ELECTROMAGNETIC CHARACTERIZATION OF BAREFACED TERRAIN FOR OIL SAND EXPLORATION

Maurice Stephen Chukwunonso Ezeoke

A thesis submitted to the

University College London

For the degree of

Doctor of Philosophy

Sensors, Systems and Circuits Group

Department of Electronic and Electrical Engineering

University College London

September 2015

Declaration

I, Maurice Stephen Chukwunonso Ezeoke confirm that the work presented in this thesis is my own. Where information has been derived from other sources, I confirm that this has been indicated in the thesis.

_____

Signature

_____

Date

Abstract

The scant difference in the electromagnetic (EM) reflectivity of barefaced terrain often imposes challenges in differentiating between such terrain types and deployment of synthetic aperture radar to oil sand exploration. Microwave remote sensing has a proven ability to provide valuable information about targets. However to derive geoscientific information, a profound understanding of the EM interaction with terrain is vital. The challenge is to identify scattering characteristics relevant to oil sand fields. While various terrain identification methods and signature databases have been developed in the optical domain, only few examples of barefaced terrain discrimination in the microwave domain have been reported. In this thesis a three step multi-sensor approach has been used to identify EM signature of barefaced terrain encompassing homogeneous and heterogeneous materials, in the optical and microwave range. The combined method also led to the development of a large database of hyperspectral reflectivity, dielectric and backscattering data relevant to geointelligence analysis.

The geochemical signature identification and prediction (GSIP) process required spectral data acquisition, chemometric model implementation and post-processing to determine the spectral fingerprints and components of two strains of Nigerian oil sands. The results were compared with available hydrocarbon databases and four new features of Nigerian oil sands were observed. The dielectric discrimination statistical model (DDSM) involved three studies of the dielectric properties of oil sands and other barefaced terrain with different weight percentage of moisture and statistical processing of data to identify the 1 – 2 GHz and 5 – 7 GHz as most suitable frequency bands for microwave imaging. The GSIP and DDSM provided new empirical data on the geochemical and electrical behaviour of oil sand particularly the contrasting effects of bitumen, sand and moisture.

Finally computer EM (CEM) models of barefaced terrain and sensors were used to identify the backscattering behaviour of the terrain for analysis in 2D/3D format. The results provided good agreement with classical surface roughness models particularly the Surface Perturbation and Kirchoffs Scattering model. They also enabled the investigation of the effect of wide variations in the sensor and terrain parameters on backscattering in order to evolve a radar signature necessary for identification of oil sand terrain for petroleum exploration. A laboratory scatterometer system (LSS) was developed and deployed in three imaging scenarios to verify aspects of the derived

microwave EM signature of the terrain. The LSS measurements and the results from the CEMs were complimentary.

Acknowledgements

First and foremost, I want to give gratitude to God for his kind mercies. I am grateful to my supervisor Dr Kenneth Kin Fai Tong for giving me the opportunity to work on such an interesting subject in order to pursue my doctoral thesis. His guidance, insight and patience throughout the past four years of my studies have been invaluable. Without his exemplary assistance, this work would have been impossible to accomplish.

I am also grateful to the members of the UCL Sensors and Circuits group particularly the members of the Radar and Terahertz teams. I want to thank Prof. Hugh Griffiths, Prof. Paul Brennan, Prof. Tony Kenyon and Prof. Karl Woodbridge for their exemplary leadership and the cooperative culture they have enshrined in to the Radar team. I want to thank Dr. Steve Hudziak and Dr. Chin-Pang Liu for their help with the geochemical signature analysis and dielectric discrimination measurements. The UCL Electronic and Electrical Engineering department was very supportive during the difficult times particularly Prof. Alwyn Seeds and Mr Paul McKenna. I extend the same gratitude to all my colleagues and co-authors who I have interacted with over these years and whose names are unfortunately too many to mention here.

I also feel privileged for meeting many great people throughout these years who have made this period an extraordinary experience: my colleagues and friends from the UCL EE Department, from London, from back home and elsewhere around the globe. In this context, I especially want to thank Dr's Matthew Ash, Raimund Mueckstein, Mathew Ritchie, Francesco Fioranelli and Allann Al-Armaghany. Also Amin Amiri, Mandan Tanha and Cristina Borda-Fortuny for being such wonderful friends but also their numerous discussions towards my research. A very special thank you goes to my partner for being such a supportive and encouraging character, especially during the last 2 years of my project.

Finally, I want to thank my family and especially my parents for their support and all the sacrifices they had to make. This project would not have been even remotely possible without the financial support of the Petroleum Technology Development Fund overseas scholarship scheme, the technical support of the National Space Research and Development Agency and the Nigerian Navy.

Abbreviations

AEM Airborne Electromagnetic Sensors/Sensing

API American Petroleum Institute

ASAR Advanced Synthetic Aperture Radar

ASTER Advanced Spaceborne Thermal Emission and Reflectance Radiometer

ATSD Agbabu Tar Sand Deposits

AVIRIS Airborne Visible/Infrared Imaging Spectrometer

Bbl Standard barrel Crude Oil (= 42 US gallons, 34.972 Imperial gallons or 158.987 litres)

BTM Barefaced Terrain Model

CASI Compact Airborne Spectrographic Imager

CDS Cubic Double Square

CEM Computer Electromagnetic Model

CHOPS Cold Heavy Oil Production

CPA Closest Point of Approach

CRIM Complex Refractive Index Method

CSS Cyclic Steam Stimulation

CST Computer Simulation Technology

dBm Decibels relative to 1mW

dBsm Decibels per square meter

DBS Doppler Beam Sharpening

DEM Digital Elevation Model

DLaTGS Deuterated, L-alanine doped Triglycine Sulfate

E&P Exploration and Production

E-field Electric Field

EM Electromagnetic

EMF Electromagnetic Force

EnviSAT Environmental Satellite

ESA European Space Agency

ETM Enhanced Thematic Mapper

FCC False Colour Composite

FEM Finite Element Method

FDTD Finite Difference Time Domain

FIT Finite Integral Techniques

FTIR Fourier Transform Infrared

FWHM Full Width at Half Maximum

GBL Geophysical Borehole Logging

GOM Geometrical Optics Model

HH Horizontal transmit, Horizontal receive

HOS Hard Oil Sand

HV Horizontal transmit, Vertical receive

HYDICE Hyperspectral Digital Imagery Collection Experiment

IF Intermediate Frequency

IR Infrared

KSM Kirchoff Scattering Model

LOS Line of sight

MSC Multiplicative Scatter Correction

MSS Multispectral Scanners

MUT Material Under Test

NASA National Aeronautics and Space Administration

NASRDA National Space and Research Development Agency

NGSA National Geological Survey Agency

NNPC Nigerian National Petroleum Corporation

NRL Naval Research Laboratory (United States)

OPEC Organisation of Petroleum Exporting Countries

OPM Open Pit Mining

PFA Polar Format Algorithm

POM Physical Optics Model

PRF Pulse Repetition Frequency

PSD Power spectral density function

PSF Point Spread Function

RADAR Radio Detection and Ranging

RadarSAT Radar Satellite

RAR Real Aperture Radar

RCS Radar Cross Section

RDA Range-Doppler Algorithm

RGB Red Green Blue

RHD Rhombohedral

SAGD Steam Assisted Gravity Drainage

SAR Synthetic Aperture Radar

SARA Saturates, Aromatics, Resins and Asphaltenes

SASI Shortwave Infrared Airborne Spectrographic Imager

SB Standard Beam

SCO Synthetic Crude Oil

SIR-C/X Spaceborne Imaging Radar C/X

SLAR Side Looking Airborne Radar

SPOT Système Pour l'Observation de la Terre series of satellites

SPM Small Perturbation Model

SWIR Short Wave Infrared

TBC Total Bitumen Content

TEM Transverse electromagnetic (Antenna)

TIR Thermal Infrared

THF Tetrahydrofuran

UK ADAS United Kingdom Agricultural Development and Advisory Service

USDA United States Department of Agriculture

UWB Ultrawideband Antenna

VH Vertical transmit, Horizontal receive

VOS Viscous Oil Sand

VV Vertical transmit, Vertical receive

WDA Wavenumber Domain Algorithm

***Wt.*%** Weight Percentage

Symbols

α	Attenuation constant in Nepers per meter (Nm^{-1})
β	Phase constant in Radians per meter ($Radm^{-1}$)
γ_g	Grazing angle
γ	Radioactivity in counts/sec
δ_p	Depth of penetration
ρ_b	Bulk density in kilograms per meter cubed (kgm^{-3})
$\varepsilon^*, \varepsilon, \varepsilon', \varepsilon''$	Complex and absolute permittivity, real and imaginary part
$\Delta\theta$	Change in aspect angle between Radar and target
ΔR_{az}	Azimuth or cross range resolution also d_{az}
ΔR_{rs}	Slant range or along-track resolution
ΔR_{rg}	Ground-Range Resolution
Δt	Sonic travel time, in μseconds per feet in (μsec/ft)
$\tan \delta$	Loss tangent
θ_B	Antenna beamwidth (3dB) of monostatic radar (= λ/d).
θ_i	Incidence angle
λ	Wavelength
λ_c	Christensen wavelength
λ_m	Material wavelength
μ	Permeability in Henrys per meter (Hm^{-1})
σ^0	Backscattering coefficient
σ_s^0	Surface scattering component
σ_v^0	Volume scattering component
σ	Standard deviation of the surface height variation in centimeters (cm)
σ	Electrical conductivity (Sm^{-1})
σ_n	n^{th} target reflectivity
τ	Pulse duration (or time resolution) or pulse width duration (PWD)
σ_{RCS}	Radar Cross Section in Decibels per square meter (dBsm or dBm^2)
ϕ	Porosity
ϱ	Resistivity in ohms meter (Ωm)
ν_c	Christensen Band
ω_c	Carrier frequency

ω_0 Bseband bandwidth

Ω_n Slow Time Doppler support band

A Absorbance

A_{cM} Size of the resolution cell

B Radar bandwidth (= $1/\tau$)

c Speed of light = $3x10^8$ meters per second (ms^{-1})

C Clay particles

C Capacitance (Farads)

C^*, C_e, C', C'' Complex conductivity, real and imaginary parts (Sm^{-1})

d Physical length of the antenna

d_a Terrain depth of pseudo-surface (derived after inversion)

dA Elemental area of terrain-target

D Electric flux density vector in Coulombs per meter squared (Cm^{-2})

D_a Terrain depth from Aircraft estimated by algorithm

dV Elemental volume

f Frequency in Hertz (H)

F Pattern propagation factor

F_f Formation factor

G_{rx}, G_{tx} Antenna gain receiver, transmitter

h Aircraft (altimeter) height

h_{rms} R.M.S height/surface roughness

I In-phase channel

I_{IR} Radiant power transmitted

$I(\mathbf{r})$ Radiant power transmitted

J Current Density Vector in Amperes per meter squared (Am^{-2})

I_0 Radiant power at source or origin

k_B Boltzmann's constant = 1.38×10^{-23} *joule/degree Kelvin*

k_p Permeability of a porous material in *milidarcy* (mD). 1 darcy $\approx 10^{-12} m^2$)

k Wavenumber

l Surface Correlation Length

ℓ Electromagnetic (EM) waves travel distances in terrain

L_{SA} Synthesized or virtual antenna array length

L_s	Radar System Losses
M	R.M.S surface slope
m	Complex index of refraction = $n - jK$ (n = real, K = imaginary part or extinction coefficient)
MPa	Mega Pascal = 10^6 Pascal or 10^6 Newton per square meter (Nm^{-2})
m_v	Volumetric soil moisture
n^*	Complex refractive index of medium
P	Power in dB
$\mathbf{psf}_t$	Point Spread Function = $\mathcal{F}^{-1}_{(\omega)}[\lvert P(\omega)\rvert^2]$
Q	Quadrature phase channel
R	Range distance between target and sensor
rx	Receiver
s	Saturation, also distance between peaks
S	Sand particles
SP	Spontaneous Potential in *millivolts* (mV)
t	Time delay of echo or fast time domain
tx	Transmitted
T_{IR}	Radiant transmittance
u	slow time or synthetic aperture domain
V	Velocity
v_m	Propagation velocity in the material in meters per second (ms^{-1})
x, y	range and cross range directions within a resolution cell
X, Y	Cartesian co-ordinates

Contents

List of Tables

List of Figures

1 Introduction

The research work is set in context and the motivation is highlighted. Remote sensing is introduced and the applications of radar remote sensing are brought to light. The chapter ends with the scientific objectives and thesis structure.

1.1. Overview

Remote sensing is the ability to detect information about an area, target-object or phenomenon by using a detecting sensor or instrument that is not in physical contact with the said area, target-object or phenomenon. Classically the human eye is a sensor that collects data in the visible electromagnetic (EM) spectrum for analysis by the brain (Lillesand *et al*., 2004). Remote sensing has varied applications to several fields including military reconnaissance, meteorology, medical imaging and mining. There are two broad methods of remote sensing; direct and indirect. Direct remote sensing involves the monitoring of specific phenomena, for instance atmospheric pressure or precipitation to forecast weather. The indirect remote sensing method is used when direct measurements are unfeasible. It therefore relies on contrasts in observable features as proxies. For example detecting polyvinyl chloride (PVC) pipes in the Amazon basin could indicate special irrigation systems necessary to cultivate illegal crops (Ezeoke & Ford, 2008). Furthermore sensors can be distinguished as passive and active types. Passive sensors like the eye, camera or a radiometer take advantage of naturally occurring radiation such as sunlight interacting with terrain or infra-red radiation from a target. Active sensors emit their own signal on to the target, detect the backscattered or returned radiation and then process it. This means they can be configured to highlight target objects in a best case manner which is useful for both direct and indirect methods of remote sensing.

The *ra*dio *d*etection *a*nd *r*anging system or radar is an active remote sensor traditionally used to detect the range of a target-object. In 1880 Heinrich Hertz demonstrated the reflection of EM waves from metal objects and using this principle, Christian Hülsmeyer patented a ship detection device, called the 'Telemobilescope' in 1904 (Lasswell, 2005). Since then research into radar systems has only increased leading to a variety of uses. In the Second World War the Chain Home radar was

successfully deployed in the battle of Britain by the Royal Air Force and present day uses include medical physics (Britannica, 2007; Swords, 1986; Neale, 1985). The typical radar first illuminates the target-object with pulse or continuous wave (CW) radiation and then receives a small portion of the signal reflected by the target back to the radar antenna before sending to a signal processor and then to the display. In this system target classification and analysis takes place on the display but regardless of where classification occurs, an in-depth understanding of the EM wave interaction with the target is necessary for analysis of the radar echo returns.

*S*ynthetic *a*perture *r*adar (SAR) was conceived by Carl Wiley in the 1950's as an expert form of radar on the premise that high resolution two-dimensional imagery can be created by coherently processing the return pulses from a target (Lasswell, 2005). SAR uses the change in Doppler as a result of motion between an antenna and target region to synthesize a large antenna from a series of spatial samples in the signal processor (Stimson, 1998). In essence a radar measures the Fourier transform of echoes observed from a given viewing angle while SAR combines viewing angles along a synthetic aperture to improve the azimuthal angular extent. Combining this powerful set of techniques with microwave imaging means that high resolution imagery is possible from air and space-borne platforms by day and night and also through cloud or inclement weather (Stimson, 1998; Skolnik, 1990). In addition to range, R and direction, it is possible to determine backscatter coefficient, σ^0 from received radiation power and surface roughness, h_{rms} from the shape of the return pulse. Such abilities are vital to derive geoscientific information from terrain.

Petroleum or crude oil is a flammable, non-renewable, fossil fuel consisting of a complex naturally occurring mixture of hydrocarbon and other compounds. Searching for petroleum is an inter-disciplinary effort. The petroleum industry requires several tools to identify the possibility of a resource, assess the quantity of crude oil and gas available for production and determine the value of the proven reserve. The first conventional oil well was discovered in 1859 at Titusville, Pennsylvania by 'Colonel' Edwin Drake who used borehole drilling to search for salt rock (Medicus, 1859; Owen, 1975). Since then significant efforts have been made in the improvement of tools for use by commercial oil companies in land and marine exploration. They include surface geology by 1900, refraction seismic from 1925, geophysical borehole logging (GBL) with electric well logs starting 1930 and analogue reflection seismic by 1935. Other

improvements include mud logging in 1940, pioneering digital reflection seismic by 1965 and 3-D reflection seismic from 1978 (Ivanhoe, 1995). Due to the location and depth of conventional oil wells the geophysical sensors must be physically placed on the terrain or marine surface to detect the acoustic vibrations from compressional (*P*) waves and shear (*S*) waves.

Sustained global demand for oil, relatively high oil prices and terminal decline in production from conventional oil fields has led to greater commercial and scientific interest in *synthetic fuels* obtained by the pyrolysis decomposition of unconventional petroleum sources such as shale rock and oil sand (Hascakir *et al*., 2008; Walsh, 2012). Unlike conventional sources which may exist on land or marine locations, oil sand and shale rock exist solely on land at comparatively shallow depths. It is estimated that over 169 billion recoverable barrels of synthetic fuel from oil sand exist globally, but only Canada and Venezuela have established exploration and production (E&P) industries. Also 22 other countries including Kazakhstan, Nigeria and Russia have an estimated 817 billion barrels that are yet to be discovered from prospective oil sand resources (Walsh, 2012; Attanasi & Meyer, 2010). This has led to greater interest to identify, explore and monitor unconventional petroleum resources such as oil sand deposits in order to produce synthetic crude oil (SCO).

EM characterization of bare face terrain for unconventional petroleum exploration of oil sand involved the use of different parts of the EM spectrum to study terrain (Ezeoke *et al*., 2014a). Across the EM spectrum modern radar operates over a wide variety of frequencies ranging from a few megahertz (MHz) to as high as 300 terahertz (THz) (Stimson *et al*., 2014). Radar spectrometers over the 1 - 18 GHz frequency range have been used to investigate the response of radar to soil moisture and surface roughness for bare soils with various degrees of success (Dobson *et al*., 1981). One study resulted in the recommendation for a 5 GHz radar operating at incident angles between 10° - 20° due to greater sensitivity to soil moisture and least sensitivity to surface roughness (Dobson & Ulaby, 1998). Rather than a radar spectrometer we first use a reflectance spectrophotometer operating in the mid (MIR) to near-infrared (NIR) region to identify the geochemical signature of the terrain classes. Thereafter we determined the intrinsic properties relevant to radar particularly the surface roughness and dielectric properties for input in to terrain models. The intrinsic properties of the barefaced terrain were measured, classified then input into 3D computer EM models

developed to distinguish oil sand from other terrain types. Finally the modelling results were post processed to indicate the EM signature of terrain and validated by empirical scattering measurements.

Reflectance spectroscopy was used to generate hyperspectral images which provided ultra-high resolution spectrograms in the frequency f varying from 12 THz to 120 THz. In wavelength this corresponds to 2.5 – 25 micrometers (μm). Previously this method has been used to study the energy reflected from a solid, liquid or gas at wavelengths that are small enough to recognize subtle changes in the underlying crystal structure of the material under test (Ezeoke *et al*., 2014b). We extend the method to characterize the different terrain types. Combinations and overtones of the different absorption (or transmission) bands that occur in the MIR and far IR regions or even crystal field transitions can be detected using spectroscopic sensors in the ultraviolet, visible and NIR spectral regions. Besides helping to distinguish between the chemical properties of terrain this process gives a brief snapshot for terrain behaviour in other EM frequencies.

Geoscientific information extraction from SAR imagery depends on two characteristics of the image. The most important is where intrinsic terrain properties such as the dielectric constant and geometry influence scene reflectivity while the second depends on the signal processing within the radar system. The dielectric properties are notoriously difficult to measure and quantify (Oliver & Quegan 2004). This PhD work focusses on modelling the effect of the material properties on barefaced terrain scattering rather than on the internal signal processing of the radar system. The performance of air and satellite borne radar for oil exploration depends on understanding the EM signature of oil sand amidst other barefaced terrain and secondly developing effective EM terrain models with SAR system configuration to enhance detection. Radar remote sensing is relevant to the investigation and monitoring of terrain due to the possibilities presented by technological advances such as SAR, multipolarization, multifrequency and interferometry (Plaut *et al*., 1999). In the past three decades beginning with the 1978 launch of the SEASAT satellite, various space and airborne SAR sensors such as Shuttle Imaging Radar series, A, B, C (SIR-A, SIR-B, SIR-C/X), Airborne Imaging Radar (AIRSAR), RADARSAT series and ENVISAT have demonstrated the sensitivity of SAR to surface roughness, backscatter and topography (Elachi *et al*., 1986; Ulabi, 1982; Evans, 2006; Lou *et al*., 1996). This raises

the possibility of using SAR for petroleum exploration and to discover oil sand resources (Ezeoke & Tong, 2012).

SAR missions are typically unique in their choice of frequency, polarization, resolution and swath width but four different bands are commonly used in radar remote sensing: P-band with wavelength, λ = 68 cm, L-band with λ = 23.5 cm, C-band with λ = 5.8 cm, and X-band with λ = 3.1 cm. To date, data gathered by SAR sensors has contributed to understanding the relationship between backscatter and surface roughness. However the ability to predict petroleum occurrence is limited. This is mostly due to a lack of oil sand terrain models accurate or otherwise. Terrain models were developed in software using the finite integration technique (FIT) in order to represent the details of an imagine scene. Computer electromagnetic models (CEM) were used to simulate the key components of the scattering process interaction between terrain and EM waves. Empirical scattering measurements were performed using a laboratory scatterometer system (LSS) configured at the University College London (UCL) for validation of the developed models and observation of EM signature (Ezeoke & Tong, 2013a). The indoor experiments with LSS were also used to calibrate the developed computational models for oil sand reservoir prediction and post-processed to determining the average reflectivity of oil sand compared to other terrain (Ezeoke *et al*., 2012; Ezeoke *et al*., 2014c). This thesis will identify suitable parameters to distinguish bare-terrain surfaces, investigate the EM signature of oil sand terrain and generate modelling and measurement data for a possible database useful for distinguishing oil sand from other terrain types. It is hoped that the developed method, models and measurement results will help advance the performance of SAR for petroleum exploration and provide a practical approach for modeling the EM radar signature of barefaced terrain for remote sensing in general.

1.2. Motivation

Fossil fuels account for 86% of global energy consumption and 80-85% of Nigeria's export revenue, however conventional (lighter oils) are increasingly difficult to find (G.O.E, 2008; Arhore, 2006). To guarantee current global energy needs and meet future expectations there is a need to rapidly identify new unconventional resources. A large potential of virtually untapped unconventional fuel resource remains hidden in oil sands located in the Dahomey Benin Basin in south Nigeria. This region

experiences heavy cloud cover and the National Space Research and Development Agency (NASRDA) is developing a Nigerian RADAR satellite to aid in oil exploration and environmental monitoring (Attanasi & Meyer, 2010; Shabba, 2010; NGSA, 2010). Potential oil sand reservoirs are located in difficult to reach environments with harsh geological settings and Nigeria has seven widely dispersed sedimentary basins with proven and unproven reserves. They include the Anambra, Benin, Benue, Bida, Bornu, Niger-Delta and Sokoto basins. Such exploration challenges require both timely large scale mapping and high resolution imagery which are conceivable with air or satellite radar sensors but unmanageable with conventional petroleum exploration methods such as GBL or seismology. Also the NASRDA radar satellite will seek to help combat growing terrorism in Nigeria's north east characterized by heavy forest, mountains and semi-arid desert terrain. As part of this research a barefaced terrain model (BTM) for land degradation was created and designed to be responsive to variation in moisture as a precursor to temporal terrain classification (Ezeoke & Tong, 2013b; Ezeoke & Tong, 2014).

It is evident that remote sensing can contribute to the detection and analysis of different environments at the local, regional and global scales however the use of spectral and microwave wavelengths for oil sand detection is not fully investigated. The purpose of this PhD research work was the EM characterization of terrain using both optical and microwave methods, development of the BTM and SAR processing models to better identify oil sand terrain. It is hoped that when the Nigerian radar satellite is built the developed models and corresponding database will help identify oil sand terrain. This will require effective characterisation of terrain backscatter which can be related to field measurements. The linking of oil sand spectral response to dielectric permittivity and empirical scattering measurements enhances the ability of radar to predict the oil sand terrain based on field samples in a manner previously undone. To the radar community this work furthers the performance of SAR radar to target measurement and produces the requirements for successful application of the modelling and measurement technique to distributed terrain. In the absence of EM scattering data from oil sands, this work has provided valid measurement data and also extracted hydrocarbon, moisture and backscatter information from processing the obtained field data.

1.3. Scientific Objectives

The stated objective of this research is to investigate the EM characterization of terrain to aid unconventional petroleum resources identification and to develop methods and strategies to understand, classify and use microwave remote sensing data for petroleum exploration. This work forms part of the effort to study the EM backscattering behaviour of various terrain classes particularly oil sand. EM scattering from distributed targets like barefaced terrain is difficult to classify due to the complexity of interaction between diverse aspects of terrain with the EM wave (Fig. 1.1). The resulting EM scattering response ranges from specular to diffuse Lambertian reflection meaning that EM signature typically overlaps.

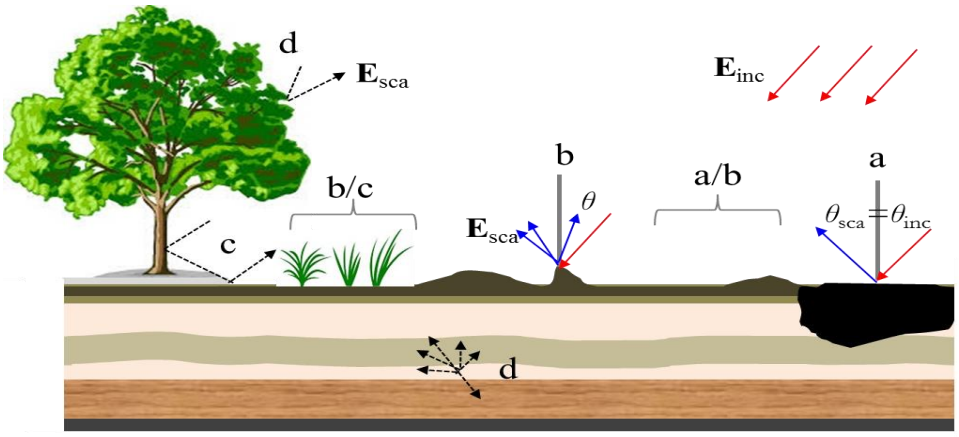

Figure 1.1: Sketch showing complex interaction between incident and scattered EM waves with land surface. Response from Barefaced terrain overlaps from specular through diffuse. Here: (a) specular (b) diffuse (c) corner reflection (d) volume scattering.

Therefore the primary objective of this research is to design and develop an effective high resolution terrain, processing and computer EM characterization models to distinguish oil sand from other barefaced terrain in order to enhance petroleum exploration of oil sand. Six barefaced terrain classes are investigated covering homogeneous terrain like beach sand, gravel and pebbles but also heterogeneous terrain such as loamy farm soil, hard oil sand and viscous oil sand. The PhD thesis demonstrated the following:

1. Identification of parameters that can aid in the detection of oil sand reservoirs and development of an earth model database. Backscattering database is included with deliverables accompanying thesis.

2. Characterization of the spectral and microwave properties of oil sand reservoir and barefaced terrain through modeling, simulation and measurement.

3. Empirical study of EM wave interaction with various barefaced terrain for description of land surface processes.

4. Demonstration and classification of the backscattering behaviour within and on the surface of terrain.

An advanced EM characterization procedure using geochemical signature prediction, dielectric discrimination statistical models, computer electromagnetic models and empirical measurements was developed to achieve this. The high quality 2D/3D models carry information on the barefaced terrain characterization that has not been seen before.

1.4. Thesis Outline

This thesis attempts to highlight the work done so far but is not an exhaustive account of all the efforts made. The work presented here concentrates on the understanding, differentiation and description of the intrinsic properties that cause backscattering from terrain but also models the scattering effect from different terrain. A BTM is suggested for barefaced terrain and validated by empirical measurements. The strategy to develop a reliable BTM, classification algorithm and empirical scattering measurements for unconventional petroleum exploration entailed several distinct stages. Consequently the thesis is split into eight chapters.

The next chapter gives a general overview of the geotechnical theory involved in oil formation and sensors used in exploration engineering. It also covers basic principles of spectroscopy and microwave remote sensing particularly focusing on SAR radar.

Chapter 3 provides a critical review of literature relevant to this work. The characteristics of known oil sand reservoirs are looked at in detail and the similarities with Nigerian locations identified. Thereafter the current performance of microwave

systems to resource monitoring is investigated. Finally backscattering phenomena that could distinguish terrain types are identified and evaluated in the context of chemical and geo-physical terrain properties.

Oil sand samples were acquired from Nigeria but other barefaced terrain were obtained locally in UK. Consequently chapter 4 and 5 both discuss the intrinsic terrain properties relevant to oil sand identification. Chapter 4 discussed the developed statistical method to obtain the geochemical signature for terrain particularly our geochemical signature identification and prediction process for Bitumen and moisture presence. The geochemical signature was used to identify bitumen and other hydrocarbons present in the oil sand using hyperspectral spectroscopy.

Chapter 5 linked the geochemical signature to the dielectric properties of terrain. The procedure and method for dielectric measurements of the terrain types was presented. Also using the measurement data, a model for the prediction of the dielectric properties of oil sand was also derived and presented.

Chapter 6 presents the modelling technique using finite integration technique (FIT) discretization for development of the computer electromagnetic models. Both a general and situation specific EM simulation technique is presented along with an analysis of the results. A large amount of scattering data was generated therefore the radar signature of oil sand results are discussed according to the effects on radar signature caused by secondary reservoir properties, water content, penetration depth, angular geometry and frequency within two broad trends.

Field measurements are necessary to further validate the BTMs. Chapter 7 discusses the measurement technique, LSS configuration and signature classification approach. The CEM backscattering results are further processed, analysed and applied to the petroleum exploration of oil sands. A discussion of the three-step electromagnetic characterization process in light of the project aim is also presented.

The thesis concludes in Chapter 8 by highlighting some achievements and considering how the models can be applied to real SAR images.

1.5. Research Contributions and Deliverables

For the advancement of research a few deliverables were provided in a 1 Terabyte portable hard drive at the completion of this work. Furthermore, the novel

contributions of this research have led to 13 conference and 2 journal papers. The deliverables and research contributions are listed below:

1.5.1. Deliverables

- PhD Thesis explaining work carried out along with relevant results.
- Hyperspectral measurement data (raw results) and Geochemical Signature Prediction Model software codes.
- Dielectric measurement data (raw results) and Dielectric Discrimination Statistical Model software codes.
- Backscattering database containing results from Computer Electromagnetic Models, Laboratory Scatterometer System and software codes.

1.5.2. Journal Papers

- Ezeoke, M., and Tong, K., (2015) "Electromagnetic characterization of oil sands for petroleum exploration ", *Journal of Petroleum Engineering*, 16 pages, [In Press].
- Ezeoke, M., Tong, K., and Shi, S. (2014), "A practical approach for modeling the electromagnetic radar signature of barefaced terrain for remote sensing ", *International Journal of Computational Methods and Experimental Measurements*, Vol. 2, No. 4, G. Carlomagno, C.A. Brebbia, W. Patrick De Wilde (Eds.), WIT Press: Southampton, UK, pp. 403 – 419.

1.5.3. Conference Papers

- Ezeoke, M., Tong, K., and C.B.Fortuny (2014), "Terrain backscatter and oil sand exploration: Average Reflectivity Analysis", *Proceedings of the 2014 IEEE Radar Conference* (Radar2014), 13-17 October, Lille, France, pp. 1-6.
- Ezeoke, M., Tong, K. and S. Shi. (2014), "Modeling Synthetic Aperture Radar Signature of Agbabu Oil Sand for Petroleum Exploration", *Energy Production and Management in the 21st Century the Quest for Sustainable Energy*, Vol.2, Eds C.A. Brebbia, E.R. Magaril and M.Y. Khodorovsky, *WIT Transactions on Ecology and the Environment*, Vol. 190, pp. 1284 – 1295.
- Lawal, A., Radice, G.M., and Ezeoke, M. (2014), "Evaluating the Potentials of an International Collaboration between Equatorial Nations by Implementing a constellation of Interferometric small SAR Satellite Network", *Proceedings of the 65th International Astronautical Congress* (2014 IAC), 29 Sep – 4 October, Toronto, Canada, IAC-2014,

IAC-14, B4, 1, 13, x27229, 2014.

- Ezeoke, M., and Tong, K. (2014), "Polarimetric SAR Classification of Terrain for Land Degradation Monitoring", *Proceedings of the 2014 IAF Global Space Applications Conference* (2014 GLAC), 2 – 4 June, Paris, France, GLAC-2014,S,6B,4,x20699.
- Ezeoke, M., Tong, K and Mubea. K.,(2014), "Electromagnetic Characterisation of Terrain for Unconventional Petroleum Exploration", *Proceedings of the 2014 IEEE Radar Conference* (RadarCon2014), 19-23 May, Cincinnati, Ohio, USA, pp.0990-0995.
- Ezeoke, M., and Tong, K. (2013), "Terrain Backscatter and Oil Sand Exploration: Initial Measurement Results", *Proceedings of the IEEE UK SIM AMSS 7th European Modeling Symposium* (EMS 2013), 20 – 22 November, Manchester, UK, pp.91-96.
- Ezeoke, M., Tong, K., Amiri, A. and Al-Armaghany, A. (2013), "Effects of Electrical and Physical Properties of Barefaced Terrain on Backscatter Response", *Proceedings of the international conference on Advances in Computing Electronics and Communication*-ACEC2013, 12-13 October, Zurich, Switzerland, pp.89-93, 2013.
- Ezeoke, M., and Tong, K. (2013), "Determining the Synthetic Aperture Radar Signature of Terrain for Earth Observation Using Computer Electromagnetic Models", *Proceedings 64th International Astronautical Congress*, IAC 2013, 23-27 September, V, 2-B3.9,x20328, Session 2-B3.9, Human Space Endeavours Young Professionals Virtual Forum. http://www.iafastro.net/iac/paper/id/20328/summary.lite/
- Ezeoke, M, Tong, K, and Shi, S. (2013), "Modeling Synthetic Aperture Radar Signature of Agbabu Oil Sands for Petroleum Exploration", *Presentation to 16th Computational Methods Experimental Measurements* (CMEM2013), A Coruna, Spain, 2-4 July, 2013.
- Ezeoke, M. and Tong, K. (2013), "Modeling Electromagnetic Reflectivity of Agbabu Oil Sands from Hyperspectral Infrared Reflectance Spectra and Dielectric Properties at L-, C- and X-band Frequencies", *5th Computational Intelligence, Communication Systems and Networks* (CICSyN2013), 5-8 June, Madrid, Spain, pp.125-130.
- Ezeoke, M. and Tong, K. (2012), "Synthetic Aperture Radar Signature of Oil Sands for Petroleum Exploration", *Proceedings of the IEEE UK SIM AMSS 6th European Modeling Symposium* (EMS 2012), 14 – 16 November, Valetta, Malta, pp.455-460, 2012.
- Ezeoke, M, Tong, K, Adole, T and Lovett, A (2012), "Determining the Geographic Effect of Gas flaring using multi-SAR Azimuth Processing", *Proceedings of IEEE 2nd International Conference on Advances in Computational Tools for Engineering Applications* (ACTEA 12), 12-15 December, Louaize, Lebanon, pp.209-213, 2012.

2 Oil Exploration and Radar Basics

We first consider the geotechnical theory involved in oil reservoir formation, the sensors used in exploration engineering prior to developing a basic understanding of spectroscopy and microwave imaging then focus on synthetic aperture radar development.

The first part of this chapter explores the details of oil sand formation and hydrocarbon exploration. They are both covered separately in literature by several texts including *Petroleum Formation and Occurrence* by B.P Tissot & D.H Welte (1984). While J.L Berry and G.L Prost provide a remote sensing perspective to finding crude oil in *Hydrocarbon Exploration* (Rencz, 1999), C. Oliver and S. Quegan give important insight to microwave imaging in *Understanding Synthetic Aperture Radar Images* (2004). The second part introduces basic concepts in spectral identification and radar engineering including synthetic aperture radar (SAR) using *The Radar Handbook* edited by M.I Skolnik (Skolnik, 1990) and *MATLAB Simulations for Radar Systems Design* by B.R Mahafza & A.Z Elsherbeni (2004).

2.1. Petroleum Formation

Petroleum means *rock oil*. It is also known as crude oil and refers to naturally occurring mixture of hydrocarbons specifically saturates, aromatics, resins and asphaltenes (SARA) with traces of nitrogenous and sulphurous compounds. It often exists in liquid form in underground reservoirs but is recoverable at typical atmospheric conditions. Analysis of elementary crude oil in weight percent (*wt*.%) includes: hydrogen (11-14 *wt*.%), carbon (83-87 *wt*.%), sulphur (0.06-8 *wt*.%), nitrogen (0.11-1.7 *wt*.%), oxygen (0.1-2 *wt*.%) and metals (up to 0.3 *wt*.%) (Hunt, 1979; Tissot & Welte, 1984). The physical properties and chemical composition vary with location but the density and constituent properties determine classification as light crude oil (LCO), heavy crude oil (HCO) or extra-heavy crude oil (EHCO) amongst others.

Petroleum is formed from the organic remains of decayed plants and animals in an ancient 3-stage process of *diagenesis*, *catagenesis* and *metagenesis*. The organic matter accumulates through geological history in a mixture of sediments to form fine-grained shale or source rock. Marine burial starts with phytoplankton entering the food

chain and causing sedimentation of zooplankton rich in proteins, carbohydrates and lipids. Terrestrial interment involves trees and shrubs which mainly deposit carbohydrates and lignin. The difference in burial process results in different mineral to organic matter fractions between land and sea reservoirs. It also results in different organic-rich sedimentary formation. Hutton (1987) classified these into oil shale, bitumen-impregnated rock such as oil sands and humic coals.

2.1.1. Oil Sand Formation

The buried organic remains settle to a sea or lake bottom and newer organic sedimentary layers are deposited in the initial process of diagenesis. Diagenesis also causes the conversion of organic matter from biopolymers to kerogen or directly to bitumen as shown in Fig. 2.1. This is done at depths ranging from surface to less than 100 meters. The bitumen eventually becomes unconventional petroleum or oil sands when Catagenesis does not fully occur and the source rock is immature.

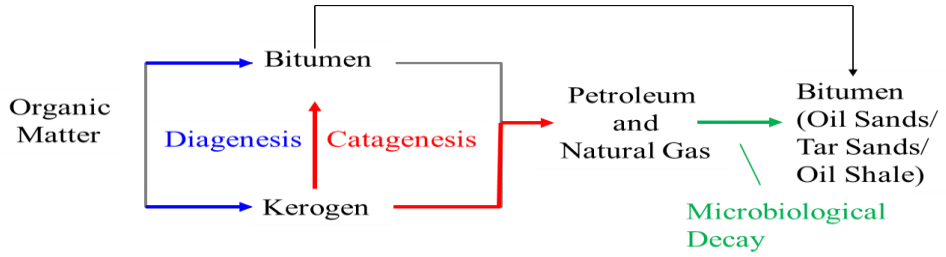

Figure 2.1: Roles of Diagenesis and Catagenesis in formation of Oil Sands.

In essence the incomplete heating of prehistoric organic materials over geological time causes the formation of unconventional petroleum such as oil sands. Where complete pyrolysis decomposition occurred, conventional crude oil and gas were formed. Oil sands are referred to as *bitumen sands* in America and *tar sands* in Nigeria. They are also called EHCO in Venezuela. They consist of an aggregate matrix of sand and clay which is saturated with water and a viscous form of petroleum called bitumen (Fig. 2.2) (CCEI, 2012). Due to the physical properties and composition, oil sands unlike crude oil cannot be pumped from the ground in natural state but are mined using open pit mining (OPM) techniques or in-situ production (ASUF, 2007). After mining, the bitumen is separated by pyrolysis decomposition and processed to produce *synthetic crude oil* (SCO). Typical oil sand reservoirs occur from surface down to depths of 300 m from surface.

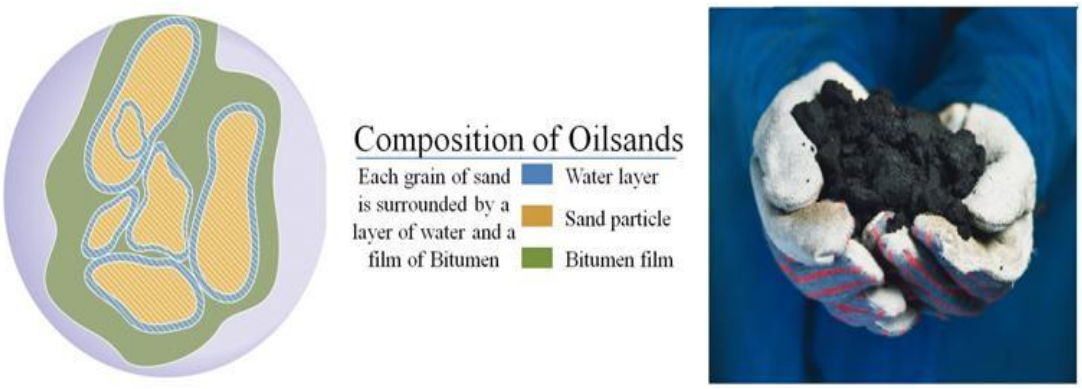

Figure 2.2: Oil sand composition. Schematic on the left shows composition of oil sands while photo on the right shows a handful of oil sand from Alberta, Canada (CCEI, 2012)

2.1.2. Crude Oil Formation

For formation of conventional petroleum resources both c*atagenesis* and *metagenesis* take place. Catagenesis occurs for organic matter further down the surface. The resulting weight forces intense geostatic pressure, about 300 to 1500 bars (30 – 150 MNm^{-2}) and heat ranging from 50˚C to 150˚C on the source rock to form liquid and gaseous hydrocarbons. The final stage of metagenesis and metamorphism results in further distillation of the organic material into crude oil and natural gas (Strakhov, 1962; Tissot & Welte, 1984). The summary of this process leading to the formation of crude oil and natural gas is shown in Fig. 2.3.

The oil eventually flows from the source rock to accumulate in thick but porous limestone or sandstone reservoirs. Movements of the earth such as folding, faulting and pinching out cause the natural gas and oil to be trapped in the reservoir rocks between layers of impermeable rock such as granite. An opposition to the assessment that oil sands were formed due to incomplete pyrolysis (section 2.1.1) is the view that oil sands are the remnants of conventional oils that have been generated then degraded by bacterial action (Attanasi & Meyer, 2010). This is due to the chemical and textural similarity with the residuum from distillation of LCO. Other discussions on the origin and formation of oil sands can be found in Stewart and MacCallum (1978) and Kendall (1976) amongst others. For this thesis we are interested in the intrinsic material properties of oil sand that could enable them to be remotely detected by electromagnetic (EM) sensors.

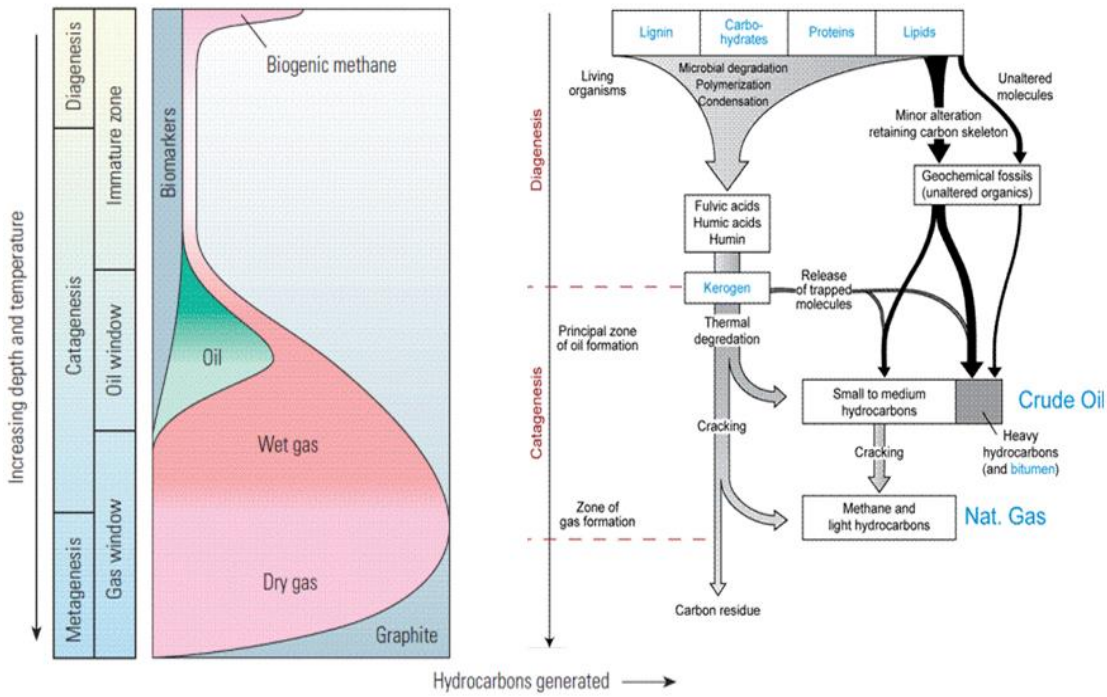

Figure 2.3: Oil Formation. Summary of the formation process is on the left and a detailed overview of the processes is on the right (Modified from Tissot & Welte, 1984).

2.1.3. Classification of Petroleum

There are many different varieties and grades of petroleum with different characteristics such as density, colour, viscosity, gas content and oxidation resistance. Consequently classification mechanism depends on the geographic area in which it is produced, sulphur content or American Petroleum Institute (˚API) gravity. Geographically, there is the West Texas Intermediate (WTI) from Texas, Brent Crude from the North Sea or Bonny Light from Nigeria amongst others. Sweet petroleum contains relatively little sulphur while sour petroleum contains substantial amounts. The ˚API gravity is a measure of the density compared to water. Mathematically,

$$\boldsymbol{API\ gravity} = \frac{\mathbf{141.5}}{\boldsymbol{SG}} - \mathbf{131.5}\,. \tag{2.1}$$

Where SG represents the specific gravity of the substance compared to water. From (2.1) API gravity for HCO with SG of 1.0 is 10.0° API, this is the same density of pure water at 60°F. If the density is greater than 10° API then it is LCO and floats on water but if it is less than 10° it is considered HCO and sinks. LCO such as the WTI with 39.6° API, is more desirable than heavy oil because it produces more gasoline

while sweet oil such as Bonny Light from Nigeria with 0.15 *wt*.% of sulphur commands a higher price than sour oil due to the lower sulphur content. The classification of conventional and unconventional crude oil with oil sand is presented in Table 2.1.

Table 2.1: Classification of Crude oil

	Conventional Oil	**Heavy Oil**	**Extra-heavy Oil**	**Oil Sand**
API Gravity (°API)	More than 20	10 − 20	Less than 10	Less than 6
Density, ρ (gcm^{-3})	Below 0.934	0.934 − 1.0	Above 1.0	Above 2.1
Viscosity, mPa.s (centipoises)	Not greater than 10000.0		Less than 10000.0	Greater than 10000.0

The presence of bitumen and sand content in oil sand reservoirs makes oil sand extremely heavy, resulting in density higher than 2.1 and less than 10.0° API. The detailed characterization of an oil sand deposit starts with the examination of a single sample and becomes more complete with subsequent field analysis. This is the approach that will be followed using EM wave models prior to empirical measurements. Having noted the method of formation and classification properties, an evaluation of exploration sensors is discussed.

2.2. Oil Exploration and Monitoring

The search for oil is an interdisciplinary undertaking but traditionally led by geologists. They focus on the identification of direct or indirect hydrocarbon evidence and the resulting data obtained, represents information about specific locations in a single point in time (Heming, 1996). In the past the typical method was to interpret surface features, surface rock, soil types and terrain to discover the right conditions for an oil trap onshore. Offshore prospecting required analysis of near-bottom waters and sediments. In modern day exploration, geologists still examine surface rocks and terrain but they also consider spectra of stressed vegetation and alteration of minerals due to onshore oil seepage (Yang *et al*., 1998; Everett *et al*., 2002). The decision to explore for petroleum and the method used depends a lot on the petroleum economy and reservoir geography.

2.2.1 Petroleum Supply and Demand

The global demand for petroleum will continue to rise for several reasons including economic expansion in emerging market economies and total population

growth. According to (IEA, 2012) the world oil consumption has increased from less than 70 million barrels of oil per day (mbpd) in 1995 to over 89 mbpd in 2011 as shown in Fig. 2.4.

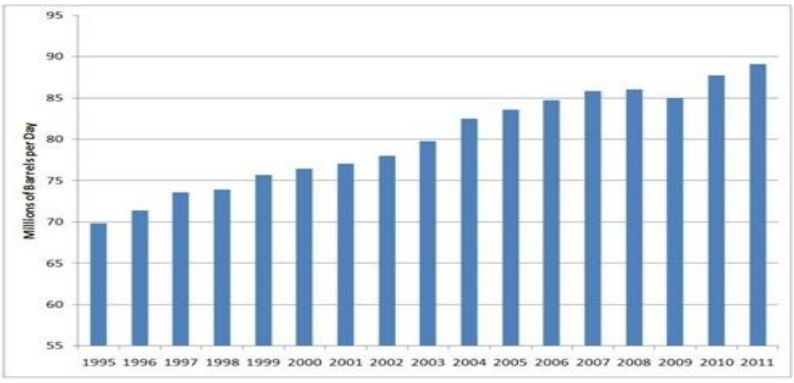

Figure 2.4: Global Oil Demand 1995 – 2011 (IEA, 2011).

Petroleum supply is more complex. It is dominated by the organization of the petroleum exporting countries (OPEC), which is an umbrella body of twelve oil-producing countries. Some countries such as America, China and Indonesia produce petroleum but are still net-importers. Other non-OPEC countries like Russia, Canada and Norway significantly affect global supply. More importantly global oil discoveries have declined each decade since 1964 as shown in Fig. 2.5. Although production from major conventional oil fields is in persistent decline it is believed that exploration and production (E&P) of unconventional petroleum resources such as oil shale and oil sands will help offset the drop (Walsh, 2012). Therefore unconventional petroleum resources such as oil shale and oil sand are set to dominate the focus of onshore E&P for fossil fuel.

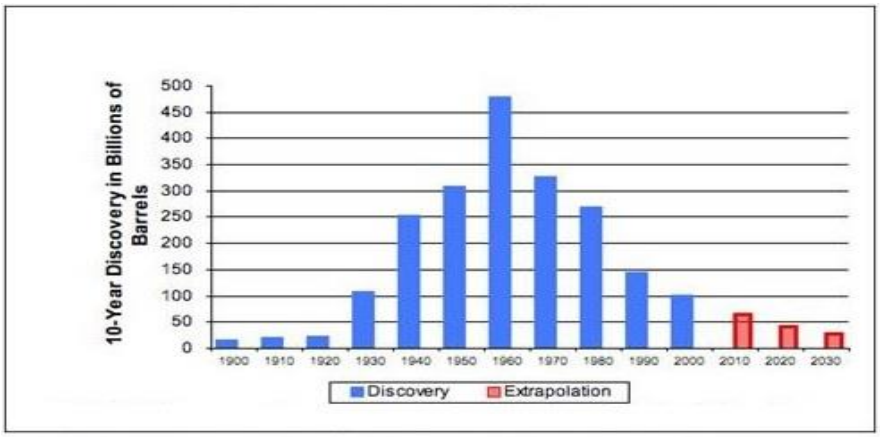

Figure 2.5: World Oil Discovery over 10 year periods (Laherre, 2002).

Estimates of possible and proven hydrocarbon reserves are prone to change in the life time of a project from initial identification, through exploration and eventual maturity (WPC, 2010). Due to the vast extent of terrain covered by oil sand reservoirs and the subtle difference between common soil and oil sand being the presence of bitumen, petroleum exploration and monitoring requires efficient technology that can be rapidly updated. However the current geophysical exploration sensors in use include gravity meters, sensitive magnetometers, electronic sniffers and most commonly seismology.

2.2.2 Geophysical Exploration Sensors

Geophysical Borehole Logging (GBL) involves drilling a borehole about 18 to 25 cm diameter or an exploration well of an area 245 cm^2 to 491 cm^2 and taking various sub-surface measurements using probes (Heming, 1996). A GBL resistivity tool is shown in Fig. 2.6(a). The principle of operation depends on the precise physical feature to be observed as shown in Fig. 2.6(b). Probe data is generated on *logs* which are classified according to type of probe, property measured and interpretation derived from measurement. Electric logs measure electric property such as spontaneous potential, resistivity, porosity and conductivity. A sample borehole induction electrical conductivity log showing both shallow and deep regions of high conductivity for a surface well is shown in Fig. 2.6(c).

Other logs measure radioactivity, velocity and mechanical strength. Gravity meters and magnetometers are sensors used with GBL**.** They both measure small changes in gravitational and magnetic fields of the earth respectively due to flowing oil. Along with electrical well logging they help in characterizing already discovered reservoirs (Bahar *et al*., 2005; Sibley *et al*., 1997; Sullivan *et al*., 2006). Granting inherent precision, the GBL method disturbs the reservoir equilibrium such as temperature or flow, represents only a small fraction of the oil field and contains limited dynamic information. Measurements are taken at depth and provide high resolution vertical data which is a good source of ground truth for reservoir characterisation. However they do not provide information on inter-well positions and therefore are best used when combined with dynamic data from gravity meters, seismology and magnetometers (Mezghani *et al*., 2000).

(a)

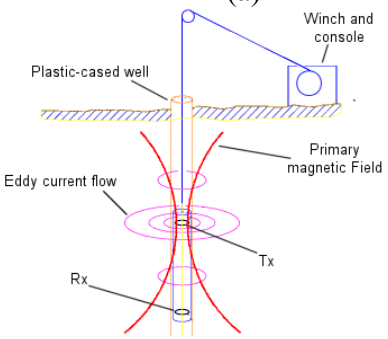

(b)

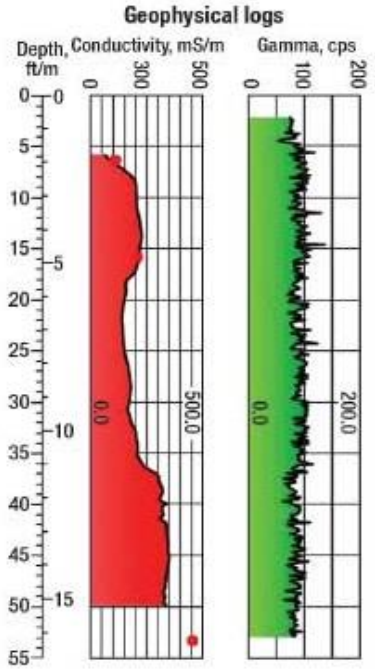

(c)

Figure 2.6: Geophysical Borehole Logging. (a) Resistivity probe with logging unit (b) Principle of operation of an electrical conductivity probe (c) Electrical conductivity log.

Other sensors detect the quality of mined oil fields such as the K40 Potassium Isotope Analyzer (PIA) and Near Infrared (NIR) Analyzer (NIA) for measuring bitumen and clay content respectively in mined oil sands (Shaw & Kratochvil, 1990; Beers, 1945). Reflectance spectroscopy exemplified by the NIA and PIA is a possible remote sensing method for measuring the components present in mined oil sands although current applications require laboratory analysis (Cloutis, 1989).

Electronic Sniffers are sensitive electronic noses that can detect the presence of hydrocarbon anomalies mostly in or near bottom waters (Phillip & Crisp, 1982). They use a *geochemical* prospecting technique such that water passing through the nose is analyzed for C1 to C4 hydrocarbon. It is used on a limited scale to search for surface chemical phenomena onshore and offshore. This is possible because oil and gas reservoir cap rocks are not completely impermeable and hydrocarbons migrate by either diffusion which is due to differences in concentration or effusion, due to differences in pressure. They can also transfer through a combination of both diffusion and effusion (Petukhov, 1977). The hydrocarbon escape causes changes in the surface soil, water and ocean sediment.

For onshore prospecting liquid hydrocarbons are less volatile and unable to reach the surface compared with gases (Sokolov, 1970). The majority of onshore sniffers try to detect ethane, propane and iso-butane because they are not produced in significant biological amounts unlike methane which is (Stahl *et al*., 1981; Davis & Squires, 1954). Due to the usually trace amounts detected, the interpretation of the results for onshore prospecting is often controversial and debated (Horvitz, 1972; Phillip & Crisp, 1982). Offshore sniffers are better preferred by petroleum explorers in a two-step process. First water sampling is used to identify the area of interest then sediment sampling helps to isolate seep location. However they are restricted to maximum depths of 300 m.

Seismology is the process through which seismic images recorded on the earth's surface are mapped to represent sub-surface properties (Scales, 1997). It involves creating a shock wave to pass through hidden rock layers then solving the inverse scattering problem as waves reflect back to the surface. The seismic technique is a geophysical method of exploration specific for sub-surface imaging. Seismic signal travel time or impedance in the earth is converted to depth (Breton *et al*., 2002). Data from shockwaves reflected back at different speeds are compared with known velocity models indicative of type and density of rock layers (Rawlinson *et al*., 2010). The velocity models aid analysis and classification.

Emergent 3D and 4D seismic reflection technology techniques allow repeated imaging of reservoirs and fluid fronts by detecting several components of *P* and *S* waves along with the direction of propagation (Heming, 1996; Bois *et al*., 1972). It is also possible for seismic data to be combined with well logs, pressure tests and other information to increase the accuracy of prediction models. Although seismology is germane to subsurface imaging there is a long interval between surveys and similar to GBL, it only applies to a very limited geographical region. The interpretations available from seismic imaging data can be grouped into three. Namely those that (a) Map the geometry of the hydrocarbon trap (b) Characterize rock and fluid properties and with 4D or time-lapse seismic it is possible to (c) Monitor fluid flow and/or pressure variation during crude oil production.

2.2.3 Remote Sensors

Effective exploration and management of petroleum resources requires knowledge of both surface and subsurface features. Airborne or satellite based remote sensors have applications in hydrocarbon exploration due to the ability to access difficult to reach regions. It is particularly useful to those reservoir basin structures that have low relief or subtle expression at the surface such as macro or micro-seepage. All remote sensing measurement occurs at some frequency *f* of the EM spectrum. Common remote sensing systems are shown in Fig. 2.7.

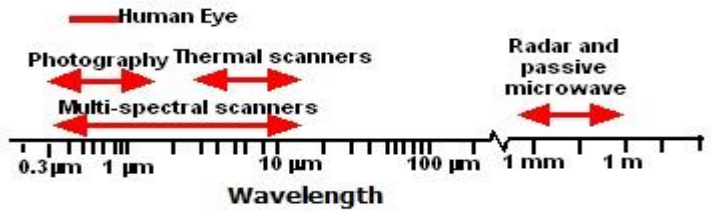

Figure 2.7: Common Remote Sensing Systems (Modified from Lillesand *et al.*, 2004).

Depending on the interaction of the sensor with terrain or target condition the EM *signature* could be considered from spatial, spectral, angular or temporal viewpoints. The commonly used frequency bands in the spectral and microwave regions are given in Table 2.2.

Table 2.2: Selected Frequency Bands

Spectral band	**Wavelength (μm = 10^{-4}.cm)**	**Frequency (THz = 10^{3}.GHz)**
Ultraviolet (UV)	0.001 – 0.4	299792-749
Visible	0.4 – 0.7	749-384
NIR	0.78 – 3	384 - 100
MIR	3 - 50	100 – 6
FIR	50 –1000	6 – 0.3
Microwave band	**Wavelength (cm =10^{4}. μm)**	**Frequency (GHz = 10^{-3}.THz)**
X	2.4 – 3.8	12.5 – 8.0
C	3.8 – 7.5	8.0 – 4.0
S	7.5 – 15.0	4.0 – 2.0
L	15.0 – 30.0	2.0 – 1.0
P	30.0 – 100.0	1.0 – 0.3

Passive sensors useful for mineral explorations are the optical and hyperspectral types. Radar is an active sensor that may also be useful. A disproportionately greater number of optical sensors have been deployed for mineral exploration compared to

radar or microwave imagers. This is due to several reasons including lack of terrain classification data for microwave imaging (See section 3.2). Some satellite optical resource sensors with fine resolution include the multispectral scanner (MSS), Landsat thematic mapper (TM) and enhanced thematic mapper (ETM+). Others include the French Système Pour l'Observation de la Terre (SPOT) series, Geo-Eye and NigeriaSat-2 (N2). The Advanced Spaceborne Thermal Emission and Reflectance Radiometer (ASTER) is a hyperspectral imager. A few characteristics of optical sensors are shown in Table 2.3. The band pass filters determine the operational wavelengths, λ through which targets are imaged.

Table 2.3: High Resolution Optical Sensors Useful for Mineral Exploration

	MSS	TM, ETM	SPOT-5	Geo-Eye	N2	ASTER
Bands	4	7	4	5	5	14
Swath (km)	185	185	120	15.2	20/300	
Pixel Size (m)						
VNIR	80	30	10	-	32	15
SWIR	-	30	-	-	-	23
TIR	-	120	-	-	-	90
PAN	-	15	2.5/5	0.5/1.65	2.5/5	
Band-pass Filters (μm)						
1 (Blue)	-	0.45-0.52	0.5-0.59	0.45-0.51	0.45-0.9	-
2 (Green)	0.5-0.6	0.52-0.6	0.61-0.68	0.51–0.58	0.52-0.6	0.52-0.6
3 (Red)	0.6-0.7	0.63-0.69	0.72-0.89	0.655-0.69	0.63-0.69	0.63-0.69
4 (NIR)	0.7-0.8, 0.8-1.1	0.76-0.9	0.5-0.74	0.78-0.92	0.76-0.9	0.76-0.86
5 (SWIR)	-	15.50-17.50 (20.80-23.50)	-	-	-	1.6-1.7, 2.145-2.185, 2.185-2.225, 2.235-2.285, 2.295-2.365, 2.36-2.43

Landsat satellite series with MSS and ETM+ have been the preferred sensors due to wide availability of continuous data. Newer high resolution imagers like N2 and SPOT-5 are used to increase the spatial resolution of MSS and ETM+ by pan-sharpening with 2.5/5 m and 10 m resolution imagery respectively as shown in Fig. 2.8. Although with less spatial resolution the ASTER has provided enhanced mineral mapping capabilities due to the high spectral resolution but without a band in the blue wavelength (van der Meer *et al*., 2012). This makes it incompatible with Landsat TM and unable to produce natural colour composite images.

Figure 2.8: NigeriaSat-2 2.5m Pan Sharpened image showing Diamond Mine covered in snow at Mirny, Russia (NASRDA, 2012).

Most optical systems provide a synoptic view of a region, operating in a variety of wavelengths and resolutions. From the Rayleigh criterion, the higher the resolution of the sensor, the smaller the swath width obtainable such that at 2.5m and 32 m resolution NigeriaSat-2 is able to achieve 20 km and 300 km swath widths respectively. Newer sensors typically attempt to be backwardly compatible with previous systems therefore the 32m ground resolution of NigeriaSat-2 is designed to be compatible with NigeriaSat-1 and Landsat TM. This creates baseline data that can aid compilation of structural and stratigraphic relationships but there is no terrain penetration (Liang, 1997; Berry & Prost, 1999).

Unlike the lack of information concerning microwave remote sensing, literature is replete with soil optical remote sensing properties backed up with laboratory analyses and field based radiometric studies (Huete, 2004). Although optical sensors are unable to image through cloud or inclement weather conditions they have been deployed to observe change in the land use pattern as a result of mining activities over time. This is seen in Fig. 2.9(a)-(d) showing reduction in Canada's boreal forests and growth of surface mines around Athabasca River. The presence of cloud in the bottom corners (Fig. 2.9b) shows a typical challenge with optical sensors which does not occur with radar sensors.

Hyperspectral sensors such as the Airborne Visible/Infrared Imaging Spectrometer (AVIRIS) and the Geoscan MkII collect data with high spectral resolution (~10 nm) and over several spectral bands between 100 and 300 bands (Vane *et al*., 1993a). They have been successful in identifying mineral species such as gold and base metals but the cost of deployment is prohibitive (Prado & Crósta, 1997; Sabine, 1999). Therefore they are used primarily as research instruments.

(a) 23 July 1984

(b) 22 June 1996

(c) 11 September 2002

(d) 03 October 2010

Figure 2.9: Landsat Images showing growth of surface mines in Alberta, Canada. (a) 23 July 1984 (b) 22 June 1996 with cloud cover in bottom right and left corner (c) 11 Sept 2002 (d) 03 Oct 2010 (NASA, 2002).

Some airborne imaging systems are highlighted in table 2.4. The height of platform determines the pixel resolution varying from 20 m-pixel at 20 km altitude to 4-5 m at lower altitudes.

Table 2.4: Airborne Imaging Systems useful for Mineral Exploration

	Geoscan Mk II	GERIS	MIVIS	AVIRIS
Bands				
VNIR	10	24	20	224 covering 400-2450nm wavelengths
SWIR	8	33	72	
TIR	6	6	10	
Resolution				
IFOV (mrad)	2	2.2	2.0	1
Pixel Size[a] (m)	8	9	8	20
Swath[a] (km)	8	6.4	6	10

[a]At 4km above ground level except AVIRIS considered at 20 km altitude

2.3. Basic Spectroscopy Theory

Whenever EM waves encounter an object, terrain or target they could be absorbed, reflected or scattered depending on the sensor characteristics of the EM wave

and the properties of the target. Spectroscopy is the study of light in relation to wavelength that has been emitted, reflected, or scattered from matter. This differential reflection and scattering of light as a function of wavelength could be due to interaction with solid, liquid or gas. Spectroscopy has potential use as a diagnostic or remote sensing tool (Clark, 1999). It could be reflectance, specular, transmission or emission spectroscopy. However a major challenge in using spectroscopy as an analytic tool is the lack of reliable models for interpreting reflectance data (Hapke, 1993).

Reflectance spectroscopy is a powerful method for determining the characteristic absorption (or transmission) spectrum of a material and has several advantages over other methods. In particular the dynamic range is large, up to four orders of magnitude in the absorption coefficient. It is also a very effective technique when the transmission- and specular reflection techniques are difficult to implement, such as when the imaginary component of the refractive index is in the range of 10^{-3} to 10^{-1}. Furthermore the sample preparation is typically straightforward. In the PhD work reflectance spectroscopy was used to measure the characteristic absorption of homogenous and heterogeneous terrain including oil sand, beach sand and loamy farm soil amongst others. Thereafter an innovative matching algorithm was developed and used to obtain the geochemical signature.

2.3.1. Imaging Spectroscopy

Every terrain type or class consists of particulate material therefore the scattering and propagation of light within non-uniform media into spectra can aid image interpretation. Mineral spectra exhibit diagnostic features at various wavelengths which can enable remote discrimination and identification. When photons impinge on mineral or terrain, some are reflected or scattered from the surface of the grains, some pass through while others are absorbed. In some situations natural surfaces emit photons in a process called *emission*. Spectrometers or spectrophotometers are used to measure the spectral response of materials. Typically the variable observed is the intensity of light while wavelength of the light or any unit directly proportional to the photon energy such as wavenumber or electron volt is the independent variable. Four parameters that describe the capability of a spectrometer namely spectral range, spectral bandwidth, spectral sampling and signal to noise ratio are described in Appendix 1. General spectral ranges in common use were shown in Table 2.2.

Spectrometers may be used in a laboratory, out in the field, in aircrafts and on satellites. This wide variation in platforms suggests that spectral signature classification results in the laboratory can be used to identify targets from air or satellite based observation. Both reflectance and emittance spectroscopy are sensitive to the chemical bonds in a material. The variations in material composition are indicated by shifts in the position and shape of absorption bands in the spectrum. This could often make spectral signatures somewhat complex and unintelligible. Therefore knowledge of the natural variation in spectral features and the causes of the shifts are vital to effective interpretation. Imaging spectroscopy has developed as a new method for mapping materials by analyzing the location and position of bonds indicative of the presence of chemical materials (Vane *et al*., 1993b). This mapping requires spectral feature analysis based on scattering and absorption.

2.3.2. Principles of Spectroscopy

Several good texts discuss the physical laws of scattering, absorption, reflection and refraction of photons in a medium including Hecht (1987) and Hapke (1993). Only the necessary principles will be highlighted here. The change in the index of refraction causes incident photons to be reflected or refracted from a medium. All materials have a complex index of refraction, m given by:

$$\boldsymbol{m = n - jK}\,. \tag{2.2}$$

Here n is the real part of the index, $j = (-1)^{1/2}$ and K is the imaginary part, sometimes called the *extinction coefficient*. In an absorbing medium, photons are absorbed according to *Beer's law*:

$$\boldsymbol{I = I_0 e^{-kx}}\,. \tag{2.3}$$

Where I is the observed intensity, I_0 is the original light intensity, k is the absorption coefficient and x is the distance travelled through the medium. The absorption coefficient as function of wavelength, describes the interaction of photons with a material. It is traditionally expressed in units of wavenumber, cm^{-1} while x is in cm. Transmittance, T_λ, is ratio of radiant power transmitted or coming out of the sample, I_T, to that incident, I_0, on the material at a given wavelength. While absorbance, A is the logarithm to the base 10 of the reciprocal of transmittance and given by:

$$A = log_{10}\left(\frac{1}{T_\lambda}\right) = -log_{10}T_\lambda = -log_{10}\left(\frac{I_T}{I_0}\right) \quad (2.4)$$

The relationship between the complex index of refraction and the absorption coefficient is given by:

$$k = \frac{4\pi K}{\lambda}. \quad (2.5)$$

Here λ is the wavelength of light. The relationship between wavenumber and wavelength is given by:

$$k\ (cm^{-1}) = \frac{10^4}{\lambda\ (\mu m)} \quad (2.6)$$

At the fundamental absorption bands the real (n) and imaginary or extinction coefficient (K) properties of the complex index of refraction vary strongly with wavelength. Typically the reflection of light, r which is normally incident onto a plane surface is described by the *Fresnel equation*:

$$r = \frac{(n-1)^2 + K^2}{(n+1)^2 + K^2}. \quad (2.7)$$

From (2.7), the reflection of light increases monotonically with K when the first media is a vacuum from a value of $r = [(n\text{-}1) / (n\text{+}1)]^2$ at $K = 0$ to $r = 1$ when $K >> 1$. In essence the imaginary component (K) of the refractive index increases the reflectivity of the boundary. This is why metals appear bright in reflected light. The frequency at which $n = 1$ is known as the *Christensen frequency* given by v_c while the corresponding wavelength is the Christensen wavelength, λ_c. From Logan *et al*. (1973), this has great use in the thermal IR remote sensing because at v_c there is small difference in the n compared to the surrounding medium and maximum emissivity occurs at the Christensen wavelength. In essence reflectance $r(\lambda_c) << 1$ and emissivity $\varepsilon_m(\lambda_c) \sim 1$. When v_c occurs at a wavelength shorter than the maximum in the extinction coefficient, K that maximum is known as the *reststrahlen band*. The amount of photons received from a surface is determined by the amount of light scattered versus the amount of light absorbed by the medium.

2.3.3. Processes in Spectroscopy

The absorption bands seen in the spectra of materials are caused by two general processes: electronic and vibrational. Vibrational processes have been discussed by

Farmer (1974) while Burns (1993) has examined details of electronic processes. Also Gaffey *et al*., (1993) has studied the causes of absorption bands in mineral for the UV, visible and NIR.

Atoms and ions have discrete energy states which can be changed to higher states on absorption of incident photons or changed to lower states on emission of photon. The energy level of shared electrons may also be smeared over a range of values called *energy bands*. In terrain, absorption may be caused by *crystal field effects* when unfilled electron shells of transition elements move to higher levels on absorption of photons or *charge transfer absorptions* where the absorbed photon causes the electron to move between ions or between ions and ligands. The crystal field varies with crystal structure from mineral to mineral. Crystal field effects result in the same ion producing different absorptions making it possible to identify specific minerals from spectroscopy. An example would be Fe^{3+} absorptions in goethite (FeOOH) and hematite (Fe_2O_3). Charge transfer effects are better suited to mineralogy identification because the resulting absorption bands are hundreds to thousands of times stronger than those of crystal field transitions and are the main cause of the red colour in iron oxides and hydroxides.

The electrochemical bonds in a crystal lattice or molecule are prone to vibration at a frequency which depends on the strength of each bond and the molecular mass. Incident radiation causes a change in the dipole moment leading to translation, rotation or vibration. A molecule with N atoms will have $3N$-6 normal modes of vibrations called *fundamentals* which themselves may have multiples called *overtones* or *combinations* when different vibration modes are involved. For instance if the frequency of fundamental vibrations are at v_1, v_2, v_3, the overtones roughly occur at $2v_1$, $3v_1$, $2v_2$ and combinations approximately at $v_1 + v_2$, v_2+v_3 or $v_1 + v_2+ v_3$. Due to variations in the strength of higher overtones and combinations, the spectrum of minerals in terrain may be complex (Clark, 1999).

Although absorption makes spectroscopy useful for diagnosis, it is the scattering of light particles that is actually measured by the spectrometer making reflectance spectroscopy possible. The optical path of incident photons reacting with each grain of a particulate of matter is a random walk. This has been discussed by Clark and Roush (1984) however it leads to notable effects. For instance if a material under test (MUT) is bright like quartz at visible wavelengths, it can expect that most photons were

scattered. If the majority of photons are absorbed like in magnetite then the grains appear dark. Grain size also has an effect on spectral results. From Beer's law (2.3), larger grain sizes have greater internal paths for photons to be absorbed meaning reflectance should decrease as grain size increases. Importantly, terrain may be classified into one of four mixtures: linear, intimate, coatings and molecular which are explained in Appendix 1. Oil sands and the other terrain investigated in this research were grouped in to linear (or homogenous), intimate (semi-heterogeneous) and molecular (heterogeneous) terrain.

2.4. Basic RADAR Theory

From the system point of view there are four basic steps in the operation of radar. First a Radio Frequency (RF) signal is generated and then this RF signal is transmitted to a target-object. Next, a fraction of the backscattered signal or *echo* from the target-object is received by the radar antenna and lastly it is processed to yield information. The derived information is mostly achieved by comparing the transmitted and received signals. Consequently, range is obtained by observing time delay between signal transmission and reception. Bearing is acquired using the antenna(s) orientation while velocity is derived from Doppler shift with respect to operating frequency. The four steps translate in to the four sections of the basic radar system shown in Fig. 2.10.

In the middle of the system are elements common to both transmit and receive channel. The duplexer enables the antenna to transmit and receive signals in a monostatic operation. When a separate antenna is used for both transmit and receive channels with considerable distance between them the arrangement is called *bistatic* radar. The coherent local oscillator or *coho* generates the reference signal, f_{ref}, which is used to detect changes in the received signal. The stable local oscillator or *stalo* provides the high frequency carrier signal, f_c, which is used to down convert the received signal and up-convert the coho prior to transmission. For transmission, the output of both coho and stalo are mixed to transmission frequency, amplified by a power amplifier and modulated to emit pulses at a given Pulse Repetition Frequency (PRF). During mixing unwanted harmonics are filtered out.

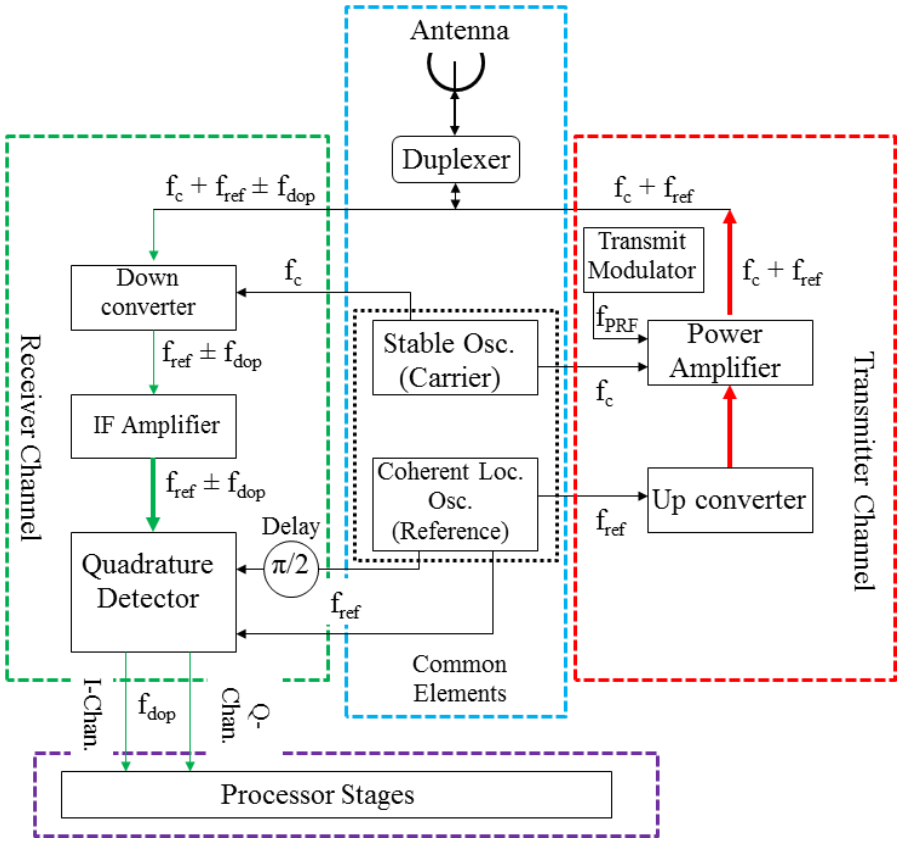

Figure 2.10: System view of basic radar structure (Mahafza & Elsherbeni, 2004).

The power of the transmission signal needs to be magnified due to the severe attenuation experienced from two-way path propagation and backscattering from the target. In the receiver, weak echo signals are down converted to an Intermediate Frequency (IF) at which most receiver elements operate. Thereafter the weak received signals are amplified on the way to the Quadrature detector where the target's echo signal is separated from the coho signal and split into two channels with a 90° phase delay. Another signal is created from a 90° delayed coho input. Splitting the target returns into in-phase (*I*) and quadrature (*Q*) channels is required to correctly identify the direction of the Doppler shift. Traditionally the I-channel is down converted using the regular coho signal but 90° phase delay is applied to the Q-channel. They are both compared then sent to the processor.

It is at the processor stage that different signal processing techniques are applied to convert *I* and *Q* channel data in to information. The processor stage itself may be divided in to real time processing and offline processing. The type and function of the radar system will determine the information processing performed. A moving target indication (MTI) radar will need to continuously identify target speed while imaging

radar will need to process phase data to create maps of terrain reflectivity in range and cross-range. A major focus of this research is to model the relationship between intrinsic material properties and terrain reflectivity. Other types of radar include frequency modulated continuous wave (FM-CW), target recognition, guidance, weather and side looking airborne radar (SLAR) to name a few.

2.4.1. RADAR Equation

The radar equation describes the fundamental relation between the characteristics of a transmitted radar signal, target and received signal (Ulaby *et al*., 1982; Stimson, 1998). The signal from the transmitter spreads spherically outwards to the target and then a fraction of this returns the same way such that the radar transmit power, P_{tx} is related to the received power, P_{rx} according to (2.8) (Skolnik, 1990).

$$\boldsymbol{P_{rx} = \frac{P_{tx} G_{tx} G_{rx} \sigma_{RCS} \lambda^2 F^4}{(4\pi)^3 R^4 L_s}}. \tag{2.8}$$

Here G_{tx}, G_{rx} are the transmitter and receiver gain and λ is the operating signal wavelength which is related to the radar carrier frequency f_0 (in Hz) by $\lambda f_0 = c$. Also F is pattern propagation factor and σ_{RCS} is the target's radar cross section (RCS). Gain refers to the ability of an antenna to focus energy in a specific direction while the pattern propagation factor is the measure of the attenuation or gain as a result of the transmission route. The RCS depends on the target backscattering properties and indicates the size of the target as observed from the radar. General radar system losses are given by L_s while R represents the target slant range. The radar equation takes several forms but they mostly agree that to double the radar maximum range, R_{max} the peak transmit power, P_{tx} must be increased by a factor of 16 (Mahafza & Elsherbeni, 2004).

The effective antenna aperture A_e is related to the antenna gain, G, aperture efficiency η and physical aperture A by

$$\boldsymbol{G = \frac{4\pi A_e}{\lambda^2}}, \tag{2.9}$$

$$\boldsymbol{A_e = \eta A \; where \; 0 \leq \eta \leq 1}. \tag{2.10}$$

Maximum detection range can also be doubled by increasing the effective aperture four times or decreasing the wavelength correspondingly (Stimson, 1998).

However the first order effect of a decrease in wavelength is offset by increased atmospheric absorption. All the parameters in (2.8) can be modified by the radar designer except the RCS, σ_{RCS} and the pattern propagation factor F. This is because σ_{RCS} depends on the target specific parameters such as size, orientation, physical shape and material characteristics while F depends on the operating environment which can vary with relative motion between radar and target (Fig. 2.11). It is possible that the radar signal travels on a direct path between radar and target, R_d, along an indirect path, R_i or a combination of both ($R_d + R_i$). This variation in range length causes phase difference between the signals and could affect return signal amplitude in accordance with superposition principle (Hecht, 1987).

In reality the returned signal strength, P_r is affected by noise. It is clearly desirable that the minimum detectable signal (S_{min}) is greater than the noise power, N which is a function of the radar operating bandwidth, B according to:

$$\boldsymbol{N = Noise\ PSD \cdot B} \tag{2.11}$$

Here PSD refers to the power spectral density function.

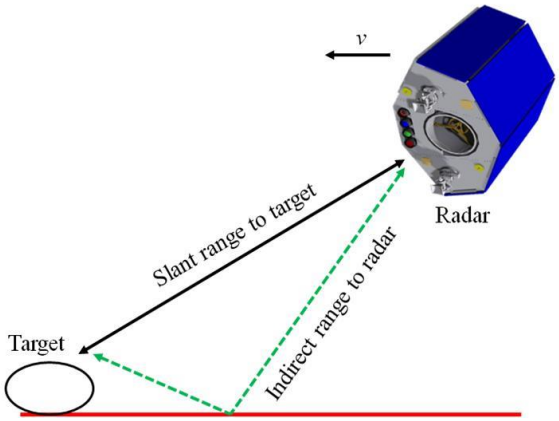

Figure 2.11: Diagram illustrating variation in propagation paths between moving radar platform and stationary target.

The input noise power to a lossless antenna is given by:

$$\boldsymbol{N_i = k_B T_e B} \tag{2.12}$$

Where Boltzmann's constant, $k_B = 1.38 \times 10^{-23}$ *joule*/degree *Kelvin* (J/K) and T_e is the effective noise temperature. Consequently it is common practice for radar

designers to be interested in the minimum signal to noise ratio $(SNR)_0$ for maximum range R_{max}, so that the Radar Equation (2.8) becomes:

$$(\boldsymbol{SNR})_{\mathbf{0}} = \frac{\boldsymbol{P_{tx}G_{tx}G_{rx}\sigma\lambda^2F^4}}{\boldsymbol{(4\pi)^3kT_eN_FBR_{max}^4L_s}}. \tag{2.13}$$

The noise figure represented by N_F is defined as the ratio of the signal, S to noise power N at the receivers input and output. Mathematically this would be:

$$\boldsymbol{N_F} = \frac{\boldsymbol{(SNR)_{in}}}{\boldsymbol{(SNR)_{0ut}}} = \frac{\boldsymbol{S_{in}/N_{in}}}{\boldsymbol{S_{0ut}/N_{0ut}}}. \tag{2.14}$$

Consequently, it can be observed that for a given maximum detection range, R_{max} the (SNR) reduces with increasing radar-target distance. It also drops with transmitted power, P_{tx} as shown in the plots comparing the (SNR) with detection range for different values of transmit power (Fig. 2.12). The code and parameters used to investigate this relationship are at Appendix 2A.

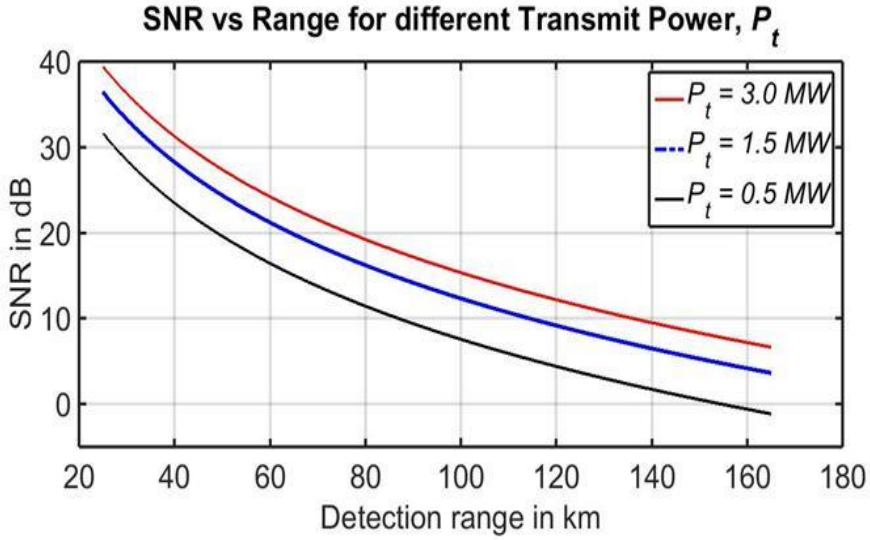

Figure 2.12: (SNR) compared with detection range for different values of peak transmit power, P_{tx}.

The type of target also affects the power considerations. There are generally two types of target; point and distributed or area targets. The lower the value of target RCS the more difficult it is for the receiver to detect. In Fig. 2.13 it can be observed that the

(SNR) value reduces with detection range, for three different values of RCS in decibels per square meter (dBsm or dBm^2), σ_{RCS} = 0 dBm^2, -10 dBm^2 and -20 dBm^2.

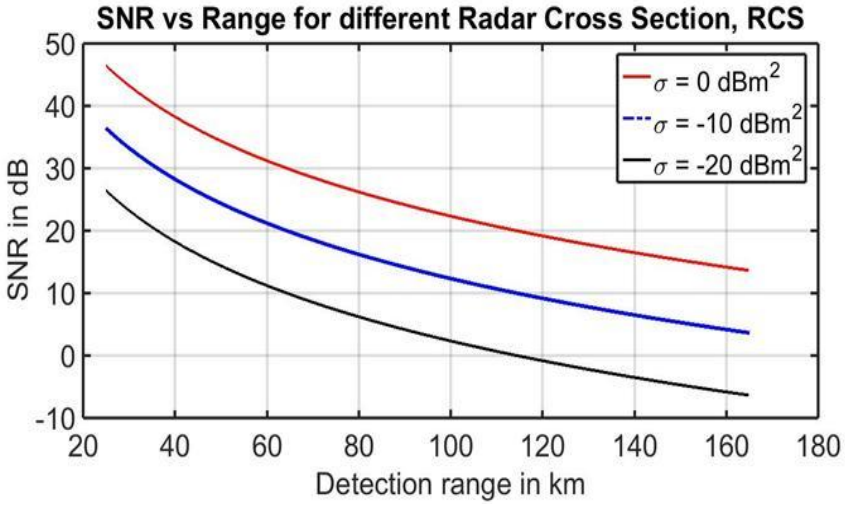

Figure 2.13: (SNR) compared with detection range for different RCS, σ_{RCS}.

A point target generally provides stronger returns per resolution cell while an area-distributed target such as oil sand or terrain occupies more than one resolution cell. A resolution cell is a rectangle whose sides correspond to an across-track or range component, d_r and an azimuth or along-track component, d_a. Together d_r and d_a, define the size of the cell (Stimson *et al*., 2014). Therefore the RCS of extended targets depends on the area illuminated by the radar in a single resolution cell, ∂A and the effective surface area that scatters incident radiation, dA_{eff}. This effective surface area responsible for scattering is measured by the backscatter coefficient σ^0, and is related to the equivalent target RCS by:

$$\boldsymbol{\sigma_{RCS} = \sigma^0 \, dA.} \tag{2.15}$$

For area extensive terrain the backscattering coefficient, σ^0 is considered as the RCS over the unit area, dA. Considering oil sand, σ^0 will depend on specific terrain parameters like texture such as surface roughness or correlation length, moisture content, dielectric constant and geometric properties and also radar system factors such as operating frequency, incident angle and polarization. In this PhD research it would be particularly interesting to study how the intrinsic terrain properties of oil sand affect the backscatter coefficient σ^0. Furthermore the possibility of any links between the geochemical properties and the dielectric properties would be investigated, in order to

reflect the outcome in the classification models. Backscattering phenomena will be discussed further in chapter 3. However dimensions of the resolution cell, ∂A is determined by the ground range and azimuth or cross-range resolution.

2.4.2. Range Resolution

Range resolution, ΔR_r describes the ability of radar to identify two or more targets in close range proximity. Range and azimuth are described in the glossary (Appendix 1). It is defined as the minimum separation between two objects of equal reflectivity along the line-of-sight (LOS), which enables them to appear individually in a processed radar image. It is referred to as *cross-track* resolution when the LOS remains perpendicular to the direction of flight. If it is assumed that the radar transmits pulses as shown in Fig. 2.14, the target range information, R can be determined from measuring the time delay, Δt between pulse transmission and reception along the two-way path between radar and target in (2.16).

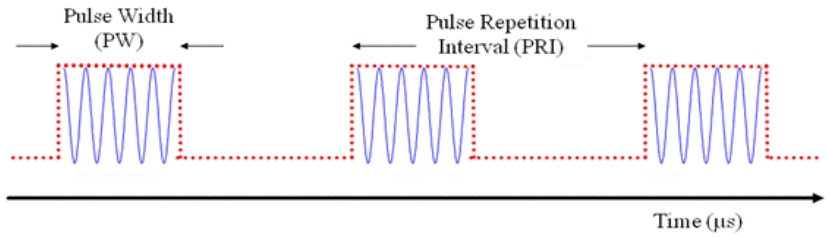

Figure 2.14: Structure of Pulse Waveform.

$$\boldsymbol{R = \frac{c\Delta t}{2}}. \tag{2.16}$$

Here c is the speed of propagation which is approximately 3 x 10^8 ms^{-1} for EM waves in air. In general a sequence of pulses are transmitted, each with pulse width duration, τ (PWD) and inter-pulse spacing equal to pulse repetition interval (PRI) as shown in Fig. 2.14. The PRI is the reciprocal of the PRF denoted by:

$$\boldsymbol{f_{PRF} = \frac{1}{T_{PRI}}}. \tag{2.17}$$

During each PRI the radar radiates energy for τ seconds and 'listens' for target echo returns for the remaining of the PRI. Therefore the echo from a target at distance R from the radar returns to the platform with time delay $t = 2R / c$ after transmission.

The radar bandwidth, B is equal to $1/\tau$ for a rectangular pulse, therefore the minimum separation for signal returns from two targets to remain distinguishable becomes:

$$\Delta R_{rs} = \frac{c\tau}{2} = \frac{c}{2B}. \qquad (2.18)$$

This suggests that for optimum radar performance ΔR_r should be greater or equal to $c\tau/2$ as shown for two targets T_1 and T_2 and corresponding range R_1 and R_2 in Fig. 2.15(b). In the case of spaceborne radar where ranges are very long the reception period does not correspond to the previous pulse. For instance the reception period for the ERS-1 radar for the N^{th} pulse corresponds to $(N\text{-}9)^{th}$ preceding pulse (Bamler & Schättler, 1993). The PRF for the ERS-1 satellite is about 1680 Hz while the beam velocity on ground, which is based on the satellite velocity in orbit, is in the order of 6700 ms^{-1} (Bamler, 2000). Therefore pulses are received every 4 m and without SAR processing objects with less than 4 m separation distance will not be discernible.

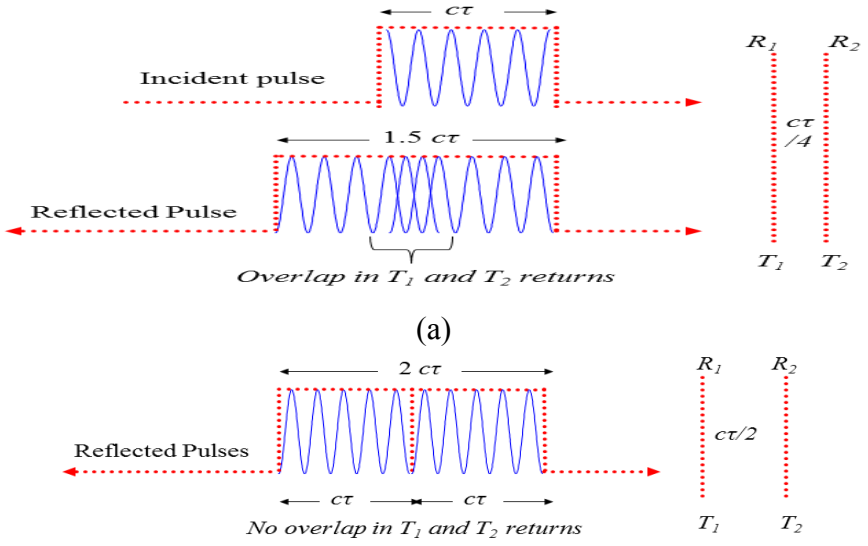

Figure 2.15: Range Resolution, ΔR_r for (a) Two unresolved targets (b) Resolved targets

Fine range resolution can only be achieved if the pulse width, τ is minimized at the risk of reducing the average transmitted power and increasing operating bandwidth. A common solution to this is to use pulse compression techniques which modulate a long pulse during transmission and match filter the received signal. The matched filter output is compressed in to a smaller period of time $\Delta\tau$.

For imaging terrain there is also slight difference between the range resolution otherwise known as *slant range resolution*, ΔR_{rs} and the *ground-range resolution*, ΔR_{rg}

as shown in Fig. 2.15. From the radar imaging platform, *depression angle*, θ_d and the off-nadir or *look angle*, θ_l are complementary ($\theta_d + \theta_l = 90°$). Similar angles are defined on the ground such that for horizontal terrain, the *incident angle*, θ_i is equal to the *look angle* ($\theta_i = \theta_l$) and assuming the flat earth principle, the *grazing angle*, γ_g is equal to the depression angle ($\gamma_g = \theta_d$). The imaging or viewing angle has an appreciable effect on the target signature. The 3D EM models and scattering measurements of oil sand and other terrain will be used to investigate the effects of this variation in sensor or viewing angle on terrain reflectivity in subsequent chapters.

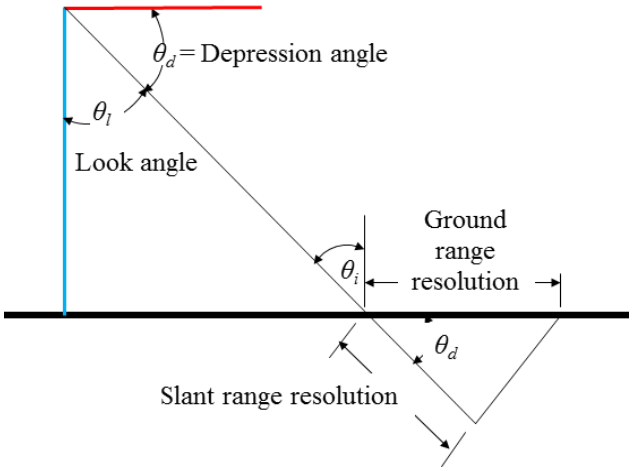

Figure 2.16: Relationships between Slant Range and Ground Range (*XZ* plane).

For *nadir* imaging when θ_d is 90° from the platform then the incident angle, θ_i is seen to be 90° from the terrain so that both the ground range and slant range resolution are equal. Modern imaging radar systems seldom operate with 90° incidence. Therefore, in the range direction, ground range resolution becomes *coarser* with increasing slant range distance. This inverse variation of ΔR_{rg} with the cosine of θ_d (or γ_g for flat terrain) is depicted by:

$$\Delta \boldsymbol{R_{rg}} = \frac{\boldsymbol{c\tau}}{\boldsymbol{2cos\gamma_g}}. \tag{2.19}$$

The flat terrain approximation is only relevant for cases of airborne radar. The effect of earth curvature which is more dominant for spaceborne radar is discussed in Appendix 2B.

2.4.3. Azimuth Resolution

The *azimuth* or *cross range* resolution, ΔR_{az} refers to the ability of radar to identify two or more targets across the line of platform flight or along track direction.

It is sometimes called *along-track* resolution. This cross range component of the radar resolution cell is related to the antenna horizontal beam width, θ_B (in radians) and the ground range, R_{rg}. This dependence means that it deteriorates with increasing ground range distance from platform due to widening of θ_B. This is shown in Fig. 2.17 for real aperture radar (RAR) moving along the y direction. The two objects at distance R_{rg2} and R_{rg3} will not be clearly distinguished. At ground range distance R_{rg1} both objects provide separate return signals due to finer azimuth resolution (narrower beam width) at this point.

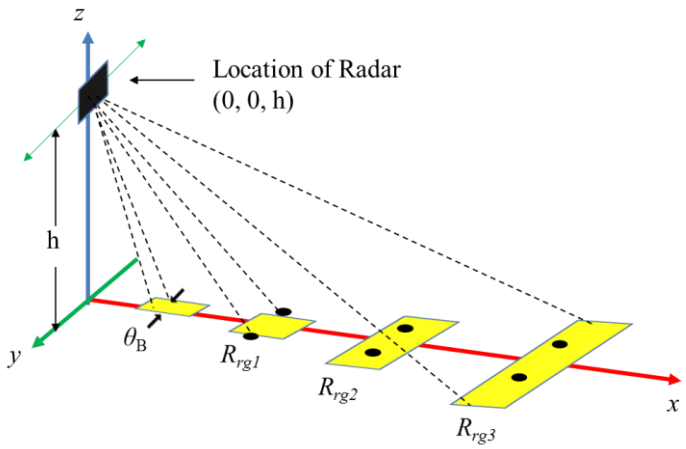

Figure 2.17: 3D Decreasing azimuth resolution for platform moving in y-direction with increasing beamwidth, θ_B for two point targets at ground range positions R_{rg1}, R_{rg2} and R_{rg3}.

From the foregoing, azimuth resolution for a RAR is given by:

$$\Delta \boldsymbol{R_{az}} = \boldsymbol{\theta_B} \cdot \boldsymbol{R_{rg}}, \tag{2.20}$$

The beam width of the antenna is itself directly proportional to the wavelength of transmitted pulse λ, and inversely proportional to the antenna aperture diameter d, i.e. $\theta_B = \lambda/d_a$ where d_a is the azimuth dimension of the antenna. This means that the azimuth component of the resolution cell as shown in Fig. 2.18 is given by:

$$\Delta \boldsymbol{R_{az}} = \frac{\boldsymbol{\lambda R_{rg}}}{\boldsymbol{d_a}}. \tag{2.21}$$

This means that for any given wavelength the azimuth resolution can be determined by either controlling the physical length of the antenna, d or synthesizing a virtual antenna array of length, L_{SA}. When the azimuth resolution depends on the

physical antenna such a radar is referred to as real aperture radar. It is called synthetic aperture radar when a large synthetic aperture is created. The data processing requirements for real aperture radar are fairly simple. However the poor azimuth resolution restricts their deployment to relatively short range, low altitude and low wavelength operations.

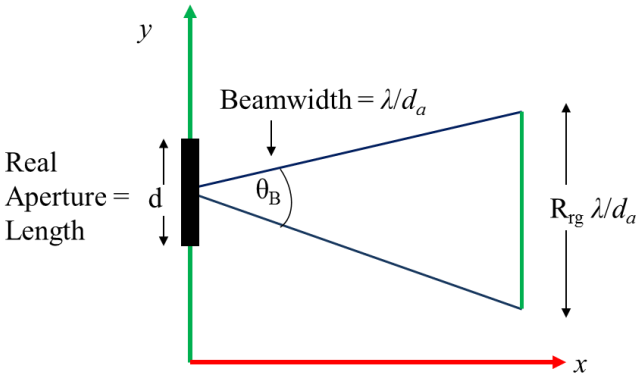

Figure 2.18: Diagram showing effect of range on Azimuth resolution (XY Plane) for RAR

2.5. Synthetic Aperture Radar Theory

The challenges with RAR are overcome in SAR which is employed in modern radar systems specifically for mapping large areas of terrain. Therefore our classification results must be determined for terrain, mapped using SAR techniques because SAR can produce high resolution two-dimensional (2D) and sometimes three-dimensional (3D) imagery of the ground. It does this by illuminating the terrain with coherent radiation and measuring the Doppler echo returns as the radar moves along, thereby creating a long synthetic aperture L_{SA} shown in Fig. 2.19. The length depends on the velocity of the platform, v and the coherent integration interval T_{ob} for each observation point, t_n (n=1, 2, 3…) such that $L_{SA} = v\ T_{ob}$.

SAR systems typically use a short physical antenna and the motion of the platform to generate fine resolution imagery through diverse processing techniques. The first SAR systems used optical processors with intensity modulated scanners which photographically recorded coherent video output in a 2D raster format on film (Stimson, 1998). After developing the film, range and Doppler (cross range) information from the video is combined to create an image using offline processing.

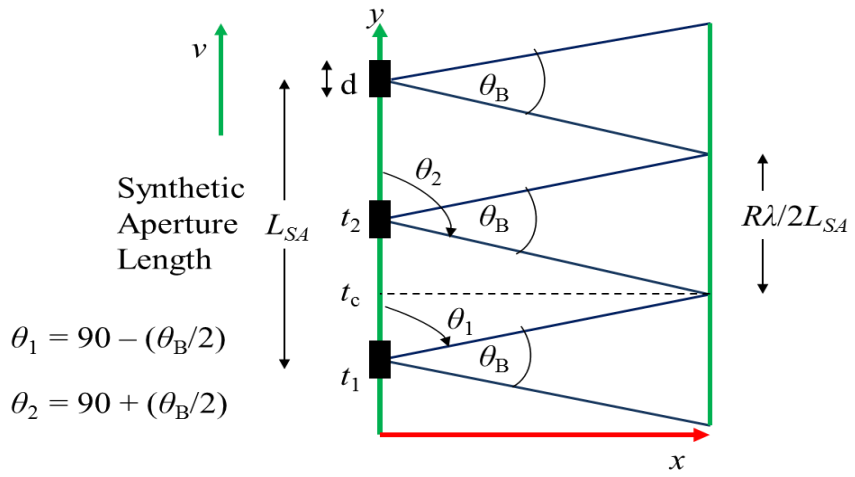

Figure 2.19: Sketch showing Doppler history computation (XY plane). Synthetic aperture length gives finer cross range resolution when compared with RAR.

It follows that the angle subtended by the synthetic aperture, $\Delta\theta$, such that two scatterers can distinctly be seen in two Doppler filter bins is:

$$\Delta\boldsymbol{\theta} = \frac{\boldsymbol{\lambda}}{\boldsymbol{2vL_{SA}sin\theta_l}}. \tag{2.22}$$

The quality of a ground map is determined by the size of the resolution cell and the dimensions of the resolution cell depend on the minimum resolvable distance in range, r_r and azimuth r_{az}. In essence the ground range resolution, ΔR_{rg} and cross range resolution, ΔR_{az} are the determinants of image quality and they depend primarily on the nature of the object to be imaged which in this case would be oil sand terrain and other barefaced terrain. The advent of low-cost and high speed processors has enabled digital processing in real time. This enables small, rugged and lightweight equipment in addition to flexible, timely and accurate operation. The imaging algorithm is a major challenge in SAR. Several SAR image processing methods are in existence. They include the range-doppler algorithm (RDA), Polar Format Algorithm (PFA), Wavenumber Domain Algorithm (WDA), wave front reconstruction and back projection to name a few (Bamler, 1992; Soumekh, 1999). Current efforts in SAR are focused on optimizing different signal processing methods. This depends on the required image accuracy, available processing time, nature of terrain and type of SAR.

2.5.1. Types of SAR

Several forms of SAR exist. For terrain imaging the interest is typically in *focused* SAR. This is the best case operation when phase information is processed and corrected for each returning pulse to achieve cross-range resolution comparable to the theoretical limit. Synthesized arrays like SAR are formed by moving a single element along an *imaginary* aperture while a *phased* array introduces delays in the transmitter and/or receiver paths to focus the radiation pattern of a physical antenna at specific points in the spatial domain. Several techniques have evolved in the development of focused SAR. A few historical examples include the SLAR, Doppler Beam Sharpening (DBS) and unfocused SAR. Present day operational modes of focused SAR include Inverse SAR, Spotlight SAR, Interferometric SAR and Stripmap SAR.

In SLAR a RAR is mounted on an aircraft and pointed perpendicular to the direction of flight such that azimuth resolution r_{az}, is ~ $R_{rg}\lambda/d$. This is the same azimuth resolution obtained with RAR (2.21). DBS is what Carl Wiley who first discovered SAR at Goodyear aerospace initially called SAR in 1951 (Wiley, 1985). For the DBS technique, echoes from a scanning beam are Doppler processed to achieve azimuth resolution which is finer than from RAR. Here the broadside cross-range resolution:

$$\boldsymbol{DBS\ r_{az} = \frac{\lambda R_{rg}}{2L_{DBS}}}. \tag{2.23}$$

L_{DBS} is the synthetic aperture length generated while the antenna scans a target. This antenna scanning operation means the length of time a ground object is within the antenna view is limited and therefore resolution is coarser. According to (Stimson, 1998) it also means azimuth resolution distance increases with range. Unfocused SAR is seldom in use since current technology enables the phase adjustment necessary to obtain focused SAR. However it was characterized by lack of phase shift before integration of coherent signals at synthetic array points and from (Cutrona, 1990), resolution was:

$$\boldsymbol{Unfoc\ SAR\ r_{az} = \frac{(\lambda R_{rg})^{1/2}}{2}}. \tag{2.24}$$

Inverse SAR (ISAR) uses the motion of the target and corresponding Doppler shift caused by changes in relative velocity to identify the type of target. This is useful

for automatic target recognition (ATR) and diagnostic measurements of RCS range for ships and aircrafts because their inherent differential motion can blur typical SAR imagery (Knott *et al*., 2004). Interferometric SAR (InSAR) was originally developed by the Jet Propulsion Laboratory (JPL) to detect moving targets or ocean currents (Goldstein & Zebker, 1989). InSAR involves coherently combining the signals from two antennas with a fixed physical separation such that target height, depth and motion can be measured. Spotlight SAR is suitable for surveillance, reconnaissance and weapon delivery applications as very fine resolution is obtained by illuminating a fixed region of terrain while radar moves along its path. Theoretically the azimuth resolution for spotlight SAR is independent of the antenna dimension, given by:

$$\boldsymbol{Spotlight\ SAR\ r_{az} = \frac{\lambda}{2\Delta\theta}}. \tag{2.25}$$

Where $\Delta\theta$ is the change in aspect angle over which the radar data are coherently processed. A Stripmap SAR is useful for imaging large areas where the precise target is unknown. Here the beam moves along with the radar over large swath or strip of terrain with theoretical resolution:

$$\boldsymbol{Stripmap\ SAR\ r_{az} = \frac{d_a}{2}}. \tag{2.26}$$

This thesis investigates the performance of Stripmap SAR to oil sand detection and develops CEM models and scattering methods to distinguish barefaced terrain types. (2.26) provides the spatial resolution assuming flat earth approximation. The detailed derivation and the corresponding expression for a spaceborne SAR is given at Appendix 2B.

2.5.2. Basic Principles

In the strictest sense SAR is a technique or technology aimed at improving the azimuth or cross-range resolution, r_{az}. However both range and cross-range must be considered for each resolution cell as they determine the footprint dimensions. The interplay of both range and cross-range processing dramatically increases the complexity with SAR therefore they will be considered separately here. Furthermore

the classification technique for oil sand terrain will be based on instantaneous models of reflectivity with specific spatial location and time.

For range imaging which is also used in altimeters or echo-location, it is assumed that the SAR is located at a known (fixed) target area in cross range, *y*. This scenario can be described by mathematical analysis based on Soumekh (1994) and Blahut *et al*., (1991). The analysis begins by considering the echo received, *s*(*t*) on illuminating a one dimensional target area in the *x* (range) domain with signal *p*(*t*):

$$\boldsymbol{s(t) = \sum_{n} \sigma_n p\left(t - \frac{2x_n}{c}\right).} \tag{2.27}$$

Where σ_n and x_n are the n^{th} target reflectivity and range respectively and $2x_n/c$ is the two way path propagation from SAR sensor to n^{th} target. If the range domain, *x* is the linear transformation of the time axis,

$$\boldsymbol{x = \frac{ct}{2}.} \tag{2.28}$$

And the *ideal* target function for the range imaging problem is given by:

$$\boldsymbol{f_0(x) = \sum_{n} \sigma_n \delta(x - x_n).} \tag{2.29}$$

Then from (2.27) and (2.28), the echoed signal model becomes

$$\boldsymbol{s(t) = f_0(x) * p(t) = f_0\left(\frac{ct}{2}\right) * p(t).} \tag{2.30}$$

Here (2.29) reflects the *forward* problem shown in Fig. 2.20.

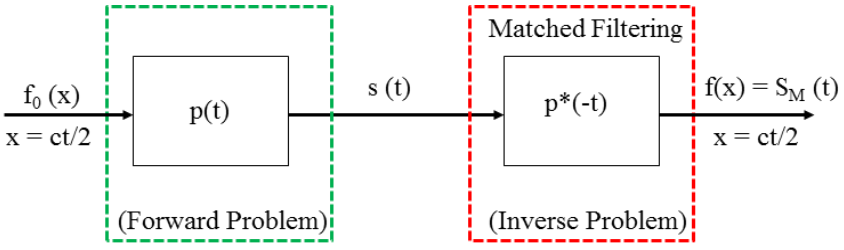

Figure 2.20: Forward and inverse system models for range imaging.

This functional property enables the determination of an output from knowledge of the impulse response and applied input. An oil sand reservoir will be composed of a

continuum of reflectors therefore the number of reflectors is infinite and the echoed signal will reflect this as:

$$s(t) = \int_x f_0(x) p\left(t - \frac{2x_n}{c}\right) dx = f_0\left(\frac{ct}{2}\right) * p(t). \tag{2.31}$$

Here $f_0(x)$ is the target reflectivity function in the continuous range domain. It is this function that the 3D EM models are used to determine and later verify with scattering measurements. However in this instance, the model in (2.31) does not account for the backscattering phenomenon which is discussed in Chapter 3. It also assumes that the target reflectivity, σ_n is invariant with radar frequency which is also not the case for oil sand terrain. The Fourier transform of the echoed signal is:

$$S(\omega) = P(\omega) \sum_n \sigma_n exp\left(-j\omega \frac{2x_n}{c}\right). \tag{2.32}$$

The procedure for cross-range imaging is similar. It is assumed that the position of the radar in the range domain, x is known or fixed but the cross range values of targets, y_n and corresponding reflectivity σ_n are unknown. Also the SAR moves along the cross-range domain beginning with position $(0, u)$ where the u domain is the synthetic aperture domain. For this SAR located at $(0, u)$ in the spatial (x, y) domain, the target falls within a cross-range interval:

$$y_n \epsilon [-Y_0, Y_0], \qquad n = 1, 2, \ldots . \tag{2.33}$$

So that $2Y_0$ is the size of the target area in the cross range domain. When the target area exists in the center of the cross-range, y domain such that its center is at the closest point of approach (CPA) to the radar, the target area is *broadside*. If the target area is skewed from the radar it is called a *squint* target area. For a SAR transmitting a signal, $p(t) = \exp(j\omega t)$, along the synthetic aperture, the recorded echo return signal will vary as u varies and can be expressed as a function of u:

$$s(t, u) = \sum_n \sigma_n p\left[t - \frac{2\sqrt{x_n^2 + (y_n - u)^2}}{c}\right],$$

(2.34)

$$= \exp(j\omega t) \sum_{n} \sigma_n exp\left[-j2k\sqrt{x_n^2 + (y_n - u)^2}\right]$$

Here $k = \omega/c$ is wavenumber and the phase function, $exp\left[-j2k\sqrt{x_n^2 + (y_n - u)^2}\right]$ is a phase-modulated (PM) signal also referred to as a spherical PM signal (Morse & Feshback, 1953). It is a nonlinear phase function of (x_n,y_n) and also u. The CPA for the n^{th} target occurs when $u = y_n$. Again it can be expected that the terrain reflectivity σ_n will vary with radar frequency ω and the synthetic aperture position u. This is similar to the aspect coordinates between target and radar. Examples of techniques for range processing of a single pulse and azimuth dimension processing are given at Appendix 2C.

2.5.3. SAR Radar Equation

The radar equation for a single pulse was given in (2.13), and in (2.15) it was noted that the RCS, σ_{RCS} is a function of the radar resolution cell, ∂A and terrain reflectivity, σ^0. From the analysis of range and cross-range imaging in the previous section the RCS can be considered as:

$$\sigma = \sigma^0 \Delta R_{rg} \Delta R_{az} = \sigma^0 \frac{c\tau}{2cos\gamma_g} \Delta R_{az} \tag{2.35}$$

Here ΔR_{az} is the azimuth resolution and (2.19) was used to replace ground resolution. Within each observation interval, $n = f_{PRF} \cdot L_{SA}/v$ pulses can be coherently integrated without ambiguity and the average radar power over this observation interval is:

$$P_{av} = \frac{P_{tx}}{B} f_{PRF} \tag{2.36}$$

Therefore for n coherently integrated pulses the radar equation becomes:

$$(SNR)_n = nSNR = n \frac{P_{tx} G_{tx} G_{rx} \sigma \lambda^2}{(4\pi)^3 k T_e B R_{max}^4 L_s} \tag{2.37}$$

Substituting (2.22), (2.26), (2.35), and (2.36) in to (2.37) yields the SAR Radar Equation. The significant difference is that better SNR is obtained because of the

coherent addition of pulses despite the reduction in the magnitude of range from R^4 to R^3.

$$(SNR)_n = \frac{P_{av} G_{tx} G_{rx} \sigma^0 \lambda^3}{(4\pi)^3 k T_e R^3 L_s} \frac{\Delta R_{rg}}{2v} csc\theta_l \tag{2.38}$$

2.6. Concluding Remarks

This chapter dealt with the main building blocks underpinning the research from a general perspective. In the first half of this chapter it was observed that high oil prices, terminal decline of conventional oil reserves along with increasing energy demand and technological progress has driven the search for unconventional petroleum reserves such as oil sands and oil shale. Current exploration sensors used to search for oil sand such as PIA and NIA are manual requiring laboratory validation. Others such as GBL and seismology enable measurements of variation in earth properties at depths which are suitable for sub-surface identification of conventional deposits in accessible terrain. Already a disproportionately larger number of earth observation sensors use the optical wavelengths for mineral exploration due to lack of terrain classification data and models for microwave imaging. Invariably there are trade-offs between geometrical and spectral resolution when considering panchromatic and multispectral passive sensors. Panchromatic imagers have poor spectral resolution but high geometrical resolution while multispectral imagers have medium geometrical resolution but high spectral resolution. Both are affected by atmospheric conditions and variations in illumination conditions depending on acquisition time.

Therefore it is believed that in addition to the high spectral resolution provided by passive multispectral imagers, the wide area spread and shallow depth of oil sand terrain will benefit from the ability of radar to achieve greater terrain penetration, see through sparse surface vegetation or cloud while allowing user control of EM illumination conditions. This will permit the use of EM remote sensing techniques such as SAR to aid exploration efforts in difficult to reach terrain either alone or in combination with other sensors. After considering the principles and processes involved in spectral identification of minerals in terrain, the chapter was concluded with basic radar theory noting that for imaging radar the spatial resolution determines the amount of detail seen from a target. The SAR was considered as a measuring instrument which provides

estimates of the complex radar reflectivity or backscattering coefficient of a scene whether spaceborne or airborne. The SAR resolution cell, ∂A depends on both ground range and cross-range. The relationship between a transmitted radar signal, target, and receiver signal for SAR was investigated. The relationship between the backscatter coefficient and EM reflectivity from terrain was highlighted. Lastly simple models for both range and cross-range image processing were mathematically implemented separately using the wave-front reconstruction theory.

3 Electromagnetic Characterization

We consider the wider picture of oil sand exploration research and the performance of electromagnetic sensors particularly hyperspectral and Synthetic Aperture Radar systems to resource monitoring. Thereafter we evaluate backscattering phenomena along with parameters that can aid terrain identification and consider diverse backscattering models.

It was identified in section 1.1 and 2.1 that relatively high oil prices have only recently made oil sand exploration and production (E&P) commercially viable. Consequently very little literature exists that is specific to oil sand exploration technology using radar or IR remote sensing and those that do exist are *commercial-in-confidence*. The use of remote sensing for mineral exploration is typically limited to mapping geology of faults and fractures that localize ore deposits or identification of hydrothermally altered rocks by the spectral signatures. This limitation creates a paucity of oil sand exploration studies for comparison or evaluation. Consequently following on section 2.1.3 the review begins by summarizing the appropriate characteristics of known oil sand reservoirs on which the subsequent electromagnetic (EM) barefaced terrain models (BTM) will be based and discussion of previous use of hyperspectral imaging to terrain identification. Thereafter it identifies parameters that may be detected by radar based on interaction of EM waves with terrain. The performance of spectral and microwave sensors to hydrocarbon exploration will be critically analyzed while the prospect of airborne electromagnetic sensing (AEM) is discussed. Together they shed light on possible sensor requirements and object characteristics that may be monitored. Literature describing oil sand EM backscatter characteristics are non-existent therefore general terrain models will be investigated as a prelude to identifying parameters for oil sand backscattering.

3.1. Oil Sand Characteristics

Oil sands are mixture of clays, quartz grains, water, trace amounts of accessory minerals and bitumen amongst other hydrocarbons (Cloutis *et al*., 1995; Majid *et al*., 1988). Accurate knowledge of the physical, dielectric and chemical properties of these materials is vital to enhancing the bitumen extraction process, understanding the oil

sand formation process and obtaining geoscientific information from optical or microwave sensors. The chemical properties vary with the constituent components. A variety of laboratory methods such as X-ray diffractometry and Fourier Transform Infrared Spectrometry (FTIR) have been used to identify the wide variety of bonds in minerals. The mineralogy of oil sands is important as it roughly requires 2 tonnes (~ 1800 kg) of oil sand to create one barrel (bbl) or 42 US gallons (158.9 liters) of synthetic crude oil (SCO).

The physical properties of sandstone reservoirs depend primarily on the average value of grain size, texture and composition as shown in table 3.1. Others such as porosity, permeability and bulk density are dependent properties (Berg, 1986; Boggs, 2006). The primary properties exert the most control on the reservoir while the secondary properties depend on the former. The tertiary properties are traditionally measured beneath the surface using geophysical borehole logging (GBL) (discussed in section 2.2). The BTM developed as part of this work are designed to include representative properties for the primary and secondary properties for an elemental area, ∂A of an oil sand reservoir.

Table 3.1: Categories of Reservoir Rock Properties (Berg, 1986)

Primary (definitive)	**Secondary (dependent)**	**Tertiary (latent)**
Composition (%)	Porosity, ϕ (%)	Resistivity, r (Ωm)
Texture (mm)	Permeability, k_p (md)	Spontaneous potential, SP (mV)
Sedimentary Structures (m)	Saturation, s (%)	Radioactivity, γ (counts/sec)
Morphology (descriptive)	Bulk density, (g/cm^3)	Sonic travel time, Δt (μsec/ft)

Reservoir rock properties vary with the local depositional environment therefore values change from region to region despite general relationships between the categories. The first task to characterize an oil sand deposit is to describe the geological setting, stratigraphy, paleogeography and nature of oil bearing zone (Wallace *et al*., 1988). This thesis does not discuss the sedimentary structures or morphology of oil sand terrain further as geological setting and stratigraphy for broad regions can be generally obtained in literature. Also the aim of the research is to develop BTM that identify oil sand on the localized terrain surface regardless of the underlying morphology. The second task is to perform an engineering evaluation to identify the secondary properties. Engineering evaluations that indicate these properties are seldom available in literature as they are used by companies to set up exploration and production (E&P) platforms (Bruney, 2014). It is also difficult to predict the dependent properties at the subsurface without understanding the definitive (primary) characteristics at the surface.

Canada and Venezuela are the two countries with the largest known oil sand reserves. The Alberta Energy and Utilities Board estimates oil sands in Northern Alberta contain about 2.5 x 10^{12} bbl (400 x 10^{19} m^3) of heavy oil (bitumen) from which roughly 7% or 180 x10^9 bbl (30 x1 0^9 m^3) are economically recoverable using existing technologies (Czarnecki *et al*., 2005). Descriptions of geology and deposits of Canadian oil sands can be found in books by Fitzgerald (1978) and Hills (1974). Canada also has the most established E&P procedures for oil sand using physical inspection and a variety of methods including open pit mining (OPM) amongst others. Therefore to determine potential oil sand reserves, several countries like Nigeria and America compare terrain characteristics with Canadian oil sands (NGSA, 2010). Most of Canada's reserves are found in north eastern Alberta and north western Saskatchewan (Prebble *et al*., 2009). The entire area shown in Fig. 3.1 covers roughly 146,000 km^2 (Moritis, 2009). The three major deposits are at Cold Lake, Athabasca-Fort McMurray and Peace River in Alberta.

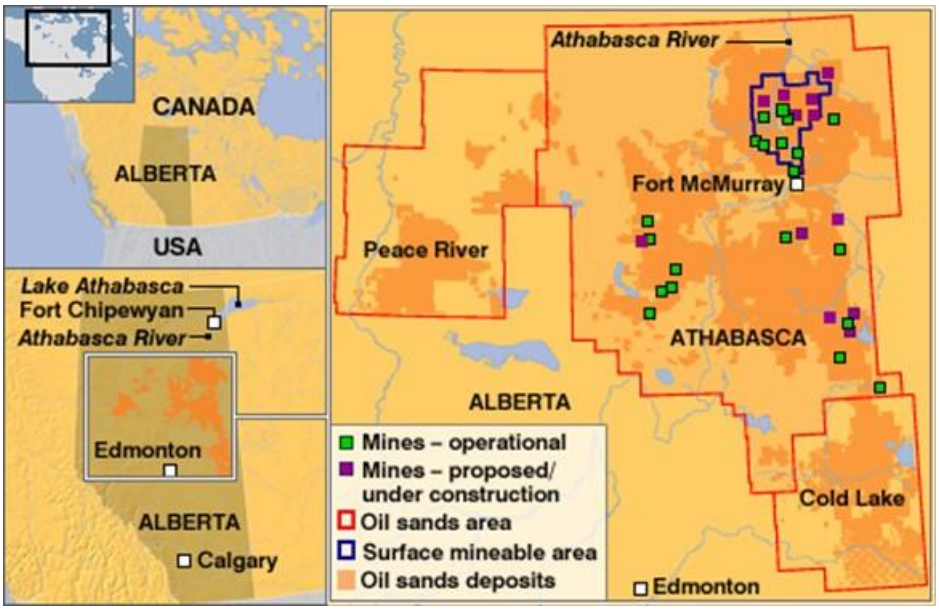

Figure 3.1: Oil sand regions in Canada showing operational and proposed exploration sites (Shenker, 2008).

The geological characteristics differ slightly. This determines the suitable E&P methods. In areas with little overburden OPM is used to dig out the oil sand from the surface prior to post-processing. In areas with medium overburden such as Cold Lake, the cold heavy oil production with sand (CHOPS) operation is used. This entails extracting oil sands with vertical wells. The steam assisted gravity drainage (SAGD)

method with cyclic steam stimulation (CSS) is employed in areas with substantial overburden (Butler, 1991). SAGD involves drilling two horizontal wells in to the oil sands and injecting steam through the upper pipes to heat the oil sands and bitumen which is collected with the bottom pipe. Consequently bitumen is mobilized and recovered from the surface. Rather than steam, some research has considered the use of microwave radiation to heat up the oil sands to reduce the viscosity of bitumen making extraction easier (Mutyala *et al*., 2009).

Furthermore, the depth of overburden often varies from place to place. In Alberta the overburden increases from east to west as shown in Alberta's geological structure (Fig. 3.2). In Nigeria the oil sand belt is generally shallow occurring from surface outcrops to 300 m depths at the eastern end of the Dahomey basin (Odunaike *et al*., 2009; Omatsola & Adegoke, 1981). This means that the Nigerian reservoirs lend themselves to OPM which is relatively cheaper to set up. The formation and disposition of oil sand reservoirs in terrain with low overburden, permit OPM before conversion to SCO. Therefore detecting Nigerian oil sand reservoirs requires a sensor that is able to quickly and effectively identify potential reservoirs from surrounding wet and dry surfaces. This raises the possibility of using EM methods such as hyperspectral imaging and SAR.

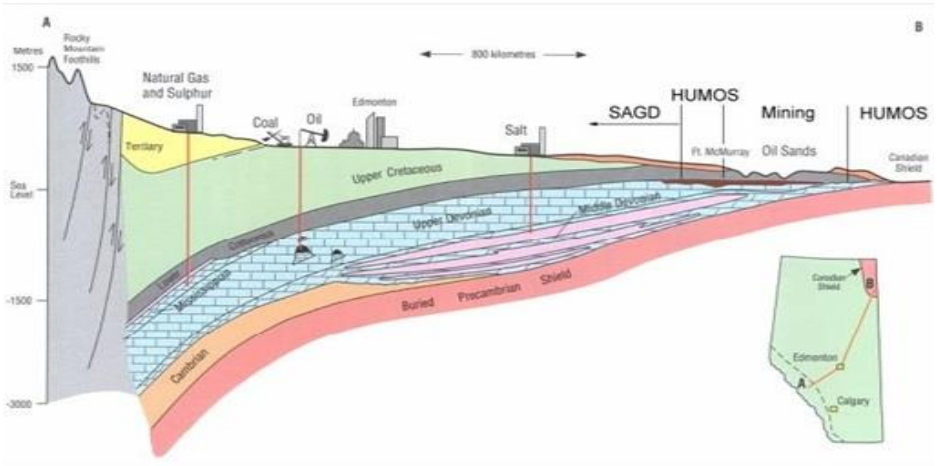

Figure 3.2: Alberta Geological Structure (Engelhardt & Todirescu, 2005).

3.1.1. Terrain Composition

Oil sands are highly complex mixtures (Bichard, 1987; Liu, 1989). Sand is the major grain ingredient while clay is the finer material or matrix that occurs between the grains. Both grains and matrix result from weathering and deposition under diagenesis

(see section 2.1.1). Bitumen is the cement that joins the grain and matrix in to a competent mass. Although researchers do not doubt the actual components present in oil sand there are two opinions on the oil sand structure. One view considers oil sands to be 'water-wet' or hydrophilic and the other 'oil-wet' or hydrophobic. In the former the bitumen is not directly in contact with the mineral phase but separated from the grains by a thin film of water while in the latter, bitumen is in direct contact with the mineral grains. Czarnecki *et al*. (2005) considered the effects of thick or thin water film cases and impact of natural surfactants on oil sands while Strausz and Lown (2003) considered the chemical properties.

Understanding terrain composition is important for identifying the source material although equilibrium of the constituent particles including bitumen may change under different conditions of temperature, pressure or injected fluids. The presence of other trace minerals means that long or short-term changes in physical and chemical environment can cause instability (Berg, 1986). In this thesis the undisturbed terrain is considered for evaluation where oil sand is at steady state. However, deposits are typically non-homogenous and may vary in water, sand, clay and bitumen content as well as particle size and distribution (Hepler, 1989). Therefore an ordered consideration was used to develop the models based on empirical evidence and measurements verified wherever possible with literature.

Bitumen is a thick, sticky, black and highly viscous form of petroleum which occurs naturally in oil sands but can be manufactured in a refinery. It may be solid or semi-liquid depending on the temperature and pressure. Both solid bedrock and viscous oil sand exist in Nigeria and were acquired from Agbabu Oil Sand Reservoir (AOSR) near Igbokoda, Ondo State in South West, Nigeria. Bitumen is the one component that differentiates oil sands from any other terrain. Consequently the physical and chemical properties of Bitumen may differentiate the behaviour of EM waves with oil sands and other terrain types such as normal wet or dry terrain. Also the arrangement of phases in oil sands is largely determined by the volume fractions of bitumen, water, quartz and clay sand (Czarnecki *et al*., 2005). Compositions of oil sand in weight percent (*wt*. %) derived from literature are shown in table 3.2.

Table 3.2: Mass Composition of Oil Sand

Material (*wt*. %)	**Dahomey Basin**	**Athabasca**	**Asphalt Ridge**
Solids (sand and clay)	80-84	83.0	89.5
Water (*wt*. %)	4-8	5.7	0.4
Bitumen (*wt*. %)	10-17	8.5 -12.5	9.9

The grade or quality of oil sand depends on the oil content and particle distribution. Usually the grain (sand) and matrix (clay) form the bulk of oil sand materials with bitumen (for rich oil sands) or water (for lean oil sands) forming the continuous phase. Carrigy (1962) has related the grain size distribution of Athabasca oil sands to the variations in oil content. From particle size analysis of 142 samples of oil sand he found a direct relationship between grain size and oil content. The oil content of oil sands decreased with the median particle diameter and as the fraction of particles in the clay-size range increases. Determination of clay-sized fractions has further application to determining oil sand reservoir structure, composition and processability.

3.1.2. Spectroscopic Applications

Multispectral or hyperspectral imaging is a passive remote sensing technique unlike microwave radar imaging which is active. In laboratory spectroscopy light is transmitted through a material under test (MUT) and the spectral content of the light before and after transmission is compared with each other (see section 2.3). This can be done for even minute samples as every molecule shows a very specific response to the incident light which could also be referred to as the *spectroscopic fingerprint* of the molecule. In the EM spectrum the infrared (IR) region is bound by the red end of the visible spectrum at high frequencies and the microwave region at low frequencies. Therefore IR radiation covers wavenumber (k) from roughly 13,000 to 10cm^{-1}, or wavelengths (λ) from 0.78 to 1000μm. From (2.3) the distance travelled by light through the sample or optical depth is important to maintain consistence in absorption or transmission spectra.

The application of multispectral or hyperspectral imaging to mineral exploration has been well documented. A lot of the early work on the application of VNIR, SWIR, MIR and TIR in geologic remote sensing resulted from the pioneering work of Hunt and Salisbury (Hunt, 1977; Salisbury *et al*., 1989). They carefully measured mineral and rock spectra which later formed the basis for airborne and spaceborne sensors but did not obtain spectra for oil sands or bitumen. Other review articles focus on aspects of passive sensor technology application including multispectral and hyperspectral remote sensing in the VNIR to SWIR and TIR parts of the EM spectrum. A few include applications of hyperspectral remote sensing in geology (Cloutis, 1996) and MIR characterization of rocks (Cooper *et al*., 2002). Also combined use of spectral remote

sensing to identify possible mineral deposits and geographic information systems (GIS) to integrate geoscience data (Rajesh, 2004).

Initially geologists developed band ratio techniques and selective principal component analysis (PCA) to produce iron oxide and hydroxyl images that could be related to hydrothermal alteration using data from the Landsat Multispectral scanner (MSS) and Thematic Mapper (TM) (Goetz & Rowan, 1981). Various false colour composite (FCC) image schemes have been used to interpret different phenomena such as the R-5/7, G-3/1, B-5 in red-green-blue (*RGB*) shown in Table 3.3 (van der Meer *et al*., 2012). Where RDN is the ratio of value in the ratio image and DN is the digital number intensity in the *i*th or *j*th channel of image acquired, the band ratio imaging is performed according to:

$$\boldsymbol{RDN_{ij}} = \frac{\boldsymbol{DN_i}}{\boldsymbol{DN_j}}. \tag{3.1}$$

Table 3.3: Qualitative interpretation scheme for FCC ratio 5/7, 3/1, 5 in *RGB*

TM ratio[a]			Image Colour	Absorption Feature
Red:5/7	Green:3/1	Blue:5		
H	L	L	Red	H_20, OH, low albedo
H	L	H	Magenta	H_20, high albedo
H	L	M	Pink	H_20, OH
L	M	L	Dark green	Weak Fe^{3+}, low albedo
L	M-H	L-M	Light green	Weak Fe^{3+}, low albedo, H_20, OH, carbonaceous materials
L	M-H	M-H	Cyan	Strong Fe^{3+}, moderate albedo, low H_20
L	L	M	Blue	Moderate albedo
L	M	H	Light blue	High albedo, moderate Fe^{3+}, low H_20
M-H	M-H	L-M	Yellow	Moderate Fe^{3+}, moderate H_20

[a] Relative ratio values: L = low; M = moderate; H = high.

Similarly the French Système Pour l'Observation de la Terre (SPOT) has been used for terrain lithologic mapping (Gad & Kusky, 2000) and semi-automatic detection of faults (Kaya *et al*., 2004). In addition to PCA and band ratio methods for spectral identification, decorrelation stretching and saturation enhancement have also been used and compared (Chavez *et al*., 1991). In these cases spectral gradients expressed as a fraction of average radiance is obtained for highly correlated images by normalizing the intensity pixel by pixel to an average value (Gillespie *et al*., 1987):

$$\boldsymbol{DDN_{ij}} = \left(\frac{\boldsymbol{DN_i - DN_j}}{\boldsymbol{DN_i + DN_j}}\right)\frac{\mathbf{2}}{\boldsymbol{\lambda_i - \lambda_j}}, \tag{3.2}$$

Where DDN_{ij} is the value of the normalized intensity for channels *i* and *j* while λ_i and λ_j are the respective wavelengths. The division by $(\lambda_i - \lambda_j)$ is necessary for DDN_{ij} to be interpreted as a spectral gradient although it does not affect image enhancement. Applying (3.2), a qualitative interpretation scheme for FCC normalized using values from Table 3.3 is presented in table 3.4. Multispectral data have been applied to a variety of other applications including oil seep detection (Macdonald *et al*., 1993) and mineral exploration (Abdelsalam *et al*., 2000) alone or in partnership with airborne geophysical survey and spaceborne radar. In both cases it was necessary to validate the results with 'ocean truth' in the former and supervised classification in the latter. More recently the introduction of the Advanced Spaceborne Thermal Emission and Reflectance Radiometer (ASTER) with three VNIR, six SWIR and five TIR channels (see table 2.3 for sensor configuration) enables the production of qualitative surface mineral maps.

Table 3.4: Qualitative interpretation scheme for FCC ratio 5/7, 3/1, 5 in *RGB*

TM ratio[a]			Image Colour	Absorption Feature
Red: 5/7(N)	Green:3/1(N)	Blue: 5		
M	L	M	Magenta	H_20
H	M-H	L	Yellow	Weak H_20, OH, Fe^{3+}
L	M	L	Dark green	Fe^{3+}
H	L	L	Red	H_20
L	M-H	M-H	Cyan	Fe^{3+}
L	L-H	M	Dark cyan	Low Fe^{3+}
M-H	L-M	L	Brown	Low Fe^{3+}, moderate H_20
H	H	H	White	

[a] Relative ratio values: L = low; M = moderate; H = high.

The narrow bands in SWIR and TIR enable mapping of mineral indices rather than mere alteration indices and has been used to map the mineralogic composition of dune fields (Abrams, 2000; Scheidt *et al*., 2011). Maps of clay (illite), sulfate (alunite), carbonate (calcite, dolomite), iron oxides (hematite, goethite) and silica (quartz) amongst others have been obtained by several proposed band ratios (Cudahy & Hewson, 2002; Rajendran, 2011; Kalinowski & Oliver, 2004). These and other authors propose a range of band combinations and ratios for mapping different minerals. The suggestion is based on the mineral response along with specific FCC's to better highlight alteration intensity.

The advent of high spectral resolution hyperspectral remote sensors has made sub-pixel surface mineralogical mapping possible. The aim of hyperspectral remote sensing (which is also referred to as imaging spectroscopy or imaging spectroscopy) is

to measure quantitatively the components of the Earth System using radiance, reflectance or emissivity spectra acquired in several, narrow and contiguous spectral bands (van der Meer *et al*., 2012). It has been applied to quantify rock or soil chemistry and even physics in combination with derivative image products. However current research focuses on indirect remote sensing where sub-pixel surface compositional information is derived from surface measurements. This requires the development of techniques to match imaged pixel spectra to library and field spectra in order to unravel mixed pixel spectra to pure end member spectra.

There are only very few attempts to link hyperspectral remote sensing to the oil and gas industry (van der Meer *et al*., 2012). These are predominantly focused on detection and characterisation through surface mineral mapping of oil seeps (van der Werff *et al*., 2007), gas seeps (van der Meer *et al*., 2002) and combination of both (Kühn, *et al*., 2004). Also hyperspectral reflectance spectra (8 cm^{-1} resolution), has been used to model the total bitumen content (TBC) in Athabasca oil sands using spectra covering both SWIR and TIR (Lyder *et al*., 2010). Both the wavelet analyses and Gaussian fitting were investigated to identify useful bitumen features at selected (2.274, 2.396, 3.725 μm) and 2.230 – 2.603 μm respectively. The validation was performed using least squares fitting. The corresponding models, extensively used features in the 2.3 μm region which is complicated by the presence of clay and/or water. A simpler prediction of TBC in oil sand used an indirect method to measure and analyze the FTIR spectra of various clay/bitumen composites compared with oil sand from Athabasca mixed in tetrahydrofuran (THF) (Yoon *et al*., 2009). The relationship between concentration ratio bitumen:clay (C^{bitu}/C^{clay}) and absorption ratio (A^{bitu}/A^{clay}) of the created clay composite was used to obtain a predictive model of TBC for Athabasca oil sand. This method is suitable for determining the reflectance data of oil sands however the use of THF could influence the results.

3.1.3. Microwave Applications

Microwaves typically refer to EM waves with frequency, f of 300 MHz to 300 GHz which corresponds to wavelengths, λ of 1 mm to 1 m or in the narrow sense 1cm to 1m (30GHz to 300 MHz). The applications of microwave radiation to oil sand E&P has generally been limited to heating up the reservoir to enhance bitumen extraction, upgrading heavy oils to remove heteroatoms and reduction of oil sands viscosity to

enable pumping to the surface (Mutyala *et al*., 2010). Other applications are shown in Table 3.5. Microwave heating differs from normal heating methods due to the compositional difference in terrain samples. The theory of microwave heating has been discussed in literature resulting in several mechanisms such as Debye (1929), Cole and Cole (1941), Frohlich (1958) and Hill *et al*. (1969) to name a few. Some components of oil sand such as sulfur will be transparent, others like copper will reflect while water molecules will absorb microwaves. A detailed analysis is beyond the scope of this research however microwave heating occurs from three main mechanisms namely: dipolar polarisation, ionic conduction and interfacial polarisation (Mingos & Baghurst, 1991).

Table 3.5: Microwave Applications to Oil Sands

Application	Investigator	Procedure	Results
Separation	Pierre *et al*., 1992	1: 570 g irradiated by 0. 915 GHz, 500 W, t = 5 min. 2: 20 L irradiated by 0.915 GHz, 1500W, t = 20 min.	S1: Several layers. S2: 3 distinct layers with bitumen on top.
	Bosisio *et al*., 1977	Extraction used quartz reactor placed in rectangular microwave (2.45 GHz, 100 W), t = 10 - 15sec, 15sec - 15 min.	Crude oil produced. EM heating increased yields from 70%-86%.
Extraction	Balint *et al*., 1981	Patented technique using microwave feeder pipes and chemicals pumped through oil sand. S1: 5.8 GHz and BTZ[a] S2: 0.915 GHz and CTC[b].	S1: Green oil on top and bitumen at the bottom from oil sand sample. S2: Kerogen extracted was 65% of initial organic content.
	Dumbaugh *et al*., 2001	Laboratory microwave used to irradiate 128 g of oil sand and oil shale. S1: 800 W, t = 10 min, S2: 1500 W, t = 15 min	Both oil sand and oil shale separated into components after 10 min and 15 min respectively.
Recovery	Sahni *et al*., 2000	EM heating used as preheating tool.	Lower frequency waves took longer time than higher frequency
Upgrading	Wolf, 1986	De-emulsification of hydrocarbons and water.	High efficiency in breaking W/O emulsions compared to conventional heating
	Fang *et al*., 1989	Separation of oil from water using gravity sedimentation, conventional heating and microwave radiation.	Microwave demulsification provides improved results.

[a] BTX, Benzene-toluene-xylene-ethylbenzene. [b] CTC, Carbon tetrachloride

Lloydminster oil sands (with oil-water-solids ration of 19:40:41) were exposed to varying frequency and exposure time in order to identify the microwave frequency

best suited for separation (Renouf *et al*., 2003). The samples separated in to a liquid upper layer and mostly solid lower layer with most samples registering little under 27% oil content by weight percent (*wt*.%) in the lower layer. The best results reportedly occurred when the samples were irradiated for 10 minutes (600 seconds) at 6.4 GHz (± 100 MHz) where the lower layer only had 19% oil content. Other results are shown in Table 3.5. Although success has been achieved for relatively small sample sizes, microwaves will not be practical for use in heating large petroleum deposits. In this research the aim is not to use microwave energy to heat, extract, separate or recover bitumen from oil sands but rather develop microwave scattering data and hyperspectral reflectance data that can aid the E&P of oil sand from airborne and spaceborne platforms.

3.2. Sensors for EM Characterization

The characterization of materials at radio frequencies (RF) has existed for over 100 years and is often referred to as *dielectric spectroscopy* (Jol, 2009). In this section we are interested in the performance of hyperspectral and SAR for conventional hydrocarbon exploration. We consider the performance of EM waves for terrain identification from both satellite and airborne platforms. In the microwave region this has been limited to either tectonic studies to guide exploration towards basins with prolific hydrocarbon reservoirs or large scale structural mapping in tropical cloudy areas. This is because it is difficult to conclusively distinguish between terrain types. However, SAR usage has led to several large petroleum discoveries such as the P'nyang gas field with 3.5 trillion cubic feet (TCF) of gas and the Shan-shan fields with 350 million barrels of oil (Berry & Prost, 1999).

3.2.1. Satellite Systems

A few SAR satellite sensors that could have generated data for oil sand exploration include the advanced SAR (ASAR) on EnviSAT, RadarSAT-1 and the Spaceborne Imaging Radar C/X (SIR-C/X) which are no more operational. Currently available satellite sensors include RadarSat-2 and TerraSAR-X amongst others. A few characteristics of commercially available SAR sensors are shown in Table 3.3. They indicate that major bands used by SAR systems are the L, C and X-bands. Also spatial resolution can be as fine as 1 m for TerraSAR-X while incident angles vary from 20 –

55° at multiple polarisations such as vertical transmit and vertical receive (VV), horizontal transmit and receive (HH) and a combination of both (either HV or VH). Multiple incidence angles permit frequent observations of terrain while multi-polarisation enable the acquisition of multi-channel information. Wide swath areas permit coverage of large areas while fine resolution enables greater spatial detail.

Table 3.6: Commercial SAR Sensors

Parameters	ASAR	SIR-C/X	TerraSAR-X	RadarSAT-1
Wavelength (cm)/Band/Freq. (GHz)	5.7/C/5.3	23.5/L/1.25 5.8/C/5.3 3.0/X/9.6	3.1/X/9.7	5.6/C/5.3
Polarisation	VV/HH HV/VH	VV/HH HV/VH	VV, HH	HH
Swath (km)	100	50-500	10-100	45-500
Incidence angle (deg)	23	20 – 55	20-55	10 - 49
Resolution (m)	28	30	1-16	8-100

The first satellite imaging spectrometer was the Lewis Linear Etalon Imaging Spectral Array (LEISA) Hyperspectral Imager (HSI) with 384 continuous spectral bands from 0.4 – 2.5 μm (Marmo *et al*., 1996). It was launched in 1997 but failed after 3 days in orbit. Based on the Lewis concept the National Aeronautics and Space Administration (NASA) launched Hyperion with 220 spectral bands (0.4 - 2.5 μm i.e. VNIR/SWIR), 30 m spatial resolution and 7.5 km by 100 km area per frame (Pearlman *et al*., 2003). It maintains a 705 km circular sun-synchronous orbit at 98.7° inclination in order to remain compatibility with Landsat 7 orbit. Also the European Space Agency (ESA) operates the Compact High Resolution Imaging Spectrometer (CHRIS) with 19 spectral bands on board the project for onboard autonomy (Proba-1). It measures directional spectral reflectance using multiple viewing and illumination geometries over 0.415 - 1.050 μm, spectral resolution of 5 - 12 nm, nadir spatial resolution of 20 m on 14 km swath (Barnsley *et al*., 2004). According to Buckingham and Staenz (2008), other sensors present or planned include ESA's MultiSpectral Imager (MSI) on the Sentinel-2 mission with 13 spectral VNIR to SWIR (4 spectral bands at 10 m, 6 bands at 20 m and 3 bands at 60 m spatial resolution). Also NASA is developing the HYperSPectral InfRared Imager (HyspIRI) with which is an imaging spectrometer that measures from VNIR to SWIR and a TIR imager both at a spatial resolution of 60m at nadir.

The interactions between frequency, polarisation, resolution and incidence angle with terrain determines the backscattering response of the terrain. The *radar signature* of terrain in the microwave region is not as unique as the *spectral fingerprint* in the IR region due to the coarser spectral resolution from microwave wavelengths (Fig. 3.3a). However the transmission of IR energy in the atmosphere is limited by molecules of water, carbon dioxide and oxygen which tend to absorb solar radiation (Fig. 3.3b). Therefore radar remote sensing is mostly achieved using the 1mm – 1m *atmospheric window* which permits the greatest transmission of microwave energy unlike hyperspectral that could sometimes be absorbed.

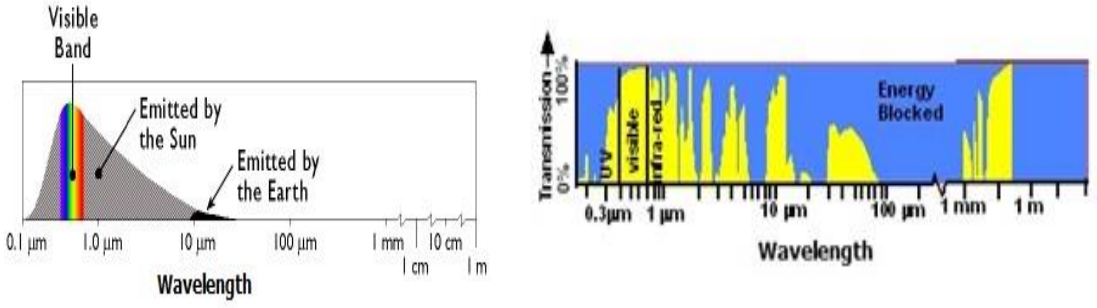

(a) (b)

Figure 3.3: Spectral characteristics of (a) energy sources (b) atmospheric transmittance (Modified from Lillesand *et al*., 2004).

A typical SAR satellite that may be used for oil sand exploration is the RadarSAT. RadarSAT-1 and 2 are Canadian remote sensing satellites launched with inbuilt SAR sensors in 1995 and 2007 respectively. Both satellites have 7 different imaging modes such as standard, wide swath and fine resolution beams. These modes differ in resolutions, swath widths and incidence angles as shown in Fig.3.4 (CSA, 2006). RADARSAT-2 is an improvement on RADARSAT-1. Unlike the former, it has finer azimuth resolution of 1m and can operate at multiple polarisations including HH, VV, HV and VH. Fine resolution (8m) RADARSAT-1 imagery acquired with standard beam 1, *SB1* (20 - 27°) and *SB7* (45 - 49°) for two different incident angles have been combined with digital elevation models (DEM) to successfully identify surficial sediments including oil sand in North Alberta, Canada (Mei & Paulen, 2009). This is a remote location region constrained by lack of infrastructure access. When *SB1* and *SB2* imagery were used to contrast radar responses from two different incident and look directions, different cover types such as wetland/organic deposits were highlighted.

This was due to the effect of the variations in incidence angles as a function of different moisture and surface roughness response.

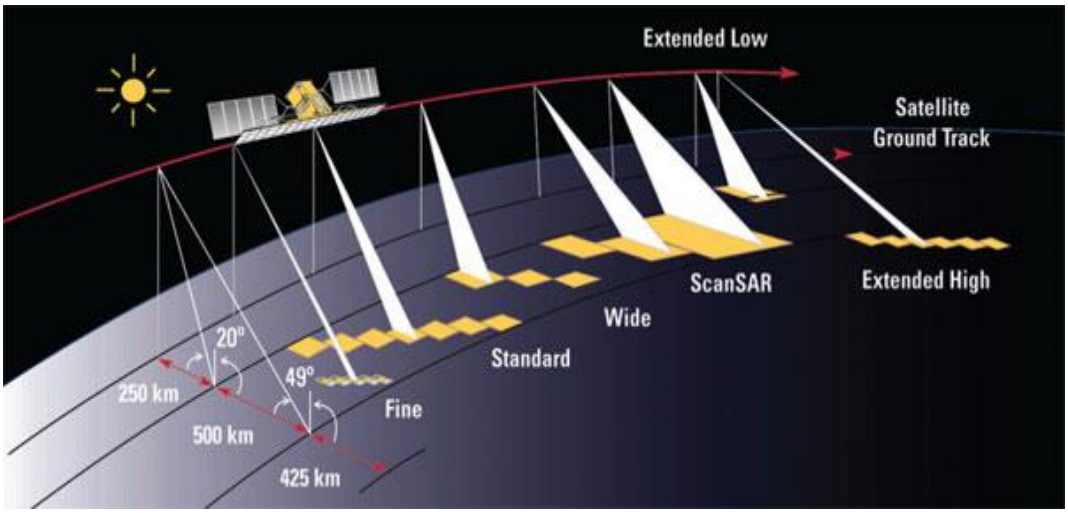

Figure 3.4: RADARSAT Imaging Modes (CSA, 2006).

3.2.2. Airborne Systems

The Airborne Visible/Infrared Imaging Spectrometer (AVIRIS) was the first imaging sensor to measure the solar reflected spectrum from 0.4 – 2.5 μm at 0.01 μm intervals in 1987 (Green *et al*., 1998). Prior to this a one dimensional profile spectrometer developed by the Geophysical Environmental Research Company had acquired data in 576 channels in 1981 (van der Meer *et al*., 2012). Since then several hyperspectral sensors have been in operation with more in development (Buckingham & Staenz, 2008). The pathfinder hyperspectral sensor is an AVIRIS that can operate from a variety of aircraft providing a high SNR and nominal 20 m spatial resolution from an altitude of 20 km (~65 000 ft). Other sensors include the Canadian Compact Airborne Spectrographic Imager (CASI), CASI 1500 and Shortwave IR Airborne Spectrographic Imager (SASI), SASI 600 described by Babey and Anger (1993). Also the US Naval Research Laboratory hyperspectral digital imagery collection experiment (HYDICE) discussed by Basedow *et al*. (1996).

More recently helicopter time domain electromagnetic (HTEM) and AEM methods are gaining prominence (Cox *et al*., 2012). Airborne SAR systems such as the EMISAR and AIRSAR have similar trade-offs with satellite SAR systems although they can obtain finer resolution due to geographic effect but require corrections for

flight trajectory (Ezeoke *et al*., 2012; Skriver *et al*., 2000; Schaber, 1999). Both frequency-domain (FDM) and time-domain techniques (TDM) have been used to focus Airborne SAR from non-linear flight tracks (Frey *et al*., 2009). Another technique that can be used for oil sand exploration is the use of AEM sensors shown in Fig. 3.5. Due to the airborne platform this technique can also cover large areas in less time than geophysical exploration methods and for cheaper cost (Fountain, 1998). The AEM technique is useful for geological exploration of electrically conducting targets (Palacky & West, 1991; Spies *et al*., 1998). It has also been used in environmental studies to map salinity distribution and hydrogeological features in alluvial aquifers amongst others (Kirkegaard *et al*., 2011; Dickinson *et al*., 2010).

The AEM operation differs slightly from SAR. Rather than just detect the magnitude of backscattering it deliberately induces current in the ground. This is done with an airborne transmitter loop acting as a magnetic dipole source to generate primary magnetic field. The induction process causes EM fields to diffuse slowly in to the conductive ground which establishes an EM response or secondary magnetic field which is detected by the receiver loop. The mathematical theory has been considered by Ward & Hohmann (1987) and this technique is still under commercial investigation (Cristall *et al*., 2004). It works on the principle that different terrain layers can be defined by electrical conductivity (or resistivity) and thickness. AEM data received from TDM or FDM surveys are inverted to estimate the bedrock topography or sediment thickness.

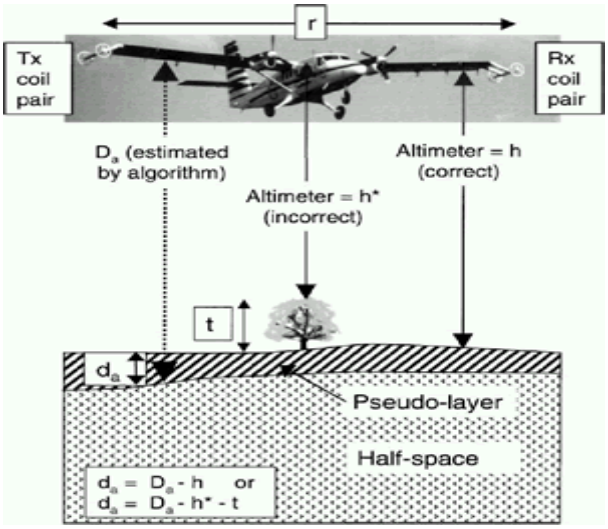

Figure 3.5: Airborne Electromagnetic Survey (Oldenburg & Jones, 2007).

3.3. Electromagnetic Interaction with Barefaced Terrain

An EM field occurs when an electromagnetic force (EMF) excites an electrically charged object. The EM field consists of a combination of electric or *E*-field and magnetic or *H*-field. The E-field expresses the relationship between two or more point charges derived from Coulombs law with units in volts per meter (Vm^{-1}). H-field sometimes referred to as the magnetic field strength is produced by the movement of electric charges and measured in amperes per meter (Am^{-1}). The electric field, magnetic field and direction of propagation are always orthogonal such that an EM wave propagating in the +*x* direction ($\overline{\boldsymbol{E}}$ x $\overline{\boldsymbol{B}}$) is given by:

$$\overline{\boldsymbol{E}} = \boldsymbol{E_{max}}\, \boldsymbol{cos}\left(\frac{\boldsymbol{2\pi x}}{\boldsymbol{\lambda}} - \boldsymbol{2\pi f t}\right)\hat{\mathbf{j}} \tag{3.3}$$

$$\overline{\boldsymbol{B}} = \boldsymbol{B_{max}}\, \boldsymbol{cos}\left(\frac{\boldsymbol{2\pi x}}{\boldsymbol{\lambda}} - \boldsymbol{2\pi f t}\right)\hat{\boldsymbol{k}} \tag{3.4}$$

Here $E_{\max}$ and $B_{\max}$ represent the electric and magnetic field strengths respectively. A time dependence form of $\overline{\boldsymbol{E}}$ and $\overline{\boldsymbol{B}}$ in (3.3) and (3.4) will be used, which implies that the actual field is determined by the real components of these vectors namely Re [$\boldsymbol{E}$] and Re [$\boldsymbol{B}$] (Ulaby & van Zyl, 1990). When an *E*-field of wave $\mathbf{E}^{inc}$ is incident on the boundary surface between different media, some of the incident field is scattered backwards, $\mathbf{E}^{ref}$ and the rest is absorbed, $\mathbf{E}^{abs}$. Therefore the *E*-field of the total signal of interaction $\mathbf{E}^{tot}$ is given by:

$$\mathbf{E}^{tot} = \mathbf{E}^{inc} + \mathbf{E}^{ref} + \mathbf{E}^{abs} \tag{3.5}$$

The SAR sensor on board a satellite or spacecraft measures the reflected or backscattered signal $\mathbf{E}^{ref}$. Opportunities exist for SAR remote sensing in low relief basins such as the Nigerian 'Dahomey' or western Canada Basin in which large amount of oil sand is assumed to exist (Amigun *et al*., 2012; Odunaike *et al*., 2010; Ako *et al*., 1983). In order to identify oil sand from amongst other terrain types it is vital to grasp the radar signature of the oil sand terrain and how it affects radar backscatter.

3.3.1. Backscattering Phenomena

The radar backscattering coefficient, σ^0 responds to two broad factors. These are physical and electrical factors. The local imaging geometry also exerts influence

(Table 3.7). Understanding the relationship between a SAR sensor and object or terrain parameters determines the use of SAR for oil sand exploration.

Table 3.7: System and Terrain Parameters Influencing Radar Backscatter

SAR Parameters	Terrain Parameters
Frequency or Wavelength	Surface roughness
Polarisation	Dielectric properties
Look or incidence angle	Slope and orientation
Resolution	Surface features

Here we consider a SAR in a fixed position relative to the terrain target. This means that we do not bother with the nature of the transmitted signal, the velocity of the sensor platform relative to the mean surface or the possibility of local motion within the surface such as leaves or grass. This enables us to focus on the terrain characterization and classification. If we consider the geometry for a SAR sensor in an instantaneous point in time with respect to an arbitrary area *dA* shown in Fig. 3.6. Then from (2.7) the general SAR radar equation can be adapted to consider backscattering within a resolution cell, ∂A.

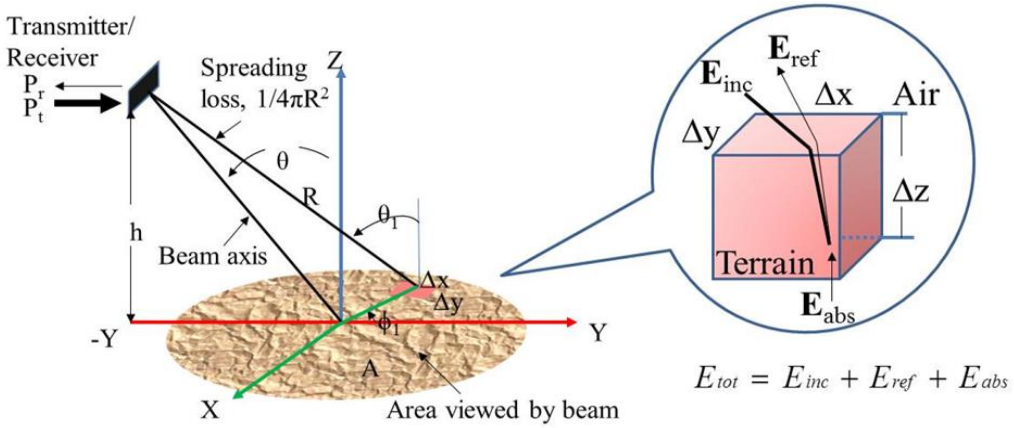

Figure 3.6: Backscattering from elemental area of terrain (Ezeoke & Tong, 2012).

In this sense the power received by the sensor, P_{rx} is given by:

$$\frac{\boldsymbol{\lambda^2}}{\boldsymbol{(4\pi)^3}} \cdot \iint_{\substack{\boldsymbol{Illuminated} \\ \boldsymbol{Area}}} \frac{\boldsymbol{P_{tx} G_{tx(\theta_i,\phi_i)} G_{rx(\theta_i,\phi_i)}}}{\boldsymbol{R^4}} \boldsymbol{\sigma^0_{rxtx}(\theta_i, \phi_i) \partial A} \tag{3.6}$$

Here $P_{tx}(\theta)$ is the transmitted power at polarisation, *tx*, and (θ_i, $\emptyset_i$) are angular coordinates to elemental area, ∂A or elemental volume $\partial V = \partial A \partial z$. Lastly, $G_{tx}(\theta_i, \emptyset_i)$

and $G_{rx}(\theta_i, \emptyset_i)$ are the transmit and receive antenna gain in direction to ∂A. In addition $\sigma^0_{rxtx}(\theta_i, \emptyset_i)$ is the backscattering coefficient of elemental area ∂A for *tx*-polarized illumination and *rx*-polarized receiver. For SAR imaging, the terrain is located at the far field of the incident *E*-field. Therefore a plane wave can be used to represent this incident field so that G_{tx}, G_{rx} and R will be constant over the beam solid angle. Also ∂A can be considered so small that σ^0_{rxtx} could be assumed to be constant i.e. σ^0. Therefore (3.4) may become,

$$\boldsymbol{P_{rx}(\theta)} = \left(\frac{\boldsymbol{P_{tx}G^2(\theta)\lambda^2}}{\boldsymbol{(4\pi)^3R^4}}\right)\sigma^0. \tag{3.7}$$

This agrees with what has been reported in Ulaby *et al*., (1982) on the premise that several individual point scatterers exist per specific area and more scatterers exist in the total illuminated area. For an elemental area, ∂A the system factors from (3.4) and (3.5) are typically constant meaning that the backscattering coefficient, σ^0 is the single differentiating factor for the representation of a target in the radar image. For extensive terrain the backscattering coefficient, σ^0 is considered as RCS over the unit area (m^2m^{-2}) or volume (m^3m^{-3}) although its units can also be considered dimensionless.

3.3.2. Physical Properties

Physical factors cover both texture and geometric properties such as porosity and roughness. Texture refers to the interrelationships among the target population and covers features such as shape, orientation, grain size and packing (Krynine, 1948). These features determine the degree of roughness or texture for a particular terrain. Two statistical parameters are used to describe the degree of roughness namely, the standard deviation of the surface height variation, σ or root mean square (r.m.s) height, h_{rms} and the surface correlation length, l (Beckmann & Spizzichino, 1963). The r.m.s height indicates the vertical roughness of the surface, h when compared to the average height, $\overline{h}$. It is given as:

$$\boldsymbol{h_{rms}} = \sqrt{\left(\frac{\sum_{i=1}^{n}(\boldsymbol{h_i} - \overline{\boldsymbol{h}})^2}{\boldsymbol{n}}\right)} \tag{3.8}$$

The manner in which EM field $\mathbf{E}^{ref}$, is reflected from a terrain target depends on the surface roughness of the boundary separating two semi-infinite media. A monostatic

SAR which has both transmitter and receiver at the same location would be unable to receive any return power from a smooth surface except at 90° incidence. As we move from the smooth to rough surface (left to right) in Fig. 3.7 the angular radiation pattern of the reflected wave changes from a delta function centered in the specular direction to non-coherent diffuse reflection. Therefore both wavelength, λ_i of the incident EM radiation and the angle of incidence, θ_i contribute to the reflected radiation. Also the magnitude of the return signal is much less than the incident wave.

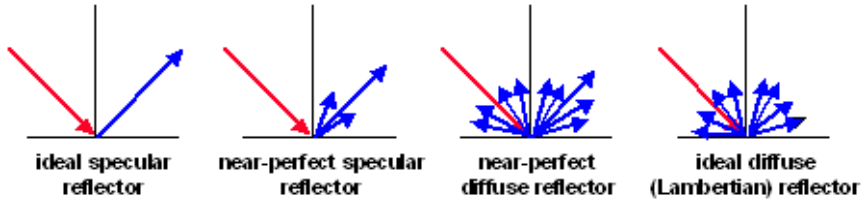

Figure 3.7: Examples of surface scattering patterns.

Due to the wide variety of texture features, several theoretical models relate the backscattering coefficient, σ^0 to physical parameters of roughness. The three most renowned models are the physical optics (POM) or Kirchhoff Scattering (KSM), geometrical optics and small perturbation models. The physical optics model (POM) developed by Beckmann-Spizzichino (1963) is useful for EM scattering from rough surfaces with relatively small slopes where both standard deviation and correlation length are larger than wavelength (Papa, 1988; Nayar *et al*., 1989). The geometrical optics model (GOM) associated with Torrance-Sparrow (1966) requires both small slopes and large Rayleigh roughness parameters to be accurate (Nayar *et al*., 1991). The small perturbation model (SPM) is useful for moderate roughness where $k\sigma = 0.5$ but unworkable where it exceeds 1.5 (De Roo & Ulaby, 1996). In order to apply a model it is important to satisfy the conditions that determine the validity of the model. Summary of the validity conditions for each model is presented in Table 3.8.

Table 3.8: Validity Conditions for Theoretical Models

Model	Validity Condition	Remarks
Physical Optics model	$m < 0.25$ $kl > 0.6$	Surface irregularities large compared to λ i.e. average radius of curvature of local surface, $R_c >> \lambda$
Geometrical Optics model	$(2k\sigma \cos \theta)2>10$, $12=2.76\sigma\lambda$	High frequency geometric optics limit, $\lambda \rightarrow 0$. Valid only when $\sigma >> \lambda$
Small Perturbation model	$m < 0.3$ $k\sigma \leq 0.3$	Required that $\sigma << \lambda$ and m should be of same magnitude as $k\sigma$.

Greffet (1992) used SPM to explain the downward shift in the Brewster angle as surface roughness increases. These theoretical models apply to surface roughness where, σ is the standard variation r.m.s height, l is the surface correlation length in terms of wavelength, m is r.m.s surface slope and k is wavenumber or propagation constant given by ($2\pi/\lambda$). These empirical models are useful guides for prediction of terrain behaviour although some investigators have achieved different results (Fung *et al*., 1974; Lentz, 1974; Ulaby *et al*., 1982). Nevertheless practical SAR studies over geological terrain have successfully classified data using the Rayleigh Criteria (Schaber *et al*., 1976; Schaber, 1999).

The relationship between wavelength, λ and incidence angle, θ_i to surface r.m.s roughness, h_{rms} has been described by Rayleigh criterion which considers a surface smooth if $h_{rms} < \lambda /8 \cos\theta$ (Beckmann & Spizzichino, 1963). Ulaby *et al*., (1982) characterize this for a random surface with $\sigma < \lambda /8\cos\theta$. Also Peake & Oliver (1971) define upper and lower values for surfaces with intermediate roughness such that clearly smooth occurs when $\sigma < \lambda /25\cos\theta$ and clearly rough if $\sigma < \lambda /4.4\cos\theta$. A more stringent condition has been suggested for modeling the scattering behaviour of natural surfaces in the far-field region. This is known as the Fraunhofer criterion given by $\sigma < \lambda /32 \cos\theta$ (Ulaby *et al*., 1982). Using typical band values from SAR systems minimum heights for scattering detection were derived (Table 3.9).

Table 3.9: Standard Deviation of Surface Height for Four Roughness Criteria

SAR Band	Wavelength (cm)	Rayleigh Transition	Rayleigh Rough	Rayleigh Smooth	Fraunhofer Smooth
25% Incidence Angle					
L	**23.5**	**3.24**	**5.89**	**1.04**	**0.81**
C	**5.7**	**0.79**	**1.43**	**0.25**	**0.20**
X	**3.1**	**0.42**	**0.78**	**0.14**	**0.11**
35% Incidence Angle					
L	**23.5**	**3.59**	**6.52**	**1.15**	**0.90**
C	**5.7**	**0.86**	**1.58**	**0.28**	**0.22**
X	**3.1**	**0.47**	**0.86**	**0.15**	**0.12**
45% Incidence Angle					
L	**23.5**	**4.15**	**7.55**	**1.33**	**1.04**
C	**5.7**	**1.01**	**1.83**	**0.32**	**0.25**
X	**3.1**	**0.53**	**0.99**	**0.17**	**0.14**
55% Incidence Angle					
L	**23.5**	**5.12**	**9.31**	**1.64**	**1.28**
C	**5.7**	**1.2**	**2.25**	**0.40**	**0.31**
X	**3.1**	**0.67**	**1.23**	**0.22**	**0.17**

A comparison of the relative surface height to produce a *Rayleigh rough* for L, C and X-bands using SAR sensor is discussed in Appendix 3. The surface standard

deviation is typically considered with the surface correlation length. Together both describe the statistical variation of the surface height relative to a reference (Ulaby *et al*., 1982). The correlation length, l is used to support height variation estimation where two horizontal points separated by a distance greater than l are considered to be statistically independent. For a perfectly smooth surface, $l = \infty$.

3.3.3. Electrical Properties

In addition to physical structure, scattering and absorption of EM waves is dependent on the electrical properties of the terrain such as the electrical permittivity, ε and magnetic permeability μ. The effects of EM field propagation in free space and attenuation within the medium also play a role. At microwave frequencies magnetic permeability is taken as unity (Peake & Oliver, 1971). The microwave dielectric properties of terrain depend on the moisture content, frequency and the textural composition (Ulaby *et al*., 1982; Ulaby, 1982). For a homogenous medium the dielectric constant is static however for oil sand terrain this is not the case and anisotropic medium modelling is more suitable. The analysis of dielectric constant relates Maxwell's equation for a source free region with the constitutive parameters of permittivity ε, in Farads per meter (Fm^{-1}) and electrical conductivity σ', in Siemens per meter (Sm^{-1}). In the time domain form, the equations for a heterogeneous media are given by (3.9) – (3.11) for stationary terrain (Jol, 2009),

$$\boldsymbol{D} = \boldsymbol{\varepsilon E} \tag{3.9}$$

Where $\boldsymbol{D}$ = electric flux density vector in Coulombs per meter squared (Cm^{-2}).

$$\boldsymbol{J} = \boldsymbol{\sigma' E} \tag{3.10}$$

Where $\boldsymbol{J}$ = current density vector in Amperes per meter squared (Am^{-2}).

$$\boldsymbol{B} = \boldsymbol{\mu H} \tag{3.11}$$

Where μ = permeability of the material or terrain in Henrys per meter (Hm^{-1}). Terrain is considered a 'lossy' dielectric material because although non-conducting it can accept EM field and in turn produce attenuation, scattering and energy loss (absorption). The behaviour of EM field with oil sand terrain has not been investigated. Permittivity refers to the ability of a material to store and release an electric charge. This ability is classically described by a capacitor. Raney (1998) considers the complex

electric permittivity, ε_c to describe the principal mediums response to an electric field. It is often called dielectric constant given by:

$$\boldsymbol{\varepsilon_c = \varepsilon' - j\varepsilon'' = \varepsilon_0(\varepsilon_r' - j\varepsilon_r'')} \quad (3.12)$$

Here vacuum permittivity, $\varepsilon_0 = 8.85 \times 10^{-12}$ (Fm^{-1}), ε' is the *absolute* real and ε_r' is the *relative* real values of the dielectric constant. For most materials both ε' and ε_r' may be found in literature but the difference between both values are sometimes unclear. The latter represents an intrinsic property of the terrain or target-object but has been cited in literature simply as *dielectric constant*. For consistency with other publications (Ulaby *et al*., 1982; Dobson & Ulaby, 1998) both ε' and ε_r' will be referred to as dielectric constant within this research. At the molecular level, the dielectric constant is a measure of the ability to obstruct microwave energy while ionic and dipole properties are measures of how the molecule adsorbs microwave energy. It would be expected that sulfur-containing and nitrogen-containing compounds would have high dielectric constants and dipole moments (Mutyala *et al*., 2010). This should mean oil sand is more sensitive to microwave radiation.

The real part of the dielectric constant influences the wave propagation, depolarisation and defines the amount of energy scattered or stored. This polarisation at the boundary between two semi-infinite layers produces a separation of electrical charges. The force of separation is defined by ε_r'. The imaginary part is a measure of the absorption or loss properties of the terrain or target-object. Consequently the relationship between the two defines the amount of energy lost in the terrain. It is common to express the loss property using the loss tangent, tan δ as:

$$\boldsymbol{\tan\delta = \frac{\varepsilon_r''}{\varepsilon_r'}} \quad (3.13)$$

For an incident pulse of EM energy propagating through a material, the loss tangent may be used as limiting expression for low loss assumptions. It describes the ratio of EM energy loss factors ($C_t' + \omega\varepsilon''$) to energy storage ($\omega\varepsilon' - C_t''$) (Jol, 2009). Here real and imaginary conductivity of the medium are given by C_t' and C_t''. This allows the propagation velocity in the material, v_m and wavelength λ_m in terrain to be approximated by (3.14) and (3.15).

$$\textbf{Velocity in terrain,} \qquad v_m = \frac{c}{\sqrt{\varepsilon\mu}} \tag{3.14}$$

$$\textbf{Wavelength in terrain,} \qquad \lambda_m = \frac{v_m}{f\ (in\ Hz)} \tag{3.15}$$

Energy transfer from incident radiation to the terrain generates a small *displacement current* which slows down the velocity of the incident propagating wave. This means that the approximate velocity of EM wave in terrain is related to the dielectric properties. As ε_r increases, velocity of EM wave propagation, v_m reduces with the wavelength, λ_m (Fig. 3.8).

The conductivity σ' refers to the ability of terrain or material to transfer electric charges in response to an applied field. In dielectric materials there are both free and bound charges, so that both conductivity and dipolar effects contribute to the dielectric loss such that:

$$\varepsilon_r'' = \varepsilon_{cond}'' + \varepsilon_{dipol}'' \tag{3.16}$$

This is typically explained by the movement of free electrons in metals or charge carrier transfer of dissolved anions and cations in fluids such as Na^+, Ca^{2+}, Cl^- and CO_3^{2-} (Jol, 2009).

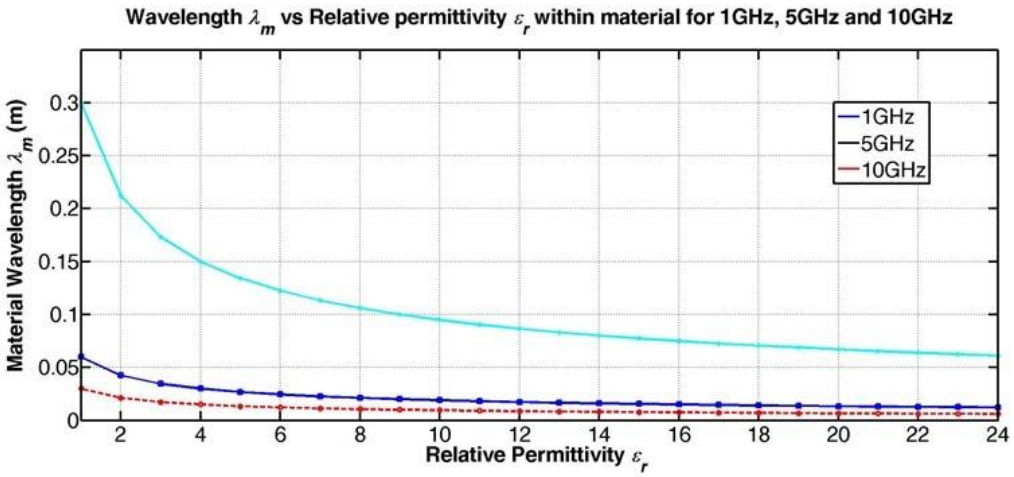

Figure 3.8: Normalized wavelength vs. relative permittivity at L, C and X-band

The conductivity contribution is dominant at low frequencies, f of applied electric field. In cases where the directly measured conductivity is frequency-independent, the loss factor is proportion to the reciprocal of applied frequency. In essence:

$$\varepsilon''_{cond} = {C'_t}/{(2\pi f \varepsilon_0)} \quad (3.17)$$

The reliability of dielectric measurements for terrain seems to vary with the investigator but most natural materials have relative permittivity, ε_r values ranging from 2 – 10 at microwave frequencies. In very dry materials microwave dielectric permittivity will range from 1.2 – 6 while the loss tangent will seldom exceed 0.1 (Ulaby, 1982). Estimated dielectric properties of materials from literature are shown in Table 3.10 where the relative permittivity values for desert dry sand were verified for antenna frequency of 100 MHz (Jol, 2009) and 14 GHz (Oliver & Peak, 1971). The default values used in the computer simulation technology (CST) microwave studio (MWS) EM model software database is also shown (CST MWS, 2012).

Table 3.10: Dielectric Constant for Different Materials at 100 MHz and 14 GHz

Material	Loss Tangent	Relative Permittivity	CST MWS Database Values
Air	0	1	1+j0
Dry sandy soil	0.004	3-6	2.53 + 0.004
Wet sandy soil	0.29	10-30	13 + j0.29
Dry loamy soil	0.0014	4-6	2.44 + j0.0014
Wet loamy soil	0.18	10-20	13.80 + j0.18

The dielectric constants for rocks and minerals with viscous properties similar to oil sands tend to vary in proportion to the density and are almost independent of frequency (Peake & Oliver, 1971). Little research has been done to evaluate the dielectric constant of oil sand terrain consequently dielectric and bitumen electrical properties are scarce in literature but those obtained vary from 2.48 – 7 (Table 3.11).

Table 3.11: Survey of Dielectric Constants obtained for Oil Sand, Asphaltenes and Bitumen

Dielectric Constant	Investigator	Remarks
6 - 7	Bertholet et al., 2010	Investigated bitumen base for road transport using GPR
4.3 – 5.4	Evdokimov & Losev, 2010	Found ε to be freq. and temp. independent
3.83	Rejon, Manero & Lira-Galeana, 2004	Used DC electric fields to characterize structural, rheological and dielectric behaviour
2.8 – 3.2	Erdogan *et al*., 2011	Used rectangular cavity resonator at 2.45 GHz
2.0-2.2, 2.7	Tao & Xu, 2006	Measured crude oil viscosity
2.48 – 2.71	Pedersen, 2000	Permittivity measurement and modeling.
2.7 – 3.0	Read & Whiteoak, 2003	Bitumen is freq. independent. ε = 2.7 at 25° but 3.0 at 100°

3.3.3.1 Penetration Depth

Another group of parameters used to describe the electrical properties of matter or terrain is the complex propagation constant, γ. It is given by

$$\boldsymbol{\gamma = \alpha + j\beta = \sqrt{(\sigma' + j\omega\varepsilon) j\omega\mu}} \tag{3.18}$$

Here the real part, α is the attenuation constant (nepers/meter) and the imaginary part β is the phase constant (radians/meter). For a plane wave propagating in the z direction in a terrain medium with parameters ε_0, ε_c, μ_0 the wavelength in vacuum $\lambda_0 = 2\pi / (\omega\sqrt{\epsilon_0 \mu_0})$ and the complex index of refraction $n_c = \sqrt{\epsilon_c}$. In this sense the depth of penetration or skin depth in the medium, δ_p is 1/ α (Oliver & Peak, 1971). It is defined as the depth at which the magnitude of the power transmitted within terrain has reduced by a factor of e^{-1} or 37% (Reynolds, 1997). Where $\mathbf{I}_{inc}$ is the intensity of the transmitted wave at the interface between two media and $\mathbf{I}(\delta_p)$ is the intensity of the wave at the depth of penetration point in the medium, then mathematically $\delta_p = \mathbf{I}(\delta_p)/ \mathbf{I}_{inc} = e^{-1}$. It is related to the radar wavelength, incident angle and attenuation loss according to:

$$\boldsymbol{I(r) = I_{inc}.e^{-\alpha\vec{r}}} \tag{3.19}$$

If scattering losses are ignored, δ_p can be expressed as (Ulaby, 1982):

$$\boldsymbol{\delta_p = \frac{\lambda_0}{4\pi|\mathrm{Im}[\sqrt{\varepsilon}]|}} \tag{3.20}$$

Where λ_0 is the wavelength in free space and $\varepsilon = \varepsilon' - j\varepsilon''$ is the relative complex dielectric constant of the terrain. For most natural terrain except water, the relationship $\varepsilon''/\varepsilon' << 1$ holds true, which leads to the approximate expression:

$$\boldsymbol{\delta_p = \frac{\lambda_0}{2\pi}\frac{\sqrt{\varepsilon'}}{\varepsilon''}} \tag{3.21}$$

For 2-way attenuation in dBm^{-1}, the attenuation loss for different depths is given (Jol, 2009) as:

$$\boldsymbol{\alpha = 8.686 \text{ x } 2 \text{ x } r \text{ x } 2\pi f\sqrt{\left(\frac{\mu_0\mu_r\varepsilon_0\varepsilon_r}{2}\left(\sqrt{1+\tan^2\delta}\right)-1\right)}} \tag{3.22}$$

Fig. 3.9 shows the increasing two-way attenuation measured against frequency at different depths for wet and dry sandy soil using data from Table 3.10. Attenuation loss in dBm^{-1} increases with the depth of penetration. Also higher frequencies experience greater loss. Theoretically for C-band, penetration depth is considered for the upper 1-2 centimeters (Löw, 2004). This research uses computer simulation tools and modeling techniques to characterize and visualize EM behaviour for different terrain at greater depths and for different frequencies and incident angles.

It is also evident that the attenuation loss in wet sand is higher than in dry sand. This can only be due to the effect of the water content on the electrical properties particularly dielectric constant and loss tangent.

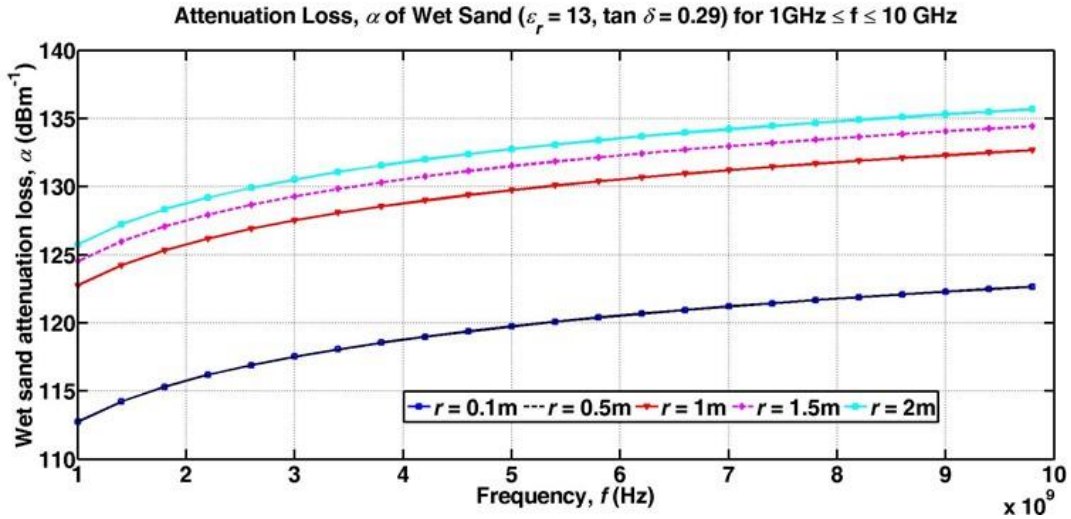

(a)

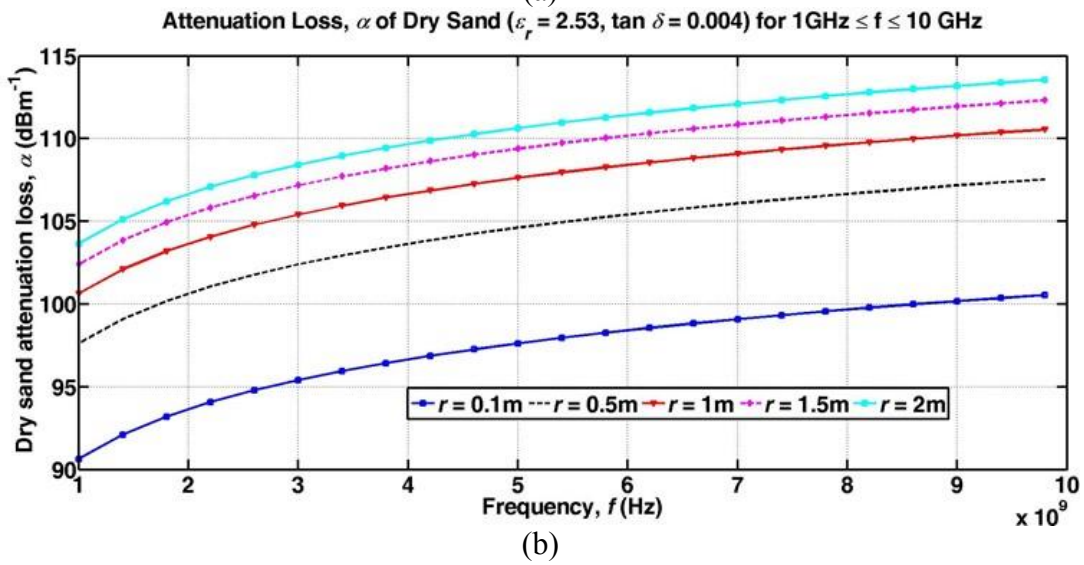

(b)

Figure 3.9: Theoretical attenuation loss for sand at various depths from the surface (a) Wet (b) Dry

3.3.3.2 Moisture and Mineral Content

Electrical conductivity, permittivity and energy dissipation increase with increasing water, soluble salts and clay contents within terrain (McNeill, 1980; Campbell, 1990). This is because electrical charge transport and storage is determined by the terrain composition and dielectric constant. The microwave spectra scale for the real ε' and imaginary ε'' permittivity of water are orders of magnitude larger than for dry materials (Ulaby, 1982). Therefore the presence of moisture will dramatically alter the behaviour of oil sand terrain under incident EM fields. The dielectric constant of liquid water has been reported in literature to be as high as 80 (Mätzler, 1987). Traditional methods of estimating soil moisture content may be destructive such as gravimetric or non-destructive like neutron thermalization. More recently EM-wave techniques such as ground penetrating radar (GPR) and time domain reflectometry (TDR) are gaining prominence. This research does not explicitly try to determine the moisture content in oil sand terrain. However during experiments to determine the geochemical signature this will become more evident in chapter 4 while the permittivity measurement of oil sand and other barefaced terrain will be investigated in chapter 5.

Water is a polar molecule which experiences permanent dipole realignment parallel to the direction of an applied electrical field. Clay particles (<0.002mm in diameter) have greater surface areas and can potentially hold more water than silt (particles 0.02 – 0.05mm in diameter) or sand (particles 0.05-2.0mm in diameter). Terrain with low salt concentrations will be more susceptible to the effects of clay particle presence on electrical conductivity than others (Klein & Santamarina, 2003). A lot of studies deal with the retrieval of soil moisture for bare soil conditions using space and airborne SAR systems (Dobson & Ulaby, 1998; Engman & Chauhan, 1995). They conclude that there are typically high spatial and temporal variations in the degree of soil moisture content. Consequently, the models developed in chapter 6 reflect variations in the overall composition of terrain rather than just soil moisture.

3.3.3.3 Dielectric Models

Water and ice are homogenous media unlike natural surfaces such as soil or vegetation. For heterogeneous substances the dielectric constant is typically determined or calculated using mixture models. Several theoretical and semi-empirical models exist in literature. They describe the dielectric behaviour as a function of moisture content

(e.g. Serbin *et al*., 2001; Peplinski *et al*., 1995; Hallikainen *et al*., 1985). For microwave remote sensing the most widely used are the dual dispersion model of Ulaby & El-Rayes (1987) for vegetation and the soil model of Hallikainen *et al*. (1985). This work is more interested in the ability to distinguish oil sands from surrounding barefaced terrain consequently the Hallikainen soil model is highlighted where,

$$\boldsymbol{\varepsilon_r = (a_0 + a_1 S + a_2 C) + (b_0 + b_1 S + b_2 C) m_v + (c_0 + c_1 S + c_2 C) m_v^2} \quad (3.23)$$

Here m_v is the volumetric soil moisture while S and C represent sand and clay components of the terrain respectively in *wt*.%. Furthermore a_n, b_n and c_n are empirically determined model coefficients which are given for the real and imaginary part of ε_r. It can be seen that this model does not account for the presence of hydrocarbons such as bitumen or other minerals, which is a core distinguishing feature between oil sand and other terrain. Therefore the geochemical signature using reflectance spectra will be determined for oil sand and other barefaced terrain prior to developing a dielectric prediction model for oil sand. Also there is need for the development of BTM's to aid investigation of oil sand backscattering behaviour as a step towards classification and characterization. Therefore the possibility of using SAR techniques to identify and distinguish between terrain types will depend on adequate electromagnetic terrain models.

3.4. Requirements and Research Needs

In this chapter we discussed the lack of oil sand exploration technology data and noted that oil sand terrain is composed of several constituents that vary with the location of the underlying reservoir. The variation of chemical, physical and dielectric properties with composition necessitates a dual EM characterization approach using hyperspectral and SAR imaging. The behaviour of EM field with oil sand terrain has not been investigated. The challenge is to retrieve surface compositional information for oil sand exploration purposes. There is more data on hyperspectral remote sensing than microwave characterization although there is little research linking their application to oil and gas exploration. Also laboratory spectroscopic procedures to derive reflectance data for oil sand terrain were discussed. FTIR is preferred to X-ray diffraction or microprobe analysis because it can better observe light elements such as C, O, H and

N. It will be used in chapter 4 to identify then derive spectral data for oil sand specimen acquired in Nigeria in addition to other barefaced terrain. Similar to Hunt and Salisbury (Hunt, 1977; Salisbury *et al*., 1989) characterizing mineral rock spectra, it is expected that the oil sand and other barefaced terrain spectra will form the basis for airborne and spaceborne hyperspectral sensors.

The Nigerian Dahomey Basin similar to parts of the West Canadian basin lacks infrastructural access but possess low overburden suggesting the possibility of using EM methods such as hyperspectral imaging and SAR. Modern uses of SAR for terrain imaging require prior knowledge, meaning there could be a need for an automatic classification system based on determined features. This was deemed to be important as any ability to gain geo-scientific information from SAR will depend on models that can explain the radar signature of oil sand terrain.

Mutyala *et al*., (2010) raise three main issues with microwave applications to oil sands after considering three decades of research. First, despite a large range of possible applications (summarized in Table 3.5), no definitive application of microwaves to oil sand and petroleum has emerged due to inappropriate dielectric properties measurement. Secondly it is difficult to correlate energy balance data as the experimental procedures contain insufficient information to ensure accurate conclusions. Thirdly they consider a lack of simplified universal experimental methods, standardized conditions and commercial dielectric measurement tools make it difficult to compare data within applications. Here we also observed that the available empirical terrain models to determine the dielectric permittivity of terrain do not account for the presence of bitumen which is the major constituent that differentiates oil sand from other terrain.

The lack of specific EM models able to adequately explain the optical or radar backscattering behaviour of oil sand terrain was also observed. The primary and secondary properties of reservoir rocks that could prove relevant to EM reflectivity of oil sand were identified. For models of EM interaction with oil sand reservoirs the steady state will be considered with fixed particle sizes and distribution. The backscattering phenomenon as it relates a SAR sensor to measureable terrain parameters was identified. These will form the characteristics of the models. The average dielectric permittivity and loss tangent of oil sand will be derived and compared with literature in chapter 5 for input in to the BTMs.

The effectiveness of multi-beam image analysis with Radar satellites typically depends on prior knowledge and experience of the interpreter. This means there is a need for an automatic classification system based on determined features. Also the AEM method relies solely on the conductivity contrast between terrain layers and involves a fitting technique where conductivity is the only parameter varied in relation to delay time and penetration depth. Therefore the received EM response is highly sensitive to sub-meter variations in the altitude of transmitter and receiver loops. This makes AEM suitable for modeling the response from oil sand layers but not a ready substitute for SAR-based oil sand exploration.

It is difficult to derive roughness parameters from field measurements because several measurements in different directions are required and natural surfaces have different roughness frequency components (Chanzy *et al*., 2003; Davidson *et al*., 2000). The terrain models developed in this thesis will represent both the surface roughness and correlation length of oil sand terrain in comparison with other terrain. This is done in chapter 6 using the systematic packing of uniform sphere theory by Graton and Fraser (1935). Furthermore, the nature of surface scattering varies from completely specular governed by the Fresnel laws to fully diffuse or Lambertian reflection (Ulaby *et al*., 1981). No one model can fully predict diffuse reflection therefore the behaviour of oil sand will need to be experimentally determined after modeling analysis in chapter 7.

3.5. Conceptual Approach to the Thesis

The ability to extract useful information from current and future hyperspectral or SAR systems depends on an understanding of the EM interaction with different terrain types represented by reflectance, R_λ and backscattering, σ^0 data. This knowledge is necessary for terrain classification, area object characterization and even features identification or detection. Therefore a four step model and measurement based approach covering two parts, was chosen to address the research needs mentioned above. Determination of the geochemical signature using hyperspectral imaging and dielectric properties using measurement techniques are necessary in order to develop intrinsic properties of barefaced terrain. These are input in to the development of the BTM with different sensor configuration from which the radar signature is obtained. Finally empirical scattering measurements are used to validate the model. The structure of the approach is shown in Fig. 3.10. The composition of oil sands with oil (bitumen)

and water which are naturally immiscible but held together by surfactants (having one hydrophilic end and one oleophilic end) suggests that each element of oil sands (bitumen, water, solids) may respond differently to EM radiation. This will help us differentiate between oil sand terrain and other barefaced terrain types.

Although the composition and properties of Canadian oil sands have been reviewed by several authors (Carrigy, 1967; Wallace *et al*., 1988; Cloutis *et al*., 1995; Lyder *et al*., 2010) this is not true of Nigerian oil sands (NGSA, 2010; Akinmosin *et al*., 2009). Chapter 4 considers our method to characterize Nigerian oil sands using hyperspectral imaging and reflectance spectroscopy in order to develop a geochemical signature R_λ.

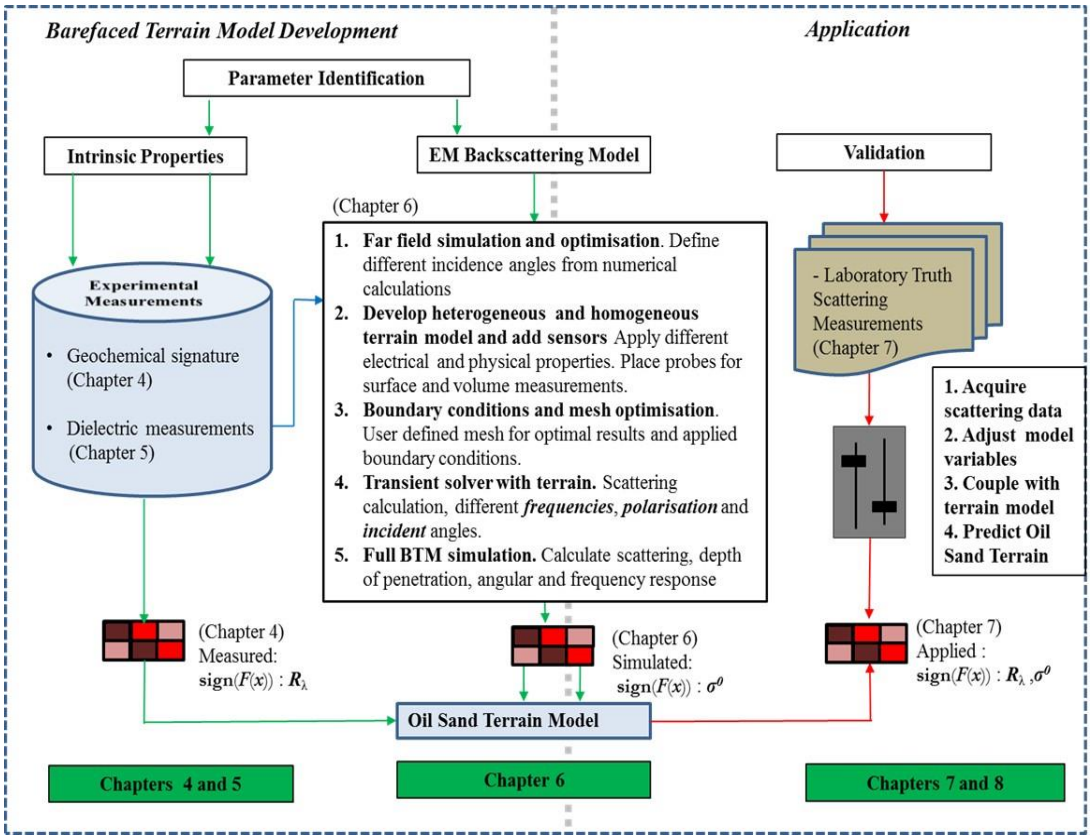

Figure 3.10: Conceptual Structure of the Thesis.

For this research backscattering phenomena considers the interaction between the backscattering coefficient and specific oil sand terrain parameters like texture, moisture content, dielectric constant and geometric properties when compared to surrounding barefaced terrain. At C-band and X-band frequencies no dielectric property measurements of oil sand have been reported however Erdogan *et al*., (2011) performed

measurements at 2.45 GHz (Table 3.11). In order to ensure robust BTM's we outline our method to determine the dielectric properties of oil sand and other barefaced terrain with different *wt*.% of water then discuss the results in chapter 5.

From (3.5) a plane wave is used as the incident electric field, $\mathbf{E}^{inc}$ for the initial simulation models in chapter 6 of this work. However for determining the polarimetric backscattering signature of oil sand, polarimetric sensors consisting of wide-band horn antenna models are developed in chapter 6 and post processed to obtain simulated backscattering signature. The laboratory validation measurements are obtained and presented in chapter 7.

4 Geochemical Signature

A multi-sensor approach for the electromagnetic characterization of barefaced terrain has been proposed to include optical and radar identification of terrain targets. The first step was to determine the geochemical signature. Spectroscopy was used to identify the components in oil sand, compare to literature and develop the geochemical signature of oil sands from Nigeria along with other barefaced terrain. The experimental procedure is discussed, results for oil sands using statistical models analysed and the bitumen and water content predicted using experimental data.

Multi-spectral and hyperspectral theory and its application to geologic remote sensing was considered in the previous chapter along with Radar backscattering. Reflectance spectra of minerals in the visible and near-IR (VNIR) wavelengths are determined by the presence or absence of transition metal ions (e.g. Fe, Cr, Co, Ni) which result in absorption (or transmission) features occurring due to electronic processes. However in the short wave IR (SWIR) and medium IR (MIR) the absorption features are dominated by the presence or absence of water and hydroxyl, carbonate and sulfate occurring due to vibrational processes. The grain or particle size also affects the light scattering and absorption due to the length of the internal optical path in the material under test (MUT) through which photons may be absorbed. Previous efforts to apply spectroscopy and spectral imaging to the characterization of oil sand and oil sand reservoirs were discussed in Section 3.1.2. Here the approach to develop the geochemical signature of oil sands from Nigeria along with other barefaced terrain is outlined based on laboratory investigations and data interpretation algorithm. Multivariate statistics particularly principal component analysis (PCA) and partial least square analysis (PLSA) were used to develop the geochemical signature prediction model while spectral angle mapping (SAM) was used to identify the mineral phases present.

4.1. Spectral Behaviour of Hydrocarbons

The spectral behaviour and physicochemical properties of hydrocarbons have been discussed by Cloutis (1989), Silverstein and Webster (1998) and Winklemann (2005). In order to investigate contaminated terrain, Winklemann (2005) observed Carbon-Hydrogen bonds (C-H, C-H_2 and C-H_3), hydroxyl groups (O-H), the double

and triple bonds of asphaltenes and aromatics, carboxyl groups (C=O), ethers (C-O-C), and amino groups (N-H) amidst other organic chemicals. He concluded that they exhibit characteristic fundamental vibrations and combination overtones. The fundamental vibrations are evident in the 2.5 μm to 6.67 μm wavelength, λ region which corresponds to wavenumber, ν covering 4000 cm^{-1} to 1500 cm^{-1} while combination overtones in the visible IR spectrum occur between 0.5 μm (20,000 cm^{-1}) and 6.67 μm (ν = 1500 cm^{-1}). The major hydrocarbon vibrations are shown in Table 4.1.

Table 4.1: Major Hydrocarbon Vibrations (Cloutis, 1989; Silverstein & Webster, 1998)

Compound		**Type of deformation**	**Vibrations**	
			cm^{-1} (ν)	μm (λ)
[1]	C-H	Axial deformation of C-H (Alkanes and Aromatics)	3032	3.30
[2]	CH_3	Methyl asymmetric axial deformation (Alkanes)	2950	3.39
[3]	CH_2	Methylene asymmetric axial deformation (Alkanes)	2920	3.42
[4]	CH_3	Methyl symmetric axial deformation (Alkanes)	2875	3.48
[5]	CH_2	Methyl symmetric axial deformation	2850	3.51
[6]	C=O	Carbonyl axial deformation	1700	5.88
[7]	C	C axial deformation (aromatic ring)	1600	6.25
[8]	CH_2 and CH_3	Methyl asymmetric angular deformation + Methylene symmetric deformation (Alkanes)	1450	6.90
[9]	CH_3	Methyl symmetric angular deformation (Alkanes)	1375	7.27
[10]	C-H	Angular deformation out of the plane of the C-H ring bonds (Mononuclear and Polynuclear Aromatics)	900-675	11.1-14.8
[11]	C-H	Angular deformation out of the plane of the C-H in Naphthenes	862-735	11.6-13.6

The overtones and combinations for the hydrocarbon molecules at specific wavelengths have been highlighted (Cloutis, 1989) and presented in table 4.2. These broad bands over the NIR (λ = 0.78 – 2.5 μm) spectrum create a lack of selectivity which prompts the development of automated methods and models to analyze the data. Therefore to identify the possible regions for determination of the geochemical signature, R_λ of oil sands, different spectra intervals was considered (Lammoglia & Souza-Filho, 2012). Aromatic structures and heavy atom bonds can be observed 11 to 25 μm but a complex interaction of vibrations between 7.6 and 11.1 μm makes identification of structural or functional groups impossible. The stretching vibrations of double and triple bonds such as C=O, C=C, C=N, C≡C, C≡N etc. have been recorded between 4.0 and 6.7 μm while between 2.5 and 4.0 μm the fundamental bands and axial deformations of light atoms such as C-H, O-H, N-H are observed.

Table 4.2: Hydrocarbon Molecules Overtones and Combinations (Cloutis, 1989)

Overtones and combinations	Wavelength	Wavenumber	Overtones and combinations	Wavelength	Wavenumber
	μm	cm^{-1}		μm	cm^{-1}
2*[1]	1.65	6061	[5]+[6]	2.2	4545
[1]+[3]	1.68	5952	[3]+[7]	2.21	4525
2*[2]	1.69	5917	[5]+[7]	2.25	4444
[1]+[6]	1.7	5882	[2]+[8]	2.27	4405
2*[3]	1.71	5848	[3]+[8]	2.29	4367
[2]+[4]	1.72	5814	[2]+[9], [4]+[8]	2.31	4329
[3]+[3]	1.73	5780	[5]+[8]	2.33	4292
2*[4]	1.74	5747	[4]+[9]	2.35	4255
2*[5]	1.75	5714	[5]+[9]	2.53	3953

The fundamental bands' combination tones and overtones are exhibited between 0.8 and 2.5 μm. VNIR reflectance spectra of oil sands exhibit several transmission features that have been used to characterize minerals present in oil sands (Cloutis *et al*., 1995). Investigation using diffuse-reflectance spectra in the 0.3 – 2.6µm was used to identify minerals such as kaolinite, illite and siderite in oil sands. Importantly, Cloutis (1989) and Yoon *et al*., (2009) conclude that the most promising interval for detection of absorption organic bands is close to 1.7 μm and between 2.2 and 2.5 μm which is conveniently within the transmittance atmospheric window for solar radiation. The spectra of oil sands and other terrain was characterized across the ν = 500 cm^{-1} to 4600 cm^{-1} (λ = 20 – 2.1 μm) region.

4.2. Laboratory Spectroscopy

For spectral characterization of the acquired oil sand samples and other barefaced terrain, Fourier Transform IR (FTIR) spectroscopy was preferred to other methods such as X-ray diffractometry due to the wider regions supported. FTIR is more suitable to study light elements such as C, O, H and N unlike X-ray diffraction or microprobe analysis. FTIR is a geo-chemical approach preferred to dispersive or filter methods of spectral analysis because it is non-destructive, mechanically simple and more precise without requiring a need for external calibration (Swann & Patwardhan, 2011). These three advantages comprise the multiplex or Fellgett advantage, aperture throughput or Jacquinot advantage and wavenumber accuracy or Connes advantage. The first refers to the ability of FTIR to measure a wide spectrum of wavenumbers. Successive scanning allows the resulting spectra to have high S/N ratio. Also a large aperture can be used as FTIR depends on the aperture area and the incident angle of

light. The Cones advantage results from the use of an He-Ne laser which emits an extremely stable monochromatic light.

In this work FTIR is used to understand the variety of bonding between oil sand components, observe the consistency of oil sand samples brought from Nigeria, determine the SARA presence and define the geochemical signature. Hyperspectral processing of FTIR spectra was used to create a molecular fingerprint of the oil sand samples amidst other terrain types. The resultant spectrum represents the molecular absorption and transmission features which are dissimilar for non-unique samples. The absorption or transmission *peaks* correspond to the frequency of vibrations between the atomic bonds that make up oil sand while the *size* of the peaks indicates the amount of material present. Almost similar to the measurement of dielectric permittivity the detector provides a spectrum that plots intensity in % Transmittance vs. Wavenumber. From (2.6) the IR bands used in the measurement are shown in Table 4.3.

Table 4.3: Spectrometric Identification Regions

	NIR	**Mid IR**	**Far IR**
Wavenumber, v (cm^{-1})	13000 - 4000	4000 - 200	200 -10
Wavelength, λ (μm)	0.78 – 2.5	2.5 - 50	50 - 1000

4.1.1. Materials

This work investigated 3 groups and 6 types of barefaced terrain including oil sand. The groups were linear (or homogenous), intimate (semi-heterogeneous) and molecular (heterogeneous) terrain types. These different groups were chosen in order to cover the possible barefaced terrain types from the Wentworth terrain classification scheme (Wentworth, 1922). The six terrain types representing the materials under test (MUT) include beach sand, loamy farm sand, 10mm pebbles, 40mm gravel, hard oil sand (HOS) and viscous oil sand (VOS) shown in Fig. 4.1. Together they represent MUT A to F respectively.

MUT A and B were relatively semi-homogenous. MUT C and D were homogenous while MUT E and F were heterogeneous. The latter represent two strains of oil sand samples which are referred to in this work as HOS and VOS. Both were obtained from six locations within the Agbabu oil sand reservoir (AOSR) in the Igbokoda areas of Ondo State, south west, Nigeria and transported to UK in 2013 and 2014. The AOSR reservoir is located within latitudes 6° 35’ 16.3’’N to 6° 37’ 13.9’’N and longitudes 4° 49’ 29’’E to 4° 50’ 20.7”E (Amigun *et al*., 2012; Ezeoke *et al*.,

2014a). The other terrain types were acquired locally in UK. A summary of the mean grain size of the MUTs are shown in Table 4.4.

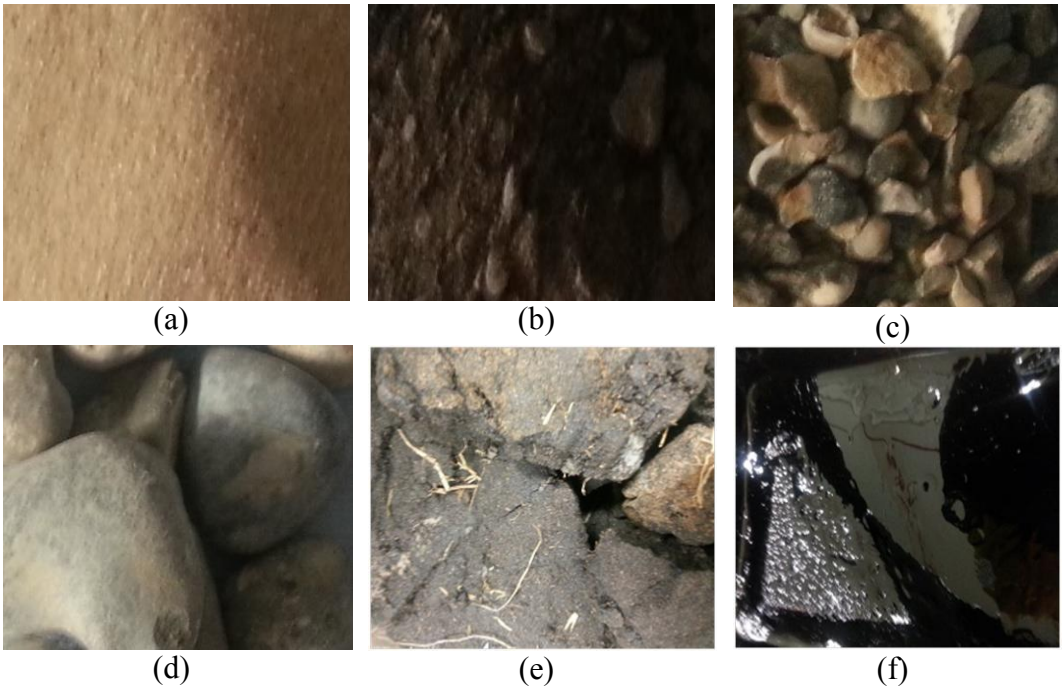

Figure 4.1: Barefaced Terrain. First row: (a) MUT A - Beach Sand (b) MUT B - Loamy Farm Sand (c) MUT C - 10mm pebbles. Second row: (d) MUT D - 40mm Gravel (e) MUT E - Hard Oil Sand (f) MUT F - Viscous Oil Sand.

Table 4.4: Mean Grain Sizes

MUT	**Name**	**Size**[a]
A	Beach Sand	< 0.5
B	Loamy Farm Soil	1 - 2
C	Pebbles	10
D	Gravel	40
E	HOS	1 - 2
F	VOS	<0.5

a. Mean particles diameter in mm from Wentworth (1922)

The determination of the grain size and relation of the mean grain sizes to Wentworth classification has been discussed previously in Ezeoke *et al*., (2013).

4.1.2. Method

The spectral reflectance of the 16 terrain samples were measured under different water saturations but similar acquisition geometries. In order to avoid influencing the results and ensuring MUTs remained in the natural state, beach sand, loamy farm sand,

VOS and HOS did not undergo any preparation before the measurement. However due to the large mean grain size of pebble and gravel, representative samples were obtained by soaking MUT C and D in deionized water and sonication using a Branson1510 ultrasonic Sonicator. This is a useful procedure to extract representative sediments of solid and non-granular terrain for spectral identification. From (2.3) the size of each MUT for spectroscopic analysis needs to be similar in order to ensure that the variation of intensity obtained in the spectra depends on the absorption coefficient k of the terrain sample not the distance x travelled through the medium. Each MUT sample was 130 μm in thickness.

The variation in water saturation was achieved by a calibrated mixing of MUT A and B with 10, 20 and 30 weight percent (*wt*.%) of water. First MUT A and B were heated using a hotplate at a modest temperature (75°C) to remove trace moisture without altering the biophysical nutrients. The *wt*.% of moisture per terrain sample was measured with analytical balance AB304-S Mettler Toledo instrument. Each 10 *wt*.% increase in water is accompanied by a corresponding decrease in terrain sample to preserve the equilibrium (Table 4.5).

All the samples were investigated using the Shimadzu IRPrestige-21 FTIR-8400S spectrophotometer located at the UCL Nanotechnology Laboratory. Spectra were acquired over the VNIR and MIR corresponding to v = 4600 - 500 cm^{-1} (2.1 – 20 μm) interval with hyperspectral resolution >2180 bands (4 cm^{-1}). This means that the major overtone and combination regions for Hydrocarbons were avoided (Table 4.2). The equipment is suited for organic polymers such as oil sand because it uses an interferometer to collect the raw data which was then translated into the IR spectrum using Fourier transform (FT) algorithms. Experiments were carried out with the assistance of Dr Steve Hudziak in the Nanotechnology Laboratory at UCL. The beam splitter of the interferometer and the Deuterated, L-alanine doped triglycine sulphate (DLaTGS) detector were illuminated by a ceramic light source and tungsten-halogen laser. DLaTGS detectors provide a linear response over a wide range of FTIR throughput which is helpful for qualitative and quantitative FTIR sampling.

Two separate procedures were performed on each MUT. The first was a transmittance/reflectance (T/R) test which proved inconclusive for HOS and VOS due to interference from the microscope slides used to prevent detector contamination (Fig. 4.2a). The second was the attenuated total reflectance (ATR) test which used sample

holders (accepting samples 130 μm thick) rather than micro-slides to provide better results (Fig. 4.2b).

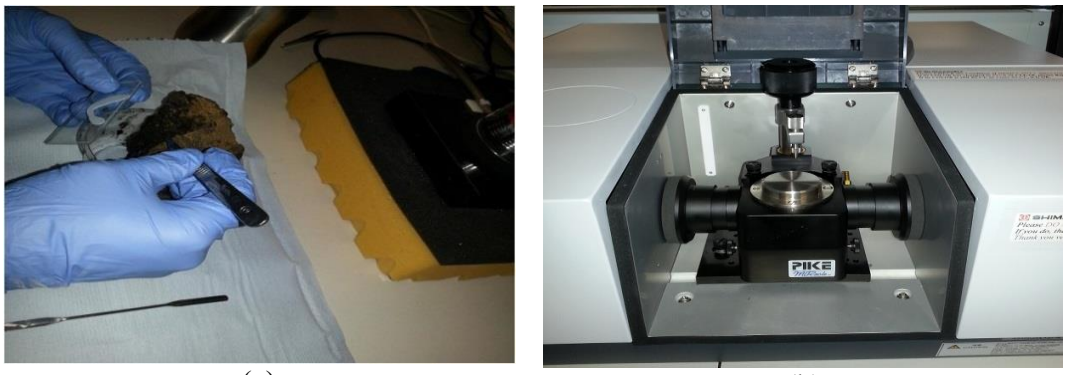

(a) (b)

Figure 4.2: HOS in (a) Premium microscope slides for T/R (b) FTIR ATR holder.

The ATR measurements involved the absorbance of IR beams by the samples with the crystal having a higher index of refraction than the sample, directly in contact with the sample. ATR transmission measurements typically avoid the problems related to T/R scattering because the limited path length in to the sample (0.5 – 2 μm) avoiding the problem of strong attenuation of the IR signal in highly absorbing sample media (Spragg, 2000). The T/R measurement approach had samples placed between premium microscope slides held together by glutamate while the ATR had the samples placed directly on the ATR accessory holder (Fig. 4.2). The thick viscosity and composition of VOS meant the surface of the ATR sample holders had to be frequently cleaned of residue in-between measurements with Isopropyl alcohol. This was also a problem in later dielectric measurements.

For each MUT a background spectrum was obtained by first measuring the spectrometer response without any sample in place. This was important as the experiments were made in ambient atmospheric conditions in the laboratory and the samples were not pre-processed by dissolving in solvent mixture. The use of solvents such as tetrahydrofuran (THF) or IR pellets can cause vast increases in background transmittance values (Yoon *et al*., 2009). The aim of the experiment was first to identify the possible presence of hydrocarbons, estimate quantity of aggregate SARA present (represented by bitumen) and determine the geochemical signature. Therefore both the position and size of the peaks were important. The sample spectra were measured relative to Potassium Bromide (KBr) crystal which is a near perfect reflector up to 25 μm region. Several measurements of each sample type were taken to establish

repeatability at room temperature (25 °C). The following spectrophotometer settings were used: number of scans, 25 - 100; resolution, 4cm^{-1}; gain, auto. Other details of the measurement campaign are shown in Table 4.5.

Table 4.5: Spectral Measurement Campaign

MUT	**Name**	**Description**
A, A10, A20, A30	Beach Sand	100% MUT A and others increasing by 10 *wt*.% water
B, B10, B20, B30	Loamy Farm Soil	100% MUT B and others increasing by 10 *wt*.% water
C	Pebbles	MUT C after sonication and sedimentation
D	Granite	MUT D after sonication and sedimentation
E: HOS1, HOS2, HOS3	HOS	HOS from 3 different locations in the AOSR
F: VOS1, VOS2, VOS3	VOS	VOS from 3 different locations in the AOSR

The acquisition and arrangement of the hyperspectral data for oil sand has been discussed in (Ezeoke & Tong, 2013c) while that for other barefaced terrain was highlighted in (Ezeoke & Tong, 2014). Despite the high level of accuracy and precision typically obtained with spectral instruments scaling differences may arise from path length effects, scattering effects, source or detector variations (Martens & Naes, 1992). Typically sample normalization preprocessing methods try to correct for such effects by identifying aspects of the MUT that should be constant between samples and correcting the scaling of all the variables based on this feature. Therefore rather than the absolute measured values it is often the relative value of variables that are used for multivariate modeling. An internal standard value was used to correct for such scaling effects since the measurements of the samples occurred over 2 years in 2013 and 2014.

After each measurement the background subtraction was performed automatically because normalization before background removal may deteriorate model performance particularly with measurements taken on different days over long periods. The main form of normalization employed to the results was the multiplicative scatter correction (MSC). The main aim of the MSC was to account for scaling and baseline offset effects (Martens & Naes, 1992). One method of doing this is to regress a measured spectrum against a reference spectrum and then correcting the measured spectrum using the slope of this fit. In this work it was performed by ensuring all the spectra were adjusted to the same baseline. In essence **x** was defined as a column vector

corresponding to the spectrum to be standardized while **r** is a vector corresponding to the reference spectrum. If *b* is the unknown multiplicative factor, then $\mathbf{x}_c$ and $\mathbf{r}_c$ are the mean centered vectors with $\bar{x}$ and $\bar{r}$ the respective means of the spectra to be standardized. The mean centered vectors are related by:

$$\mathbf{r}_c \boldsymbol{b} = \mathbf{x}_c \tag{4.39}$$

Then the unknown multiplicative factor *b* was obtained from:

$$\boldsymbol{b} = (\mathbf{r}_c^{\mathrm{T}} \mathbf{r}_c)^{-1} \ \mathbf{r}_c^{\mathrm{T}} \mathbf{x}_c \tag{4.40}$$

While the corrected spectrum $\hat{x}$ is then given by

$$\hat{\boldsymbol{x}} = \frac{\mathbf{x}_c}{\boldsymbol{b}} + \bar{r}\mathbf{1} \tag{4.41}$$

Where **1** is a vector of ones then $\mathbf{r}_c$ and $\mathbf{x}_c$ are related to $\bar{r}1$ and $\bar{x}1$ by $\bar{r}1 = r - \mathrm{r}_c$ and $\bar{x}1 = \mathrm{x} - \mathrm{x}_c$ respectively.

4.1.3. Chemometrics

Analysis of spectra typically requires statistical or mathematical methods. This is particularly important in NIR and SWIR regions due to superimposition of several individual peaks as overtones and combination bands that represent the hydrocarbon's reflectance spectrum. Unlike chemical characterization methods such as high performance liquid chromatography (HPLC), spectroscopy does not resolve components in a sample and information is embedded in multiple absorption bands (Aske *et al*., 2001). Due to this complexity in interpreting spectra and defining the geochemical signature multivariate statistics (chemometrics) based on principal component analysis (PCA) and partial least square analysis (PLSA) was used. A geochemical signature analysis model was built for both prediction and interpretation using MATLAB® (MATLAB, 2012b). The algorithm sequence is shown in Fig. 4.3 and written code presented in Appendix 4.

Literature has discussed the applicability of PCA and PLSA to interpretation of hydrocarbon transmittance and absorbance spectra (Aske *et al*., 2001; Freitas *et al*., 2013; Lammoglia & Souza Filho, 2011). In this study it was observed that the application is case specific even for MUT with similar spectral features like oil sand.

Both were used to model a response variable particularly when there are a large number of predictor variables and the predictors are highly correlated or perhaps collinear. In both PCA and PLSA new predictor variables or components are created as linear combinations of the original predictor variables. However while PCA creates components to explain the observed variability in the predictor without considering the response at all, PLSA considers the response variable.

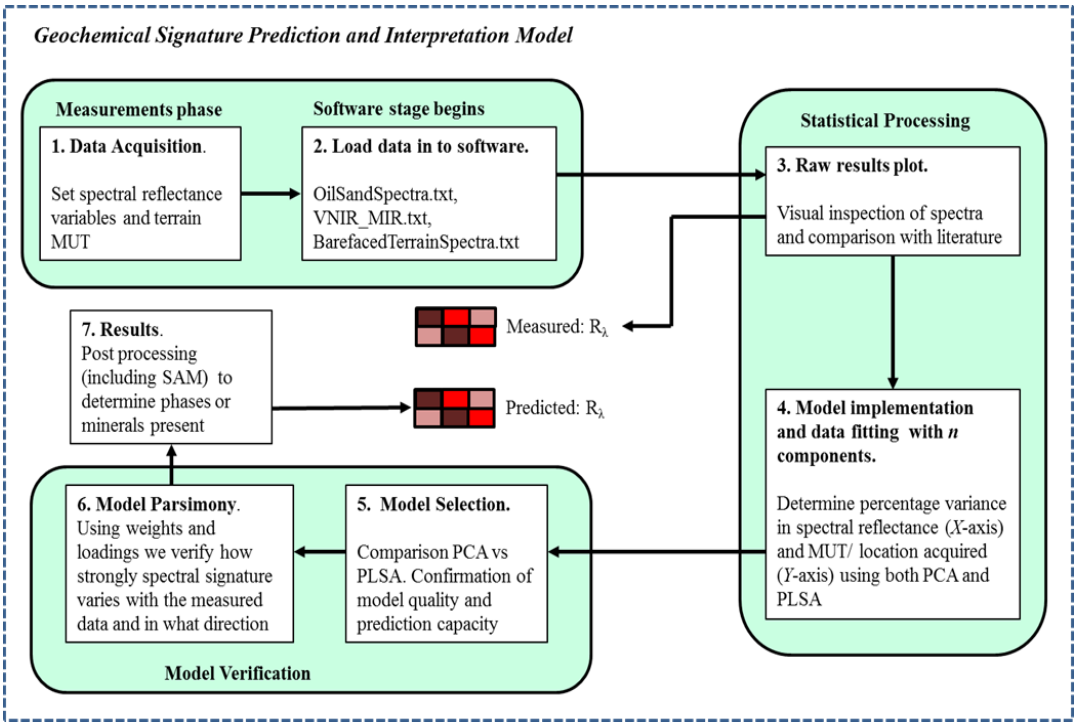

Figure 4.3: Geochemical signature determination process.

Mathematically, PCA is based on an eigenvector decomposition of the covariance matrix of the variables in our data set. Therefore for data matrix **X** with *m* rows of samples and *n* columns of variables, the covariance matrix of **X** is given by:

$$\mathbf{cov}\,(\mathbf{X}) = \frac{\mathbf{X^T X}}{\boldsymbol{m-1}}. \tag{4.42}$$

This results in a decomposition of the data matrix X into principal components called score and loading vectors given as:

$$\mathbf{X}_{n\times m} = \mathbf{t_1 p_1^T} + \mathbf{t_2 p_2^T} + \mathbf{t}_i\mathbf{p}_i^{\mathbf{T}} \ldots . + \mathbf{t}_k\mathbf{p}_k^{\mathbf{T}} + \mathbf{E}_{n\times m} \tag{4.43}$$

Where $\mathbf{t}_i$, $\mathbf{p}_i$ and $\mathbf{E}$ represent score vector, loading vector and residual matrix respectively. The score and loading vectors contain information on how the samples and variables relate to each other. Aske *et al*., (2001) suggest that for NIR data usually more than 95% of original variation is described by 2 – 5 principal components.

PLSA was used to fit data from the data matrix **X** to the response vector **y**. For this application, the data matrix was the measured oil sand and barefaced terrain spectra data while the response is the observed SARA values as a function of location (for oil sand) and MUT for terrain. Finally the spectral angle mapper (SAM) implementation of the Shimadzu IR Solution software viewer was used to identify the mineral phases present. The SAM classifier helps provide a comparative diagnostic qualitative analysis to determine the major and minor mineral phases present per sample by matching the peaks and troughs of measured spectra. Our method to determine the specific concentration of bitumen and water in the oil sand will be discussed in the next section.

4.1.4. Content Prediction

For the prediction of water and bitumen content in MUT E and MUT F the ratio of concentration of the MIR spectra at specific diagnostic wavenumber bands was used. For an absorbing medium the photons are absorbed according to Beer's law given in (2.3). If applied to the main components of oil sand, then for clay, bitumen and water:

$$\mathbf{A}^{water} = \mathbf{a}^{water}(\boldsymbol{v})\mathbf{c}^{water} = -\boldsymbol{log}_{\mathbf{10}}\left(\frac{\boldsymbol{I}^{\mathbf{water}}(\boldsymbol{v})}{\boldsymbol{I}_{\mathbf{0}}^{\boldsymbol{water}}(\boldsymbol{v})}\right). \tag{4.44}$$

$$\mathbf{A}^{clay} = \mathbf{a}^{clay}(\boldsymbol{v})\mathbf{c}^{clay} = -\boldsymbol{log}_{\mathbf{10}}\left(\frac{\boldsymbol{I}^{\mathbf{clay}}(\boldsymbol{v})}{\boldsymbol{I}_{\mathbf{0}}^{\boldsymbol{clay}}(\boldsymbol{v})}\right). \tag{4.45}$$

$$\mathbf{A}^{bitumen} = \mathbf{a}^{bitumen}(\boldsymbol{v})\mathbf{c}^{bitumen} = -\boldsymbol{log}_{\mathbf{10}}\left(\frac{\boldsymbol{I}^{\mathbf{bitumen}}(\boldsymbol{v})}{\boldsymbol{I}_{\mathbf{0}}^{\boldsymbol{bitumen}}(\boldsymbol{v})}\right). \tag{4.46}$$

Where $A(v)$, $a(v)$, c, I, $I(v)$, $I_0(v)$ are the absorbance, absorption coefficient, concentration, length of IR cell, transmitted light intensity and incident light intensity respectively (Yoon *et al*., 2009). For this work there were no separate pellet cells of pure clay, bitumen or water therefore the parameter I which depends on the IR pellet preparation had to be removed by dividing (4.6) and (4.8) by (4.7) to obtain:

$$\frac{\boldsymbol{c}^{\mathbf{water}}}{\boldsymbol{c}^{\mathbf{clay}}} = \left(\frac{\boldsymbol{a}^{\mathbf{clay}}}{\boldsymbol{a}^{\mathbf{water}}}\right)\left(\frac{\boldsymbol{A}^{\mathbf{water}}}{\boldsymbol{A}^{\mathbf{clay}}}\right). \tag{4.47}$$

$$\frac{\boldsymbol{c}^{\mathbf{bitumen}}}{\boldsymbol{c}^{\mathbf{clay}}} = \left(\frac{\boldsymbol{a}^{\mathbf{clay}}}{\boldsymbol{a}^{\mathbf{bitumen}}}\right)\left(\frac{\boldsymbol{A}^{\mathbf{bitumen}}}{\boldsymbol{A}^{\mathbf{clay}}}\right). \tag{4.48}$$

From (4.9) and (4.10) the ratio of concentration, *c* is proportional to the ratio of absorbance, *A*, but the ratio of absorption coefficients, *a*, is inversed. The absorbance *A* was obtained from the hyperspectral data. The absorption coefficient ratio for clay and water can be estimated from the linear least square fitting of MUT A or MUT B with calibrated *wt*. % of water to keep the concentration ratio constant then obtaining the absorbance. The absorption coefficients of both clay and bitumen have a similar range of values (10^3 - 10^4) (Koike *et al*., (1982). However for bitumen and clay in MUT E and MUT F concentration ratio was obtained by determining the ratio of absorbance, *A* for both HOS and VOS, and input in to (4.11) from Yoon *et al*., (2009):

$$\frac{\boldsymbol{c}^{\mathbf{bitumen}}}{\boldsymbol{c}^{\mathbf{clay}}} = (\mathbf{0.57 \pm 0.095})\left(\frac{\boldsymbol{A}^{\mathbf{bitumen}}}{\boldsymbol{A}^{\mathbf{clay}}}\right) + (\mathbf{0.00247 \pm 0.027}). \tag{4.49}$$

In order to use equations (4.6), (4.7) and (4.8) the strongest IR bands needed to be selected for moisture, bitumen and clay in MUT E and MUT F.

4.2. Statistical Model

The discussion on the statistical model is based on the pure oil sand data however a similar geochemical signature interpretation and prediction model was implemented for the barefaced terrain data with different *wt*.% of water. The software implementation of the statistical model is presented in Appendix 4. The spectral plot of the data is presented in Fig. 4.4 for the oil sand samples from 6 locations in the AOSR, Nigeria.

In order to implement the model the next step is to curve fit the data to understand the number of principal components (PCs) necessary to fit the original data (observed response) with the predicted response (fitted response). The outcome for both PLSA and PCA models having 2 and 3 components based on the oil sand spectra data is shown in Fig. 4.5.

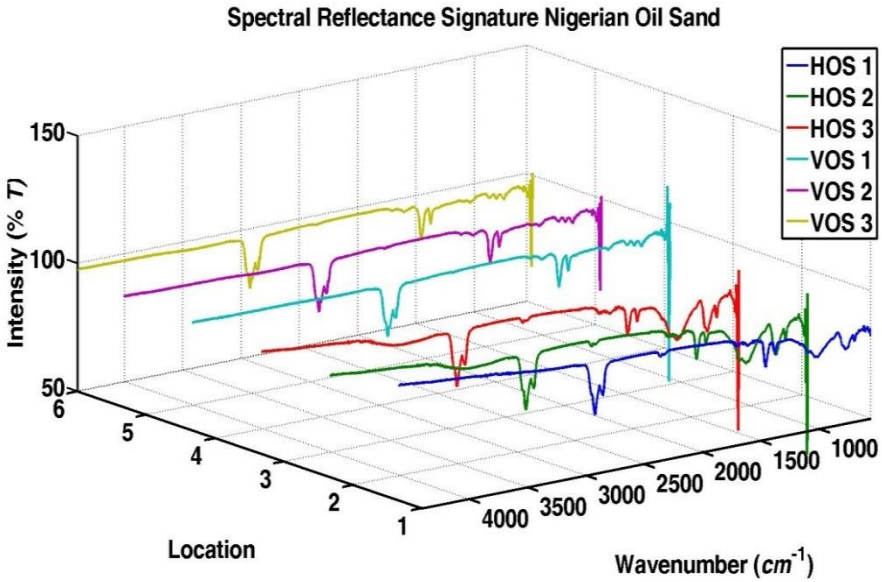

Figure 4.4: Spectral signature Nigerian Oil Sands (wavenumber 550 – 4400 cm^{-1}).

This shows that the Oil Sand Geochemical Signature Model is best implemented for PLSA with 2 components and PCA with 3 components (Fig. 4.5b) rather than both PLSA and PCA having 2 components (Fig. 4.5a).

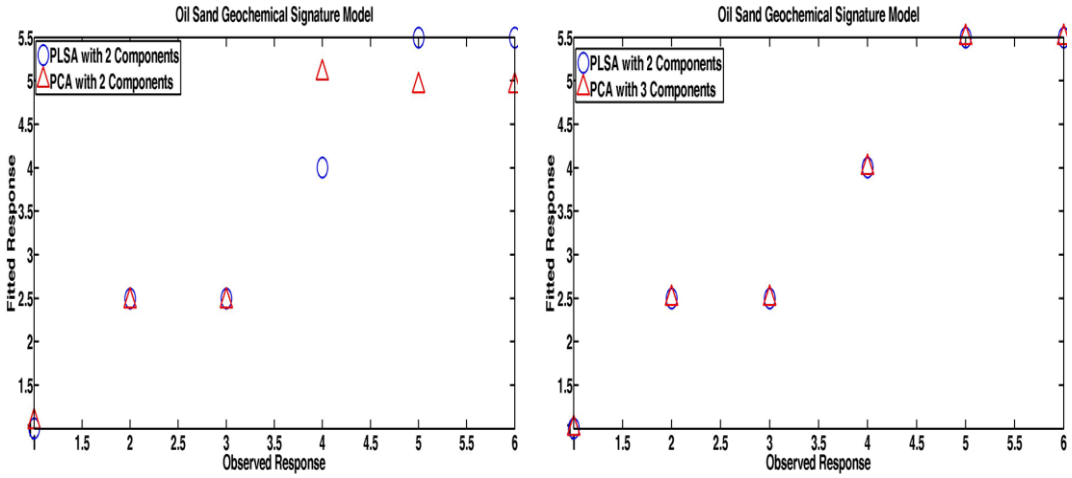

Figure 4.5: Observed vs fitted response for model implementation (a) 2 PCs (b) 3 PCs.

The effect of the PCs on variance is presented in Fig. 4.6. This shows the number of PC's for PLSA and PCA and the percentage variance they explain with respect to spectral response with acquisition location (*y* axis) and the 2162 ultra-spectral intensity wavenumber values (*x* axis). It is clear that while 2 PCs can explain for 85% of the variation in the *y* axis, three PC's account for 95% of the variation (Fig. 4.6a). Also

along the *x* axis 3 PCs represent over 90% of the variation in the 2162 spectral values. However the 3 components of the PLSA model marginally explain less variance in the observed data than the first 3 PCs of the PCA (shown by the area under the curve in Fig. 4.6b).

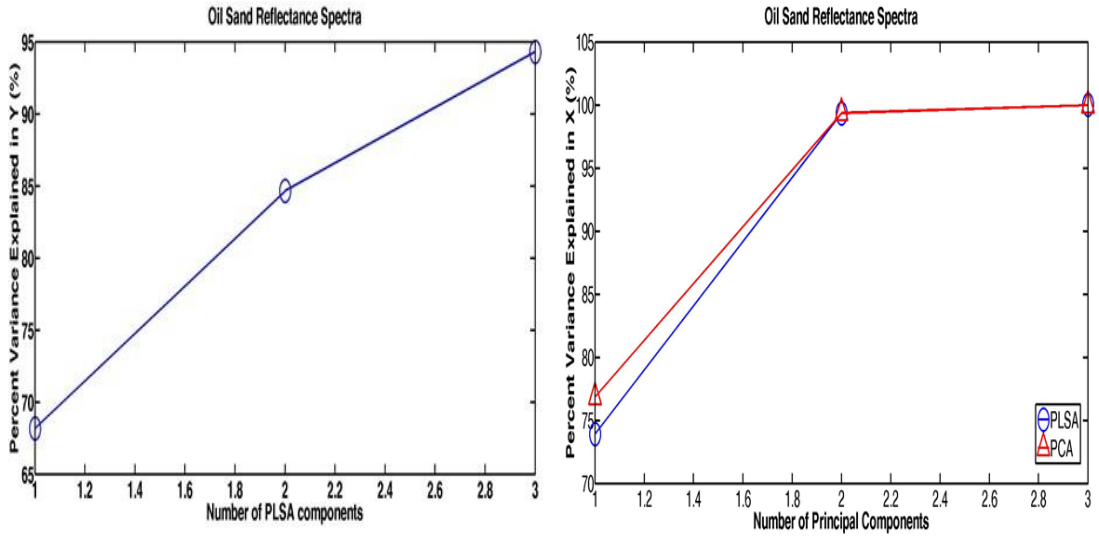

Figure 4.6: Effect of PC's on variance for Oil Sand spectra (a) *y* axis (b) *x* axis.

Therefore the quality of the PCA model with 3 components is better suited to determine the geochemical reflectance signature R_λ of the oil sand data. Errors in the calibration and prediction models are typically expressed by the root mean squared error (RMSE), where the RMSE for the prediction (RMSEP) is given by:

$$\mathbf{RMSEP} = \sqrt{\sum_{i} (\boldsymbol{y_{ip}} - \boldsymbol{y_{ir}})^2 \div \boldsymbol{n}}. \tag{4.50}$$

Here y_{ip}, y_{ir} and n represent the value of the response (y) parameter estimated for ith sample, reference value for the sample and the number of samples. This error is the average of the prediction errors. The RMSE of calibration (RMSEC) is the measurement of the adjustment and quality of the model based only on the calibration samples values. Ultimately both model quality and predictive capacity can be evaluated through R^2 which is the square of the correlation coefficient between predicted values and measured values. The results for the geochemical signature model for oil sand and barefaced terrain data is presented in Table 4.6. This shows that the PLSA is the best prediction model for both oil sand and barefaced spectra data. However PCA with 3 PCs outperforms that with 2 PCs.

Table 4.6: Geochemical Signature Prediction Model: R^2

	PLSA	PCA (2 components)	PCA (3 components)
Oil Sand	0.94	0.84	0.94
Barefaced Terrain	0.98	0.67	0.79

Finally for the statistical model implementation, the parsimony of the model was determined. Using weights or scores, the strength of the relationship between each component of the model and the original measurement was determined along with the direction. This is shown by the direction of the first, second and third PC's. From (4.5) they are the scores and loading vectors for PCA ($\mathbf{t}_1\mathbf{p}_1$, $\mathbf{t}_2\mathbf{p}_2$ and $\mathbf{t}_3\mathbf{p}_3$) and weights for PLSA. These are lines in the variable space that best describes the variation in the data matrix X which is the oil sand spectra for Fig. 4.7. The direction of the second PC is given by the line that best describes the variation not described by the first PC. The variable loadings and weights both illustrate that for models generated with HOS and VOS spectra the most important variables concentrate in three regions: 1000 - 1100 cm^{-1}, 1400 - 1450 cm^{-1} and 2900 - 2950 cm^{-1}.

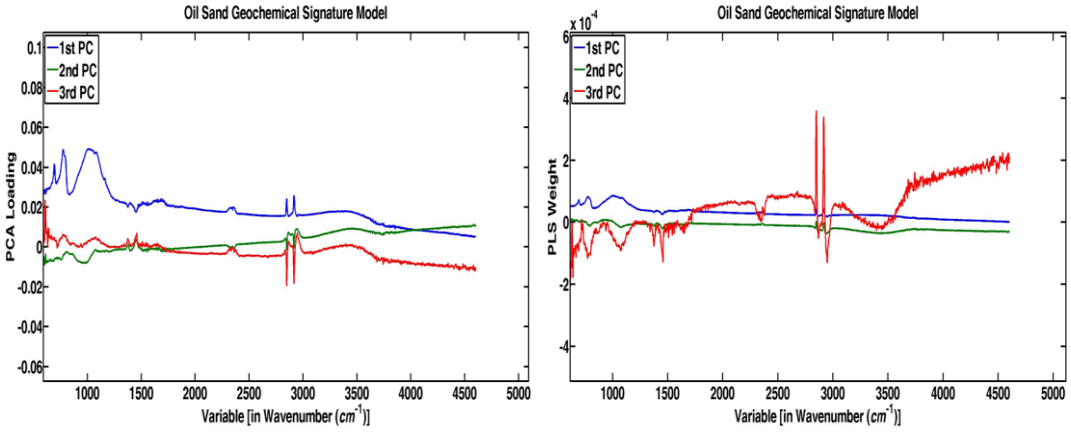

Figure 4.7: Model parsimony with wavenumber (cm^{-1}) for oil sand geochemical signature interpretation and prediction (a) PCA loading (b) PLS weight.

Therefore the original large data set has been described using the PCs instead of the original variables without any loss of information and the relationship between the 6 oil sand samples is indicated. A slight difference is evident in both representations due to the statistical method inherent in the model. In PLS, scores and loadings (called weights) are vectors that have the highest covariance with response vector **y** such that the decomposition in (4.5) is followed by a regression between the weights and the response. However for PCA the scores and loadings are vectors that best describe the variance of the matrix **X** therefore have a larger magnitude scale in this case.

The SAM with Shimadzu IRSolution® software was used to identify the major and minor phases present in oil sand. A table summary of the result showing the bonds present in the samples after SAM classification and database matching is shown in Table 4.7. The SAM classifier compared the prevalence of identified bonds with components already existing in the Shimadzu database. A detailed T/R report and contamination analysis of the constituent bonds and ions has been presented in (Ezeoke, 2013). The variety and types of bonds obtained indicated the presence of hydrocarbons in VOS and HOS (MUT E and F) but none was recorded in any of the other samples.

Table 4.7: Raw Mineral Phases Identified in Barefaced Terrain MUT A-F

Terrain	Major constituents	Minor constituents	Remarks
Beach sand	Glass, Silica gel (SiO_2)	Humic acid, Sucrose, Silica-1	No hydrocarbon present but similar silica oxide features with HOS.
Loamy farm soil	$NaNO_3$, KNO_3	Oleamide, Mg Stearate, polyamide (nylon12)	No hydrocarbon present.
Pebbles	Glass, Polystyrene film, granular $Si0_2$	$Si0_2$, Diatomaceous earth, Silica-1, silica-2	No hydrocarbon present.
Gravel	Glass, SiO_2	Diatomaceous earth/SiO_2, silicon rubber	No hydrocarbon present.
HOS	Glass, Diatomaceous earth (SiO_2)	Hydrocarbon polyethylene	Presence of bitumen and clay sand detected as major constituent.
VOS	Hydrocarbon – polyethylene, Humic acid	AL(OH)3, Ba(NO3)2, Stearate Mg, Silicon Oil, Silicon grease, Silicon Rubber	Presence of bitumen and clay sand detected as major constituent. Humic acids and hydrocarbon are main constituents of oil sands (Hutton, 1987).

4.3. Analysis of Geochemical Signature Results

The MIR transmittance reflectance spectra from 550 cm^{-1} to 4600 cm^{-1} and 60 to 110 % transmittance for MUT A - F is presented in Fig. 4.8. Use of the Pearson correlation coefficient (PCC) identified the greatest statistical linearity for HOS was between HOS 2/HOS 3 while for VOS it was between VOS 2/VOS 3. Therefore the measurement data from HOS 3 and VOS 3 were subsequently used to represent MUT E and MUT F respectively and for the prediction of the bitumen and water content using statistical derivation. Across the spectra and from visual observation the first observation is the overall emergence of three separate spectral profiles in line with the

intrinsic constituents of the MUT. Above 2000 cm^{-1} the spectral curves correlate with the sample homogeneity. Therefore the transmittance values for homogenous (MUT C and D), heterogeneous (MUT E and F) and semi-heterogeneous (MUT A and B) are in close proximity. Although the percentage intensity of transmittance (% T) varies for the non-normalized case, it can be seen that beach sand, 10mm pebbles and 40mm gravel/granite produce similar peaks in the 2800 cm^{-1} – 3000 cm^{-1} region. This is not seen for loamy farm soil but is opposite and larger in both HOS and VOS. A diagnostic spectral feature assessment was used to gauge the underlying cause of the peaks.

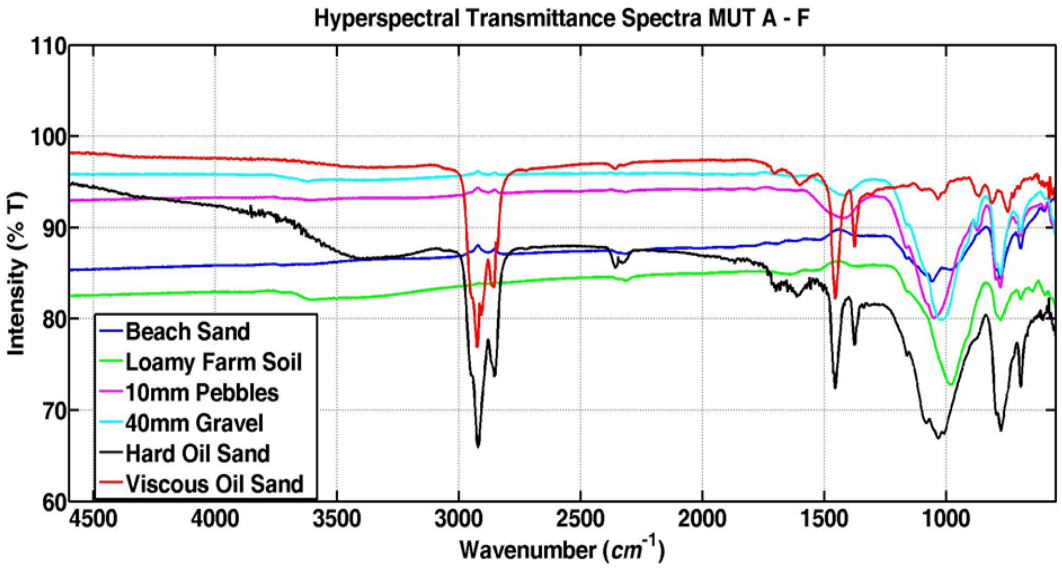

Figure 4.8: VNIR/MIR transmittance spectra of barefaced terrain MUT A-F (without normalization or common baseline applied).

4.3.1. Bitumen and Grain Presence

The heterogeneous terrain produces two broad observations. First both strains of oil sands have a uniquely similar spectral profiles with matching similarity in the spectral location of wavenumber bands (*x* axis) but with different transmittance peaks (*y* axis) *%T*. Where the wavenumber band matching occurs, this indicates the presence of similar diagnostic spectral features in oil sand (Fig. 4.9). Almost all the major hydrocarbon features expected from Table 4.1 are observed except at 3032 cm^{-1} while unreported extra features are seen at 2361 cm^{-1}, 1084 cm^{-1}, 1032 cm^{-1}, 773 cm^{-1} and 692 cm^{-1}. From Cloutis (1989), Silverstein and Webster (1998), Winklemann (2005) and Bukka *et al*. (1991), the features can be interpreted as follows: 1 – Methyl asymmetric stretching at 2950 cm^{-1} (ν_{as}= CH_3); 2 – Asymmetrical stretching methylene

at 2924 cm^{-1} (ν_{as}= CH_2); 3 – Symmetric stretching of methyl at 2867 cm^{-1} (ν_s= CH_3). Typically C-H stretching vibrations associated with methyl and methylene groups may be observed between 2960 and 2850 cm^{-1}.

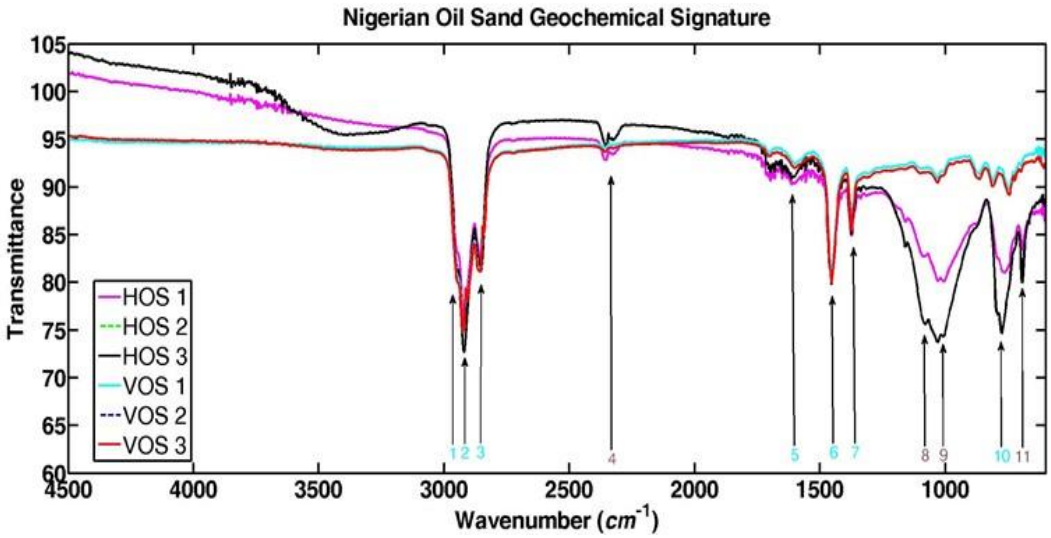

Figure 4.9: Nigerian oil sand transmittance spectra in VNIR/MIR showing diagnostic spectral features (with normalization).

Other spectral features observed for Nigerian oil sands include: 4 – Symmetric stretching of hydrogen silicon trioxide at 2361 cm^{-1} (ν_sSi-H); 5 – Skeletal vibrations involving C-C stretching within the ring of aromatic compounds at 1605 cm^{-1} (νC-C); 6 – Asymmetric bending vibrations of methyl with in-plane bending of methylene at 1456 cm^{-1} (δ_{as} CH_3+ δ_s CH_2) and 7 – Symmetric bending vibration of alkane methyl at 1373 cm^{-1} (δ_s CH_3). Although unmarked the small bands at 1620 - 1640 cm^{-1} are known to be due to distortion vibration of adsorbed water molecules (Yoon *et al*., 2009). Furthermore it can be seen that: feature 8 and feature 9 – Antisymmetric unfolded vibration of silicon oxide at 1084 cm^{-1} and 1032 cm^{-1} respectively (ν_a SiO_2) which is indicative of clay or sand granules. Also 10 – Angular deformation of silicon carbon with methylene rocking at 773 cm^{-1} (νSi-C, ϱ_s CH_3) was observed. Finally 11 – Symmetric stretching of silicon oxide at 692 cm^{-1} (ν_s SiO_2). Note that in the nomenclature used here, ν = stretching, δ = bending, ϱ = rocking, a = antisymmetric and s = symmetric.

From the 11 identified diagnostic spectral features in the Nigerian oil sands, 7 exhibit the expected features indicative of hydrocarbon presence. These are numbers 1, 2, 3, 5, 6, 7 and 10 corresponding to compound [2], [3], [4], [7], [8], [9] and [10] of

Table 4.1. However four new peaks were discovered in the oil sand spectra namely numbers 4, 8, 9 and 11. The two wavebands at 1084 cm^{-1} and 1032 cm^{-1} (8 and 9) have been discussed by Bukka *et al*., (1991) as associated with the antisymmetric unfolded vibration of Si-O-Si. In essence they are characteristic of clay materials. When the spectra are normalized using (4.1) – (4.3), the area under the curve (AUC) from all six Nigerian oil sand samples intensities is standardized to the group median (Fig. 4.9). After normalization a novel technique was used to predict the amount of bitumen and water content in the Nigerian oil sand samples based on the variation in intensity. The feature at 4 indicates the presence of hydrogen silicon trioxide ($H\text{-}SiO_3$). It is what gives oil sand the cohesive nature so that HOS is more brittle than VOS which contains more moisture but fewer hydrocarbons than HOS.

From Bukka *et al*. (1991) and Yoon et al. (2009), two of the strongest bands to estimate bitumen presence in oil sand occur at 2924cm^{-1} and 1456 cm^{-1} respectively. This corresponds to identified signature 2 and 6 of the Nigerian oil sands (Fig. 4.9). The effect of bitumen is to reduce the overall reflectance (absorption effects) of band depths in both HOS and VOS. The greater amount of clay sand in HOS is indicated by the larger absorption experienced in the 1084 cm^{-1} and 1032 cm^{-1} bands compared with VOS. From (4.7), (4.8) and (4.10) the bitumen content for each of the 3 samples of MUT E and MUT F was predicted with our measurement data presented in Table 4.8.

Table 4.8: Prediction of Bitumen content using absorbance in FTIR spectra

MUT	**Clay absorbance at 1032 cm^{-1}**			**Bitumen absorbance at 2924 cm^{-1}**			$\left(\frac{A^{\text{bitumen}}}{A^{\text{clay}}}\right)$	**Predicted Bitumen wt.%**
	I	I_0	A^{clay} (-log (I/I₀))	I	I_0	A^{bitumen} (-log (I/I₀))		
HOS 1	50.35	95.12	0.276	73.1	96.12	0.118	0.427	20.3 ± 2.1
HOS 2	43.77	97.01	0.346	78.28	96.67	0.092	0.266	12.6 ± 2.0
HOS 3	43.77	97.01	0.346	78.28	96.67	0.092	0.266	12.6 ± 2.0
VOS 1	61.07	94.96	0.191	75.09	95.00	0.102	0.53	24.2 ± 1.5
VOS 2	60.59	94.69	0. 194	74.73	95.37	0.106	0.54	24.6 ± 1.5
VOS 3	60.59	94.69	0. 194	74.73	95.37	0.106	0.54	24.6 ± 1.5

The results indicated that HOS contains less bitumen (12.6% - 20.3%) compared with VOS (24.2% - 24.6%) but more sand particles based on the absorbance caused by clay although they both have similar geochemical signatures. This technique employing the use of IR spectra to predict the bitumen content can be easily achieved in the field if the oil sand has similarities with oil sand from Athabasca (Canada) or Agbabu (Nigeria).

The predicted results compare favorably with the 12 – 22 *wt*.% of bitumen seen in Nigerian oil sands (NGSA, 2010). HOS and VOS were expected to have a higher bitumen content and lower clay content than Canadian deposits based on (NGSA, 2010; Amigun *et al*., 2012). Typically the wave bands between 1000 and 400 cm^{-1} are also characteristic for clay materials therefore the intensity of feature 11 further buttresses the fact that there is more clay and sand grains in HOS than VOS. This is better seen in the effect of grain size on the other terrain.

4.3.2. Grain Size

The NIR and MIR spectrum for soil and sand (MUT B and MUT A respectively) depends on the underlying composition. These include the vibrational signatures for organic matter, quartz (sand), kaolinite and smectite (clays), carbonates (lime), iron and aluminum oxides to name a few. The presence of several overtones due to contributions from the diverse components meant that the PLSA and PCA models were used to analyze both qualitative and quantitative features between the spectral signatures and physicochemical properties. Fig. 4.10 presents the geochemical signature of MUT A-D over VNIR (4600 – 4000 cm^{-1}) and MIR (4000 - 550 cm^{-1}) first without normalization and later with preprocessing applied to show the relative peak positions. After normalization the general profile trends based on MUT homogeneity is still evident but the spectra indicate greater overtones (Fig. 4.10b). Consequently the spectral finger prints are indicated in the non-normalized view (Fig. 4.10a).

The spectral diagnostic signature indicated: feature 1 – and feature 2 – represent twin peaks at 2924 and 2851 cm^{-1}. These are due to the fundamental alkyl stretching vibrations of ($-CH_2$) and ($-CH_2$) respectively. They are close to but lower than those reported by Kalme *et al*., (2008) and Forrester *et al*., (2012). A strong distinguishing feature between oil sands and other terrain is the very strong peaks attributed to the methyl groups in the three wavebands from 2850 – 2950 which is inverted and much weaker in MUT A to MUT D. Also feature 3 – represents overlap due to carbonate minerals at 2316 cm^{-1} which has been reported over 2600-2500 cm^{-1} (Forrester *et al*., 2012).

The spectral diagonostic feature 4 – indicates the fundamental $-CO_3$ stretching vibration near 1450 cm^{-1} which may have been shifted by specular reflectance distortion to 1439 cm^{-1}. For higher wavebands clay presence was detected from absorption bands between 1000 and 400 cm^{-1} therefore feature 5 – represents several combinations of

HSi-O-SiH (ν_a = Si-O) and silicon suboxide, Si-O-Si (ν_a = Si-O-Si) at 983 cm^{-1} (for MUT B), 1053 cm^{-1} (for C/D) and 1150 cm^{-1} (for MUT A) respectively. This region also overlaps with the region for quartz (sand), aluminosilicate clay or kaolinite and calcite ($CaCO_3$) (Nguyen *et al*, 1991). Lastly, feature 6 – corresponds to symmetric stretching of silicon oxide at 775 cm^{-1} (ν_s SiO_2).

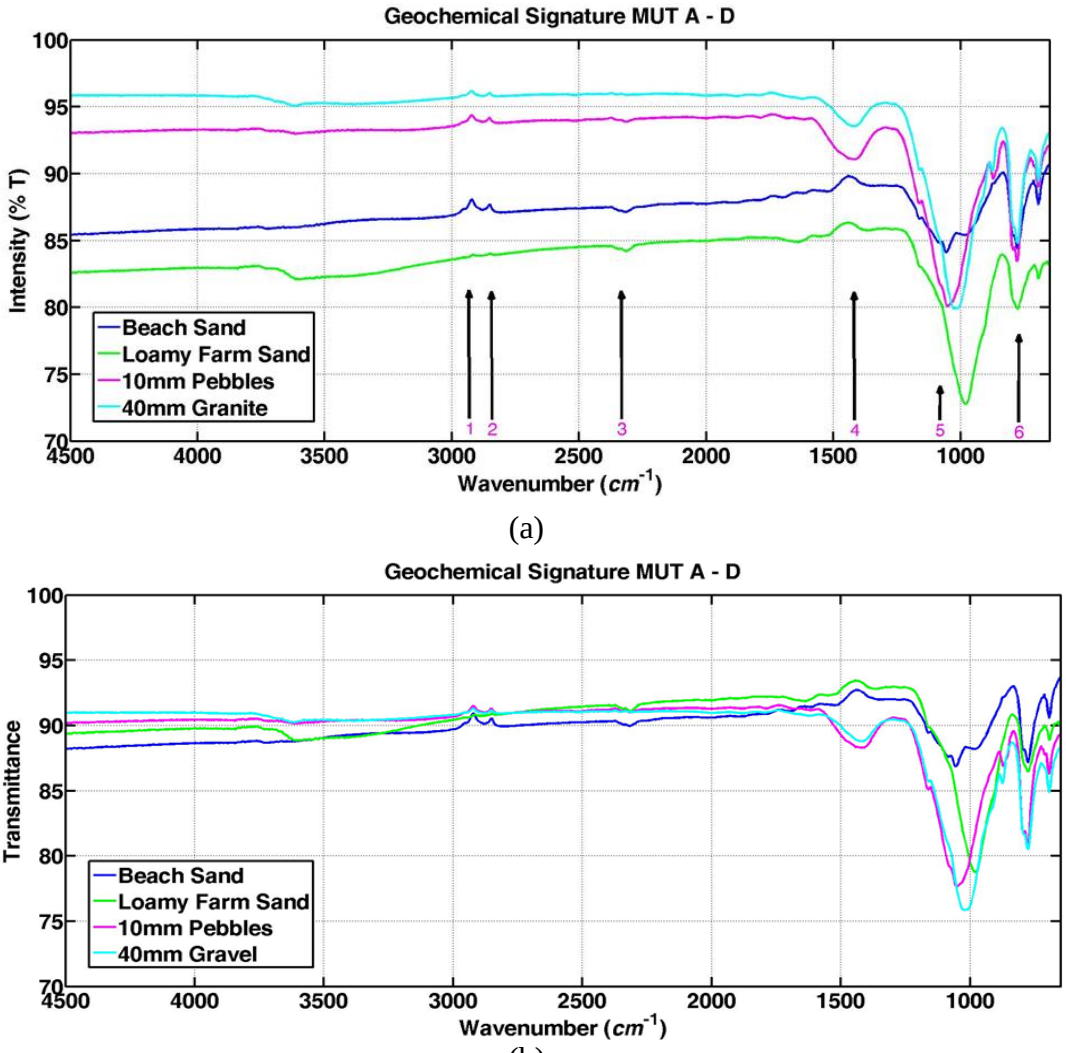

Figure 4.10: Transmittance spectra in NIR/MIR for MUT A - D showing diagnostic spectral features (a) without normalization (b) with normalization.

From the 6 selected diagnostic spectral features in the barefaced terrain, 3 exhibit features revealing silicon presence. These are 4, 5, and 6. Importantly the 6th corresponds to oil sand diagnostic feature 9 which indicates clay and sand particles. It is also clear that HOS and loamy farm soil contain more clay than VOS and beach sand causing greater absorption features in this region. In the pre-standardized view gravel

and pebbles have roughly similar amounts of clay which seems less than in loamy farm soil from feature 6. After standardization it is obvious that both have more clay sediments than loamy farm soil but there is a spectral shift around feature 5, due to the particle size (Ezeoke *et al*., 2014b). The normalized reflectance spectra for MUT A to MUT F is shown in Fig. 4.11.

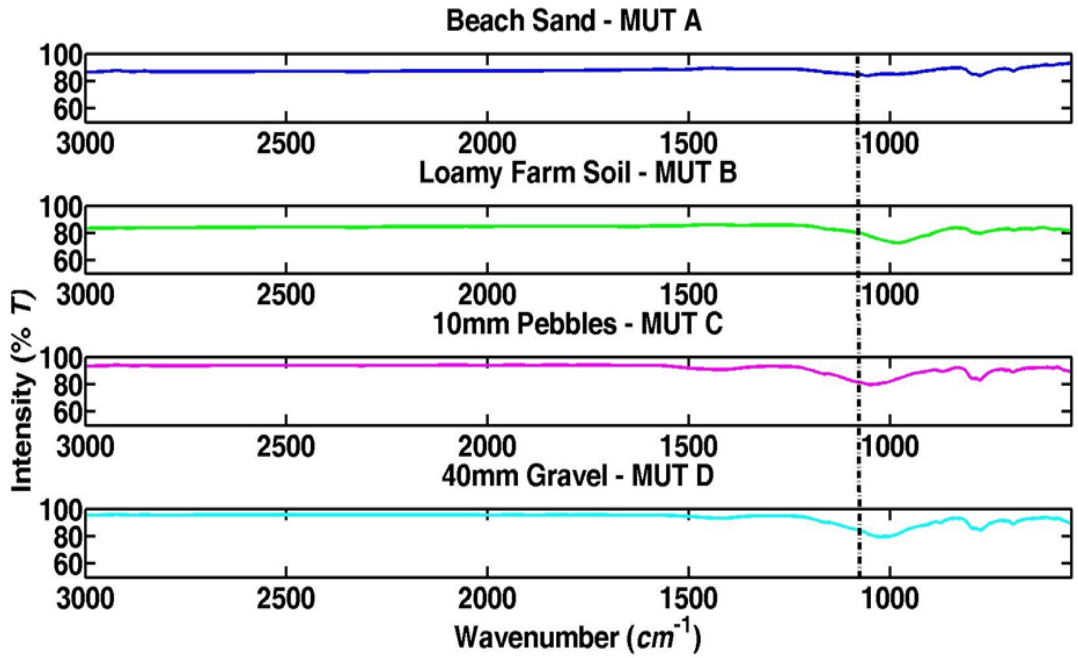

Figure 4.11: Normalized IR showing reststrahlen effect at v = 1100cm^{-1} for MUT A.

A slight reststrahlen effect is witnessed at v = 1100 cm^{-1} in beach sand compared to gravel, pebbles and loamy farm soil. This is a slight shift from the 1150 cm^{-1} waveband at which Willey (1986) also observed this effect. He considered it to be caused by the presence of quartz which causes an inability of the EM radiation within the narrow energy to propagate within beach sand. Furthermore both 40mm gravel and 10mm pebbles share similar geochemical signature with only slight difference in the magnitude of absorption peaks due to the relatively larger sediment (or grain size) of gravel. This means that hyperspectral imaging has applications to particle grain size determination. In addition to the observation of the reststrahlen effect for beach sand it is believed that the homogeneity and smaller grain size of beach sand particles also contributed to the lower absorption profile except in the higher wavenumber region.

4.3.3. Moisture Presence

The climate of the AOSR in south west Nigeria is prone to rainfall. Therefore an interesting part of the geochemical signature evaluation process was to determine the effect of moisture on the surrounding terrain and also develop an empirical formula to predict the presence of moisture in oil sands that may have similar phyisico-chemical properties with Nigerian oil sands.

The transmission and absorption spectra of water is very complex due to the relative abundance of the six isotopologues of water ($H_2{}^{16}O$, $H_2{}^{18}O$, $H_2{}^{17}O$, $HD^{16}O$, $HD^{18}O$, and $HD^{17}O$) and heavy water (D_2O). Water molecules impact the remote sensing analysis of both terrain and space objects while water vapor spectra is germane to atmospheric science. Consequently various species of water have been discussed severally in literature (Bernath, 2002; Tennyson *et al*., 2014). Detailed characterization of the transmission and absorption feature of water molecules alone have been discussed by (Maréchal, 2003; Maréchal, 2011).

We experimentally obtained the spectra for water over the MIR region at room temperature. Thereafter the effect of water on the properties of barefaced terrain was studied as a precursor to the development of an empirical model. Water at room temperature was used as control for the change in terrain geochemical signature with 10 - 30 *wt*.% of water variation. The results for 10 and 20 *wt*.% of water is shown (Fig. 4.12). Here 4 of the spectral features at 742 cm^{-1}, 1640 cm^{-1}, 2400 cm^{-1} and 3350 cm^{-1} were selected to highlight the presence and effect of increasing moisture content to barefaced terrain MUT A and B (Fig. 4.12). Both the pre-normalized and normalized spectra are shown although selected diagnostic spectral features are only indicated in the pre-normalised spectra (Fig. 4.12.a).

Here the features: 1 – indicates weak rocking H-bonds in the H_2O molecules, ϱ_{H2O} at 742 cm^{-1}. However in: 2 – the relatively smaller water bands compared to 1, 3 and 4 at 1620 – 1640 cm^{-1} is shown as bending bands, $\delta_{H\text{-}O\text{-}H}$ representative of band vibration of H-O-H angle at 1640 cm^{-1}. According to Yoon *et al*., (2009) these occur due to the distortion vibration of adsorbed water molecules. This is reasonable, considering the predictable increase in terrain physicochemical properties around this region. Feature 3 – represents the OD stretch bands in the region 2000 - 2800 cm^{-1} with peak at 2400 cm^{-1} while feature 4 – covers OH stretch bands in the region from 2700 – 3600 cm^{-1} with peak at (ν_s = O-H) stretch occurring at 3350 cm^{-1}.

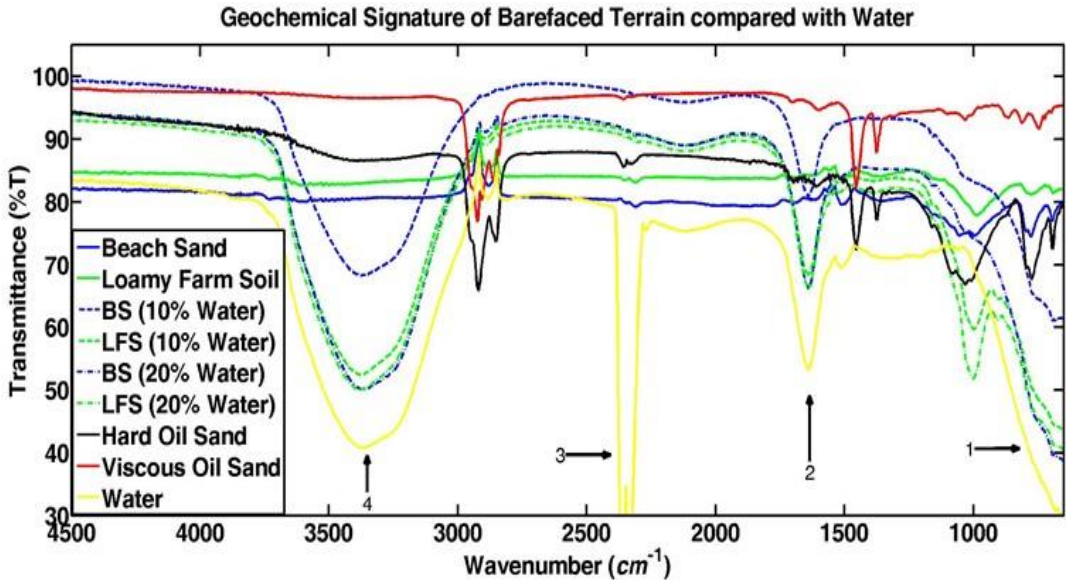

(a)

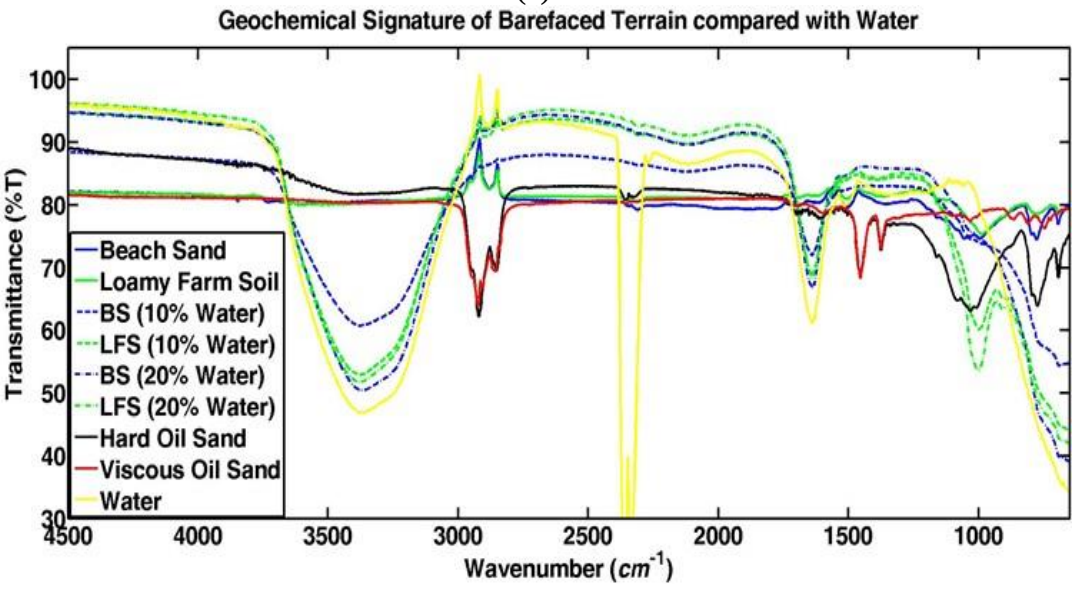

(b)

Figure 4.12: Geochemical signature selected barefaced terrain showing diagnostic spectral features with 10 and 20 *wt*.% of water (a) without normalization (b) with normalization.

From (4.3), (4.4) and (4.6) the water content in each of the 3 samples of MUT E and MUT F was predicted. Since there was no empirical equation similar to (4.8) for water content, an empirical equation was derived to determine this relationship. Spectra for MUT A was used to generate the empirical equation because the response of MUT A to clay at the 1032 cm^{-1} band was closest to VOS. Also increasing *wt*.% of water was better defined for MUT A at the OH stretch band peak at 3350 cm^{-1} (Fig. 4.13).

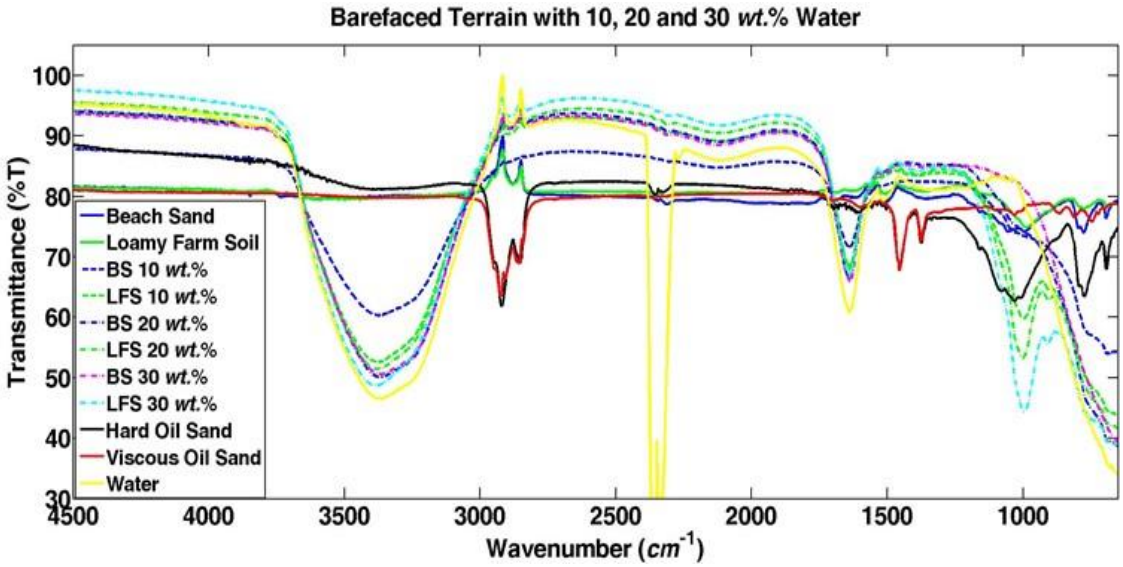

Figure 4.13: Normalized spectra of barefaced terrain with 10, 20 and 30 *wt.*% water showing better defined response for MUT A in 1032 cm^{-1} and 3350 cm^{-1} wavenumber bands.

The first step in the development of the empirical equation to determine the water content in the Nigerian oil sands was the determination of the absorbance ratio for water and clay (A^{water}/A^{clay}). This was based on the relationship between the concentration ratio (c^{water}/c^{clay}) at the specific wavenumber bands representing the peak response for clay and water (table 4.9).

Table 4.9: Determination of water empirical relationship from MUT A FTIR spectra

MUT A	**Conc. Ratio** $\left(\frac{c^{water}}{c^{clay}}\right)$	**Clay absorbance at 1032 cm^{-1}**			**Water absorbance at 3350 cm^{-1}**			$\left(\frac{A^{water}}{A^{clay}}\right)$
Water content (%)		***I***	***I*₀**	A^{clay} **(-log (I/I₀))**	***I***	***I*₀**	A^{water} **(-log (I/I₀))**	
3	0.03	74.58	80.35	0.0324	80.16	81.28	0.006	0.186
10	0.1	75.17	82.43	0.0400	60.58	86.23	0.153	3.829
20	0.2	75.10	83.25	0.0447	50.21	91.74	0.266	5.955
30	0.3	82.70	88.90	0.0314	50.93	93.56	0.264	8.412

The R^2 value indicating linearity was 0.9606. The measured data and the line of best fit using least square fitting are shown (Fig.4.14). The slope which is the indicated ratio of absorption coefficient seems reasonable based on coefficient values from Yoon *et al*., (2009) and Koike *et al*., (1982).

The derived empirical equation (4.13) relates the inverse of the absorbance to the concentration of the components based on MUT A spectra. Thereafter (4.13) was

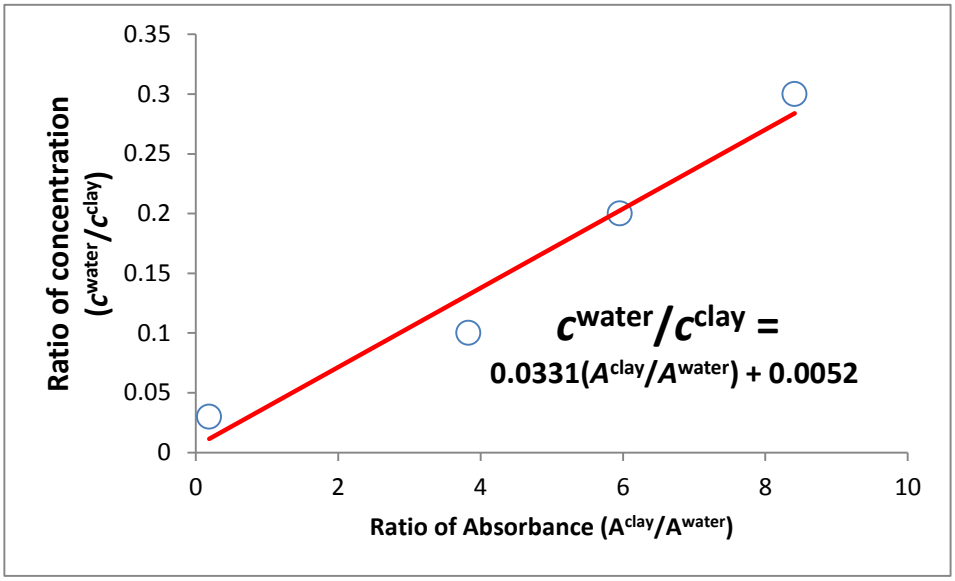

Figure 4.14: Relationship between concentration ratio (c^{water}/c^{clay}) and absorbance ratio (A^{clay}/A^{water}) shown by blue circle. Empirical equation obtained by least square fitting is inset while result is shown as solid red line.

applied to experimental measurement data for MUT E and MUT F in order to estimate the moisture content in Nigerian oil sands as shown in in Table 4.10.

$$\frac{c^{water}}{c^{clay}} = (0.0331)\left(\frac{A^{clay}}{A^{water}}\right) + 0.0052. \tag{4.51}$$

Table 4.10: Prediction of Water in Oil Sands Content using absorbance in FTIR Spectra

MUT	Clay absorbance at 1032 cm^{-1}			Water absorbance at 3350 cm^{-1}			$\left(\frac{A^{clay}}{A^{water}}\right)$	Predicted Water wt.%
	I	I_0	A^{clay} (-log (I/I₀))	I	I_0	A^{water} (-log (I/I₀))		
HOS 1	80.52	88.25	0.0398	96.8	102	0.0227	1.752	6.3 ± 2.0
HOS 2	73.92	88.93	0.0802	95.59	104.2	0.0375	2.144	7.6 ± 2.0
HOS 3	73.92	88.93	0.0802	95.59	104.2	0.0375	2.144	7.6 ± 2.0
VOS 1	91.2	95.01	0.0178	94.16	95.05	0.0041	4.350	14.9 ± 2.0
VOS 2	90.59	95.69	0.0238	93.86	95.42	0.0072	3.323	11.5 ± 2.0
VOS 3	90.59	95.69	0.0238	93.86	95.42	0.0072	3.323	11.5 ± 2.0

From Table 4.10, HOS water content varies from 6.3 *wt*.% to 7.6 *wt*.% while VOS varies from 11.5 *wt*.% to 14.9 *wt*.%. The results indicate that HOS contains less water than VOS and the empirical formula is valid for oil sands with similar geochemical signature of oil sand. Therefore despite seemingly similar geochemical

signatures the empirical study discovered that HOS had less bitumen and water content but more sand particles than VOS.

4.4. Concluding Remarks

Barefaced terrain have slightly different texture, orientations, mixing phases and material compositions. This chapter determined the unique spectral signature of oil sands which was distinguished based on VNIR and MIR spectroscopy data. Ultra-high resolution spectrograms were generated in the frequency region varying from 12 THz to 120 THz corresponding to wavelength in 2.5 – 25 μm. HOS and VOS measurement data along with beach sand, loamy farm soil, quartz and pebbles were analyzed with multivariate methods including PLSA and PCA. The diagnostic spectral features of oil sands were linked to the chemical composition and fundamental molecular vibrations. ATR measurements provided better response than emissivity and T/R measurements for oil sand.

The experimental results indicated that: (i) spectral features can be recognized for VOS, HOS, pebbles, granites and various *wt*. % of beach sand and loamy farm soil; (ii) different oil sand samples can be qualitatively distinguished based on the spectral features, therefore despite higher viscosity of VOS more bitumen was present in VOS than HOS; (iii) this also applied to measurements simulated at the spectral resolution of hyperspectral and multispectral sensors. The statistical models generated with HOS and VOS spectra indicated that for oil sand the most important variables concentrated in three regions: 1000-1100 cm^{-1}, 1400-1450 cm^{-1} and 2900-2950 cm^{-1} (Fig. 4.9).

An empirical formula based on statistical analysis of oil sands from the AOSR was developed to predict the presence of bitumen hydrocarbon (Table 4.8) and moisture (Table 4.9) for the MUTs. Also 11 diagnostic spectral features were identified in Nigerian oil sands with 7 exhibiting the expected features indicative of hydrocarbon presence (Fig. 4.9 and Table 4.1). Furthermore four new peaks corresponding to features 4, 8, 9 and 11 were observed with the two wavebands at 1084 cm^{-1} and 1032 cm^{-1} consistent to clay materials. Spectroscopy raises the possibility of remotely detecting and characterizing oil sand and other barefaced terrain through optical remote sensing. The suggested geochemical signature determination process can be applied to other spectra samples with high accuracy and has important applications to geointelligence analysis.

5 Dielectric Measurements

In line with the multi-sensor approach for terrain characterization, the second step involves determination of the electrical properties that govern the interaction between synthetic aperture radar electromagnetic waves and oil sand. The experimental procedure to determine dielectric properties of barefaced terrain, develop a dielectric discrimination model for oil sand and analysis using statistical models is presented.

Radar scattering by barefaced terrain is determined by two main attributes. First is the geometry of the air-terrain boundary and second is the microwave dielectric properties of the terrain medium. There has been little interest in dielectric properties of oil sand terrain which are intrinsic and therefore empirically determined unlike physical features such as surface roughness or correlation length that have been standardized and described by several authors. Information on earth dielectric permittivity may be useful in problems of electric power transmission and environmental pollution but this study considers its relevance to developing models for geological mapping. Some electrical properties of the surrounding barefaced terrain types have been discussed (Table 3.11). Both bitumen and oil sands literature revealed several contrasting dielectric constants, within the range of 2.48 – 7.0. Therefore it was important to determine the dielectric behaviour of oil sands across radar frequencies of L-, C- and X-band. If the dielectric dispersion is not accurately applied it would interfere with the precision of developing the barefaced terrain models and also affect post-processing data interpretation. Also a dielectric discrimination statistical model (DDSM) was developed to determine possible frequency of operation for the characterizing sensor models.

5.1. Electrical Properties of Terrain

The electrical properties of terrain are the primary properties of dielectric polarization (charge separation) and electric conduction (charge transport). The dielectric permittivity of a material is the ability of the material to be polarized while the electrical conductivity is its ability to conduct an electrical current when a potential difference is applied between two locations. Polarization occurs when free dipoles within the material (or terrain) are reoriented due to the presence of an electric field. In the microwave frequency of interest (0.9 – 10 GHz) the mechanism responsible for

dielectric polarization of oil sand terrain can be expected to be interfacial polarization (Schön, 1998). This behavior is also called the Maxwell-Wagner effect and occurs in heterogeneous materials due to non-uniform charge distribution at boundary regions. Such regions exist at grain boundaries or other discontinuities like minerals or moisture within the solid rock matrix and expectedly have different electrical properties depending on the type and extent of the discontinuity.

The only previously known effort to empirically determine dielectric property of oil sands at radar frequencies was by Erdogan *et al*., (2011). In that study a cavity resonator was used to measure three grades of oil sand from Alberta at 2.49 GHz. The results indicated that the real and imaginary parts of permittivity increased with the quality of the oil sands as shown in (Fig. 5.1). These results are of limited use because they are valid for only one specific frequency and with oil sands from one location.

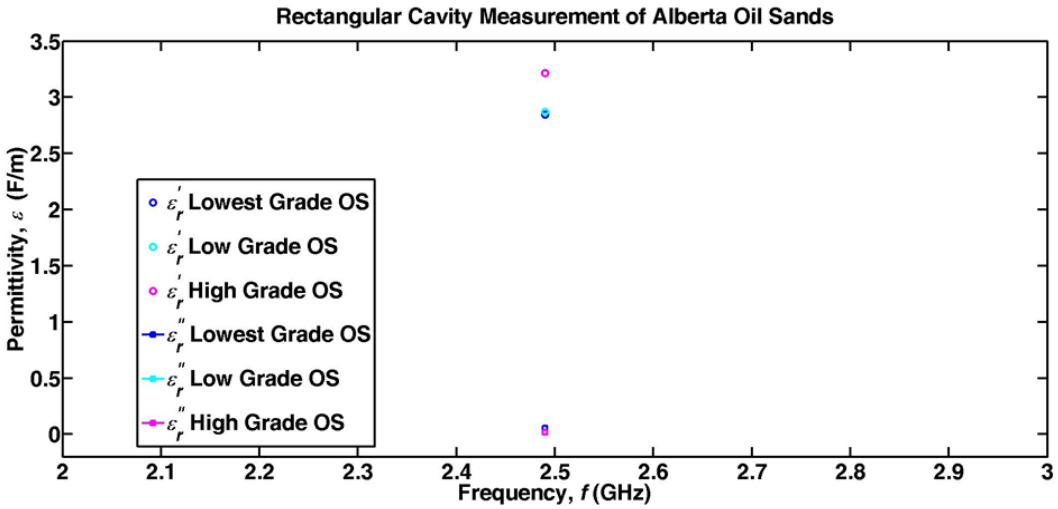

Figure 5.1: Electrical characteristics of Alberta oil sands using rectangular cavity at 2.49 GHz. Real and imaginary permittivity (Erdogan *et al*., 2011).

Terrain resistivity has been evaluated by direct observation using dipole-dipole resistivity soundings and magnetotelluric resistivity methods (Keller, 1963). However such measurements were supplemented by laboratory measurements of the electrical properties for higher reliability. Other efforts at much lower frequency (0.1 – 100 kHz) determined the resistivity of oil-based muds with oil being the non-conductive continuous phase of the emulsion (Laasted *et al*., 2000). Amigun *et al*. (2012) investigated the magnetic and electrical resistivity of Nigerian oil sands using vertical electrical sounding (VES) to determine lateral continuity of the Agbabu oil sand reservoir (AOSR). This is the same region from which the hard oil sand (HOS) and viscous oil sand (VOS) material's under test (MUTs) were obtained. Also Odunaike *et*

al. (2010) determined Nigerian oil sands resistivity to fall within the 110 – 1800 Ωm values seen in oil rich sands from Athabasca (Canada). However they did not measure permittivity behavior.

At higher frequencies (100 MHz – 1 GHz) the permittivity for dry Indian limestone and dry Boise sandstone has been examined (Rau & Wharton, 1982) while Shen (1985) investigated the dielectric properties of oil but observed no dispersion in the frequency range 800 MHz to 1.2 GHz. From the discussion of previous results it is expected that water content will be the main variable influencing permittivity however the study would further determine if the presence of bitumen has any effect. The effect of pressure and temperature was not studied because no significant effect on the dielectric properties was expected (Ezeoke *et al*., 2014a; Olhoeft, 1981).

5.2. Dielectric Mixing Models

Dielectric mixing models are used to explain the dielectric behaviour of diverse media, objects or terrain. Rodríguez and Abreu (1990) developed a mixing model for saturated porous media consisting of rock, water and oil. Each component was assigned an exponent β_w, β_n and β_g corresponding to the material presence of water saturation, oil saturation and rock matrix respectively. Also Alvaro *et al*., (2009) successfully used the sand-bitumen ratio (S-Br) to determine the effect of conductivity in heterogeneous material such as a combination of asphalt mortar and fillers for bitumen not exceeding 6% S-Br. Evolving a sand-bitumen-water ratio resulted in a dielectric constant, ε that was higher than bitumen alone since measured values of water had ε = 74 and conductivity, σ' = 3.53 Sm^{-1}. In petrophysics a few other mixing laws have been proposed mainly to estimate rock properties such as porosity and water saturation using electrical measurements in the laboratory and field measurements at wellbores (Banhegyi, 1988). The two most well-known are Archie's Law and the Complex Refractive Index Method (CRIM).

5.2.1. Archie's Law

For water saturated rocks consisting of matrix minerals that are non-conducting, the empirical relationship known as Archie's Law has been used to analyze the electrical properties. The relationship between in-situ electrical conductivity, C_t of a

sedimentary rock to its porosity, ϕ and brine saturation, s_w is given by (Archie, 1942; Winsauer & Shearin, 1952):

$$\boldsymbol{C_t = \frac{1}{a} C_w \phi^m s_w^n}. \quad (5.1)$$

Here C_w represents the brine electrical conductivity, m is the cementation exponent of the rock (1.8 – 2.0 for sandstones), n is the saturation exponent (usually close to 2) and a, is an error or diffusion term also known as the tortuosity factor. It is possible to rearrange (5.1) in terms of electrical resistivity, ρ_t (in Ωm):

$$\boldsymbol{\rho_t = a \phi^{-m} s_w^{-n} \rho_w}. \quad (5.2)$$

The formation factor, F_f loosely refers to the resistivity factor of the formation. In essence, it is the ratio of the resistivity of 100% water saturated rock to the resistivity of the water with which it is saturated as in (5.3). The significance of the measured resistivity recorded by the electrical logs depends on the empirical relationship established in a laboratory between aspects of the physical property of reservoir rocks and the formation factor. This is given by:

$$\boldsymbol{F_f = \frac{a}{\phi^m} = \frac{\rho_o}{\rho_w}}. \quad (5.3)$$

Where ρ_o is the resistivity of the rock filled with only water such that $s_w = 1$ (or 100%) and ρ_w is the resistivity of the water with which the rock is saturated. The term 'formation factor' was originally used because it was roughly constant for any given formation (Glover, 2010). It varies from unity, $F_f = 1$, which represents the case when $C_t = C_w$ (i.e., when $\phi \rightarrow 1$) and increases when porosity decreases with $F_f \rightarrow \infty$ as $\phi \rightarrow 0$. Archie's experimental work also led to the empirical deduction that:

$$\boldsymbol{F_f = a \phi^{-m}}. \quad (5.4)$$

An advantage that Archie's law has over other mixing laws such as Waff's model (Waff, 1974), Hashin-Shtrikman bounds (Hashim & Shtrikman, 1962) and the parallel, perpendicular and random models (Glover *et al*., 2000), is that the cementation exponent gives it a flexibility of application. Smaller values of a, and m, qualitatively indicate well interconnected pore spaces. The cementation exponent, m can be inferred from electrical conductivity measurements at brine-saturated intervals. Also electrical

resistivity logs are typically used to determine the values of resistivity while brine conductivity can be measured directly from the water samples produced. For oil sands and other barefaced terrain the investigation used dielectric probe kits (DPK) and suitable vector network analyser (VNA) to determine the dielectric permittivity because both materials from Nigeria are either solid like HOS or semi-solid in VOS. Although the relationship inherent in Archie's law is now a standard it is best used to describe flow of ions (such as sodium, Na^+ and chloride) in clean terrain with varying intergranular porosity as the only electrical conduction is assumed to be in (and due to) water. Consequently, it is best suited for electrical well log interpretation as it relates the measured borehole electrical conductivity to hydrocarbon presence because for fluid saturated rock the hydrocarbon presence will be $1 - s_w$. This is not valid for oil sand terrain.

A broader discussion of Archie's law and a list of papers discussing various *a*, and *m* values for specific rocks such as clean sandstones have been provided by Keller (1982). Subsequent studies have used down-hole log data, core data and laboratory measurements to confirm the relationship between porosity and resistivity (Jackson *et al*., 1978; Ioannidis *et al*., 1997). Archie's Law is not applicable in terrain containing significant percentage of clay because clay provides a conductive matrix which negates a fundamental assumption rendering the application invalid. From Ezeoke and Tong (2013) and spectral models in Chapter 4, VOS and HOS contain significant presence of clay. Also for our microwave applications the frequency of operation is several magnitudes higher than often used for resistivity mapping. Although Huang and Fraser (2002), developed a system for both dielectric permittivity and resistivity mapping from airborne sensors, resistivity, ρ is more prevalent at very low frequencies (VLF) (< 15 kHz) for which Archie's Law is better suited.

5.2.2. Complex Refractive Index Method

The CRIM does not consider geometry dependent parameters. Furthermore unlike Archie's law, CRIM neither depends on the diameters of the pores (or porosity) nor does it have a great deal of published data to back it up (Rodríguez & Abreu, 1990). However it is directly related to the interpretation of dielectric well logs and is defined by (5.5):

$$\sqrt{\boldsymbol{\varepsilon}^*} = \boldsymbol{s_w}\,\boldsymbol{\phi}\sqrt{\boldsymbol{\varepsilon_w^*}} + (\mathbf{1} - \boldsymbol{s_w})\boldsymbol{\phi}\sqrt{\boldsymbol{\varepsilon_n}} + (\mathbf{1} - \boldsymbol{\phi})\sqrt{\boldsymbol{\varepsilon_g}}. \qquad (5.5)$$

Here ε^* is the complex dielectric constant of the mixture, while ε_w^*, ε_n and ε_g are the dielectric constants of water, oil and rock respectively. The CRIM equation is derived by assuming that electromagnetic (EM) waves travel distances ℓ_w, ℓ_n and ℓ_g through a three layered medium. For such a system the total travel time, t, through the three components will be:

$$\boldsymbol{t = t_w + t_n + t_g}. \tag{5.6}$$

Since $t = \frac{\ell}{v}$, where v is the wave velocity ($= \frac{c}{n^*}$) in a medium of complex refractive index n^* and c is the velocity of light in vacuum. It (5.6) may also be expressed in terms of the travel distance, ℓ as:

$$\boldsymbol{n^* = \frac{\ell_w}{\ell}\, n_w^* + \frac{\ell_n}{\ell}\, n_n^* + \frac{\ell_g}{\ell}\, n_g^*}. \tag{5.7}$$

Substituting $n^* = \sqrt{\varepsilon^*}$ in (5.7) to obtain:

$$\sqrt{\boldsymbol{\varepsilon^*}} = \frac{\ell_w}{\ell}\sqrt{\boldsymbol{\varepsilon_w^*}} + \frac{\ell_n}{\ell}\sqrt{\boldsymbol{\varepsilon_n}} + \frac{\ell_g}{\ell}\sqrt{\boldsymbol{\varepsilon_g}}. \tag{5.8}$$

In essence (5.8) relates the dielectric constant of a medium with the dielectric constant of each component through parameters that depend on the spatial arrangement of the components. The CRIM equation in (5.5) is derived from the simple case when incidence angle i, is perpendicular to the three parallel layers such that the relationship may be written as volume fractions in (5.9):

$$\frac{\ell_w}{\ell} = \boldsymbol{s_w \phi}\,; \qquad \frac{\ell_n}{\ell} = \boldsymbol{(1 - s_w)\phi}; \qquad \frac{\ell_g}{\ell} = \boldsymbol{(1 - \phi)}. \tag{5.9}$$

CRIM is a good approximation in the static low frequency case and has shown some agreement at higher frequencies up to 2 GHz using an EM propagation tool (EPT) (Rau & Wharton, 1982) but higher frequency measurements have not been conclusive. Besides CRIM, most other mixing models available in literature for petrophysics are for electrical conductivity in porous media (Table 5.1) (Glover, 2010). They are highlighted in Table 5.1 but will not be discussed further. In order to improve CRIM, Rodríguez & Abreu (1990), introduced coefficients which contain information about the geometry of each component but it is difficult to speculate about the geometrical distributions of water and oil in oil sands.

Table 5.1: Other Mixing Models for Electrical Properties in Porous Media

Name	Equation	Reference	Remarks
Parallel model	$C_{eff} = \sum_{i=1}^{n} \phi_i C_i$	Luo *et al.* (1994), Guégen & Palciauskas (1994)	Arithmetic mean. Parallel layers of constant thickness with conductivity, C_i arranged axially to current flow.
Perpendicular model	$1/C_{eff} = \sum_{i=1}^{n} \phi_i / C_i$	Guégen & Palciauskas (1994), Luo *et al.* (1994)	Harmonic mean. Parallel layers of constant thickness with conductivity, C_i arranged normally to current flow.
Random model	$C_{eff} = \prod_{i=1}^{n} C_i^{\phi_{i_i}}$	Somerton (1992)	Geometric mean. Conductivity, C_i is arbitrary shaped and in oriented volumes distributed randomly
Lichtenecker-Rother equation	$C_{eff} = (C_1^{1/m}(1-\phi_2) + C_2^{1/m}\phi_2)^m$	Lichtenecker & Rother (1936)	Based on the theory of functional equations under appropriate boundary conditions. Leads to Archie's law if $\phi_1 = 0$.
Generalized Archie's law	$C = \sum_{i}^{n} C_i \phi_i^{m_i}$ With exact solution $m_j = \log(1 - \sum_{i \neq j} \phi_i^{m_i}) / \log(1 - \sum_{i \neq j} \phi_i)$ And first order approximation $m_j = \sum_{i \neq j} \phi_i^{m_i} / \sum_{i \neq j} \phi_i$	Glover (2010)	Derived from conventional Archie's law by considering boundary conditions implied by geometrical constraints

Furthermore oil sands (both VOS and HOS) do not exist in separate layers as grains, water and bitumen but rather in 'water-wet' arrangement where bitumen is in direct contact with the water and grains (see section 3.1.1). Consequently an empirical study of HOS and VOS along with other terrain was performed.

5.3. Dielectric Materials and Investigative Methods

There are four main methods to determine the complex electrical properties of a substance, terrain or material. These include the transmission line, resonant cavity, coaxial probe and parallel plate techniques. Each method typically requires placing samples of the MUT in to a capacitor arrangement, waveguide array or resonant cavity except the coaxial probe technique which places a probe either on the surface or inside the MUT. A summary of these methods along with a basic description and requisite operating frequency of investigation is provided (Table 5.2). Several factors including accuracy, frequency range, precision and the shape or form of the MUT determines the

best approach for measurement. In this research work the coaxial probe technique was best suited for investigation of the dielectric properties of the terrain MUT. This is because the barefaced terrain models (BTM) are expected to be developed for multi-frequency Radar sensors operating across a range of frequencies from L-band to X-band. Also the physical characteristics of the terrain made the coaxial probe technique a great fit as HOS samples (Fig. 5.2) were irregularly shaped while VOS samples (Fig. 5.3) were mostly semi-solid.

Consequently the coaxial probe technique was used to empirically determine the dielectric material properties of oil sand and other barefaced terrain. The dielectric properties investigated include the real and apparent parts of the permittivity and the loss tangent (ε', ε'' and tan δ) respectively. The results indicate the value of dielectric permittivity for each MUT with frequency. Statistical models were developed to identify the frequencies with the greatest impact on permittivity values and result accuracy was improved by minimizing measurement errors, recalibration with standard materials, least square fitting of results and measurement repetition for consistency.

Table 5.2: Dielectric Measurement Techniques

Method	Operating Frequency	Description
Parallel plate/free space	Less than 1 GHz	Operates at low frequency. MUT is emplaced between 2 electrodes to form a capacitor. This is a capacitive method.
Coaxial probe	200 MHz – 50 GHz	Open ended coaxial probe is placed in MUT. In addition to irregularly shaped HOS it was also useful to VOS as it increases contact area for semi-solid objects.
Resonant cavity	5 GHz – 60 GHz	MUT is inserted at the maximum electric field of cavity resonating at a specific frequency, f_c and shifts f_c lower. This offers the best lost factor resolution but is subject to errors (perturbation analysis) particularly for low loss samples due to comparatively low Q-factor of empty waveguide cavity. Also requires VNA to have excellent frequency resolution (1 Hz).
Transmission/ reflection line	100 KHz – 18 GHz	General purpose method may be used with waveguide, coaxial and free space with medium level losses as MUT is placed inside a portion of enclosed transmission line.

5.3.1. Materials

This work investigated 14 samples of oil sand consisting of 10 HOS samples and 4 VOS samples along with 2 samples of beach sand and loamy farm soil at three different *wt*.% of water. The samples investigated cover MUT A, B, E and F (from Fig. 4.1). The acquisition of MUT E and F from the AOSR located within latitudes 6° 35' 16.3''N to 6° 37' 13.9''N and longitudes 4° 49' 29''E to 4° 50' 20.7"E has been discussed previously in this thesis (and Ezeoke *et al*., 2014b). The 10 HOS fragments from 3 spatial locations are shown in Fig. 5.2. HOS 1 to HOS 10 are irregularly shaped

and were numbered in increasing sizes from 1 to 10. For optimum measurement accuracy the high temperature probe requires the MUT diameter, thickness and granule size to be (Agilent AN5988, 2003):

$$\textbf{Diameter}: > \mathbf{20}\ \boldsymbol{mm} \tag{5.10}$$

$$\textbf{Thickness}: > \frac{\mathbf{20}}{(\sqrt{|\boldsymbol{\varepsilon_r^*}|})}\ \mathbf{mm} \tag{5.11}$$

$$\textbf{Granule size}: < \mathbf{0.3}\ \boldsymbol{mm} \tag{5.12}$$

Figure 5.2: Hard oil sand (HOS1 – HOS10) from 3 spatial locations within the AOSR.

The VOS samples were also arranged in increasing volume from 1 to 4 (VOS 1 – VOS 4). The volumetric quantity covered 100 ml, 450 ml, 900 ml and 2000 ml respectively (Fig. 5.3). The different mass and volume sizes were necessary to understand the effect of size and volume of oil sand on permittivity. Other barefaced terrain representing MUT A and B at different *wt*.% of water are not shown but they are listed in Table 5.3. From Fig. 5.2 and Fig. 5.3 it can be seen that VOS 1, HOS 1, HOS 2 and HOS 3 did not meet the thickness criteria set in (5.10).

Table 5.3: Dielectric investigation campaign

MUT	Name	Description
A, A10, A20, A30	Beach Sand	100% MUT A and others increasing by 10 *wt*.% water
B, B10, B20, B30	Loamy Farm Soil	100% MUT B and others increasing by 10 *wt*.% water
E: HOS 1 – HOS 10	Hard oil sand	10 fragments of oil sand with irregular shapes from 3 randomly selected locations in the AOSR
F: VOS 1 – VOS 4	Viscous oil sand	4 volumes of VOS with 100, 450, 900 and 2000 ml from 3 randomly selected locations in the AOSR

5.3.2. Method

Three sets of measurements were performed at the University College London (UCL) Microwave laboratory located in the Department of Electronic and Electrical Engineering. The first was carried out in 2013 on VOS 1, HOS 3 and HOS 6. For this measurement the dielectric properties were investigated using an Agilent 85070E dielectric probe kit (DPK) and Agilent ENA 9 kHz – 8.5 GHz VNA series. The DPK consists of a high temperature probe, short block and associated cables (inset Fig. 5.4a). The ENA VNA for the first measurement was only able to investigate properties up to 8.5 GHz. The other two studies were carried out in January and April 2014 using the DPK and Agilent PNA N5227A 10MHz – 67 GHz VNA. The PNA VNA is theoretically able to investigate properties up to 67 GHz but this is limited to 20 GHz by the high temperature probe (Agilent AN5988, 2003).

The generic experimental set up for measurement of the dielectric properties is shown (Fig. 5.4a), along with an inset of the high temperature probe and shorting device. During measurements the high temperature probe was mounted on a laboratory stand before insertion in to the sample as shown (Fig. 5.4b). The aim of the stand is to keep stable the high temperature 20 GHz cable (Agilent 1250-1743 also included in the DPK kit) stable along with the high temperature probe. The 20 GHz cable was connected from the high temperature probe to a high frequency RF coaxial cable. The high frequency RF coaxial cable (shown with black covering in Fig. 5.4.) is directly connected to the VNA ports in order to reduce possible transient errors.

Cable stability, air gaps and sample thickness are three main sources of operator errors. Therefore the stand was used to take care of cable stability while air bubbles were monitored by inserting the probe in water for calibration and then wiping clean with soft cloth before each measurement. In essence due to the nature of the oil sands,

a range of preventive actions were employed to minimize measurement errors. One was to calibrate the probes before each sequence of measurements and then to use air and water as control samples.

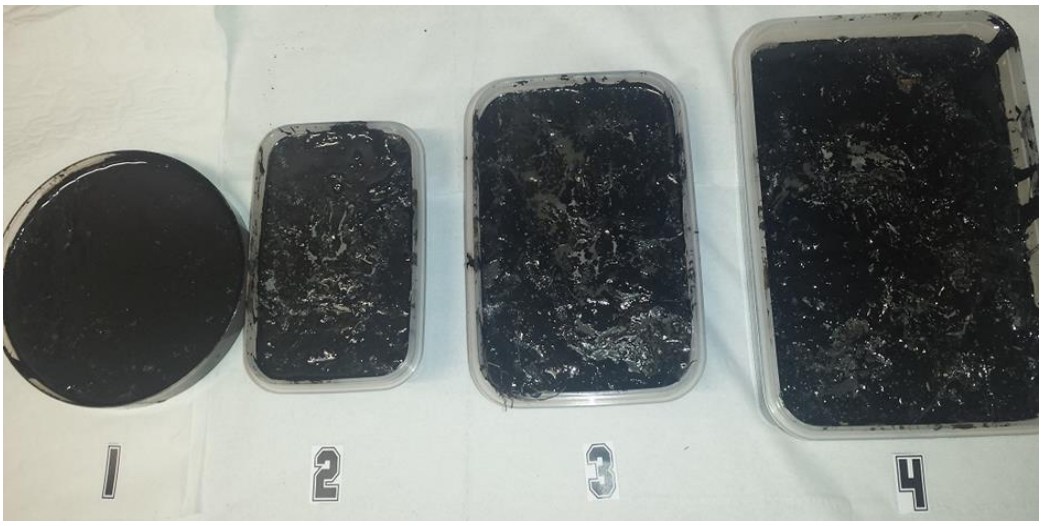

Figure 5.3: Viscous oil sand (VOS1 – VOS4) from 3 spatial locations within the AOSR.

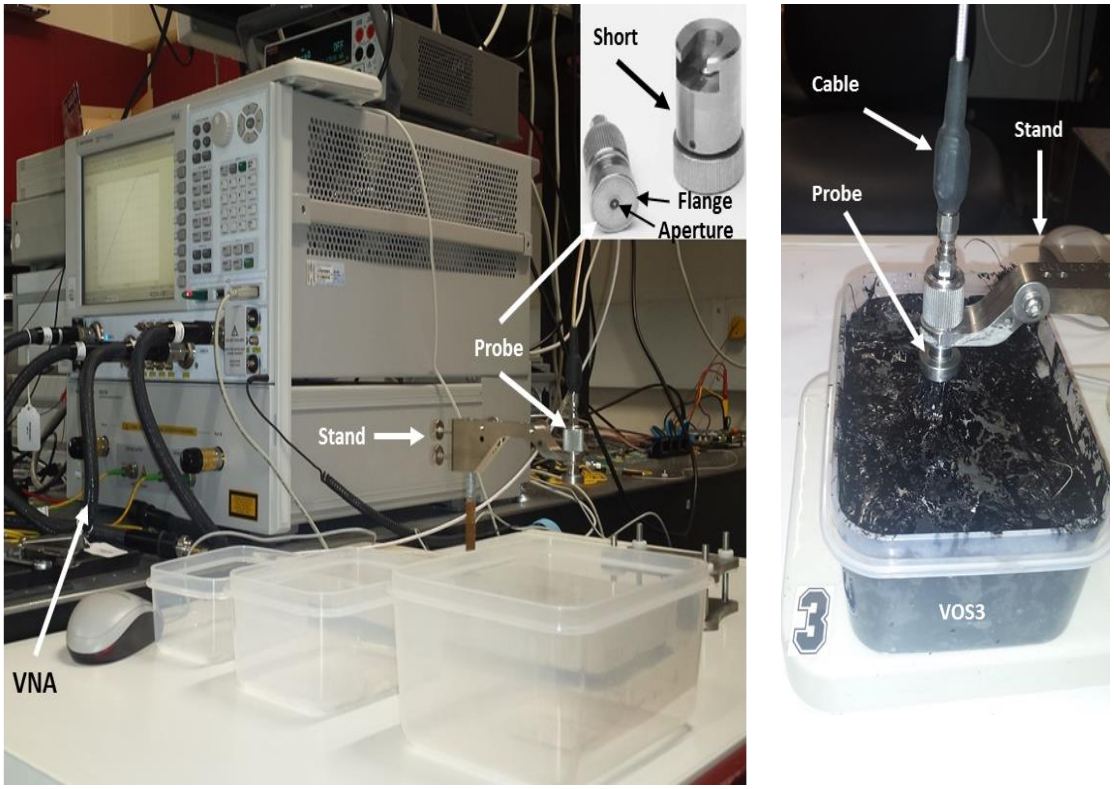

Figure 5.4: (a) Generic experimental setup for measurement of dielectric properties showing PNA N5227A VNA, probe, stand and empty VOS containers (inset: high temperature probe and shorting block) (b) Probe inserted into VOS3 sample.

Open, short and load (50 ohms) (OSL) calibrations were performed for the high RF coaxial cables coming from the VNA before each data acquisition sequence to eliminate systematic measurement errors. Each standard was connected to the extended end of the high temperature probe before insertion. After calibration, the high temperature probe was left exposed to air and an air sample was measured to verify the calibration (Fig. 5.5a). The flange and aperture of the probe had to be rubbed thoroughly with soft non-abrasive laboratory cloth wipes and Isopropanol cleaning solvent each time the oil sands were measured. This was due to the sticky brown deposits from HOS and VOS. The thick viscosity of VOS meant the surface of the flange and aperture of the probe (Fig. 5.4a) had to be cleaned more frequently than with the HOS MUT.

After the use of Isopropanol and disconnecting the probe to confirm both the probe flange and aperture was free of sediments then the OSL calibration was performed before measurement to neutralize the effect of repeatable errors. The frequent staining was also a problem in previous hyperspectral measurements. Consequently water was used as control substance post-calibration to verify the calibration performance by comparison with the Cole-Cole model (Fig. 5.5b). This was repeated after each measurement sequence. The implementation of the Cole-Cole model using MATLAB® (MATLAB, 2012) is included at Appendix 5. In addition to cleaning, both air and water control measurements were taken before each sequence of measurements to ensure measurement accuracy.

To obtain the necessary variation in *wt.*% of water for loamy farm soil and beach sand a calibrated mixing was performed as explained in Ezeoke *et al*. (2013) and (Section 4.2.2 of) this thesis. When the calibration results were satisfactory the MUT was interfaced with the high temperature probe for investigation of the material properties. After calibration care was taken to avoid changes to the measurement system between calibration and measurement, because cable movements can introduce perturbations to the systematic errors. If cable movement does happen such variations in the systematic errors due to the new perturbation would not have been accounted for during calibration.

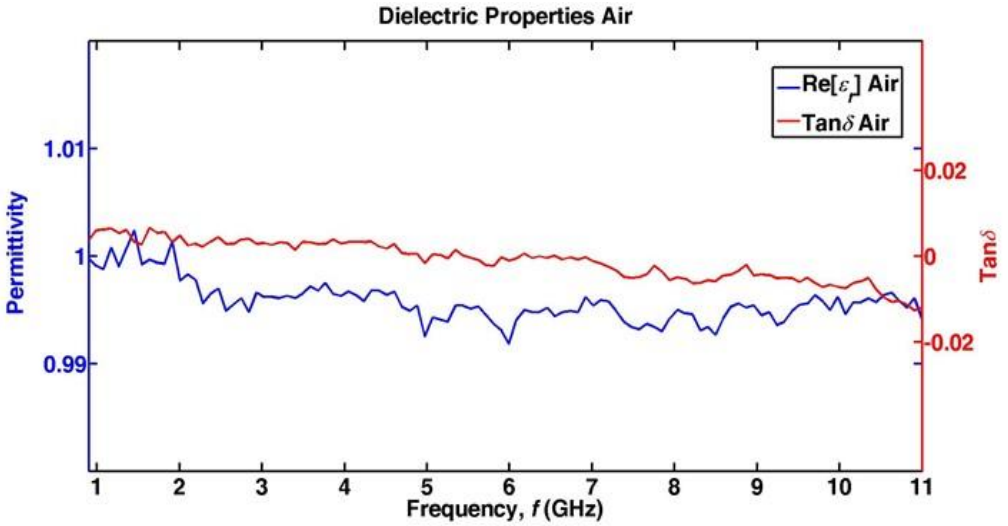

(a)

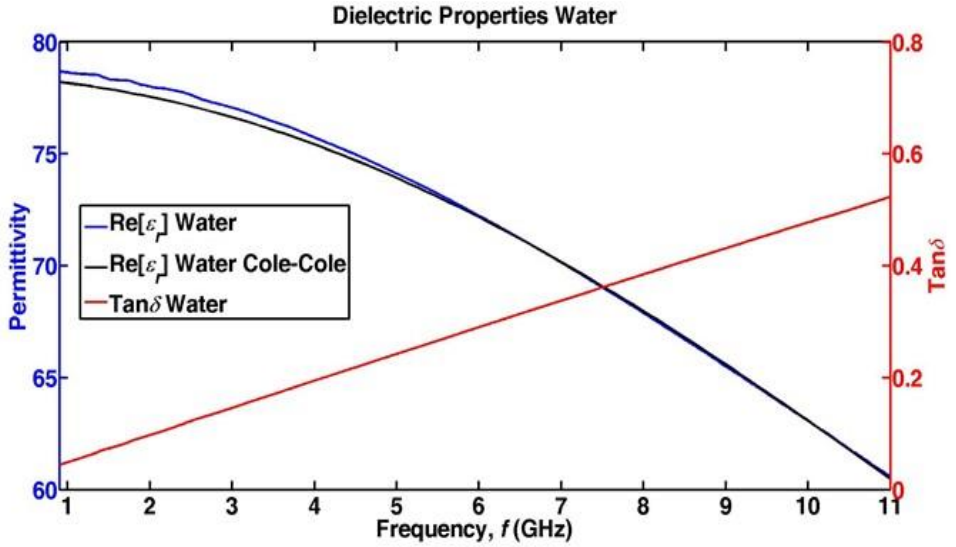

(b)

Figure 5.5: Dielectric properties (real permittivity and loss tangent) 0.9 – 11 GHz for control materials (a) air and (b) naturally occurring water compared to Cole-Cole prediction model.

5.3.2.1 Computing Material Properties

All the MUT were measured over a range of frequencies covering 1 GHz (L-band) through C-band (4 - 7 GHz) and up to 11 GHz (X-band). The VOS samples did not undergo any preparation before the measurement nor did other barefaced terrain samples. However due to the irregular surface of the HOS fragments the surfaces were smoothed with an engineering file to ensure a single continuous, smooth and flat surface for optimum contact at the probe interface with MUT. This is best seen in HOS 9 and HOS 10 (left side of Fig. 5.2). Generally, coaxial probes are designed to assume an infinite ground plane and semi-infinite sample size (Blackham & Pollard, 1997). First,

the VNA measured the reflection coefficient from the probe aperture and material interface. Then an inverse coaxial probe model is used to compute the permittivity of the MUT in contact with the probe from measurements of the coaxial aperture reflection coefficient.

If the oil sand samples are represented by a capacitance, *C* parallel to a resistor the admittance will be represented by:

$$\boldsymbol{Y(\omega) = G(\omega) + j\omega C(\omega)} \tag{5.13}$$

Here the real part is denoted by the conductance, *G* and the imaginary with the capacitance. In order to compute the MUT properties the cell geometry ought to be considered but unlike spectroscopic analysis the MUT is taken as an infinite material if it satisfies (5.10). Where ε_e and ε_0 are the effective and vacuum permittivity respectively ($\varepsilon_0 = 8.85 \times 10^{-12}$ (Fm^{-1})), then the effective complex conductivity for the parallel circuit is given by:

$$\boldsymbol{\sigma'_e \cdot (\omega) = \sigma'_e(\omega) + j\omega\varepsilon_e\varepsilon_0(\omega)} \tag{5.14}$$

The geometry factor *K* relates electrical conductivity with admittance according to (Patil *et al.,* 2010) as:

$$\boldsymbol{\sigma' (\omega) = {Y(\omega)}/{K}} \tag{5.15}$$

For the high temperature probe the geometry factor, *K* is that of a cylindrical resistance/capacitor,

$$\boldsymbol{K = \frac{2\pi l}{\ln\left({r_0}/{r_i}\right)}} \tag{5.16}$$

Where r_0 and r_i are the outer and inner radii of the flanges respectively and *l* is the length of the cell. Equating the real and imaginary parts of *Y* and *C** in (5.13), (5.15) and (5.16) it can be observed that:

$$\boldsymbol{\sigma'_e(\omega) = KG(\omega) = \frac{G(\omega)}{2\pi l}\ln\left({r_0}/{r_i}\right)} \tag{5.17}$$

$$\boldsymbol{\varepsilon_e(\omega) = \frac{KC(\omega)}{\varepsilon_0} = \frac{C(\omega)}{2\pi l\varepsilon_0}\ln\left({r_0}/{r_i}\right)} \tag{5.18}$$

Patil *et al.* (2010) observes that the results could be interpreted as a non-ideal resistor or a loss prone capacitor. Fuller and Ward (1970) consider it as a combination of both and provide the following relations for an effective measurement value of rocks (which may be applied to terrain) as:

$$\boldsymbol{\sigma'_{eff} = \sigma' + \omega \varepsilon''_r \, \varepsilon_0} \tag{5.19}$$

$$\boldsymbol{\varepsilon_{eff} = \varepsilon'_r + \frac{\sigma''}{\omega \varepsilon_0}} \tag{5.20}$$

Oil sands are highly resistive (Amigun *et al*., 2012; Odunaike *et al*., 2010) therefore it can be assumed that any conduction effects are negligible. Therefore the system can be interpreted as a lossy dielectric capacitor with real and imaginary permittivity given by:

$$\boldsymbol{\varepsilon'_r(\omega) = \frac{C(\omega)}{2\pi l \varepsilon_0} \mathrm{In}\left({}^{r_0}/_{r_i}\right)} \tag{5.21}$$

$$\boldsymbol{\varepsilon''_r(\omega) = \frac{G(\omega)}{2\pi l \omega \varepsilon_0} \mathrm{In}\left({}^{r_0}/_{r_i}\right)} \tag{5.22}$$

5.3.2.2 Verification Measurements

The typical accuracy of the dielectric constant measurements using the high temperature probe are $\varepsilon'_{r\_\mathrm{actual}} = \varepsilon'_{r\_\mathrm{measured}} \pm 0.05 \, |\varepsilon_r^*|$ and $\varepsilon''_{r\_\mathrm{actual}} = \varepsilon''_{r\_\mathrm{measured}} \pm 0.05 \, |\varepsilon_r^*|$ while the loss tangent measurements are $\pm 0.05\%$ (Agilent AN5988, 2003). The initial OSL calibration of the probe is expected to correct for systematic errors of the cables and connections due to directivity (e_d), frequency response tracking (e_r) and source matching (e_s). These errors may cause the measured reflection coefficient (Γ_m) to differ from the actual reflection coefficient (Γ_a) such that:

$$\boldsymbol{\Gamma_m = e_d + \frac{e_r \Gamma_a}{1 - e_s \Gamma_a}} \tag{5.23}$$

The OSL calibration which is also known as vector error correction amends the systematic deviation by measuring the OSL reflection coefficients over the frequency of interest. This way the errors are mathematically removed from subsequent measurements (Fitzpatrick, 1978) to provide the actual reflection coefficient as:

$$\Gamma_a = \frac{\Gamma_m - e_d}{e_s(\Gamma_m - e_d) + e_r} \tag{5.24}$$

Furthermore the accuracy of experimental set up was measured using air and water as control standards. Air, a short circuit and water are readily available as well-defined calibration materials. The reflection coefficient of a short circuit connected to the probe aperture is -1 while the reflection coefficients for air and water were determined using known values for both in a forward coaxial probe model. Since the permittivity value of water changes with frequency a Cole-Cole prediction model was implemented. The real dielectric permittivity ε', loss factor ε'' and loss tangent tan δ of these standard materials was measured between 0.9 and 11 GHz. For air both ε' and ε'' are essentially independent of frequency (Fig. 5.5a) with the dielectric properties of air mostly constant ($\varepsilon' = 1$, $\varepsilon'' = 0$) across the frequency range from 0.9 – 11 GHz. However for water, there was a pronounced drop in real permittivity corresponding with a rise in loss factor with increasing frequency. This drop in real permittivity can be explained by the Cole-Cole model for water at room temperature (25° C) given by (Cole & Cole, 1941):

$$\varepsilon^* = \varepsilon' - j\varepsilon'' = \varepsilon_\infty + \frac{\varepsilon_s - \varepsilon_\infty}{1 + (j\omega\tau)^{1-\alpha}} \tag{5.25}$$

Where ε^* is the complex dielectric constant, ε_s and ε_∞ are the static and infinite frequency dielectric constants. Also ω is the angular frequency while τ is the relaxation time constant. The exponent parameter, α which can take a value between 0 and 1 allows different spectral shapes so that when $\alpha = 0$, the Cole-Cole model reduces to the Debye model and when $\alpha > 0$ the relaxation is stretched and extends over a wide range on a logarithmic scale. The value of permittivity as a function of frequency for water is accurately known. The control measurements compare well to values computed using a Cole-Cole model (Hasted, 1972) for deionized water at 25° C with parameters ε_s = 78.6, ε_∞ = 4.22, $\tau = 8.8 \times 10^{-12}$ s and $\alpha = 0.013$ included for comparison. Since oil sands occur naturally, in the absence of natural water, tap water rather than deionized (DI) water was used as control. However although the relaxation time constant of DI water is well known that for tap water was not and using curve fitting techniques, it was determined to be $\tau = 12.8 \times 10^{-12}$ s (in Fig. 5.5b). To obtain the real permittivity (5.25) is decomposed to:

$$\varepsilon' = \varepsilon_\infty + \frac{\varepsilon_s - \varepsilon_\infty[1 + (\omega\tau)^{1-\alpha}\sin(\frac{1}{2}\alpha\pi)]}{1 + 2(\omega\tau)^{1-\alpha}\sin(\frac{1}{2}\alpha\pi) + (\omega\tau)^{2(1-\alpha)}} \tag{5.26}$$

$$\varepsilon'' = \frac{(\varepsilon_s - \varepsilon_\infty)(\omega\tau)^{1-\alpha}\cos(\frac{1}{2}\alpha\pi)}{1 + 2(\omega\tau)^{1-\alpha}\sin(\frac{1}{2}\alpha\pi) + (\omega\tau)^{2(1-\alpha)}}$$

The implementation of this model is at Appendix 5. Subsequently the measured value for air and water was compared with literature to obtain the accuracy of the experimental set up using:

$$\varepsilon_r(\%) = \frac{\left|\varepsilon_{r\_true\_i} - \varepsilon_{r\_measured\_i}\right|}{\varepsilon_{r\_true\_i}} 100\%, \tag{5.27}$$

Where ε_{r_true} represent values from literature (Hasted, 1972; Ulaby *et al*., 1986) for air and normal water and $\varepsilon_{r\_measured}$ denotes values from the measurement set up. Also the standard deviation (SD) of the data was derived using (5.28):

$$SD = \sqrt{\frac{1}{N-1}\sum_i^N (x_i - \bar{x})^2} \tag{5.28}$$

Here N is the total number of observations while x_i is the measured and $\bar{x}$ is the mean value. Table 5.3 shows the measured mean and standard deviation values for air and water across the 0.9 – 11 GHz region. For water the high SD is due to the large frequency drop in real permittivity across frequency range of measurement. Thus a better gauge of accuracy for water is the ε_r (%) as it compares each data point value-wise. The Pearson correlation coefficient (PCC), was used to gauge the statistical strength of the linear association between the measured and true real permittivity values on a scale from 0 to 1 for water. The PCC was determined with R in (5.29):

$$R = \frac{\sum_{i=1}^N \left(\varepsilon_{r_{true\,i}} - \overline{\varepsilon_{r_{true}}}\right)\left(\varepsilon_{r_{measured\,i}} - \overline{\varepsilon_{r_{measured}}}\right)}{\sqrt{\sum_i \left(\varepsilon_{r_{true\,i}} - \overline{\varepsilon_{r_{true}}}\right)^2}\sqrt{\sum_i \left(\varepsilon_{r_{measured\,i}} - \overline{\varepsilon_{r_{measured}}}\right)^2}} \tag{5.29}$$

The PCC for ε'_r of water was 0.9992 indicating that both true and measured values for water had strong positive correlation. Ultimately the measurement accuracy

can be evaluated through R^2 which is the square of the correlation coefficient between true values (from Cole-Cole prediction model) and the measured values. The value of R^2 which is also known as the coefficient of determination was 0.9984 for the water control sample. In order to ensure a high level of measurement accuracy for the oil sand and barefaced terrain, four dielectric permittivity measurements were taken for each sample and in the case where the measurements did not perfectly coincide, the two with the highest correlation values ($R \rightarrow 1$) were selected.

Table 5.4: Error Estimation of Measurement in Frequency Range 0.9 – 11 GHz

Control Material	**Permittivity**	**Agilent PNA N5227A 10MHz – 67 GHz VNA and Agilent 85070E DPK**			
		Mean	**N**	ε_r%	**SD**
Air	ε'= 1	0.996	118	0.429	0.002
Water	ε'= 78 - 60 (over 0.9 - 11 GHz)	71.47	1043	0.260	5.478

5.4. Statistical Model

The large amount of data values obtained from the measurements necessitated the development of a statistical model to determine the main principal components (PC) of the different terrain types. The objective of the statistical models was to (1) identify the unique features of the relationship between measured dielectric properties and the frequency for each MUT and (2) pinpoint the frequency or range of frequencies with the highest discrepancy or variation for use in development of the sensor and BTM in Chapter 6. The method for implementation of the statistical model is similar to the geochemical signature and interpretation model in the preceding chapter therefore the focus here will be on the results rather than the procedure. The implementation code using MATLAB and data are presented in Appendix 5.

The major focus of the dielectric discrimination model here will be the oil sand data however the same procedures were implemented for the barefaced terrain mentioned previously (Table 5.3). The real permittivity for two measurements each of HOS 1 to HOS 10 and VOS 1 to VOS 4 data are shown in Fig. 5.5. Generally it can be seen that the real permittivity slightly rises with frequency and then tapers off for both VOS and HOS. The actual real permittivity value ranged from 2.1 to 4.5 for MUT E as shown in Table 5.5.

Table 5.5: Measurement Values obtained for Hard Oil Sand fragments

MUT	1st Measurement			2nd Measurement		
	ε_r'(min)	ε_r'(max)	ε_r'(avg)	ε_r'(min)	ε_r'(max)	ε_r'(avg)
HOS 1	2.86	3.04	2.99	2.36	2.52	2.48
HOS 2	2.14	2.3	2.25	2.48	2.69	2.62
HOS 3	2.10	2.18	2.15	2.15	2.25	2.22
HOS 4	2.88	2.99	2.96	3.68	3.81	3.76
HOS 5	3.76	3.87	3.82	3.77	3.88	3.82
HOS 6	3.86	4.00	3.95	3.92	4.04	3.99
HOS 7	3.56	3.67	3.62	3.35	3.47	3.41
HOS 8	4.26	4.53	4.39	4.38	4.51	4.42
HOS 9	4.04	4.20	4.13	3.89	4.08	4.01
HOS 10	3.62	3.95	3.85	3.51	3.88	3.77

The median permittivity varied with the sample thickness for HOS and with the sample depth for VOS. In essence the real permittivity values increased from HOS 1 – HOS 10 and VOS 1 – VOS 4 with exceptions that HOS 10 and VOS 4 were closer to the mean values of 3.75 for HOS and 4.25 for VOS. The real permittivity value varied between 2.6 and 4.7 for MUT F shown in Table 5.6.

Table 5.6: Measurement values obtained for Viscous Oil Sand volumes

MUT	1st Measurement			2nd Measurement		
	ε_r'(min)	ε_r'(max)	ε_r'(avg)	ε_r'(min)	ε_r'(max)	ε_r'(avg)
VOS 1	2.63	2.80	2.74	2.62	2.85	2.77
VOS 2	4.43	4.70	4.60	3.88	4.08	4.0
VOS 3	4.40	4.70	4.58	4.32	4.53	4.44
VOS 4	4.17	4.35	4.27	4.14	4.41	4.30

Also the results for both measurements of VOS 1, HOS 1, HOS 2, HOS 3 and HOS 4 were markedly lower than the rest due to the thickness being less than $\frac{20}{(\sqrt{|\varepsilon_r^*|})}$ mm and for HOS 1 the diameter was < 20 mm. For these 5 the maximum thickness was 6 mm, 8 mm, 10 mm, 11 mm and 12 mm respectively. Therefore these results will be subsequently discarded and not used in the development of the dielectric discrimination statistical model (DDSM). They were only presented here to indicate the accuracy of the experimental measurement approach because the values recorded for these fragments of oil sand were expectedly lower than other fragments.

The HOS 7 fragment shows a seemingly large discrepancy between both measurements (Fig. 5.6a). This is believed to be due to two reasons. First the measurement probe was placed at two different points on the surface of the fragment. This was also applied to all the other measurements. However for HOS 7 there is a large variation in the intrinsic material properties which can best be seen by the different colouration in the HOS 7 fragment (Fig. 5.2). The upper part of the fragment is light brown in comparison to the lower part of the fragment that is slightly darker. Also both real permittivity measurements for VOS 1 (Fig. 5.6b) were remarkedly lower due to the lower thickness of the MUT.

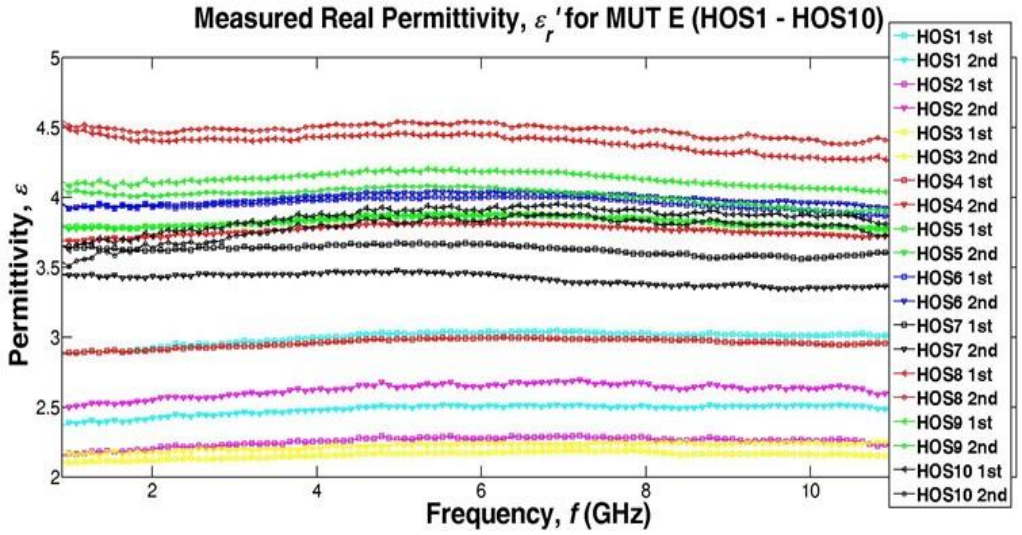

(a)

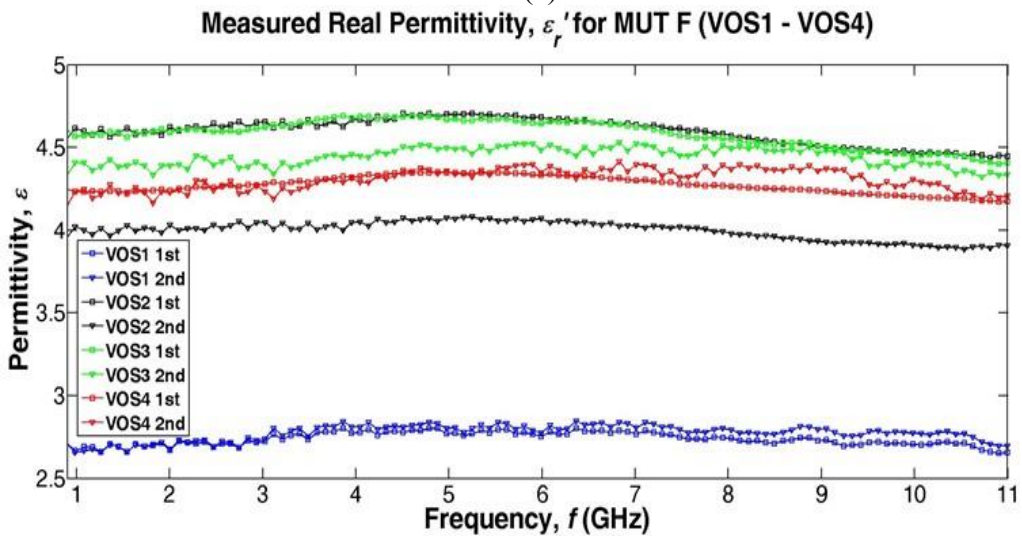

(b)

Figure 5.6: Experimental results for real permittivity, $\boldsymbol{\varepsilon_r'}$ change with frequency (0.9 – 11 GHz) showing two measurements each of (a) MUT E: HOS1 – HOS10 and (b) MUT F: VOS1 – VOS4

Similarly the loss factor for VOS 1, HOS 1, HOS 2, HOS 3 and HOS 4 was distinctively lower than for the other samples. The experimental loss factor results for two measurements each of HOS 1 to HOS 10 and VOS 1 to VOS 4 was determined and presented in (Fig. 5.7). They indicate the amount of energy dissipated by the MUT. Generally for all MUT E samples, the loss factor for HOS is <0.03 while for MUT F it is <0.05 indicating that VOS is more lossy than HOS.

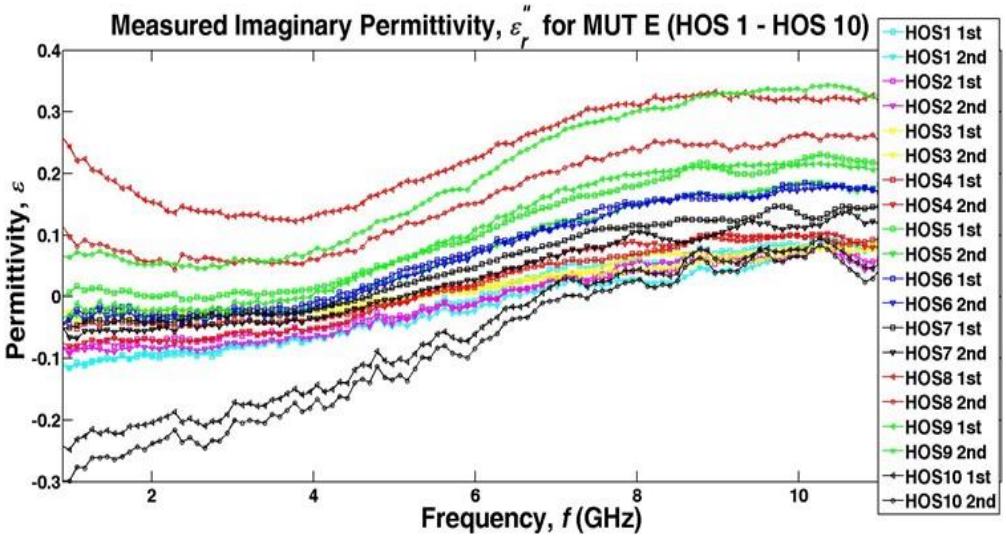

(a)

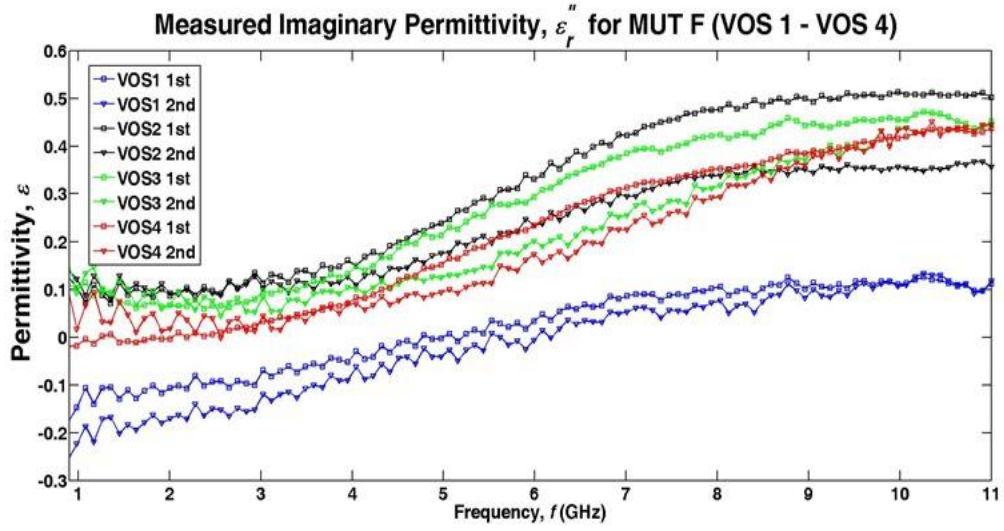

(b)

Figure 5.7: Experimental results for imaginary permittivity, $\boldsymbol{\varepsilon_r''}$ change with frequency (0.9 – 11 GHz) showing two measurements each of (a) MUT E: HOS1 – HOS10 and (b) MUT F: VOS1 – VOS4

Both HOS and VOS loss factors show a slight drop between 2 GHz – 4 GHz and a steep increase between 6 GHz – 8 GHz. The drop from 1 GHz to 2 GHz is more pronounced for HOS compared to VOS due to the lower effect of moisture as HOS was

predicted to have roughly half the amount of moisture present in VOS (6.3 *wt*.% - 7.6 *wt*.% in HOS compared to 11.5 *wt*.% - 15 *wt*.% in VOS). It could also be dampening effect of the larger amount of grains (or clay sand) in HOS compared to VOS.

The statistical model was developed to determine what frequency or frequency range in the measurement scope (0.9 – 11 GHz) indicated the largest variation in dielectric permittivity. The variation could be positive or negative. This is important because the intent is to identify the best possible EM signature that can distinguish oil sands from other terrain. The principal component analysis (PCA) and partial least squares analysis (PLSA) technique discussed in section 4.2.3 was used. The applicability of PCA and PLSA for identification of optimum frequency of interest in permittivity response has not been investigated. This is implemented here to create a scientific basis for dielectric discrimination of the permittivity of HOS, VOS and other barefaced terrain. The inclusion of PCA values is for future reference. Our main interest was the performance of PLSA to achieve the dielectric discrimination because unlike PCA, PLSA considers the response variable which in this case is the dielectric permittivity measurements. This is clear from Table 5.7 where the PLSA provides a better statistical representation than PCA. It is indicated by R^2 which shows the correlation between the DDSM and the original measurement results data. Notice that in the dielectric discrimination model development, the results for HOS 1 – HOS 7 and VOS 1 are left out. First each terrain group is considered separately beginning with MUT A, B, E and F and later they are combined in to two, oil sand and barefaced terrain classes.

Table 5.7: Dielectric discrimination statistical model: R^2

MUT	Measurements	PLSA	PCA (2 components)	PCA (3 components)
A, A10, A20, A30	16	0.9015	0.3691	0.8415
B, B10, B20, B30	16	0.9199	0.8404	0.9192
E: HOS8 – HOS10	12	0.8435	0.7382	0.8291
F: VOS2 – VOS4	12	0.6392	0.2043	0.5440
Oil Sands	24	0.4148	0.2778	0.3137
Barefaced Terrain	32	0.4067	0.2742	0.3747

The dielectric discrimination with frequency is best seen in the model parsimony. Using weights (loading or scores), the algorithm checked how strongly each component of the developed model depends on the original measurement data and in

what direction. This is shown by the direction of the first, second and third PC's. From (4.2) these are the scores and loading vectors for PCA ($\mathbf{t}_1\mathbf{p}_1$, $\mathbf{t}_2\mathbf{p}_2$ and $\mathbf{t}_3\mathbf{p}_3$) and weights for PLSA. Conventionally these lines in a variable space best describe the variation in the data matrix X for each of the measurement results (rows in the leftmost column of Table 5.7). The parsimony for the VOS and HOS datasets are shown in Fig. 5.8 and resulting implementation codes is at Appendix 5. Only 3 PCs are used where the second describes the variation not described by the first PC and the third describes the variation not seen in the first and second. Since the PLSA provides higher correlation between measurements and discrimination model our analysis follows the parsimony provided by the PLSA.

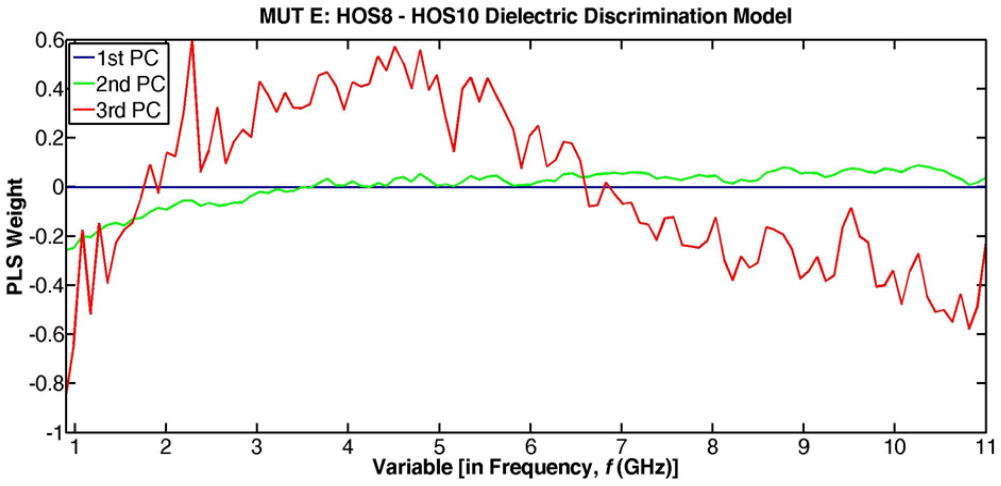

(a)

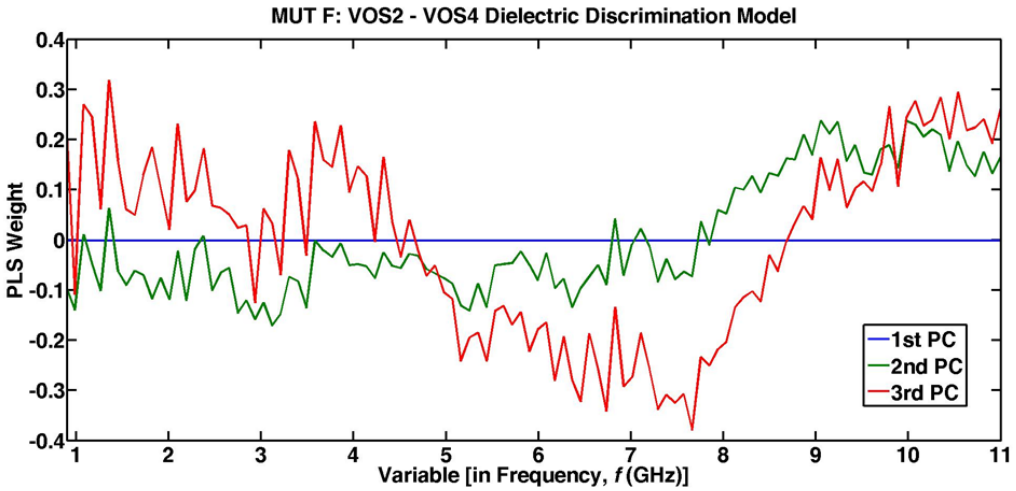

(b)

Figure 5.8: Model parsimony with frequency (0.9 – 11 GHz) for Dielectric Discrimination Model (a) MUT E: HOS 8 – HOS 10 (b) MUT F: VOS 2 – VOS 4.

The variable weights result illustrate that, for the dielectric discrimination models generated with HOS and VOS dielectric measurements the 1st PC has no

distinguishing variable due to the similarity in terrain permittivity. Both HOS and VOS models considered 12 sets of measurements each comprising of both real and imaginary permittivity values. However for HOS a large contrast emerges between 6 – 8 GHz while this is between 5 – 7 GHz for VOS. The statistical interpretation is that the 5 - 7 GHz and 6 - 8 GHz frequency band regions could provide the best window to differentiate between VOS and HOS or generate the radar signature of either terrain.

On application of the statistical models to the dielectric permittivity results for MUT A and MUT B it was observed that the 1st PC has no distinguishing variable along the frequency for both terrain types (Fig. 5.9). The statistical models were used to investigate 16 sets of measurements for both MUT A and MUT B. The results indicated that at low microwave frequencies (1 - 2 GHz) MUT A has a marked overtone while MUT B experiences a mild droop with frequency for the 2nd PC and a marked rise in the 3rd PC. Therefore the 1-2 GHz frequency band may best differentiate between both terrain types due to the steep variation in the 2nd and 3rd PC along this frequency range.

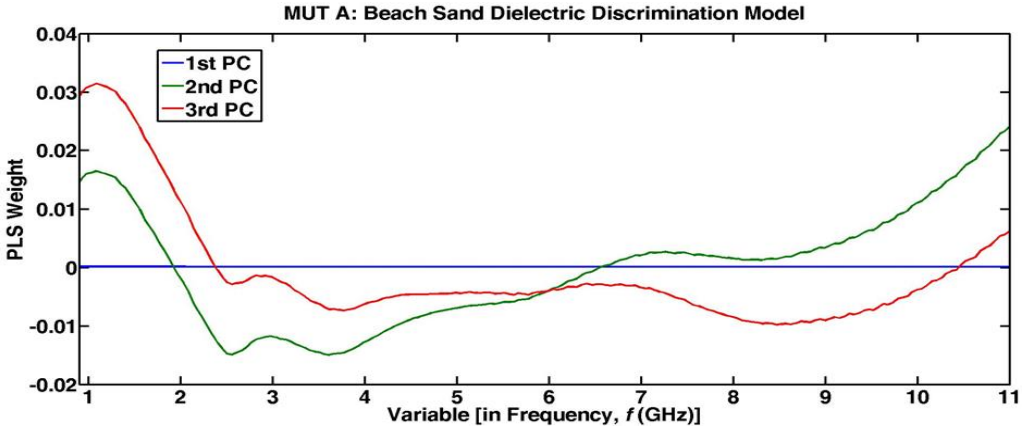

(a)

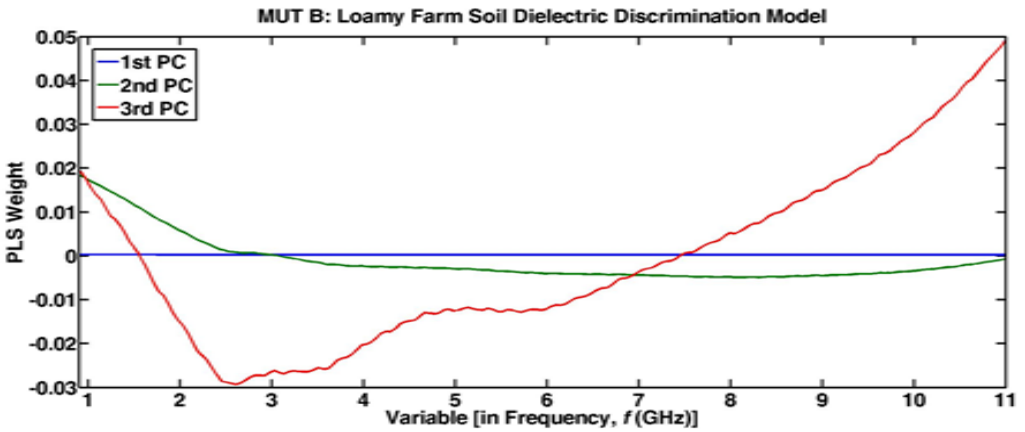

(b)

A comparison of the DDSM parsimony for the MUTA, MUT B, MUT E and MUT F also shows that while the results for non-oil sand terrain are clear without

Figure 5.9: Model parsimony with frequency (0.9 – 11 GHz) for Dielectric discrimination model (a) MUT A: Beach Sand (b) MUT B: Loamy Farm Soil.

ripples, the oil sand terrain show fluctuations at each frequency point. This is because the measurement results for oil sand are due to the intrinsic heterogeneous properties while MUT A and MUT B are more homogeneous materials.

The statistical models were also used to investigate the experimental permittivity values of homogeneous terrain (MUT A and MUT B) grouped together as barefaced terrain and heterogeneous terrain (MUT E and MUT F) clustered as oil sands (Fig. 5.10).

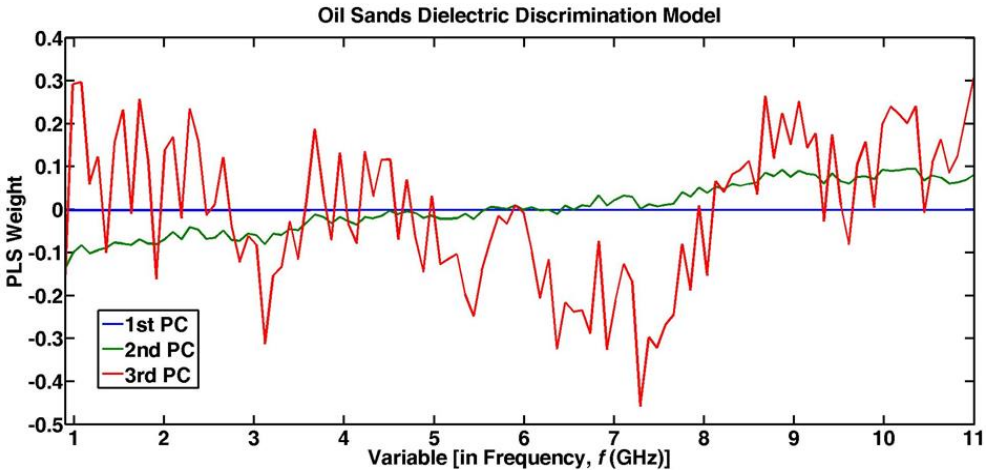

(a)

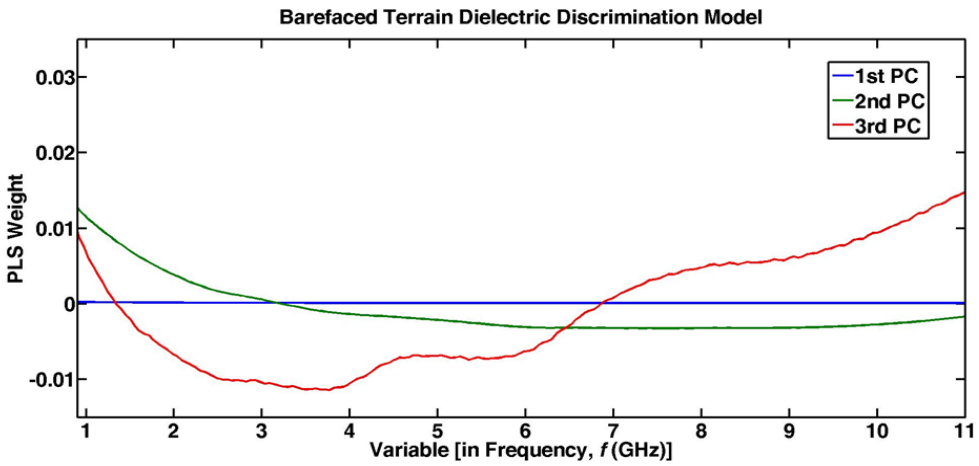

(b)

Figure 5.10: Model parsimony with frequency (0.9 – 11 GHz) for dielectric discrimination model (a) Oil Sands (b) Barefaced Terrain.

For both groups, the correlation values R^2 (from table 5.5) between the DDSM and measurement data are average (> 0.4) as an indication of the difference between

the datasets and the models. Nevertheless a few plausible trends emerge (Fig. 5.10). The 1st PC is again constant for both groups. In the oil sand group the highest variation of the data with frequency occurs between 5 and 7 GHz but for the barefaced terrain group the steepest slope for the PC of the data occurs between 1 and 2 GHz. This reinforces the previous observation that the 1 - 2 GHz and 5 - 7 GHz microwave region show great potential for radar remote sensing if only dielectric properties are considered.

5.5. Analysis of Permittivity Results

Earlier it was observed that three sets of dielectric measurements were performed on the oil sand data due to the originality of investigation. The first series of measurements were in 2013 (Ezeoke & Tong, 2013c) while the last two were in January and April 2014 (Ezeoke *et al,* 2014c*).* The measurement set up was similar except that the ENA VNA for the 2013 experiments limited the results to 8.5 GHz and only 3 samples, VOS 1, HOS 3 and HOS 6 were investigated. In 2014 the PNA VNA was specified to function up to 67 GHz although the probe cables limited this to 20 GHz in reality. There was a slight difference in the results which will be discussed below.

5.5.1. Resonance Effect

The 2013 measurements of VOS 1, HOS 3 and HOS 6 produced a visible resonance in the real permittivity around 6.5 – 7.5 GHz region. A comparison of real permittivity for the 2014 measurement results of HOS 10 and VOS 4, the results from Erdogan *et al*. (2011) and results for both MUT A and MUT B is presented (Fig. 5.11). While there is a slight curve in the real permittivity with frequency for the 2014 results, it is not as pronounced as the 2013 results. There is greater statistical correlation between the 2013 results with literature (Erdogan *et al*., 2011). Furthermore in comparison to the 2014 results, the 2013 measurements were not repeated subsequently. However both January and April measurements of HOS 1 – HOS 10 and VOS 1 – VOS 4 produced the same results.

The loss factor for the 2013 dielectric measurements is similar in profile to the real permittivity with a large drop between 6.5 GHz and 7. 5 GHz. Interestingly there is greater correlation between the 2014 results and literature (Erdogan *et al*., 2011). Also the 2013 results are much higher than both 2014 measurements and normal terrain

(Fig. 5.12). It is also significant to note that the results suggest a negative permittivity of up to 3.5 which could not be explained conventionally except perhaps that the immiscibility of water and hydrocarbon caused an anomalous behaviour.

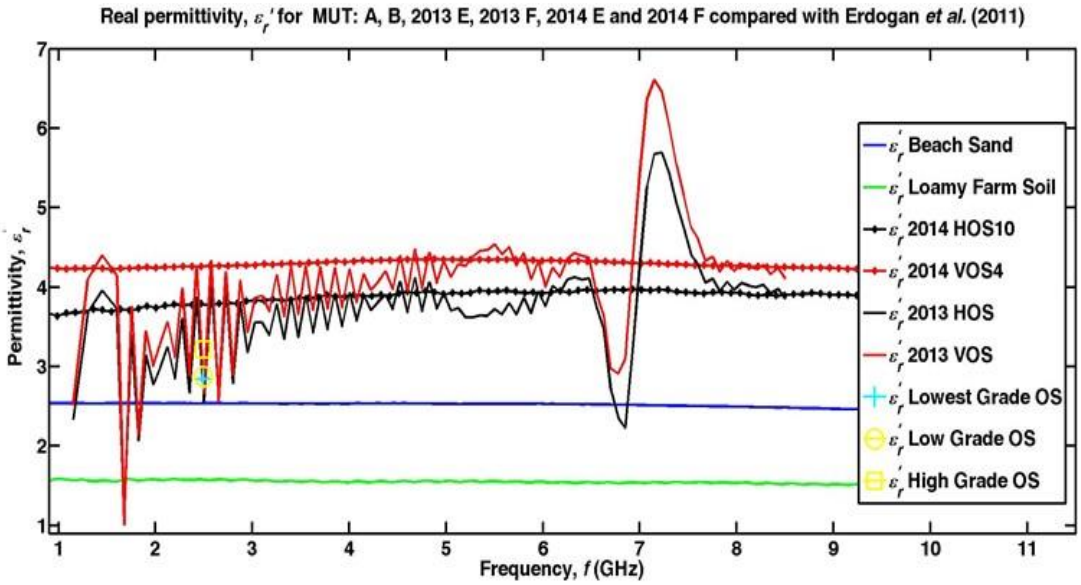

Figure 5.11: Resonance effect in real permittivity of oil sands compared with normal terrain.

The 2013 results also indicated the presence of a Kramers-Krönig relationship between the real and imaginary parts of the permittivity. The Kramers-Krönig relations (Krönig, 1926; Kramers, 1927) are an appropriate tool to check the correctness of the frequency response of linear systems. This follows from the fact that both real and apparent permittivity are conjugate functions given by:

$$\boldsymbol{\varepsilon'(\omega) - \varepsilon_\infty = -\int_0^\infty \frac{\varepsilon''(v)v dv}{v^2 - \omega^2}, \text{and } \varepsilon''(\omega) = \frac{2}{\pi}\int_0^\infty \frac{[\varepsilon'(v) - \varepsilon_\infty]\omega dv}{v^2 - \omega^2}} \tag{5.30}$$

Here v is a vector in the complex plane. Dielectric materials may be regarded as causal linear systems ($h(t) = 0$ for $t < 0$), therefore the consistency between both real and imaginary permittivity for the 2013 results ought to validate the measurements. However the precision of the 2013 results could not be validated due to the inability to repeat them therefore the results were not used in the subsequent BTMs (in Chapter 6). The strong resonance witnessed in the 2013 results has been mentioned here due to the possibility of future researchers observing a similar trend with oil sands or any other

similar heterogeneous material. It is believed that the large resonance in (Fig. 5.11) and (Fig. 5.12) could be due to measurement errors which affected results from the three MUTs investigated in 2013. Therefore the resulting measurement data are considered unreliable for further use in the research.

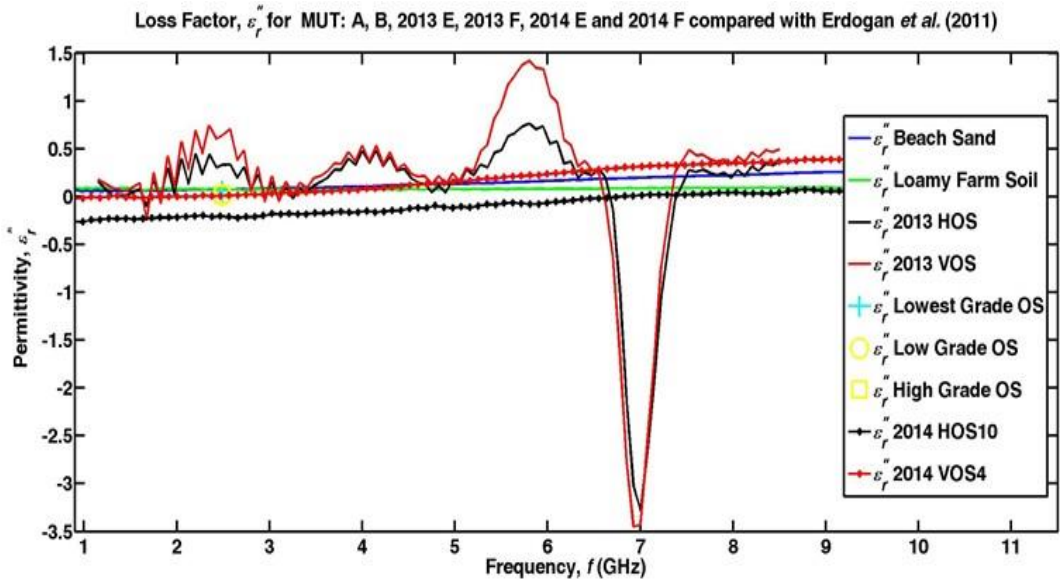

Figure 5.12: Resonance effect in loss factor of oil sands compared with normal terrain.

It was also observed that for homogenous terrain like MUT A and MUT B, the dielectric constant was static across the frequencies when there is no moisture added. However for oil sand terrain this is not the case as the permittivity varies with frequency. For such materials, anisotropic modelling may be more suitable. The effect of the dielectric properties on the velocity of signal propagation and wavelength in a material was given in (3.12) and (3.13). The dielectric permittivity acts to slow down EM radiation in terrain and also decrease the wavelength. Therefore materials with high ε_r will cause greater attenuation of signals compared to materials with lower ε_r. This may be the difference between detection and classification of terrain types.

5.5.2. Moisture Effect

As noted previously the AOSR located in southern Nigeria experiences heavy rains with double maxima rainfall and a short dry season falling between the rain-fall peaks (Ezeoke *et al*., 2012). Therefore a curious part of the dielectric experiments was to determine the effect of bitumen hydrocarbon and water in HOS and VOS on the dielectric permittivity. A challenge was to do this without having to create pseudo oil sands. In terms of bitumen content, the data for HOS and VOS were input in to (4.11)

and then they were predicted to contain bitumen ranging from 12.2 ± 2.3 *wt*. % to 20.3 ± 2.0 *wt*. % while VOS is believed to hold 24.2 ± 1.5 *wt*. % to 24.6 ± 1.5 *wt*. %. We used the lower values of 12% and 24% bitumen in HOS and VOS respectively.

Due to the lack of a similar empirical equation for prediction, an empirical model was developed (4.13) based on the spectral IR data and then used to predict the amount of moisture in both VOS and HOS. The HOS was estimated to contain 6.3 *wt*.% to 7.6 *wt*.% of water while VOS was determined to consist of 11.5 *wt*.% to 14.9 *wt*.% water content. Again by using a conservative approach the lower values of 6.3 *wt*.% and 11.5 *wt*.% water content were accepted for both HOS and VOS respectively. In order to determine the effect of moisture content in oil sands with other terrain the dielectric properties of other barefaced terrain with 10, 20 and 30 *wt*.% moisture was investigated. The real permittivity of oil sands with other terrain is presented (Fig. 5.13). The real permittivity of normal terrain (with 2 - 3 *wt*.% water) is flat and frequency independent as observed for rocks and minerals (Peake & Oliver, 1971). This was not seen for oil sands.

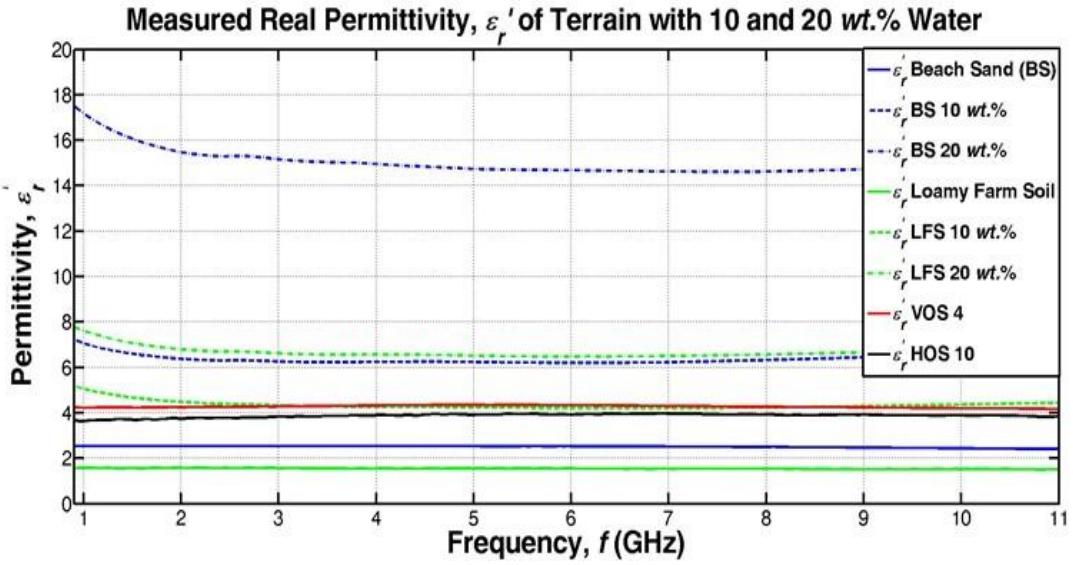

Figure 5.13: Measured real permittivity of terrain with 10 and 20 *wt*.% water.

Furthermore, the effect of moisture on MUT A and MUT B is clearly seen by the increase in permittivity with moisture content. The permittivity of MUT B is lower than MUT A while both HOS 10 and VOS 4 (used to represent HOS and VOS) permittivity is in between normal beach sand and loamy farm soil with 10 *wt*.% water at the extremities of L-band and X-band. Over C-band frequencies VOS 4 permittivity is slightly higher than MUT B with 10 *wt*.% water due to the curve in permittivity from

5 GHz to 8 GHz as noted with the DDSM. Also the presence of water causes the terrain permittivity to drop at L-band frequencies but this is not seen in the oil sand.

Similarly for terrain the presence of water causes a dispersion in permittivity at L-band frequencies. Prior to the saturation point which roughly coincides with 30 - 40 *wt*.% for MUT A the loss factor continues to drop with increasing frequency similar to the Cole-Cole model for water. For MUT A with 20 *wt*.% the water presence causes a mild increase with increasing frequency particularly at X-band frequencies. The behavior of the loss factor of oil sands is vastly different from real permittivity (Fig. 5.14). This is because both HOS and VOS loss factor are lower than normal terrain. However the resultant value increases with frequency until VOS is the same with MUT A with 10 *wt*.% and MUT B with 10 and 20 *wt*.% water.

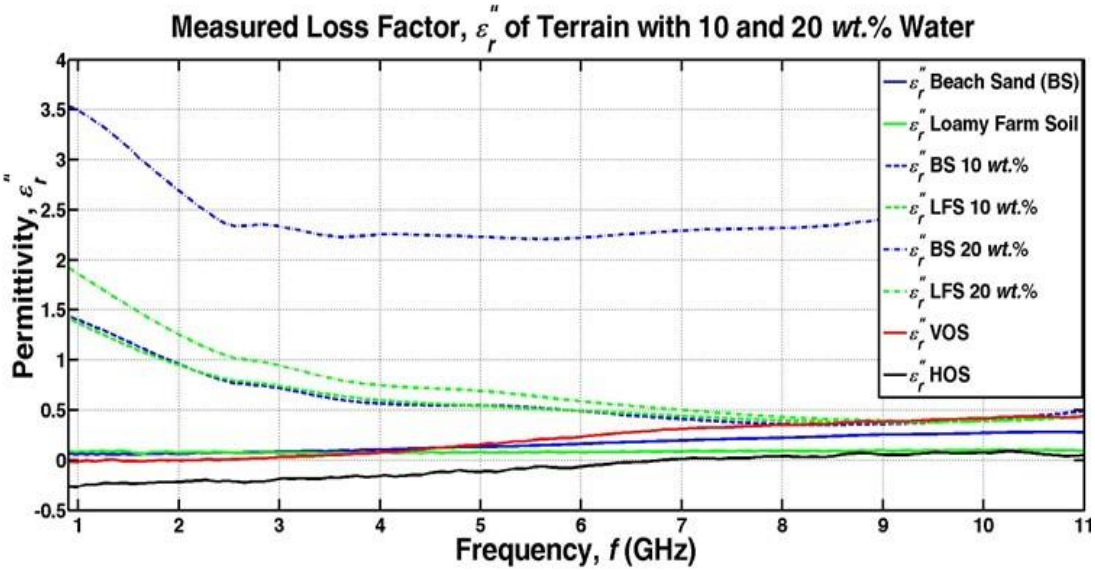

Figure 5.14: Measured loss factor of terrain with 10 and 20 *wt*.% water.

The increase in the lossiness of oil sands is due to the presence of bitumen. Similarly, the much higher increase in VOS compared to HOS owes to the greater amount of bitumen in the former compared to the latter. The loss factor varied along an S-shaped curve meaning that the intrinsic properties of HOS and VOS will cause greater losses around the 4.5 to 8.5 GHz frequency region.

5.6. Concluding Remarks

An experimental study of the dielectric properties (ε_r', ε_r'' and tan δ) of oil sand and other barefaced terrain in the frequency range from 0.9 to 11 GHz was presented. The 14 samples of Nigerian oil sands (consisting of 10 HOS fragments and 4 VOS

volumes) and other barefaced terrain with calibrated 10, 20 and 30 *wt*.% water were used to derive a dielectric discrimination model of oil sand behavior. Measurements were performed in 2013 then repeated January and April 2014 to ensure consistency of results and repeatability. Accuracy of the measurement system was determined with standard materials such as air and water as control. Control measurements for water compared well to values computed using a Cole-Cole model for deionized water at 25° C with parameters $\varepsilon_s = 78.6$, $\varepsilon_\infty = 4.22$, $\tau = 8.8\text{x}10^{-12}$ s and $\alpha = 0.013$. As oil sands occur naturally rather than deionized water, tap water was used as control and the relaxation time constant was determined with curve fitting techniques to be $\tau = 12.8\text{x}10^{-12}$ s.

The DDSM involved a statistical component which was used to analyze the derived empirical results. They indicated that for the 0.9 – 11 GHz range: (i) the ε_r' of normal terrain was flat and almost independent of frequency; (ii) the ε_r' of oil sands varied mildly with frequency particularly across C-band frequencies; (iii) both HOS and VOS ε_r' varied between normal beach sand and loamy farm soil with 10 *wt*.% water content; (iv) the loss factor, ε_r'' for terrain varied mildly with frequency but for oil sand there was steeper increase with frequency following an S-curve shape; (v) the presence of bitumen caused more dampening in permittivity response of HOS and VOS; (vi) HOS terrain fragments tended to have comparatively lower ε_r', ε_r'' and tan δ in comparison to VOS.

Furthermore the derived DDSM for barefaced terrain: (i) compared well with those for beach sand and loamy farm soil; (ii) relative ε_r decreased with f up to 2 GHz and then generally increased afterwards with increasing water content; (iii) this slight decrease in ε_r'' up to 2 GHz was also observed for both HOS and VOS although the drop was steeper in HOS. The study of the dielectric behavior performed in the UCL Microwave Laboratory was compared to the hyperspectral analyses carried out at the UCL Nanotechnology Laboratory. This indicated that while the presence of moisture ought to increase ε_r, the effect of bitumen was to lower ε_r for both oil sand types.

The study also showed the most important dielectric property variables for bareface terrain and oil sands concentrate in two frequency bands: 1 - 2 GHz and 5 - 8 GHz respectively. The mild dielectric resonance effect observed for oil sands in the C-band frequency, could have important ramifications for airborne and space-borne radar exploration of oil sands and assessment of oil sand reservoirs.

6 Computer Electromagnetic Model

The third step in our method to establish the spectral and radar signature of oil sand for petroleum exploration is to develop computer electromagnetic models that generate scattering data for each barefaced terrain class. The models consist of electromagnetic sensors and barefaced terrain models that generate surface and volume scattering data for terrain classification. The chapter discusses the modelling technique for adaptable 3D terrain models, electromagnetic sensors, remote sensing configuration, simulation procedure and results.

Backscattering theory has inherent challenges when trying to apply it to oil sand reservoir exploration due to the strong similarities between oil sand and other barefaced terrain. Therefore a multi-sensor approach was adopted in this research. First hyperspectral imaging was used to obtain the geochemical signature for an electro-optical (EO) imager and the distinguishing components of oil sands was identified. Then the dielectric properties of diverse terrain types was empirically determined while statistical discrimination models were developed to identify frequencies that most influence terrain radar signature. In this chapter 3D computer electromagnetic (CEM) models that describe and enable the visualization of the complex interactions between electromagnetic (EM) waves and diverse terrain are developed. The interrelationships enable understanding of the oil sand scattering process for the retrieval of geophysical parameters. The CEM comprise microwave sensors and a barefaced terrain model (BTM). The microwave sensors are distinguished by the frequency of operation, f polarization, p and incident angle geometry, θ_i with respect to the terrain. BTM were designed to closely resemble barefaced terrain and embody the differences in surface roughness and dielectric properties. The 3D terrain models were made to represent the material under test (MUT) A - MUT F, namely: beach sands, loamy farm soils, pebbles, gravel and also hard and viscous oil sands. The modelling technique used finite integration technique (FIT) discretization. Prior to this work no microwave EM scattering models of oil sand terrain are known to exist in literature. Previous terrain models neither account for the presence of bitumen and other hydrocarbons nor the intrinsic electrical properties. This chapter advances the theory of microwave SAR for

oil sand exploration then discusses development of CEMs for investigating the larger context of terrain scattering effects from multiple frequencies and incidence angles.

6.1. Model Components

In Section 2.4 we considered the response of an isolated point target in order to better understand the system resolution. Distributed targets such as terrain however, present unique imaging problems for radar remote sensing due to the presence of multiplicative speckle noise. Unlike coherent point targets which are easier discriminated from surrounding objects due to discernible physical features, distributed targets are best determined from the average or dominant scattering mechanism which serves to blur the EM response (Cloude & Pottier, 1996; Cloude & Pottier, 1997; Ezeoke *et al*., 2014c). In this case, target information is described by the radar cross section (RCS) or scattering coefficient, σ for point targets and average normalized RCS (nRCS) per unit area or backscattering coefficient, σ^0 for distributed targets. Both depend on target geometric and dielectric properties as well as sensor parameters like incident geometry, polarization and spatial resolution (Table 3.7). Therefore in the CEM, σ^0 will need to be characterized for specific frequency, f and polarization of incident (θ_i, ϕ_i) and scattered (θ_s, ϕ_s) wave directions.

The interpretation of SAR imagery is non-linear and varies along a gray scale palette where low backscattered signals are dark and high backscattered signals are slightly brighter. Therefore it is often better to first model the EM wave interaction with the terrain target or scattering systems as shown (Fig. 6.1). Here an incident polarized wave, $\mathbf{E}^i$ interacts with a distributed terrain scatterer [M] through combination of wave propagation, attenuation and scattering. In (Cloude & Pottier, 1996), the classical Stokes vector of a wave was solved for an intensity vector, **k** to give a Mueller matrix relationship for incident and scattered waves directions with [M] as (Fig. 6.1 and (6.1)):

$$\mathbf{k}_s = [\boldsymbol{M}] + \mathbf{k}_i. \tag{6.1}$$

In the ideal scattering plane, θ_S is the scattering angle where $\theta_S = 0°$ is forward scatter and $\theta_S = 180°$ is backscattered. In reality the scattering response particularly from distributed scatterers is not so clear cut. For terrain the resulting scattered field,

$\mathbf{E}^{sca}$ is due to a coherent addition of scattered waves, $\mathbf{E}^{sca}{}_k$ (k = 1, 2 … N) from independent targets that model the extended target.

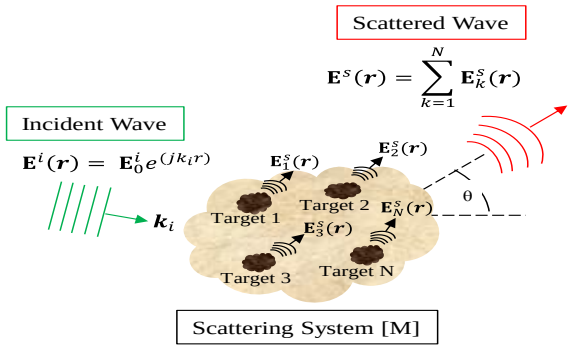

Figure 6.1: General scattering geometry showing interaction of EM wave and extended target (Ezeoke *et al*., 2014c).

Therefore the incident and scattered EM waves, $\mathbf{E}^{inc}$ and $\mathbf{E}^{sca}$ at a distance **r** can be represented by a Jones vector (6.2) and (6.3):

$$\mathbf{E}^{i}(\mathbf{r}) = \mathbf{E}_{\mathbf{0}}^{i} e^{(j\mathbf{k}_1\mathbf{r})} \tag{6.2}$$

$$\mathbf{E}^{s}(\mathbf{r}) = \sum_{k=1}^{N} \mathbf{E}_{k}^{s}(\mathbf{r}) \tag{6.3}$$

The CEMs developed here are expected to help identify and then present the radiometric properties of an imaged terrain or area. Therefore the best way to identify the components required to develop the models is to explain how the radar reflectivity of a scene imaged from an airborne or satellite EM sensor is translated to image brightness. Several good radar remote sensing texts cover this translation such as Ulaby *et al*., (1982), Oliver and Quegan (2004) and Stimson *et al*., (2014). Our analysis loosely follows the description by Oliver & Quegan (2004).

6.1.1. Complex Reflectivity

Considering SAR as a linear measurement system for geoscientific purposes, then the general description for the scattering behaviour of a point target (which is the simplest possible target) is given by the *complex scattering amplitude*, S_{pq}. The complex scattering amplitude or complex reflectivity, quantifies the scattering, from the point target into the polarization state p of an incident plane wave with wave polarization q and is given by (Van Zyl & Ulaby, 1990):

$$\begin{pmatrix} \mathbf{E}_p^s \\ \mathbf{E}_q^s \end{pmatrix} = \frac{e^{2\pi jr/\lambda}}{\mathbf{r}} \begin{pmatrix} S_{pp} & S_{pq} \\ S_{qp} & S_{qq} \end{pmatrix} \begin{pmatrix} \mathbf{E}_p^i \\ \mathbf{E}_q^i \end{pmatrix} \quad (6.4)$$

Here there is free space propagation from the EM sensor at an observation point **r** which is in the far-field of the (terrain) scatterer. The incident electric field has complex (*p*, *q*) components represented by $\mathbf{E}_p^i$ and $\mathbf{E}_q^i$ or in some cases by the three coordinates (*x*, *y*, *z*) by $\mathbf{E}_x^i$, $\mathbf{E}_y^i$ and $\mathbf{E}_z^i$ where the absolute value for all three is $\mathbf{E}_{abs}^i$. Also the scattered field components may be similarly defined as $\mathbf{E}_p^s$ and $\mathbf{E}_q^s$ or $\mathbf{E}_x^s$, $\mathbf{E}_y^s$ and $\mathbf{E}_z^s$ with $\mathbf{E}_{abs}^s$the absolute value for all three coordinates. A full discussion is at (Van Zyl & Ulaby, 1990). The 2 x 2 matrix on the right hand of (6.4) is known as the *scattering matrix*. In this study we post-processed the results from the CEM's in order to present the scattering matrix as radiometric brightness in one dimensional (*x*, *y* or *z* plots) and two dimensional (*x*/*y*, *x*/*z* or *y*/*z*) reflectivity views.

6.1.2. Radar Cross Section

A detailed analysis of the scattering matrix would need to consider bistatic geometry. However in the second year of this research, it was decided that the monostatic backscattering case was more relevant. This is because currently available commercial airborne and satellite sensors are monostatic while the practical application of radar remote sensing to oil sand exploration requires knowledge of the monostatic RCS (Ezeoke & Tong, 2012). In many situations the phase of a point scatterer is of less interest than the backscattered power therefore the RCS is a more commonly used descriptor for a point scatterer (Oliver & Quegan, 2004). It is given by (Van Zyl & Ulaby, 1990):

$$\sigma_{pq} = 4\pi |S_{pq}|^2 \quad (6.5)$$

For SAR imaging we consider a point scatter to have a complex reflectivity *S* at azimuth or cross range position *y′* and slant range *R* when the platform is at azimuth position *y*. For a pulse emitted at time *t* = 0, after pulse compression the received echo signal is:

$$E(y) = S\, K'(R) h_r \left(t - \frac{2R}{c}\right) a\left(\frac{y - y'}{R}\right) e^{-4\pi jR/\lambda} \quad (6.6)$$

Where $K'(R)$ is a term that accounts for the elevation antenna pattern, processing gain during range compression and the range spreading loss which is proportional to R^{-2}. The two way amplitude azimuth antenna pattern is given by $a(\phi)$. The term $h_r(t - 2R/c)$ describes the time delay in the range point spread function (PSF) (see (2.27)) and in this case allows the positioning of the target in the range direction. Conventionally, the three terms in (6.6): $K'(R)$, $a(\phi)$ and $h_r(t - 2R/c)$ vary more slowly with range, R than the phase of the exponential term $4\pi jR/\lambda$. Therefore for the three terms, R may be replaced by R_0 which is the closest point of approach (CPA) for the range.

The variation of range, R with along-track separation $y - y'$ can be described as:

$$\boldsymbol{R = R_0 + \frac{\lambda\beta}{4\pi}(y - y')^2} \tag{6.7}$$

Here β is the focusing parameter. We have already derived expressions for β in the airborne and space-borne cases in (2C.13) and (2C.14). For the situation where range migration is negligible or corrected in radar processing the received echo signal from (6.6) may be written in terms of the CPA for the range, R_0 as:

$$\boldsymbol{E(y) = S\,K(R_0)a\left(\frac{y - y'}{R}\right)\exp(-i\beta[y - y']^2)} \tag{6.8}$$

Where

$$\boldsymbol{K(R_0) = K'(R_0)h_r\left(t - \frac{2R_0}{c}\right)\exp(-4\pi iR_0/\lambda)} \tag{6.9}$$

More detailed analysis of the coupling between range and azimuth in the signal processing of SAR imagery has been discussed by (Curlander & McDonough, 1991; Bamler & Shättler, 1993). To determine the backscattering coefficient, σ^0, for different terrain types, the effect of backscattered or echo signal at an instantaneous point in time is considered where the radar sensor is in a fixed position relative to the terrain target. Therefore mutual coupling between azimuth and range is constant and negligible.

6.1.3. Differential Backscattering Coefficient

By considering the spatial extent in azimuth and at range, R_0 to be a scattering system $[M]$ made up of elementary scattering areas represented by delta functions, then (6.8) can be generalized to include a continuous reflectivity function $S(y, R)$. For this

spatial extent, $R = R_0$ and $S(y, R)$ can be abbreviated as $S(y)$. From (6.3) and (6.8) the received echo signal is a convolution given as:

$$\boldsymbol{E(y) = K(R_0)} \int_{-\infty}^{\infty} \boldsymbol{S(y')a}\left(\frac{\boldsymbol{y - y'}}{\boldsymbol{R_0}}\right)\mathbf{exp}(-\boldsymbol{i\beta}[\boldsymbol{y - y'}]^{\mathbf{2}})\boldsymbol{dy'} \tag{6.10}$$

$$= \boldsymbol{K(R_0)S(y)} * \boldsymbol{k(y)}$$

Where

$$\boldsymbol{k(y)} = a\left(\frac{\boldsymbol{y}}{\boldsymbol{R_0}}\right)\mathbf{exp}(-\boldsymbol{i\beta y^2}) \tag{6.11}$$

In (6.11), $k(y)$ can be regarded as a prefilter containing two effects: the *beam weighting* given by the antenna in the azimuth direction and the *range variation* caused by the relative motion between the platform and the scatterer (Harger, 1970; Raney & Bamler, 1994). For distributed targets represented by the continuous form of $S(y)$ the phase of the scattered field has a correlation length that is shorter than the resolution of the radar measurement (Oliver & Quegan, 2004). Therefore for resolution comparable with the correlation length, l, the target has a well-defined RCS enabling us to derive the *differential backscattering coefficient* as:

$$\boldsymbol{\sigma^{\circ}\Delta A} = \mathbf{4}\boldsymbol{\pi R^2}\frac{\boldsymbol{P_{sca}}}{\boldsymbol{P_{inc}}} \tag{6.12}$$

Where ΔA is the elemental spatial area over which the phase is effectively constant, P_{inc} is the incident power per unit area, P_{sca} is the power per unit area backscattered from the spatial area ΔA (or ∂A) and observed at a range R. It is expected that different aspects of the terrain will contribute independent phases so that the electric field observed at the sensor will experience interference effects or *speckle* (Stimson *et al*., 2014).

The elemental spatial area, ∂A represents the surface of the terrain area or BTM that is illuminated by the EM sensor. It ought to embody the physical and electrical properties that represent each of the terrain types covered in MUT A to MUT F. The BTMs were specifically designed to represent this spatial area. Also for proper EM characterization of the terrain types the actual spatial extent considered for each terrain type, must be the same so that both the energy backscattered and absorbed $\mathbf{E}^{ref}$ and $\mathbf{E}^{abs}$ respectively from (3.3) can be compared for each BTM. For this work, ∂A was set to

$1m^2$ although resolution as fine as $0.5m^2$ has been investigated (Ezeoke *et al*., 2014c; Ezeoke *et al*., 2014b; Ezeoke *et al*., 2014a). Furthermore to derive volume scattering at depths of up to 1m an elemental volume ∂V of $1m^3$ was implemented for the 3D BTMs.

6.1.4. Illumination Source

In order to obtain the average or mean value of backscattering coefficient, σ° the returns over the area illuminated by the EM sensor need to be normalized (6.12). The power incident on ∂A, P_{inc} depends on power transmitted by the EM sensor, P_{tra}. As a result there are three imaging effects accounted for when trying to recover σ° for a real world system, namely: (1) the scaling of σ° due to field propagation, antenna pattern and processing effects; (2) system noise that could cause a bias in σ°; and also (3) spatial correlation induced by processing. Only (1) and (3) were observed in the CEMs and different approaches were used to correct for them based on the sensor type.

6.1.5. Range

The EM energy incident, backscattered and absorbed, $\mathbf{E}^{inc}$, $\mathbf{E}^{sca}$ and $\mathbf{E}^{abs}$ in a distributed target depends on the range distance between the antenna sensor and the target (Fig. 6.2). In some applications such as detection of buried mines, geological monitoring or archeological excavation the sensor could be in contact with the ground or some distance above it. These regions correspond to the reactive or near field. In the reactive near-field both the electric and magnetic field are quadrature out of phase so that the maximum amplitude of the radiating field varies with respect to the distance in the medium. The interaction of the incident EM energy with terrain at the reactive near field region will be strong for low permittivity terrain but weak for high permittivity terrain (such as with increasing moisture content).

For applications of microwave heating to oil sands such close proximity is suitable because the antenna operates in the radiating near-field or Fresnel region with relevant absorption, heating and cooling mechanisms (Pierre *et al*., 1992; Sahni *et al*., 2000). In this region the electric field is semi-reactive with weak power density at the center ensuring that surface heating occurs when the sensor interacts with terrain. However for the coverage of the large areas in spatial extent, required for oil sand exploration the EM sensors are expected to be in the far field. Therefore environmental factors such as propagation losses in air, texture or surface roughness, attenuation and

electrical properties may be more dominant (Fig. 6.2). In the far field region the range of the EM sensor (or antenna) from the terrain is greater than:

$$\boldsymbol{Far\ field} > \frac{\boldsymbol{2D^2}}{\boldsymbol{\lambda}} \tag{6.13}$$

Where D, is the antenna or EM sensor dimensions and the wavelength, λ depends on the frequency, f, at which the antenna sensor operates. In this region the incident field is characterized as a plane wave with a cosine distribution such that the electric and magnetic fields are in phase with each other during transmission.

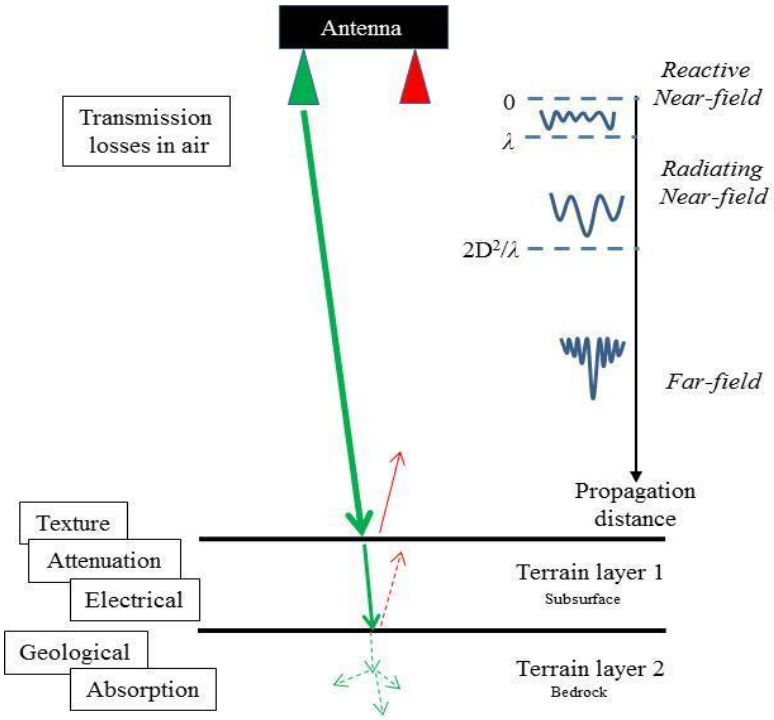

Figure 6.2: Schematic showing the effect of range between EM source and terrain on environmental variables and antenna field distribution at different zones.

Importantly the radiated energy decreases with the square of the propagating distance as range spreading loss is proportional to R^{-2}. In this thesis the EM sensor producing the radiated field is considered to be in the far field region at a distance greater than 10 λ although the models are adaptable.

6.1.6. Processing

For modern airborne or spaceborne radar the range compressed raw data, $E(y)$ would be digital and built up sequentially at each range gate (or bin) as pulse echo returns and saved in to memory. From (6.8) the azimuth processing is a correlation with

this stored data and may be represented as a 'second' filtering operation so that the output is:

$$\boldsymbol{\xi(y) = E(y) * l(y) = K(R_0)S(y) * h_a(y)} \tag{6.14}$$

Where

$$\boldsymbol{h_a(y) = k(y) * l(y)} \tag{6.15}$$

In (6.15), $h_a(y)$ is the azimuth PSF and $l(y)$ is the SAR processing filter. The filter may contain an amplitude weighting term $W(y/R_0)$ and its main purpose is to remove the quadratic phase terms (Stimson *et al*., 2014). It has the form:

$$\boldsymbol{l(y) = W\left(\frac{y}{R_0}\right)\exp(i\beta y^2)} \tag{6.16}$$

Therefore (6.15) may be rewritten as:

$$\boldsymbol{h_a(y) = \exp(i\beta y^2)\int_{-\infty}^{\infty} a\left(\frac{-x}{R_0}\right)W\left(\frac{x-y}{R_0}\right)\exp(-2i\beta xy)dx} \tag{6.17}$$

The range PSF, $h_r(t)$ is much more straight forward since it is really a delayed and scaled version of the transmitted pulse (see simple form in (2.27) and detailed derivation in 2D.5). It is often called the autocorrelation function and given here as:

$$\begin{aligned}\boldsymbol{h_r(t)} &= \boldsymbol{\int_{-\tau/2}^{\tau/2}\exp(i\beta S^2)\exp(-i\beta[s+t]^2)rect\left(\frac{s+t}{\tau}\right)\,ds} \\ &= \boldsymbol{(\tau-|t|)\,\mathrm{sinc}\left(\frac{\beta}{\pi}\right)t[\tau-|t|])\,\mathrm{rect}\left(\frac{t}{\tau}\right)}\end{aligned} \tag{6.18}$$

When the beam shape is uniform over the beamwidth, θ_B and zero elsewhere we can equate $a(\phi)$ = W(ϕ) = rect(ϕ / θ_B) so that a point target response for $h_a(y)$ and $h_r(y)$ gives the same result except for the range dependent term $K(R_0)$. For linearly polarized plane wave as radiating source, the magnitude of the backscattering coefficient is approximately the same for the azimuth (y) and range (x) aspects of the CEM. Therefore the absolute value of the scattered field, $\mathbf{E}_{abs}^{s}$ was determined for individual terrain classes.

6.1.7. Noise and Losses

The complete translation of the radar reflectivity from an imaged scene to image brightness stored in memory will necessarily encounter system noise. In order to include this in the azimuth processing model in (6.8), (Oliver & Quengan, 2014) introduced noise term $n(y)$ so that:

$$\begin{aligned}\boldsymbol{\xi(y)} &= \big(\boldsymbol{C(R)S(y)} * \boldsymbol{k}\,\boldsymbol{(y)} + \boldsymbol{n(y)}\big) * \boldsymbol{l(y)} \\ &= \boldsymbol{C(R)S(y)} * \boldsymbol{h_a(y)} + \boldsymbol{n(y)} * \boldsymbol{l(y)}\end{aligned} \tag{6.19}$$

The coefficient $C(R)$ absorbs the range dependent system terms given in (6.9) with magnitude given by:

$$|\boldsymbol{C(R)}|^2 = \left(\frac{\boldsymbol{P_t G_r^2 \lambda^2 G_p}}{\boldsymbol{(4\pi)^3 R^4 L}}\right) \tag{6.20}$$

Where P_t is the peak transmitted power, G_r is the one way power gain of the antenna pattern at range R, L represents system losses and G_p is the processing gain due to range compression. Typical system noise appearing in each range gate after range compression is expected to be white, zero mean and Gaussian because it will typically be unaffected by antenna pattern or Doppler shifts. Therefore we do not include noise in the CEMs. Although the voltage equation (6.19) is applicable to any form of target, it is more useful to consider the observed backscattered power in magnitude dB, dBm or Vm^{-1}. All three were employed.

Finally the mean power in the signal received by the sensor from a uniform distributed target with backscattering coefficient can be written:

$$\langle|\boldsymbol{\xi(x)}|^2\rangle = |\boldsymbol{C(R)}|^2 \boldsymbol{\sigma^0}\, \boldsymbol{E_{h_a}} + \boldsymbol{N E_l} \tag{6.21}$$

where

$$E_{h_a} = \int_{-\infty}^{\infty} |h_a(x)|^2 \; dx$$

is the energy in h_a or the SAR processor gain and E_l is similarly defined. It is (6.21) that connects the power observed at the sensor to the geophysical quantity σ^0. For SAR the mean power from the uniform distributed target exhibits an R^{-3} dependence as E_{h_a} is roughly linearly proportional to R. In order to characterize the scattering coefficient of different terrain over a broad range covering L-band, C-band and X-band frequencies both linearly polarized and co-polarized radiation was used. The latter was best achieved through ultrawideband (UWB) antennas.

6.2. Ultrawideband Antenna Theory

Although the history of early radio has been well studied, the development of UWB antenna has not been similarly researched (Aitken, 1985; Lewis, 1991). Schantz (2005) tried to bridge this gap by chronicling the development of UWB from James Clerk Maxwell's equations to the efforts of Heinrich Hertz who discovered Radio waves. Progress in UWB benefitted from Oliver Lodge who invented 'syntonic' radio, Jagadis Chandra Bose who invented horn antennas and Guglielmo Marconi who first commercialized radio as a means of long-range communication amongst others. Here we briefly discuss UWB antennas as precursor to its use as a sensor in the CEMs.

UWB antennas have been defined by several criteria. The Defense Advanced Research Projects Agency (DARPA) requires a UWB antenna to have a fractionating bandwidth greater than 0.25 while the US Federal Communications Commission (FCC) places the limit at 0.2 (Schantz, 2005). In essence the fractionating bandwidth (*bw*) for UWB is defined as:

$$\boldsymbol{bw = 2\frac{f_H - f_L}{f_H + f_L} \geq \begin{cases} 0.25 & DARPA \\ 0.20 & FCC \end{cases}} \tag{6.22}$$

Where f_H is the upper or high end and f_L is the bottom or lower end of the antenna's operational band respectively. The FCC also provides an alternative definition where UWB antenna is defined as having a -10 dB bandwidth (*BW*) greater than 500 MHz (US 47 C.F.R, 2003). Difficulties appear when we try to extend traditional narrowband antenna behavior to UWB antennas as exemplified by the contradiction between constant gain antennas and constant aperture antennas. The former has a fixed pattern and minimal dispersion while the latter has narrowing field of view (FOV) and exhibits waveform dispersion at the edge of the FOV.

The different UWB antennas fall into either of these archetypes. UWB antennas such as Vivaldi, spiral, double-ridged, transverse electromagnetic (TEM) and bow-tie, are important parts of high resolution radar imaging systems. Double-ridged and TEM horn antennas have been used for satellite ground station communications, EM weapons, impulse radars, monitoring underground reservoirs, ground penetrating radar and oil well monitoring amongst others (Oloumi *et al*., 2013; Wright *et al*., 1984; Guo & Liu, 2010; Panzner *et al*., 2010).

A typical antenna is composed of three parts: a feed line to connect to the radio frequency (RF) front end, a feed region to transition between the feed line and one or

more radiating elements and the radiating element. The radiating elements aid the coupling between radiation fields and the guided fields in the antenna's feed line. A standard horn or conical plate antenna starts at a feed point and includes two parallel conducting plates of length *l*, usually with a fixed plate angle (α) and a fixed plate pitch angle (β). A model of this is shown in (Fig. 6.3). It was developed using computer simulation technology (CST) microwave studio (MWS) EM model software (CST MWS, 2014).

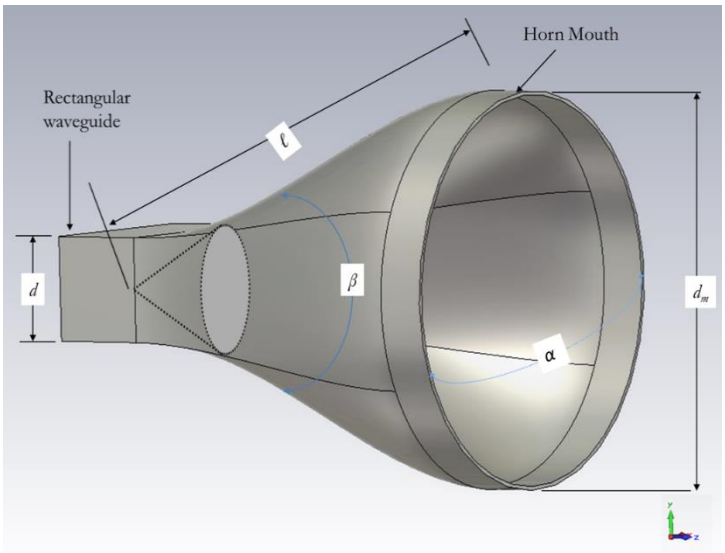

Figure 6.3: A conventional conical plate horn antenna comprising conducting plates with length *l*, fixed plate angle (α) and fixed plate pitch angle (β) with rectangular waveguide gradually flared into the horn mouth directly.

For (King, 1950) the diameter of the horn antenna, d_m was used rather than (β). Also both dominant wave (TE_{10}) excitation in rectangular wave guide and TE_{11} wave excitation in circular waveguides were found to exhibit the same behavior. For characterization across a broad frequency range, a tapered double ridged wave-guide was added to the conical plate antenna to make it a standard gain horn (SGH) antenna. Ridged wave guides have been used since the 1960's (Lai *et al*., 1987). The SGH are essentially flared or tapered transmission lines able to transmit and receive EM energy in one or more particular directions with constant gain.

The SGH developed here is a directive antenna and therefore can only transmit and receive in one specific direction (Fig. 6.4). The tapered double ridge creates a capacitive effect that increases the bandwidth by lowering the cutoff frequency of the dominant mode (TE_{10}) while increasing the cutoff frequency of the next dominant mode

(Schantz, 2005; Ezeoke *et al*., 2014c). Furthermore ridge slot loading contributes to a better impedance matching behavior while broadening the impedance bandwidth (Tenigeer *et al*., 2013). The SGH antenna was designed using CST MWS EM Modeler module for use as a far field dielectric probe.

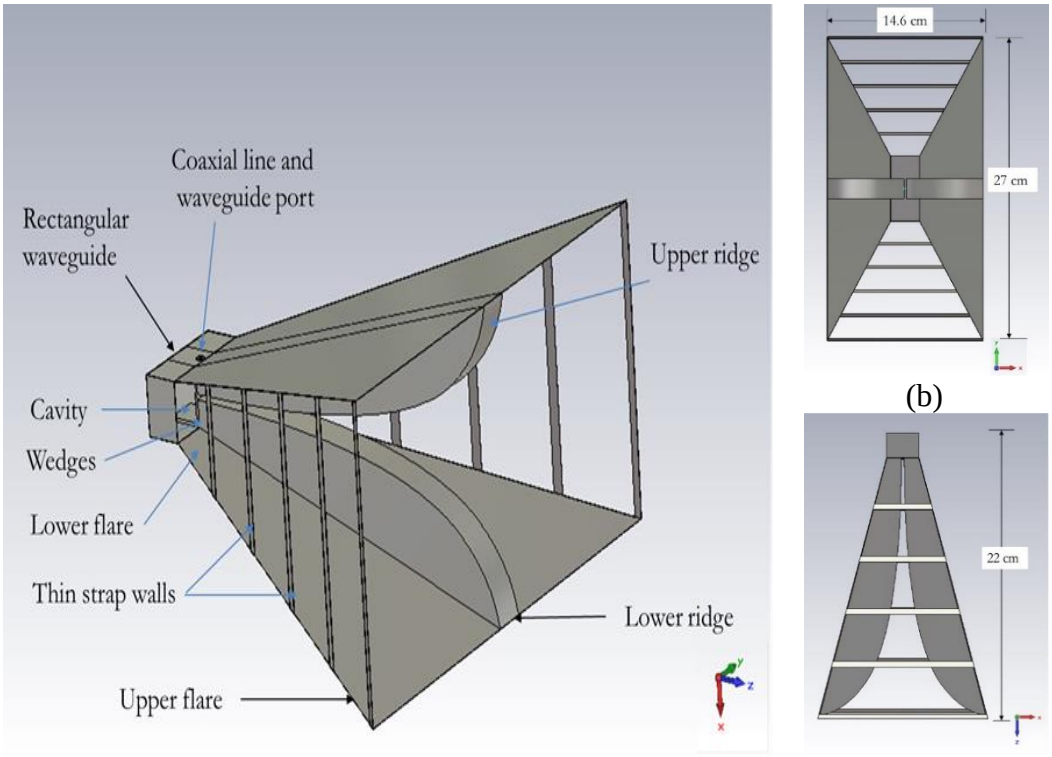

(a) (b) (c)

Figure 6.4: Double ridged wave-guide SGH antenna designed in CST MWS showing views: (a) perspective (b) front (c) top.

The sensor consists of a coaxial line and waveguide port input connector with optimal dielectric constant ε_r = 2.05, a cavity below the coaxial input section, two exponentially shaped ridges, two wedges and two lower and upper *H* plane flares (Fig. 6.4). The overall box dimensions (L x W x H) are 22 x 14.6 x 27 cm^3 (Fig. 6.4) while the metal parts were modeled as perfect electrical conductor (PEC). The thin strap walls help to control the width of the *E* plane radiation pattern at lower frequencies but do not have any measurable effect above 4 GHz (Bruns *et al*., 2003). The taper profile slope, *S* of the continuous metallic ridge in the *z* direction along the horn flare is exponential and governed by the expression (Olver *et al*., 1994; Notaros *et al*., 2001):

$$\boldsymbol{S_{exp}(z) = S_{exp}(0)\, e^{pz}} \tag{6.23}$$

with,

$$p = \frac{1}{L} \ln \frac{S_{exp}(L)}{S_{exp}(0)}, \qquad 0 \leq z \leq L \tag{6.24}$$

Here L is the length adjacent to the taper on the horn radial axis and $S(z)$ is the gap between the upper and lower ridges at the wedge end. For our model, L = 22 cm and $S(z)$ = 0.5 cm. The ridges were chamfered so that only a very small gap for $S(z)$ existed between the ridges at the feed point. The chamfer angle was 45°. Propagating fields are excited by the coaxial line probe inserted in to the waveguide port (Fig. 6.4). The gradual outward progression of the flare from the lower to upper stages acts as a broadband impedance transformer from the 50-ohm feed to the 377-ohm impedance of the free space (Giacomini *et al*., 2011). The antenna was single linear polarized able to transmit and receive horizontally (HH) or vertically (VV).

The low frequency limit is dictated by the overall length of the antenna while the high frequency limit is governed by the mechanical precision of the feed. UWB antennas require a smoothly varying impedance profile to ensure a good broadband match (Andersen, 1982). While narrowband antennas have specific impedance for the frequency they operate at, UWB antennas suffer because of the wide range of frequencies they work at. This has to be considered when designing the antenna. An analytical solution for the impedance of conical plate horns exist in literature using elliptical integrals and mathematics (Yang & Lee, 1976). There are several other termination techniques used in horn antennas such as serration of an edge, rolled edges and resistive termination amongst others (Burnside & Chuang, 1982; Chang & Burnside, 2000).

6.3. Modelling and Simulation

In EM signature classification the main goal is the determination of the quantitative description of the known scatterer(s) size, location, permittivity, conductivity, scattering coefficient or other property from remote sensing measurement obtained away from the scatterer (Lillesand *et al*., 2008). For the numerical solution the volume integral equation is an appropriate method because the calculation domain is an inhomogeneous closed space for most situations. In some general applications a good approximation of the signature is useful. Several approximation techniques have been developed based on the physical optics (POM) or Kirchoff scattering model (KSM),

Small Perturbation Model (SPM) or geometric optics (GOM) approximations (Beckmann & Spizzichino, 1963; Torrance & Sparrow, 1966).

When the profile of the surface deviates only a little from that of a smooth surface, perturbation solutions can be used (Oh *et al*., 1992). For the classical treatment of SPM the root mean square (r.m.s) height, h_{rms} must be much smaller than the wavelength, λ,while the r.m.s slope, m, is on the same order of magnitude as the wavenumber ($k = 2\pi/\lambda$) times the r.m.s height (Rice, 1951). The KSM applies when the surface irregularities are large compared to wavelength so that there is a large radius of curvature at each point on the surface along with small slopes (Beckmann & Spizzichino, 1963; Ulaby *et al*., 1986). Various modifications and improvements to the models can be found in literature even extending the region of validity of both KSM and SPM to composite surfaces (Brown, 1978). Similarly a few books and papers have been devoted to the general scattering model with increasingly sophisticated techniques and descriptions of the scattering problem (Ulaby *et al*., 1986; Fung, 1996).

All three models depend on statistical surface properties and do not say much about achieving the radiometric brightness of a scene although efforts have been made to do this (Nayar *et al*., 1989). Furthermore there is still a large gap between the scattering medium described in most models and the reality of what is contained in the scattering cell because some quantities necessary for the scattering models are difficult to measure reliably such as detailed dielectric properties (ε', ε'' and tan δ) of a medium (Oliver & Quegan, 2004). Similarly other quantities such as the correlation length, l or surface roughness, h_{rms} may exhibit rapid spatial variation making it difficult to define a meaningful representative value for insertion in to a scattering model. Another weakness with most modeling approaches is the assumption of infinite plane waves and infinite media whereas in reality the satellite measures a structured scene (Soumekh, 1999). Next we discuss the choice of solver, modelling method and simulation procedure.

6.3.1. Numerical Study

The measurement of the EM interaction inside barefaced terrain and reflections from and within oil sand is a serious challenge for geophysicists working in petroleum exploration and radar engineers tasked with developing responsive radar remote sensing systems. There is a wide variety of choice with regards to EM sensors, platforms and configurations on one hand but very little difference in attributes between

barefaced terrain and oil sands on the other. One solution to this situation is to develop CEMs for understanding the scattering behavior of oil sand terrain before empirical measurements to validate modeling results. Both analytical and numerical methods may be employed for EM characterization of terrain particularly determination of backscattering and reflectivity. In the analytical methods, Maxwell's equations are mathematically solved for diverse geometry while numerical solutions employ computer simulation based on approximating algorithms. In particular, Maxwell's equations subject to the boundary conditions are addressed in analytical approaches but physical models based on simplifying assumptions are developed for numerical methods (Lee & Tong, 2012).

Several numerical methods exist and have been applied to different problems. They include full wave solvers such as method of moments (MoM) or bi-conjugate gradient method (BCG) (Ezeoke *et al*., 2014b). There are also approximate methods such as the finite difference time domain (FDTD) method, the finite-element method (FEM) or the finite integral technique (FIT). Full wave solvers provide greater accuracy however other methods can provide good approximations of the exact solution.

Currently, the FDTD and the FIT methods are the most dominant (Davidson, 2008). FDTD has been used to investigate the characteristics of new antenna types (Tong *et al*., 1997). The FDTD algorithm solves Maxwell's time dependent curl equations by filling up the computation space with several Yee cells or grid mesh as they are currently referred to (Tong *et al*., 1997; Taflove & Brodwin, 1975). Typically field components are approximated at the center of each cell during each iteration within which a finite difference analog of the time dependent Maxwell's equations for the model is repeatedly solved. Rather than at cell centers, the FEM technique analyses the field components at the nodes of the cell (Coulomb, 2008).

6.3.2. Simulation Architecture

Only little research has been carried out to understand the EM scattering obtained from oil sand terrain (Ezeoke & Tong, 2012; Ezeoke & Tong, 2013c; Ezeoke *et al*., 2014c). This means that no meaningful comparison of backscattering from oil sand and other barefaced terrain has been conducted as a means to differentiating barefaced terrain types. However aspects of the general scattering problem have been discussed by several authors including Wei *et al*., (2007) and Ulaby *et al*., (1982) amongst others. In this research work, we primarily consider the monostatic

configuration in which there is an EM transmitter and receiver (transceiver) source on the same platform. The EM waves are incident on a multilayer medium where the medium consists of $N + 1$ layers separated by N planar sections as shown (Fig. 6.5).

For such a monostatic configuration, the EM source and receiver are in the same layer *a*, the transmission medium (air) occupies layer *b* while the MUT which is any of the barefaced terrain types will be in a layer *c*. Subsequent layers may occupy up to $N - 1$ in the case of deep terrain imaging such as ground penetrating radar or archeological applications. If the EM source is in the z direction then layer i will exist between z_{i-1} and z_i, while the real and imaginary dielectric permittivity for each layer is given by $\varepsilon'_{r,i}$ and $\varepsilon''_{r,i}$ respectively. Therefore the electrical properties of layer *a*, *b* and *c* are given by the complex permittivity's: ε_a^*, ε_b^* and ε_c^* respectively.

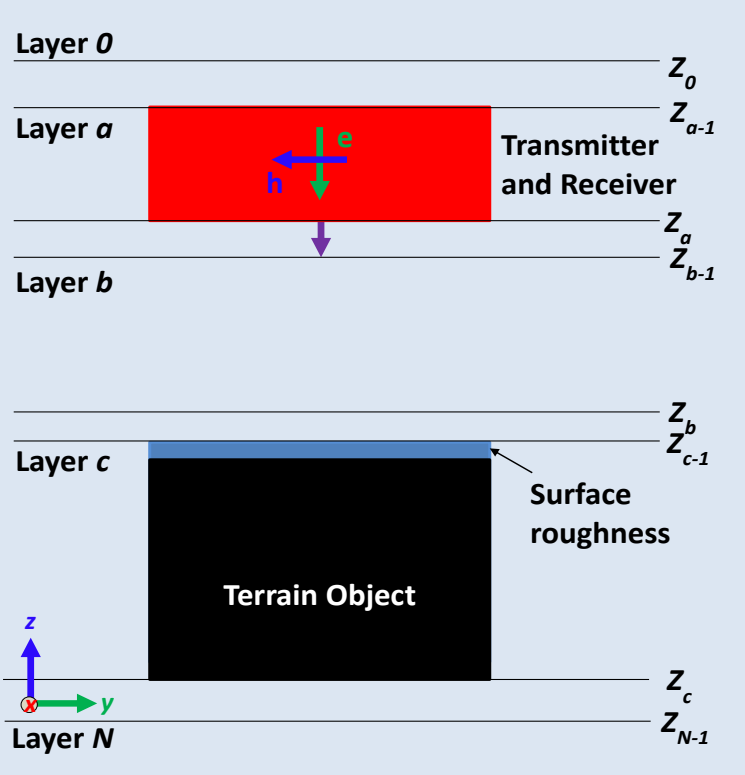

Figure 6.5: Generic scattering problem with terrain object present in multilayer medium. EM transmitters and receivers are located in layer *a* while the computational domain (*D*) comprises layers *a*, *b* and *c*. Electrical properties of layer *a*, *b* and terrain object in *c* are characterized by complex permittivity's ε_a^*, ε_b^* and ε_c^* respectively while the physical properties are characterized by the surface roughness and terrain object properties in *c*.

In (Wei *et al*., 2007) the transmitter and receiver were in a bistatic formation and not included in the calculation. For simplicity and easy adoption for other

applications such as land degradation monitoring besides oil sand exploration, our approach includes layers *a* through to layer *c* with both transmitter and receiver sources in a radar monostatic mode (Ezeoke & Tong, 2014; Ezeoke *et al*., 2014d). For the CEMs we consider the magnetic permeability μ to be constant with both EM transmitter and EM receiver in the far field region. This is expected for radar sensors borne on air or satellite platforms (Ezeoke & Tong, 2012; Lillesand *et al*, 2008). The far field distance, d_f is related to the wavelength, λ of the EM field being transmitted by an antenna of dimension, *D* according to (6.13).

In the forward problem case the dielectric properties were derived for input in to the predictive CEM based on measurement technique and results from the DDSM described previously (Chapter 5). Rather than models of dielectric behavior, the actual measurement values would be input in to the BTMs for accuracy and to enhance the CEMs with real world intrinsic terrain data.

For an object in the far field, the total electric field at a point **r** which is within the dielectric object (terrain in this case) will be caused by the transmitter located at position $\mathbf{r}_T$. For monostatic radar configurations the receiver will be located at position $\mathbf{r}_R$. Based on the superposition principle the total electric field in the terrain object is a summation of the incident and scattered fields given by (Wei *et al*., 2007) as:

$$\mathbf{E}(\mathbf{r}, \boldsymbol{r_T}) = \mathbf{E}^{\boldsymbol{inc}}(\mathbf{r},\ \mathbf{r_T}) + (\boldsymbol{k_c^2} + \boldsymbol{\nabla\nabla}\cdot)\int_{\boldsymbol{D}} \mathbf{G}_{\boldsymbol{cc}}^{\boldsymbol{AJ}}(\mathbf{r}, \mathbf{r}') \cdot \boldsymbol{\chi}(\mathbf{r}')\mathbf{E}(\mathbf{r}', \mathbf{r_T})\boldsymbol{d}\mathbf{r}', \mathbf{r} \in \boldsymbol{D}, \tag{6.25}$$

Here $\mathbf{G}_{cc}^{AJ}(\mathbf{r}, \mathbf{r}')$ is an auxiliary dyadic Green's function which represents the magnetic vector potential. This equation can also be written with the electric dyadic Green's function $\mathbf{G}_{ac}^{EJ}$ at the observation point **r** in layer *a*, which is related to the unit current source at a point $\mathbf{r}'$ in layer *c*. The wavenumber in layer *c* is given by $k_c^2 = \omega^2\mu_c\,\varepsilon_c^*$ and χ(r) is the contrast given by:

$$\boldsymbol{\chi}(\mathbf{r}) = \frac{\boldsymbol{\varepsilon}^*(\mathbf{r})}{\boldsymbol{\varepsilon}_c^*} - \mathbf{1}. \tag{6.26}$$

After the total electric field in the computation domain, *D* is solved using the 'object' equation (i.e. (6.25)) then the scattered field at any location *S* can be calculated from:

$$\mathbf{E}_a^{sca}(\mathbf{r}, \boldsymbol{r}_T) = j\omega\varepsilon_c^* \int_D \mathbf{G}_{ac}^{EJ}(\mathbf{r}, \mathbf{r}') \cdot \chi(\mathbf{r}')\mathbf{E}(\mathbf{r}', \mathbf{r}_T)d\mathbf{r}', \quad \mathbf{r} \in S \tag{6.27}$$

This integral equation which defines the scattered field at the observation point *S* is called the 'data' equation. The forward modelling case uses the object (6.25) and scattered (6.27) field equations to solve for the scattered field reflected from and within the terrain object. It is the solution to these integral equations that solvers such as MoM, BCG, FDTD, FEM and FIT are used to solve. In this work the FIT implemented by the CST MWS (CST MWS, 2014) commercial software tool was used because it uses less computer central processing unit (CPU) time and memory than full wave solvers. It also decomposes the computational domain *D* into a finite number of smaller mesh cells, *d* in a primary grid **G**, which can be modified to select regions of greater interest. An internal second or dual mesh $\widetilde{\mathbf{G}}$ is set up orthogonally to the primary grid. The CST discretization scheme is shown (Fig. 6.6).

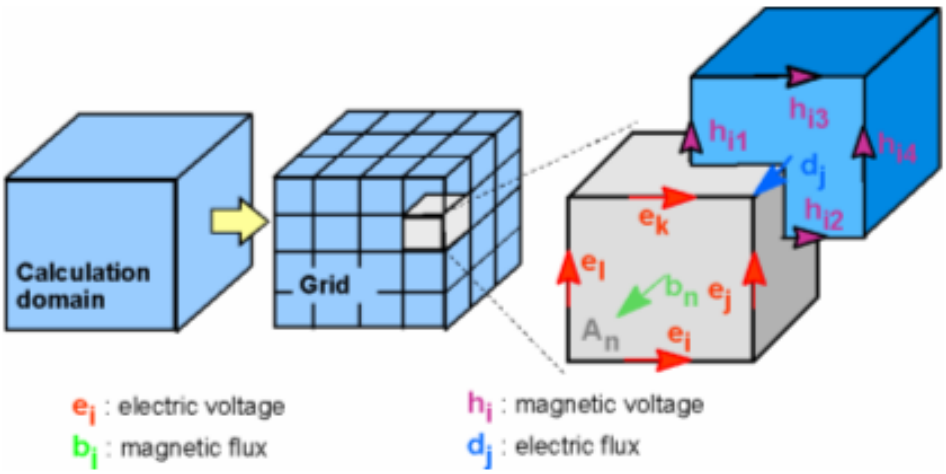

Figure 6.6: Computer Simulation Technology implementation of the Finite Integral Technique (CST MWS, 2014).

The Maxwell equations are applied to each mesh cell. This spatial discretization permits flexibility in the geometric attributes such as surface roughness of terrain and the addition of arbitrary material properties such as real and imaginary permittivity, loss tangent (tan δ) dispersion, non-linearity and anisotropy which is a true reflection of terrain behavior. In essence the constitutive equations from (3.7), (3.8) and (3.9) become:

$$\mathbf{D} = \boldsymbol{d}_{\varepsilon'}\mathbf{E}; \tag{6.28}$$

$$\mathbf{B} = \boldsymbol{d}_{\mu}\boldsymbol{H} \tag{6.29}$$

$$\mathbf{J} = \boldsymbol{d}_{\sigma}\mathbf{E}. \tag{6.30}$$

In this way $d_{\varepsilon'}$, d_{μ} and d_{σ} from (6.28), (6.29) and (6.30) represent the permittivity, permeability and conductivity matrices respectively. The basic idea of FIT is to approximate the scattered field relative to attributes of the scatterer and the source dependent diagonal scattering tensor within the grid complexes $\mathbf{G}$ and $\widetilde{\mathbf{G}}$. We can evaluate both surface and volume integrals this way. With the transmitter-dependent diagonal scattering tensor, $\Gamma(\mathbf{r}, \mathbf{r}_T) = \text{diag}[\psi x, \psi y, \psi z]$, then the scattered field for any distance within the scattering domain, $\mathbf{r} \in D$ can be written as:

$$\mathbf{E}^{\boldsymbol{sca}}(\mathbf{r}, \mathbf{r}_{\boldsymbol{T}}) \approx \boldsymbol{\Gamma}(\mathbf{r}, \mathbf{r}_{\boldsymbol{T}}) \cdot \mathbf{E}^{\boldsymbol{inc}}(\mathbf{r}, \mathbf{r}_{\boldsymbol{T}}), \qquad \mathbf{r} \in \boldsymbol{D} \tag{6.31}$$

Other details of the FIT method can be found in (Clemens & Weiland, 2001) and (Weiland, 1996). The model development technique along with the simulation procedure and analysis involved an iterative process. The general simulation method for the CEM's are shown (Fig. 6.7). The design, development and modeling of the CEMs along with the simulations, post-processing and analysis of results in this chapter were performed using CST MWS and MATLAB® software (MATLAB, 2012b).

A finite calculation domain, D enclosing the barefaced terrain and the radiating source or sensor, was created in order to solve each problem. Models of terrain and the EM wave source were the basic unit of each CEM. Thereafter a mesh system is defined to split the domain in to several grid cells with a specific number of lines to represent each wavelength in D so that a balance between accuracy, mesh density, CPU processing time and memory was achieved.

The CEMs consist of two main components that embody the variables that determine backscattering from terrain (Table 3.7). These are the BTM and the EM radiation source or representative sensors. A variety of measurement sensors were placed within the calculation domain to monitor various aspects of the backscattering response such as the E-field, electric energy density, far field and power loss density at specific frequencies. The modeling aspect began with the characterization of the plane wave sensor in free space using a predefined mesh and open space boundary. The angle

of incidence, θ_i was varied by mathematical computation to alter the geometry. When the source signal design was completed various BTM's were created with different electrical and physical properties reflective of real life situation. A significant challenge in the BTM development was configuring and presenting the texture and composition of the terrain and accurately representing the variation in dielectric constants with frequency.

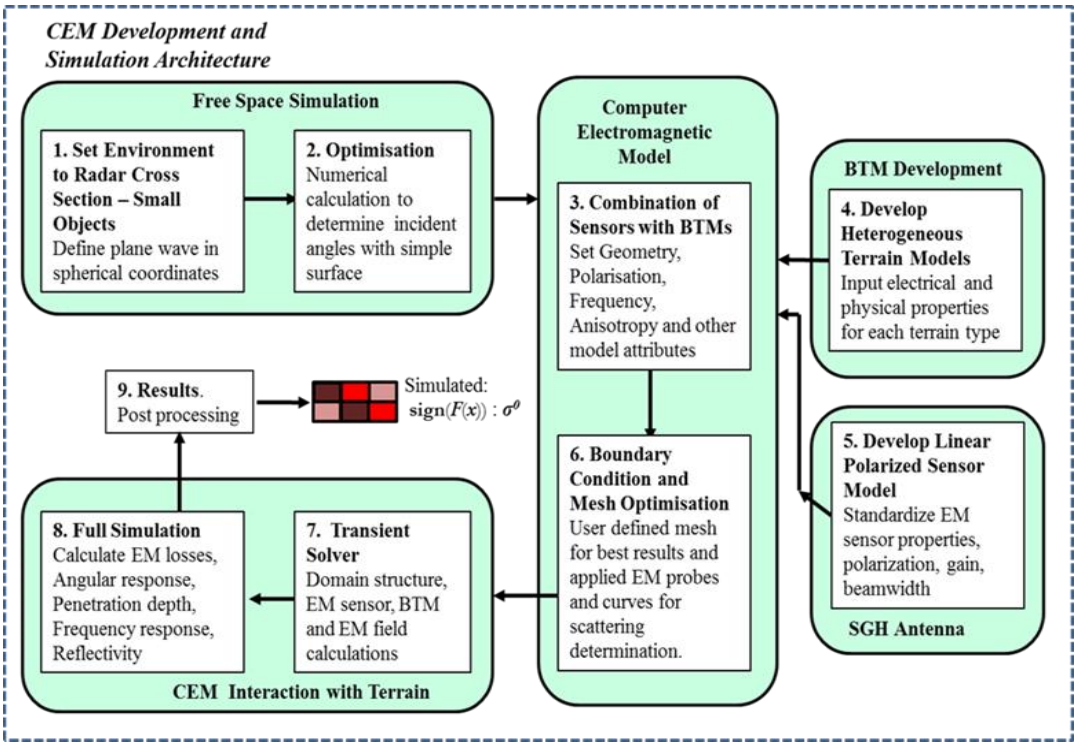

Figure 6.7: General Computer Electromagnetic Models development and simulation architecture

6.3.3. Barefaced Terrain Modeling

The BTM development covers the efforts to represent layer *c* of the general scattering model (Fig. 6.5). Natural terrain is often made up of relative proportions of sand, silt and clay. This raises questions on the level of detail possible. Wentworth (1922), provides a measure for grain size classification based on the major particle size within the population variation. Usually this is determined experimentally using sieve analysis. The detailed Wentworth scale and relative sizes of grain particles are shown in Appendix 6. Several attempts to represent tiny grain particles such as silt and clay on a vast terrain scale proved inconclusive. One previous solution was to consider only a small elemental volume, ∂V (0.125 m^3) in the calculation domain (Ezeoke & Tong,

2012; Ezeoke & Tong, 2013c). This corresponds to a spatial resolution (∂A) of 0.5m^2 and reduces the simulation time by 50% compared to coarser resolution. Very few commercial SAR sensors have resolutions below 1m^2 (Stimson *et al*., 2014; Lawal *et al*., 2014). Therefore baseline terrain volume for computation, ∂V was 1m^3.

A complementary approach could have included approximating a ratio of the relative sizes of the terrain features to each other. Although this could help in differentiating the barefaced terrain it would not sufficiently represent reality to the standards demanded by the research objective. Furthermore literature is replete with different composition for terrain types. The developed BTMs included both physical and electrical properties of terrain. Importantly, both the US Department of Agriculture (USDA) and the UK Agricultural Development and Advisory Service (ADAS) suggest soil texture (or roughness) is also affected by silt not just sand and clay. They reflect this in the soil texture triangle shown in Appendix 6.

The approach adopted in this research involved incorporating primary and secondary reservoir rock properties in to each BTM (Berg, 1986; Ezeoke & Tong, 2012). Secondary properties like porosity, bulk density and saturation were also inculcated in the BTM. However primary properties of texture and composition were implemented with surface roughness and dielectric permittivity matrices.

6.3.3.1 Porosity and Packing

The porosity, ϕ of oil sand and other terrain typically varies from 25 - 50%. In (Graton & Fraser, 1935) the relationship between the geometric distribution of points and particles was investigated and used to explain porosity and permeability. Such morphological analysis permits the development of the solid space to consist of particles represented by spheres or agglomeration of spheres (Coskuner & Huang, 2014). For the BTMs the four models developed by (Graton & Fraser, 1935) were used as building blocks to represent different terrain structures, then modified to investigate the behavior of the models when incident with EM waves. Each layer can be visualized as a series of strata in square or rhombic configurations (Fig. 6.8).

For rock and terrain reservoirs secondary properties such as porosity, ϕ (%), permeability, k_p in milidarcy (md) and packing are related. The effect of such dependent properties on volume scattering will be more than on surface backscattering. In comparison to rock reservoirs, the packing or arrangement of terrain particles is difficult

to both estimate and implement. Yet, secondary reservoir rock properties of porosity, ϕ and permeability, k_p depend on this relative packing (Table 3.1).

Recent technological advances such as digital rock physics (DRP) may enable prediction of relative permeability and capillary pressure from fluid flow simulations based on high resolution 3D images of the terrain media (Coskuner & Huang, 2014). This technology is still under development and solely focused on flow related properties within the pore space of the material. DRP is inapplicable because this work was interested in the microwave EM backscattering from and within the media

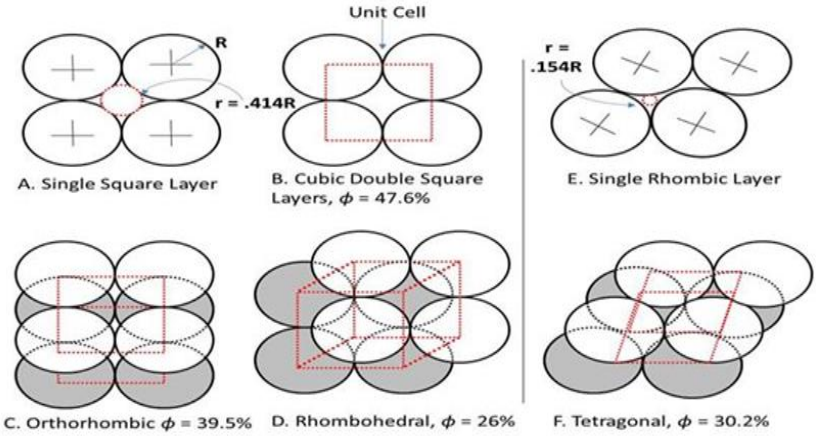

Figure 6.8: Systematic packing of uniform spheres applied to BTMs. Top view with porosity, ϕ given for principal packing (modified from (Graton & Fraser, 1935)).

The effect of packing was investigated using two different packing models, namely the rhombohedral (RHD) and the cubic double square (CDS) (Fig. 6.9). The RHD configuration is more compact with ϕ = 26% while the CDS arrangement is the least compact with ϕ = 48%. A third arrangement considered was a random packing arrangement which was discarded because it was difficult to identify porosity or permeability. The magnified top and side view for the RHD and CDS formations are shown (Fig. 6.9). In the initial implementation, bitumen and water were used as substrate in between pores for oil sand while only water was used for wet sand (Ezeoke, 2013). This method was complex with limited abstraction and required greater CPU time both to develop the models and perform simulations. Subsequently, the inclusion of representative electrical parameters reduced the necessity for multiple components while simplifying the model response across frequency.

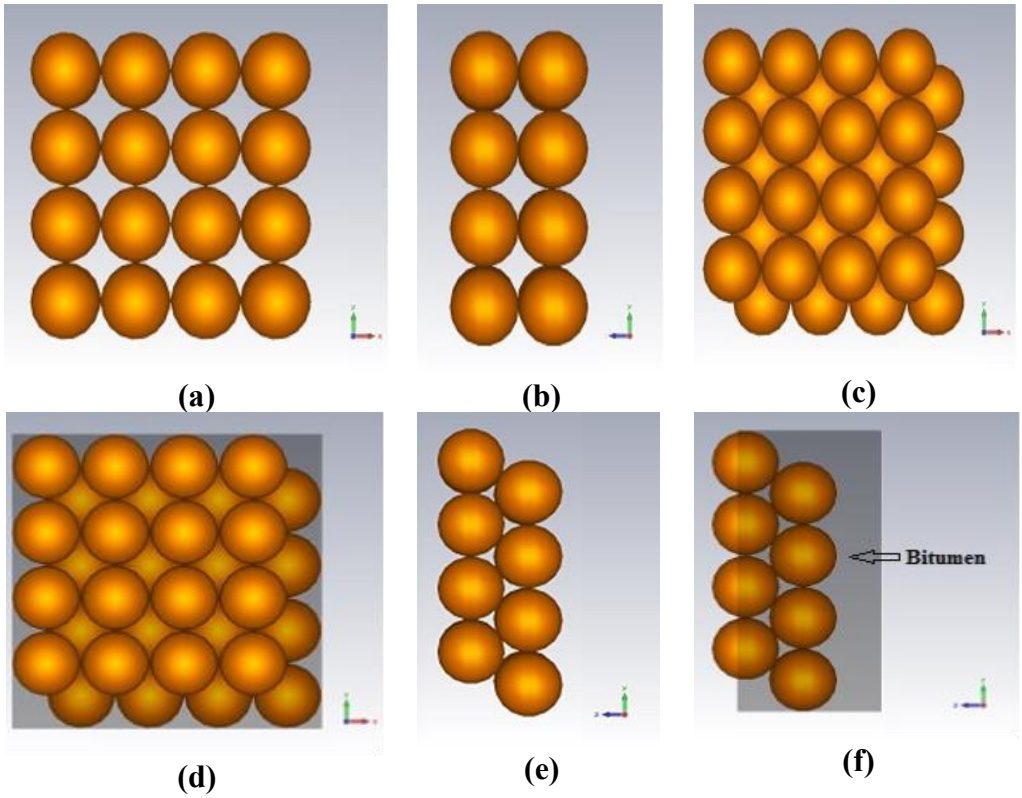

Figure 6.9: Physical packing of barefaced terrain models enlarged view cubic double square and rhombohedral (a) CDS Top View (b) CDS side view (c) RHD Top view (d) RHD top with bitumen substrate (e) RHD side view (f) RHD with bitumen.

6.3.3.2 Bulk Density

The bulk density of the actual terrain, ρ_b was derived using unit samples of MUT A to MUT F and then comparing with industrial measurements from (Walker, 2013) as reference. Bulk density was considered rather than just density because this measure includes the mass of the grains, air spaces and bitumen content in pores for MUT E and MUT F. Although natural bitumen density varies from 1.1 - 1.6 gcm^{-3} (1100 - 1600 kgm^{-3}), the compactness of oil sand terrain with moisture and hygroscopic grains gave much higher bulk density.

The bulk density of the samples was obtained by weighing 100g mass of each terrain MUT in relation to the volume. For HOS we measured the dimensions, displaced water and then derived the bulk density. The mass of 100 ml (100 cm^{-3}) of each barefaced terrain sample was measured with analytical balance AB304-S Mettler Toledo instrument in the UCL Nanotechnology Laboratory (Ezeoke *et al*., 2013). Values used in BTMs are shown (Table 6.1). Conventionally 1 cm^3 of water weighs 1g since water density is 1 gcm^{-3} (1000 kgm^{-3}). This was used to check for errors and reset

the balance whenever the sensitivity varied even slightly. The measured results for MUT A to MUT F compared favorably with literature.

Table 6.1: Measured bulk density values compared with literature

Terrain	Measured ρ_b (kgm^{-3})	Literature[a,b] ρ_b (kgm^{-3})	BTM ρ_b (kgm^{-3})
MUT A	1522	1442	1441
MUT B	1203	1249	1249
MUT C	1550	1682	1550
MUT D	2350	2403	2350
MUT E	2400	2200	2300
MUT F	2210	N/A	2100

[a]The industrial measurements of MUT A – D for literature values were obtained from Walker (2013)
[b]The classification value for MUT E was given by Attanasi & Meyer (2010)

The density measurement procedure was also used to determine the ρ_b for terrain with different weight percentage (*wt*. %) of moisture. The measured density values for MUT A with 10 *wt*.%, 20 *wt*.% and 30 *wt*.% moisture were 1602 kgm^{-3}, 1922 kgm^{-3} and 1922 kgm^{-3}. Similarly for MUT B with 10 *wt*.%, 20 *wt*.% and 30 *wt*.% moisture, the measured density was 1442 kgm^{-3}, 1602 kgm^{-3} and 1730 kgm^{-3}. Since there was no readily verifiable literature source, these values were used in the models to depicting terrain with changing water content. The primary reservoir rock property of composition was best accounted for using the electrical properties of the barefaced terrain.

6.3.3.3 Electrical Properties

The results from the DDSM (Chapter 5) helped to identify the most important frequencies for the sensor development and for the placement of field monitors at L-, C- and X-band. Thus to account for dielectric dispersion and enhance model accuracy, the empirical measurement results for the different barefaced terrain types (MUT's) at normal and increasing *wt*.% of water were input in to the BTM as a matrix $\boldsymbol{d}_{\varepsilon'}$ using (6.28). Therefore there was no need to individually model the heterogeneous components of the terrain nor separately implement the diverse electrical properties of water, bitumen, sand and silt components of oil sand.

This was possible because the previous empirical measurements and statistical processing of the barefaced terrain dielectric properties gave the aggregate property for each terrain class as a group. For BTMs without corresponding experimental measurements, the standard permittivity values for the individual components such as bitumen, sand, silt and water would be required making the model implementation more

complex. This was done in (Ezeoke & Tong, 2012; Ezeoke, 2013). The dielectric permittivity measurement result values for MUT A, B, E and F along with different *wt*.% of water for MUT A and MUT B were used to update the CST MWS database. Consequently future researchers have a ready database of permittivity values for terrain with similar composition to those considered in this work.

There was no need to experimentally determine the dielectric properties for MUT C and D because they have been properly investigated in literature with good agreement between results (Schneider & Dante, 2009; CST MWS, 2014; Peak & Oliver, 1971). For gravel and pebbles the respective permittivities were taken to be constant across frequency with real permittivity of 2.15 and loss tangent 0.004 (0.08 Peak & Oliver, 1971). The measurement in (Peake & Oliver, 1971) was at 35 GHz which is outside the range of interest therefore the loss tangent values from (Schneider & Dante, 2009) were used in the BTMs for MUT C and MUT D.

6.3.3.4 Surface Roughness

One important physical property for the BTM modeling is the development of the surface roughness layer. This is the top most strata that exist at the dielectric discontinuity between terrain and air media. The classical models use statistical distribution to create the surface roughness as a random Gaussian or power law correlation (Papa, 1988). Statistically, the surface roughness component can be represented by two types of model: the height distribution model and the slope distribution model. The height distribution is quantified in terms of r.m.s height, h_{rms} and autocorrelation coefficient, $C(s)$. The $C(s)$ is a property that determines the relationship or lack of independence between random values representing height h at two surface points (x_1, y_1) and (x_2, y_2) separated by distance s. For a normal (or Gaussian) distribution the probability of h (Nayar, 1989) is given as:

$$\boldsymbol{P_h(h) = \frac{1}{\sqrt{2\pi}\sigma_h} e^{-\frac{h^2}{2\sigma_h^2}}} \tag{6.32}$$

While autocorrelation coefficient may be represented by the general function:

$$\boldsymbol{C(s) = e^{-\frac{\tau^2}{T^2}}} \tag{6.33}$$

Here σ_h is the standard deviation of h and equal to h_{rms} while T is the correlation distance for which $C(s)$ drops to the value e^{-1}. In theory by varying h_{rms} and T, surfaces

can be generated to match the appearance of almost any rough surface. It is also possible to consider a surface as a collection of planar micro-facets or slopes. Statistically the slope distribution represents the orientation angle, α of individual micro-facets around a mean surface orientation, $\boldsymbol{n}$. The normal distribution for the facet slope, α is:

$$\boldsymbol{P_{\alpha}(\alpha) = \frac{1}{\sqrt{2\pi}\sigma_{\alpha}} e^{-\frac{\alpha^2}{2\,\sigma_{\alpha}^2}}} \tag{6.34}$$

Here σ_{α} is the standard deviation of α. The slope distribution model only requires one parameter which may lead to weak models for smaller values of σ_{α} (Ulaby *et al*., 1982).

Comparison between both slope and height distribution methods abound in literature and the in the implemented empirical method, BTMs were developed with both considered. The hyperspectral measurements (Chapter 4) showed that bitumen and silicon acted as an adhesive to bond the grains of HOS together so that the vertical roughness of the surface, h when compared to the average height $\overline{h}$ of the HOS particles was larger. To represent the surface roughness, an adaptation of the points and particle representation from (Graton & Fraser, 1935) was made to vary the slope orientation angel, α. The aim was to achieve the typical variation in texture height (h_{rms}), retain separation spacing between peaks and vertices, s and investige the effects of slope orientation angle, α on overall scattering response (Fig. 6.10).

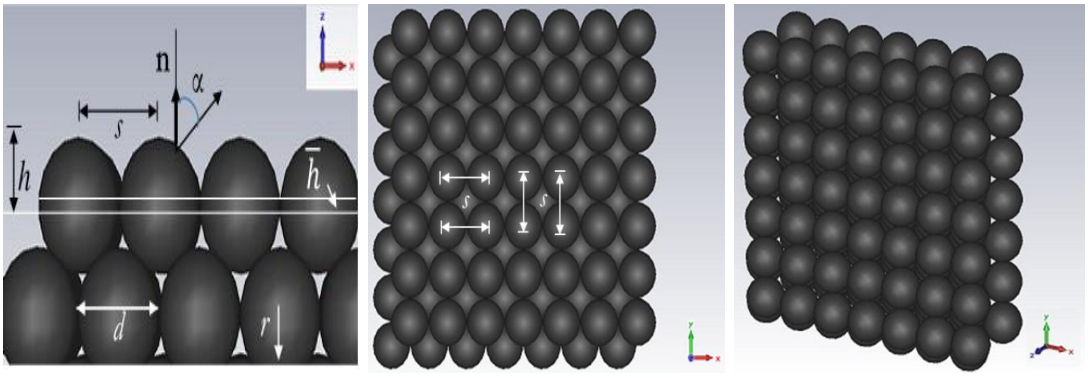

(a) (b) (c)

Figure 6.10: Surface roughness of HOS top most layer using normal Graton spheres with no segments and constant separation between peaks and vertices (a) side (b) top (c) perspective.

The jagged edge of most terrain features was mathematically represented by extending the normal Graton sphere model to three, four, five and eight segment or facets. The orientation of each BTM was set to -z direction in order for the surface roughness layer to face the EM radiation source in the +z direction. Beginning with the normal Graton spheres which has no segment (or 0 Seg.), spheres with more than four facets or segments in either plane above or below the diameter, d yielded a relatively milder texture with smaller slope angle, α (Fig. 6.11). A zoomed in view of the milder surface roughness slope, m, implementation using the HOS (d = 160mm) as an example in RHD configuration (ϕ = 26%) with 5 and 8 facets corresponding to vertices angles, γ of 72° and 45° respectively is presented (Fig. 6.11).

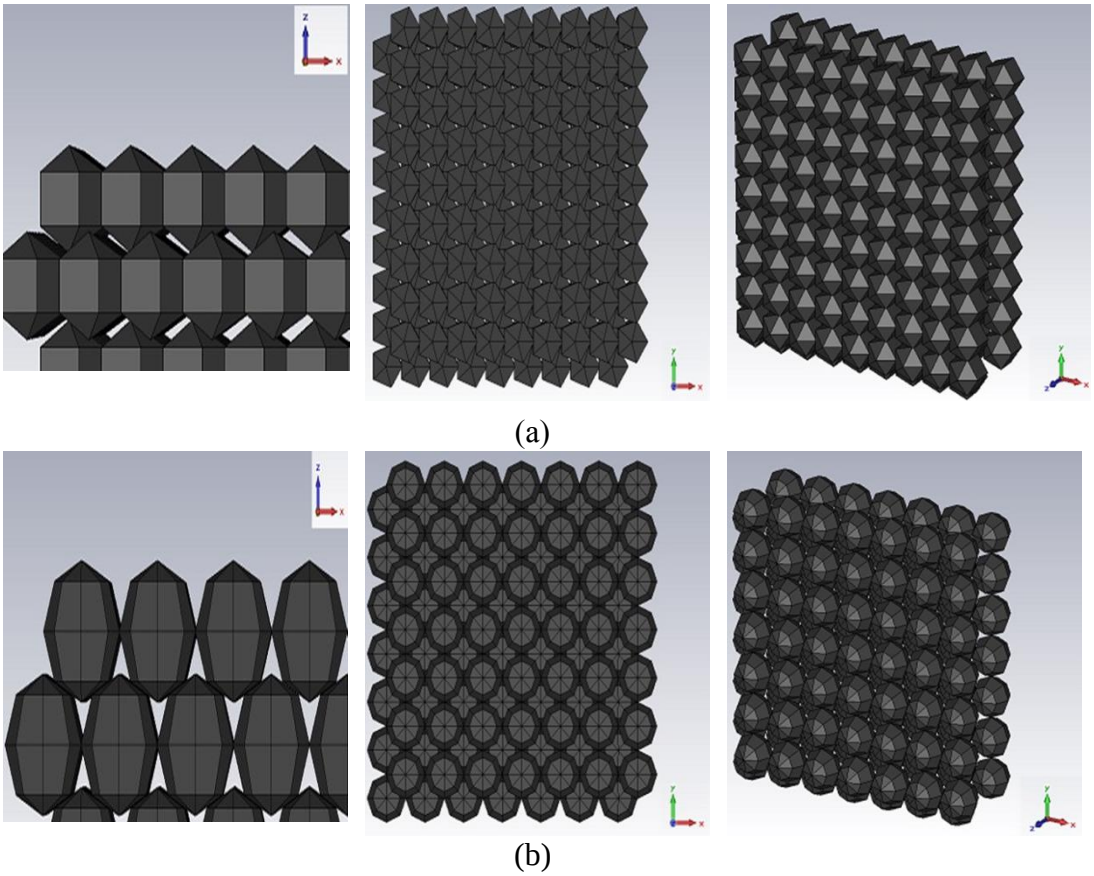

(a)

(b)

Figure 6.11: Mild surface roughness representation magnified view of HOS top most layer (without underlying substrate layers). Left to right views indicate side, top and perspective for (a) Graton Sphere modified to 5 segments (b) Graton Sphere modified to 8 segments.

When there are fewer facets such as 3 or 4 with vertex angles, γ = 120° and 90° respectively sharper edges and steeper slopes result. This leads to a coarser surface texture (Fig. 6.12). In such surface roughness representation the disparate edges

exposed the bottom bedrock layer (not shown). Therefore the underlying layers will contribute to the backscatter response as seen from the adjacent gaps in the perspective views (Fig. 6.12). When the segmentation was 4 (HOS 4 Seg.) there is a better fit for individual layers from both the top and side views but this feature was not possible when there were 3 facets.

In terms of the height distribution, *h*, the average grain size measurements (Table 4.4) were performed using sieves of different diameters according to the Wentworth classification scale. In order to measure HOS grain particles, there was a need to crush it in to a paste which still retained a lot of viscosity. The VOS sample had to be dissolved in tetrahydrofuran (THF) to obtain the representative particles. The original clumping of HOS and VOS was referred to in this work as the 'agglomerated size'. Agglomeration refers to the coarse accumulation of blocks of material, rock or terrain.

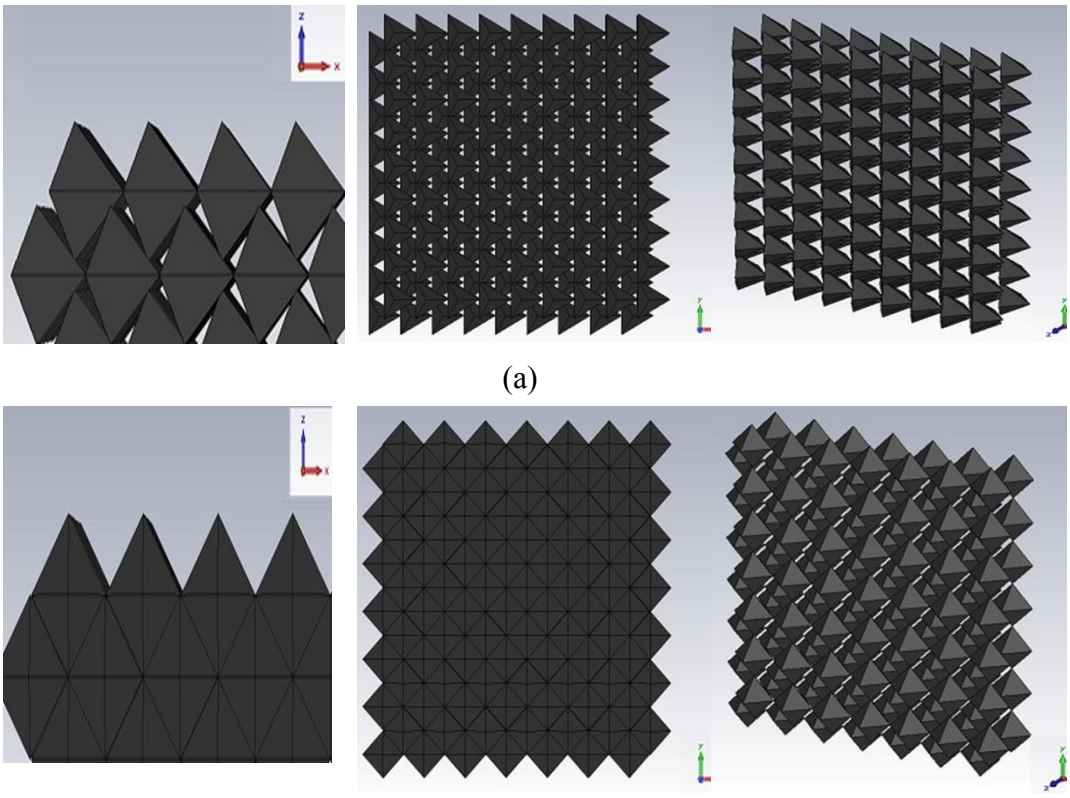

(a)

(b)

Figure 6.12: Coarse surface roughness representation magnified view of HOS top most layer (without underlying substrate layers). Left to right views indicate side, top and perspective for (a) Graton circles modified to 3 segments (b) Graton circles modified to 4 segments.

For both HOS and VOS the grain size differed from the agglomerated size (Fig. 6.13). This peculiarity of bitumen infused rock such as shale rock and oil sands mean that rather than grain size the agglomerated size was used to create the surface roughness layer for the BTMs. Similarly for beach sand and loamy farm soil with increasing water saturation a milder form of agglomeration was seen and has been reported previously (Ezeoke *et al*., 2013). Consequently the average values for the agglomerated particles were used in the models of HOS and VOS rather than the grain size measurements because an airborne or space-borne radar satellite would image the terrain as clumped rocks rather than individual grains (Sabins, 1997; Schaber, 1999).

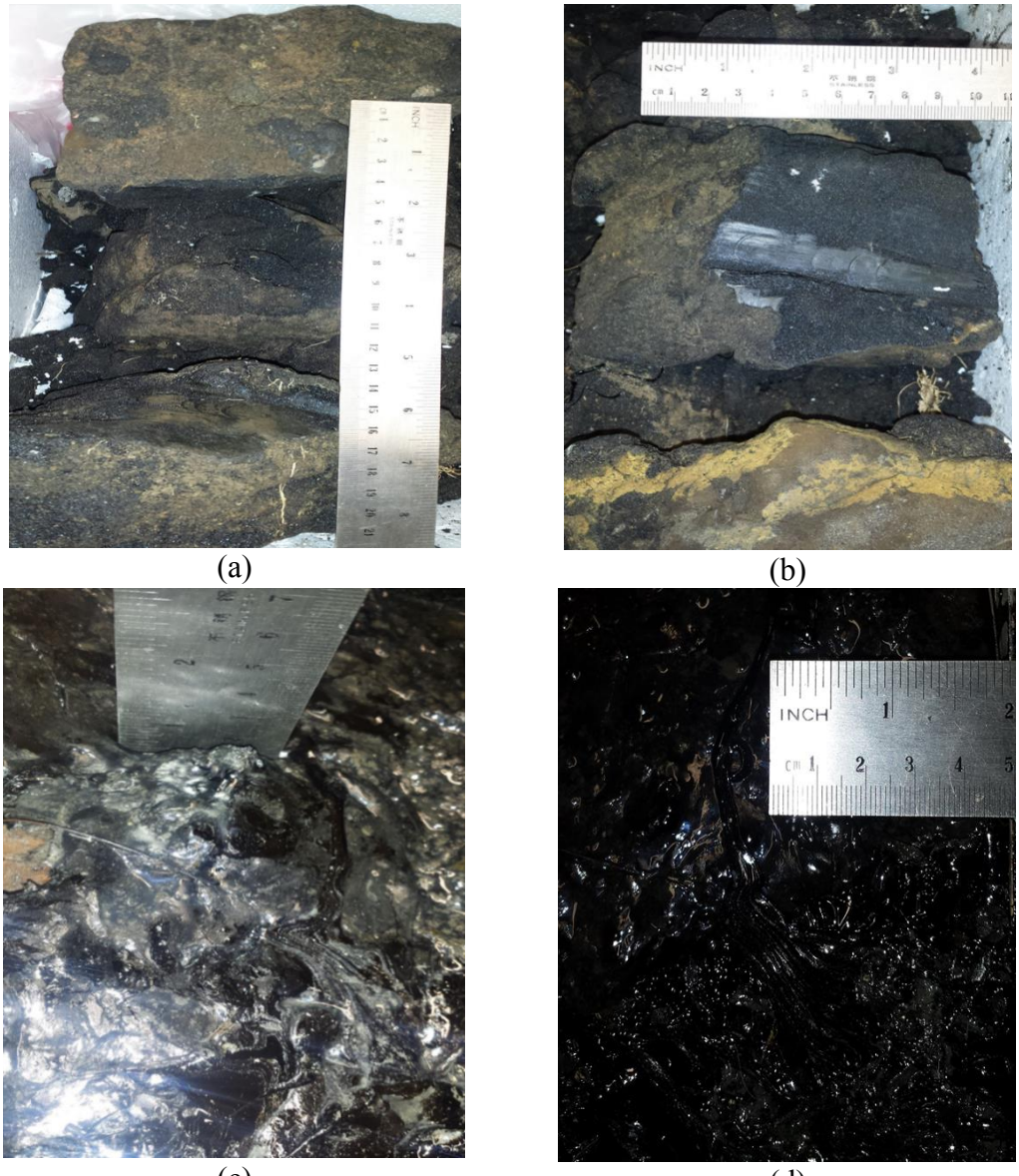

(a) (b)

(c) (d)

Figure 6.13: Agglomeration of oil sands acquired from Nigeria (a) HOS side view (b) HOS top view (c) VOS side view (d) VOS top view.

This is also the case for saturated beach sand and loamy farm soil at 10 *wt*.%, 20 *wt*.% and 30 *wt*.% water content. When the water saturation exceeds 30 *wt*.% for beach sand and 40 *wt*.% for loamy farm soil the aggregation is lost (Ezeoke *et al*., 2013). Neither beach sand nor loamy farm soil exhibited any particle gathering or agglomeration in the normal state only with increasing moisture was clumping seen due to the relative presence of clays identified during the hyperspectral analysis.

For a broad based investigation, all six barefaced terrain types covered the Wentworth terrain classification scheme (Wentworth, 1922). Without water saturation, the normal state BTM represented both beach sand and loamy farm soil with mild and coarse surface approximations using the modified Graton model spheres with 0 and 3 segments for mild and coarse respectively. This was done due to the relatively uniform geometric properties of both homogeneous terrain types and the very small dimensions.

Uniform spheres with milder surface roughness (5 and 8 segments) were used to represent gravel and pebbles (Table 6.2). VOS was implemented with mild and coarse surface roughness because the viscous behavior creates a range of roughness (see Fig. 6.13c). Due to the irregular forms of HOS, 4 different representations covering both mild and coarse surface roughness were used to implement HOS BTMs. A summary of the grain size for the barefaced terrain types and agglomeration size used in BTM models along with the EM roughness ($k\sigma$) is shown (Table 6.2). The validity criteria for the classical models SPM, KSM and GOM have been presented (see Table 3.8), however we can see that to validate our modelling the radiance using more than one classical model will be required.

Table 6.2: Summary of average grain and agglomeration size with surface roughness

Terrain	Mean grain size (mm)	Agglomerated Size (mm)	BTM sphere diameter, *d* (mm)	BTM segments	EM roughness, $k\sigma$		
					L	C	X
MUT A	< 0.5	No change[a]	1	0, 4	0.013	0.06	0.1
MUT B	1-2	No change[a]	4	0, 3	0.053	0.22	0.4
MUT C	10	No change	20	5, 8	0.27	1.1	2.0
MUT D	40	No change	80	5, 8	1.1	4.4	8.1
MUT E	1-2	80	160	0, 4, 5, 8	2.1	8.8	16.2
MUT F	<0.5	10	20	0, 3	0.27	1.1	2.0

[a]No change except when moisture is added

The physical clumping observed with increasing moisture content up to 30 *wt*.% water content for beach sand and 40 *wt*.% for loamy farm soil, was represented with larger diameter spheres for mild and coarse surface roughness. The smaller particles

took longer for BTM development using the CST MWS Modeler®. Furthermore the subsequent simulation took longer to run for 0, 5 and 8 segmentation compared to 3 and 4 segments due to the larger number of mesh cells required to create the models. The number of mesh cells also increased with frequency from L- to X-band and inclination geometry of the EM sensor from normal (90°) through low (20° – 35°), high grazing (55° – 60°) and moderate (45°) angles respectively.

The measured electrical properties and bulk density were input in to the BTMs. A flat rate for bulk density based on laboratory measurements was used but the electrical properties were input in a dispersion matrix due to the slight variations with frequency. This was to ensure that the BTMs better reflect real world terrain. Similarly the physical properties were implemented with RHD configuration for packing arrangement and the various surface roughness representations already discussed. The completed BTMs have the surface roughness layer emplaced on a bottom elemental layer covering a volume of $1m^3$ for 3D BTM implementation (Fig.6.14). Here loamy farm soil and Gravel BTMs show the surface roughness variation ($+z$ direction) on the elemental $1m^3$ volume, ∂V of terrain. The surface area, ∂A of $1m^2$ represents the spatial extent or resolution of the pixel in x and y coordinates while the 1m depth (z) enabled observation of EM energy behavior inside oil sand and other barefaced terrain. In this way both surface and volume scattering were obtained for all 6 terrain types.

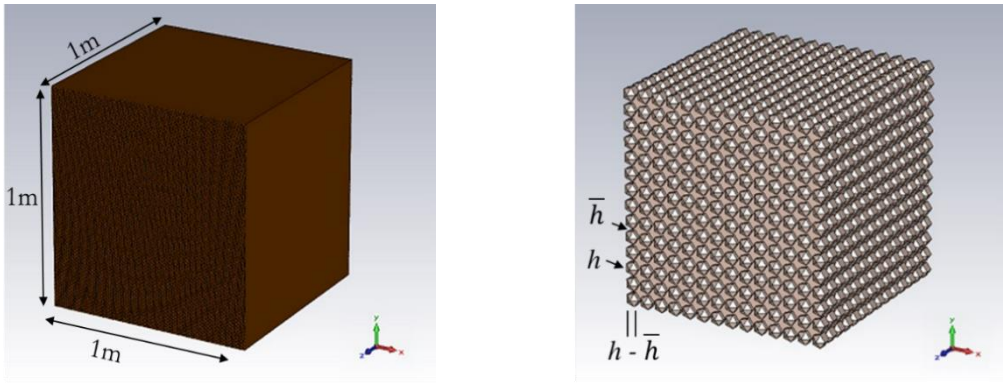

(a) (b)

Figure 6.14: Selected BTM perspective view (a) Loamy farm soil (b) Gravel.

For accurate comparison of radar signature, all the terrain types were created with the same ∂V but different geometric and electrical properties congruent with their electrical and physical properties. BTMs for HOS and VOS shown (in Fig. 6.15).

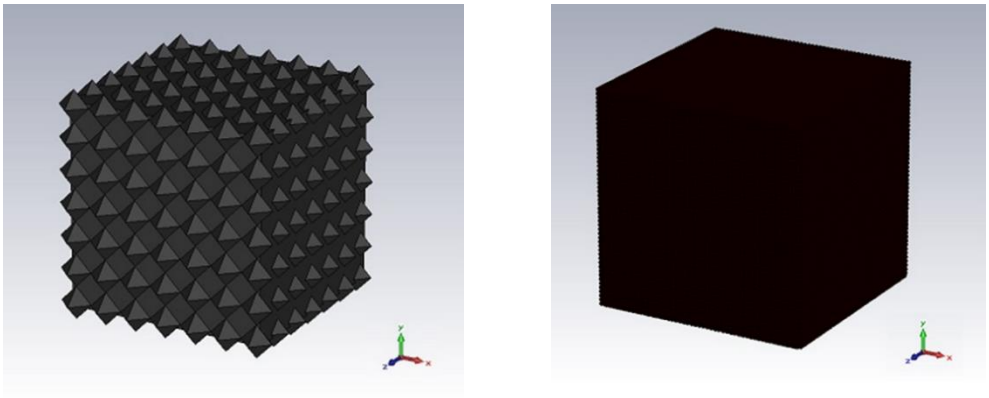

(a) (b)

Figure 6.15: Oil sand BTM perspective view (a) Hard oil sand with 4 segment (b) Viscous oil sand with 0 segment representation.

To represent the different surface roughness implementations 26 BTMs were developed as generic BTM models. Although the base BTMs remained unchanged, the addition of sensor variations in terms of polarization, frequency and incident angles led to more diverse modeling and simulation.

6.3.4. Sensor Modeling

The basic quantity observed in a satellite or airborne radar image of terrain at each pixel is a voltage or power relation. The values measured represent the effect of the imaged terrain on the transmitted wave in an indirect way (Lewis & Henderson, 1998). However the system bandwidth in range and azimuth implies that the measured values are a weighted average from a region determined by the point spread function (PSF) of the SAR. The necessary post processing is performed to convert the measured voltage or power relationships to geophysical units that correspond to the RCS, backscattering coefficient, σ° or complex reflectivity of the scene. Therefore SAR sensor imaging fundamentally depend on the EM scattering processes.

Two sensors were used as EM excitation source. First was a plane wave and the second was the SGH antenna. Unlike the SGH antenna the plane wave excitation source does not enable the calculation of S-parameters but with probes and monitors the differential RCS, nRCS and surface scattering value (per $1m^2$ pixel) can be calculated after post-processing the results. Both linear and left circular plane wave excitation polarization were used. The propagation normal frame was adjusted to provide different incident angles, θ_i for the EM waves impinging on the BTMs covering normal, low, medium and high grazing angles (Table 6.3). The electric field vector was orthogonal

to the propagation normal and had its components specified to 5 Vm^{-1}. The different incident angles were obtained by adjusting the relationship between propagation normal and electric field. After mathematical calculation, values to obtain θ_i = 20°, 30°, 35°, 45°, 55°, 60° and 90° are shown (Table 6.3).

Table 6.3: Plane wave incident angle geometry

Propagation Normal			**E-field Vector (Vm^{-1})**			**Sensor Angle, θ_i**	**Grazing Angle**
X	**Y**	**Z**	**X**	**Y**	**Z**		
5, 0, -13.737			4.698, 0, 1.710			20°	Low
5, 0, -8.65			4.328, 0, 2.502			30°	
5, 0, -7.14			4.095, 0, 2.868			35°	
5, 0, -5			3.535, 0, 3.535			45°	Moderate
7.14, 0, -5			2.868, 0, 4.095			55°	High
8.65, 0, -5			2.502, 0, 4.328			60°	
0, 0, -5			5, 0, 0			90°	Normal

For linear polarization the **E** and **H** fields are at right angles to each other (Fig. 6.16a). The direction of propagation of the EM waves is at right angle to both. It is this direction of propagation that is configured to different incident angles corresponding to normal, high, medium and low grazing angles. The orientation for plane wave with θ_i = 90°, 60° and 30° is shown (Fig. 6.16).

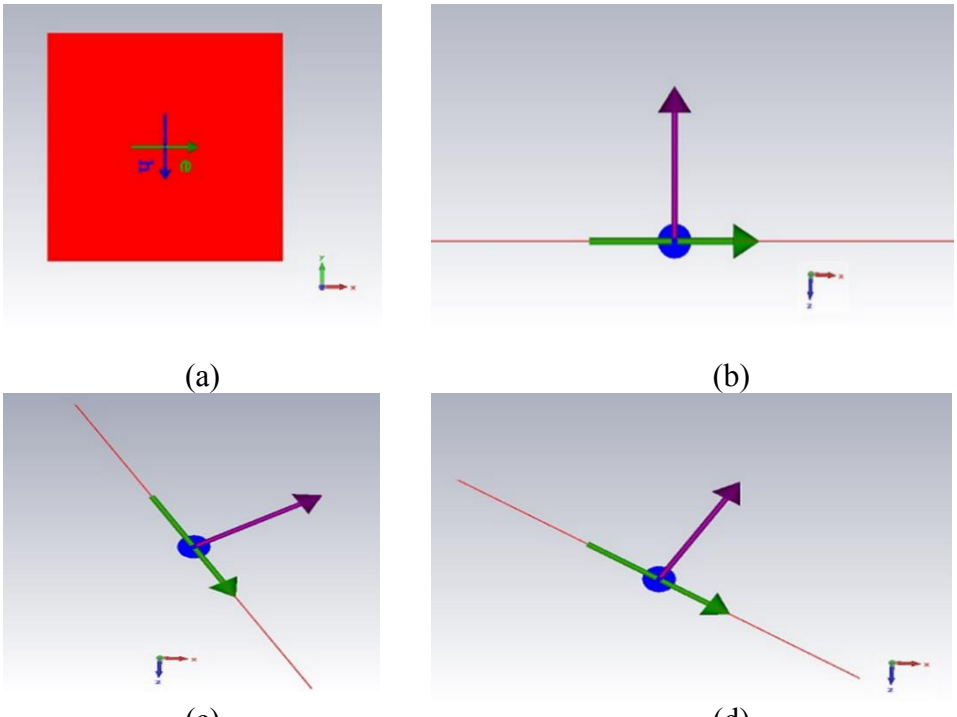

(a) (b)

(c) (d)

Figure 6.16: Plane wave with linear polarization showing propagation normal in direction (a) E and H field orientation *xy* plane (b) propagation normal 90° *xz* plane (c) propagation normal 60° *xz* plane (d) propagation normal 30° *xz* plane.

The mathematical combination is the same for both linear and circular polarization however for the latter a reference frequency and polarization was set. The reference frequency of 5.7 GHz depended on the frequency range of the simulation (0.9 – 10.5 GHz). The plane wave was excited by a Gaussian signal with narrow pulse width. The use of a narrow pulse provides a large bandwidth since the null-to-null bandwidth of the spectral lobe of a stream of independent single pulses (Stimson *et al*., 2014) is:

$$\boldsymbol{BW_{nn}} = \frac{\mathbf{2}}{\boldsymbol{\tau}} \tag{6.35}$$

However for a coherent pulse train with line spacing, f_r, inter-pulse period, T_p and number of pulses in the train, N the greater the number of pulses the better the spectral resolution as the null-to-null line width is given by:

$$\boldsymbol{LW_{nn}} = \frac{\mathbf{2}}{\boldsymbol{N}}\boldsymbol{f_r} = \frac{\mathbf{2}}{\boldsymbol{NT_p}} \tag{6.36}$$

Therefore for higher frequency (spectral) resolution, a train of 20 and 100 coherent pulses were used in the simulation depending on the receiver distance (either 2m or 5m). This is because the longer the time period over which echoes are recorded, the better the ability of the radar to discern targets. In practice the limiting value for echo reception depends on the range resolution of the target and the azimuth resolution expected of the air or space-borne sensor (Soumekh, 1999). Some also add the radar velocity (Stimson *et al*., 2014).

The second sensor was the SGH antenna for a radar model, operating over the frequency range, f from 0.9 - 10.5 GHz. It was designed then created in CST MWS using the principles discussed previously (Section 6.2). The main characteristic of the SGH antenna used in the radar model is presented in Table 6.4. The taper section of the horn is defined by 10 points which are joined by a fitted spline according to (6.23) and (6.24). The points scale with the flare dimensions. The waveguide port drives the coaxial feed section which contains the dielectric. Magnetic symmetry was used in the *xy* plane and the initial results were simulated using the CST MWS transient solver. For the sensor alone the global mesh was set at 10 lines per wavelength with a lower mesh limit of 5 and mesh line ratio limit 10. Also the local mesh refinements were set as: *Dx* = ridge_spacing/2; *Dy* = *Dz* = coaxial_inner_diameter/2 set on the pin but *Dy* = *Dz* = coaxial_outer_diameter/6 was set on the dielectric. This way we used the same antenna for multi-frequency analysis at f = 1, 5, 7 and 10 GHz.

Table 6.4: Summary of characteristics of the Radar Model Antenna

Property	Radar Model
Receiver gain[a]	7.5-14.3 dBi
Transmitter gain	7.5-14.3 dBi
Beamwidth[b] (3dB) E x H	87.8-15° x 60.9-30.3°
Losses[c]	Nil
Output power	0 dB
Transmitted Waveforms	Gaussian

[a]The gain varies with *f*

[b]Varies with *f*. For model E: 87.8° (1 GHz) to 15° (10 GHz) and H: 60.9° (1 GHz) to 30.3° (10 GHz)

[c]For a satellite or airborne radar there will be losses in monostatic configuration but typically corrected during calibration

Although connectors used were approximated with simple structures the dielectric material components were not ignored unlike in (Foged *et al*., 2005). This increases accuracy at the expense of simulation time. The radiation pattern of the transmit antenna in terms of **E** and **H** planes is shown in Fig. 6.17 for L-, C- and X-band frequencies.

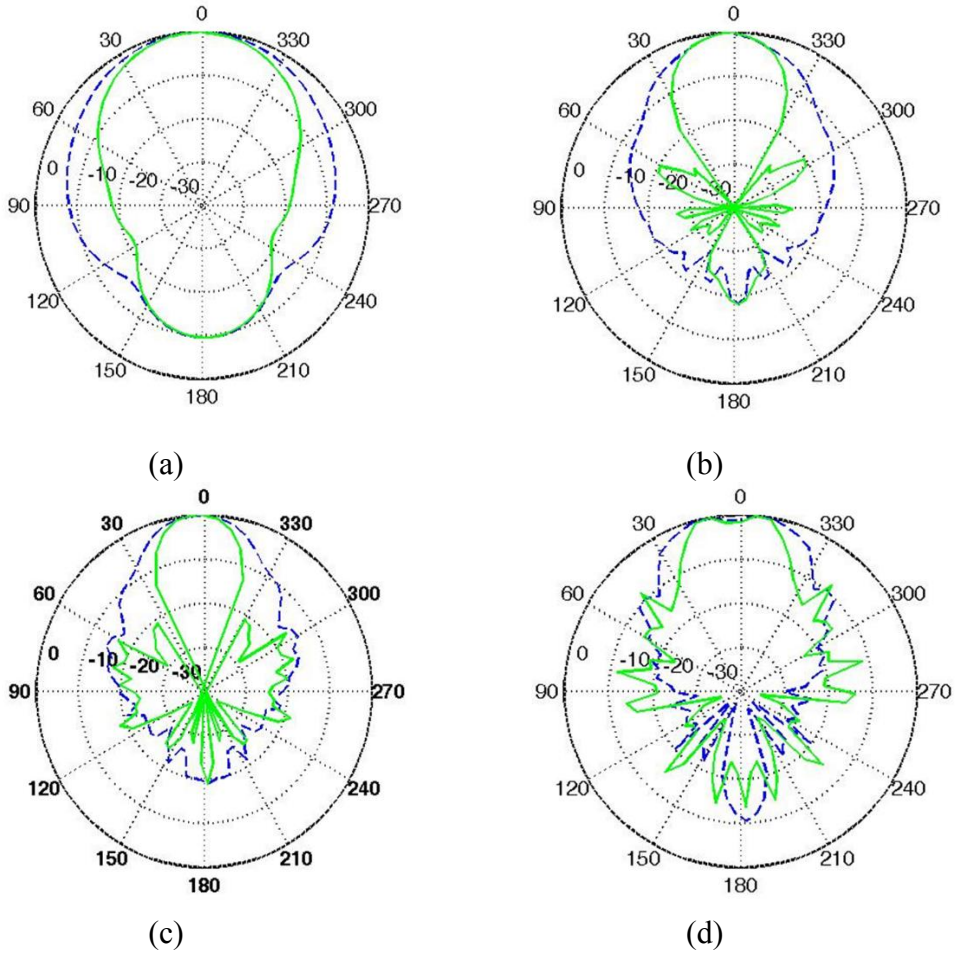

Figure 6.17: Radiation pattern transmit antenna for radar model. Co-polarized E-field (blue) and H-field (green) (a) 1 GHz (b) 5 GHz (c) 7 GHz (d) 10 GHz.

In linearly polarized antenna the electric or E-field determines the antenna polarization. For horizontal (H) polarization, the E-field coincides with the azimuth (*Az*.) plane and the magnetic or H-field coincides with the elevation (*El.*) plane. This is reversed for vertical (V) polarization where the E-field coincides with the *El.* plane and the magnetic or H-field coincides with the *Az*. Plane.

For the antenna used in the radar model, there are several groups of time domain signals that are useful in UWB engineering such as sinc, step (or edge) and Gaussian amongst others. Sinc signals are bounded in one domain but broad in the other domain. Step or 'edge' signals are useful in modeling transients. Sine and truncated sine waves are easy to generate and useful when time domain compactness is critical while Gaussian signals offer a good balance between time domain and frequency domain compactness. The signal transmitted in this work was a Gaussian pulse waveform with amplitude 1 and width of 1*n*s in time duration contributed by the feed region and the return signal radiated in the azimuthal plane.

6.3.5. Microwave Simulation Procedure

An important way to observe, demonstrate and understand the backscattering properties of barefaced terrain is to develop models and then simulate diverse mechanisms. Both structural and textural information can be combined to develop such simulators in order to train both human observers and automatic analysis algorithms (Lewis & Henderson, 1998; Nayar, 1989). Conventional SAR images consist of scenes of specific spatial resolutions. Therefore the scenes represented by the surface of the BTMs consist of unit areas, ∂A with homogeneous texture. BTMs can be combined to form regions where the edges of the regions may be defined by known boundaries or indicated by variations in parameter values. In the CEMs, each BTM was separately simulated with homogeneous texture and the intrinsic properties.

The simulation technique was designed to produce the scattering response of oil sands and other barefaced terrain at the frequencies most common to SAR and then to investigate the radar signature at the greatest dispersion frequency (Ezeoke *et al*., 2014a). It is difficult to discriminate between barefaced terrain when shown in a radar image whether visually or using statistical tests (Oliver, 1988). Therefore the CEMs were used as a deterministic solution to model the full physics of the scattering process based on the developed simulation architecture (Section 6.3.2). This enabled

investigation of the slightly different EM wave reflectivity observed between barefaced terrain and oil sands (Ezeoke & Tong, 2012).

The results were used to provide a comparison of the backscattering behavior between common soil, oil sand and other barefaced terrain. The results also provide useful reference for the design of optimum SAR system for oil sand resource discovery and an understanding of the RCS fluctuations for terrain (Ezeoke & Tong, 2012). Consequently for the CEMs several SAR imaging scenarios were implemented to reflect different frequencies, surface roughness, incident geometries and polarizations. The data sets were post processed to derive the scattering profiles for EM probes placed at different heights and depths from the BTM surface.

The generic simulation set up (Fig. 6.18) shows the *xy* plane as the dielectric boundary with free space in +*z* direction, terrain model in –*z* direction and plane wave with circular polarization at 90° incident angle. The EM waves were designed to be incident from +*z* direction on to terrain which is usually spread in the *X* and *Y* coordinates to reflect range, *x* and cross range, *y* directions of a resolution cell, ∂A. The consideration of the depth *z* coordinate extended the resolution cell to a unit volume of the BTM representing each barefaced terrain class, ∂V.

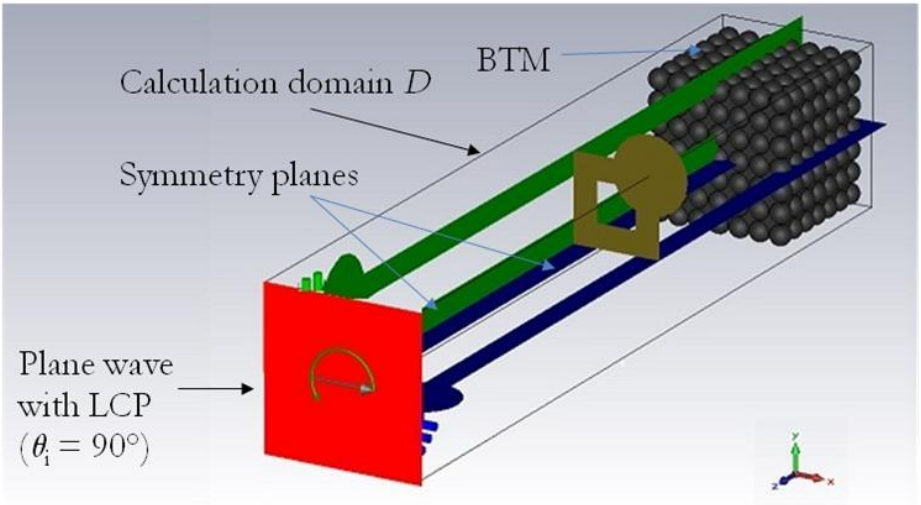

Figure 6.18: General simulation setup (perspective view) showing HOS BTM model and plane wave sensor with circular polarization at $\theta_i = 90°$ incident angle (-*z*), $1m^3$ of terrain volume and symmetry planes (*yz* plane, $E = 0$; *xz* plane, $H = 0$).

When the sensor is at normal incidence (i.e. 90°) the simulation time was reduced by defining boundary conditions for the symmetry planes where *yz* plane for the electric or E-field = 0 and for the *xz* plane the magnetic, H-field = 0. This reduces

the mesh cells by a factor of 4. The 'open (add space)' boundary condition was used. It operates like free space, where waves can pass the boundary with minimum reflection but also adds extra space for farfield RCS calculations (CST MWS, 2014). The selected open access boundary condition enables the free passage of EM waves reflected from the terrain (Ezeoke & Tong, 2012).

Scattering from different layers becomes progressively weaker so 3D EM probes were used to investigate surface scattering, σ_s^0, backscattering received at the receiver, σ_r^0 and volumetric scattering, σ_v^0 at deeper depths, δ_p ranging from 0.01m to 0.5m in to the terrain (Fig. 6. 19a). The probes were placed within the calculation domain D to record the x, y and z components of the EM field at specified locations within, on the surface and above the BTMs during the transient analysis. The probe results were processed to automatically derive frequency domain results for the x, y and z or an absolute combination of all three components of the EM field normalized to 1 Watt (W) or 30 decibel-milliwatts (dBm) for each frequency point. Here the power in dBm:

$$\boldsymbol{P_{(dBm)} = 10\log_{10}\left(1000\,\frac{P_{(W)}}{1W}\right) = 10\log_{10}\left(\frac{P_{(W)}}{1W}\right) + 30} \tag{6.37}$$

In essence the frequency domain data represents a transmission function between the stimulation port or transmitter and the EM field at the probes position and orientation. This is also true for the power scattered from the BTM which represents the transmission function between the power incident on the BTM surface and the power scattered from the surface. For polarization measurements the average reflectivity value was obtained by post processing the E-field observed over the $1m^2$ surface of the terrain ($+z$) direction to obtain the horizontal σ_{HH}^0 and vertical σ_{VV}^0 scattering coefficients for the terrain classes (Fig. 6. 19b).

Field monitors were also used to calculate the E-field, power loss density/SAR, electric energy density and far field/RCS at specific frequencies within the 0.9 – 10.5 GHz simulation frequency range. The Transient Solver in CST MWS was used with a Gaussian time pulse signal as excitation source for the plane wave sensors. The simulation accuracy was set to stop when either the remaining energy in the calculation domain (and the port signals) decreased to a value of -40 dB or the simulation time spent equaled a total number of 100 pulses.

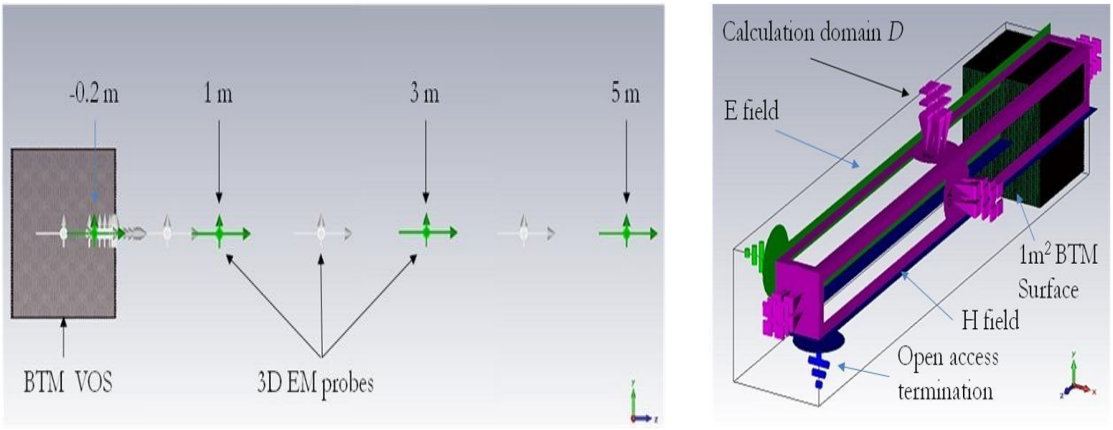

(a) **(b)**

Figure 6.19: Simulation setup showing VOS BTM model with $1m^3$ of terrain volume (surface occupies $1m^2$) (a) 3D EM Probes (*yz* plane) with probes at -0.2m, -0.1m, 1m, 3m and 5m highlighted (b) Open access termination (perspective view) to permit E^{inc} and E^{sca} waves pass through computation domain *D* with minimum reflection, surface selected for post-processing, green (E field), blue (H field).

One major difficulty with this approach is the necessity to repeat the simulations for each BTM and also each variation of sensor parameter. Consequently, a large amount of data was generated. The nuanced repetition was necessary to cover all the different realizations for microwave imaging with changing parameters. Consequently a database of aspects of the radar signature for oil sands and other barefaced terrain has been generated for both present and future radar remote sensing community. Next we discuss aspects of the radar signature.

6.4. Barefaced Terrain Radar Signature

There is typically only slight difference between the physical and electrical properties of barefaced terrain at microwave frequencies when considered separately. Therefore to generate a responsive radar signature, the backscattering response had to be examined from diverse sensor and terrain combinations using CEMs as a deterministic process that models the full physics of the scattering process. The derived data models describe elemental volumes of homogenous texture which can be regarded as single realizations of the radar scattering process. Therefore to fully investigate the microwave aspects of the EM characterization of terrain to aid unconventional petroleum resources identification a large amount of data was generated. Each data set derived from the 26 basic BTMs comprised of 168 values of backscattering coefficient corresponding to 168 combinations of sensor parameters per BTM. Therefore the

corresponding discussion of the results will only cover aspects of the microwave backscattering behaviour of barefaced terrain surfaces while highlighting the relevance to radar use in the petroleum exploration of oil sands. The full database in its present form is included with the research deliverables (Section 1.5.1). First modeling results are compared with the classical solution. Therafter using different EM imaging scenarios, unique trends in the frequency and angular response were highlighted inorder to distinguish between the barefaced terrain types.

6.4.1. Comparison with Classical Solution

This section evaluates the compatibility of the empirical modeling method developed in this research with the SPM and KSM models relevant to the BTMs. Expressions for the backscattering coefficient, σ^0 and the regions of validity have been discussed by (Ulaby *et al*., 1982; Oh *et al*., 1992) and summarized previously in this work (Table 3.8). The roughness conditions for all 6 barefaced terrain in the $k\sigma$ space have been identified in Table 6.2. According to (Oh *et al*., 1992) some of the surface roughness conditions fall outside the regions of validity of all three models while some BTMs satisfy the model conditions. In order to compare the BTM results with the model predictions MUT A and MUT B were selected for comparisoin with SPM while MUT E and MUT F were compared with KSM at normal incidence.

6.4.1.1 Small Perturbation Model

The scattering pattern of the individual scatterers that dominate a surface become more directional with increasing frequency. This is because the relative size of the scatterers (represented by modified Graton spheres) on the surface roughness layer increases when compared to decreasing wavelength for a plane wave from normal incidence. This was almost negligible for relatively flat homogeneous terrain such as MUT A and MUT. The modeled response for coarse and mild surface representations of MUT A and MUT B are shown in Fig. 6.20, together with scatter plots calculated using the SPM for a normalized Gaussian function of the form given by (6.32) and radiance equation from (Nayar, 1989).

The backscattering coefficient was derived from CST simulations by processing the far field absolute value (*x, y* and *z*) component of the returned backscattered signals from the terrain surface. The absolute values were measured by the 3D EM probes for each frequency point (1, 1.27, 5, 5.25, 7, 9.67 and 10 GHz) respectively (shown in Fig.

6.20). For homogeneous terrain with low surface roughness compared to the wavelength ($h - \overline{h} << \lambda$), the scattering at low frequencies is almost indistinguishable. Both mild (0 seg.) and rough (4 seg.) representations of beach sand produced identical scattering response indicative of the difficulty in distinguishing between homogeneous terrain classes using radar.

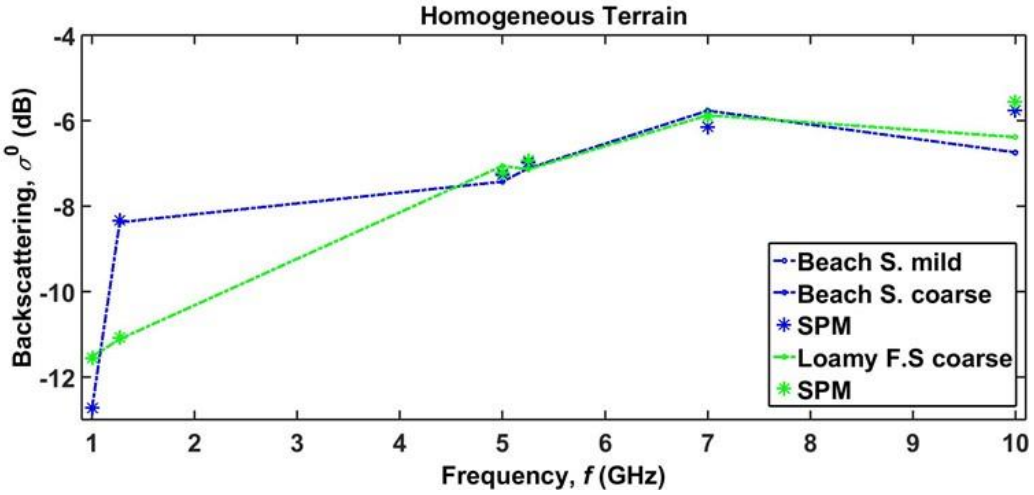

Figure 6.20: Backscattering (in dB) from homogeneous barefaced terrain models compared with SPM (Gaussian function) for plane wave sensor with linear polarization.

From (Oh *et al*., 1992) the calculated curves required a coherent component to account for strong backscatter response near normal incidence. Overall, SPM with Gaussian function provided an excellent fit for σ^0 determined from our modelling technique due to the precise and narrow region of validity for which the SPM may be applied. Applying the empirical modelling method to homogenous terrain with different *wt*.% of moisture the general observation of increased backscattering with frequency also held true. However the models also revealed a difference in the effect of moisture on the backscattering response for beach sand and loamy farm soil at low frequencies. For beach sand at low frequencies, normal terrain provides greater surface backscatter by up to 4dB when the moisture content changes by 10 *wt.*% at 1.27 GHz (Fig. 6.21). At high frequencies the presence of moisture is more important than surface roughness causing lower returns in the more coarse representation.

The ability of farm land or loamy terrain to absorb larger amounts of water compared to beach sand was indicated by the larger backscatter seen by loamy farm soil with 10 *wt*.% water (Fig. 6.22). At C-band there is little difference between the backscatter observed for loamy farm soil with moisture regardless of surface roughness.

At high frequencies, moisture presence determines backscattering from farmlands therefore normal loamy farm soil terrain yielded a higher reflectivity performance as would be expected (Huete, 2004).

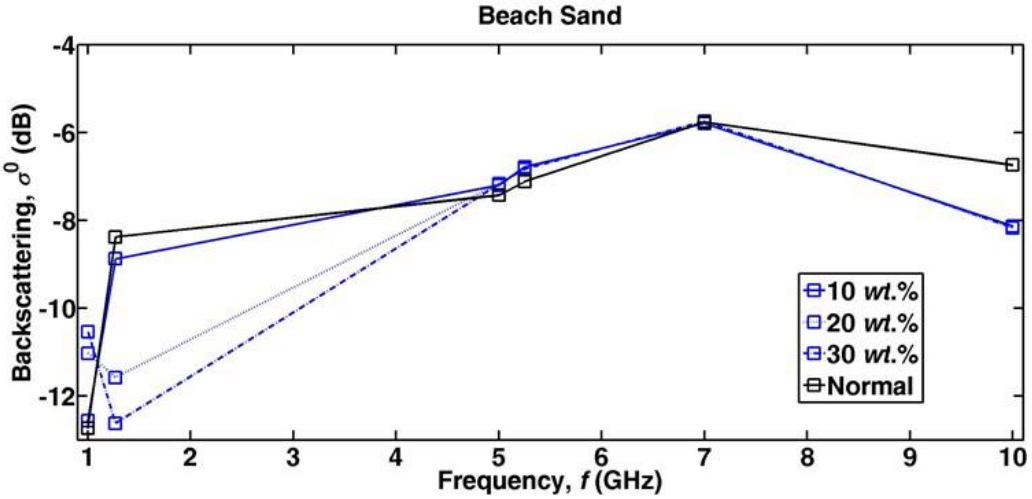

Figure 6.21: Scattering response from Beach sand models with varying moisture content.

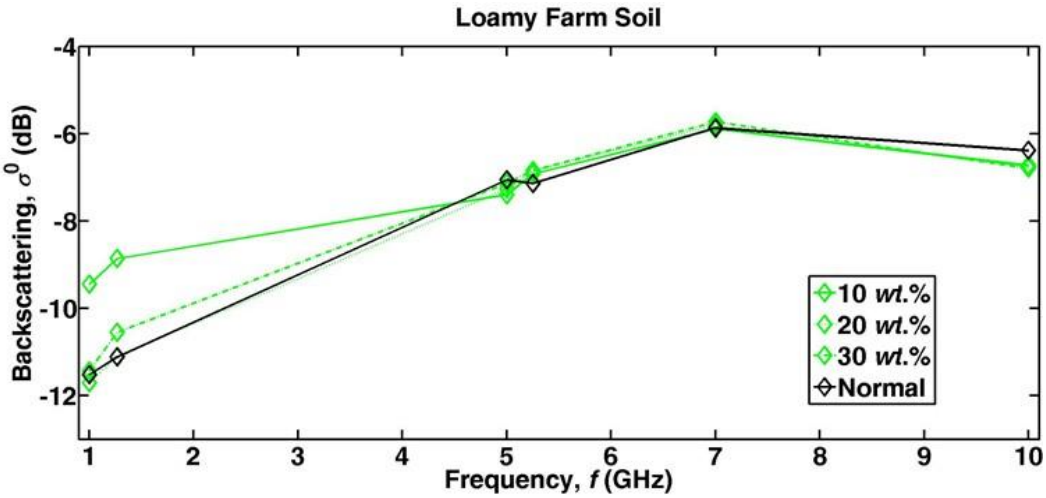

Figure 6.22: Scattering response Loamy farm soil models with varying moisture content.

6.4.1.2 Kirchoff Scattering Model

A lot of the surface roughness conditions examined in this study fall within the region of validity of the KSM. Since we are interested in oil sands we chose the HOS and VOS modelling results for detailed examination in this section. The plots shown in Fig. 6.23 and Fig. 6.24 show that the KSM model provides relatively good agreement for the HOS and VOS modelling results at normally incident plane wave ($\theta_i = 90°$). But the KSM Gaussian correlation model both underestimates the coarse HOS response and overestimates the mild HOS response at frequencies below 8 GHz (Fig. 6.23). However

for higher frequencies there is a convergence at 10 GHz (i.e. $\lambda = 3.1$ cm) where the EM roughness ($k\sigma$) increases.

A similar comparison was performed for the VOS BTM models. Here the KSM Gaussian correlation model underestimates both coarse and mild VOS roughness BTMs until f = 7 GHz where the deviation is up to 4 dB (Fig. 6.24). The VOS BTM backscattering response was also interesting as the mild surface representation (0 seg.) yielded higher backscatter response (4.5 dB) in comparison to the rougher VOS representation (3 seg.) at 7 GHz. Nevertheless with a plane wave sensor, the trend of increasing backscatter with frequency could be observed in the VOS terrain models. Verification of the modeling results is carried out in Chapter 7.

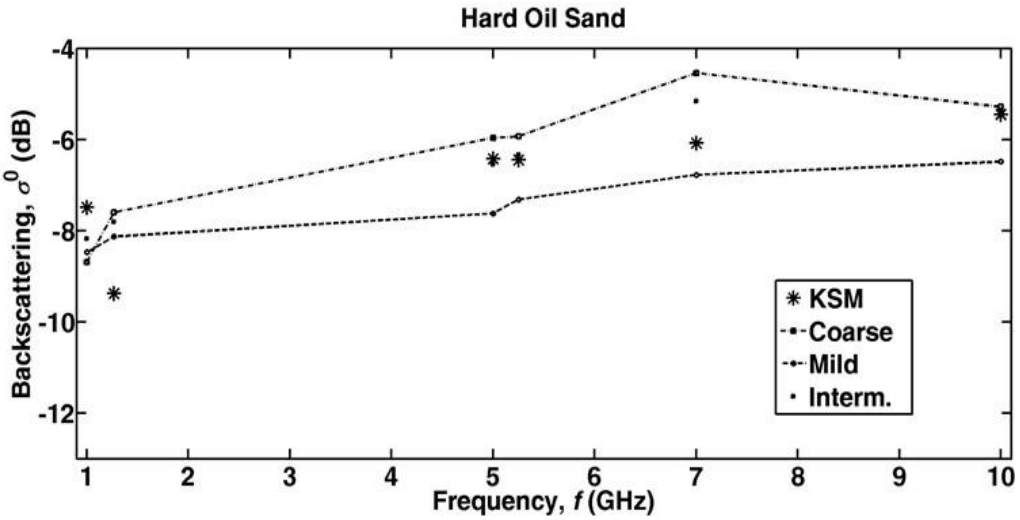

Figure 6.23: Backscattering (in dB) from Hard Oil Sand BTMs compared with KSM (Gaussian function) for plane wave sensor with linear polarization.

The effect of permittivity is best seen with the VOS BTM due to the low surface height variation compared to wavelength ($h - \overline{h} << \lambda$). The KSM Gaussian model for VOS behaved like a mirror at low frequency resulting in low scattering response (-11.8 dB) received at 1.27 GHz. At high frequency σ^0 for the KSM model increases to -6 dB at 10 GHz which is similar for coarse VOS. The drop in σ^0 for the mild representation could be due to low EM roughness causing less scattered energy to the sensor (Oliver & Quegan, 2004). For VOS both coarse (3 seg.) and mild (0 seg.) surface roughness experienced (approximately) higher scattering of -7 dB and -8.5 dB at 9.5 GHz compared to -8.7 dB and -8.8 dB respectively at 1 GHz (Fig. 6.24). In summary, HOS ($\varepsilon_r' = 3.85$) has a lower average real permittivity than VOS ($\varepsilon_r' = 4.5$), however the larger

backscattering experienced from HOS is also due to the larger surface roughness compared to wavelength.

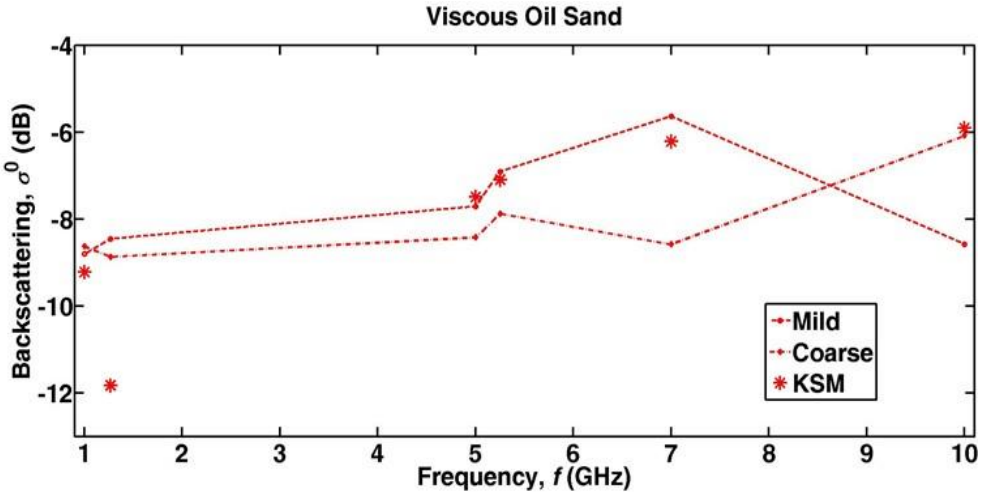

Figure 6.24: Backscattering (in dB) from Viscous Oil Sand BTMs compared with KSM (Gaussian function) for plane wave sensor with linear polarization.

Previous research simulated the effect of different levels of EM roughness for HOS (Ezeoke *et al*., 2014d). That study investigated the full effect of scatterer orientation on backscattering and the current results indicate that the effects of sharper facets and edges is more pronounced at X-band. Across the frequency of observation, greater scattering was consistently seen from the HOS BTMs with the coarse edges (4 seg.) compared with milder representations (8 seg). Also the EM roughness increased with frequency as classically expected for any terrain surface (Fung, 1996).

Overall the KSM Gaussian normalized models provided good agreement with the BTM models particularly at high frequencies. Having verified the validity of the models developed with this approach, the backscattering behaviour for the different terrain types was identified. The use of the BTMs enabled detailed observation of both surface and volume scattering from the barefaced terrain in 3D. The comparative magnitude of both types of contribution depends on the penetration depth of the EM wave relative to the terrain, the angle of incidence, the radar frequency and the surface roughness representation. Therefore the effect from low, medium and high frequency EM sensors on the backscattering behaviour will now be discussed.

6.4.2. Frequency Response

As the radar frequency was scanned from 0.9 to 10.5 GHz covering L-, C- and X-band microwave frequencies respectively, it was generally observed that the

magnitude of surface roughness increased with frequency. The response also showed a weaker dependence of the scattering coefficient, σ^0 with the angle of incidence θ_i compared to increasing frequency except at normal incidence (θ_i = 90°). Also the penetration depth, δ_p, of the microwaves into the barefaced terrain decreased with increasing frequency. For normal barefaced terrain which act as non-dispersive media unlike oil sands, and for which the permittivity is relatively independent of frequency the propagation losses are primarily due to absorption with penetration depth, δ_p varying as f^{-1} (Ulaby *et al*., 1982). For oil sands the variation was between f^{-2} and f^{-3} due to the heterogeneous nature of the material.

6.4.2.1 Low Frequency

Low frequency considers the backscattering behaviour of oil sands and other barefaced terrain over the L-band frequency range 0.9 – 2 GHz. Three field monitors were designed to monitor the E-field, power loss density and electric field density at 1 GHz and 1.27 GHz (corresponding to λ = 30 cm and 23 cm). The boundary conditions for all the models were the same. The resulting E-field for the 6 terrain types grouped into homogeneous (MUT A and B), semi-homogeneous (MUT C and D) and heterogeneous (MUT E and F) at 1 GHz is shown. For uniformity in presentation the absolute value in Vm^{-1} is normalized from 0 to 10 Vm^{-1} however the 2D maximum in Vm^{-1} is highlighted. At 1 GHz both the coarse and flat approximation models (not shown) for homogeneous terrain are similar. The longer wavelengths penetrated both beach sand (Fig. 6.25) and loamy farm soil (Fig. 6.26) but caused different propagation effects due to the terrain packing and permittivity.

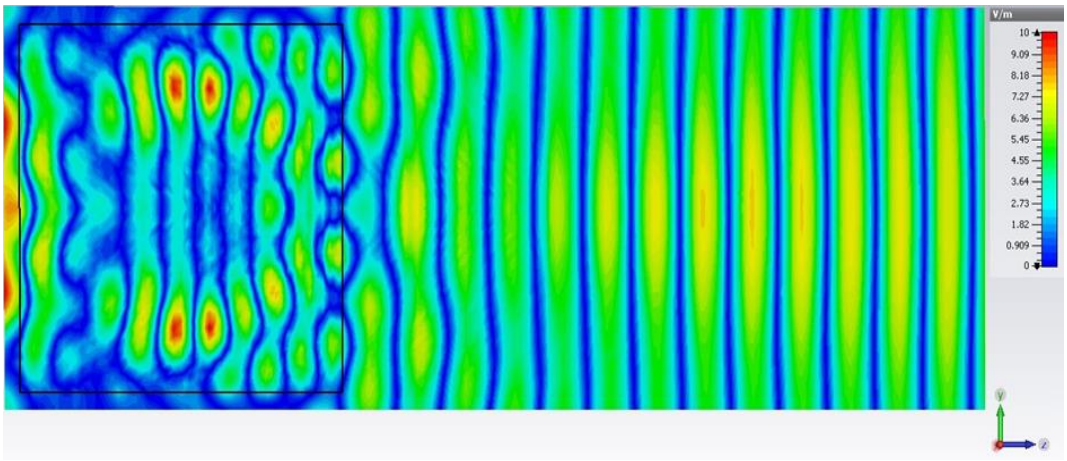

Figure 6.25: EM wave propagation (normalized to 10 V/m) in Beach Sand at 1GHz *yz*-plane. EM fields shown from base of terrain model to 2 m above surface.

Signal penetration in beach sand is higher than loamy farm soil (Cassidy, 2009). This was seen by the broader EM wave within beach sand while a tapering of signal is observed in loamy farm soil. Prior to normalization the maximum E-field for beach sand and loamy farm soil measured by the sensor at 2m above the model surface were 13.94 Vm^{-1} and 9.62 Vm^{-1} respectively. This indicates of the higher reflectivity from normal beach sand compared to loamy farm soil terrain.

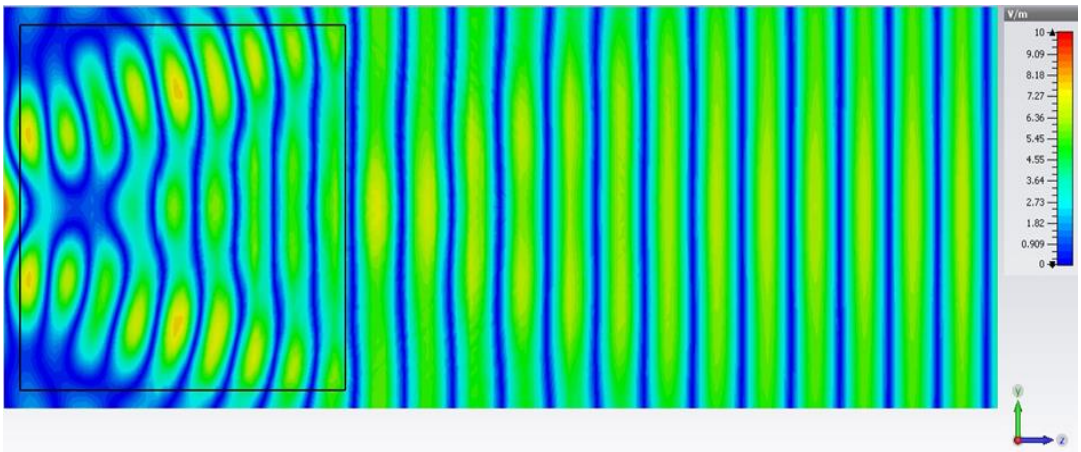

Figure 6.26: EM wave propagation (normalized to 10 V/m) in Loamy Farm Soil at 1GHz *yz*-plane. EM fields shown from base of terrain model to 2 m above surface.

The increased dielectric permittivity due to moisture and the effect on backscattering has been used to monitor land degradation (Ezeoke & Tong, 2014). Here it can be seen that the interaction of moisture and homogeneous terrain increases the amount of EM energy absorbed within both beach sand (Fig. 6.27) and loamy soil (Fig. 6.28) with 10 *wt*.% water content.

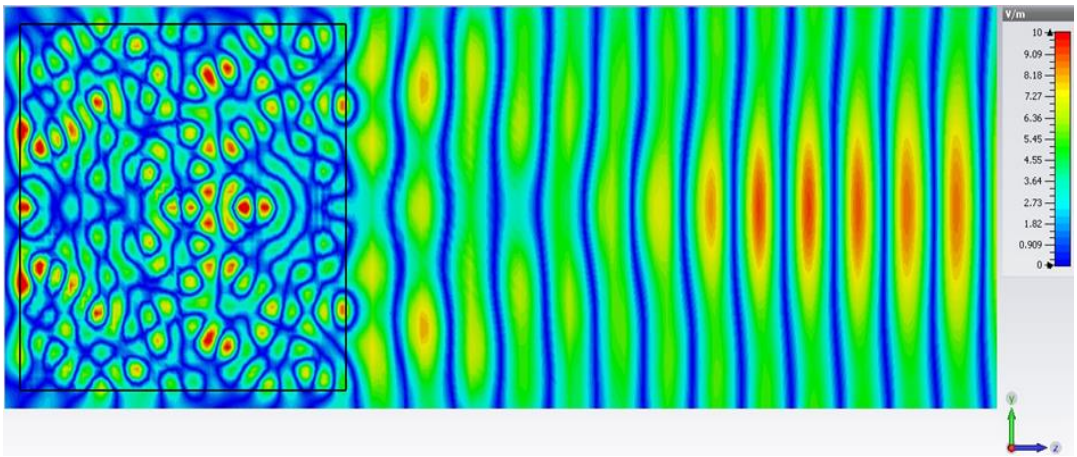

Figure 6.27: EM wave propagation (normalized to 10 V/m) in Beach Sand with 10 *wt.*% at 1 GHz *yz*-plane.

The differences in EM propagation between both homogeneous terrain types is due to the increased water in the terrain pores. Variations in the matrix material (grains) and pore space (air) creates field centers within the terrain. The 2D/3D results for increased moisture level provide a good indicator of what to expect in granular porous materials that contain natural moisture.

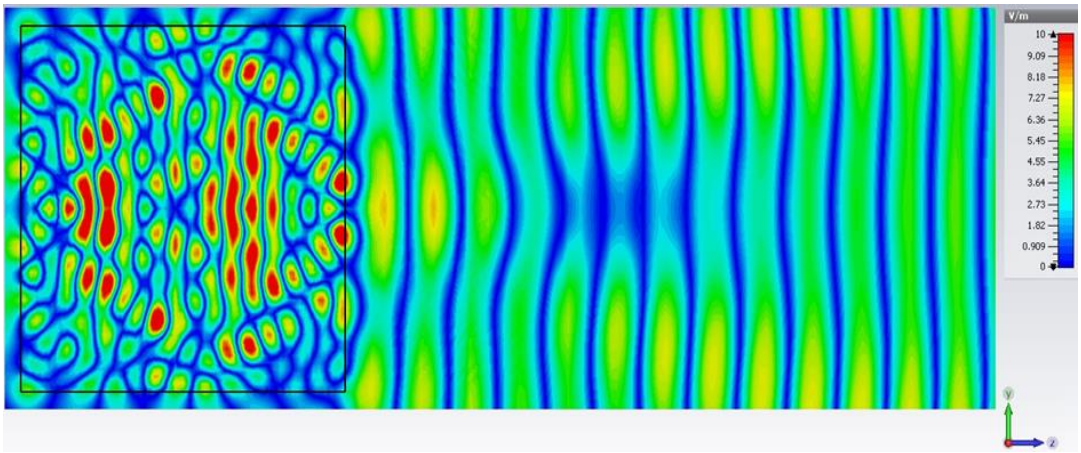

Figure 6.28: EM wave propagation (normalized to 10 V/m) in Loamy Farm Soil with 10 *wt.*% at 1 GHz *yz*-plane.

Compared to homogeneous terrain at 1 GHz, greater reflectivity was seen from both gravel and pebble than homogeneous terrain. The maximum E-field for pebbles (Fig. 6.29) and gravel (Fig. 6.30) was 17 Vm^{-1} and 19.9 Vm^{-1} respectively due to the difference in surface roughness. Both terrain were developed with a composite of uniform layers of varying dimensions with coarse surface representation (8 seg.). The EM propagation within both media at 1 GHz is due to the granular scale effects of the grain shape, porosity and density (Friedman, 1998).

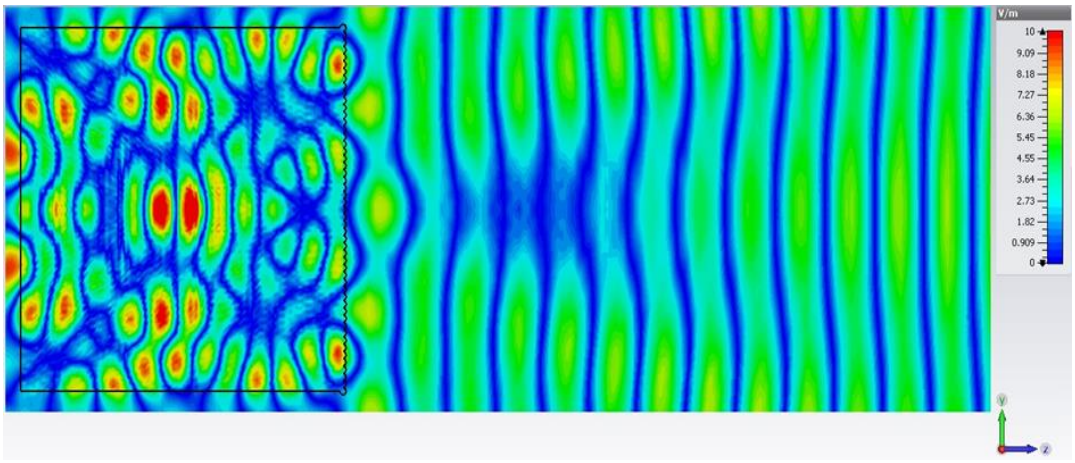

Figure 6.29: EM wave propagation (normalized to 10 V/m) in Pebble terrain at 1GHz *yz*-plane.

The smaller granular size of pebbles permitted higher penetration of EM waves into the terrain and less attenuation.

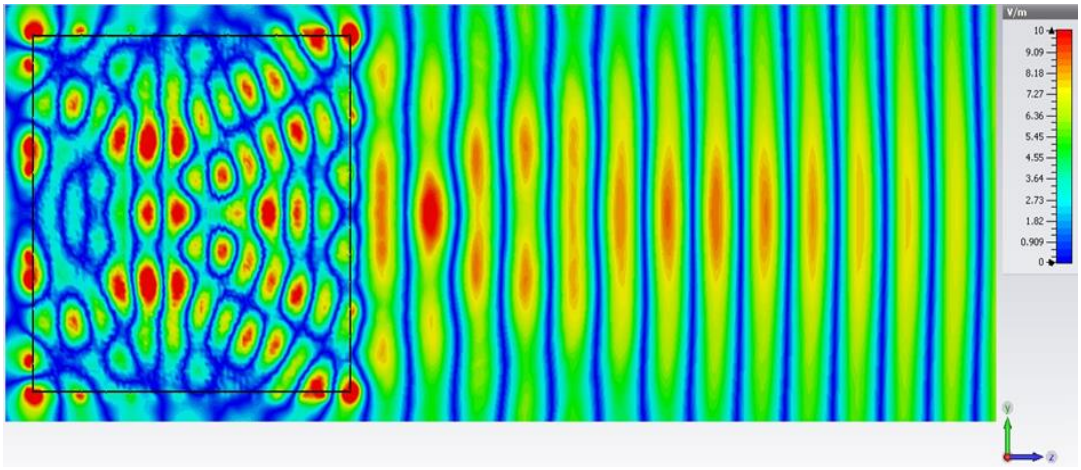

Figure 6.30: EM wave propagation (normalized to 10 V/m) in Gravel terrain at 1GHz *yz*-plane.

For oil sands however the presence of bitumen and moisture caused volumetric scattering within the terrain at 1 GHz. This was seen by the larger amount of low magnitude E-field interspersed with high intensity fields. This is a combination of diffuse reflectance with specular spikes within the terrain (Nayar, 1989). In HOS and VOS the peak E-field measured by the sensor at 2m above the terrain model surface was 14.3 Vm^{-1} and 18.6 Vm^{-1} respectively. The larger correlation length of the scatterers, *ks* on the HOS surface (Fig. 6.31) reduced the expected surface scattering while the larger amount of moisture present in VOS (Fig. 6.32) caused the higher EM fields observed within the terrain.

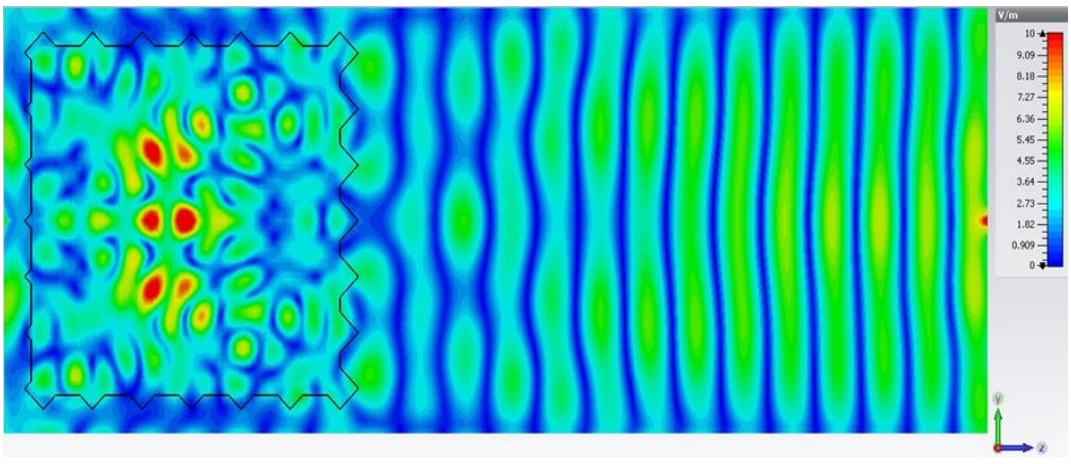

Figure 6.31: EM wave propagation (normalized to 10 V/m) in Hard Oil Sands at 1GHz *yz*-plane.

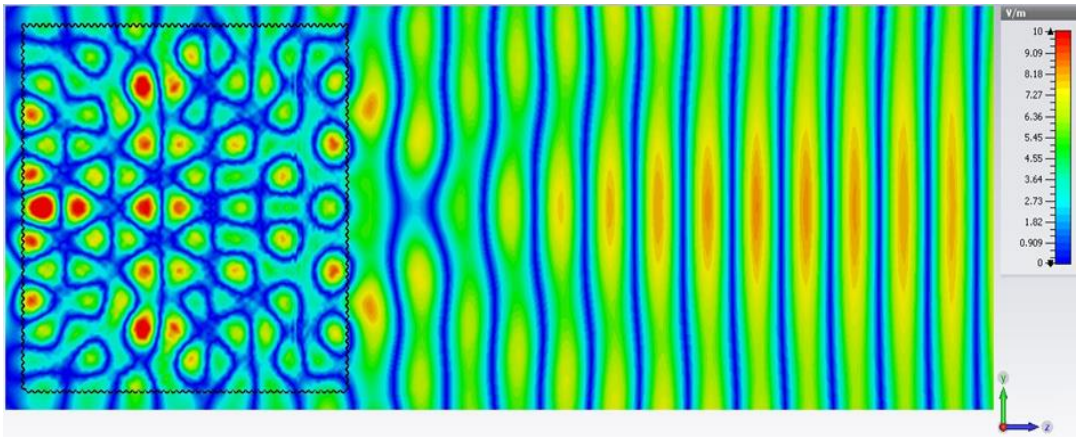

Figure 6.32: EM wave propagation (normalized to 10 V/m) in Viscous Oil Sands at 1GHz *yz*-plane.

6.4.2.2 Medium Frequency

The DDSM identified the 5 – 7 GHz region occupying the microwave C-band layer, as most significant to oil sand exploration due to the greater possibility of differentiation. To discern the behavior of barefaced terrain in this frequency range, another three field monitors were designed and placed at 2m above the terrain surface. They were set to monitor E-field, power loss density and electric field density at 5 GHz, 5.25 GHz and 7 GHz corresponding to λ = 6 cm, 5.7 cm and 4.3 cm respectively. The increased frequency and shorter wavelength of the incident EM wave produced higher reflectivity from homogeneous terrain. The total recorded EM energy was higher than at 1 GHz for both beach sand (18.6 Vm^{-1}) and loamy farm soil (19.3 Vm^{-1}) due to the higher frequency (5 GHz) involved. The natural moisture inherent in beach sand caused much higher signal attenuation within beach sand BTM (Fig. 6.33) compared to loamy farm soil (Fig. 6.34).

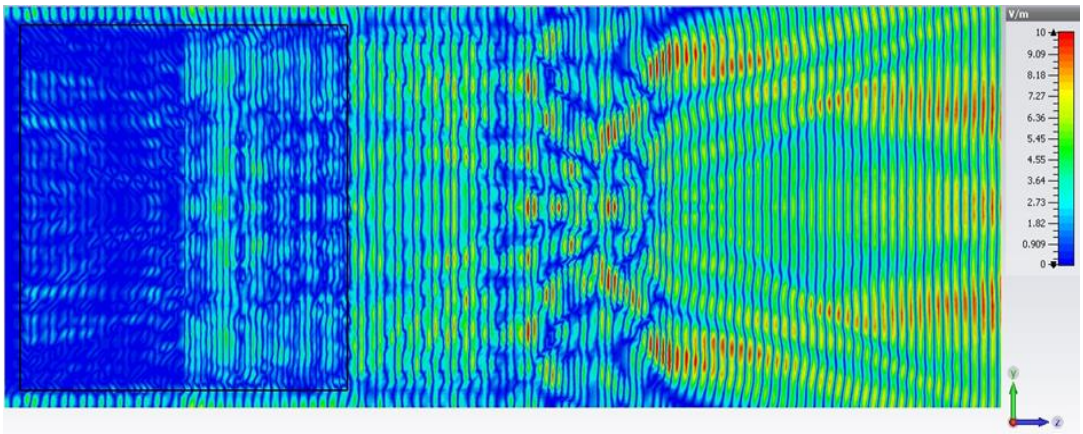

Figure 6.33: EM wave propagation (normalized to 10 V/m) in Beach Sand at 5.25 GHz *yz*-plane.

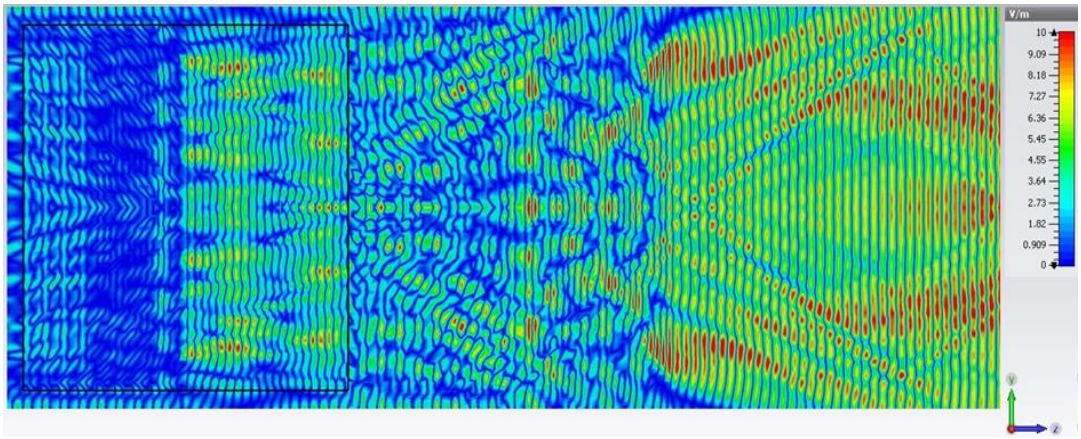

Figure 6.34: EM wave propagation (normalized to 10 V/m) in Loamy Farm Soil at 5.25GHz *yz*-plane.

For pebbles and gravel higher EM wave energy was also measured with peak E-field of 28 Vm^{-1} and 34.8 Vm^{-1} respectively. The scattering from pebbles (Fig. 6.35) and gravel (Fig. 6.36) was mostly due to the surface configuration although scattering within gravel was more diffuse due to the large correlation length from coarse spheres at the surface layer.

Similar to other barefaced terrain, the increased incident frequency of 5.25 GHz resulted in higher recorded E-fields from the oil sand models. The sensor models for HOS and VOS recorded 15.8 Vm^{-1} and 32.5 Vm^{-1} which was higher than the 14.3 Vm^{-1} and 18.6 Vm^{-1} measured at 1 GHz. The observed scattering within both HOS (Fig. 6.37) and VOS (Fig. 6.38) was more diffuse than other terrain types due to the macroscopic effects of bitumen, water and grains.

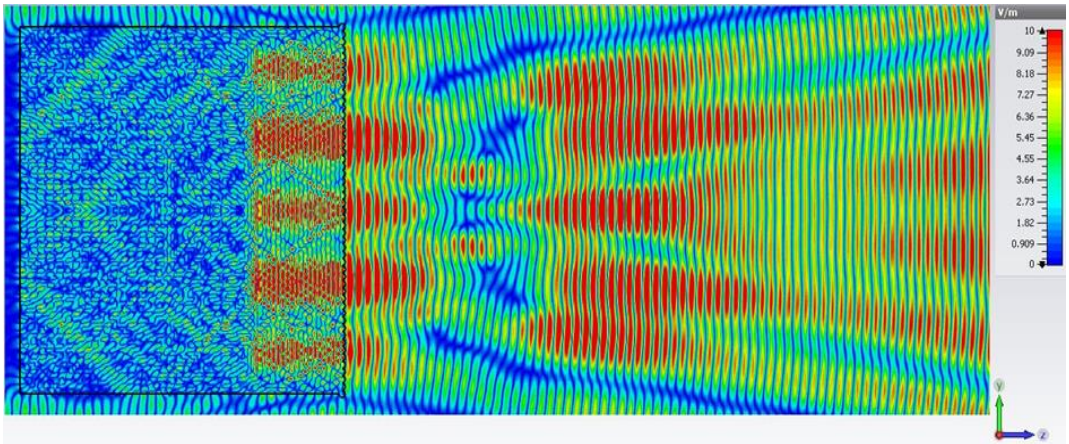

Figure 6.35: EM wave propagation (normalized to 10 V/m) in Pebble terrain at 5.25 GHz *yz*-plane.

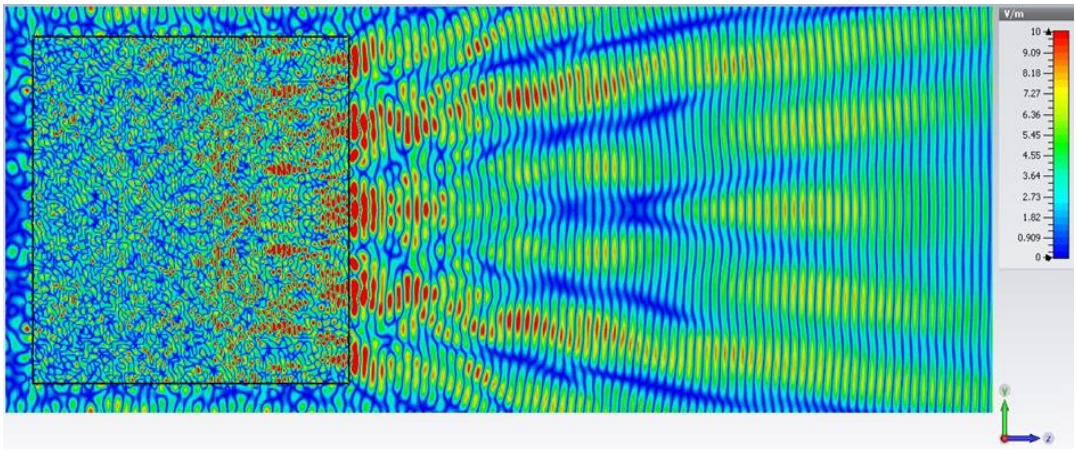

Figure 6.36: EM wave propagation (normalized to 10 V/m) in Gravel terrain at 5.25 GHz *yz*-plane.

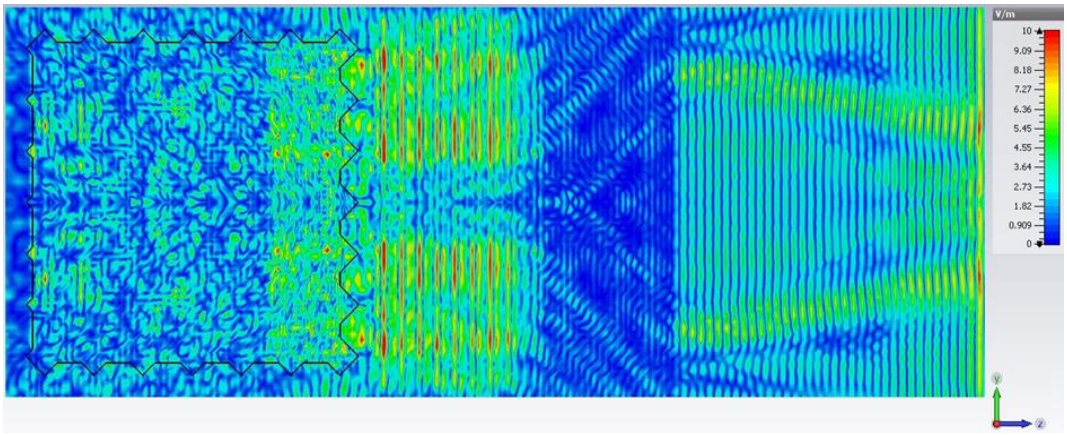

Figure 6.37: EM wave propagation (normalized to 10 V/m) in Hard Oil Sands at 5.25 GHz. Diffuse scattering seen.

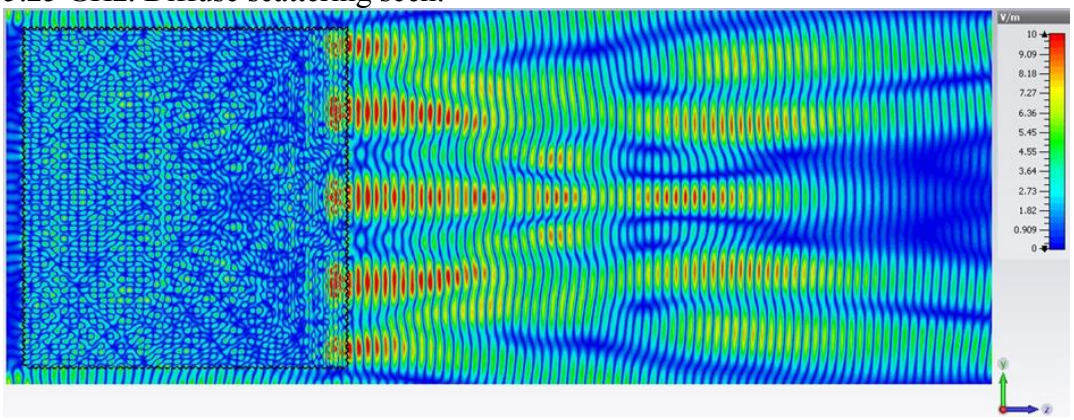

Figure 6.38: EM wave propagation (normalized to 10 V/m) in Viscous Oil Sands at 5.25 GHz *yz*-plane.

Furthermore, the effect of the heterogeneous nature of oil sands can be seen in the electric energy density plots. The presence of bitumen combined with low moisture and high grain content in HOS served to retain diffused energy within the HOS terrain (Fig. 6.39). In contrast, the greater amount of moisture in VOS which resulted in higher

dielectric permittivity when considered with the lower amount of grains can be seen in the smaller skin depth. This caused almost no energy beyond the top 10 cm for incident EM waves at 5.25 GHz (Fig. 6.40). Within the top layer of VOS, peak electric energy was 11 x 10^{-9} Joules per cubic meter (Jm^{-3}) compared to 3 x 10^{-9} Jm^{-3} for HOS.

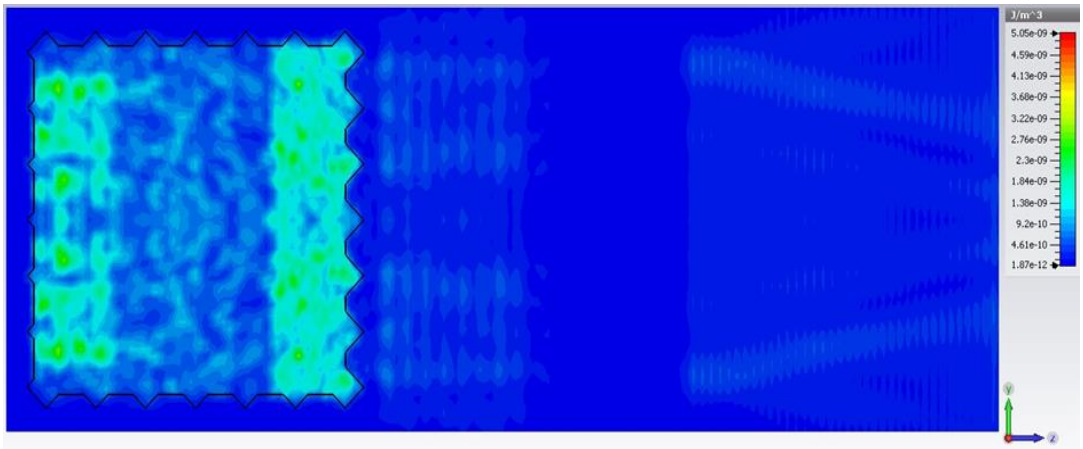

Figure 6.39: Electric energy density (Jm^{-3}) within Hard Oil Sands at 5.25 GHz *yz*-plane. Diffuse energy retained within HOS terrain.

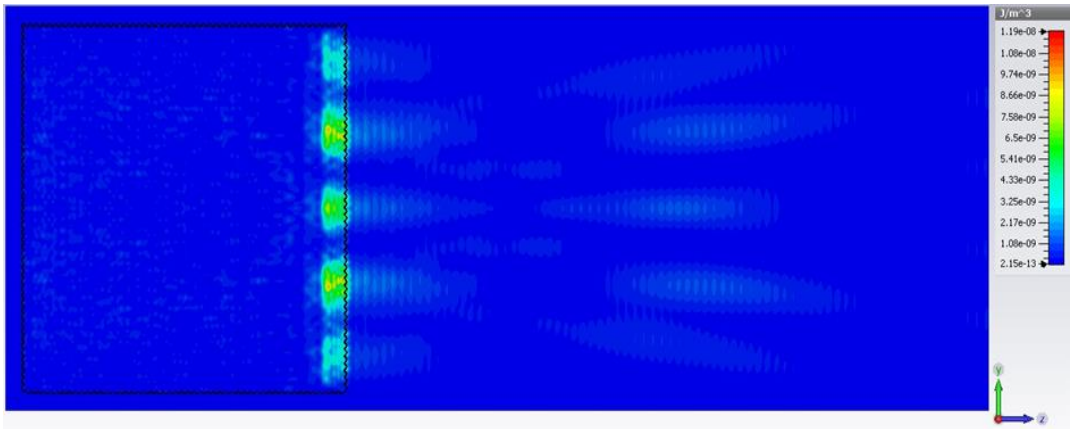

Figure 6.40: Electric energy density (Jm^{-3}) within Viscous Oil Sands at 5.25 GHz *yz*-plane. High moisture content increases absorption beyond 10 cm skin depth while bitumen retains energy on the surface of VOS.

6.4.2.3 High Frequency

The behavior of barefaced terrain at X-band was characterized with the aid of two E-field and electric field density monitors at both 9.67 GHz and 10 GHz, corresponding to λ = 3 cm and 3.1 cm respectively. At 10 GHz the σ^0 is almost exclusively due to scattering by the surface roughness layer. This top layer appears to be a semi-infinite layer of terrain to differing extents based on the ground parameters.

Due to the variation in physical properties the magnitude of 'ground echo' varies with terrain type because shorter wavelengths better separate surface facets (Moore, 1990).

For homogenous terrain the effect of the high frequency was to produce a 'mirror reflection' or shadowing in the area directly above the terrain from both *x* and *y* cut-planes. Although only the coarse representation of beach sand (Fig. 6.41) and loamy farm soil (Fig. 6.42) is shown, this mirroring of the ground was observed for both coarse and mild surface roughness implementations. In order to adequately understand the interaction of EM waves with the 6 terrain types the design of the CEM's allowed the free passage of EM waves around the terrain. The unhindered passage of EM fields around both terrain models confirm the mirrored ground echo was due to the terrain itself and not an artefact of processing.

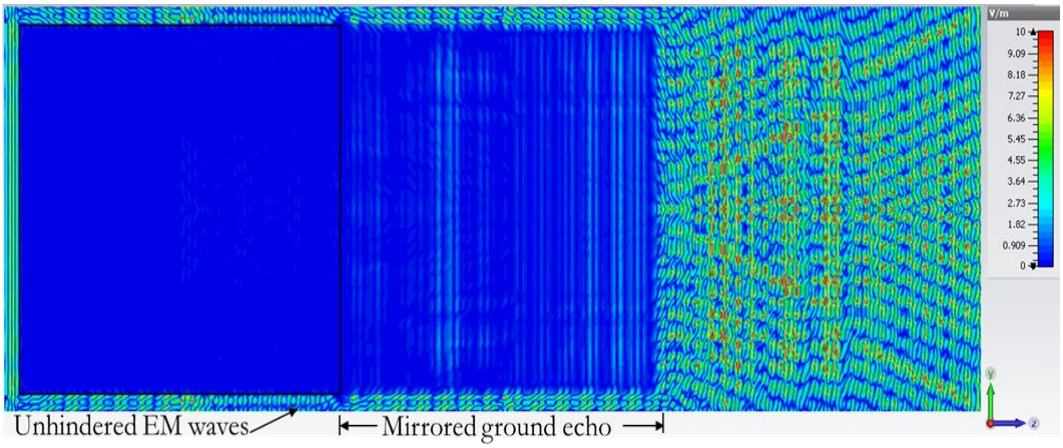

Figure 6.41: EM wave propagation (normalized to 10 V/m) in Beach Sand at 10 GHz *yz*-plane. Mirrored ground echo occurs opposite terrain model while EM waves pass unhindered where terrain is absent.

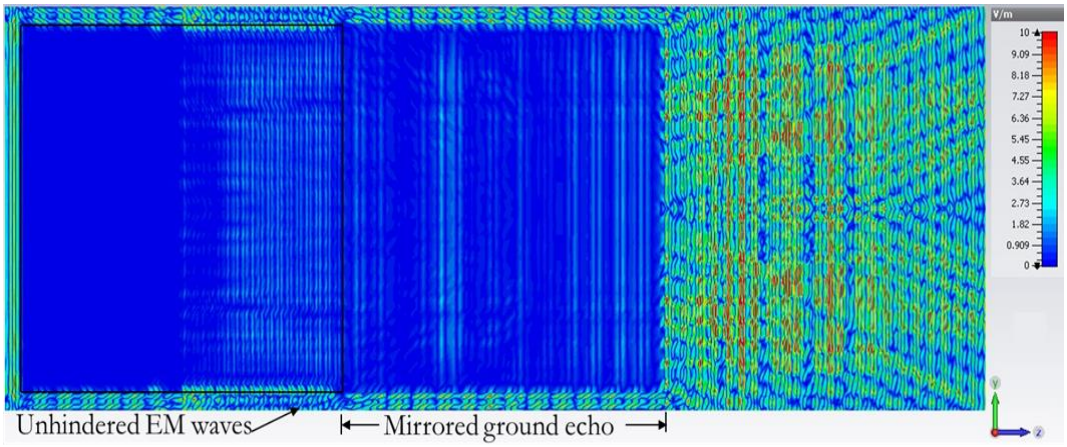

Figure 6.42: EM wave propagation (normalized to 10 V/m) in Loamy Farm Soil at 10 GHz. Mirrored ground echo occurs opposite terrain model while EM waves pass unhindered where terrain is absent.

Pebbles and gravel recorded higher peak E-fields of 56 Vm^{-1} and 51 Vm^{-1} with peak energy density of 32×10^{-9} Jm^{-3} and 26.25×10^{-9} Jm^{-3} due to the higher frequency involved. The peak electric energy distribution for pebbles (Fig. 6.43) and gravel (Fig. 6.44) at 10 GHz extended to similar depths (δ_p = -25cm). Due to the longer separation spacing between peaks, s for gravel scatterers the EM probes embedded (δ_p = -50cm) within gravel recorded 5dB difference in comparison to pebbles (Fig. 6.45).

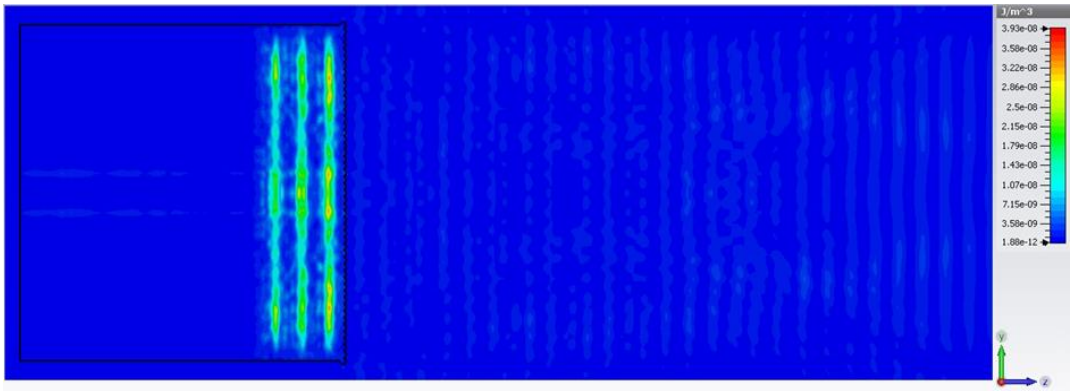

Figure 6.43: Electric energy density (Jm^{-3}) within Pebbles at 10 GHz *yz*-plane.

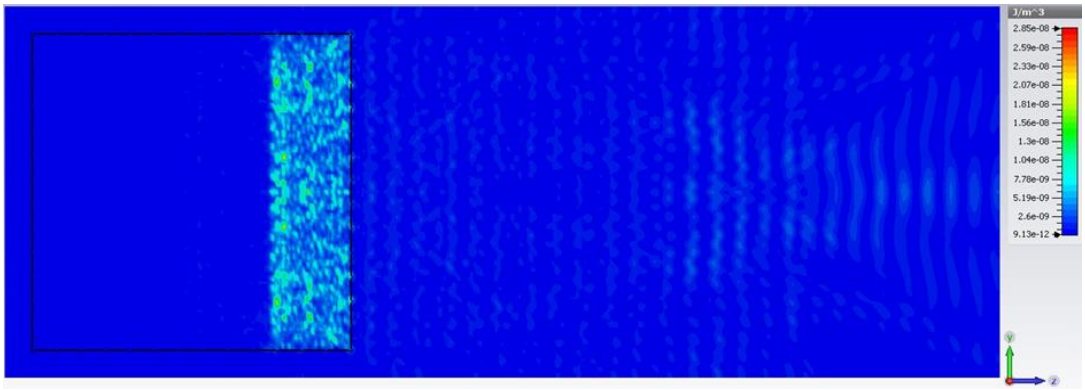

Figure 6.44: Electric energy density (Jm^{-3}) within Gravel at 10 GHz *yz*-plane.

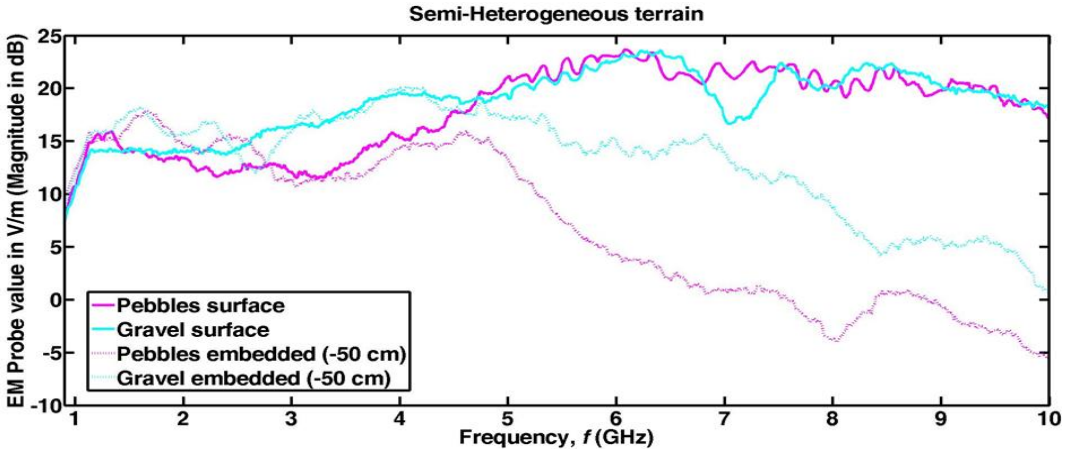

Figure 6.45: EM probe measurements from semi-heterogeneous terrain surface and embedded (δ_p = -50cm).

Compared to the similarities within other terrain groups, oil sands showed remarkably different responses at X-band. First there was low E-field penetration into HOS (Fig. 6.46) compared to VOS (Fig. 6.47). The unhindered passage of EM waves around the BTM shows that the top layer of HOS terrain acted as a semi-infinite layer. This was also seen in the electric density plot for HOS at 10 GHz (not shown). The interaction of bitumen and moisture in VOS caused a centralization of EM energy which was also seen in the electric density plot for VOS at 10 GHz (not shown). This centralization of E-field in VOS raises the prospect of heating VOS terrain for extraction and recovery purposes (Sahni *et al*., 2000; Bosisio *et al*., 1977). Rather than extraction, the research is interested in applications to identification and classification.

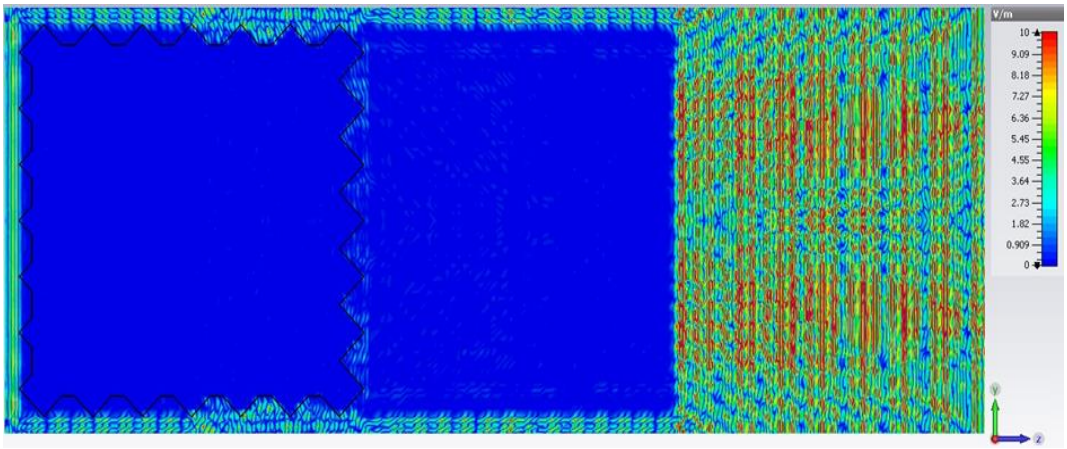

Figure 6.46: EM wave propagation (normalized to 10 V/m) in Hard Oil Sands at 10 GHz *yz*-plane.

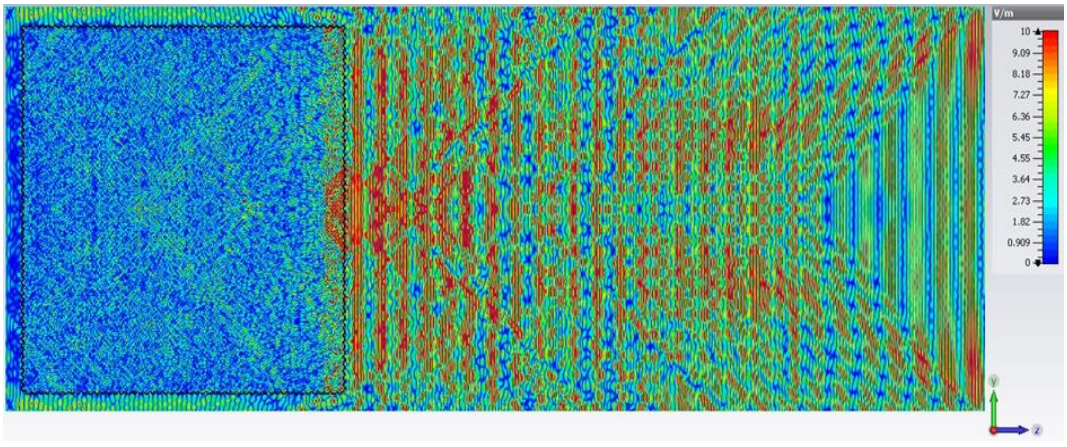

Figure 6.47: EM wave propagation (normalized to 10 V/m) in Viscous Oil Sands at 10 GHz *yz*-plane.

Importantly both surface and embedded probes indicated a clear E-field transition for HOS within the 6.5 – 7.5 GHz region (Fig. 6.48). Although there was not

a similar drop for probes inserted on the surface and within VOS (δ_p = -50 cm is shown), there was a 3 dB drop and later on increase within the 6.5 – 7.5 GHz microwave region for the surface probe. For the probe embedded (at δ_p = -50 cm) within VOS there was a slight fluctuation which could reflect the mild resonance observed in the dielectric permittivity. These results confirmed the DDSM identification of bitumen influence in the dielectric permittivity values over this microwave region for both HOS and VOS.

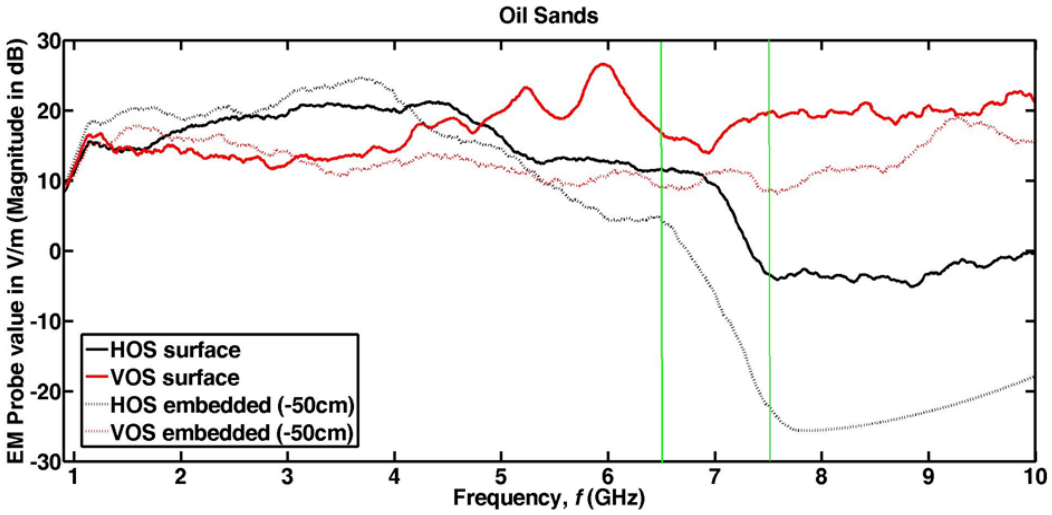

Figure 6.48: EM probe measurements from Oil Sands surface and embedded (δ_p = -50cm)

6.4.3. Angular Response

Modern commercial SAR satellites operate in 'agile' modes with the capabilities for different sensor viewing angles mostly to benefit from radar interferometry or stereoscopic effects (Elachi & Van Zyl, 2006). For airborne imaging radar most of the ground returns vary with the radar platform height and speed (Stimson *et al*., 2014). Therefore the Doppler resolution and relative amplitude of ground echo remains the principal means of discerning target echoes from the ground. In this application, the terrain is the target and there is little possibility of other point scatterers that are relatively straightforward to determine. Therefore it is necessary to understand the amplitude of the terrain returns under different conditions and how they compare with other barefaced terrain returns in varying situations.

By convention geometrical effects due to variation in the incidence angle would influence an imaged scene through processes such as shadowing (Oliver & Quegan, 2004). In the region of interest where oil sands are located such as the Agbabu Oil Sand Reservoir (AOSR) in Nigeria or the Canada basin, the possibility of shadowing from

foliage, trees or houses is minimal. Nevertheless in the likelihood or absence of shadowing, it is important to recognize the effect of incident geometry on surface and volume scattering in order to differentiate terrain target from clutter return (Mahafza & Elsherbeni, 2004). The possibility of deriving greater information from an imaged scene is shown by varying effects of angular relationship between sensor geometry and barefaced terrain on the radar signature.

Surface scattering is caused by the dielectric discontinuity between two media such as air and terrain while volume scattering is due to the spatial inhomogeneity in a volume at a scale comparable to the wavelength of the incident wave (Ulaby, 1982; Ezeoke & Tong, 2012). In terms of environmental remote sensing using radar, the volumes hitherto considered have been vegetation and snow cover (Ulaby, 1982; Ulaby *et al*., 1982). Therefore the E-field response in diverse terrain as a function of sensor geometry and barefaced terrain was investigated. In terms of the angular behaviour of σ^0 , oil sands and other barefaced terrain were grouped into 4 different perspectives namely: normal (90°), low (20° – 35°), moderate (45°) and high (55° – 60°) grazing angles.

6.4.3.1 Normal Grazing Angle

The normal look angle is the default SAR imaging mode when the sensor points down to the scene at 90° angle. This imaging perspective is the preferred look angle for Radar altimeters and scatterometers (Ulaby, 1982). Furthermore for airborne radars fitted with front or rear sensors there is the risk of 'altitude return' which is a peculiar problem that occurs when there is ground echo or clutter directly beneath the aircraft (Stimson *et al*., 2014). Clutter refers to the unwanted returns from the ground when a satellite or airborne radar is trying to image a target of interest. For our work the ground is the target. The EM characteristics of barefaced terrain during this imaging mode has been discussed in Section 6.4.1. Generally terrain penetration reduced with frequency i.e. δ_p varied with f^{-1} to different extents in MUT A, MUT B, MUT C and MUT D. Surface dispersion differed according to the terrain types. A comparison of the scattered signal ($\boldsymbol{E}^{tot}$ - $\boldsymbol{E}^{inc}$) dispersion directly on the surface (where $\boldsymbol{E}^{abs}$ is lowest) for the 6 terrain types at f = 10 GHz but normalized to 10 Vm^{-1} is presented (Fig. 6.49). Other surface scattering plots for f = 1 GHz and 5 GHz when $\theta_i = 90°$ are at Appendix 6.

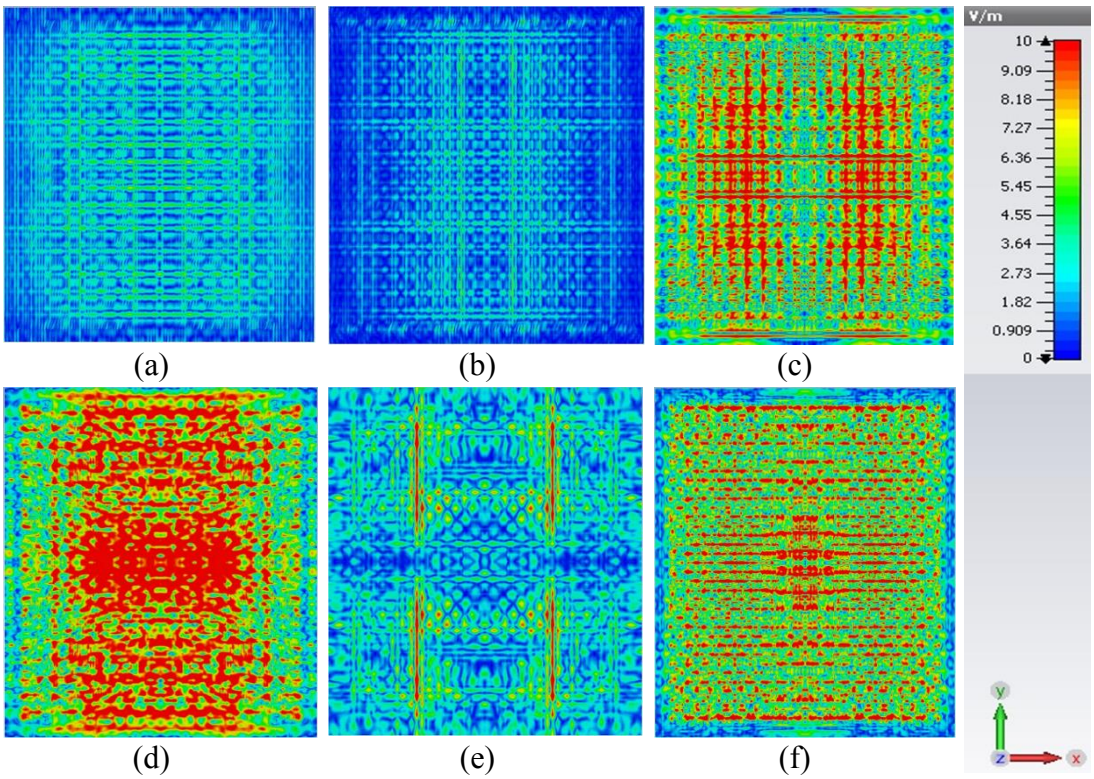

Figure 6.49: 2D/3D E-field normalized (10 Vm^{-1}) scattering plot from barefaced terrain surface *xy*-plane with $\theta_i = 90°$ and $f = 10$ GHz: (a) MUT A (b) MUT B (c) MUT C (d) MUT D (e) MUT E (f) MUT F.

For this geometry ($\theta_i = 90°$), the EM wave strikes the terrain at right angles in the middle of ∂A and then disperses like a drop on a surface. This is most evident in the lower intensity scattering plots for the terrain at 1 GHz, where the highest return amplitudes occur at the center for MUT A, MUT C, MUT D and MUT F (Fig. 6B.1). It is strikingly similar for 5 GHz incident radiation although the dimensions of the incident wave footprint is smaller than at 1 GHz with higher intensity returns in MUT A, MUT B, MUT C and MUT F (Fig. 6B.2). At 10 GHz the scattering plot for all the terrain types shows the wave front extending from the center outwards (Fig. 6.49).

For 10 GHz, MUT A had a higher dispersion spread and σ^0 than MUT B despite the lower surface roughness but higher permittivity in the former. This was also seen for MUT C and MUT D despite having exactly the same permittivity (Fig. 6.49). We ordinarily would expect greater scattering from MUT D owing to the surface roughness however the peak E-field value was higher for MUT C (Table 6.5). This behavior is due to the higher number of scatterers in MUT C and longer correlation length between scatterers in MUT D. Although a higher σ^0 from MUT E was expected this was also not the case due to the effect of the mirrored ground echo and overlapping returns from HOS scatterers which halved the total E-field observed in the CEM (Table 6.5). In

essence the total E-field detected during post-processing was low due to vector addition of voltage return process representing each scatterer (Stimson *et al*., 2014). This effect is also seen when gas flaring stacks are included as dominant scatterers in multi-SAR imaging (Ezeoke *et al*., 2012). The very large returns seen for VOS is due to the concentration of waves in the center of the BTM. Table 6.5 shows the absolute peak E-field scattered from terrain, $\boldsymbol{E}_{\mathbf{sca}}$ compared with the incident E-field, $\boldsymbol{E}_{\mathbf{inc}}$ when the BTM is not within the computation domain, D and the total E-field, $\boldsymbol{E}_{\mathbf{tot}}$. The lower total E-field values for MUT A, MUT B and MUT E at 10 GHz were due to the mirror ground reflection discussed previously.

Table 6.5: Peak E-field (Vm^{-1}) surface scattering with $\theta_i = 90°$ and f = 1, 5, 10 GHz

Terrain	1 GHz			5 GHz			10 GHz		
	$\boldsymbol{E}_{\mathbf{sca}}$[a]	$\boldsymbol{E}_{\mathbf{inc}}$[b]	$\boldsymbol{E}_{\mathbf{tot}}$[c]	$\boldsymbol{E}_{\mathbf{sca}}$	$\boldsymbol{E}_{\mathbf{inc}}$	$\boldsymbol{E}_{\mathbf{tot}}$	$\boldsymbol{E}_{\mathbf{sca}}$	$\boldsymbol{E}_{\mathbf{inc}}$	$\boldsymbol{E}_{\mathbf{tot}}$
MUT A	9.5	5.2	11.1	18.1	13.5	15.2	8.2	8.5	6.3
MUT B	2.8	5.4	5.3	20.4	11.4	22.0	7.5	6.4	6.5
MUT C	8.9	5.0	12.9	14.9	12.8	10.5	26.4	16.3	30.9
MUT D	6.4	5.0	8.4	13.9	13.3	19.0	23.9	25.6	23.6
MUT E	7.0	11.8	13.9	12.0	7.0	13.5	17.9	18.16	9.0
MUT F	10.6	5.0	14.1	18.3	12.6	13.5	32.7	20.3	27.4

[a] Absolute (Abs) value from CEM surface of terrain, $\mathbf{E}_{\mathbf{sca}}$
[b] Absolute (Abs) from CEM with BTM removed from calculation domain i.e. $\mathbf{E}_{\mathbf{inc}}$
[c] Absolute (Abs) from CEM both planewave sensor and BTM i.e. $\mathbf{E}_{\mathbf{tot}}$

6.4.3.2 Low Grazing Angle

At low look angles the incident EM wave strikes the terrain surface almost parallel to the terrain surface. In this research these angles were defined to cover 20° – 35°. Typically for low grazing angles the effective area of the terrain model surface, ∂A_{eff} covered depends on the azimuth beamwidth and compressed pulse length from an airborne radar antenna. Here the scattering response for $\theta_i = 30°$ at X-band (10 GHz) for MUT A – F is presented (Fig. 6.50) while the response at 1 GHz and 5 GHz is shown in Appendix 6.

It can be seen that the magnitude of surface scattering for all the terrain types when the sensor geometry, $\theta_i = 30°$ was lower than $\theta_i = 90°$ for all the frequencies. This is because the multiple scatterers in the imaged area ∂A add their returns in the radar beam. Each individual scatterer will possess its own RCS and phase angle, relative to its range from the radar (Stimson *et al*., 2014). At 1 GHz the EM waves impinge on the terrain from the right side leading to higher E-field observed in the first 30 cm of ∂A for MUT C, MUT D and MUT F (Fig. 6B.3).

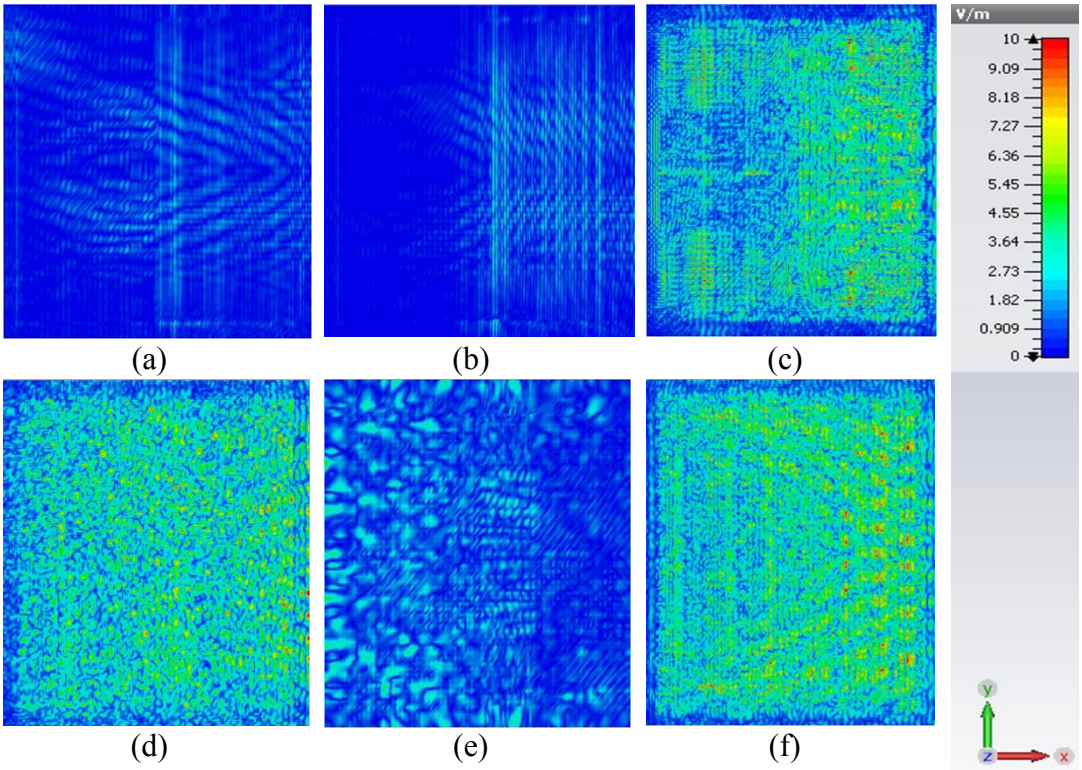

Figure 6.50: 2D/3D E-field normalized (10 Vm^{-1}) scattering plot from barefaced terrain surface *xy*-plane with $\theta_i = 30°$ and $f = 10$ GHz. (a) MUT A (b) MUT B (c) MUT C (d) MUT D (e) MUT E (f) MUT F

With increased energy and smaller wavelengths at 5 GHz, the direction of incident waves is more apparent. Also the EM wave footprint is clearly smaller for MUT A, MUT B, MUT C and MUT F but the scattering plots yield more intensity (Fig. 6B.4). The footprint of the EM waves is more pronounced for the left side of individual plots except for HOS which experiences shadowing away from the receiver. Despite the change in sensor angles there was slight ground echo mirroring for MUT A and MUT B so that the peak total E-field, $\boldsymbol{E}_{\mathbf{tot}}$ was lower than $\boldsymbol{E}_{\mathbf{sca}}$ when the incident frequency was 5 GHz and 10 GHz.

The difference between the $\boldsymbol{E}_{\mathbf{inc}}$ and $\boldsymbol{E}_{\mathbf{sca}}$ is due to absorption and propagation losses. At 1 GHz the scattered field on the surface was low for all the barefaced terrain with almost no returns seen for loamy farm soil (Fig. 6B.3). At 5 GHz the scattering that occurred was due to the effective area of the terrain model surface, ∂A_{eff} (Fig. 6B.4). The summary of the peak E-fields obtained for $\theta_i = 30°$ with $f = 1$, 5 and 10 GHz agrees with this assessment and is presented in Table 6.6.

Table 6.6: Peak E-field (Vm^{-1}) surface scattering with $\theta_i = 30°$ and $f = 1$, 5, 10 GHz

Terrain	1 GHz			5 GHz			10 GHz		
	E_{sca}	E_{inc}	E_{tot}	E_{sca}	E_{inc}	E_{tot}	E_{sca}	E_{inc}	E_{tot}
MUT A	6.5	5.1	11.3	20.7	8.7	16.1	5.1	5.2	4.7
MUT B	1.7	5.1	5.7	18.1	8.7	15.0	5.4	4.5	4.6
MUT C	9.2	5.0	10.8	11.1	7.5	13.2	16.1	8.5	18.3
MUT D	8.7	5.0	11.7	12.85	8.7	15.7	14.3	11.4	15.3
MUT E	7.6	5.1	10.8	11.2	5.8	13.7	6.4	4.8	6.9
MUT F	10.3	5.0	15.2	10.4	8.4	15.5	15	11.5	15.2

6.4.3.3 Moderate Grazing Angle

Here the moderate or medium look angle was defined to be 45° but for conventional radar, the definition varies with system design, commercial considerations and operator use. Having characterized terrain in the microwave frequencies over a geometric inclination from θ_i = 20° through to 90°, it was appropriate to consider θ_i = 45° as the moderate grazing angle. At this angle the incident waves achieve greater terrain penetration but also with a larger effective area, ∂A_{eff} when compared to lower grazing angles. Therefore there is more likelihood of backscatter compared to low grazing angles (Fig. 6.51). The values obtained for the barefaced terrain show this and the summary of the peak E-fields obtained for θ_i = 45° with f = 1, 5 and 10 GHz is presented in Table 6.7. The geometric position of scatterers is more pronounced for moderate grazing angles. The EM footprint seems larger in comparison to the low grazing angles because there is more uniformity of backscatter (Fig. 6.51). The relatively lower surface scattering can be seen by the shadowing on the left side of each individual terrain plot along with less intense region along the middle for MUT A, MUT B and MUT E (Fig. 6.51).

Table 6.7: Peak E-field (Vm^{-1}) surface scattering with θ_i = 45° and f = 1, 5, 10 GHz

Terrain	1 GHz			5 GHz			10 GHz		
	E^{sca}	E^{inc}	E^{tot}	E^{sca}	E^{inc}	E^{tot}	E^{sca}	E^{inc}	E^{tot}
MUT A	5.3	5.0	7.8	13.9	8.5	16.8	9.4	9.4	4.1
MUT B	1.8	5.0	6.1	18.2	7.6	20	5.8	5.8	4.0
MUT C	8.4	5.0	11.5	10.2	6.4	14.0	22.2	7.7	21.3
MUT D	9.5	5.0	13.5	11.5	6.6	14.0	15.1	8.9	17.0
MUT E	9.6	5.0	12.6	15.1	8.3	17.1	7.3	5.6	5.5
MUT F	13.4	5.0	15.2	15.1	6.0	16.4	15.0	9.1	15.8

This is particularly pronounced in beach sand and loamy farm soil with low surface roughness conditions even at 10 GHz. The same shadowing effect was not seen in MUT C and MUT D. The lower backscatter from HOS compared to gravel at 10

GHz despite having larger surface roughness variation can also be attributed to the greater penetration of the incident waves into HOS. Across the grazing angles there was more penetration at $\theta_i = 45°$.

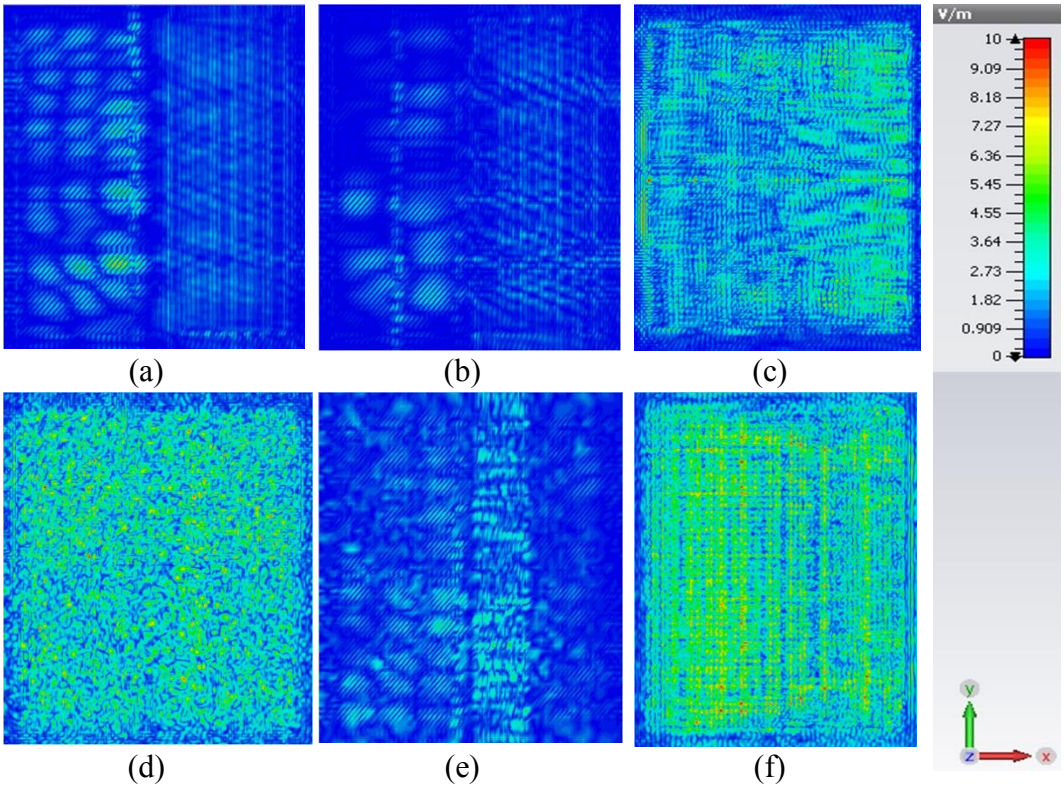

Figure 6.51: 2D/3D E-field normalized (10 Vm^{-1}) scattering plot from barefaced terrain surface *xy*-plane with $\theta_i = 45°$ and $f = 10$ GHz. (a) MUT A (b) MUT B (c) MUT C (d) MUT D (e) MUT E (f) MUT F

The shadowing effect was not seen at $f = 1$ GHz due to the longer wavelengths of the incident waves (Fig. 6B.5). The scattering response was due to a combination of the incident geometry and media permittivity with almost no surface response from MUT B (Fig. 6B.5). At 5 GHz, the effect of surface roughness and incident geometry played an increasing role. The right hand side of the surface scattering plot of MUT A and MUT B yielded more scattering returns with the left hand side seemingly shadowed (Fig. 6B.6). This is because they behaved like pure mirror reflectors, also seen to a less extent in MUT F. MUT E experienced double bounce scattering from volume effects so that the opposite was true and the side away from the receiver looked more reflective at 5 GHz (Fig. 6B.6).

6.4.3.4 High Grazing Angle

For this research, when EM waves are incident above 50° the sensor is said to operate at high incident angles. At large grazing angles, the area covered on the ground may be defined by both azimuth and elevation beamwidths of the antenna or EM source (Stimson *et al*., 2014). Consequently terrain ought to appear mirror like but with larger and almost specular backscatter. At 1 GHz the backscatter footprint, ∂A_{eff} was broader than previous grazing angles for MUT A, MUT B, MUT C, MUT D, MUT E and MUT F (Fig. 6B.7). This was also true at f = 5 GHz but with higher scattering intensity (Fig. 6B.8). Due to the large wavelengths the incident fields at 1 GHz yielded the same value of 5 Vm^{-1} indicating minimal losses whether from absorption on the surface or to scattering outside the open boundary conditions of the computational domain D.

The correspondingly lower scattering at 10 GHz supports the view of specular backscatter from MUT A and MUT B (Fig. 6.52). For both homogeneous terrain, the left hand side of the scattering plots did not give appreciable backscatter. This was not the case for MUT C which had more coherent returns of higher magnitude than at θ_i = 30° and 45° indicating the effect of surface roughness (Fig. 6.52).

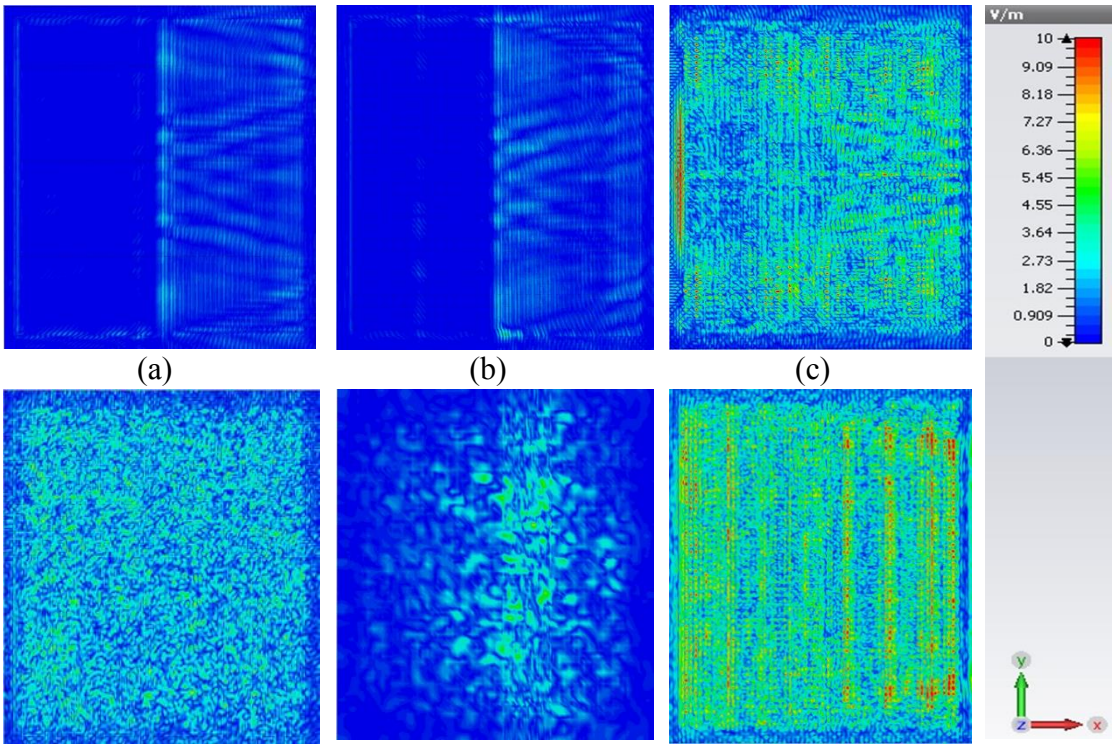

Figure 6.52: 2D/3D E-field normalized (10 Vm^{-1}) scattering plot from barefaced terrain surface xy-plane with θ_i = 60° and f = 10 GHz. (a) MUT A (b) MUT B (c) MUT C (d) MUT D (e) MUT E (f) MUT F

The peak E-field obtained for MUT A along with other terrain across L-, C- and X-band is presented in Table 6.8. The coherent effect of surface roughness was also seen for MUT D and MUT F but not to the same extent for MUT E indicating one method of distinguishing between the terrain types. MUT D had more E-field scattering at moderate grazing angles compared to low and high. The backscatter footprint for MUT E seemed smaller due to shadowing at 10 GHz but there was no shadowing for MUT E at 1 GHz (Fig. 6B.7). The right side of MUT E produced greater scattering intensity at 5 GHz due to higher grazing angle (Fig. 6B.8). This was also repeated at 10 GHz for MUT E however there was no shadowing across the frequencies for MUT F.

Table 6.8: Peak E-field (Vm^{-1}) surface scattering with $\theta_i = 60°$ and $f = 1, 5, 10$ GHz

Terrain	1 GHz			5 GHz			10 GHz		
	E^{sca}	E^{inc}	E^{tot}	E^{sca}	E^{inc}	E^{tot}	E^{sca}	E^{inc}	E^{tot}
MUT A	4.8	5.0	6.9	11.6	11.5	12.3	4.5	9.0	8.5
MUT B	2.3	5.0	5.3	11.0	9.3	10.1	5.9	9.1	8.9
MUT C	9.4	5.0	11.9	11.4	6.7	14.7	25.1	10	23.4
MUT D	9.5	5.0	13.5	10.9	7.1	14.3	10.8	13.5	15.3
MUT E	6.3	5.0	10.0	17.1	14.9	23.4	8.7	8.1	8.8
MUT F	12.0	5.0	13.8	11.4	5.5	14.7	21.6	13.0	21.1

6.4.4. Scatter Plots

An example EM signature comprising scattered power received, P_r for $\theta_i = 20°$ to 90° for HOS and VOS is presented in a scatter plot. The received scattered power σ^0 for 3 monitors placed at 1 GHz, 7 GHz, and 10 GHz for the oil sand models are presented in Fig. 6.53 to Fig. 6.55. Over the 20° – 90° angular range σ^0 exhibits larger dynamic range of 8 dB at $f = 1$ GHz, 4 dB at $f = 7$ GHz and 3 dB at $f = 10$ GHz. It can be seen that at $f = 1$ GHz, both VOS surfaces with flat approximation (smooth) and 3 segment (slightly rougher) surface roughness exhibit similar radar response (Fig. 6.53).

The sensitivity of backscattering coefficient, σ^0 to surface roughness of oil sands is evident at higher frequencies such as $f = 7$ GHz and $f = 10$ GHz where terrain scattering response is higher and the dynamic range of the radar response is lower (Fig. 6.54 and Fig. 6.55). The EM signature for both oil sand terrain varied with θ_i and f. Also for transmit power, P_t of 5W (r.m.s) incident on terrain the magnitude of received power, P_r does not exceed -3 dB due to propagation path effects and attenuation corresponding to the round trip distance between transmitter, terrain and receiver from (2.8) and (3.4) and (3.5).

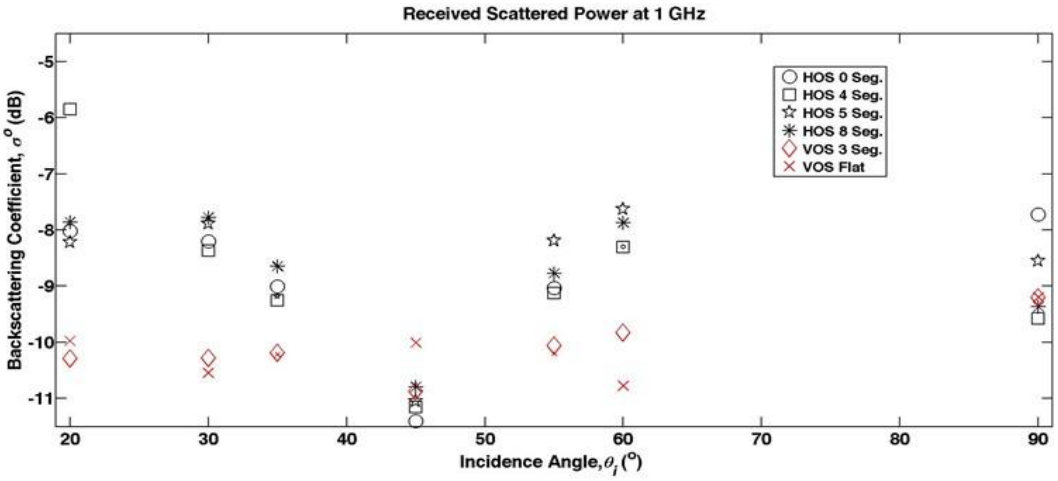

Figure 6.53: Scatter plot showing angular response of σ^0 for six different surface roughness implementations of oil sand BTMs at f = 1 GHz.

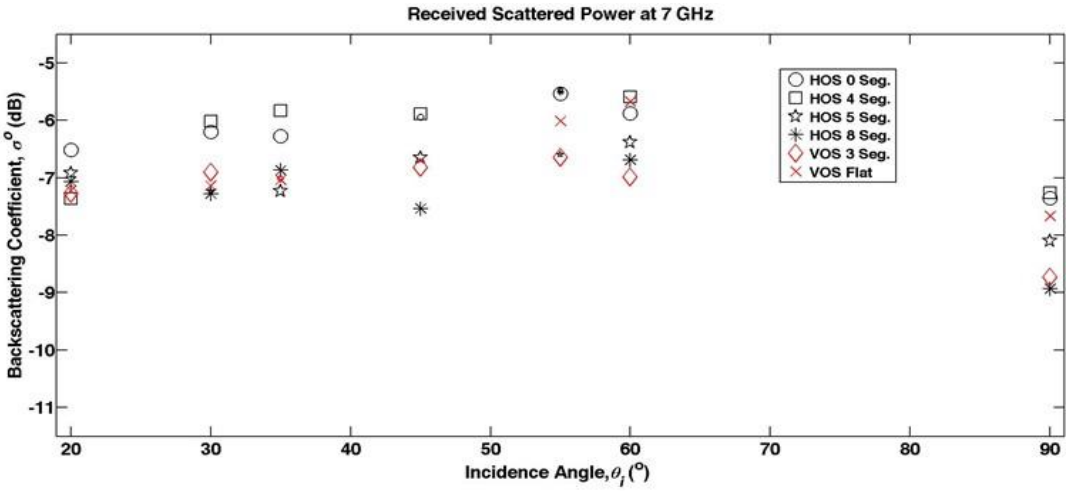

Figure 6.54: Scatter plot showing angular response of σ^0 for six different surface roughness implementations of oil sand BTMs at f = 7 GHz.

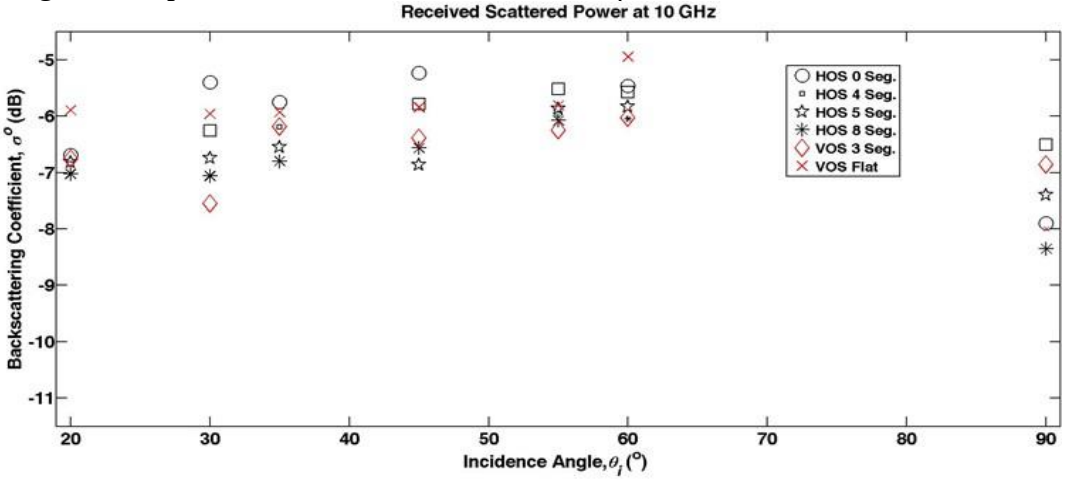

Figure 6.55: Scatter plot showing angular response of σ^0 for six different surface roughness implementations of oil sand BTMs at f = 10 GHz.

6.5. Concluding Remarks

The scattering process for six barefaced terrain classes was investigated using CEM models. The CEM models were created to examine the EM wave interactions for inhomogeneous layers of oil sands and other barefaced terrain using 3D sensors and terrain models. The models covered homogeneous terrain like beach sand, gravel and pebbles but also heterogeneous terrain such as loamy farm soil, hard oil sand and viscous oil sand. The study considered several SAR imaging scenarios. The use of computer simulation and intrinsic terrain models enabled EM characterization of the interaction of EM field with oil sand terrain at different geometries (20°, 30°, 35°, 45°, 55°, 60° and 90°), polarization (linear and circular), depths (1 - 3 cm, 5cm, 10cm, 15cm, 20cm, 25cm and 50cm) and frequencies (0.9 GHz – 10.5 GHz). The results were post-processed in order to present the scattering matrix as radiometric brightness in one dimensional (x, y or z plots) and two dimensional (x/y, x/z or y/z) reflectivity views. The high quality 2D/3D models carried previously unseen information on barefaced terrain characterization.

The complexity and wide diversity of natural surface covers make it difficult to exactly model such surfaces and the corresponding backscatter behaviour as a function of changing sensor parameters like illumination geometry, frequency and polarization. Physical measurement of the grain size of VOS and HOS in this study indicated the prevalence of clumping. This habit of bitumen infused rock enabled high resolution models to be developed with agglomerated rather than grain size. A milder form of clumping seen in homogeneous terrain with increasing moisture level was used in model representations. Previous terrain models do not account for the presence of bitumen. It was included here using raw dielectric permittivity data obtained from EM measurement techniques for each terrain class.

A large amount of scattering data was generated therefore radar signature results were mainly discussed according to the effects caused by frequency and angular geometry on the scattering process. Other factors such as polarization, water content, secondary reservoir properties, and penetration depth amongst others were considered under both themes. It was observed that the values of σ^0 for all 6 terrain types had a clear dependence on radar frequency, f. The appearance of surface roughness to microwave imaging, was inversely dependent on the radar wavelength. At higher wavelengths the scatterers appear smaller giving smaller values for σ^0. However as the

frequency increased the surface scatterers appeared proportionately larger and the surface scatterers appeared rougher with an attendant increase in the σ^0. At X-band, beach sand, loamy farm soil and HOS produced ground echo mirroring or "quasi-specular backscatter" (Stimson *et al*., 2014). At low frequency the variation in penetration depth with frequency was between f^{-2} and f^{-3} due to the heterogeneous nature of oil sands. At high frequency the interaction of bitumen and moisture presence caused a concentration of energy in the center of VOS although this was not seen in HOS where the greater presence of sand caused ground echo mirroring.

The contrast in dielectric permittivity, ($\varepsilon'_{r,i}$ and $\varepsilon''_{r,i}$) and surface roughness, χ between the different layers *a*, *b*, and *c* of the CEM models enabled the post processing of the scattering coefficient and identification of the EM signature of HOS and VOS. The BTM research and development proved that 26 BTMs adequately represented the range of surface roughness conditions witnessed for the 6 MUTs. The results from the CEMs provide a comparison of backscattering behavior between barefaced and oil sand terrain. It was further observed that the σ^0 from oil sands consisted of contributions to both surface and volume scattering due to the non-complementary effect of moisture, grains and bitumen. Moisture ought to increase the backscatter by reducing penetration depth, δ_p of EM waves. However the bitumen present in oil sands served to reduce backscatter while grains (sand) served to increase the reflectivity. Consequently, at the boundary of air-oil sand terrain (models) surface scattering occurred while volume scattering occurred within the oil sand terrain itself. The CEM model results also demonstrated excellent agreement with classical scattering models for each terrain type particularly SPM and KSM. Therefore CEM modelling provided a new competent method to characterize, classify and visualize EM scattering from barefaced terrain and is inherently useful to barefaced terrain classification.

7 Validation

The development of a laboratory scatterometer system and the deployment to measure the reflectivity of terrain is highlighted then the results are analysed.

This chapter has two main segments. First a method to examine the diversity of terrain backscattering was developed to analyze the results of the three step electromagnetic (EM) characterization process then the results were compared with previous computer electromagnetic (CEM) models and literature. The approach to measure the relationship between sensor configuration and terrain backscatter involved microwave modeling and measurement techniques. Based on previous CEM model scattering, the investigation measured the far field EM wave reflectivity of six different barefaced terrains at microwave frequencies (1 – 8 GHz) in an open laboratory and also anechoic chamber. The results provided a comparison of backscattering response for different terrain types particularly bitumen rich terrain such as oil sands at L-, C- and X-band. The resulting information is vital for deploying synthetic aperture radar (SAR) systems for petroleum exploration.

7.1. Scattering Parameter Model

Previously the dielectric discrimination statistical models (DDSM) and the general analysis based on the results from the CEMs identified a mild resonance effect for oil sands in the 6 GHz to 7 GHz region (Ezeoke & Tong, 2013c; Ezeoke *at al*., 2014a). Investigating the average reflectivity of barefaced terrain, particularly at different polarizations and frequency could further verify the ability to discriminate amongst barefaced terrain types (Ezeoke & Tong, 2013a; Ezeoke *et al*., 2014b). This is because geoscientists interpretation of radar imagery uses the same 'clues' utilized for identification from aerial photographs (Lewis & Henderson, 1998). Such clues include tone, texture, shape, size, pattern and shadow amongst others. They occur in radar imagery due to the EM backscatter rather than reflection of sunlight. Therefore the validation of the backscattering behavior at specific frequencies is vital to determining the possible roles and applications of synthetic aperture radar (SAR) (Ulaby, 1982).

Owing to the complex interaction between incident EM fields, $\boldsymbol{E}^{\mathbf{inc}}$ from SAR and the Earth leading to backscattered fields, $\boldsymbol{E}^{\mathbf{sca}}$, ground based measurements are

typically used to calibrate and validate existing remote sensing data products. In the absence of high resolution satellite or airborne radar imagery over specific geographic regions, empirical measurements of land surface parameters can aid in the development of an inversion strategy for SAR data (Ezeoke & Tong, 2013a). For the monostatic operation considered in this thesis the same radar antenna was used for transmission and reception but two or more antennas are used in the bistatic and multistatic cases respectively. Backscattering datasets can be recorded using monostatic (S_{11}), bistatic (S_{12}) or multi-static techniques depending on the sensor configuration.

A 'scatterometer' is the conventional radar sensor used to investigate the backscattering cross section of surface areas illuminated by sensor antenna (Elachi & van Zyl, 2006; Whitt *et al*., 1990, Dobson & Ulaby, 1981). Scatterometers could be spaceborne like the SEASAT scatterometer or ground based such as the truck mounted Millimeterwave Network Analyzer based polarimetric (MNAP) scatterometer. They have been used to measure ocean backscatter as a means to deriving the wind vector, differential scattering from vegetation canopies as a function of range and measurement of farmland (Ulaby *et al*., 1988; Ulaby *et al*., 1978). The primary function of such systems was to make absolute measurements of the backscattering coefficient, σ^0, usually as a function of the incidence angle, θ_i. In most cases the quantity measured by the scatterometer is the magnitude of the received signal so that the strength of the radar backscatter is proportional to the target or terrain properties.

For a single terrain scatterer the radar range equation from (3.7) can be adapted for the polarimetric case as:

$$\frac{P_{r\,(h,v)}}{P_{t(h,v)}} = \frac{G_t\, G_r \lambda^2 \sigma_{(h,v)}}{(4\pi)^3 R^4} \tag{7.1}$$

Where P_r and P_t are the received backscattering signal power and transmit signal power for two polarizations either horizontal h or vertical v. The polarized radar cross section (RCS) of such a single scatterer will be given by the $\sigma_{(h,\,v)}$. Also G_t, G_r, R and λ represent transmit and receive antenna gains at specific polarizations, target range and wavelength respectively. From (7.1) the RCS or normalized RCS (nRCS) can be derived by measuring transmit and receive power ratio at specific frequencies for a fixed range target (Zhang *et al*., 2010). In contrast to conventional magnitude only scatterometers a laboratory scatterometer system (LSS) was developed and configured

to measure the co-polarized scattering matrix $\boldsymbol{S}_{HH}$ and $\boldsymbol{S}_{VV}$. With change in sensor the LSS may also measure the cross polarized scattering matrix $\boldsymbol{S}_{HV}$ and $\boldsymbol{S}_{VH}$.

7.2. Laboratory Scatterometer System

Terrain calibration with SAR satellite data requires access to relevant imagery over a known area of interest (Sabine, 1999; Löw, 2004). The ability of radar to penetrate cloud while operating day and night with global coverage means that SAR has vital applications for military purposes particularly surveillance, reconnaissance and monitoring. Consequently relevant data and specialized image processing software is often unavailable due to barriers including political restrictions, geographic location of user and high costs (Ezeoke & Tong, 2013). Therefore the LSS was used to circumvent this difficulty. The LSS comprised of a standard gain radar horn (SGH) antenna that could operate over 0.8 – 12 GHz, telescopic tripod mount, vector network analyzer (VNA), Styrofoam polystyrene (SFP) box and coated black stand for room measurements. The VNA and SGH are the main components of this system.

7.2.1. Network Analyzer Operation

In general VNA's are used to measure the magnitude and phase characteristics of linear networks relative to a reference or standard (Whitt *et al*., 1990). This is usually performed by carrying out both transmission and reflection measurements to obtain the network characteristics. When a terrain sample is inserted as the test network there are several possible measurements that can be used to characterize the terrain sample such that the network analyzer behaves as a scatterometer (Fig. 7.1). The principles of magnitude-only scatterometers have been discussed by several authors (Ulaby *et al*., 1986; Whitt *et al*., 1990). A basic VNA system consists of (1) a radio frequency (RF) source, (2) an RF to IF converter, (3) an IF signals detector and analog to digital (A/D) converter and (4) a digital microprocessor with display. The VNA based LSS terrain characterization model is shown (Fig. 7.1).

The RF source or sensor was used to supply the incident signal to the terrain rather than a test network. When the terrain is inserted as test device the total wave energy in the system from (3.3) may be modified to consider the transmitted term, $\boldsymbol{E}^{\mathbf{tran}}$ which depends on the extent of the medium:

$$\boldsymbol{E}^{\mathrm{tot}} = \boldsymbol{E}^{\mathrm{inc}} + \boldsymbol{E}^{\mathrm{ref}} + \boldsymbol{E}^{\mathrm{abs}} + \boldsymbol{E}^{\mathrm{tran}} \tag{7.2}$$

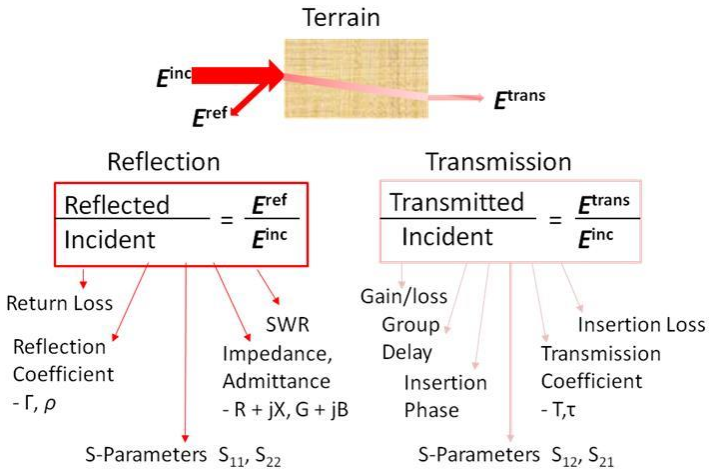

Figure 7.1: Terrain characterization model with possible measurements.

The signal from the RF source, $\boldsymbol{E}^{\mathbf{inc}}$ is coupled to free space with the SGH antenna rather than a coaxial cable or waveguide and travels through the air medium to the terrain samples where it may be absorbed, $\boldsymbol{E}^{\mathbf{abs}}$ in addition to being transmitted or reflected. The signal reflected from the terrain, $\boldsymbol{E}^{\mathbf{ref}}$ is received by the SGH antenna after separating transmitting and receiving channels or another antenna for a dual antenna system. The backscattered field, $\boldsymbol{E}^{\mathbf{ref}}$ is a perturbation that occurs when the terrain body is introduced in to the incident field that previously existed in space. In forward scatter alignment (FSA) convention the polarization unit vectors are considered relative to the propagating wave but in the backscatter alignment they are defined relative to the radar antenna (IEEE, 1983). Therefore the horizontal, $\boldsymbol{h}$ and vertical $\boldsymbol{v}$ component of the incident wave, $\boldsymbol{E}^{\mathbf{inc}}$ is given by (Kuga *et al*., 1990):

$$\boldsymbol{E}^{\mathbf{inc}} = \boldsymbol{E}^{\mathbf{inc}\text{-}}\boldsymbol{v} + \boldsymbol{E}^{\mathbf{inc}\text{-}}\boldsymbol{h} \tag{7.3}$$

While the backscattered wave, $\boldsymbol{E}^{\mathbf{ref}}$ may be written as:

$$\boldsymbol{E}^{\mathbf{ref}} = \boldsymbol{E}^{\mathbf{ref}\text{-}}\boldsymbol{v} + \boldsymbol{E}^{\mathbf{ref}\text{-}}\boldsymbol{h} \tag{7.4}$$

Therefore the scattering matrix, S from (6.4) may be rewritten in terms of the components of the incident and scattered fields. Where R is the distance from the scatterer to the receiving antenna and k_0 (= $2\pi/\lambda$) is the wavenumber of the illuminating wave, then the backscattering will be (Van de Hulst, 1981):

$$\boldsymbol{E}^{\mathbf{ref}} = \frac{e^{ik_{0R}}}{R} S\boldsymbol{E}^{\mathbf{inc}} \tag{7.5}$$

Although (7.4) was defined for simple point targets such as spheres, dihedral, planar or corner reflectors, it was used for investigation of terrain samples with the LSS. This is because for the validation study, the terrain samples were placed in (1) SFP boxes over a terrain pit for the open room experiment and (2) SFP boxes alone in the anechoic chamber using the measurement configuration shown (Fig. 7.2). The sharp sand in the terrain pit covered 1 m x 1 m x 0.2 m (length x breadth x height - LBH) but the SFP boxes were 0.468 m x 0.368 m x 0.3 m (LBH) and 0.564 m x 0.4 m x 0.352 m (LBH) external dimension. The plastic box that contained VOS was 0.55 m x 0.37 m x 0.36 m in the open room experiment (Fig. 7.2a).

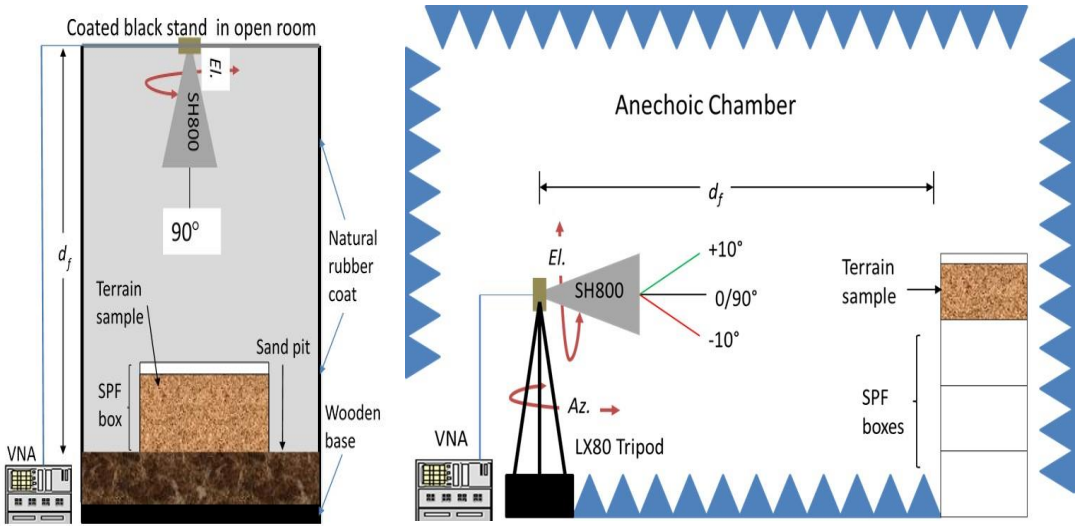

(a) (b)

Figure 7.2: Configuration of measurement system for acquisition of L-, C- and X-band terrain scattering (a) Coated black stand in open room (b) Anechoic Chamber.

The scattering amplitudes of the complex scattering matrix, S for the individual terrain types was a function of frequency, f, incident geometry, θ_i, reflecting angles, θ_r, and the target aspect angle (TAA). Each element is therefore represented as (Kuga *et al.*, 1990):

$$S = S_{pq}(\theta_{\text{ref}}\, \phi_{\text{ref}};\ \theta_{\text{inc}}\, \phi_{\text{inc}};\ \theta_{\text{TAA}}\, \phi_{\text{TAA}}) \tag{7.6}$$

Here (θ_{TAA}, ϕ_{TAA}) is the orientation angle of the scatterer with respect to the antenna. The surface normal of the terrain targets (+ z) are listed in Table 7.1. Since the

SPF box was emplaced on a base of sharp sand covering 1 m x 1 m (LB), there was an overlap in backscattering from the sharp sand in the open room experiment. This was filtered out in the post processing when necessary by measuring the backscattering from the sharp pit sand alone, then with the SPFB box without terrain and finally with the terrain samples.

Table 7.1: Surface normal of terrain targets in SPFB

Scatterer	Anechoic Chamber (LH)	Coated Black Stand (LB)
MUT A	0.42 m x 0.25 m	0.42 m x 0.32 m
MUT B	0.42 m x 0.25 m	0.42 m x 0.32 m
MUT C	0.42 m x 0.25 m	0.42 m x 0.32 m
MUT D	0.42 m x 0.25 m	0.42 m x 0.32 m
MUT E	0.51 m x 0.30 m	0.51 m x 0.35 m
MUT F	0.51 m x 0.20 m	0.50 m x 0.35 m

The surface normal is important because it is the view that causes the most reflection to the sensor. Typically the two port device in RF circuits is used to describe the device under test (DUT). When applied to the terrain MUT it could be described by four scattering parameters S_{11}, S_{21}, S_{22} and S_{12}. The relationship between incident and reflected waves for the two port model when the terrain body is introduced in to the field is presented (Fig. 7.3).

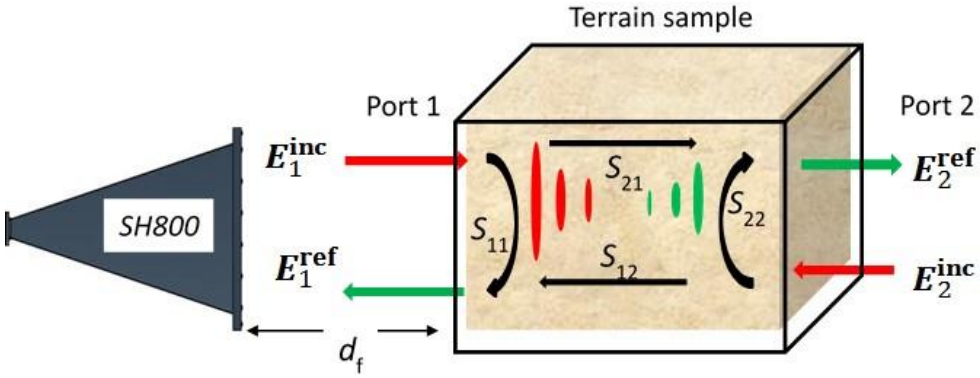

Figure 7.3: Two-port S-parameter schematic model showing SH800 antenna, terrain in SPF box holder with monostatic (S_{11}, S_{22}) and bistatic (S_{12}, S_{21}) configuration with transmitted and reflected waves.

The reflected wave $\boldsymbol{E}^{\mathbf{ref}}$ for both ports is given by:

$$\boldsymbol{E}_1^{\mathbf{ref}} = S_{11}\boldsymbol{E}_1^{\mathbf{inc}} + S_{12}\boldsymbol{E}_2^{\mathbf{inc}} \qquad (7.7)$$

$$\boldsymbol{E}_2^{\mathbf{ref}} = S_{21}\boldsymbol{E}_1^{\mathbf{inc}} + S_{22}\boldsymbol{E}_2^{\mathbf{inc}} \tag{7.8}$$

It can also be described by a matrix equation:

$$\begin{bmatrix} \boldsymbol{E}_1^{\mathbf{ref}} \\ \boldsymbol{E}_2^{\mathbf{ref}} \end{bmatrix} = \begin{bmatrix} S_{11} & S_{12} \\ S_{21} & S_{22} \end{bmatrix} \cdot \begin{bmatrix} \boldsymbol{E}_1^{\mathbf{inc}} \\ \boldsymbol{E}_2^{\mathbf{inc}} \end{bmatrix} \tag{7.9}$$

In the monostatic case $\boldsymbol{E}_2^{\mathbf{inc}} = 0$, therefore the S_{12} and S_{22} have no effect and (7.9) simplifies to:

$$\begin{bmatrix} \boldsymbol{E}_1^{\mathbf{ref}} \\ \boldsymbol{E}_2^{\mathbf{ref}} \end{bmatrix} = \begin{bmatrix} S_{11} \\ S_{21} \end{bmatrix} \cdot \left[\boldsymbol{E}_1^{\mathbf{inc}}\right] \tag{7.10}$$

From (6.13), a longer far field distance, d_f between the sensor and terrain is required at low microwave frequencies. However by using the wide band horn antenna this limitation was overcome so that the terrain was placed at 10 λ away. This varied from 2m in the open coated stand to 4m in the anechoic chamber. The main system driver is the UWB antenna and VNA characteristics (Ezeoke *et al*., 2014c).

7.2.2. Measurement Campaign and Imaging Scenarios

Three measurement scenarios were implemented. Scenario 1 was the general terrain response while scenario 2 and 3 were the SAR scatterometer profile and incident geometry effect respectively. The first and second involved the LSS on a natural black rubber coated stand with an underlying sandpit in an open room while the third had the LSS set up in an anechoic chamber (Fig. 7.2). The black coat is 6mm thick and made of natural rubber to act as a microwave absorbent layer while the sharp sand in the open pit was composed of sand, small pebbles and silicon to resemble under-surface terrain. The measurement system consisted of the SATIMO Dual Ridge reference horn SH800 wideband antenna which can operate over 0.8 – 12 GHz and terrain samples in the SPF box for both configurations. The SH800 was used as both transmitter and receiver at port 1 of the Spectrum Analyser for the open room scenario 1 and 2 measurements. For scenario 3 the SH800 was connected to the VNA in the anechoic chamber.

The Spectrum analyser and VNA were used as the RF and IF processor when connected to a laptop PC for automatic control. Both HH and VV polarizations were investigated. Previous work measured the RCS of rough surfaces using fully polarimetric radar ranges operating at 100 GHz and 240 GHz with actuated stepper

motors to control the azimuth (Az.) and elevation (El.) of the MUT (DiGiovanni *et al*., 2013). Rather than adjust the position of the terrain target (MUT) which differs from real airborne or satellite radar we have previously varied the antenna elevation using the LX80 tripod mounts (Ezeoke & Tong, 2013). However the volume, ∂V of terrain investigated earlier was smaller 0.013 m^3 with a surface normal: 0.15m x 0.368m. Also only MUT A, MUT C, MUT D and MUT E were studied without any underlying bottom layer. Therefore the measurements were expanded to consider the open room case with corresponding 'bedrock' layer made of sharp sand, while an extra 64 kg of terrain particularly oil sands from Nigeria were acquired in 2014.

In the open room measurements (Fig. 7.2a) the coated black stand dimension was 2 m x 1 m x 1 m and the underlying sand pit reached a depth of 0.2 m (20cm). The SGH antenna was placed on an aluminum horizontal stand which was wedged on SPF pads for extra height and stability. In the Anechoic chamber the Hewlett-Packard 85052D calibration system, Rohde & Schwarz ZNB40 VNA and Meade Instruments LX80 tripod and telescopic mounts were configured as shown (Fig. 7.2b).

7.2.2.1 Barefaced Terrain

The terrain samples roughly occupied $\partial V = 0.034$ m^3 but when considered with the sharp sand base doubled to 0.06 m^3 which is less than the CEM $\partial V = 1$ m^3. The materials studied included beach sand (MUT A), loamy farm soil (MUT B), pebbles (MUT C), gravel (MUT D), hard oil sand (HOS) (MUT E) and viscous oil sand (VOS) (MUT F). They were investigated across L-band (1 - 2 GHz), C-band (5 – 7 GHz) and X-band (8 GHz) as well as incident geometry θ_i from +20° to -20°. MUT A to MUT E were held in SPF boxes. These polysterene boxes had a measured dielectric permittivity, $\varepsilon_r = 1.03$ and were used both as support stand in the anechoic chamber and holding container. This is an improvement on (DiGiovanni *et al*., 2013) because with ε_r close to air ($\varepsilon_r = 1$), they permit unhindered passage of EM waves with negligible effect on scattering. The dielectric permittivity of the SPF boxes were measured using Agilent dielectric probe kit.

In the natural black rubber coated stand open room nadir measurements the antenna points downwards and only the edge of the boxes are 'seen' by the sensor. The empty SPF boxes were also illuminated on the open pit terrain to act as reference. MUT F was in a plastic box measuring 0.55 m x 0.37 m x 0.36 m for the open room measurement due to the difficulty in handling VOS while the VOS terrain itself

occupied 0.50 m x 0.34 m x 0.18 m. It was however put in an SPF box for the anechoic chamber measurement and discarded afterwards.

7.2.2.2 Coated Black Stand

The basic open room measurement using the coated black stand set up is shown (Fig. 7.4) while the measurement sequence is at Appendix 7. For the natural rubber coated black stand or open room measurements, the Rohde & Schwarz FSH8 spectrum analyzer and 3.65mm high performance SUCOFLEX-100 microwave cable were calibrated with FSH Z28 calibration kit.

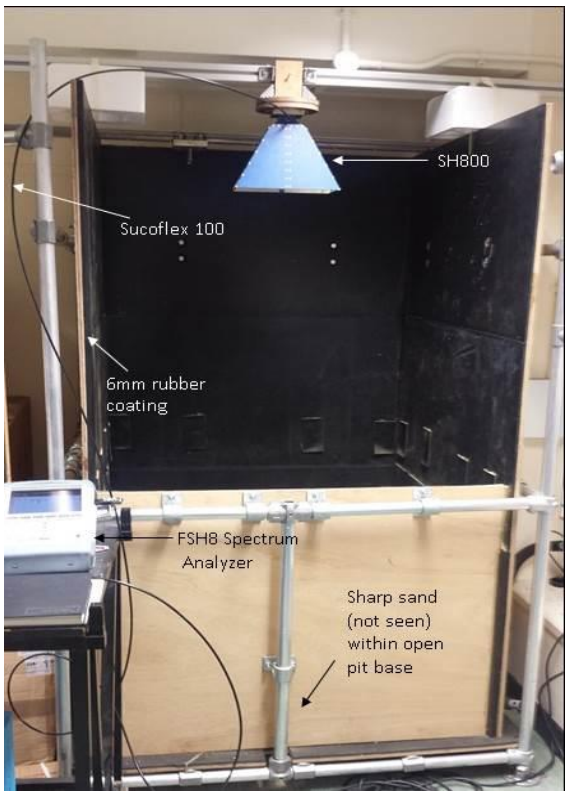

Figure 7.4: Measurement set up for natural rubber coated black stand nadir geometry measurements (terrain pit with sharp sand and terrain samples not seen).

One port calibration for open, short and load (OSL) was performed. The FSH stimulus was set to sweep in steps of 10 kHz resolution bandwidth (RBW) covering 0.9 – 8 GHz. Altogether 48 datasets were acquired with each measurement performed twice for Scenario 1 but 336 datasets were acquired for Scenario 2. Data files from the FSH8 Spectrum analyzer were received as *.set files and processed using the FSH4 viewer which is a proprietary analyzer software from Rohde and Schwarz before post-processing in MATLAB® software (MATLAB, 2012b).

7.2.2.3 Anechoic Chamber

The basic measurement set up is presented (Fig. 7.5) while sequence indicating how the 88 datasets were acquired is presented at Appendix 7. In addition to LSS components a Rohde & Schwarz ZNB40 VNA, Hewlett-Packard 85052D calibration system and 5mm flexible copper-cored LBC 195-1 low loss coaxial cable were used. For uniformity, the stimulus was set to $f = 0.9 – 8$ GHz as in open room measurements and one port calibration for short, open, load and through (SOLT) performed.

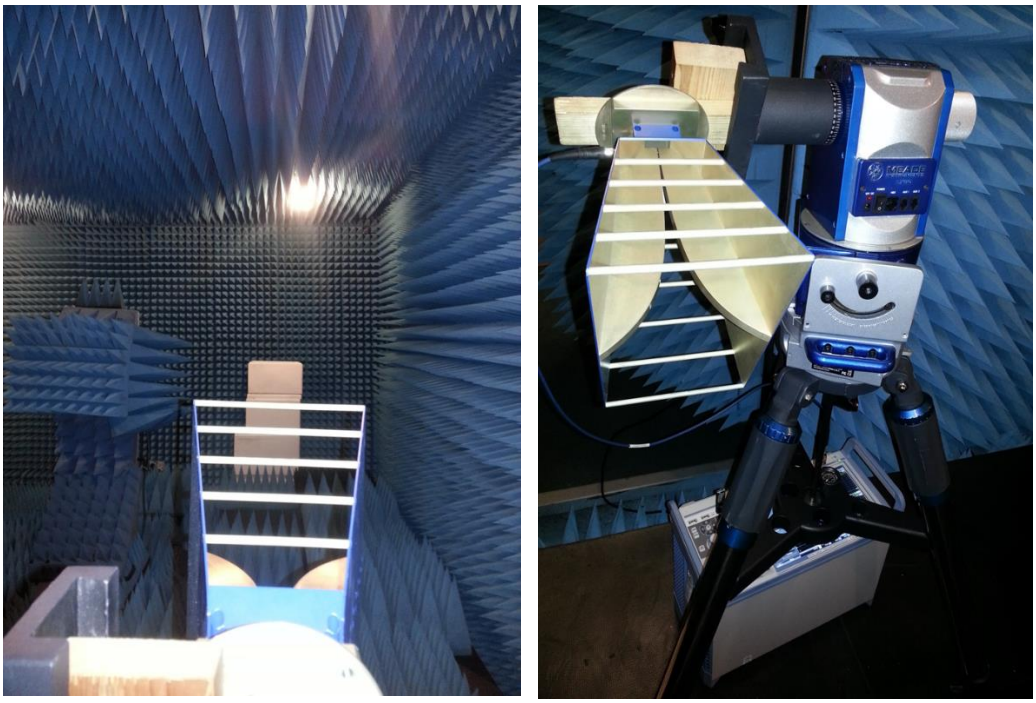

(a) (b)

Figure 7.5: Measurement set up anechoic chamber (a) Rear view: SH800 facing terrain in SPFB (white box) (b) Front view: SH800 (HH polarization) on LX80 Tripod and connected to VNA beneath.

The VNA stimulus was also set to sweep in steps of 10 kHz resolution bandwidth (RBW) covering 0.9 – 8 GHz. The main aim of the chamber was to permit the calibrated change in geometry measurements using the LX80 tripod mounts. Data files from the ZNB40 VNA were acquired in *.s2p format, imported in to Excel and uploaded as *.txt in to MATLAB software for processing (MATLAB, 2012b).

7.2.2.4 Calibration

In the LSS measurement, errors could occur due to noise and interference reflections from the room environment, instrument internal drifting errors, cabling and

system connections. Accurate calibration with standard targets were completed before performing the sensitive measurements. Cable effects were accounted for by internal calibration of the system and cabling prior to connection with the sensor. Planar, dihedral and trihedral reflectors coated with aluminum were used to calibrate the results for both co-polarized horizontal transmit, horizontal receive (HH) and vertical transmit, vertical receive (VV) S-parameter measurement (Fig. 7.6). The calibration of polarimetric radar systems has been well researched. A technique introduced by Riegger *et al*., (1987) characterizes system errors in terms of coupling coefficients between aspects of the theoretical and measured scattering matrix while the method proposed by Sarabandi *et al*., (1990) calibrates the cross talk errors by measuring any arbitrary depolarizing target.

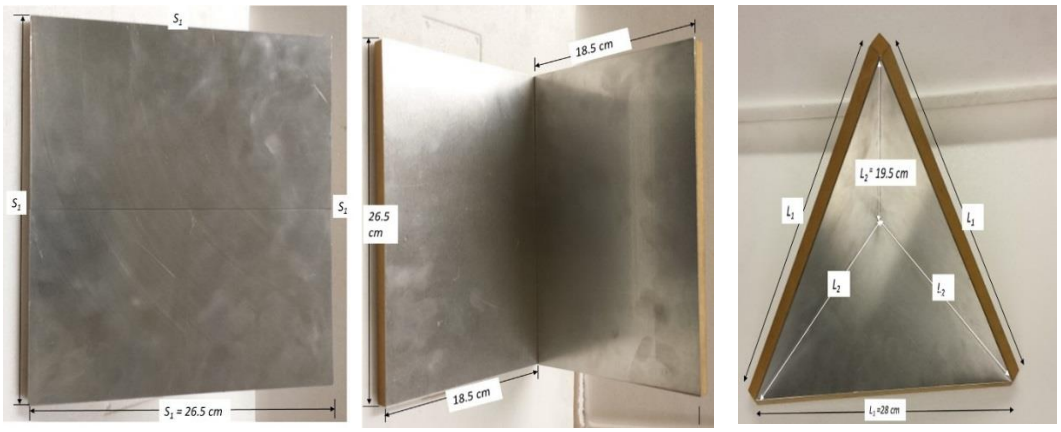

(a) (b) (c)

Figure 7.6: LSS Calibration Targets (a) Planar (b) Dihedral (c) Trihedral.

In this work the reflectors were used as non-depolarizing targets to correct for co-polarized channel imbalance and absolute magnitude errors. They were measured to determine the distortion matrices that characterize the effect of the measurement system on the VNA trace which represents the transmitted and received waves. The background scattering matrix $\bar{\boldsymbol{B}}$ which represents the direct scattering measured by removing the target, raw measurement of the targets represented by scattering matrix $\bar{\boldsymbol{M}}$ and the target scattering matrix $\bar{\boldsymbol{N}}$ are related by: $\bar{\boldsymbol{N}} = \bar{\boldsymbol{M}} - \bar{\boldsymbol{B}}$. In practice the scattering signatures of the system components were zeroed out by normalizing background trace. Details of this generalized calibration technique (GCT) approach and how the actual scattering matrix $\bar{\boldsymbol{P}}$ was obtained has been discussed (Whitt *et al*., 1990). For cross-polarization coupling errors, unknown targets would be required however

only co-polarized operation of the LSS was considered. The co-polarized calibration is generally more straightforward than cross-polarization (Dubois & van Zyl, 1994).

7.3. Terrain Backscattering

A conventional radar scatterometer measures the radar returns as a function of range with returns isolated for each range using time gating (Ulaby *et al*., 1988). With the LSS the backscattered power as a function of frequency, f for the different terrain types placed in the SPF boxes at distance $r \geq 10\ \lambda$ was measured. Also rather than time gated responses the frequency response (loss return) due to the interaction of the small volume, ∂V of terrain with transmit and receive antenna was considered. In this way the received power ratio P_r/P_t (or S_{11}) versus frequency (0.9 – 8 GHz) from (7.1) was determined, as well as the phase values. For identification of sensor geometry effects at further distances ($r > 20$ m), a scatterometer requires fine angular resolution (Ulaby *et al*., 1988). This may be achieved with a small-beamwidth antenna necessitating an increase in antenna aperture size. This need was avoided by careful selection of d_f and use of the Tripod mounts to alter θ_i in elevation (look angle).

Four aspects of the validation results will be highlighted. First the preliminary system response without terrain is considered and compared to the radar model in open space. This effect has to be 'zeroed' out in order to obtain the terrain reflectivity alone then the general terrain response will be discussed in light of three reflectivity scenarios.

7.3.1. Preliminary Results

The performance of the LSS was measured without any terrain obstruction in the open air for room environment and anechoic chamber then compared with the radar model sensor simulation (Fig. 7.7). The radar model sensor (Table 6.4) was developed using CST MWS (2014). The simulation results compare favorably with the measured results. The return loss here indicates the pass band of the simulated radar system using the UWB horn antenna and the LSS using an optimized SATIMO SGH SH800. Both were below -10 dB meaning that more than 90% of the energy is used by the simulated and measured systems. For both simulated and measured results they have a pass band from 1 to 8 GHz. At low frequencies below 3 GHz, the S_{11} results for the LSS in the open room environment and anechoic chamber was similar. However at higher frequencies the performance within the chamber is marginally better than in open air.

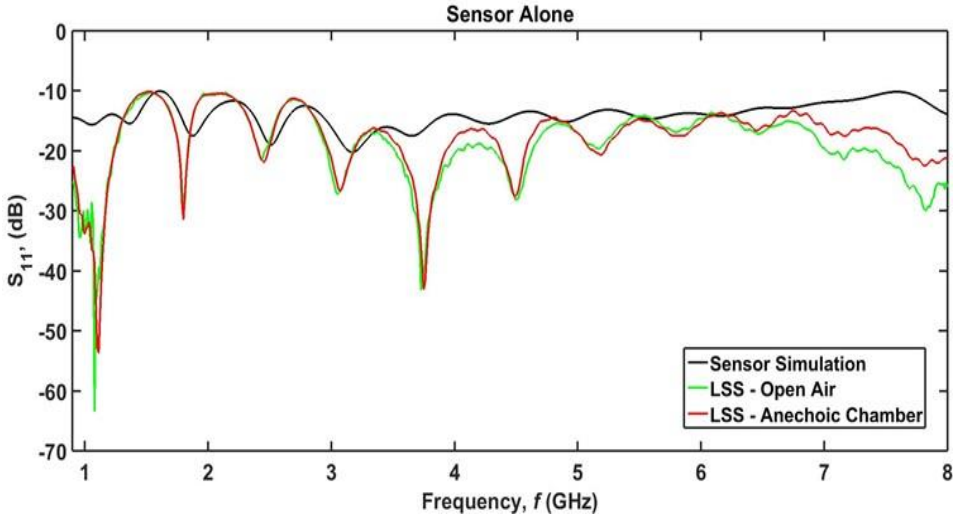

Figure 7.7: S_{11} with frequency. Electrical performance of LSS in anechoic chamber and open air without any terrain compared with simulation.

Also the backscattering at L-band was higher than at higher frequencies such as C- or X-band (8 GHz). This was considered as the measured noise background level and was subtracted from the measured soil backscatter data coherently to improve the signal to noise ratio (Oh *et al*., 1992). The measurement of the dielectric properties of the SPF box using a coaxial probe also indicated an average dielectric permittivity ε_r = 1.02 (Fig. 7.8). The loss tangent, tan δ was also very low (average 0.001). Together both mean that the SPF boxes which were used as stand and holding device did not significantly affect the measurement result as the incident EM waves passed through with minimal reflection and absorbance.

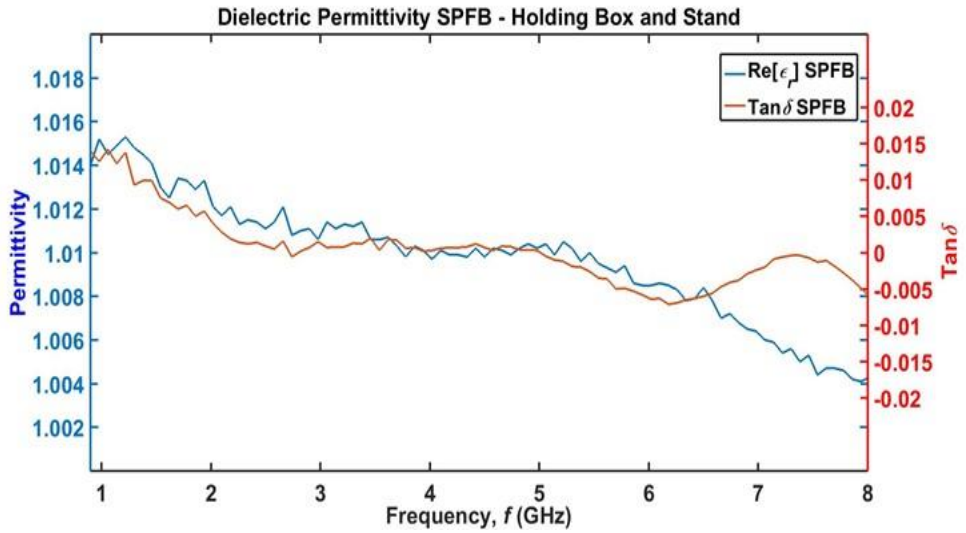

Figure 7.8: Measured dielectric permittivity of Styrofoam Polystyrene Foam box which is used as sample stand and holding box.

7.3.2. Scenario 1: General Terrain Response

In characterizing the behavior of the terrain with the LSS both the manner in which the returns change with time and the distribution of the signal return power with frequency was determined. Fortunately both frequency domain representation and time domain representation can be interchanged. The inverse Fourier transform converts the frequency domain function to a time function while the Fourier transform does the opposite. Techniques such as frequency domain and time domain analysis which have applications to geology, remote sensing and image processing were required to achieve high sensitivity and noise immunity over the broadband range. One preliminary method employed was the intermediate frequency (IF) bandwidth control which can limit overall receiver noise power (Zhang *et al*., 2010). Here a narrow IF bandwidth of 10 kHz was used. A 20 *ns* passband window which corresponds to a 3 m round trip distance was applied to the transformed time domain signal but only the 12 *ns* passband window was centered on the distance to the terrain target. In order to avoid aliasing and maintain an adequate range resolution with the frequency span of 7.1 GHz the alias free range was given by:

$$R_{\max} = \frac{v_{\mathrm{p}}}{\Delta f}, \tag{7.11}$$

Where v_{p} is the phase velocity of light in the specific propagation media (air = 3 x10^8 ms^{-1}) and Δf is the frequency step size related to the total frequency span in GHz, ΔF. The relationship between the frequency step size and the number of data points in the frequency domain N is given by:

$$\Delta f = \frac{\Delta F}{N-1}. \tag{7.12}$$

For the LSS the number of data points was set to 631 meaning that up to 27 meters of alias free measurement could be obtained. This was sufficient to cover the measurement range and provide good data resolution over frequency span of 7.1 GHz. In this way mathematical transformation of the reflectivity response of the data from the frequency domain to the time domain was performed using MATLAB software.

Polarization refers to the direction of the electric vector in an EM wave. It has been used as a useful discriminant in SAR image analysis (Brisco & Brown, 1998). For microwave radar applications the linear applications of horizontal (H) and vertical (V) polarization states for transmit and receive antennas give the HH, VV, HV and VH connotations. From reciprocity HV = VH (cross polarization) while VV and HH are the

copolarization. The LSS in the present configuration considered only co-polarization effects (HH and VV). The co-polarized average time domain signature response for the barefaced terrain is presented (Fig. 7.9). A moving average convolution was used to smooth the data sets. In the measurement HH occurs when the long side of the SPFB with terrain is aligned with the long side (H plane) of the SH800 antenna. VV mode corresponds to the short side of the antenna (E plane) aligning to the long side SPFB.

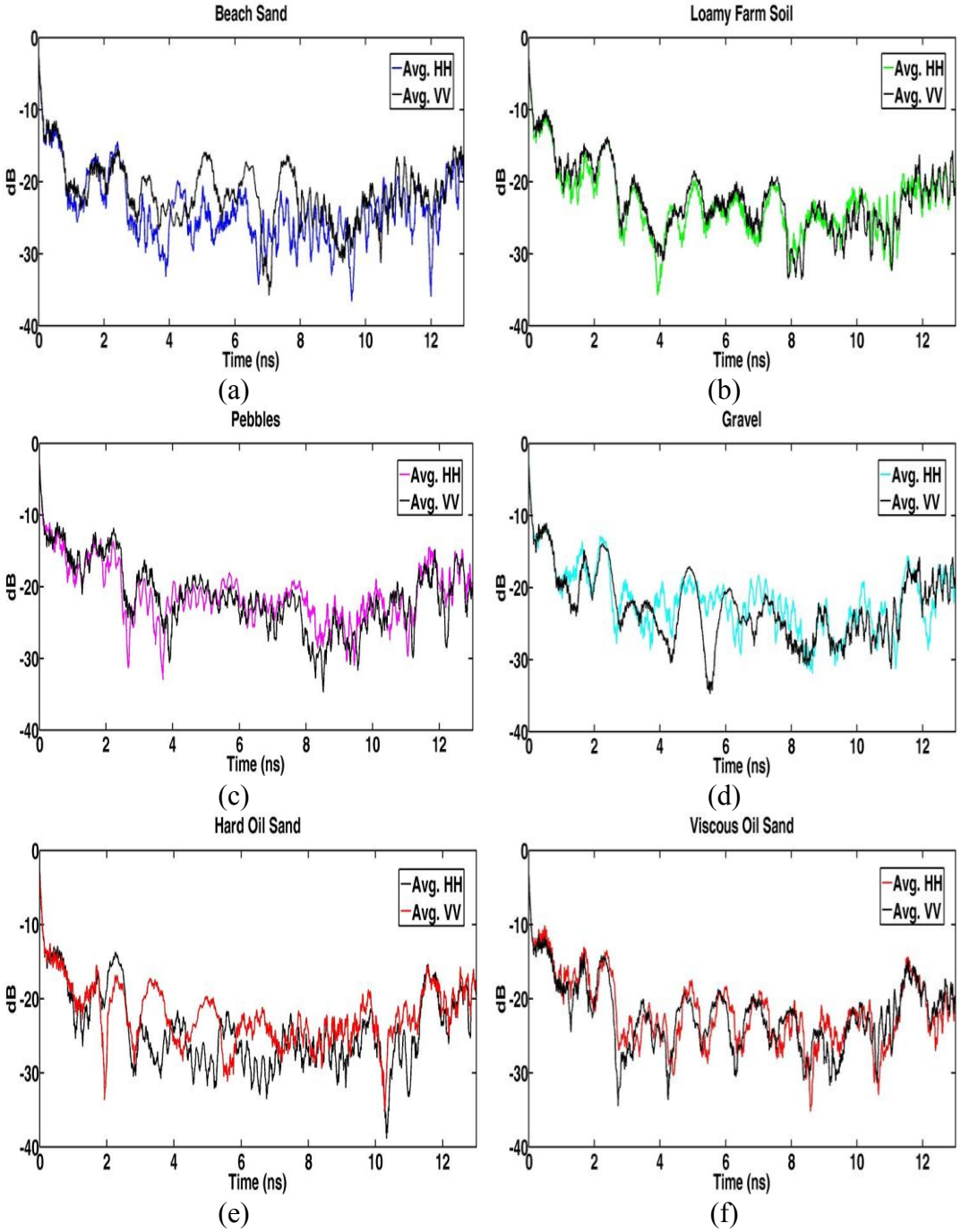

Figure 7.9: Barefaced terrain Time-Domain signature nadir imaging ($\theta_i = 90°$) (a) Beach Sand (b) Loamy Farm Soil (c) Pebble (d) Gravel (e) HOS (f) VOS.

The time domain signature for the 6 barefaced terrains helps establish the measurement accuracy as well as the response behavior (Zhang *et al*., 2010). Especially as the time domain is preferred for studying the response from wide bandwidth or transient systems such as UWB (Schantz, 2005).

In (Zhang *et al*., 2010) the time domain signature was used with a laboratory scatterometer to identify the polarimetric EM signature of icy hydrometers. Here the response behavior was considered along the signal spectrum path and over the range gate covering the terrain. Considering the HH response for VOS as the base response, all the terrain types display visible peaks at times corresponding to the expected distances from the sensor. The magnitudes seem visually comparable for pebbles, gravel, HOS and VOS at 12 ns HH but not for beach sand and loamy farm soil, therefore a statistical comparison was performed.

For measurements performed at 95 GHz the VV and HH polarized levels of backscattering have been found to be within 2 dB of each other (Ulaby *et al*., 1998). This was not true in this case. The VV time signature was not similar to HH because the orientation of the SPF box surface containing the terrain was changed. The magnitude variation in dB response suggested that depending on the surface roughness, terrain is anisotropic and therefore polarization sensitive to varying degrees.

The statistical strength of the linear association between the measured time domain signatures along the entire signal path and at the terrain point (11.5 - 12.6 ns) for each terrain type compared with VOS HH was derived using the Pearson correlation coefficient (PCC) given in (5.26) and presented in Table 7.2.

Table 7.2: Statistical comparison of Time Domain Signature response using PCC

MUT	**Entire signal path**		**Terrain**	
	HH	**VV**	**HH**	**VV**
MUT A	0.613	0.536	0.34	0.42
MUT B	0.729	0.725	0.81	0.875
MUT C	0.732	0.687	0.85	0.65
MUT D	0.828	0.829	0.82	0.87
MUT E	0.71	0.675	0.91	0.86
MUT F	1	0.85	1	0.91

The statistics software was used (Wessa, 2014). For loamy farm soil and gravel there was stronger correlation between HH and VV returns due to the orientation of smaller irregular scatterer embedded within. Importantly at the 12 ns point both HOS

and VOS had identical scattering peaks indicative of the similar intrinsic properties. This was different when the entire signal path was considered due to the effect of surface roughness on backscattering. This was also seen to a lesser extent in pebbles and gravel terrain.

7.3.3. Scenario 2: Scatterometer SAR Profiling

In the CEM models it was possible to place probes at different layers of terrain to observe both the surface and volume backscattering. This is not typically possible with real SAR imaging from airborne or spaceborne platform therefore Scenario 1 was extended to collect and process high azimuth resolution SAR measurements. It was achieved by moving the sensor linearly over the barefaced terrain with the horn antenna sensor at cross range, y intervals (∂Az.) of 1cm along the track length for a distance of 55cm. Geometry showing modifications to Scenario 1 to obtain high azimuth resolution (SAR) measurement is presented (Fig. 7.10).

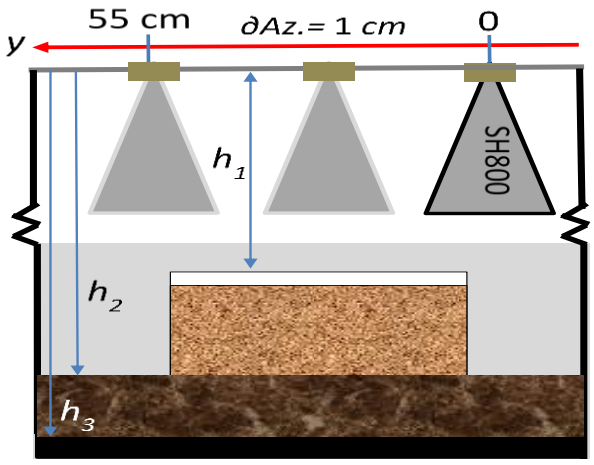

Figure 7.10: Schematic of SAR Scatterometer Measurement with LSS.

In essence 56 antenna measurements were captured for each of the 6 barefaced terrain types then the 336 datasets were processed using a time delay SAR algorithm. This enabled development of 1cm Az. resolution image of the 6 barefaced terrain types while presenting the terrain scattering matrix as a two dimensional reflectivity scene. The typical radar scatterometer measures the Fourier transform of echoes observed from a given viewing angle. The SAR technique combines views along the synthetic aperture to improve azimuthal resolution. Unlike ground penetrating radar or single point targets there are several possible scatterers in the scene. The closest point of

approach (CPA) to the antenna track, h for each scatterer can be considered as h_1, h_2 and h_3 respectively for the terrain target, the sand pit layer and the wooden base. The two way range to the target R_{2w} in (7.13) and (7.14) considers the along-track Az. distance the antenna moves, y and the center to center distance between the transmitter and receiver antenna separation, d as:

$$R_{2w}(y) = R_t(y) + R_r(y), \tag{7.13}$$

And

$$R_{2w}(y) = \left(h^2 + \left(y - \frac{d}{2}\right)^2\right)^{\frac{1}{2}} + \left(h^2 - \left(y - \frac{d}{2}\right)^2\right)^{\frac{1}{2}}. \tag{7.14}$$

For the monostatic case, $d = 0$ as the same sensor is used to transmit and receive. The range profile at each point from $y = 0$ to 55 cm was merged in to a single coherent image by combining both the amplitude and phase measurement using SAR techniques. The MATLAB code used to present the backscattering from the received echo signal using (6.6), (6.8), (7.13) and (7.14) for each terrain is at Appendix 7.

In the normal image when signal multipath effects are not considered, the only notable feature is the presence of 'ground' echo mirroring for beach sand, loamy farm soil and HOS. The beach sand SPFB started at LSS position, $y = 9$ which is where the ground mirror reflection started (Fig. 7.11).

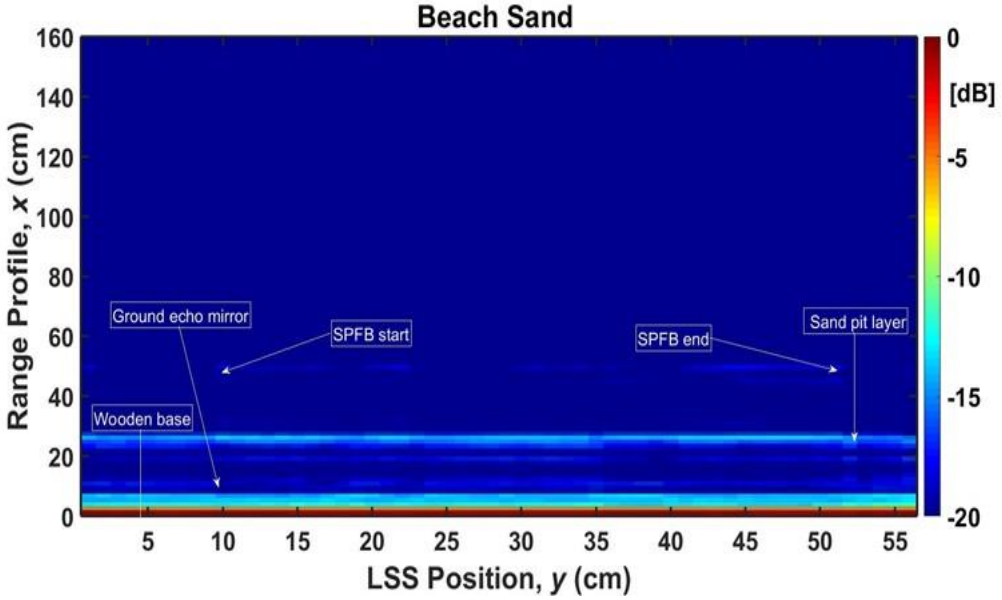

Figure 7.11: Beach Sand echo mirror.

The reflection from the wooden base and sand pit layer can also been seen at range profile distance 0 – 2 cm and up to 22 cm respectively. The latter corresponds to

the actual position of the sharp sand. EM scattering from the sand pit layer was removed from the datasets to better observe the terrain backscatter. Therefore the resulting scene reflectivity for each range profile was due to the effect of sensor and terrain. Visually smooth beach sand acted as a mirror causing low backscatter (Fig. 7.12). This can best be seen from the relatively higher E-field intensities at along track positions (*y*) from 17 - 22 cm and 34 – 40 cm.

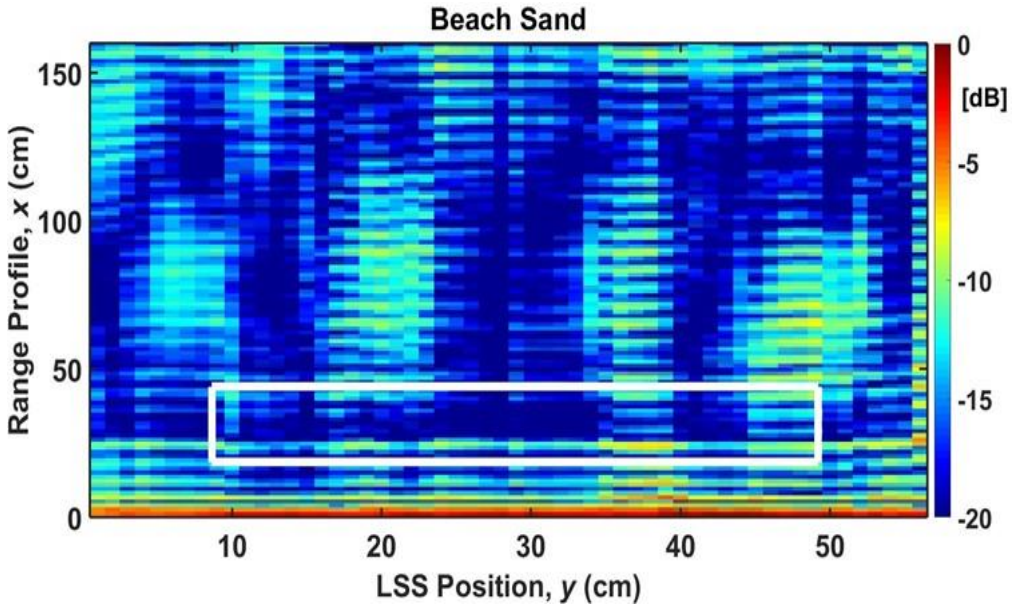

Figure 7.12: Range profile image Beach sand located *y* (9 - 51 cm), *x* (25 - 50 cm).

Along the same along track positions (*y*) from 17 - 22 cm and 34 – 40 cm, loamy farm soil produced higher backscattering intensity than beach sand (Fig. 7.13). This was due to the relatively larger surface roughness of the loamy soil terrain.

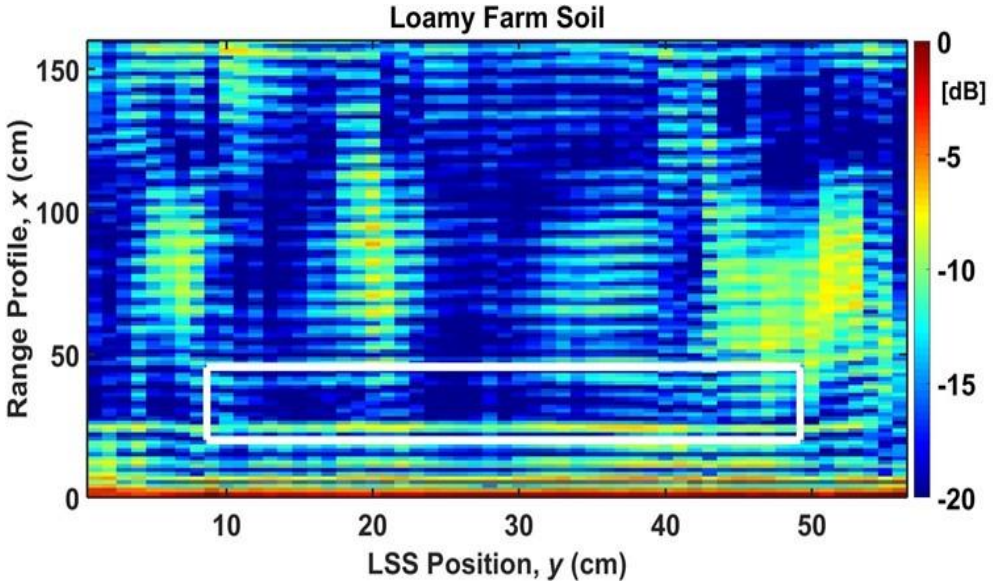

Figure 7.13: Range profile image Loamy Soil located *y* (9 - 51 cm), *x* (25 - 50 cm).

The backscattering from both beach sand and loamy soil was much lower than pebbles or gravel (Fig. 7.14) and (Fig.7.15) respectively. The sensor position at the top of both images also indicates the higher backscattering returns.

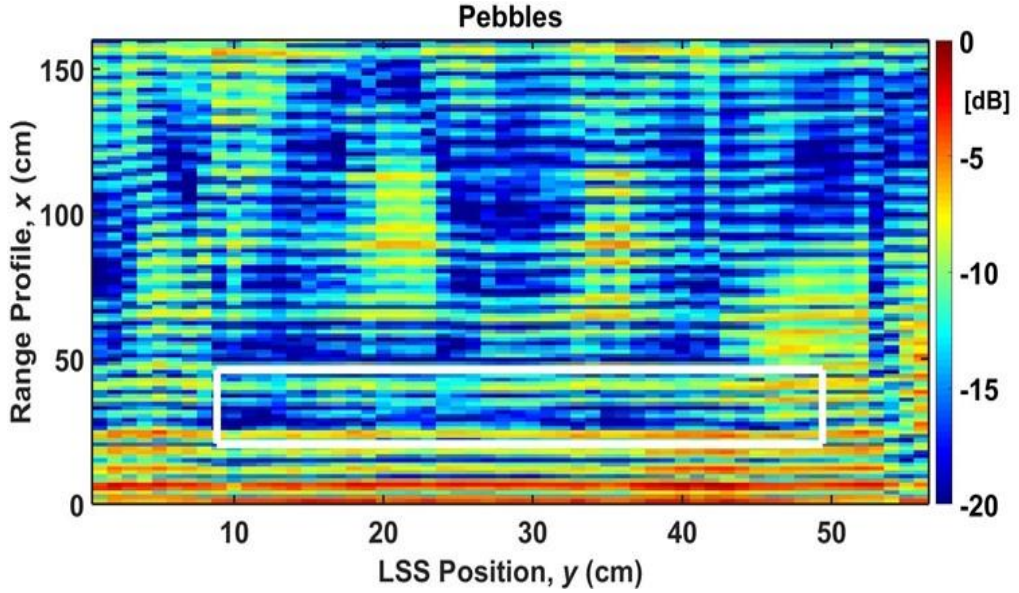

Figure 7.14: Range profile image Pebbles located *y* (9 - 51 cm), *x* (25 - 50 cm).

The backscatter from gravel was of higher intensity and covered a broader sensor range than pebbles due to the larger surface roughness (Fig. 7.15). The wider sensor aperture received both stronger reflected waves and over a wider field of view. This was not effectively shown by the CEM models due to correlation length for fixed position scatterers being longer than actual terrain with increasing surface roughness.

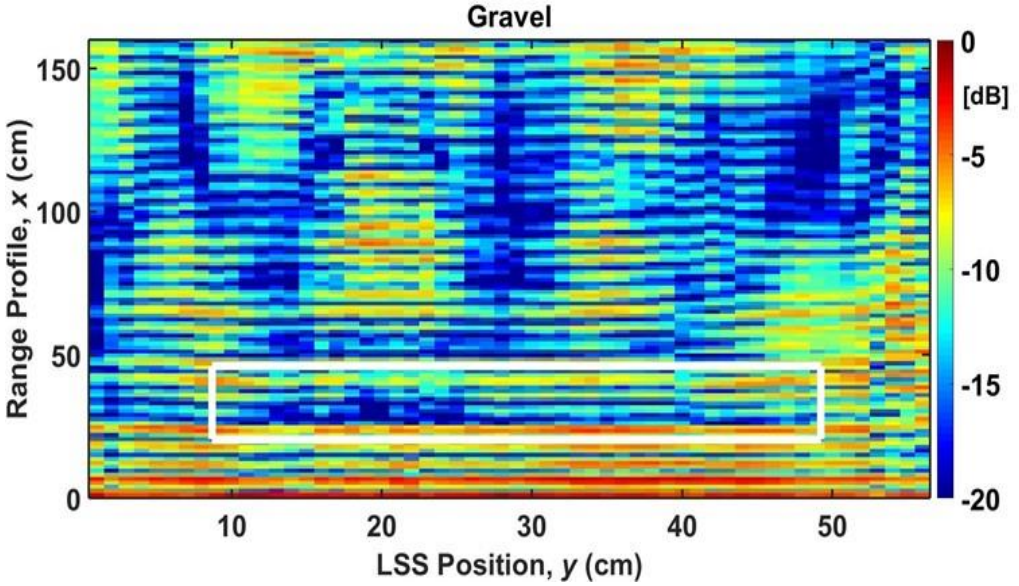

Figure 7.15: Range profile image Gravel located *y* (9 - 51 cm), *x* (25 - 50 cm).

Similar to the CEM results the effect of heterogeneity can be seen in the HOS and VOS results (Fig. 7.16 and Fig. 7.17). Despite the larger surface roughness the effect of sand grains, bitumen and moisture produced diffuse response from HOS (Fig. 7.16). The backscattered returns from HOS were stronger than loamy soil and beach sand but weaker than both pebbles and gravel. However the effect of bitumen and moisture can be seen in the high wave attenuation so that the reflectivity of the wood base is much less than previous terrain results and almost not evident after y = 22 cm.

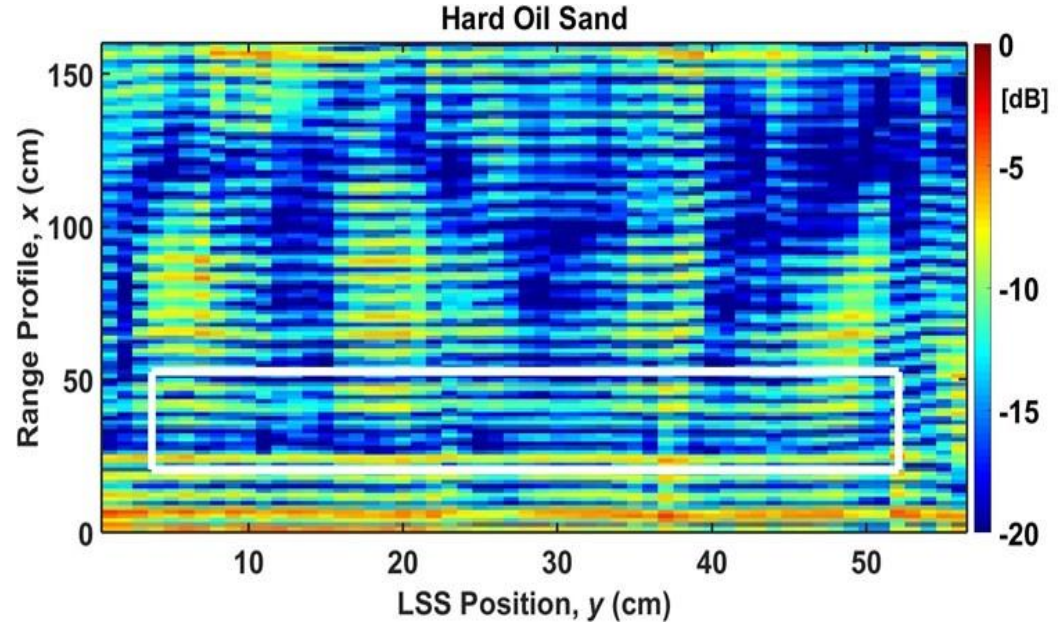

Figure 7.16: Range profile image HOS located y (3 - 54 cm), x (25 - 55 cm).

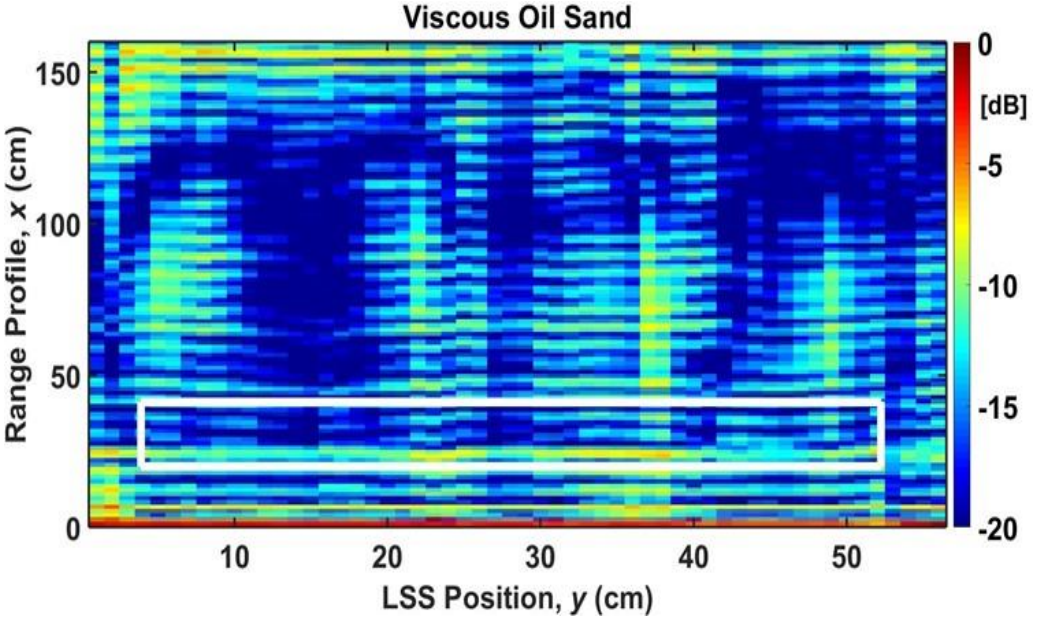

Figure 7.17: Range profile image VOS located y (3 - 54 cm), x (25 - 43 cm).

The effect of moisture on E-field absorption is best seen in the low VOS scattering returns between the terrain and sensor (Fig. 7.17). The intensity of returns at the sensor is higher than both beach sand and loamy farm soil where the visually smooth surfaces cause anisotropic scattering but also not as low as the dielectric permittivity would suggest. Values of the mean backscattering values for the 6 barefaced terrain are presented in Table 7.4 corresponding to the sensor in the middle of the terrain sample location.

7.3.4. Scenario 3: Incident Geometry Effect

The effect of incident geometry was studied by using the LX80 tripod mounts for off nadir imaging in the anechoic chamber. A 10° change in the look direction of the LSS corresponds to very high grazing angle (80°) which is still close to nadir imaging (Fig. 7.18). The mean values of backscattered response for all six surfaces at different incident angles is presented in Table 7.4 and compared to published results for rocks, 'visually smooth sand' and 'visually rough sand' obtained by Whitt *et al*., (1990) at f = 35 GHz and θ_i = 26°. For f =10 GHz and similar grazing angle (10°), Stimson *et al*., (2014) obtained , σ^0 value of -20 dB for desert terrain which is similar to the beach sand value obtained during this study (Ezeoke *et al*., 2013). The data presented in Table 7.3 for θ_i = 90° corresponds to a single measurement when the LSS is pointing towards the center of the terrain while θ_i = 80° has the antenna askew by 10°.

Table 7.3: Mean values of backscatter, σ^0 in dB for all 6 terrain types measured with LSS at two different incident angles

Surface	**Nadir Imaging,** θ_i = 90°		**Off-Nadir,** θ_i = 80°		**Comparison**[a]		
	HH	**VV**	**HH**	**VV**	**HH**	**VV**	**Description**
MUT A	-23.6	-21.32	-20.45	-20.2	-15.2	-12.6	Smooth sand
MUT B	-22.6	-22.1	-22.0	-22.1	-15.2	-12.6	
MUT C	-20.7	-20.1	-19.8	-23.0	N/A		
MUT D	-19.5	-19.4	-18.5	-22.2	-7.5	-7.1	Rocks
MUT E	-21.9	-20.9	-21.7	-20.6	N/A		
MUT F	-21.6	-21.4	-21.1	-20.8	-13.1	-12.1	Rough sand

[a]Whitt *et al*., (1990, pg. 255)

The measurement results obtained here compared favourably with literature and the little discrepancy is due to the wide variation in frequency. The values obtained from the study are suitably lower as should be expected for a centimeter-wave scatterometer compared to the millimeter-wave polarimeter results of Whitt *et al*.,

(1990). In line with the measurement validation results from Scenario 2 (Fig. 7.11 to Fig. 7.17), the magnitude of backscattering for pebbles and gravel were much larger than beach sand and loamy farm soil with the response from oil sand in between.

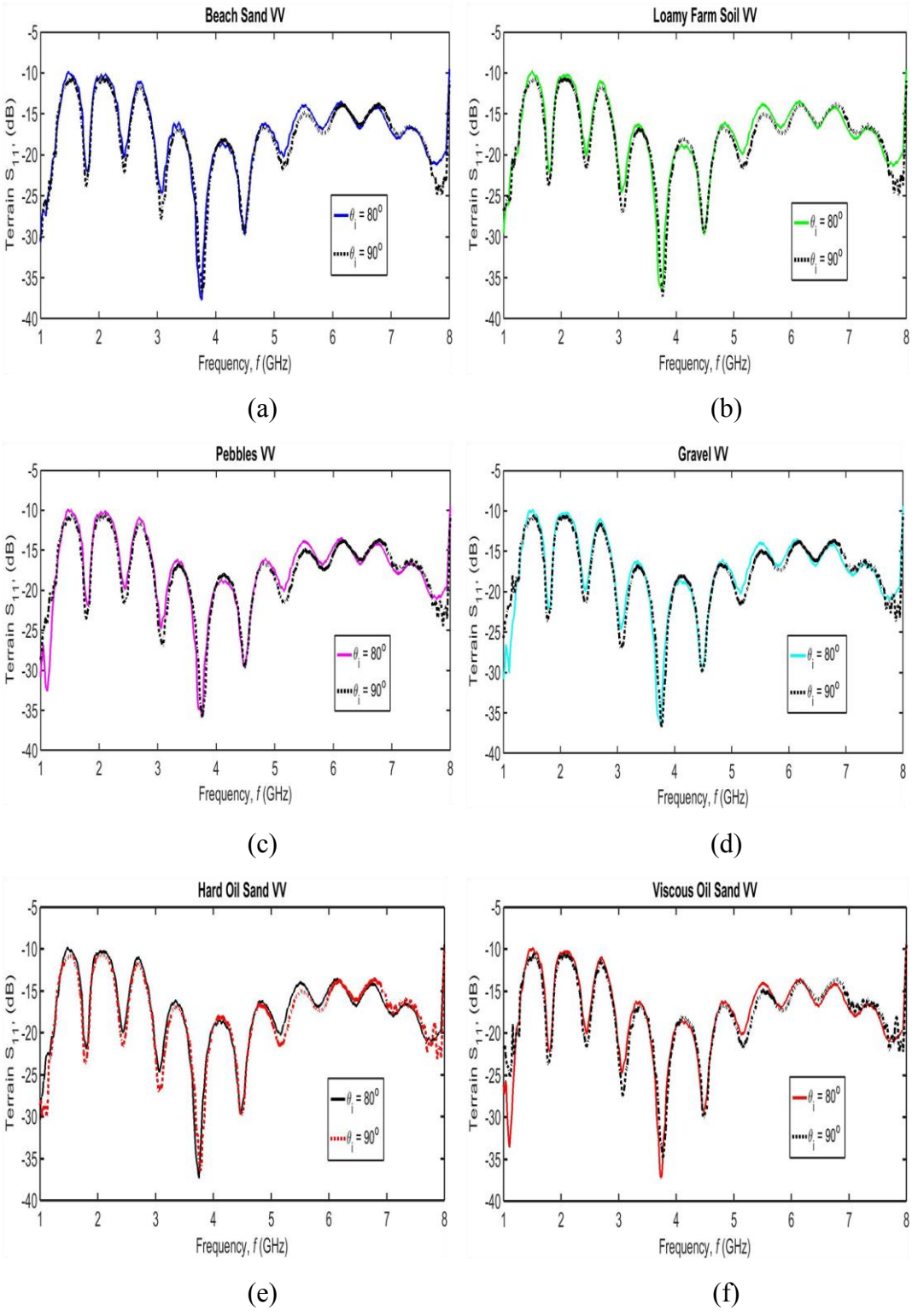

Figure 7.18: Barefaced terrain backscattering response with frequency, f = 1- 8 GHz and imaging geometry, θ_i = 80° and 90° for (a) Beach Sand (b) Loamy Farm Soil (c) Pebble (d) Gravel (e) HOS (f) VOS

Despite the closeness in look angle, the effect of a 10° change in sensor position relative to terrain, caused tangible response in the magnitude of backscattering for both HH and VV polarization, although only the latter is presented (Fig. 7.18). For all the terrain types the nadir imaging (when sensor is pointing straight down at $\theta_i = 90°$) produced less backscatter at low frequencies ($f < 3.75$ GHz). However for $\theta_i = 90°$ greater reflectivity response was seen at higher frequencies ($f > 7$ GHz) when compared to the reflectivity obtained at $\theta_i = 80°$. This is because at low frequencies the EM waves achieve greater penetration than at high frequency in line with the modeling results discussed in Chapter 6. Furthermore less perturbations in the reflectivity were seen for the homogeneous terrain (Fig. 7.18a-b) due to the much lower surface roughness of beach sand and loamy farm soil compared to the other terrain at $f = 7 – 8$ GHz.

7.4. Validation with LSS

Expressions such as ‘data validation’ or ‘model verification’ in literature connote various meanings that differ from what real validation should encompass. It is impossible or nearly impossible to sample terrain at the scales needed to validate modelling or measurement results. This is because there are either too few samples collected to represent the variability, the samples are too small to represent the average of a pixel or they are collected over too restricted a spatial area to represent image variability (Ustin *et al*., 2004). Therefore it is a difficult task to account for scene variance when using field sensors that look at small areas particularly with wide beam sensors such as the SGH in the LSS.

It must be noted that there was no cause to particularly validate the hyperspectral imaging results. This is because for optical systems the illumination itself is incoherent such that interference effects for contact measurements are not a significant concern (Raney, 1998). For Radar however the image impulse response is typically due to coherent filter operations post-detection so that these interference effects continue in to the final image. This why a scatterometer was used to validate the microwave imaging responses because they act as incoherent radars that simply add the detected returns from a sequence of pulses (Ulaby & Dobson, 1989). This is also known as post detection integration. By setting the VNA to continuous sweep and waiting for stable returns before data capture a large number of ‘pulses’ were summed thereby reducing noise ambiguity and improving the signal to noise ratio.

Sequel to the results capture it was important to compare and contrast CEM modelling with the LSS performance in three areas. The CEM approach entailed the creation of both a barefaced terrain model (BTM) for the different terrain types and sensor models with diverse configurations. For the BTM development, the area extent, volume coverage and terrain structure differed with the LSS (Table 7.4). This was due to the amount of oil sand terrain acquired from Nigeria, size of the SPF holding boxes and structure of the coated black stand structure. Therefore the magnitude of backscatter obtained from the CEM models was consistently higher due to the larger surface area from which the EM scattering echo emanated from.

Table 7.4: Comparison CEM BTMs with LSS based validation

Parameters	**BTM**	**LSS Terrain**					
MUT		**Coated Black Stand**			**Anechoic Chamber**		
		A-D	E	F	A-D	E	F
Elemental area, ∂A (m^2)	1	0.134	0.179	0.175	0.105	0.153	0.102
Elemental volume, ∂V (m^3)	1	0.06	0.09	0.07	0.034	0.054	0.035
Terrain structure	Rigid: 26 surface representations for all 6 classes	Natural: movement of SPF boxes could cause natural realignment of surface roughness but less so for pebble, gravel and HOS.					

The measurement environment and sensors deployed in the CEM and the LSS also differed slightly. The LSS validation was conducted in open room environment using a coated black stand (Scenario 1 and 2) and electrically insulated anechoic chamber (Scenario 3). Therefore there was the possibility of cable and instrument losses with multi-path scattering compounding the results particularly within the coated black stand environment. However scattering from the CEM models were computed within the CST calculation domain, D without any corresponding environmental losses. Furthermore both sensors gain and beamwidth vary. A comparison of the CEM radar model sensor described in Section 6.3.4 with the LSS sensor is presented (Table 7.5). In the absence of terrain the measured and simulated results for the LSS and CEM sensor were found to be largely similar with slight variation at certain frequencies. The discrepancy in the reflection coefficient and bandwidth could be due to the optimization of the SH800 antenna used in the LSS by SATIMO manufacturers.

Table 7.5: Comparison of characteristics of the CEM Radar Model sensor and LSS

Property	CEM Radar Model Sensor	LSS Sensor
Receiver gain[a]	7.5-14.3 dBi	6.25 – 14.5 dBi
Transmitter gain	7.5-14.3 dBi	7 – 15 dBi
Beamwidth[b] (3dB) E x H	87.8-15° x 60.9-30.3°	100-18° x 63-35°
Losses[c]	Nil	0.5 dB
Output power	0 dB	0 dB
Transmitted Waveforms	Gaussian	Trace stimulus

[a]Excluding losses mentioned in this table for the LSS antenna. Also the gain varies with f

[b]Beamwidth varies with f. For model E: 87.8° (1 GHz) to 15° (10 GHz) and H: 60.9° (1 GHz) to 30.3° (10 GHz)

[c]Minor cable and VNA losses in monostatic configuration which are typically corrected during calibration

The free space loss between the measured and simulated results were co-plotted to allow ready comparison in Fig. 7.7. Furthermore the CEM plane wave sensor used an inbuilt CST mathematical representation for the far field propagation. The configuration of the sensor for different incident angles, θ_i was obtained by variation of the relationship between the propagation normal and electric field vector. For the LSS the variation was achieved using an LX80 tripod mount and the range of incident angles limited by the amount of terrain visible from the sensor.

Despite the differences highlighted between CEM modelling and LSS deployment, both studies produced notable findings when terrain was present. The intrinsic property of VOS and HOS, caused identical time domain signatures using the LSS while LSS scenario 2 highlighted the effect of bitumen and moisture in both HOS and VOS at θ_i = 90. For normal sensor incidence, the 'mirror reflection' due to the presence of sand grain was seen in both CEM models (Fig. 6.41, Fig. 6.42, Fig. 6.46) and LSS results (Fig. 7.11). This was also observed singularly for the beach sand, loamy farm soil and HOS terrain types in the CEM models in Chapter 6. The absorption and centralization of E-field within VOS due to the qualitative heterogenous properties was observed in CEM model at f =10 GHz (Fig. 6.47) and LSS (Fig. 7.17). For HOS, the concentration of E-field intensity at points corresponding to terrain scattering centers was seen in the CEM model at f =5.25 GHz (Fig. 6.37) and LSS (Fig. 7.16).

Similar to CEM modeling results (Fig. 6.33, Fig. 6.34) greater scattering was observed from loamy farm soil in comparison to beach sand with the LSS (Fig. 7.12, Fig. 7.13). Also in line with increasing surface roughness as observed with CEM models (Fig. 6.35, Fig. 6.36), the scattering from pebbles and gravel in the LSS study (Fig. 7.14, Fig. 7.15) was higher than beach sand and loamy farm soil. Yet, unlike CEM model results where pebbles with shorter surface correlation length produced greater

backscattering than gravel, the reverse was seen in the LSS results. The latter better fits with theoretical expectations (Ulaby *et al*., 1978) and literature (Sabins, 1997; Schaber, 1999). Due to the size of terrain available it was not possible to consider the effect of low, moderate and high grazing angles on terrain scattering but the measured mean value of backscatter compared favourably with literature (Table 7.3).

7.5. Concluding Remarks

An improved method to model and validate aspects of the microwave signature of barefaced terrain through the development and deployment of a low cost LSS was presented. Three imaging scenarios were implemented to investigate the general terrain backscatter behaviour, study range profile in high az. resolution using SAR processing techniques and examine the effect of incident geometry on backscatter signature. The results provided important information on the EM signature of the 6 barefaced terrain studied including oil sands. Finally comparison between the results from the LSS validation method and CEM model simulations was performed, buttressing the effectiveness of the developed approach. In situations where satellite calibration imagery is too expensive or airborne scatterometers are unavailable, this low cost laboratory method is proposed for investigation of the monostatic scattering properties of barefaced terrain.

8 Conclusions and Future Work

The research is concluded, achievements are highlighted and future work is considered.

High resolution imaging sensors have become essential tools for remote sensing and military intelligence, surveillance and reconnaissance (ISR) but also have civil applications such as oil sand exploration. Geointelligence harnesses greater information content from multiple sources of ISR sensor data through pattern recognition, proximity relationships and connectivity flows amongst others. In this work the representation of targets in electro-optical and radar imagery was investigated through the reflectance, R_λ and backscattering, σ^0 signature. The contrast due to the longer wavelengths of radar was exploited particularly the different electromagnetic (EM) scattering from targets compared with wavelengths at spectral frequencies. The possibility of extracting further information from current or future hyperspectral or synthetic aperture radar (SAR) systems requires greater knowledge of the EM interaction with different media represented by the reflectance, R_λ and backscattering, σ_0 data. Such knowledge has a variety of uses including terrain classification, area object characterization and even feature identification, extraction or detection.

Consequently, the investigation of the spectral reflectivity and radar backscattering response of natural terrain surfaces are both important problems in remote sensing. This is due to the potential to retrieve relevant parameters of the surface such as chemical composition or grain size from the former and surface roughness or moisture content from the latter. When combined they provide a powerful tool to differentiate between media surfaces. The problem of EM wave scattering from random surfaces has been investigated for many years due to the complexity of theoretical solutions. These solutions only exist for limiting cases which do not cover the peculiar heterogeneity inherent in oil sands. This PhD work focused on modelling then measuring the effect of the material properties on barefaced terrain scattering rather than on the internal signal processing of the radar system. In this research an empirical multi-sensor remote sensing approach was implemented to investigate the behavior of 6 barefaced terrains within the infrared and radar region of the EM spectrum. The 6 barefaced terrains with slightly different physical, chemical and electrical properties

that were investigated include: beach sand, loamy farm soil, pebbles, gravel, hard oil sand (HOS) and viscous oil sand (VOS). The approach involved the empirical determination of the geochemical signature, experimental measurement of the intrinsic dielectric properties and development of easily adaptable computer electromagnetic (CEM) models that presented 2D/3D views of the surface and volume scattering process. Thereafter aspects of the EM signature of the terrain were validated using a low cost laboratory scatterometer system (LSS) developed at the University College London (UCL).

8.1. Summary of Findings

The work presented in this thesis involved a multi-sensor approach for the EM characterization of barefaced terrain and formed part of the effort to study the EM backscattering behaviour of various terrain classes particularly oil sand. The aim was to develop a method to investigate the behavior of terrain in the presence of EM waves. A database of terrain response or EM signature in the optical and microwave regions of the EM spectrum can help geoscientists discriminate between terrain classes for oil sand exploration but also enhance remote sensing of surfaces using both radar and multispectral sensors. In this work the proposed practical strategy led to the analysis and prediction of terrain geochemical signature, dielectric property discrimination models and characterization of terrain microwave response through processing of CEM model results. Both optical and microwave sensor interaction with barefaced terrain represented by the reflectance, R_λ and backscattering, σ_0 data were investigated. The three step model and measurement approach was implemented according to the conceptual approach to the thesis outline (Section 3.5). A summary of the results will be highlighted with application to oil sands exploration.

The geochemical signature identification and prediction model required data acquisition, statistical model implementation and post processing to determine the mineral phases present prior to content prediction. Spectral reflectance data of 16 terrain samples with varying weight percent (*wt*.%) of moisture was acquired using a reflectance spectrophotometer operating over the very near infrared (VNIR) and medium IR (MIR) with wavenumber, $v = 4600 - 500$ cm^{-1} (2.1 – 20 μm). This data was used to obtain the geochemical signature for the barefaced terrain. Statistical modelling indicated that for oil sand the most important variables concentrated in the three

regions: 1000 - 1100 cm^{-1}, 1400 - 1450 cm^{-1} and 2900 - 2950 cm^{-1}. For Nigerian oil sands 11 diagnostic spectral features were identified and shown in Fig. 4.9. They included 7 features that accurately depict hydrocarbon presence from Table 4.1 and four previously unreported peaks at 2361 cm^{-1}, 1084 cm^{-1}, 1032 cm^{-1} and 692 cm^{-1}. An empirical model based on the ratio of concentration of the MIR spectra at specific diagnostic wavenumber bands was used to predict the quantity of bitumen and moisture in Nigerian oil sands and shown in Table 4.8 and Table 4.10 respectively. This empirical model can be applied to oil sand terrain from other regions with characteristics similar to the Nigerian oil sands used to develop the models. The predictive statistical techniques could also find application in geointelligence analysis.

The high level of remote sensing accuracy observed with hyperspectral data is not feasible in the microwave region of the EM spectrum because the wavelengths in the IR region are orders of magnitude finer (1 μm = 10^{-6} m). This is one reason why airborne and spaceborne hyperspectral sensors are easily obstructed by cloud cover unlike microwave sensors such as radar. However it also makes the EM signature of barefaced terrain more difficult to predict in the microwave region. Therefore to characterize the radar backscatter behavior of a target whether point targets such as trucks, aircrafts or urban features or distributed targets such as terrain required two sets of parameters: target parameters and sensor parameters. The target parameters included physical shape factors like surface roughness and correlation length but also dielectric properties. Sensor parameters covered wave frequency, f, incidence angle, θ_i, polarization, HH, VV and cell dimensions illuminated by the radar, ∂A.

In terms of terrain modeling, the most contested target parameter is the dielectric property. Therefore three empirical studies of the dielectric properties (ε_r', ε_r'' and tan δ) of oil sand amidst other barefaced terrain was carried out prior to the development of a dielectric discrimination statistical model (DDSM). The DDSM identified the 1 GHz to 2 GHz and 5 GHz to 7 GHz as most significant for discrimination between the terrains investigated. There was also better correlation for the DDSM based on partial least square analysis (PLSA) model compared to the principal component analysis (PCA) model (Table 5.7). Analysis of the results indicated that despite the level of moisture present in VOS compared to HOS and other barefaced terrain, the ε_r' values for both oil sands were dampened by the presence of bitumen. Therefore real ε_r' values ranged from 2.1 to 4.5 for HOS and 2.6 to 4.7 for VOS shown in Table 5.5 and Table

5.6 respectively. The raw dispersion results also indicated a mild resonance which was observed in both ε_r' and ε_r'' data between 5 GHz to 8 GHz as shown for HOS and VOS (Fig. 5.6).

For the other barefaced terrain it was observed that after correction for errors there was a slight variation of permittivity with frequency. This variation with frequency was more pronounced with increasing *wt*.% moisture. Lack of relevant material dielectric properties data has been identified as the bane of accurate microwave terrain backscatter modelling and real life imagery interpretation. Therefore the raw permittivity results obtained for oil sands could be applied to better understand dielectric dispersion in microwave remote sensing products for oil sand reservoirs. Although the dielectric behavior does not provide a unique or diagnostic signature similar to spectral identification it however raises the possibility of remote identification of oil sand amidst other barefaced terrain using radar sensors. The dispersion results of the dielectric study along with material density properties were input in to barefaced terrain models (BTM) that embodied the terrain parameters.

The development of the BTM's included 3 practical considerations. First in order to include both height, h_{rms} and slope, m, effects in the 3D terrain models an innovative adaptation of the points and particle representation was made to also vary the slope orientation angle, α. In this way it was possible to vary the texture height (h_{rms}), retain the separation spacing between peaks and vertices, s while investigating the effects of slope orientation angle, α on overall scattering response. Secondly the prevalence of clumping or agglomeration in oil sands provided a larger particle size for surface roughness modelling while the inclusion of the intrinsic dielectric properties was made possible by our use of the finite integration technique (FIT) discretization within the Computer Simulation Tool Microwave Studio Suite (CST MWS). In this way 26 generic BTM's were developed to cover the properties of the 6 barefaced terrains including such features as texture or surface roughness, porosity and packing, bulk density and dielectric properties amongst others.

Similarly two sensors representing a planewave signal and ultrawideband (UWB) standard gain horn (SGH) antenna were used to investigate the effect of frequency, f, polarization, HH/VV and incident geometry, θ_{i}. The SGH was developed using the CST MWS. The CEMs developed with an empirical approach, comprised models representing both target and sensor parameters. The interaction of EM field with

the 6 barefaced terrains was modelled to provide information on surface (∂A = 1 m^2) and volume (∂V = 1 m^3) scattering from the BTM using the sensors. For typical radar systems target classification and analysis takes place on the display. Here the CEM models provided an indepth understanding of the EM wave interaction with the terrain target and backscatter coefficient, σ^0 after processing the received radiation power.

In reality microwave imagery is understood using the same technique as for optical photographs where the analyst considers image features such as tone, shape, size and pattern amongst others. Therefore the CEM models were used as a deterministic tool to embody the full physics of the scattering process based on the proposed simulation architecture (Section 6.3.2). Thereafter the behaviour of barefaced terrain in the presence of EM radiation was investigated. The derived data models describe elemental volumes of homogenous texture which can be regarded as single realizations of the radar scattering process. First the results from the CEM modeling were compared to the classical surface roughness representation based on the validity conditions for EM roughness. While excellent agreement between the BTMs and small perturbation model (SPM) was achieved for homogenous terrain only good agreement was seen between the oil sand BTMs and Kirchoffs Scattering Model (KSM) which is also known as the Physical Optics model. High resolution 2D/3D image results in the *xy*- and *yz*- plane were presented and analysed for the different terrain at specific frequencies and imaging angles.

General observations from the CEMs include: (1) Surface roughness had a greater effect on the scattered field than the electrical properties of the medium; (2) For volume scattering (i.e. within terrain) the electrical properties influence the penetration depth, δ_p as well as cause volume scattering; (3) Substantial shadowing and masking of adjacent surface points occurs with reducing angle of incidence depending on the surface roughness. More specific to oil sands: (1) the variation of losses due to penetration depth varied between f^{-2} and f^{-3} due to the heterogenous nature of the material; (2) the centralization of EM energy in VOS at 10 GHz raises the prospects of extracting VOS via microwave heating although this was not relevant to our identification purposes; (3) Both HOS and VOS responded differently to EM radiation with surface texture more responsible for backscattering from the surface; (4) The dispersion of EM waves on the surface of HOS and VOS (*xy* plane) was highly dependent on the backscatter footprint, ∂A_{eff}, which itself depended on the sensor

orientation angle θ_i with respect to terrain; (5) The backscattering coefficient, σ^0 from oil sands consisted of contributions to both surface and volume scattering due to the non-complementary effect of moisture, bitumen and grains (sand).

In order to validate some of the observations from the CEM's, the LSS was designed and configured to obtain centimeter-wavelength data over 1 – 8 GHz frequency. This cut across the L-, C- and X-band microwave region of the EM spectrum. The LSS was used to obtain empirical validation of the CEM model results and to do this was deployed in 3 imaging scenarios. The first scenario involved the LSS at nadir imaging geometry illuminating the terrain sample at a single point and the time domain signature was obtained. The second scenario involved the LSS being moved in cross range intervals of 1 cm along a 55 cm track to achieve high azimuth resolution (∂Az. = 1cm) images of the terrain using SAR processing techniques. In the third scenario, the LSS was configured to observe the effect of change in the sensor look angle using an LX80 tripod stand.

The cross correlation of the time domain signature obtained from Scenario 1 for the 6 barefaced terrains indicated identical scattering peaks at the 12 ns point for HOS and VOS indicative of the similar intrinsic properties for oil sands. The high azimuth resolution range profile image effectively characterized the terrain scattering response in vivid detail and compared favourably with the CEM modeling results. Also the effect of incident geometry was verified with the mean scattering coefficient for off-nadir imaging ($\theta_i = 80°$) lower than nadir imaging ($\theta_i = 90°$) while the measured scattering coefficient had grood agreement with literature (listed in Table 7.4). There were slight differences in the CEM results compared to LSS validation. This was due to rigid BTM structure compared to natural terrain and differences in: (i) ∂A (and ∂V) owing to available amount of oil sands acquired from Nigeria, (ii) measurement environment and (iii) EM sensors as the LSS and CEM sensor varied slightly in performance due to optimization of the LSS antenna.

A multidisplinary approach was implemented in the research work. This thesis identified suitable parameters like geochemical composition, dielectric properties, porosity, packing, density and texture to distinguish barefaced terrain. The EM signature of oil sand terrain was investigated using various analytical, numerical and simulation techniques generating a large database of terrain backscattering data. The developed models and measurement results will help advance the performance of

hyperspectral sensors and SAR for petroleum exploration. The proposed characterization method will provide a practical approach for modelling the EM signature of barefaced terrain for remote sensing in general.

8.2. Contribution

- New simplified terrain modelling approach. Although developed for the unique case of oil sand petroleum exploration and monitoring, this practical modeling approach has universal application and was also useful to land degradation monitoring (Ezeoke *et al*., 2013; Ezeoke *et al*., 2014b). The approach addresses dielectric property ambiguity, surface roughness components and infinite media challenges without recourse to classical statistical EM models (Ezeoke & Tong, 2012). Use of FIT with dielectric data meant that there was no need to individually model the heterogeneous components of terrain nor separately implement the diverse electrical properties of water, bitumen, sand and silt components of oil sand (Ezeoke, 2013). This simplifies the modeling process.
- Intelligent analytics. Application of multivariate methods including PLSA and PCA to geochemical signature analysis and dielectric property discrimination (Ezeoke & Tong, 2015). The suggested geochemical signature determination and analysis process can be applied to other spectra samples with high accuracy while the statistical processing models could have important applications to geointelligence analysis.
- Geochemical signature. An empirical content estimation and prediction model was developed based on Nigerian oil sands (Ezeoke *et al.*, 2012; Ezeoke & Tong, 2015). It provides a quick method to calculate constituent properties of oil sands in the field and could be applied to oil sands with similar heterogeneous properties.
- Dielectric property data. One major challenge in developing earth data models of terrain backscattering is lack of dielectric property data. Therefore the results from this research were input into the CST MWS software database. The CST MWS library of material permittivity values was expanded to include frequency related dielectric permittivity measurement values for: (a) Beach sand at 10, 20, and 30 *wt.*%; (b) Loamy farm soil 10, 20, and 30 *wt.*%; (c) Hard oil sand; (d) Viscous oil sand (Ezeoke *et al*., 2013; Ezeoke & Tong, 2013c). The raw dielectric data could be subsequently incorporated in to future terrain or material models.

- CEM results. CEM modeling enabled investigation of the slightly different EM wave reflectivity observed between barefaced terrain and oil sands (Ezeoke & Tong, 2012; Ezeoke & Tong, 2013b). The results provided a comparison of the backscattering behavior between common soil, oil sand and other barefaced terrain in a range of sensor configurations (Ezeoke *et al*., 2014b). The data sets were post processed to derive the scattering profiles for EM probes placed at different heights and depths from the BTM surface (Ezeoke *et al*., 2014c).
- LSS configuration. In contrast to conventional magnitude only scatterometers the LSS implemented in this work also measured angular effects of backscattering (Scenario 3) and yielded high resolution imagery through use of SAR processing techniques (Scenario 2) (Ezeoke & Tong, 2015). Therefore the anisotropic behaviour of of barefaced terrain and its effect on polarization was illustrated using the LSS (Ezeoke & Tong, 2013a; Ezeoke & Tong, 2015).

8.3. Future Work

Extraction of geoscientific information from radar or SAR imagery depends on both the system properties and intrinsic terrain properties. Therefore to perform classification of actual airborne or satellite derived SAR data would also require consideration of the signal processing within each individual airborne or spaceborne radar system. Perhaps a method to avoid the nuanced repetition of the simulations for each variation in sensor and terrain parameters would be welcome in future. Also the CEMs did not consider the system noise that may cause bias in the backscattered signal because the focus was on the radiometric properties of a homogeneous unit of imaged terrain or area. Theoretically, from the Radar Equation in (2.8), (3.4) and (3.5) the system properties are the same for each terrain surface imaged and only the backscatter coefficient which depends on the intrinsic properties of the terrain varies. However to test the approach with real SAR imagery would require implementation of the actual system performance rather than the plane wave or UWB sensor used in this work.

Furthermore the CEM's considered an imaging resolution or cell size of 1 m. However to adequately resolve larger features such as vehicles, houses, small buildings or even coastlines would require larger cell sizes. This could entail much more computing power as the signal processing requirements would likely increase in proportion to the number of resolution cells per unit area of the model. Therefore there will still be room for the statistical models such as KSM, SPM or geometric optics

approximations to name a few. However the proposed empirical method will be best implemented for the prediction of EM scattering from low loss dielectric barefaced terrain media due to the ease of deployment and adaptability.

References

Abdelsalam, M.G., Stern, R.J., and Berhane, W.G. (2000), "Mapping gossans in arid regions with Landsat TM and SIR-C images: the Beddaho Alteration Zone in northern Eritrea", *Journal of African Earth Sciences*, Vol. 30, pp. 903–916.

Abrams, M. (2000), "The Advanced Spaceborne Thermal Emission and Reflection Radiometer (ASTER): data products for the high spatial resolution imager on NASA's Terra platform", *International Journal of Remote Sensing*, Vol. 21, pp.847–859.

Agilent Application Note AN5988, (2003), Technical Overview, *Agilent 85070E Dielectric Probe Kit 200 MHz to 50 GHz*, Agilent literature number 5988-9472EN, May 9, 2003, pp. 1 – 12.

Aitken, H.G.J. (1985), *Syntony and Spark: The Origins of Radio*, Princeton: Princeton University Press, 366 pp.

Akinmosin, A., Osinowo, O.O. and Oladunjoye, M.A (2009), "Radiogenic components of the Nigerian Tar Sand Deposits", *Earth Sciences Research Journal*, Vol. 13, No. 1, June 2009, ISSN 1794-6190.

Ako, B.D., Alabi, A.O., Adekoe, O.S., and Enu, E.I. (1983), "Application of resistivity sounding in the exploration for Nigeria Tar Sand", *Energy Exploration and Exploitation*, Vol. 2, No. 2, pp:155-164.

Alvaro, G., Schlangen, E, van de Ven, M and Liu, Q. (2009), "Electrical conductivity of mortar containing conductive fibers and fillers", *Journal of Construction and Building Materials*, Vol. 23, pp. 3175-3181.

Amigun, J.O., Adelusi, A.O., and Ako, B.D (2012), "The application of integrated geophysical methods in oil sand exploration in Agbabu area of South western Nigeria", *International Research Journal of Geology and Mining*, Vol. 2, No. 9, pp.243-253, November 2012

Andersen, J.B. (1982), Low- and medium- gain microwave antennas, in *The Handbook of Antenna Design*, Vol. 1, Rudge, A.W., Milne, K., Olver, A.D., and Knight, P. (Eds.), Peter Peregrinus Limited, London, UK, pp. 506 – 580.

Archie, G.E. (1942), "The electrical resistivity log as an aid in determining some reservoir characteristics", *Transactions of the American Institute Mining Engineering*, Vol. 146, pp. 54-62.

Arhore, G. (2006), "Nigeria and the Future Global Gas Market", presentation at the Baker Institute Energy Forum, Houston, Texas, May 2006, pp. 10.

Aske, N., Kallevik, H., and Sjöblom, J. (2001), "Determination of Saturate, Aromatic, Resin and Asphaltenic (SARA) components in crude oils by means of Infrared and Near-infrared spectroscopy", *Energy & Fuels*, Vol. 15, pp. 1304-1312.

ASUF (2007), Report by United States Task Force on Strategic Unconventional Fuels, *America's Strategic Unconventional Fuels*, 2007, last accessed on 22/10/2012 online from www.unconventionalfuels.org/publications/reports/Volume_III_ResourceTechProfiles(Final).pdf

Attanasi, E.D. and Meyer, R.F. (2010), Natural Bitumen and Extra-Heavy Oil, *Survey of Energy Resources*, 22nd Ed, Clarke, A and Trinnaman, J (Ed), World Energy Council, pp.123-140.

Attanasi, E.D and Meyer, R.F. (2010), Natural Bitumen & Extra-Heavy Oil, *Survey of Energy Resources*, 22nd Ed, Clarke, A & Trinnaman, J (ed), World Energy Council, pp.123-140.

Babey, S.K., and Anger, C.D. (1993), "Compact airborne spectrographic imager (casi): a progress review". In *Proceedings of the SPIE Conference on Imaging Spectrometry of the Terrestrial Environment*, 14 April 1993, Orland, Flordia, Edited by G. Vane, SPIE, Bellingham, Washington. Proceedings of SPIE Volume 1937, pp. 152 – 163.

Balint, V., Pinter, A., Mika, G. (1981), Process for the recovery of shale oil, heavy oil, kerogen, or tar from their natural sources, US Patent 4419214, December 6, 1981.

Bamler, R. (1992), "A comparison of Range-Doppler and Wavenumber Domain SAR Focusing Algorithms", *IEEE Transactions on Geoscience and Remote Sensing*, Vol. 30, No. 4, July 1992, pp.706-713.

Bamler, R., and Schättler, B. (1993), "SAR Data acquisition and image formation," *SAR Geocoding: Data and Systems*, G. Schreier (Ed.), Karlsruhe: Wichmann, pp. 53-102.

Banhegyi, G. (1988), "Comparison of electrical mixture rules formulae" *Colloid and polymer science*, Vol. 266, pp. 1 – 11.

Barnsley, M.J., Settle, J.J., Cutter, M.A., Lobb, D.R., and Teston, F. (2004), "The PROBA/CHRIS mission: a low-cost smallsat for hyperspectral multi-angle observations of the earth surface and atmosphere". *IEEE Transactions on Geoscience and Remote Sensing*, Vol. 42, pp. 1512–1520.

Basedow, R.W., Aldrich, W.S., Colwell, J.E., and Kinder, W.D. (1996), "HYDICE system performance: an update", In *Proceedings of the SPIE Conference on Hyperspectral Remote Sensing and Applications*, 5 August 1996, Denver, Colorado, Edited by S.S. Shane, SPIE, Bellingham, Washington. Proceedings of SPIE Volume 2821, pp. 76 – 84.

Beckmann, P and Spizzichino, A. (1963), *The Scattering of Electromagnetic Waves from Rough Surfaces*. New York: Elsevier, 515 pp.

Berg, R.R (1986), *Reservoir Sandstones*, Prentice-Hall, Inc., Englewood Cliffs, New Jersey 07632. ISBN 0-13-774373-4 01, 481 p.

Bernath, P.F. (2002), "The spectroscopy of water vapour: Experiment, theory and applications", *Physical Chemistry Chemical Physics*, Vol. 4, No. 9, pp. 1501-1509.

Berthelot, C, Podborochynski, D, Saarenketo, T., Marjerison, B, Prang, C. (2010), Ground-Penetrating Radar Evaluation of Moisture and Frost across typical Saskatchewan Road Soils, *Advances in Civil Engineering*, Vol. 2010, pp:1-9, doi:10.1152/2010/416190

Beers, R.F. (1945), "Radioactivity and Organic Content of Some Paleozoic Shales", *American Association of Petroleum Geologists,* Vol. 29, Issue 1, pp.1-22.

Berry, J.L and Prost, G.L. (1999), Hydrocarbon Exploration, in *Remote Sensing for the Earth Sciences – Manual of Remote Sensing*, 3rd Ed., Vol. 3, A.N. Rencz, (Ed.) John Wiley & Sons, pp. 449-508.

Bichard, J.A. (1987), "Oil Sand Composition and Behaviour Research', AOSTRA Technical Publication Series No. 4, 1987.

Blackman, D.V., and Pollard, R.D. (1997), "An improved technique for permittivity measurements using a coaxial probe", *IEEE Transactions on Instrumentation and Measurements*, Vol. 46, No. 5, October 1997, pp. 1093-1099.

Blahut, R., Miller Jr, W., and Wilcox, C (eds.) (1991), *Radar and Sonar*, Part I, New York: Springer Verlag.

Bois, P, La Porte, M, Lavergne, M, Thomas, G, (1972), "Well-to-well seismic measurements" *Geophysics* 37, pp.471-480.

Boggs, S. (2006), *Principles of Sedimentology and Stratigraphy*, 4th Ed., Pearson Prentice Hall, Upper Saddle River, New Jersey, 662 p.

Bosisio, R.G., Cambon, J.L., Chavarie, C., Klvana, D. (1977), "Experimental results on the heating of Athabasca tar sand samples with microwave power", *Journal of Microwave Power*
Vol. 12 (4), pp. 301–307.

Bowers, S.A., Hanks, A.J. "Reflection of radiant energy from soil". *Soil Science* 100, pp.130-138, 1965.

Breton, P., Crepin, S., Perrin, J.C., Esmersoy, C., Hawthorn, A., Meehan, R., Underhill, W., Frignet, B., Haldorsen, J., Harrold, T., Raikes, S.,Well Positioned Seismic Measurements. *Oilfield Review* 2002, pp. 32-45.

Brisco, B., and Brown, R.J. (1998), Agricultural Applications With Radar, in *Principles and Applications of Imaging Radar – Manual of Remote Sensing*, 3rd Ed., Vol. 2, F.M Henderson, A.J. Lewis (Ed.) John Wiley & Sons, pp. 381-398.

Britannica (2007), *Encyclopaedia Britannica*, Enclyclopaedia Brittanica Online, Chapter Radar.

Brown, G.S. (1978), "Backscattering from a Gaussian distributed perfectly conducting rough surface", *IEEE Transactions on Antennas Propagation*, Vol. AP-26, pp. 472-482, May.

Bruns, C., Leuchtmann, P., and Vahldieck, R. (2003), "Analysis and Simulation of a 1 – 18 GHz Broadband Double Ridged Horn Antenna", *IEEE Transactions on Electromagnetic Compatibility*, Vol. 45, No. 1, February 2003, pp. 55-60.

Bruney, J. (2014), Process safety management in upstream and Gas: The Chevron Way, private presentation to 2014 Safety and Chemical Engineering Workshop, Chevron Technology Center, Richmond, California, 17 – 20 August, 2014.

Buckingham, R., and Staenz, K. (2008), "Review of current and planned civilian space hyperspectral sensors for EO", *Canadian Journal of Remote Sensing*, Vol. 34, Supplementary 1, pp. S187 – S197.

Bukka, K, Miller, J.D. and Oblad, A.G. (1991), "Fractionation and characterization of Utah tar-sand bitumen's: influence of chemical composition on bitumen viscosity". *Energy & Fuels*, Vol. 5, No. 2, pp. 333-340.

Burns, R. (1993), *Mineralogical Applications of Crystal Field Theory*, 2nd Ed., Cambridge University Press, Cambridge, 551 pp.

Burnside, W.D., and Chuang, C.W. (1982), "An aperture matched horn design", *IEEE Transactions on Antennas and Propagation*, Vol. 30, July 1982, pp. 790 – 796.

Butler, R.M. (1991), *Thermal Recovery of Oil and Bitumen*, Prentice-Hall, Englewood Cliffs, New Jersey, 528 p.

Campbell, J.E. (1990), "Dielectric properties and influence of conductivity in soils at one to fifty megahertz", *Soil Science Society of America Journal*, Vol. 54, pp. 332-341.

Carrigy, M.A. (1962), "Effect of texture on the distribution of oil in the Athabasca Oil Sands, Alberta, Canada", *Journal of Sediment Petroleum*, Vol. 32(2), pp. 312-315.

Carrigy, M.A. (1967), "The physical and chemical nature of a typical tar sand: bulk properties and behaviour", *Proceedings 7th World Petroleum Congress*, Vol. 3 Tar Sands Section, Mexico City, pp. 573-581.

Cassidy, N.J. (2009), Electrical and Magnetic properties of rocks, soils and fluids, in *Ground Penetrating Radar Theory and Applications*, Jol, H.M. (Eds), Elsevier Science: Amsterdam, 509 pp.

CCEI (2012), "Energy from Athabasca" *Canadian Center for Energy Information*, 2012, pp.3 accessed 02/08/12.

Chamaani, S., Mirtaheri, S.A. and Abrishamian, M.S. (2011), "Improvement of time and frequency domain performance of Antipodal Vivaldi Antenna using Multi-Objective Particle swarm optimization", *IEE Transactions on Antennas and Propagation*, Vol. 59, No. 5, pp. 1738-1742.

Chang, L.T., and Burnside, W.D. (2000), "An ultrawide-bandwidth tapered resistive TEM horn antenna", *IEEE Transactions on Antennas and Propagation*, Vol. 48, No. 12, December 2000, pp. 1848-1857.

Chanzy, A., Molineaux, B., Zribi, M. (2003), "Influence of surface roughness frequency components on radar backscattering: Consequences on roughness sampling", *Proceedings of IEEE International Geoscience RS Symposium*, 21 – 25 July 2003, Toulouse, Vol. 2, pp. 1414-1416.

Chavez, P.S., Sides, S.C., Anderson, J.A. (1991), "Comparison of 3 different methods to merge multiresolution and multispectral data—Landsat TM and SPOT panchromatic", *Photogrammetric Engineering and Remote Sensing*, Vol. 57, pp.295–303.

Chevalier, C.T., Kory, C.L., Wilson, J.D., Wintucky, E.G., and Drayton, J.A. (2003), "Travelling wave tube cold test circuit optimization using CST Microwave Studio", *IEEE Transactions on Electronic Devices*, Vol. 50, No. 10, pp. 2179 – 2180.

Clemens, M. and Weiland, T. (2001), "Discrete Electromagnetism with the Finite Integration Technique," *Progress in Electromagnetics Research,* PIER 32, pp. 65-87.

Cloude, S.R., and Pottier, E. (1996), "A review of target decomposition theorems in radar polarimetry", *IEEE Transactions on Geoscience and Remote Sensing*, Vol. 34, No. 2, March 1996, pp. 498-518.

Cloude, S.R. and Pottier, E. (1997), "An entropy based classification scheme for land applications of polarimetric SAR", *IEEE Transactions on Geoscience and Remote Sensing*, Vol. 35, No. 1, Jan 1997, pp. 68-78.

Cloutis, E.A. (1989), "Spectral reflectance properties of hydrocarbons: remote sensing implications", *Science* 245, pp.165-168.

Cloutis, E.A., Gaffey, M.J. and Moslow, T.F. (1995), "Characterization of minerals in oil sands by reflectance spectroscopy" *Fuel*, Vol. 74, Issue 2, pp. 874-879.

Cloutis, E.A. (1996), "Hyperspectral geological remote sensing: evaluation of analytical
Techniques", *International Journal of Remote Sensing*, Vol. 17, pp. 2215–2242.

Clark, R.N. (1999), Spectroscopy of Rocks and Minerals and Principles of Spectroscopy, in *Remote Sensing for the Earth Sciences – Manual of Remote Sensing*, 3rd Ed., Vol. 3, A.N. Rencz, (Ed.) John Wiley & Sons pp. 3–58.

Cole, K.S. and Cole, R.H. (1941), "Dispersion and absorption in dielectrics. I. alternating current field", *Journal of Chemical Physics*, Vol. 9, pp. 341-351.

Cooper, B.L., Salisbury, J.W., Killen, R.M., and Potter, A.E. (2002), "Midinfrared spectral features of rocks and their powders", *Journal of Geophysical Research*, Vol. 107, No. E4, pp 1-17.

Coskuner, G. and Huang, H. (2014), "Digital Rock in Heavy Oil: Another Window on Petrophysics", *Journal of Canadian Petroleum Technology*, Vol. 53, No.6, November 2014, pp. 322-326.

Coulomb, J.-L. (2008), Introduction to Nodal Finite Elements, in *The Finite Element Method for Electromagnetic Modelling*, Meunier, G. (Ed.), ISTE Ltd, London, UK pp. 1 – 68.

Cox, L.H., Wilson, G.A., Zhadanov, M.S., Rudd, J. and Wilson, J. (2012), "Large-scale 3D inversion of helicopter electromagnetic surveys for Oil sands exploration near Fort McMurray, Alberta" *Geoconvention 2012:Vision* available at http://www.cspg.org/documents/Conventions/Archives/2012/052_GC2012_Large-scale_3D_Inversion_of_Helicopter_Electromagnetic_Surveys.pdf

Cristall, J., Farquharson, C., and Oldenburg, D. (2004), Airborne Electromagnetic Inversion applied to oil sands: Expanded Abstract, Canadian Society of Exploration Geophysics. Annual meeting cited by D.R. Schmitt in "Heavy and Bituminous Oils:Can Alberta Save the World?" *Preview* October 2005, pp:25

CSA (2006), RadarSAT-1 Components and Specifications, Canadian Space Agency, last accessed 21 Nov. 12 from www.asc-csa.gc.ca/eng/satellites/radarsat1/components.asp

CST (2012), *Computer Simulation Tool Microwave Simulation suite* 2012.

CST MWS (2014), Microwave Studio: HF design and analysis Tutorial. *In CST-Computer Simulation Technology* 2014 version.

CST MWS (2015), "Corporate", https://www.cst.com/company, 2014, online and accessed 15 March 2015.

Cudahy, T., and Hewson, R. (2002), ASTER geological case histories: porphyry-skarnepithermal, iron oxide Cu-Au and Broken hill Pb-Zn-Ag. In: Annual General Meeting of the Geological Remote Sensing Group 'ASTER Unveiled', Burlington, House, Piccadilly, London, UK.

Curlander, J.C. and McDonough, R.N. (1991), *Synthetic Aperture Radar: Systems and Signal Processing*, New York: J. Wiley & Sons, 672 pp.

Cutrona, L.J. (1990), "Synthetic Aperture Radar," in M. Skolnik, *Radar Handbook*, 2nd Ed., New York:McGraw-Hill, 1990; 1st Ed., New York:McGraw-Hill, 1970.

Czarnecki, J., Radoev, B., Schramm, L.L and Slavchev, R. (2005), "On the nature of Athabasca Oil Sands", *Advances in Colloid and Interface Science*, Vol.114-115, pp. 53-60.

Davidson, M., Letoan, T., Mattia, F., Satalino, G., Manninen, T., and Borgeaud, M. (2000), "On the characterization of agricultural soil roughness for radar remote sensing studies, *IEEE Transactions Geoscience and Remote Sensing,* Vol. 38, No. 2, pp.630-640.

Davidson, D.B (2008), Computational Electromagnetics for RF and Microwave Engineering, Cambridge University Press, 2008, pp. 432.

Davis, J.B. and Squires, R.M. (1954), Detection of microbially produced gaseous hydrocarbons other than methane. *Science,* 119, pp.381-382.

De Roo, R.D. and Ulaby, F.T. (1996), "A modified physical optics model of the rough surface reflection coefficient", *Conference proceedings of Antennas and propagation society international symposium AP-S Digest*, Vol. 3, pp. 1772-1775.

Debye, P. (1929), Polar Molecules, *Chemical Catolog*, New York.

Dickinson, J.E., Pool, D.R., Groom, R.W., and Davis, L.J. (2010), "Inference of lithologic distributions in an alluvial Aquifer using airborne transient electromagnetic surveys", *Geophysics*. Vol.75, No.4. pp.WA141-WA161.

DiGiovanni, D.A., Gatesman, A.J., Giles, R.H., and Nixon, W.E. (2013), "Backscattering of Ground Terrain and Building Materials at Milimeter-Wave and Terahertz Frequencies", *Proceedings of SPIE*, *Vol. 8715, Passive and Active Milimeter-Wave Imaging XVI*, D. A. Wikner and A.R. Luukanen, (Eds.), pp. 1-17.

Dobson, M.C., and Ulaby, F.T. (1998), Mapping soil moisture distribution with imaging radar, in Henderson and Lewis (Ed.), *Principles and applications of imaging radar, Manual of Remote Sensing*, Vol. 2, pp. 407 – 430.

Dobson, M.C. and Ulaby, F.T. (1981), "Microwave Backscatter dependence on Surface Roughness, Soil Moisture and Soil Texture: Part III- Soil Tension", *IEEE Transactions Geoscience and Remote Sensing*, Vol. GE-19, No. 1, pp. 51 – 61, January.

Dobson, M.C. and Ulaby, F.T. (1998), Mapping Soil Moisture Distribution with Imaging Radar, in *Principles and Applications of Imaging Radar – Manual of Remote Sensing*, Henderson, F.M and Lewis, A.J (ed) 3rd Ed., Vol. 2, John Wiley & Sons, Inc.

Dobson, M.C., Ulaby, F.T., Hallikainen, M.T., El-Rayes, M.A. (1985), "Microwave dielectric behavior of wet soil – Part II: Dielectric Mixing Models", *IEEE Transactions on Geoscience and Remote Sensing*, Vol. GE-23, No. 1, pp. 35-46.

Dubois, P.C., and van Zyl, J. (1994), "An Empirical Soil Moisture Estimation Algorithm using Imaging Radar", *Proceedings of IGARSS'94*, August 8 – 12, Pasadena, California, pp. 1573-1575.

Dumbaugh, W.H., Lawless, W.N., Malmendier, J.W., Wexell, D.R. (2001), Extraction of oil
from oil shale and tar sand, Canadian Patent, 1108081, Sept. 2001.

Elachi, C., Cimino, J.B., and Settle, M. (1986), "Overview of the Shuttle imaging Radar-B preliminary scientific results", *Science*, 232 (4757), pp.1511-1516.

Elachi, C. and van Zyl, J. (2006), *Introduction to the Physics and Techniques of Remote Sensing*, 2nd Edition, John Wiley & Sons, Inc, 547 pp.

Engelhardt, R., and Todirescu, M. (2005), "An Introduction to Development in Alberta's Oil Sands" University of Alberta School of Business report.

Engman, E.T., and Chauhan, N. (1995), "Status of Microwave soil moisture measurements with remote sensing", *Remote sensing of the Environment*, Vol. 51, pp. 189 – 198.

Erdogan , L., Akyel, C. and Ghannouchi, F.M. (2011), "Dielectric properties of oil sands at 2.45 GHz with TE1,0,11 mode determined by a rectangular cavity resonator", *Journal of Microwave Power and Electromagnetic Energy*, 45(1), 2011, pp.15-23.

Evans, D.L. (2006), Spaceborne imaging radar –C/X band synthetic aperture radar (SIR-C/X/SAR): A look back on the tenth anniversary, *IET Proc. Rad. Son. and Nav.,* Vol. 153, (2), pp.81-85.

Evdokimov, I.N., and Losev., A.P. (2010), "Electrical conductivity and dielectric properties of solid asphaltenes", *Energy and Fuels*, Vol. 24, No. 7, pp. 3959-3969.

Everett, J.R., Staskowski, R.J., Jengo, C. (2002), "Remote Sensing and GIS enable future exploration success" *World Oil* Vol. 223, No. 11, pp.59-60, 63-5, 2002.

Ezeoke, M., and Tong, K., (2015) "Electromagnetic characterization of oil sands for petroleum exploration", *Journal of Petroleum Engineering,* 16 pages, [In Press].

Ezeoke, M.S.C and Ford, T (2008), Satellite remote sensing, Information Communication Technology and Peace Support, United Nations Institute of Training and Research supported project, April 2008 available at http://www.peaceopstraining.org/theses/ezeoke.html

Ezeoke, M.S.C and Tong, K (2012), "Understanding the Synthetic Aperture Radar Signature for Oil Sand Exploration" *Proceedings of the 6th European Modelling Symposium*, EMS 2012, 14-16 November 2012, Valetta, Malta, pp.419-424.

Ezeoke, M., Tong, K., Adole, T and Lovett, A. (2012), "Determining the Geographic Effect of Gas flaring using multi-SAR Azimuth Processing", *Proceedings of IEEE 2nd International Conference on Advances in Computational Tools for Engineering Applications* (ACTEA 12), 12-15 December, Louaize, Lebanon.

Ezeoke, M. (2013), Synthetic Aperture Radar Signature of Oil Sands for Petroleum Exploration, *MPhil to PhD Transfer Thesis Department of Electronic and Electrical Engineering University College London,* 9th April 2013, 130 pp.

Ezeoke, M and Tong, K (2013a), "Terrain Backscatter and Oil Sand Exploration: Initial Measurement Results", *Proceedings of the IEEE UK SIM AMSS 7th European Modeling Symposium* (EMS 2013), 20 – 22 November, Manchester, UK, pp.85-89, 2013.

Ezeoke, M and Tong, K (2013b), "Determining the Synthetic Aperture Radar Signature of Terrain for Earth Observation Using Computer Electromagnetic Models", *Proceedings 64th International Astronautical Congress*, IAC 2013, 23-27 September, V, 2-B3.9,x20328, Session 2-B3.9, Human Space Endeavours Young Professionals Virtual Forum. http://www.iafastro.net/iac/paper/id/20328/summary.lite/

Ezeoke, M. and Tong, K. (2013c), Modeling electromagnetic reflectivity of Agbabu Oil Sands from hyperspectral Infrared reflectance spectra and dielectric properties at L-, C- and X-band Frequencies, *Proceedings of the 5th Computational Intelligence, Communication Systems and Networks* (CICSyN2013), 5-8 June, Madrid, Spain, pp.125-130, 2013.

Ezeoke, M., Tong, K., Amiri, A., and Al-Armaghany, A. (2013), Effects of electrical and physical properties of Barefaced terrain on backscatter response, *Proceedings of the international conference on Advances in Computing Electronics and Communication*-ACEC2013, 12-13 October, Zurich, pp.89-93, 2013.

Ezeoke, M., Tong, K., and Shi, S. (2014a), "Modeling Synthetic Aperture Radar Signature of Agbabu Oil Sand for Petroleum Exploration", *Energy Production and Management in the 21st Century the Quest for Sustainable Energy*, Vol.2, Eds C.A. Brebbia, E.R. Magaril and M.Y. Khodorovsky, *WIT Transactions on Ecology and the Environment*, Vol. 190, pp. 1284 – 1295, 2014.

Ezeoke, M., Tong, K and S.Shi (2014b), A practical approach for modelling the electromagnetic radar signature of barefaced terrain for remote sensing, *International Journal of Computational Methods and Experimental Measurements*, Vol. 2, No. 4, G. Carlomagno, C.A. Brebbia, W. Patrick De Wilde (Eds.), WIT Press: Southampton, UK, pp. 403 – 419.

Ezeoke, M., Tong, K and Fortuny, C.B (2014c), "Terrain backscatter and oil sand exploration: Average Reflectivity Analysis", *Proceedings of the 2014 IEEE Radar Conference* (Radar2014), 13-17 October, Lille, France, pp. 1-6.

Ezeoke, M., Tong, K and Mubea. K. (2014d), "Electromagnetic Characterisation of Terrain for Unconventional Petroleum Exploration", *Proceedings of the 2014 IEEE Radar Conference* (RadarCon2014), 19-23 May, Cincinnati, Ohio, USA, pp. 0990 - 0995.

Ezeoke, M., and Tong, K (2014), "Polarimetric SAR Classification of Terrain for Land Degradation Monitoring", *Proceedings of the 2014 IAF Global Space Applications Conference* (2014 GLAC), 2 – 4 June, Paris, France, GLAC-2014,S,6B,4,x20699, 2014.

Fang, C.S., Lai, P.M.C., Chang, B.K.L., Klaila, W.J. (1989), "Microwave demulsification", *Journal of Environmental Progress*, Vol. 8, pp.235–238.

Fitzgerald, J.J. (1978), *Black gold with grit*, Sidney, BC: Grays Publishers, 264 p.

Fitzpatrick, J. (1978), "Error models for systems measurement", *Microwave Journal*, Vol. 21, pp. 63-66, May 1978.

Fountain, D. (1998), "Airborne electromagnetic systems-50 years of development", *Exploration Geophysics*, Vol. 29, pp. 1 – 11.

Farmer, V.C. (Ed.), (1974), *The Infra-red Spectra of minerals*, Mineralogical Society, London, 539 pp.

Foged, L., Giacomini, A., Duchesne, L., Leroux, E. ., Sassi, L., Mollet, J. (2005), "Advanced modelling and measurement of wideband horn antenna", *Proceedings of the 11th International Symposium on Antenna Technology and Applied Electromagnetics* (ANTEM 2005), 15-17 June, Saint-Main, France, 2005, pp. 1-6.

Frey, O., Magnard, C., Ruegg, M., and Meier, E. (2009), "Focusing of airborne synthetic aperture radar data from highly non-linear flight tracks", *IEEE Transactions on Geoscience and Remote Sensing,* Vol. 47, No. 6, June 2009. Pp.1844-1858.

Friedman, S.P. (1998), "A Saturation degree-dependent composites spheres model for describing the effective dielectric constant of unsaturated porous media", *Water Resources Research*, Vol. 34, No. 11, pp. 2949-2961.

Forrester, S.T., Janik, L.J., Mclaughlin, M.J., Soriano-Disla, J.M, Steward, R., Dearman, B. (2012), "Total petroleum hydrocarbon concentration prediction in soils using diffuse reflectance infrared spectroscopy", *Soil Science Society of American Journal*, Vol. 77, pp. 450 – 460.

Frohlich, H. (1958), *Theory of Dielectrics*, 2nd Ed., Oxford University Press, London.

Fuller, B.D., and Ward, S.H. (1970), "Linear system description of electrical parameters of rocks", *IEEE Transactions on Geoscience Electronics*, Vol. GE 8, No. 1, pp. 7 – 18.

Fung, A.K., Axline, R.M and Chan, H.L. (1974), "Exact scattering from a known randomly rough surface", in *Proceeding URSI Commission II Specialist Meeting on Microwave Scattering and Emission from the Earth,* Berne, Switzerland.

Fung, A.K., (1996), *Microwave Scattering and Emission Models and their Applications*, Norwood, MA: Artech House.

Gad, S., and Kusky, T. (2006), "Lithological mapping in the Eastern Desert of Egypt, the Barramiya area, using Landsat thematic mapper (TM)", *Journal of African Earth Sciences*, Vol. 44, pp. 196–202.

Gaffey, S.J., McFadden, L.A., Nash, D., and Pieters, C.M. (1993), "Ultraviolet, visible and near infrared reflectance spectroscopy: laboratory spectra of geologic materials, in

Remote Geochemical Analysis: Elemental and Mineralogical Composition, C.M. Pieters and P.A.J. Englert, (Eds.), Cambridge University Press, Cambridge, pp.43-78.

Giacomini, A., Potenza, A., Morbidini, R., Foged, L. (2011), "Quad-ridge dual polarized antenna for use in the 2-32 GHz band", *Proceedings of the IEEE 6th European Conference on Antennas and Propagation* (EUCAP), pp.769-772.

Gillespie, A., Kahle, A., and Walker, R.E. (1987), "Color enhancement of highly correlated
images. II. Channel ratio and chromaticity transformation techniques", *Remote Sensing of Environment* Vol. 22, pp. 343–365.

Glover, W.J. (2010), "A generalized Archie's law for *n* phases", *Geophysics*, Vol. 75, No. 7, pp. E247 – E265.

Glover, P.W., Hole, P.J. and Pous, J. (2000), "A modified Archie's law for two conducting phases", *Earth and Planetary Science Letters*, Vol. 180, No. 3 – 4, pp. 369-383.

Goldstein, R.M., and Zebker, H.A (1987), "Interferometric radar measurement of ocean currents," *Nature*, Vol. 328, pp.707-709.

Goetz, A.F.H, Vane, G., Solomon, J.E. (1985), "Imaging spectrometry for earth remote sensing", *Science* 228, pp.1147-1153.

Goetz, A.F.H., and Rowan, L.C. (1981), "Geologic remote-sensing", *Science*, Vol. 211, pp. 781–791.

Graton, L.C and Fraser, H.J. (1935), "Systematic packing of spheres with particular relation to porosity and permeability", *The Journal of Geology*, Vol. 43, pp. 785-909.

Grefett, J.J (1992), "Theoretical model of the shift of the Brewster angle on a rough surface," *Optics Letters*, Vol. 17, No. 4, pp. 238 -240, February 1992.

Green, R.O., Eastwood, M.L., Sarture, C.M., Chrien, T.G., Aronsson, M., Chippendale, B.J.J,A., Pavri, B.E., Chovit, C.J., Solis, M., Olah, M.R., and Williams, O. (1998), "Imaging Spectroscopy and the airborne visible/infrared imaging spectrometer (AVIRIS)", *Remote Sensing of Environment*, Vol. 65, No. 3, pp. 227 – 248.

Guégen, Y., and Palciauskas, V. (1994), *Introduction to the physics of rocks*, Princeton University Press, 304 pp.

Guo, C., and Liu, R.C. (2010), "A borehold imaging method using electromagnetic short pulse in oil-based mud", *IEEE Geoscience and Remote Sensing Letters*, Vol. 7, No. 4, October 2010, pp. 856 – 860.

Hallikainen, M.T., Ulaby, F.T., Dobson, M.C., El-Rayes, M.A., Wu, L. (1985), "Microwave dielectric behavior of wet soil – Part I: Empirical models and experimental observations", *IEEE Transactions on Geoscience and Remote Sensing*, Vol. GE-23, No. 1, pp. 25-34.

Hapke, B. (1993), *Theory of Reflectance and Emittance Spectroscopy Topics in Remote Sensing 3*, Cambridge University Press, New York, 455 pp.

Harger, R.O. (1970), *Synthetic Aperture Radar Systems, Theory and Design*, New York: Academic Press, 240 pp.

Hascakir, B., Babadagli, T., and Akin, S. (2008), "Experimental and Numerical Simulation of Oil Recovery from Oil Shales by Electrical Heating" *Energy and Fuels* 2008, Vol. 22, pp.3976-3985.

Hashin, Z., and Shtrikman, S., (1962), "A variational approach to the theory of effective magnetic permeability of multiphase materials", *Journal of Applied Physics*, Vol. 33, No. 10, pp. 3125 – 3131.

Hasted, J.B. (1972), "Liquid water: Dielectric properties," in *The Physics and Physical Chemistry of Water: Water – A comprehensive Treatise*, F. Franks (Ed.), New York: Plenum, 1972, Vol. 1, Ch. 7, pp. 255 – 309.

Hecht, E. (1987), *Optics*, 2nd Ed., Addision-Wesley Publishing, Reading Mass., pp 676.

Hepler, L.G (1989), *Alberta Oil Sands Technology and Research Authority technical handbook on oil sands, bitumens and heavy oils*, Edmonton; pp. 14 [chapter 2].

Heming, R.F. (1996), "Impact of information technology on the earth sciences" *Technology in Society,* Vol.18, No.3, pp. 297-319.

Hill, N., Vaughan, W.E., Price, A.H. and Davies, M. (1969), "Dielectric properties and molecular behavior", *Von Nostrand*, New York.

Hills, L.V. (Ed.) (1974), *Oil Sands Fuel of the Future*, Canada Society of Petroleum Geologist Memoir, Vol. 3, 263 p.

Horvitz, L. (1978), "Near surface evidence of hydrocarbon movement from depth. In: Problems of Petroleum Migration", *American Association of Petroleum Geology Student. Geologist,* Vol. 10, pp. 241-270.

Huete, A. (2004) Remote Sensing of Soils and Soil processes. In: *Remote Sensing for Natural Resources Management and Environmental Monitoring: Manual of Remote Sensing*, 3rd ed., Vol. 4, John Wiley & Sons, Inc. ISBN: 0471-31793-4.

Hunt, G.R. (1979), *Petroleum Geochemistry and Geology*, W.H. Freeman and Company, San Francisco, 617 pp.

Hunt, G.R. (1977), "Spectral signatures of particulate minerals in the visible and near infrared", *Geophysics*, Vol. 42, pp. 501-513.

Hutton, A.C. (1987), "Petrographic classification of oil shales" *International Journal of Coal Geology* 8, 203-231.

IEA (2011), International Energy Agency – Oil Market Reports, last accessed 20 November 2012 from http://omrpublic.iea.org/omrarchive

IEEE (1983), Standard Definitions of Terms for Antennas, *IEEE Transactions on Antennas and Propagation*, Vol. AP-31, No. 6, 1983.

Ioannidis, M.A., Kwiecien, M.J., and Chatzis, I. (1997), "Electrical conductivity and percolation aspects of statistically homogeneous porous media", Transport in Porous Media, Vol. 29, No. 1, pp. 61–83.

Ivanhoe, L.F. (1995), Future Oil Supplies: There is a finite limit, *World Oil*, October 1995, pp.77-88.

Jackson, P.D., Taylor-Smith, D., and Stanford, P.N. (1978), "Resistivity-porosity-particle shape relationships for marine sands", *Geophysics*, Vol. 43, No. 6, pp. 1250-1268.

Jol, H.M. (Eds) (2009), *Ground Penetrating Radar Theory and Applications*, Elsevier Science: Amsterdam, 509 pp.

Keller, G.V. (1963), "Electrical properties in the deep crust", *IEEE Transactions on Antennas and Propagation*, Vol. 11, No. 3, May 1963, pp. 344-357.

Keller, G.V. (1982), Electrical properties of rocks and minerals: in Carmichael, R. S. (Ed), *Handbook of physical properties of rocks*, Vol. I., CRC Press, Boca Raton, pp. 217 – 294.

Kendall, G.H (1976), "Geology of the Heavy Oil Sands-Alberta", Geological Association of Canada and Miners Association of Canada (GAC/MAC) Symposium, 19-21 May, 1976.

Kalinowski, A and Oliver, S. (2004), "ASTER Mineral Index Processing Manual", *Remote Sensing Applications Geoscience*, Australia, pp. 1- 37.

Kaya, Ş., Müftüog˜lu, O., and Tüysüz, O. (2004), "Tracing the geometry of an active fault using remote sensing and digital elevation model: Ganos segment, North Anatolian Fault zone, Turkey", *International Journal of Remote Sensing*, Vol. 25, pp. 3843–3855.

Kalme, S., Parshetti, G., Gomare, S., and Govindwar, S. (2008), "Diesel and kerosene degradation by *Pseudomonas desmolyticm* NCIM 2112 and *Nocardia hydrocarbonoxydans* NCIM 2386", *Current Microbiology*, Vol. 56, pp. 581 – 586.

Kirkegaard, C, Sonnenborg, T.O, Auken, E., and Jorgenson, F. (2011), "Salinity distribution in heterogeneous coastal aquifers mapped by airborne electromagnetics", *Vadoze Zone Journal*, Vol. 10, No.1 (February 2011), pp.125-135.

Klein, K.A. & Santamarina, J.C. (2003), "Electrical conductivity of soils: Underlying Phenomena", *Journal of Environmental and Engineering Geophysics*, Vol. 8, No. 4, pp. 263 – 273.

Knott, E.F., Shaeffer, J.F., and Tuley, M.T. (2004), *Radar Cross Section*, 2nd Ed., Raleigh, NC: SciTech.

Koike, C., Hasegawa, H., and Hattori, T. (1982), "Mid and far infrared extinction coefficients of hydrous silicate minerals", *Astrophysics and Space Science*, Vol. 88, pp. 89 – 98.

Kramers, H.A. (1927), *Atti del Congress Internazione dei Fisici* (*Transactions of Volta Centenary Congress*) (*Como*), Vol. 2, pp. 545-557.

Krönig, R.L. (1926), *Journal Optical Society of America*, Vol. 12, pp. 547.

Krynine, P.D. (1948), "The megascopic study and field classification of sedimentary rocks", *Journal of Geology*, Vol. 56, pp. 130-165.

Kuga, Y., Whitt, M.W., McDonald, K.C. and Ulaby, F.T. (1990), Scattering Models for Distributed Targets, in *Radar Polarimetry for Geoscience Applications*, F.T Ulaby and C. Elachi (Eds.), Artech House, Inc:Norwood, MA, pp. 111 - 190.

Kühn, F., Oppermann, K., Hörig, B. (2004), "Hydrocarbon index—an algorithm for hyperspectral detection of hydrocarbons", *International Journal of Remote Sensing*, Vol. 25, pp. 2467–2473.

Laasted, H., Haukefaer, E., Young, S., Tehrani, A., Delaunay, P., Feather, K., Phillips, J., and Marca, S. (2000), "Water-based formation imaging and resistivity logging in oil based drilling fluids-Today's reality", Paper SPE 62977 presented at the SPE Annual Technical Conference and Exhibition, Dallas 1-4 October.

Laherre, J (2002), "Forecasting future production from past discovery", *International Journal of Global Energy Issues*, Vol. 18, No. 2 – 4, pp.218-238.

Lai, H., Franks, R., Kong, D., Kuck, D., and Gackstetter, T. (1987), "A broad band high efficient quad ridged horn", *IEEE Antennas and Propagation Society International Symposium*, Vol. 25, pp. 676 – 679.

Lammoglia, T., and Souza Filho, C.R. (2011), "Spectroscopic characterization of oils yielded from Brazilian offshore basins: Potential applications of remote sensing", *Remote Sensing of Environment*, Vol. 115, pp. 2525-2535.

Lammoglia, T., and Souza-Filho, C.R. (2012), "Satellite determination of API gravity and SARA components of offshore petroleum seeps", *Revista Brasileira de Geofisica*, Vol. 30, No. 4, pp. 419-430.

Lasswell, S.W. (2005), History of SAR at Lockheed Martin (previously Goodyear Aerospace), *Proc. SPIE* Vol. *5788*, Radar Sensor Technology IX, 1: doi:10:1117/12.603927 Also available at http://dx.doi.org/10.1117/12.603927.

Lawal, A., Radice, G.M., Ezeoke, M. (2014), "Evaluating the Potentials of an International Collaboration between Equatorial Nations by Implementing a

constellation of Interferometric small SAR Satellite Network", *Proceedings of the 65th International Astronautical Congress* (2014 IAC), 29 Sep – 4 October, Toronto, Canada, IAC-2014, IAC-14, B4, 1, 13, x27229.

Lee, K.F., and Tong, K.F. (2012), "Microstrip patch antennas – basic characteristics and some recent advances", *Proceedings of the IEEE*, Vol. 100, No. 7, July 2012, pp. 2169 – 2180.

Lewis, T. (1991), *Empire of the Air: The Men Who Made Radio*, New York, HarperCollins, 421 pp.

Lewis, A.J. and Henderson, F.M. (1998), Radar Fundamentals: The Geoscience Perspective, in *Principles and Applications of Imaging Radar – Manual of Remote Sensing*, 3rd Ed., Vol. 2, F.M Henderson, A.J. Lewis (Ed.) John Wiley & Sons, pp. 131-176.

Liang, S. (1997), An investigation of remotely sensed soil depth in the optical region, *International Journal of Remote Sensing*, Vol. 18, No. 16, pp. 3395-3408.

Lichtenecker, K., and Rother, K. (1936), "Die Herleitung des logaritmishen Mischungsgesetzen als algemeinen Prinzipen der statonaren Stromung", *Physikalische Zeitschrift*, Vil. 32, pp. 256–660

Lentz, R.R (1974), "A Numerical Study of Electromagnetic Scattering from Ocean-Like Surfaces", *Radio Science*, Vol. 9, pp. 1128 – 1146.

Lillesand, T.M., Kiefer, R.W. and Chipman, J.W. (2004), *Remote Sensing and Image Interpretation*, 5th Ed, John Wiley & Sons, Inc, 820 pp.

Lillesand, T.M., Kiefer, R.W. and Chipman, J.W. (2008), *Remote Sensing and Image Interpretation*, 5th Ed, New York, John Wiley & Sons, Inc, 768 pp.

Liu, J.K. (1989), In AOSTRA Technical Handbook on Oil Sands, Bitumen and Heavy Oils, L.G Hepler and C. His.

Logan, L., Hunt, G., Salisbury, J., and Balsamo, S. (1973), "Compositional implications of Christiansen frequency maximums for infrared remote sensing applications", *Journal of Geophysical Research*, 78, pp.4983-5003.

Löw, A. (2004), Coupled modelling of land surface microwave interactions using Envisat ASAR data, *Dissertation der Fakultät für Geowissenschaften der Ludwig Maximilians Universität München,* 25th August, 270 pp.

Lou, Y., Kim, Y., and van Zyl, J. (1996), The NASA/JPL airborne synthetic aperture radar system, *Summaries of the 6th Annual AIRSAR Earth Science Workshop*, JPL Publ. 96-4, Vol. 2, Jet Propulsion Laboratory, California Institute of Technology, Pasadena, Calif., pp. 51-56.

Luo, M., Wood, J.R., and Cathles, L.M. (1994), "Prediction of thermal conductivity in reservoir rocks using fabric theory," *Journal of Applied Geophysics*, Vol. 32, No. 4, pp. 321-334.

Lyder, D., Feng, J., Rivard, B., Gallie, A., Cloutis, E. (2010), "Remote bitumen content estimation of Athabasca oil sand from hyperspectral infrared reflectance spectra using Gaussian singlets and derivative of Gaussian wavelets", *Fuel*, Vol.89, Issue (3), pp. 760-767.

Macdonald, I.R., Guinasso, N.L., Ackleson, S.G., Amos, J.F., Duckworth, R., Sassen, R.,
Brooks, J.M. (1993), "Natural oil-slicks in the Gulf-of-Mexico visible from space", *Journal of Geophysical Research—Oceans*, Vol. 98, pp. 16351–16364.

Mahafza, B.R and Elsherbeni, Z (2004), *MATLAB Simulations for Radar Systems Design*, Chapman & Hall/CRC Press LLC, ISBN 1-58488-392-8, 682 pp.

Majid, A., Ripmeester, J.A and Kodama, H (1988), "Mineralogy of heavy mineral concentrates from oil sands" *Fuel*, Vol. 67, Issue (3), pp. 443-444.

Maréchal, Y. (2003), "Observing the water molecule in macromolecules and aqueous media using infrared spectrometry", *Journal of Molecular Structure*, Vol. 648 (1-2), pp. 27-47.

Maréchal, Y. (2011), "The molecular structure of liquid water delivered by absorption spectroscopy in the whole IR region completed with thermodynamics data", *Journal of Molecular Structure*, Vol. 1004 (1-3), pp. 146-155.

Marmo, J., Folkman, M.A., Kuwahara, C.Y. and Willoughby, C.T. (1996), "Lewis hyperspectral imager payload development", *Proceedings SPIE*, Vol. 2819, Imaging Spectrometry II, 80 (November 13, 1996); doi:10.1117/12.258089.

MATLAB and Statistics Toolbox Release 2012b, The MathWorks, Inc., Natick, Massachusetts, United States.

Martens, H., and Naes, T. (1992), *Multivariate Calibration*, John Wiley & Sons, New York, 438 pp.

Mätzler, C. (1987), "Applications of the interaction of microwaves with the natural snow cover", *Remote Sensing Reviews*. Vol. 2, pp. 259 – 387.

McNeill, J.D. (1980), Electrical conductivity of soils and rock, Technical Note TN-5, *Geonics Limited*, Mississauga, Ontario, Canada, p 21.

Medicus (No initials) (1859), Discovery of a subterranean fountain of oil, *Sandusky Register* on 16 Sept. 1859 last accessed 22/08/12 from http://www.newsinhistory.com/blog/world's-first-successful-oil-well--drilled-1859.

Mei, S and Paulen, R (2009), "Using multi-beam RADARSAT-1 imagery to augment mapping surficial geology in northwest Alberta, Canada", *Canada Journal of Remote Sensing,* Vol. 35, No. 1, pp. 1-22.

Mezghani, M, van Lingen, P, Consentino, L, and Sengul, M. (2000), "Conditioning Geostatistical Models to Flow Meter Logs". Conference Paper Society of Petroleum Engineers 65122-MS presented at the *SPE European Petroleum Conference*, Paris, 24-25 October. DOI: 10.2118/65122-MS.

Moore, R.K. (1990), Ground Echo, in *Radar Handbook* (2nd Ed.), M.I. Skolnik (Ed.), McGraw-Hill, New York, Chapter 12, pp. 12.1-12.40.

Mingos, D.M.P. and Baghurst, D.R. (1991), "Applications of microwave dielectric heating effects to synthetic problems in chemistry", *Chemical Society Reviews* Vol. 20, pp. 1–47.

Moritis, G. (2009), "Special report forecasts moderate Alberta oil sands production growth", *Oil and Gas Journal* Vol. 107, Issue 26 last accessed 30 Nov. 2012 from http://www.ogj.com/articles/print/volume-107/issue-26/Drilling___Production/special-report-forecasts-moderate-alberta-oil-sands-production-growth.html

Morse, P.M. and Feshback, H. (1953), *Methods of Theoretical Physics*, New York: McGraw-Hill, parts 1 and 2.

Mutyala, S., Fairbridge, C., Jocelyn Paré, J.R., Bélanger, J.M.R., Ng, S. and Hawkins, R. (2010), "Microwave applications to oil Sands and petroleum: a review", *Fuel Processing Technology*, Vol. 91, pp. 127-135.

National Aeronautics and Space Administration, (2002) Athabasca Oil Sands, *world of change* accessed http://earthobservatory.nasa.gov/Features/WorldOfChange/athabasca.php

National Space Research and Development Agency image of Diamond Mine in Russia last accessed 28/08/12 from http://www.sstl.co.uk/media-gallery/images/nigeriasat-2?imagepath=%2fMedia-Gallery%2fImages%2fDiamond-Mine--Mirny--Russia

Nayar, S.K, Ikeuchi, K, and Kanade, T. (1989), *Surface Reflection: Physical and Geometrical Perspectives*, CUM Publications, Carnegie Mellon University, Pittsburgh, Pennysylvania, pp. 1 – 53.

Nayar, S.K, Ikeuchi, K, and Kanade, T. (1991), "Surface Reflection: Physical and Geometrical Perspectives," *IEEE Transactions on Pattern Analysis and Machine Intelligence*, Vol. 13, No. 7, July 1991.

Nigerian Geological Survey Agency (NGSA) (2010), Tarsands and Bitumen Exploration Opportunities in Nigeria, report published by *Nigerian Ministry of Mines and Steel Development*, pp. 1-19.

Notaros, B.M., McCarrick, C.D., and Kasilingam, D.P. (2001), "Two numerical techniques for analysis of pyramidal horn antennas with continuous metallic ridges", in *Proceedings IEEE International Symposium Antennas Propagation Digest*, Vol. 2, Boston, Massachussets, pp. 560-563.

Nguyen, T.T., Janik, L.J., and Raupach, M. (1991), "Diffuse reflectance infrared Fourier transform (DRIFT) spectroscopy in soil studies", *Australian Journal of Soil Research*, Vol. 29, pp.49–67.

Odunaike, R.K, Ijeoma, G.C, Edigbe, R.O and Babatope, A.H. (2009), "Oil Sands Exploration in Ijebu-Imushin using magnetic and electrical resistivity methods", 11th SAGA Biennial Technical Meeting and Exhibition, Swaziland, 16 – 18 September 2009, pp. 247-252.

Odunaike, R.K, Laoye, J.A., Fasunwo, O.O., Ijeoma, G.C, and Akinyemi, L.P. (2010), "Geophysical mapping of the occurrence of shallow oil sands in Idiopopo at Okitipupa area, South-western Nigeria", *African Journal of Environmental Science and Technology*, Vol. 4, No. 1, pp. 034-044.

Oldenburg, D.W. and Jones, F.H.M (2007), Inversion for Applied Geophysics: learning resources about geophysical inversion, University of British Columbia Inversion Facility. Also available at www.eos.ubc.ca/ubcgif/iag/index.htm.

Olhoeft, G.R. (1981), Electrical properties of rocks. In *Physical Properties of Rocks and Minerals,* Y.S. Touloukian, W.R. Judd and R.F Roy (Ed.), pp. 257-329, New York:McGraw Hill.

Omatsola, M.E and Adegoke, O.S. (1981), "Tectonic evolution and Cretaceous Stratigraphy of the Dahomey Basin", *Journal of Mining and Geology*, Vol. 18, pp: 130-139.

Oh, Y., Sarabandi, K., and Ulaby, F.T. (1992), "An Empirical Model and an Inversion Technique for Radar Scattering from Bare Soil Surfaces", *IEEE Transactions on Geoscience and Remote Sensing*, Vol. 30, No. 2, March, pp. 370 - 381.

Oliver, C., and Quegan, S. (2004), *Understanding Synthetic Aperture Radar Images*, SciTech Publishing, Inc, Raleigh, NC 27613, 479 pp.

Oliver, C.J. (1988), "Representation of Correlated Clutter in Coherent Images," *Inverse Problems*, Vol. 4, pp. 843-866.

Oloumi, D., Mousavi, P., Pettersson, M.I., and Elliott, D.G. (2013), "A modified TEM Horn Antenna customized for oil well monitoring applications", *IEEE Transactions on Antennas and Propagationi*, Vol. 61, No. 12, December, pp. 5902 – 5909.

Olver, A.D., Clarricoats, P.J.B, Kishk, A.A. and Shafai, L. (1994), Microwave Horns and Feeds, Vol. 39, *IEE Electromagnetic Waves Series*, London*:* Institution of Engineering and Technology Publishers, 512 pp.

Owen, E.W (1975), *Trek of the oil finders: a history of exploration for petroleum*, American Association of Petroleum Geologists Publishers, Tulsa, Oklahoma.

Palacky, G.J. and West, G.F. (1991), Airborne Electromagnetic Methods, In *Electromagnetic Methods in Applied Geophysics – Volume 2 Applications* Part B, M.N. Nabighian, (Ed.), Society of Exploration Geophysicists, ISBN 1-56080-22-4, Tulsa, Oklahoma, pp. 811-879.

Patil, P.A., Gorek, M., Folberth, M., Hartmann, A., Forgang, S., Fulda, C., and Reinicke, K.M. (2010), "Experimental study of electrical properties of oil based mud in the frequency range from 1 to 100 MHz", *Society of Petroleum Engineering Drilling and Completion*, September 2010, pp. 380 – 390.

Panzner, B., Jostingmeier, A., and Omar, A., (2010), "A compact double-ridged horn antenna for ground penetrating radar applications", in *Proceedings of the 18th International Conference of Microwave Radar and Wireless Communications* (MIKON), 14 – 16 June, 2010, pp. 1 – 4.

Papa, R.J and Lennon, J.F. (1988), "Conditions for the validity of physical optics in rough surface scattering", *IEEE Transactions on Antennas and Propagation*, Vol. 36, No. 5, May 1998, pp.647-649.

Peake, W.H., and Oliver, T.L. (1971), The response of terrestrial surfaces at microwave frequencies, Ohio State University, Electro-science Laboratory, 1440-7, Technical Report AFAL-TR-70-301, Columbus, Ohio, 279 pp.

Pearlman, J.S., Barry, P.S., Segal, C.C., Shepanski, J., Beiso, D. and Carman, S.L. (2003), "Hyperion, a space-based imaging spectrometer", *IEEE Transactions on Geoscience and*
Remote Sensing, Vol. 41, pp. 1160–1173.

Pedersen, C. (2000), Asphaltene characterization: permittivity measurements and modeling, *PhD Thesis*, Technical University: Lyngby, Denmark, 2000.

Peplinski, N.R., Ulaby, F.T., Dobson, M.C. (1995), "Dielectric properties of soils in the 0.3 – 1.3 GHz range", *IEEE Transactions on Geoscience and Remote Sensing*, Vol. 33, No. 3, pp. 803 – 807.

Petukhov, A.V., Principal Structural elements of the field of concentrations of hydrocarbon gases. *Dokl. Acad. Sci. USSR, Earth Sci.* Sect., 233, pp.189-191.

Phillip, R.P., Crisp, P.T., Surface Geochemical Methods used for oil and gas prospecting-A review, *Journal of Geochemical Exploration,* Vol. 17, Issue 1, September 1982, pp:1-34, ISSN 0375-6742, 10.1016/0375-6742(82)90016-6.

Pierre, E.P. (1992), Microwave separation of bituminous material from tar sands, Canadian
Patent 1293943, January 7, 1992.

Plaut, J.J, Rivard, B, D'lorio, M.A (1999), Radar: Sensors and Case Studies in *Remote Sensing for the Earth Sciences – Manual of Remote Sensing*, Rencz, A.N (ed) 3rd Ed., Vol. 3, John Wiley & Sons, pp. 613-642.

Prado, I.D.M and Crósta, A.P (1997), Evaluating Geoscan AMSS Mk-II for gold exploration in the Fazenda Maria Preta District, Rio Itapicuru Greenstone Belt, Bahia State, Brazil. *Bol. Ig-USP, Sér.Cient.,* Vol.28, pp. 63-83.

Prebble, P., Coxworth, A., Simieritsch, T., Dyer, S., Huot, M and Walsh, H. (2009), "Carbon Copy: Preventing Oil Sands Fever in Saskatchewan", *Pembina Foundation, Saskatchewan Environmental Society, Canadian Parks and Wilderness Society*.

Rajendran, S., Thirunavukkarasu, A., Balamurugan, G., Shankar, K. (2011), "Discrimination
of iron ore deposits of granulite terrain of Southern Peninsular India using ASTER data", *Journal of Asian Earth Sciences*, Vol. 41, pp. 99–106.

Rajesh, H.M. (2004), "Application of remote sensing and GIS in mineral resource mapping—an overview", *Journal of Mineralogical and Petrological Sciences*, Vol. 99, pp. 83-103.

Raney, R.K. (1998), Radar Fundamentals: Technical Perspective, in *Principles and Applications of Imaging Radar – Manual of Remote Sensing*, 3rd Ed., Vol. 2, F.M Henderson, A.J. Lewis (Ed.) John Wiley & Sons, pp. 9-120.

Raney, R.K., and Bamler, R. (1994), "Comments on SAR signal and noise equations", *Proceedings IGARSS* 94, Pasadena, California, pp. 298 – 300.

Raney, R.K. (1998), Radar Fundamentals: Technical Perspective, in *Principles and Applications of Imaging Radar – Manual of Remote Sensing*, 3rd Ed., Vol. 2, F.M Henderson, A.J. Lewis (Ed.) John Wiley & Sons, pp. 9-120.

Rau, R.N. and Wharton, R.P. (1982), "Measurement of core electrical parameters at ultrahigh and microwave frequencies", *Journal of Petroleum Technology*, Society of Petroleum Engineers SPE-9380-PA, Vol. 34, No. 11, pp. 2689-2700.

Rawlinson, N., Pozgay, S. And Fishwick, S., Seismic Tomography: A window into deep Earth. *Physics of the Earth and Planetary Interiors* 2010, Vol. 178 (3) pp. 101-135.

Read, J. and Whiteoak, D. (2003), *The Shell Bitumen Handbook*, 5th Ed., Thomas Telford Publishing, London, 462 pp.

Rencz, A.N. (ed) (1999), *Remote Sensing for the Earth Sciences – Manual of Remote Sensing*, 3rd Ed., Vol. 3, John Wiley & Sons, 707 pp.

Renouf, G., Scoular, R.J. and Soveran, D. (2003), "Treating heavy slop oil with variable frequency microwaves", *Canadian International Petroleum Conference*, July 1, 2003.

Rejon, L., Manero., O., and Lira-Galeana, C. (2004), "Rheological, dielectric and structural characterization of asphaltene suspensions under DC electric fields", *Fuel*, Vol. 83, pp. 471-476.

Rice, S.O. (1951), "Reflection of electromagnetic waves by slightly rough surfaces", *Communications on Pure and Applied Mathematics*, Vol. 4, pp. 351 – 378.

Riegger, S., Wiesbeck, W., and Sieber, A.J. (1987), "On the Origin of Cross-polarization in Remote Sensing", *Proceedings of IGARSS'87 Symposium*, Ann Arbor, MI, Vol. 1, pp. 577-580, May.

Rodríguez, A., and Abreu, R. (1990), A mixing law to model the dielectrics properties of porous media, *Society of Petroleum Engineers SPE 21096*, SPE Latin American Petroleum Engineering Conference, Rio de Janeiro, October 14 – 19, 1990.

Sabins, F.F. (1997), *Remote Sensing – Principles and Interpretation*, 3rd ed., Freeman, New York, 494 pp.

Sabine, C (1999), Remote Sensing Strategies for Mineral Exploration, in *Remote Sensing for the Earth Sciences – Manual of Remote Sensing*, 3rd Ed., Vol. 3, Rencz, A.N. (ed) John Wiley & Sons, pp. 375-447.

Salisbury, J.W., and Walter, L.S. (1989), "Thermal infrared (2.5-13.5 MU-M) spectroscopic remote sensing of igneous rock types on particulate planetary surfaces", *Journal of Geophyisical Research*-Solid Earth and Planets 94, 9192-9202.

Salisbury, J.W., Walter, L.S., and Vergo, N. (1989), "Availability of a library of infrared (2.1-25.0 MU-M) mineral spectra", *American Mineralogist*, Vol. 74, 938-939.

Sahni, A., Kumar, M., and Knapp, R. (2000), "Electromagnetic heating methods for heavy oil reservoirs, *Society of Petroleum Engineers*, SPE-62550 presented at the SPE/AAPG
Western Regional Meeting held in Long Beach, California, June 19–23, 2000.

Sabins, F.F. (1997), *Remote Sensing – Principles and Interpretation*, 3rd ed., Freeman, New York, 494 pp.

Sarabandi, K., Ulaby, F.T. and Tassoudji, M.A. (1990), "Calibration of Polarimetric Radar Systems with Good Polarization Isolation", *IEEE Transactions on Geoscience and Remote Sensing*, Vol. GE-28, pp. 70 – 75.

Scales, J (1997), *Theory of Seismic Imaging Lecture Notes in Earth System Sciences*, Vol. 2, Springer-Verlag Berlin and Heidelberg, GmbH and Co, ISBN-10: 354059051X.

Schaber, G.G. (1999), "SAR studies in the Yuma Desert, Arizona: Sand Penetration, Geology and the Detection of military ordnance debris", *Remote Sensing of the Environment*, Vol. 67, pp. 320-347.

Schaber, G. G., Berlin, G. L., and Brown, W. E., Jr. (1976), "Variations in surface roughness within Death Valley, California: Geological evaluation of 25-cm wavelength radar images." *Geological Soceity of America Bulletin*, Vol. 87, No.1, pp.29-41

Schantz, H. (2005), *The Art and Science of Ultrawideband Antennas*, The Artech House Antenna and Propagation Library, Norwood, MA:Artech House Incorporated, 331 pp.

Schneider, J.M., and Dante, F. (2009), "Time-domain reflectometry – parametric study for the evaluation of physical properties in soils", *Canadian Geotechnical Journal*, Vol. 46, No. 7, pp. 753 – 767.

Scheidt, S., Lancaster, N., Ramsey, M. (2011), "Eolian dynamics and sediment mixing in the Gran Desierto, Mexico, determined from thermal infrared spectroscopy and remote-sensing data", *Geological Society of America Bulletin*, Vol. 123, pp. 1628–1644.

Schön, J.H., (1998), *Physical Properties of Rocks: Fundamentals and Principles of Petrophysics*, 2nd Edition, Vol. 18, Amsterdam, The Netherlands, Elsevier, 600 pp.

Schumacher, D.F. (1996), "Hydrocarbon-induced alteration of soils and sediments" *American Association of Petroleum Geologist* Vol. 66, pp.71-89.

Serbin, G., Or, D., Blumberg, D.G. (2001), "Thermodielectric effects on radar backscattering from wet soils" *IEEE Transactions on Geoscience and Remote Sensing*, Vol. 39, No. 4, pp. 897 – 901.

Shabba, H.A (2010), Nigerian Space Program and African Region, presentation to the United Nations Office on Outer Space Affairs last accessed 24/08/12 from http://www.oosa.unvienna.org/pdf/pres/stsc2012/2012ind-03E.pdf.

Shaw, R, C and Kratochvil, B. (990), Near-infrared diffuse reflectance analysis of Athabasca Oil Sand. *Anal. Chem.,* Vol. 62, No. 2, pp.167-174. DOI: 10.1021/ac00201a016

Shen, L.C. (1985), "Problems in dielectric constant logging and possible routes to their solutions", *The Log Analyst*, Vol. 26, No. 6, pp. 14-25.

Shenker, S., (2008), "Canada's black gold oil rush", Article for the British Broadcasting Corporation, last accessed online 18 March 2015 from http://news.bbc.co.uk/1/hi/world/americas/7762226.stm

Sibley, M.J., Bent, J.V., and Davis, D.W., Reservoir Modelling and Simulation of a Middle Eastern Carbonate Reservoir. *SPERE*, Vol. 12, No. 2, pp. 75. Paper 36540-PA. DOI: 10.2118/36540-PA.

Silverstein, R.M. and Webster, F.X. (1998), "Infrared spectroscopy" in *Spectrometric Identification of Organic Compounds*, 6th Ed., John Wiley and Sons, Inc., New York, pp. 70-105.

Skriver, H, Schou, J and Dierking, W. (2000), "Mapping by Airborne Synthetic Aperture Radar", *International Archives of Photogrammetry and Remote Sensing*, Vol. XXXIII, Part B1, Amsterdam, 2000.

Skolnik, M.I. (Ed) (1990), *Radar Handbook,* Vol. 2, McGraw-Hill Book Company, 1328 pp.

Somerton, W. H. (1992), *Thermal properties and temperature-related behaviour of rock/fluid systems*, Developments in Petroleum Science, Vol. 37, Elsevier, 257 pp.

Soumekh, M., (1999), *Synthetic Aperture Radar Signal Processing with Matlab Algorithms*, New York:John Wiley & Sons, Inc-Interscience Publication, 616 pp.

Soumekh, M., (1994), *Fourier Array Imaging*, Englewood Cliffs, NJ:Prentice Hall.

Spragg, R.A. (2000), "IR spectroscopy sample preparation methods", in *Encyclopedia of spectroscopy and spectrometry*, J.C. Lindon (Ed.), New York: Academic Press, pp.1058-1066.

Spies, B, Fitterman, D, Holladay, S, and Liu, G (Eds) (1998), Proceedings of the International Conference on Airborne Electromagnetics (AEM 1998), *Exploration Geophysics*, Vol. 29, Issues 1 and 2, pp:1-262.

Stahl, W., Faber, E., Carey, B.D and Kirksey, D.L. (1981), "Near surface evidence of migration of natural from deep reservoirs and source rocks", *Bulletin American Association of Petroleum Geology,* Vol. 65, pp.1543-1550.

Strakhov, N.M (1962), *Principles of the theory of Lithogenesis*, Izdat. Akad. Nauk SSSR, Moscow, (in Russian), Translation by Consultants Bureau and Oliver and Boyd, Edinburgh and London, I, 1967; II, 1969.

Strausz, O.P., and Lown, E.M. (2003), "The Chemistry of Alberta oil sands, bitumen and heavy oils", Alberta Energy Research Institute, Calgary, AB, pp. 588–592.

Stewart, G.A and MacCallum, G.T. (1978), *Athabasca Oil Sands Guide Book*, Canada Society of Petroleum Geologists, Calgary, Canada, 33 pp.

Stimson, G.W. (1998), *Introduction to Airborne Radar*, 2nd Ed., SciTech Publishing Inc, Edison: New Jersey, 584 pp.

Stimson, G.W., Griffiths, H.D., Baker, C.J., Adamy, D., (2014), *Introduction to Airborne Radar*, 3rd Ed., SciTech Publishing Inc, Edison: New Jersey, 745 pp.

Sullivan, M.J., Belanger, D.L., Skalinski, M.T., Jenkins, S.D., and Dunn, P., (2006), Permeability from Production Logs-Method and Application. Paper SPE102894-MS presented at the SPE Annual Technical Conference and Exhibition, San Antonio, Texas, 24-27 Sept 2006. DOI 10.2118/102894-MS.

Swann, G.E., and Patwardhan, S.V. (2011), "Application of Fourier Transform Infrared Spectroscopy (FTIR) for assessing biogenic silica sample purity in geochemical analyses and palaeoenvironmental research", *Climate of the Past,* Vol. 7, pp. 65-74.

Taflove, A., and Brodwin, M. (1975), "Numerical solution of the steady state electromagnetic scattering problems using the time-dependent Maxwell's equations", *IEEE Transactions on Microwave Theory and Techniques*, Vol. 23, No. 8, pp. 623-630.

Tao, R., and Xu, X. (2006), "Reducing the viscosity of crude oil by pulsed electric or magnetic field", *Energy & Fuels*, Vol. 20, pp. 2046-2051.

Tenigeer, N.Z., Qui, J., Zhang, P., and Zhang, Y. (2013), "Design of a novel broadband EMC double ridged guide horn antenna", *Progress in Electromagnetics Research C*, Vol. 39, pp. 225 – 236.

Tennyson, J., Bernath, P.F., Brown, L.R., Campargue, A., Császár, A.G., Daumont, L., Gamache, R.R., Hodges, J.T., Naumenko, O.V., Polyansky, O.L., Rothman, L.S., Vandaele, A.C., Zobov, N.F. (2014), A database of water transitions from experiment and theory (IUPAC Technical Report), Pure Applied Chemistry, Vol. 86, pp. 71-83.

Tissot, B.P and Welte, D.H (1984), *Petroleum Formation and Occurrence*, 2nd Ed., Springer-Verlag, Berlin Heidelberg New York Tokyo, ISBN 0-387-13281-3, 728 pp.

Tong, K.F., Luk, K.M., Lee, K.F., Shum, S.M. (1997), "Analysis of broadband U-slot microstrip antenna", *IEE Conference publication 10th International Conference on Antennas and Propagation*, 14 – 17 April, 1997, pp.1.110 – 1.113.

Torrance, K., and Sparrow, E. (1966), "Off-specular peaks in the directional distribution of reflected thermal radiation," *Journal of Heat Transfer*, Vol. 88, pp.223-230, May 1966.

Ulaby, F.T., Batlivala, P.P. and Dobson, M.C. (1978), "Microwave backscatter dependence on surface roughness, soil moisture and soil texture, Part 1: Bare soil," *IEEE Transactions on Geoscience Spectron*, Vol. GE-16, October, pp. 286-295.

Ulaby, F.T., El-Rayes, M.A. (1987), "Microwave dielectric spectrum of vegetation – Part 2: Dual Dispersion Model", *IEEE Transaction on Geoscience and Remote Sensing*, Vol. 25, No. 5, pp. 551-557.

Ulaby, F.T., Moore, R.K., and Fung, A.K., (1981), *Microwave Remote Sensing: Active and Passive, volume I, Microwave Remote Sensing Fundamentals and Radiometry*, Reading:MA, Addision-Wesley, 456 pp.

Ulaby, F.T (1982), "Radar Signatures of Terrain: Useful Monitors of Renewable Resources", *Proceedings of the IEEE*, Vol. 70, No. 12, December, pp. 1410 - 1428.

Ulaby, F.T., Moore, R.K., and Fung, A.K., (1982), *Microwave Remote Sensing: Active and Passive, volume II, Radar Remote Sensing and Surface Scattering and Emission Theory*, Reading:MA, Addision-Wesley, 1064 pp.

Ulaby, F.T., Moore, R.K., and Fung, A.K., (1986), *Microwave Remote Sensing: Active and Passive, volume III, Volume Scattering and Emission Theory, Advanced Systems, and Applications*, Reading:MA, Addision-Wesley, 2162 pp.

Ulaby, F.T., Haddock, T.F., East, J.R. and Whitt, M.W. (1988), "A millimeterwave network analyzer based scatterometer", *IEEE Transactions in Geoscience and Remote Sensing*, vol. 26, No. 1, January, pp. 75-81.

Ulaby, F.T. and Dobson, M.C. (1989), *Handbook of Radar Scattering Statistics for Terrain*, Artech House, Norwood, MA, 372 pp.

Ulaby, F.T., Nashashibi, A., El-Rouby, A., Li, E.S., De Roo, R.D., Sarabandi, K. (1998), "95 GHz Scattering by Terrain at Near-Grazing Incidence", *IEEE Tansactions on Antennas and Propagation*, Vol. 46, No. 1, January, pp. 3 – 13.

US 47 C.F.R. (2003), Part 15 Subpart F 15.503(a-d), Ultra-Wideband operation (October 1, 2003 edition), p. 767 in United States Code of Federal Regulations Title 47 containing the Federal Communication Commission's rules and regulations

Ustin, S. (ed.) (2004), *Remote Sensing for Natural Resources Management and Environmental Monitoring: Manual of Remote Sensing*, 3 ed., Vol. 4, John Wiley & Sons, Inc ISBN:978-0-471-31793-7, 736 pp.

Ustin, S.L., Zarco-Tejada, P.J., Jacquemoud, S., Asner, G.P., (2004), Remote Sensing of the Environment: State of the Science and New Directions, in *Remote Sensing for Natural Resources Management and Environmental Monitoring – Manual of Remote Sensing*, 3rd Ed., Vol. 4, S. Ustin (Ed.) John Wiley & Sons, pp. 679-729.

Valim de Freitas, L., Rodrigues de Freitas, A.P.B., Veraszto, E.V., Marins F.A.S. and Silva, M.B. (2013), *European International Journal of Science and Technology*, Vol. 2, No. 9, pp. 87 – 92.

Van de Hulst, H.C. (1981), *Light Scattering by Small Particles*, pp. 28 - 57, Dover Publications Inc, Mineola, New York, 1981.

van der Meer, F., van Dijk, P., van der Werff, H., Yang, H. (2002), "Remote sensing and petroleum seepage: a review and case study", *Terra Nova* , Vol. 14, pp. 1–17.

van der Werff, H.M.A., Noomen, M.F., van der Meijde, Kooistra, J.F. and van der Meer, F.D. (2007), Use of hyperspectral remote sensing to detect hazardous gas leakage from pipelines, in *New Developments and Challenges in Remote Sensing*, Bochenek, Z. (Ed), Millpress, Rotterdam, pp. 707 - 715.

Van Zyl, J.J. and Ulaby, F.T. (1990), Scattering matrix representation for simple targets, in *Radar Polarimetry for Geoscience Applications*, F.T. Ulaby and C. Elachi (Eds.), Norwood, MA: Artech House, 1990, pp. 17 – 52.

Vane, G., Green, R.O., Vhrien, T.G., Enmark, H.T., Hansen, E.G. and Porter, W.M. (1993a), "The airborne visible/infrared imaging spectrometer (AVIRIS)", *Remote Sensing of Environment*, Vol. 44, pp.127-143.

van der Meer, F.D., van der Werff, H.M.A, van Ruitenbeen, F.J.A, Hecker, C.A., Bakker, W.H., Noomen, M.F., van der Meijde, M., Carranza, E.J.M., Boudewijn de Smeth, J. and Woldai, T. (2012), "Multi- and hyperspectral geologic remote sensing: A review", *International Journal of Applied Earth Observation and Geoinformation*, Vol. 14, pp. 112-128.

Vane, G., Duval, J.E. and Wellman, J.B. (1993), Imaging spectroscopy of the Earth and other solar system bodies, in *Remote Geochemical Analysis: Elemental Mineralogical Composition*, C.M. Pieters and P.A.J. Englert, eds., Cambridge University Press, Cambridge, pp.121-143.

Waff, H.S. (1974), "Theoretical consideration of electrical conductivity in a partially molten mantle and implications for geothermometry", *Journal of Geophysical Research*, Vol. 70, No. 26, pp. 4003 – 4010.

Wallace, D., Starr, J., Thomas, K.P, and Dorrence, S.M. (1998), "Characterisation of Oil Sand Resources", *Report on the activities concerning Annex 1 of the US-Canada Cooperative Agreement on Tar Sand and Heavy Oil*, Alberta Oil Sands Technology and Research Authority, Edmonton. ISBN 0-555006-101-1.

Walker, R. (2013), Mass and density of 300 'dry' materials. Last accessed online on 02.12.2014 from www.simetric.co.uk/si_materials.htm

Walsh, B. (2012), "The Truth about Oil", featured article in Time Magazine, Vol. 179, No. 14, April 2012, pp. 19-27.

Ward, S.H, and Hohmann, G.W. (1987), Electromagnetic Theory for Geophysical Applications, in *Electromagnetic Methods in Applied Geophysics – Volume 1 Theory*, M.N. Nabighian (Ed), pp. 131-311, Society of Exploration Geophysicists, ISBN 0-931830-51-6, Tulsa, Oklahoma.

Wei, B., Şimşek, E., Yu, C. and Liu, Q.H. (2007), "Three-dimensional electromagnetic nonlinear inversion in layered media by hybrid diagonal tensor approximation: Stabilized bi-conjugate gradient fast Fourier transform method", *Journal of Waves in Random and Complex Media*, Vol. 17, No. 2, Taylor & Francis, pp. 129-147.

Weiland, T. (1996), "Time Domain Electromagnetic Field Computation with Finite Difference Methods", International Journal of Numerical Modelling: Electronic Networks, Devices and Fields, Vol. 9, 295-319.

Wentworth, C.K. (1922), "A scale of grade and class terms for clastic sediments", *Journal of Geology,* Vol. 30, No. 5, (July – August 1922), pp.377-392.

Wessa P. (2014), Pearson Correlation (v1.0.9) in Free Statistics Software (v1.1.23-r7), Office for Research Development and Education, last accessed 22 March 2015: http://www.wessa.net/rwasp_correlation.wasp/

Whitt, M.W., Ulaby, F.T. and Sarabandi, K. (1990), Polarimetric Scatterometer Systems and Measurements, in *Radar Polarimetry for Geoscience Applications*, Ulaby, F.T. and Elachi, C. (Eds.), Artech House, Inc:Norwood, MA, pp. 191 – 271.

Wiley, C. (1985), "Synthetic Aperture Radars," *IEEE Transactions Aerospace and Electronic Systems*, vol. AES-21, pp. 440-443, May 1985.

Willey, R.R. (1986), "Emittance and reflectance of various materials in the 2 to 20 micrometer spectral region", *SPIE Vol. 643, Infrared, Adaptive and Synthetic Aperture Optical Systems,* pp. 93-100.

Winkleman, K.H. (2005), On the applicability of imaging spectrometry for the detection and investigation of contaminated sites with particular consideration given to the detection of fuel hydrocarbon contaminants in soil. Doctore thesis, Universidade de Cottbus, Alemanha, 236 pp.

Winsauer, W.O., and Shearin, H.M., Jr. (1952), "Resistivity of brine-saturated sands in relation to pore geometry", American Association of Petroleum Geology Bulletin., Vol. 36, pp.253–277.

Wright, D.L., Watts, R.D., and Bramsoe, E. (1984), "A short-pulse electromagnetic transponder for hole-to-hole use", *IEEE Transactions Geoscience and Remote Sensing*, Vol. GRS-22, No. 6, November, 1984, pp. 720 – 725.

Wolf, N.O. (1986), Use of microwave radiation in separating emulsion and dispersions of hydrocarbons and water, U.S. Patent 4,582,629, April 15, 1986.

World Petroleum Council Report on the Guidelines for the Application of the Petroleum Resources Management System, 2010.

Yang, H., Zhang, J., Van der Meer, F.D., and Kroonenberg, S.B. (1998), "Geochemistry and field spectrometry for detecting hydrocarbon microseepage" *Terra Nova*, 10, pp. 231-235.

Yang, F.C. and Lee, K.S.H. (1976), "Impedance of a two conical plate transmission line," *Sensor and simulation note #221*, pp. 1 – 34.

Yoon, S., Son, J., Lee, W., Lee, H.Y., and Lee, C.W. (2009), "Prediction of bitumen content in oil sand based on FTIR measurement", *Journal of Industrial and Engineering Chemistry*, Vol. 15, pp.370-374.

Zhang, Y., Huston, A., Mallo, M., Li, Z., and Zhang, G. (2010), "A Scatterometer System for Laboratory Study of Polarimetric Electromagnetic Signatures of Icy Hydrometeors", *IEEE Transactions on Instrumentation and Measurement,* Vol. 59, No. 3, March, pp. 671 – 681.

APPENDIX 1: Glossary of Terms

Azimuth: This is the direction of travel of the platform bearing the radar usually perpendicular to the direction of the range. Hence the words “azimuth”, “cross-range” or “along-track” are used to describe this. In this work it is generally considered to be in the *y* direction. The platform could be an aircraft then the radar is said to be airborne or a satellite such that the radar is spaceborne.

Barrels (bbl): The standard barrel of crude oil or other petroleum product (abbreviated bbl) is 42 US gallons (34.972 Imperial gallons or 158.987 L). Measurement originated in the early Pennsylvania oil fields, and permitted both UK and US traders to refer to the same unit, based on the old English wine measure, the tierce. By 1866 the oil barrel was standardized at 42 US gallons. Although oil has not actually been shipped in barrels since the introduction of oil tankers, the 42-US-gallon size is still used as a unit for measurement, pricing, and in tax and regulatory codes. The extra “b” to become "BBL," has a historical note. In the early 1860's, when oil production began, there was no standard container for oil, so oil and petroleum products were stored and transported in barrels of all different shapes and sizes (beer barrels, fish barrels, molasses barrels, turpentine barrels, etc.). By the early 1870's, the 42-gallon barrel had been adopted as the standard for oil trade. This was 2 gallons per barrel more than the 40-gallon standard used by many other industries at the time. The extra 2 gallons was to allow for evaporation and leaking during tranport (most barrels were made of wood). Standard Oil began manufacturing 42 gallon barrels that were blue and the use of a blue barrel, abbreviated "bbl," guaranteed a buyer that this was a 42-gallon barrel.

FWHM: The Full Width at Half Maximum is the width in wavelength at the 50% response level of the function. For a spectrometer this is also the definition of the width of the bandpass. Modern spectrometers such as AVIRIS and VIMS sample at half-Nyquist which is approximately equal to the FWHM.

Mixture, Coating: Material under test is coated by another such that each coating is a separate scattering-transmitting layer with optical thickness varying with material properties and wavelength.

Mixture, Linear: Material under test is optically separated so that there is no multiple scattering between components. This is also called “areal mixture” because the

combined signal is the sum of the fractional area multiplied by the spectrum of each component.

Mixture, Molecular: Material under test comprises two components mixed on a molecular level such as gasoline spilled on soil or water adsorbed onto a mineral. The close contact of the mixture components cause band shifts in the asorbate.

Mixture, Intimate: Material under test consists of different materials in intimate contact on a scattering surface such as the mineral grains in soil. The resulting signal may be a highly non-linear combination of the end-member spectra depending on the optical properties of each component.

Range: This is the distance from the radar track to the platform bearing the radar. It is the direction in which the electromagnetic radiation propagates and usually perpendicular to the direction of the azimuth. Hence the words "range" or "cross-track" are used to describe this. In this work it is generally considered to be in the *x* direction. The platform could be an aircraft then the radar is said to be airborne or a satellite such that the radar is spaceborne.

Reststrahlen Band: The location of fundamental vibrational stretching modes in the near and mid-infrared. These are narrow bands of wavelengths which give strong vibrational bans of solids in the infrared. It is German for "residual rays".

Spectral Bandwidth: The width of an individual channel in the spectrometer. The narrower the spectral bandwidth the narrower the absorption feature the spectrometer will measure accurately.

Spectral Range: The scope of wavelengths covered by a spectrometer. There are general spectral ranges in common use to a first order and controlled by detector technology.

Spectral Sampling: The distance in wavelength between the spectral bandpass profiles for each channel in the spectrometer as a function of wavelength. This should not be confused with bandpass although sometimes they are grouped together and considered spectral resolution.

Spectral Signal to Noise Ratio: The SSNR depends on detector sensitivity, spectral bandwidth and intensity of light reflected or emitted from the surface being measured. When spectral features are strong, an SSNR of 10 could be adequate, however when they are weak SSNR values of several hundred or higher may be required to ensure the spectrum is measured with enough precision to record details of the spectrum.

APPENDIX 2A: Code for Comparison of Generic RCS

Parameters Used in Simulation

Symbol	Description	Value	Units	Status
Pt	**Peak power**		**Watts**	**Input**
Freq	**Radar center frequency**		**Hz**	**Input**
G	**Antenna gain**		**dB**	**Input**
Sigma	**Radar Cross Section (RCS)**		**m^2**	**Input**
Te	**Effective noise temperature**		**Kelvin**	**Input**
B	**Bandwidth**		**Hz**	**Input**
Nf	**Noise Figure**		**dB**	**Input**
Loss	**Radar losses**		**dB**	**Input**
Range	**Radar range to target**		**Meters**	**Input**
Snr	**Signal to noise ration**		**dB**	**Output**

```
% Use this program to compares radar cross section with SNR and also detection range with SNR.
close all
clear all
pt = 1.5e+6; % peak power in Watts freq = 5.0e+9; % radar operating frequency in Hz, C-band
g = 45.0; % antenna gain in dB sigma = 0.1; % RCS in m squared per meter square
te = 290.0; % effective noise temperature in Kelvins
b = 5.0e+6; % radar operating bandwidth in Hz nf = 3.0; %noise figure in dB
loss = 6.0; % radar losses in dB
range = linspace(25e3,165e3,1000); % range to target from 25 Km 165 Km, 1000 points
snr1 = radar_eq(pt, freq, g, sigma, te, b, nf, loss, range); snr2 = radar_eq(pt, freq, g, sigma/10, te, b, nf, loss, range);
snr3 = radar_eq(pt, freq, g, sigma*10, te, b, nf, loss, range); % plot SNR versus  detection range for three different values of RCS
figure() rangekm  = range ./ 1000; plot(rangekm,snr3,'-r',rangekm,snr1,'-.b',rangekm,snr2,'--k'); grid
legend('{\it\sigma_R_C_S} = 0 dBsm','{\it\sigma_R_C_S} = -10dBsm','{\it\sigma_R_C_S} = -20 dBsm')
xlabel ('Detection range in Km'); ylabel ('SNR in dB'); title('SNR vs Range for different Radar Cross Section, RCS')


% plot SNR versus detection range for three different values of transmit % power
snr1 = radar_eq(pt, freq, g, sigma, te, b, nf, loss, range); snr2 = radar_eq(pt/3, freq, g, sigma, te, b, nf, loss, range);
snr3 = radar_eq(pt*2.0, freq, g, sigma, te, b, nf, loss, range);


figure () plot(rangekm,snr3,'-r',rangekm,snr1,'b-.',rangekm,snr2,'--k'); grid
legend('{\itP_t_x} = 3.0 MW','{\itP_t_x} = 1.5 MW','{\itP_t_x} = 0.5 MW'); xlabel ('Detection range in km');
ylabel ('SNR in dB'); title('SNR vs Range for different Transmit Power, P_t_x')
```

APPENDIX 2B: Azimuth Processing for Spaceborne SAR

In Figure 2.16 we considered the Earth as flat. This is a simplification which is apt for the airborne radar case however for a NASRDA satellite the radar will be spaceborne and therefore the Earth's curvature is important. The spherical geometry relevant to such a case is illustrated below in Figure 2B.1 (a) where the satellite at altitude h travels in the azimuth direction and illuminates the Earth's surface with pulses of electromagnetic radiation. R_{rg} is the ground range and R_E is the radius of the earth. Also evident is a schematic diagram Figure 2B.1 (b) illustrating the power transmitted in either direction with a main beam and lower power side lobes.

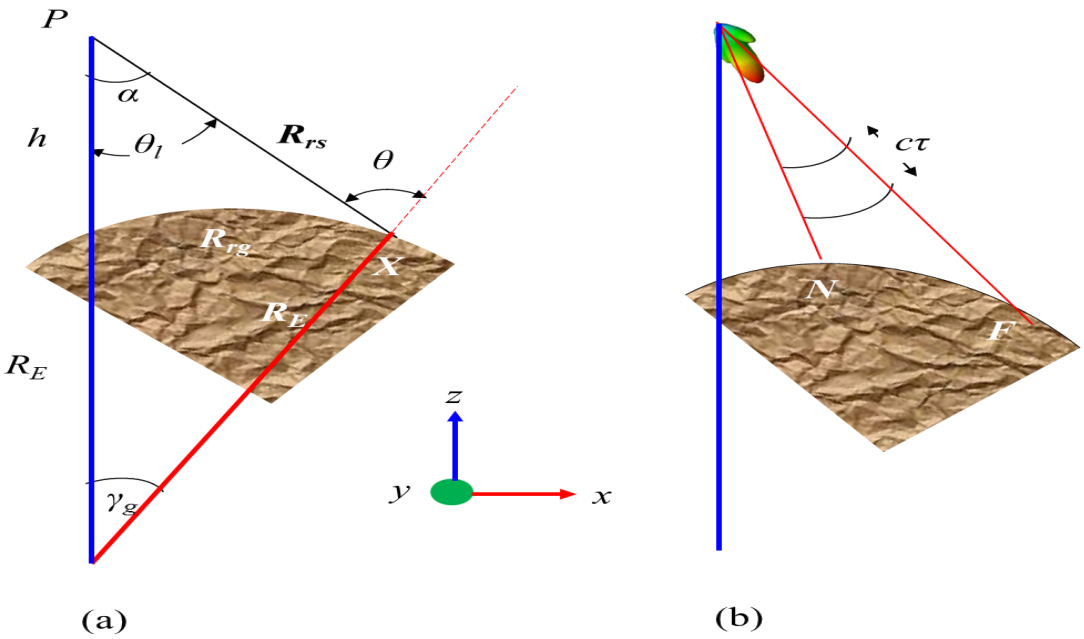

Figure 2B.1: (a) The spherical geometry appropriate to spaceborne SAR and (b) illustration of pulse spreading with duration τ

The angular distribution of power from the antenna means that the power per unit area (dA) received at a point on the ground depends on which part of the beam is illuminating the point. The minimum and maximum ranges are marked N and F in Figure 2C.1 (a). The distance between N and F is the *swath width* and the slant range is R_{rs}. Next we consider the simple case of a perfectly spherical Earth with radius R_E (≅ 6370 km) and local incidence angle, θ using geometric relations:

$$\boldsymbol{R_{rs} = (R_E + h)\frac{\sin\gamma}{\sin\theta} \approx (R_E + h)\frac{\gamma}{\sin\theta}.} \tag{2B.52}$$

$$\boldsymbol{R_{rs}^2 = R_E^2 + (R_E + h)^2 - 2R_E(R_E + h)\cos\gamma} \tag{2B.53}$$

$$\boldsymbol{R_{rg} = R_E\,\gamma} \tag{2B.54}$$

$$\boldsymbol{\gamma = \theta - \alpha} \tag{2B.55}$$

$$\boldsymbol{\sin\alpha = \frac{R_E}{R_E + h}\sin\theta} \tag{2B.56}$$

The approximation in Eqn. 2B.5 is for small γ. The slant range R_{rs} is inferred directly from the time delay using Eqn. 2.18 however given either R_{rs}, R_{rg}, θ, α, or γ the other four can be derived. For airborne imaging $h << R_E$ therefore Eqn (2B.1 and 2B.2) reduce to the flat earth approximations:

$$\boldsymbol{R_{rs} = \frac{R_{rg}}{\sin\theta}} \tag{2B.57}$$

$$\boldsymbol{R_{rs}^2 = h^2 + R_g^2} \tag{2B.58}$$

It is important to realise that the ground range, R_{rg} resolution varies linearly across the swath which has important meaning for image properties particularly spaceborne radar.

Next we develop the analogous expressions for an orbital SAR with more or less the same results. Using the same geometry shown in Figure 2C.1 (a) we assume the orbital plane of the satellite lies in the *yz* plane (with *y* in the azimuth direction as used throughout this research work). If we define the *xz* plane using a point *X* fixed on the Earth's surface such that $X = R_E$ (sin γ, 0, cos γ) and ignoring the Earth rotation, the satellite sweeps past X with angular velocity Ω rads s^{-1}. From Oliver & Quegan (2004), the position of the satellite at time *t* is therefore:

$$\boldsymbol{P} = (\boldsymbol{R_E} + \boldsymbol{h})\ (\boldsymbol{0}, \boldsymbol{\sin \Omega t}, \boldsymbol{\cos \Omega t}). \tag{2B.59}$$

Given that *X* is broadside to the satellite at time 0. The distance *R* between the satellite and *X* will be:

$$\boldsymbol{R} = |\boldsymbol{X} - \boldsymbol{P}| \approx \boldsymbol{R_0}\ \frac{\boldsymbol{R_E}\ (\boldsymbol{R_E} + \boldsymbol{h})\ \boldsymbol{\cos \gamma \Omega^2 t^2}}{\boldsymbol{2R_0}}. \tag{2B.60}$$

$$= \boldsymbol{R_0} + \frac{\boldsymbol{R_E \cos \gamma\ s^2}}{\boldsymbol{2R_0(R_E + h)}} \tag{2B.61}$$

Where R_0 is the CPA of the satellite to *X* and $s = (R_E + h)\ \Omega t$ is the distance along the satellite track. The approximation assumes the azimuth beamwidth is small so that only small values of Ω*t* (when the *X* is in the radar beam) are of interest and hence $s << R_0$. Evidently the distance between the satellite and *X* has a variation that is approximately quadratic in both time and along track distance. The corresponding two-way phase delay is given by:

$$\boldsymbol{\phi(t)} \approx -\frac{\boldsymbol{4\pi R_0}}{\boldsymbol{\lambda}}\ -\frac{\boldsymbol{2\pi}}{\boldsymbol{\lambda}}\frac{\boldsymbol{R_E\ (R_E + h) \cos \gamma\ \Omega^2 t^2}}{\boldsymbol{R_0}} \tag{2B.62}$$

This is equivalent to linear frequency modulation (FM) in which the frequency variation:

$$\boldsymbol{f_d}\ = \frac{\boldsymbol{1}}{\boldsymbol{2\pi}}\frac{\boldsymbol{d\phi}}{\boldsymbol{dt}}\ \approx -\frac{\boldsymbol{2}}{\boldsymbol{\lambda}}\frac{\boldsymbol{R_E\ (R_E + h)}}{\boldsymbol{R_0}}\boldsymbol{\cos \gamma\ \Omega^2 t}\ \ \textbf{[Hz]} \tag{2B.63}$$

can be interpreted as Doppler shift.

The time for which the target *X* will be illuminated depends on the beamwidth on the ground (i.e. from (2.20), $R_{rg}.\theta_B$) and the velocity of the beam on the ground where $V = R_E\ \Omega \cos \gamma$. Therefore the illumination time is:

$$\boldsymbol{\tau} = \frac{\boldsymbol{R_{rg}\,.\,\theta_B}}{\boldsymbol{V}} = \frac{\boldsymbol{R_{rg}\,.\,\theta_B}}{\boldsymbol{R_E \Omega \cos \gamma}} \tag{2B.64}$$

The azimuth (Doppler) bandwidth will now be:

$$\boldsymbol{B = \frac{2}{\lambda}(R_E + h)\Omega\theta_B \quad [Hz]} \tag{2B.65}$$

with associated time resolution $1/B$. In this time the beam moves a ground distance V/B so that the azimuth resolution on the ground is:

$$\boldsymbol{\Delta R_{az} = \frac{R_E}{R_E + h}\cos\gamma\frac{\lambda}{2\theta_B}} \tag{2B.66}$$

Using the approximation $\theta_B = \lambda/d_a$ and noting that γ is small, the azimuth resolution for a spaceborne Stripmap SAR theoretically improves from Eqn. 2.26 to become:

$$\boldsymbol{\Delta R_{az} = \frac{R_E}{R_E + h}\cos\gamma\frac{d_a}{2} \approx \frac{R_E}{R_E + h}\frac{d_a}{2}} \tag{2B.67}$$

APPENDIX 2C: SAR Range and Azimuth Processing

In section 2.3.2 we considered the echo received $s(t)$ on illuminating a one dimensional target area in the x (range) and later y (azimuth) with a signal $p(t)$ without considering the transmitted signal $p(t)$. In many SAR systems this transmitted waveform $p(t)$ is of the form:

$$\boldsymbol{p(t) = \exp\{i(w_0 t + \beta t^2)\} for |t| \le \tau/2.} \tag{2C.1}$$

Where w_0 is the carrier frequency of the radar expressed in radians/s^{-1}. The phase of the signal is therefore:

$$\boldsymbol{\phi(t) = w_0 t + \beta t^2 \qquad [radians]} \tag{2C.2}$$

And the instantaneous frequency (given by the time derivative of the phase) is:

$$\boldsymbol{f(t) = \frac{w_0 + 2\beta t}{2\pi} \qquad [Hz]} \tag{2C.3}$$

The frequency changes linearly with time so may be referred to as linear *frequency modulation* (FM) or chirp with an FM rate of β/π Hz/s^{-1}. (Plots of phase, real part, imaginary part and instantaneous frequency of the complex envelope $\exp(i\,\beta t^2)$ against time are shown in Figure 2C.1 (Use Matlab code saved as Appendix2DLFM in appendices folder. Here use figures 16 for phase 2 for real part, 4, for imaginary part and 17 for up chirp in Figure 2C.1 quadrants).

The total frequency sweep or bandwidth will be seen to be:

$$\boldsymbol{B = \frac{\beta\tau}{\pi} \qquad [Hz]} \tag{2C.4}$$

The pulse shown in figure 2D.1 has $B = 100$MHz and $= 10^{-6}$ seconds. In order to process the returned echo signal the carrier frequency will be stripped off and matched filtering (correlation of the signal with a copy of the transmitted signal) will be performed. For the pulse given in Eqn 2D.1 the return from a point scatterer is a delayed, scaled version of the transmitted pulse which after matched filtering produces a response whose shapes is given by:

$$\boldsymbol{h_r(t) = \int_{-\tau/2}^{\tau/2} \exp(i\beta s^2)\exp(-i\beta[s+t]^2) rect\left(\frac{s+t}{\tau}\right)\, ds} \tag{2C.5.a}$$

$$= (\tau - |t|)\mathbf{sinc}\left(\frac{\beta}{\pi}\right) t[\tau - |t|])\mathbf{rect}\left(\frac{t}{\tau}\right) \tag{2C.5.b}$$

Where $\text{rect}(t) = \begin{cases} 1 & |t| \leq \frac{1}{2} \\ 0 & |t| > \frac{1}{2} \end{cases}$ and $\text{sinc}(t) = \frac{\sin \pi t}{\pi t}$

The output $h_r(t)$ is formed by correlating the signal modulation $k(t) = \exp(-i\beta t^2)$ with itself and referred to as the *autocorrelation function* (ACF) of $k(t)$. Imaging radars are designed so that the *time-bandwidth product B* is large and a good approximation solution for the time resolution is $r_t \approx 1/B$. The *compression ratio* is the ratio of the resolution after processing to the original pulse length:

$$\textbf{compression ratio} = \frac{\tau}{r_t} = B\tau \tag{2C.6}$$

so the compression ratio is equal to the time bandwidth product. For example the ERS-1 satellite has a compression ratio of 575 therefore the 37.1μs pulse has resolution equivalent to a simple pulse duration 64.5 ns. The *ideal* form of the SAR point spread function occurs for a large time-bandwidth product where $h_r(t)$ is written to a good approximation as:

$$\boldsymbol{h_r(t) \cong \tau\, \mathbf{sinc}\left(\frac{\beta\tau t}{\pi}\right) = \tau\, \mathbf{sinc}\,(Bt)} \tag{2C.7}$$

Azimuth processing is the source of a lot of the complexity in SAR. After range processing the measurement in each range gate contains contribution from each scatterer azimuthally extended in accordance with the azimuth bandwidth. SAR processing exploits the nearly quadratic range variation of a point scatterer as the beam passes over it. From Figure 2C.1 where azimuth coordinates is y the distance between platform and spatial position X satisfies $R^2 = R_0^2 + y^2$. For a narrow beam, X is only illuminated when $y << R_0$, in which case:

$$\mathbf{R} \approx \boldsymbol{R_0 + \frac{x^2}{2R_0}} \tag{2C.8}$$

The corresponding two-way phase delay at the carrier frequency is:

$$\boldsymbol{\emptyset(x) = -\frac{4\pi R_0}{\lambda} - \frac{2\pi x^2}{\lambda R_0}} \tag{2C.9}$$

With an associated rate of change of phase with distance given by:

$$\frac{d\emptyset}{dx} = -\frac{4\pi x}{\lambda R_0} \tag{2C.10}$$

This is equivalent to linear FM in the distance variable. Spatially the *synthetic aperture length* L_{SA}, is the azimuth distance illuminated at range:

$$L_{SA} = R_0 \theta_B \tag{2C.11}$$

Applying results for a chirp pulse the spatial bandwidth is given by (Oliver & Quegan, 2004):

$$\frac{1}{2\pi} \text{ x } \frac{4\pi}{\lambda R_0} \text{x } L_{SA} = \frac{2}{d_a} \tag{2C.12}$$

Recalling that $\theta_B = \lambda/d_a$ then the associated spatial resolution for Stripmap SAR becomes:

$$r_{az} = \frac{d_a}{2} \tag{2C.13}$$

And for a spaceborne SAR it is (Raney, 1991):

$$r_{az} = \frac{R_E}{R_E + h} \frac{d_a}{2} \tag{2C.14}$$

Oliver, C., and Quegan, S., (2004), *Understanding Synthetic Aperture Radar Images*, SciTech Publishing, Inc, Raleigh, NC, ISBN 1-891121-31-6.

Raney, R.K. (1991),"Considerations for SAR Image Quantification Unique to Orbital Systems", *IEEE Transaction on Geoscience and Remote Sensing*, Vol. 29, pp. 754 – 760.

APPENDIX 3A: Surface Roughness Variation

We discuss the requirements to produce 'Raleigh roughness' based on table 3.9. The variation in surface height necessary to produce a rough response at an incidence angle, θ_i of 25° is 3.24 cm at L-band, 0.79 cm at C-band and 0.42 cm at X-band.

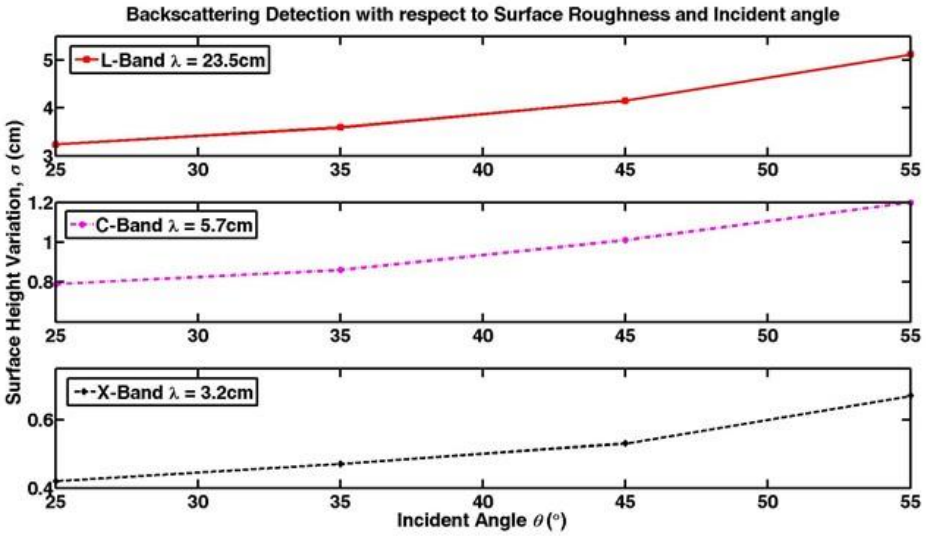

Figure 0A.**1**: Surface scattering detection for L, C and X-band.

The X-band value of σ, which differentiates the Rayleigh transition between EM fields seen as smooth by the SAR or rough at θ_i = 55° is 0.67 cm but 5.12 cm if we consider this at L-band Fig. 3.9.

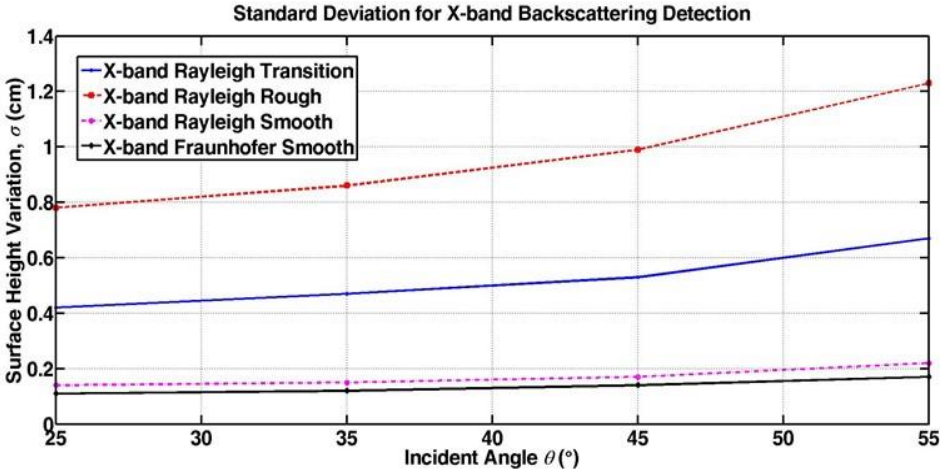

Figure 0A.2: Standard deviation for backscattering detection at X-band.

Similarly the variation that marks the Rayleigh Smooth and Fraunhofer Smooth surface at X-band is 0.17 cm and 0.14 cm at 45° respectively. This would need to be 1.33cm and 1.04 cm at L-band respectively Fig. 3A.3.

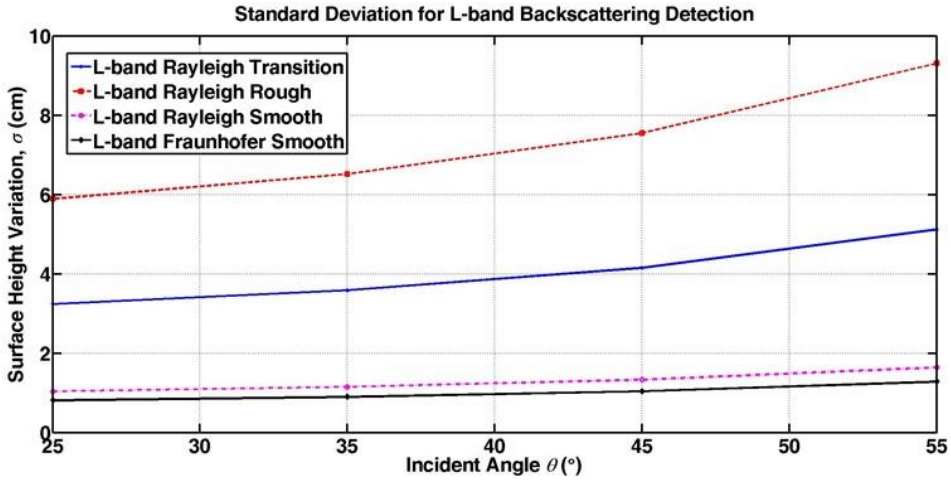

Figure 0A.3: Standard deviation for backscattering detection L-band.

A comparison of the Rayleigh smooth and Fraunhofer smooth roughness criteria values for L, C and X-band are shown in Fig. 3A.4. They will help to explain the type of backscatter to characterize different terrain when using these SAR bands to detect oil sand amongst surrounding terrain.

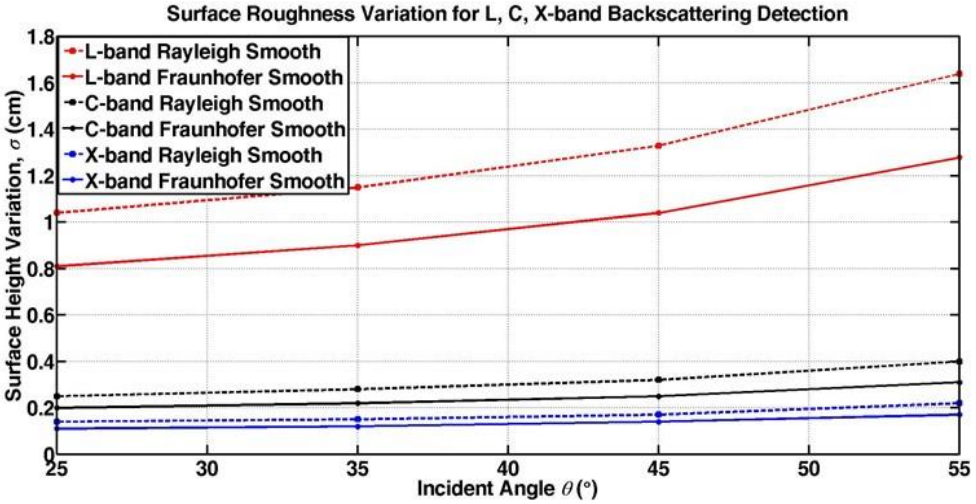

Figure 0A.4: Surface roughness variation for L, C and X-band backscattering.

APPENDIX 4: Code Geochemical Signature Analysis Model

```
%%%%%%%%%%%%%%%%%%%%%%%%%%%%%%%%%%%%%%%%%%%%%%%%%%%%%%%%%%%%%%%%%%%%%%%%
% FTIR Multivariate Analysis using Shimzada FTIR Shimadza Equipment %
% First we preliminary plot the oil sands data in the first section  %
% then we perform Partial Least Squares Analysis (PLSA) and         %
% Principal Components Analysis on the data to highlight the best   %
% method of modelling the response variable
%%%%%%%%%%%%%%%%%%%%%%%%%%%%%%%%%%%%%%%%%%%%%%%%%%%%%%%%%%%%%%%%%%%%%%%%

%%%%%%%%%%%%%%%%%%%% Part One. Plotting Data. %%%%%%%%%%%%%%%%%%%%%%%%%%%%
clear all
 % Load test soil data
 %Hard oil sand data
 load hsand_atr1_Used.txt
load hsand_atr2_Used.txt
load hsand_atr3_Used.txt
load hsand_atr1_3DUsed.txt %with Location included 1
load hsand_atr2_3DUsed.txt %with Location included 2
load hsand_atr3_3DUsed.txt %with Location included 3
 %Viscous oil sand data
load vsand_atr1_Used.txt
load vsand_atr2_Used.txt
load vsand_atr3_Used.txt
load vsand_atr1_3DUsed.txt %with Location included 4
load vsand_atr2_3DUsed.txt %with Location included 5
load vsand_atr3_3DUsed.txt %with Location included 6
% Assign data Hard oil sand
Xh2=hsand_atr1_3DUsed(80:2179,1);    % ATR Measurement for HOS from Location 1
Yh2=hsand_atr1_3DUsed(80:2179,2);    % ATR Measurement for HOS from Location 1
Zh2=hsand_atr1_3DUsed(80:2179,3);    % ATR Measurement for HOS from Location 1
Xh3=hsand_atr2_3DUsed(80:2179,1);    % ATR Measurement for HOS from Location 2
Yh3=hsand_atr2_3DUsed(80:2179,2);    % ATR Measurement for HOS from Location 2
Zh3=hsand_atr2_3DUsed(80:2179,3);    % ATR Measurement for HOS from Location 2
Xh4=hsand_atr3_3DUsed(80:2179,1);    % ATR Measurement for HOS from Location 3
Yh4=hsand_atr3_3DUsed(80:2179,2);    % ATR Measurement for HOS from Location 3
Zh4=hsand_atr3_3DUsed(80:2179,3);    % ATR Measurement for HOS from Location 3
Xh5=hsand_atr1_Used(:,1); Yh5=hsand_atr1_Used(:,2); Xh6=hsand_atr2_Used(:,1);
Yh6=hsand_atr2_Used(:,2); Xh7=hsand_atr3_Used(:,1); Yh7=hsand_atr3_Used(:,2);
% Assign data viscous oil sand
Xv1=vsand_atr1_3DUsed(80:2179,1);    % ATR Measurement for VOS from Location 4
Yv1=vsand_atr1_3DUsed(80:2179,2);    % ATR Measurement for VOS from Location 4
Zv1=vsand_atr1_3DUsed(80:2179,3);    % ATR Measurement for VOS from Location 4
Xv2=vsand_atr2_3DUsed(80:2179,1);    % ATR Measurement for VOS from Location 5
Yv2=vsand_atr2_3DUsed(80:2179,2);    % ATR Measurement for VOS from Location 5
Zv2=vsand_atr2_3DUsed(80:2179,3);    % ATR Measurement for VOS from Location 5
Xv3=vsand_atr3_3DUsed(80:2179,1);    % ATR Measurement for VOS from Location 6
Yv3=vsand_atr3_3DUsed(80:2179,2);    % ATR Measurement for VOS from Location 6
Zv3=vsand_atr3_3DUsed(80:2179,3);    % ATR Measurement for VOS from Location 6
Xv4=vsand_atr1_Used(:,1);   Yv4=vsand_atr1_Used(:,2); Xv5=vsand_atr2_Used(:,1);
Yv5=vsand_atr2_Used(:,2);  Xv6=vsand_atr3_Used(:,1); Yv6=vsand_atr3_Used(:,2);

% Combination of Results HOS and VOS
figure(1) % combined FTIR results
plot(Xh5, Yh5, '-m', Xh6, Yh6, '--g',Xh7, Yh7, '-k', Xv4, Yv4, '-c',Xv5, Yv5, '--b',
Xv6, Yv6, '-r'); set(gca, 'XDir','reverse'); xlabel('Wavenumber ({\itcm}^{-1})');
ylabel('Intensity (% \itT)'); grid on
title ('Nigerian Oil Sand Geochemical Signature');
legend ('HOS 1', 'HOS 2', 'HOS 3', 'VOS 1','VOS 2', 'VOS 3'); axis tight
%%%%%%%%%%%%%%%%%%%%%%%%For Normalisation of OilSand %%%%%%%%%%%%%%%%%%%%%%%%%%%%%
 % MUT E, F from three different locations
% in one data set with 2179 datapoints
load NormalisedOilSandSpectra.txt

% Assign Data (No X column)
YMUTE_Yh5=NormalisedOilSandSpectra(:,1); YMUTE_Yh6=NormalisedOilSandSpectra(:,2);
YMUTE_Yh7=NormalisedOilSandSpectra(:,3); YMUTF_Yv4=NormalisedOilSandSpectra(:,4);
YMUTF_Yv5=NormalisedOilSandSpectra(:,5); YMUTF_Yv6=NormalisedOilSandSpectra(:,6);
% Using msnorm for the oil sand terrain
OilSandNorm=msnorm(Xh5, NormalisedOilSandSpectra(:,[1 2 3 4 5 6]));

figure(2) % combined oil sand results NORMALISED and Baseline Corrected
```

```
plot(Xh5,OilSandNorm(:,1),'-m',Xh6,OilSandNorm(:,2),'--g',Xh7,OilSandNorm(:,3),'-
k',Xv4, OilSandNorm(:,4),'-c',Xv5, OilSandNorm(:,5),'--b', Xv6,OilSandNorm(:,6),'-r');
set(gca, 'XDir','reverse'); xlabel('Wavenumber ({\itcm}^{-1})');
ylabel('Transmittance');
grid on
title ('Nigerian Oil Sand Geochemical Signature');
legend ('HOS 1', 'HOS 2', 'HOS 3', 'VOS 1','VOS 2', 'VOS 3')

figure(3) % combined FTIR results with Location
plot3(Xh2,Zh2, Yh2, '-b', Xh3, Zh3, Yh3, '--r',Xh4, Zh4,Yh4, '--k', Xv1, Zv1, Yv1, '-
c',Xv2, Zv2, Yv2, '-g', Xv3, Zv3, Yv3, '-k'); set(gca, 'XDir','reverse');
xlabel('Wavenumber ({\itcm}^{-1})'); ylabel('Location'); zlabel('Intensity (% \itT)');
grid on
title ('Spectral Reflectance Signature Nigerian Oil Sands')
legend ('HOS 1', 'HOS 2', 'HOS 3', 'VOS 1','VOS 2', 'VOS 3'); axis tight

%%%%%%%%%%%%%%%%%%%% Part Two. PLSA vs PCA. Oil Sand Spectra %%%%%%%%%%%%%%%%
% PLSA and PCA are used to model the geochemical signature for a response %
% variable in the presence of a large number of predictor variables that  %
% are correlated. Both construct new predictor variables or components as %
% a linear combination of the original predictor variables but in different%
% ways. Refer to Chapter 4 of Thesis for how they do this. Here we present%
% the second part of the code for obtaining the geochemical signature     %
%%%%%%%%%%%%%%%%%%%%%%%%%%%%%%%%%%%%%%%%%%%%%%%%%%%%%%%%%%%%%%%%%%%%%%%%%%%

% Load the data
% First Data set comprises the spectral measurements of 6 samples of oil sand at
% 2126 wavelengths and the measurement location. The data acquisition process has been
discussed in Thesis Chapter 4 and in 3 papers:
% • M.Ezeoke, K. Tong and S. Shi (2014), "Modeling Synthetic Aperture Radar Signature
% of Agbabu Oil Sand for Petroleum Exploration", Energy Production and Management
% in the 21st Century the Quest for Sustainable Energy, Vol.2, Eds C.A. Brebbia,
% E.R. Magaril and M.Y. Khodorovsky, WIT Transactions on Ecology and the Environment,
% Vol. 190, pp. 1284 - 1295.
% • Ezeoke, M. and Tong, K. (2013), "Modeling Electromagnetic Reflectivity
% of Agbabu Oil Sands from Hyperspectral Infrared Reflectance Spectra and
% Dielectric Properties at L-, C- and X-band Frequencies",
% Proceedings of the 5th Computational Intelligence, Communication Systems
% and Networks (CICSyN2013), 5-8 June, Madrid, Spain, pp.125-130, 2013
% • M.Ezeoke and K.Tong (2014), "Polarimetric SAR Classification of Terrain for Land
% Degradation Monitoring", Proceedings of the 2014 IAF Global Space Applications
% Conference (2014 GLAC), 2 - 4 June, Paris, France,
% GLAC-2014,S,6B,4,x20699, 2014.
% The Oil Sand data were combined in to one large stream OilSandSpectra
% The Terrain data were combined in to BarefacedTerrainSpectra
load OilSandSpectra2.txt
load OilSandSpectra.txt
load Location.txt
load VNIR_MIR2.txt
load VNIR_MIR.txt

whos VNIR_MIR2 Location VNIR_MIR

% Assign data Oil Sand Spectra

XOSS=OilSandSpectra(1,:);    % ATR Measurement wavenumber same for all Loc
                             % First row and all 2126 columns
YHOS1=Location(1,1); % all the rows but first column
YHOS2=Location(2,1); YHOS3=Location(3,1); YVOS1=Location(4,1);
YVOS2=Location(5,1); YVOS3=Location(6,1); ZHOS1=VNIR_MIR(1,:);
ZHOS2=VNIR_MIR(2,:); ZHOS3=VNIR_MIR(3,:); ZVOS1=VNIR_MIR(4,:);
ZVOS2=VNIR_MIR(5,:); ZVOS3=VNIR_MIR(6,:);

%%%%%%%%%%%%%%%%%%%%%%%%%%%%%  Arrange data and plot 3D %%%%%%%%%%%%%%%%%%
[dum,v] = sort(Location); % creating 'dum' & 'v' with values 1-6
L80 = repmat(1:2126,6,1); % create 6 x 2126 Array with 6 rows and 2126
                          % columns. Each column contains the same value
                          % which is equal to the column number i.e 1, 2
                         % Therefore each row is identical from 1...2126

for n = 1:6                % Assign each row the value of wavenumber for plot
    L80(n, 1:2126) = VNIR_MIR2(1,:); %spectral wavenumber in 1st row VNIR_MIR2
end
```

```
oldorder=get(gcf,'DefaultAxesColorOrder');set(gcf,'DefaultAxesColorOrder',jet(6));% 6
loc
figure (4) plot3(L80',repmat(Location(v),1,2126)',VNIR_MIR(v,:)');
xlabel('Wavenumber ({\itcm}^{-1})'); ylabel('Location');zlabel('Intensity (% \itT)')
set(gca, 'XDir','reverse'); title ('Spectral Reflectance Signature Nigerian Oil
Sand');
legend ('HOS 1', 'HOS 2', 'HOS 3', 'VOS 1','VOS 2', 'VOS 3'); grid on
axis('tight');
figure (5) plot3(L80',repmat(Location(v),1,2126)',VNIR_MIR(v,:)');
xlabel('Wavenumber ({\itcm}^{-1})'); ylabel('Location');zlabel('Intensity (% \itT)')
set(gca, 'XDir','reverse'); axis('tight')
title ('Spectral Reflectance Signature Nigerian Oil Sand');
legend ('HOS 1', 'HOS 2', 'HOS 3', 'VOS 1','VOS 2', 'VOS 3'); grid on

%%%%%%%%%%%%%%%%%%%%%%%%%%%%%%%% Fit Data with components %%%%%%%%%%%%%%%%%%%%%%%%%%%%%%%%
% Fitting the Data with Two Components. We Use the |plsregress| function to fit a PLSA
% % model with five PLS components and one response
%%%%%%%%%%%%%%%%%%%%%%%%%%%%%%%%%%%%%%%%%%%%%%%%%%%%%%%%%%%%%%%%%%%%%%%%%%%%%%%%%%%%%%%
MyX = VNIR_MIR; MyY = Location; [m,p] = size(MyX); % let the array take extent of X
[Xloadings,Yloadings,Xscores,Yscores,betaPLS, PLSPctVar] = plsregress(MyX,MyY,3);
MyfitPLS = [ones(m,1) MyX]*betaPLS;
 % Using three components to explain the variations in the observed |y|
% Next we plot the % of variance in the measurements as function of the
% components i.e. 3 component model. From cross validation it is clear from
% figure 16 that 3 components account for 95% of the variation compared with
% only 85% from 2 components
figure (6) plot(1:3,cumsum(100*PLSPctVar(2,:)),'-bo');
xlabel('Number of PLSA components'); ylabel('Percent Variance Explained in Y');
title ('Oil Sand Reflectance Spectra');
%%%%%%%%%%%%%%%%%%%%%%%%%%%%%%%% Fit PCA model %%%%%%%%%%%%%%%%%%%%%%%%%%%%%%%%%%%%%%%%
% First we perform PCA on X using |pca| function and retaining 2 principal components
for % Figure 7. Then we use 3 principal components for better accuracy in Figure 8. In
% % essence PCA is a linear regression of the response variable on the three
components.
%%%%%%%%%%%%%%%%%%%%%%%%%%%%%%%%%%%%%%%%%%%%%%%%%%%%%%%%%%%%%%%%%%%%%%%%%%%%%%%%%%%%%%%
[PCALoadings,PCAScores,PCAVar] = pca(MyX,'Economy',false);
betaPCA = regress(MyY-mean(MyY), PCAScores(:,1:2));
% Converting PCA results to original spectral data by transforming to
% regression coefficients for the original uncentered variables
betaPCA = PCALoadings(:,1:2)*betaPCA; betaPCA = [mean(MyY) - mean(MyX)*betaPCA;
betaPCA];
MyfitPCA = [ones(n,1) MyX]*betaPCA;

%%%%%% Plot fitted vs. observed response for the PLSR and PCR fits %%%%%%%%%%%%%%%%%%%
% For 2 components
figure (7) % For 2 components plot(MyY,MyfitPLS,'bo',MyY,MyfitPCA,'r^');
xlabel('Observed Response'); ylabel('Fitted Response');
title ('Oil Sand Geochemical Signature Model');
legend({'PLSA with 2 Components' 'PCA with 2 Components'}, 'location','NW');
% For 3 components
betaPCA3 = regress(MyY-mean(MyY), PCAScores(:,1:3)); betaPCA3 =
PCALoadings(:,1:3)*betaPCA3; betaPCA3 = [mean(MyY) - mean(MyX)*betaPCA3; betaPCA3];
MyfitPCA3 = [ones(n,1) MyX]*betaPCA3;
figure (8)  % For 3 components PCA plot(MyY,MyfitPLS,'bo',MyY,MyfitPCA3,'r^');
xlabel('Observed Response'); ylabel('Fitted Response');
title ('Oil Sand Geochemical Signature Model');
legend({'PLSA with 2 Components' 'PCA with 3 Components'},'location','NW');
% In order to confirm which does a better job at fitting the variation in the samples
or % location |y|, we look at the horizontal scatter of fitted values in the plot. We
also % % determine this using the r-squared value from both the PCA and PLSA to
confirm. R     % % squared refers to the model quality determined by square of the
correlation coefficient % between predicted values and measured values
TSS = sum((MyY-mean(MyY)).^2); RSS_PLS = sum((MyY-MyfitPLS).^2);
rsquaredPLS = 1 - RSS_PLS/TSS   % model quality determined by square of the
                                % correlation coefficient between predicted
                                % values and measured values
% 2 Components
RSS_PCA = sum((MyY-MyfitPCA).^2);
rsquaredPCA = 1 - RSS_PCA/TSS   % model quality determined by square of the
% 3 Components
RSS_PCA3 = sum((MyY-MyfitPCA3).^2);
rsquaredPCA3 = 1 - RSS_PCA3/TSS  % model quality determined by square of the
```

```
% We finally confirm the predictive power of both models by plotting the response
% % variable against the 2 component and 3 component predictors first for PLS analysis
and %later PCA in Figure 9 and 10 below First for PLSA
figure (9) plot3(Xscores(:,1),Xscores(:,2),MyY-mean(MyY),'bo');
title ('Oil Sand Geochemical Signature Model'); legend('PLSA');
grid on; view(-30,30);
% Next for PCA with 2 components
figure (10) plot3(PCAScores(:,1),PCAScores(:,2),MyY-mean(MyY),'r^');
title ('Oil Sand Geochemical Signature Model'); legend('PCA'); grid on; view(-30,30);
% Next for PCA with 3 components
% While the three PLSA components better predict the observed |MyY|,
% Figure 11 shows that they marginally explain less variance in the observed |MyX|
% than the first three principal components used in the PCA.
figure (11) plot(1:3,100*cumsum(PLSPctVar(1,:)),'b-o',1:3,
100*cumsum(PCAVar(1:3))/sum(PCAVar(1:3)),'r-^');
xlabel('Number of Principal Components'); ylabel('Percent Variance Explained in X');
title ('Oil Sand Reflectance Spectra'); legend({'PLSA' 'PCA'},'location','SE');
% Cross validation can help us predict the mean squared prediction error
% (MSEP) using a 5-fold cross validation.  for PLSA
[Xl,Yl,Xs,Ys,beta,pctVar,PLSmsep] = plsregress(MyX,MyY,3,'CV',3);
 % For PCA |crossval| combined with a function to calculate the sum of
% squared errors for PCA may be used to estimate MSEP with 3 fold C-V
%Crossval2 uses Kfold as 3 for three runs rather than 10. Saved it in the
%folder for calling out. Also changed 'leave out' in Crossval2 to refer to
%3 rather than 1 multiple. For Fig 12 only plotted the first 3 components
%for both PCAmsep and PLSmsep too.
PCAmsep=sum(crossval2(@pcrsse,MyX,MyY,'leaveout',3),1)/m;
% We can plot the MSEP for PLSA and PCA to discover how many components are
% required to get the same prediction accuracy. Here we see that three
% components suffice. Also the second component in PCA seems to have slightly
% increased the MSE prediction error of the model. This means that the
% combination of predictor variables contained in that component is not strongly
% correlated with |MyY| or the location. This is explained by the fact that
% PCA constructs components to explain variation in |X| (spectral reflectance)
% not the location or samples |MyY|.
figure (12) plot(1:3,PLSmsep(2,1:3),'b-o',1:3,PCAmsep(1,1:3),'r-^');
xlabel('Number of components'); ylabel('Estimated Mean Squared Prediction Error');
title ('Oil Sand Geochemical Signature Model'); legend({'PLSA'
'PCA'},'location','NE');


%%%%%%%%%%% Model Parsimony %%%%%%%%%%%%%%%%%%%%%%%%%%%%%%%%%%%%%%%%%%%%%%%%%%%%%
% Using weights we can check how strongly each component in the PLSA depends on the
% % original variables and in what direction
% In variable alone
[Xl,Yl,Xs,Ys,beta,pctVar,mse,stats] = plsregress(MyX,MyY,3);
figure (13) plot(1:2126,stats.W,'-');
xlabel('Variable (wavenumber)'); ylabel('PLS Weight');
title ('Oil Sand Geochemical Signature Model');
legend({'1st Component' '2nd Component' '3rd Component'},'location','NW');
% In wavenumbers alone
[Xl,Yl,Xs,Ys,beta,pctVar,mse,stats] = plsregress(MyX,MyY,3);
figure (14) plot(L80(1,1:2126),stats.W,'-');
xlabel('Variable [in Wavenumber ({\itcm}^{-1})]'); ylabel('PLS Weight');
title ('Oil Sand Geochemical Signature Model');
legend({'1st PC' '2nd PC' '3rd PC'}, 'location','NW');
% Using PCA loadings we can check how strongly each component in the PCA
% depends on the original variables and in what direction
% In variable alone
figure (15) plot(1:2126,PCALoadings(:,1:3),'-');
xlabel('Variable'); ylabel('PCA Loading'); title ('Oil Sand Geochemical Signature
Model'); legend({'1st PC' '2nd PC' '3rd PC'},'location','NW');
% In wavenumbers alone
figure (16) plot(L80(1,1:2126),PCALoadings(:,1:3),'-');
xlabel('Variable [in Wavenumber ({\itcm}^{-1})]'); ylabel('PCA Loading');
title ('Oil Sand Geochemical Signature Model');
legend({'1st PC' '2nd PC' '3rd PC'},'location','NW');

%%%%%%%%%%%%%%%%%%%% Part Three. PLSA vs PCA Barefaced Terrain%%%%%%%%%%%%%%%
load BarefacedTerrainSpectra.txt
load LocationBarefacedTerrain.txt
load VNIR_MIR_BTS.txt
load VNIR_MIR_BTS2.txt

whos VNIR_MIR_BTS LocationBarefacedTerrain VNIR_MIR_BTS2
 % Assign data BarefacedTerraub Spectra
```

```
 XBTS=VNIR_MIR_BTS2(1,:);     % ATR Measurement wavenumber same for all Loc
                              % First row and all 2179 columns
YSand100=LocationBarefacedTerrain(1,1); % all the rows but first column
YSand90=LocationBarefacedTerrain(2,1); YSand80=LocationBarefacedTerrain(3,1);
YSand70=LocationBarefacedTerrain(4,1); YSoil100=LocationBarefacedTerrain(5,1);
YSoil90=LocationBarefacedTerrain(6,1); YSoil80=LocationBarefacedTerrain(7,1);
YSoil70=LocationBarefacedTerrain(8,1);

ZSand100=VNIR_MIR_BTS(1,:); % first column but all the rows
ZSand90=VNIR_MIR_BTS(2,:);   ZSand80=VNIR_MIR_BTS(3,:);  % third column but all the
rows
ZSand70=VNIR_MIR_BTS(4,:);  ZSoil100=VNIR_MIR_BTS(5,:);  % Fifth column but all the
rows
ZSoil90=VNIR_MIR_BTS(6,:);  ZSoil80=VNIR_MIR_BTS(7,:);  % Seventh column but all the
rows
ZSoil70=VNIR_MIR_BTS(8,:);  % Eighth column but all the rows
 %Change Absorbance to Transmittance%
ZSand100T=100./(10.^ZSand100);  ZSand90T=100./(10.^ZSand90);
ZSand80T=100./(10.^ZSand80);    ZSand70T=100./(10.^ZSand70);
ZSoil100T=100./(10.^ZSoil100);  ZSoil90T=100./(10.^ZSoil90);
ZSoil80T=100./(10.^ZSoil80);    ZSoil70T=100./(10.^ZSoil70);
% Water Details
load WaterUsed.txt
XWaterab=WaterUsed(:,1); YWaterab=WaterUsed(:,2);
%Change Absorbance to Transmittance
XWaterabT=100./(10.^XWaterab);   YWaterabT=100./(10.^YWaterab);
% Oil Sand
load hsand_atr2_Used.txt
load vsand_atr2_Used.txt
% Assign data ATR Hard oil sand     - MUT E
Xah2=hsand_atr2_Used(:,1); % Second ATR Results
Yah2=hsand_atr2_Used(:,2); % Second ATR Results
% Assign ATR data viscous oil sand  - MUT F
Xav2=vsand_atr2_Used(:,1); % Second ATR Results
Yav2=vsand_atr2_Used(:,2); % Second ATR Results
%Hundred Percent Terrain
load HundredPercentSand.txt
load HundredPercentSoil.txt
load NinetyPercentSand.txt
load NinetyPercentSoil.txt
load EightyPercentSand.txt
load EightyPercentSoil.txt
X100abSand=HundredPercentSand(:,1); Y100abSand=HundredPercentSand(:,2);
X100abSoil=HundredPercentSoil(:,1); Y100abSoil=HundredPercentSoil(:,2);
X90abSand=NinetyPercentSand(:,1); Y90abSand=NinetyPercentSand(:,2);
X90abSoil=NinetyPercentSoil(:,1); Y90abSoil=NinetyPercentSoil(:,2);
X80abSand=EightyPercentSand(:,1); Y80abSand=EightyPercentSand(:,2);
X80abSoil=EightyPercentSoil(:,1); Y80abSoil=EightyPercentSoil(:,2);

%Change Absorbance to Transmittance
Y100abSandT=100./(10.^Y100abSand); Y100abSoilT=100./(10.^Y100abSoil);
Y90abSandT=100./(10.^Y90abSand);  Y90abSoilT=100./(10.^Y90abSoil);
Y80abSandT=100./(10.^Y80abSand);  Y80abSoilT=100./(10.^Y80abSoil);


figure(17) % combined FTIR results 100% - 80% Terrain WITH Water
plot(X100abSand, Y100abSandT, '-b', X100abSoil, Y100abSoilT, '-g', X90abSand,
Y90abSandT, '--b', X90abSoil, Y90abSoilT, '--g', X80abSand, Y80abSandT, '-.b',
X80abSoil, Y80abSoilT, '-.g', XBTS, ZSoil70T, '-.m',Xah2, Yah2, '-k', Xav2, Yav2, '-
r', XWaterab, YWaterabT, '-y')
set(gca, 'XDir','reverse'); xlabel('Wavenumber ({\itcm}^{-1})');
ylabel('Transmittance');
grid off; title ('Geochemical Signature of Barefaced Terrain compared with Water');
legend ('Beach Sand', 'Loamy Farm Soil', 'BS (10 {\itwt.%} Water)', 'LFS (10 {\itwt.%}
Water)', 'BS (20 {\itwt.%} Water)', 'LFS (20 {\itwt.%} Water)', 'LFS (30 {\itwt.%}
Water)','Hard Oil Sand', 'Viscous Oil Sand', 'Water');


figure(18) % % Normalised FTIR results 100% - 80% Terrain WITH Water but dont
normalise VOS (Yav2) with self
plot(X100abSand, Y100abSandT./Yav2, '-b', X100abSoil, Y100abSoilT./Yav2, '-g',
X90abSand, Y90abSandT./Yav2, '--b', X90abSoil, Y90abSoilT./Yav2, '--g', X80abSand,
Y80abSandT./Yav2, '-.b', X80abSoil, Y80abSoilT./Yav2, '-.g', Xah2, Yah2./Yav2, '-k',
Xav2, Yav2/100, '-r', XWaterab, YWaterabT./Yav2, '-y'); set(gca, 'XDir','reverse');
xlabel('Wavenumber ({\itcm}^{-1})'); ylabel('Transmittance'); grid off;
title ('Geochemical Signature of Barefaced Terrain compared with Water');
```

```
legend ('Beach Sand', 'Loamy Farm Soil', 'BS (10 {\itwt.%} Water)', 'LFS (10 {\itwt.%}
Water)', 'BS (20 {\itwt.%} Water)', 'LFS (20 {\itwt.%} Water)', 'Hard Oil Sand',
'Viscous Oil Sand','Water');

%%%%%%%%%%%%%%%%%%%%%%%%For normalisation Terrain with water %%%%%%%%%%%%%%%%%%%%%%%%
load HundredPercentSand.txt
load HundredPercentSoil.txt
load NinetyPercentSand.txt
load NinetyPercentSoil.txt
load EightyPercentSand.txt
load EightyPercentSoil.txt
load SeventyPercentSand.txt
load SeventyPercentSoil.txt

X100abSand=HundredPercentSand(:,1); Y100abSand=HundredPercentSand(:,2);
X100abSoil=HundredPercentSoil(:,1); Y100abSoil=HundredPercentSoil(:,2);
X90abSand=NinetyPercentSand(:,1); Y90abSand=NinetyPercentSand(:,2);
X90abSoil=NinetyPercentSoil(:,1); Y90abSoil=NinetyPercentSoil(:,2);
X80abSand=EightyPercentSand(:,1); Y80abSand=EightyPercentSand(:,2);
X80abSoil=EightyPercentSoil(:,1); Y80abSoil=EightyPercentSoil(:,2);
X70abSand=SeventyPercentSand(:,1); Y70abSand=SeventyPercentSand(:,2);
X70abSoil=SeventyPercentSoil(:,1); Y70abSoil=SeventyPercentSoil(:,2);
%Change Absorbance to Transmittance
Y100abSandT=100./(10.^Y100abSand);  Y100abSoilT=100./(10.^Y100abSoil);
Y90abSandT=100./(10.^Y90abSand);  Y90abSoilT=100./(10.^Y90abSoil);
Y80abSandT=100./(10.^Y80abSand);  Y80abSoilT=100./(10.^Y80abSoil);
Y70abSandT=100./(10.^Y70abSand);  Y70abSoilT=100./(10.^Y70abSoil);

% MUT A, B, E, F with different weight percentages of A and B along with Water
% in one data set with 2179 datapoints
load TerrainWithWater_Transmittance.txt

% Assign Data (No X column)
YMUTA100P=TerrainWithWater_Transmittance(:,1); %all the rows but first column
YMUTB100P=TerrainWithWater_Transmittance(:,2); %all the rows but second column
YMUTA90P=TerrainWithWater_Transmittance(:,3);
YMUTB90P=TerrainWithWater_Transmittance(:,4);
YMUTA80P=TerrainWithWater_Transmittance(:,5);
YMUTB80P=TerrainWithWater_Transmittance(:,6);
YMUTEHOS=TerrainWithWater_Transmittance(:,7);
YMUTFVOS=TerrainWithWater_Transmittance(:,8);
YWatr=TerrainWithWater_Transmittance(:,9);

% Using msnorm for the terrain types with water
TerrainWaterNorm=msnorm(X100abSand, TerrainWithWater_Transmittance(:,[1 2 3 4 5 6 7 8
9]));

figure(19) % combined FTIR results 100% - 80% Terrain WITH Oil Sand and Water
NORMALISED TO BeachSand and Baseline Corrected
plot(X100abSand, TerrainWaterNorm(:,1), 'b', X100abSoil, TerrainWaterNorm(:,2), 'g',
X90abSand, TerrainWaterNorm(:,3), '--b', X90abSoil, TerrainWaterNorm(:,4), '--g',
X80abSand, TerrainWaterNorm(:,5), '-.b', X80abSoil, TerrainWaterNorm(:,6), '-.g',
Xah2, TerrainWaterNorm(:,7), '-k', Xav2, TerrainWaterNorm(:,8), '-r', XWaterab,
TerrainWaterNorm(:,9), '-y')
set(gca, 'XDir','reverse')
xlabel('Wavenumber ({\itcm}^{-1})')
ylabel('Transmittance')
grid off
title ('Geochemical Signature of Barefaced Terrain compared with Water')
legend ('Beach Sand', 'Loamy Farm Soil', 'BS (10% Water)', 'LFS (10% Water)', 'BS (20%
Water)', 'LFS (20% Water)', 'Hard Oil Sand', 'Viscous Oil Sand', 'Water')
 %%%%%%%%%%%%%%%%%%%%%%%%%%%%%%%  Arrange data and plot 3D %%%%%%%%%%%%%%%%%%
[dum,v] = sort(LocationBarefacedTerrain); % creating 'dum' & 'v' with values 1-8
LBT80 = repmat(1:2179,8,1); % create 8 x 2179 Array with 8 rows and 2179
                            % columns. Each column contains the same value
                            % which is equal to the column number i.e 1, 2
                           % Therefore each row is identical from 1...2179

for n = 1:8                 % Assign each row the value of wavenumber for plot
    LBT80(n, 1:2179) = VNIR_MIR_BTS2(1,:); %spectral wavenumber in 1st row
VNIR_MIR_BTS2
end
```

```
oldorder = get(gcf,'DefaultAxesColorOrder'); set(gcf,'DefaultAxesColorOrder',jet(8));
% 8 samples of barefaced terrain
figure (20)
plot3(LBT80',repmat(LocationBarefacedTerrain(v),1,2179)',100./(10.^VNIR_MIR_BTS(v,:))'
);
xlabel('Wavenumber ({\itcm}^{-1})'); ylabel('Location');zlabel('Intensity (% \itT)')
set(gca, 'XDir','reverse'); title ('Spectral Reflectance Signature Barefaced
Terrain');
legend ('Sand 100{\itwt.%}', 'Sand 90{\itwt.%}', 'Sand 80{\itwt.%}', 'Sand
70{\itwt.%}', 'Soil 100{\itwt.%}', 'Soil 90{\itwt.%}', 'Soil 80{\itwt.%}', 'Soil
70{\itwt.%}');
grid on; axis('tight');

figure (21)
plot3(LBT80',repmat(LocationBarefacedTerrain(v),1,2179)',100./(10.^VNIR_MIR_BTS(v,:))'
);
xlabel('Wavenumber ({\itcm}^{-1})'); ylabel('Location');zlabel('Intensity (% \itT)');
set(gca, 'XDir','reverse'); axis('tight')
title ('Spectral Reflectance Signature Barefaced Terrain');
legend ('Sand 100{\itwt.%}', 'Sand 90{\itwt.%}', 'Sand 80{\itwt.%}', 'Sand
70{\itwt.%}', 'Soil 100{\itwt.%}', 'Soil 90{\itwt.%}', 'Soil 80{\itwt.%}', 'Soil
70{\itwt.%}'); grid on


%%%%%%%%%%%%%%%%%%%%%%%%%%%%%% Fit Data with components %%%%%%%%%%%%%%%%%%
% Fitting the Data with Two Components. % We Use the |plsregress| function to fit a
PLSA % model with five PLS components and one response
%%%%%%%%%%%%%%%%%%%%%%%%%%%%%%%%%%%%%%%%%%%%%%%%%%%%%%%%%%%%%%%%%%%%%%%%%%%%%%%%
MyX = VNIR_MIR_BTS;  MyY = LocationBarefacedTerrain; [m,p] = size(MyX); % let the
array take extent of X
[Xloadings,Yloadings,Xscores,Yscores,betaPLS, PLSPctVar] = plsregress(MyX,MyY,3);
MyfitPLS = [ones(m,1) MyX]*betaPLS;
% Using three components to explain the variations in the observed |y|
% Next we plot the % of variance in the measurements as function of the
% components i.e. 3 component model. From cross validation it is clear from
% figure 16 that 3 components account for 95% of the variation compared with
% only 85% from 2 components
figure (22) plot(1:3,cumsum(100*PLSPctVar(2,:)),'-bo'); xlabel('Number of PLSA
components'); ylabel('Percent Variance Explained in Y');
title ('Barefaced Terrain Reflectance Spectra');


%%%%%%%%%%%%%%%%%%%%%%%%%%%%%% Fit PCA model %%%%%%%%%%%%%%%%%%%%%%%%%%%%%%%%%
% First we perform PCA on X using |pca| function and retaining 2 principal components.
% % Then we use 3 principal components for better  accuracy. In essence PCA is a linear
% % % regression of the response variable on the three components.
%%%%%%%%%%%%%%%%%%%%%%%%%%%%%%%%%%%%%%%%%%%%%%%%%%%%%%%%%%%%%%%%%%%%%%%%%%%%%%%%
[PCALoadings,PCAScores,PCAVar] = pca(MyX,'Economy',false);
betaPCA = regress(MyY-mean(MyY), PCAScores(:,1:2));
% Converting PCA results to original spectral data by transforming to
% regression coefficients for the original uncentered variables
betaPCA = PCALoadings(:,1:2)*betaPCA; betaPCA = [mean(MyY) - mean(MyX)*betaPCA;
betaPCA];
MyfitPCA = [ones(n,1) MyX]*betaPCA;
%%%%%% Plot fitted vs. observed response for the PLSR and PCR fits %%%%%%
% For 2 components
figure (23)              % For 2 components
plot(MyY,MyfitPLS,'bo',MyY,MyfitPCA,'r^'); xlabel('Observed Response');
ylabel('Fitted Response'); title ('Barefaced Terrain Geochemical Signature Model');
legend({'PLSA with 2 Components' 'PCA with 2 Components'},  'location','NW');
% For 3 components
%[PCALoadings,PCAScores,PCAVar] = pca(MyX,'Economy',false);
betaPCA3 = regress(MyY-mean(MyY), PCAScores(:,1:3));
betaPCA3 = PCALoadings(:,1:3)*betaPCA3;
betaPCA3 = [mean(MyY) - mean(MyX)*betaPCA3; betaPCA3];
MyfitPCA3 = [ones(n,1) MyX]*betaPCA3;


figure (24)              % For 3 components PCA
plot(MyY,MyfitPLS,'bo',MyY,MyfitPCA3,'r^'); xlabel('Observed Response');
ylabel('Fitted Response'); title ('Barefaced Terrain Geochemical Signature Model');
legend({'PLSA with 2 Components' 'PCA with 3 Components'}, 'location','NW');
% In order to confirm which does a better job at fitting the variation in
% the samples or location |y|, we look at the horizontal scatter of fitted
% values in the plot. We also determine this using the r-squared value from
% both the PCA and PLSA to confirm. R squared refers to the model quality
% determined by square of the correlation coefficient between predicted values
% and measured values
```

```
TSS = sum((MyY-mean(MyY)).^2); RSS_PLS = sum((MyY-MyfitPLS).^2);
rsquaredPLS = 1 - RSS_PLS/TSS   % model quality determined by square of the

% 2 Components
RSS_PCA = sum((MyY-MyfitPCA).^2); rsquaredPCA = 1 - RSS_PCA/TSS   % model quality

% 3 Components
RSS_PCA3 = sum((MyY-MyfitPCA3).^2); rsquaredPCA3 = 1 - RSS_PCA3/TSS  % model quality

% We finally confirm the predictive power of both models by plotting the response
%variable against the 2 component and 3 component predictors first for PLS analysis
and %later PCA below First for PLSA
figure (25)
plot3(Xscores(:,1),Xscores(:,2),MyY-mean(MyY),'bo');
title ('Barefaced Terrain Geochemical Signature Model'); legend('PLSA');
grid on; view(-30,30);

% Next for PCA with 2 components
figure (26)
plot3(PCAScores(:,1),PCAScores(:,2),MyY-mean(MyY),'r^');
title ('Barefaced Terrain Geochemical Signature Model'); legend('PCA');
grid on; view(-30,30);

% While the three PLSA components better predict the observed |MyY|,
% Figure shows that they marginally explain less variance in the observed |MyX|
% than the first three principal components used in the PCA.
figure (27)
plot(1:3,100*cumsum(PLSPctVar(1,:)),'b-o',1:3, ...
    100*cumsum(PCAVar(1:3))/sum(PCAVar(1:3)),'r-^');
xlabel('Number of Principal Components'); ylabel('Percent Variance Explained in X');
title ('Barefaced Terrain Reflectance Spectra'); legend({'PLSA'
'PCA'},'location','SE');

% Cross validation can help us predict the mean squared prediction error
% (MSEP) using a 5-fold cross validation.  for PLSA
[Xl,Yl,Xs,Ys,beta,pctVar,PLSmsep] = plsregress(MyX,MyY,3,'CV',3);

% For PCA |crossval| combined with a function to calculate the sum of
% squared errors for PCA may be used to estimate MSEP with 3 fold C-V
PCAmsep=sum(crossval2(@pcrsse,MyX,MyY,'leaveout',3),1)/m;

% We can plot the MSEP for PLSA and PCA to discover how many components are
% required to get the same prediction accuracy. Here we see that three
% components suffice. Also the second component in PCA seems to have slightly
% increased the MSE prediction error of the model. This means that the
% combination of predictor variables contained in that component is not strongly
% correlated with |MyY| or the location. This is explained by the fact that
% PCA constructs components to explain variation in |X| (spectral reflectance)
% not the location or samples |MyY|.

figure (28) plot(1:3,PLSmsep(2,1:3),'b-o',1:3,PCAmsep(1,1:3),'r-^');
xlabel('Number of components'); ylabel('Estimated Mean Squared Prediction Error');
title ('Barefaced Terrain Geochemical Signature Model');
legend({'PLSA' 'PCA'},'location','NE');

%%%%%%%%%%% Model Parsimony %%%%%%%%%%%%%%%%%%%%%%%%%%%%%%%%%%%%%%%%%%%%%%%%%
% Using weights we can check how strongly each component in the PLSA
% depends on the original variables and in what direction
% In variable alone
[Xl,Yl,Xs,Ys,beta,pctVar,mse,stats] = plsregress(MyX,MyY,3);
figure (29) plot(1:2179,stats.W,'-'); xlabel('Variable (wavenumber)');
ylabel('PLS Weight'); title ('Barefaced Terrain Geochemical Signature Model');
legend({'1st Component' '2nd Component' '3rd Component'}, 'location','NW');
% In wavenumbers alone
[Xl,Yl,Xs,Ys,beta,pctVar,mse,stats] = plsregress(MyX,MyY,3);
figure (30) plot(LBT80(1,1:2179),stats.W,'-');
xlabel('Variable [in Wavenumber ({\itcm}^{-1})]'); ylabel('PLS Weight');
title ('Barefaced Terrain Geochemical Signature Model');
legend({'1st PC' '2nd PC' '3rd PC'}, 'location','NW');
% Using PCA loadings we can check how strongly each component in the PCA
```

```
% depends on the original variables and in what direction
% In variable alone
figure (31) plot(1:2179,PCALoadings(:,1:3),'-'); xlabel('Variable');
ylabel('PCA Loading'); title ('Barefaced Terrain Geochemical Signature Model');
legend({'1st PC' '2nd PC' '3rd PC'},'location','NW');
% In wavenumbers alone
figure (32) plot(LBT80(1,1:2179),PCALoadings(:,1:3),'-');
xlabel('Variable [in Wavenumber ({\itcm}^{-1})]'); ylabel('PCA Loading');
title ('Barefaced Terrain Geochemical Signature Model');
legend({'1st PC' '2nd PC' '3rd PC'},'location','NW');


%%%%%%%%%%%%%%%%%%%%%%%%For normalisation Terrain with water
% MUT A, B, E, F with 10 and 20 weight percentages of A and B along with Water
% in one data set with 2179 datapoints
load TerrainWithWater_Transmittance2.txt
% Assign Data (No X column)
YMUTA100P2=TerrainWithWater_Transmittance2(:,1); %all the rows but first column
YMUTB100P2=TerrainWithWater_Transmittance2(:,2); %all the rows but second column
YMUTA90P2=TerrainWithWater_Transmittance2(:,3);
YMUTB90P2=TerrainWithWater_Transmittance2(:,4);
YMUTA80P2=TerrainWithWater_Transmittance2(:,5);
YMUTB80P2=TerrainWithWater_Transmittance2(:,6);
YMUTA80P2=TerrainWithWater_Transmittance2(:,7);
YMUTB80P2=TerrainWithWater_Transmittance2(:,8);
YMUTEHOS2=TerrainWithWater_Transmittance2(:,9);
YMUTFVOS2=TerrainWithWater_Transmittance2(:,10);
YWatr2=TerrainWithWater_Transmittance2(:,11);


% Using msnorm for the terrain types with water
TerrainWaterNorm2=msnorm(X100abSand, TerrainWithWater_Transmittance2(:,[1 2 3 4 5 6 7
8 9 10 11]));
figure(33) % combined FTIR results 100% - 80% Terrain WITH Oil Sand and Water
NORMALISED
plot(X100abSand, TerrainWaterNorm2(:,1), 'b', X100abSoil, TerrainWaterNorm2(:,2), 'g',
X90abSand, TerrainWaterNorm2(:,3), '--b', X90abSoil, TerrainWaterNorm2(:,4), '--g',
X80abSand, TerrainWaterNorm2(:,5), '-.b', X80abSoil, TerrainWaterNorm2(:,6), '-.g',
X70abSand, TerrainWaterNorm2(:,7), '-.m', X70abSoil, TerrainWaterNorm2(:,8), '-
.c',Xah2, TerrainWaterNorm2(:,9), '-k', Xav2, TerrainWaterNorm2(:,10), '-r', XWaterab,
TerrainWaterNorm2(:,11), '-y'); set(gca, 'XDir','reverse'); xlabel('Wavenumber
({\itcm}^{-1})'); ylabel('Transmittance'); grid off
title ('Barefaced Terrain with 10, 20 and 30 {\itwt.}% Water');
legend ('Beach Sand', 'Loamy Farm Soil', 'BS (10% Water)', 'LFS (10% Water)', 'BS (20%
Water)', 'LFS (20% Water)','BS (30% Water)', 'LFS (30% Water)', 'Hard Oil Sand',
'Viscous Oil Sand', 'Water');
```

APPENDIX 5: Code Dielectric Discrimination Statistical Model

```
%%%%%%%%%%%%%%%%%%%%%%%%%%%%%%%%%%%%%%%%%%%%%%%%%%%%%%%%%%%%%%%%%%%%%%%%%%%%%%%%%%%%%%
% The code first plots the control material properties (a) air (b) water using the
Cole Cole   %% % model Implementation for Real Permittivity of water. Thereafter the
DDSM is implemented based % % on data obtained as follows: Dielectric Measurements
PNA Network Analyser N5227A 10MHz-67GHz %
% and Agilent Dielectric Probe Kits. Measurement Campaign from 19July - 2August2013
and April - % % May 2014. Used for Dielectric permittivity processing For two bare
face terrain samples with % % different quantities of water in weight percent. They
include:                                      % (A) BSand = Beach Sand aka Sand:(1)
A100 = 100% dry BEACH sand no water  = HundredPercentSand %    % (2) A10W = 90% (wt%)
sand & 10% (wt%) water = NinetyPercentSand; (3) A20W = 80% (wt%) sand % % % & 20%
(wt%) water = EightyPercentSand; (4) A30W = 70% (wt%) sand & 30% (wt%) water = %
Seventy% % PercentSand; (B) LFsoil = Loamy Farm soil aka Soil. (1) B100 = 100% dry
BEACH sand no water = % % HundredPercentSand; (2) B10W = 90% (wt%) soil & 10% (wt%)
water = NinetyPercentSand;        %
% (3) B20W = 80% (wt%) soil & 20% (wt%) water = EightyPercentSand;(4) B30W = 70% (wt%)
soil & 30% %(wt%) water = SeventyPercentSand;(C) Air. Used as control = AirUsed;(D)
Water. Used as control.%                   % = WaterDielectric_Used; Also for four out
of Six bare face terrain samples namely: MUT A, B, E % and F: (A) BSand = Beach Sand.
(B) LFSand = Loamy farm soil. (C) TenStone = 10mm pebbles.    %
% (D) FourtyStone = 40 mm pebbles. (E) HSand = Hard oil sand. (1) HardOilSand_test1 =
2013 first % test results. (2) HardOilSand_test2 = 2013 Second test results. (3) 2
measurements (2014):   % % HOS1, HOS2, HOS3, HOS4, HOS5, HOS6, HOS7, HOS8, HOS9,
HOS10. (4) An average measurement result for each HOS1-HOS10 (F) ViscousOilSand =
Viscous Oil Sand. (1) ViscousOilSand_test1 = 2013 first test results. (2)
ViscousOilSand_test2_Used_v2.txt = 2013 Second test results. (3) 2 measurements %
(2014): VOS1, VOS2, VOS3, VOS4. (4) An average measurement result for each VOS1-VOS4
%%%%%%%%%%%%%%%%%%%%%%%%%%%%%%%%%%%%%%%%%%%%%%%%%%%%%%%%%%%%%%%%%%%%%%%%%%%%%%%%%%%%%%
clear all

% Load Measured  data
%Beach Sand Dielectric data - MUT A
load A100_Used.txt % 100 Percent terrain dry BEACH sand without water
load A10W_Used.txt % 10 Percent water in terrain i.e. Ninety Percent Terrain
load A20W_Used.txt % 20 Percent water in terrain i.e. Eighty Percent Terrain
load A30W_Used.txt  % 30 Percent water in terrain i.e. Seventy Percent Terrain
load Dielectric_BeachSand.txt % All beach sand including 100% BEACH sand without water

% Assign 100 percent beachsand with complete frequency
XBSD=Dielectric_BeachSand2(1,:)/1e9;    % Dielectric Permittivity frequency which is
same for all
                                        % Beachsand, LoamyFarmSoil and Barefaced
terrain: 1st row & all 200 columns
ZBSD100P_1Re=Dielectric_BeachSand(1,:); % first column Real but all the rows
ZBSD100P_1Im=Dielectric_BeachSand(2,:);  % second column Imaginary but all the rows
%Loamy farm soil ATR data - MUT B
load B100_Used.txt  % 100 Percent terrain dry Loamy Farm soil
load B10W_Used.txt  % 10 Percent water in terrain i.e. Ninety Percent Terrain
load B20W_Used.txt  % 20 Percent water in terrain i.e. Eighty Percent Terrain
load B30W_Used.txt  % 30 Percent water in terrain i.e. Seventy Percent Terrain
load Dielectric_LoamyFarmSoil.txt % All loamyfarmsoil data including 100% LFS without
water

% Assign 100 percent LoamyFarmSoil with complete frequency
XLFSD=Dielectric_LoamyFarmSoil2(1,:)/1e9;    % Dielectric Permittivity Measurement
frequency
ZLFSD100P_1Re=Dielectric_LoamyFarmSoil(1,:); % first column but all the rows
ZLFSD100P_1Im=Dielectric_LoamyFarmSoil(2,:);  % second column but all the rows
%10mm pebbles data - MUT C
%40mm stones data - MUT D
%Hard Oil Sand data - MUT E
load HardOilSand_test1_Used.txt    %2013 First test results 2013
load HardOilSand_test2_Used.txt    %2013 Second test results 2013
load HOS9_v1_Used.txt              %2014 Aggregate of HOS9 (1), (2), (3)
load HOS9_v2_Used.txt              %2014 Aggregate of HOS9 (1), (2)
load HOS10_v1_Used.txt              %2014 Aggregate of HOS10 (1), (2), (4)
```

```
load HOS10_v2_Used.txt              %2014 Aggregate of HOS10 (2), (3)
load HOS1_2_Used.txt               % 2014 HOS1 2nd Measurement
load HOS1_3_Used.txt               % 2014 HOS1 3rd Measurement
load HOS1_Avg_Used.txt % 2014 HOS1 Average 2nd & 3rd load HOS2_1_Used.txt
% 2014 HOS2 1st Measurement load HOS2_2_Used.txt % 2014 HOS2 2nd Measurement
load HOS2_Avg_Used.txt % 2014 HOS1 Average 1st & 2nd load HOS3_1_Used.txt
% 2014 HOS3 1st Measurement load HOS3_2_Used.txt  % 2014 HOS3 2nd Measurement
load HOS3_Avg_Used.txt % 2014 HOS3 Average 1st & 2nd load HOS4_1_Used.txt
% 2014 HOS4 1st Measurement load HOS4_3_Used.txt % 2014 HOS4 3rd Measurement
load HOS4_Avg_Used.txt % 2014 HOS4 Average 1st & 3rd load HOS5_2_Used.txt
% 2014 HOS5 2nd Measurement load HOS5_4_Used.txt % 2014 HOS5 4th Measurement
load HOS5_Avg_Used.txt % 2014 HOS5 Average 2nd & 4th load HOS6_2_Used.txt
% 2014 HOS6 2nd Measurement load HOS6_3_Used.txt % 2014 HOS6 3rd Measurement
load HOS6_Avg_Used.txt % 2014 HOS6 Average 2nd & 3rd load HOS7_1_Used.txt
% 2014 HOS7 1st Measurement load HOS7_3_Used.txt % 2014 HOS7 3rd Measurement
load HOS7_Avg_Used.txt % 2014 HOS7 Average 1st & 3rd load HOS8_1_Used.txt
% 2014 HOS8 1st Measurement load HOS8_3_Used.txt% 2014 HOS8 3rd Measurement
load HOS8_Avg_Used.txt % 2014 HOS8 Average 1st & 3rd load HOS9_1_Used.txt
% 2014 HOS9 1st Measurement load HOS9_2_Used.txt % 2014 HOS9 2nd Measurement
load HOS9_Avg_Used.txt % 2014 HOS9 Average 1st & 2nd load HOS10_2_Used.txt
% 2014 HOS10 2nd Measurement load HOS10_4_Used.txt % 2014 HOS10 4th Measurement
load HOS10_Avg_Used.txt % 2014 HOS10 Average 2nd & 4th



%Viscous oil sand data - MUT F
load ViscousOilSand_test1_Used.txt  % First test results 2013
load ViscousOilSand_test2_Used.txt    % Second test results 2013
load ViscousOilSand_test2_Used_v2.txt % Second test results smoothened out
load VOS4_v1_Used.txt              %2014 Aggregate of VOS4 (1), (2), (3)
load VOS4_v2_Used.txt              %2014 Aggregate of VOS4 (2), (3)
load VOS4_v3_Used.txt              %2014 Direct result of VOS4 (2)
load VOS1_2_Used.txt               % 2014 VOS1 2nd Measurement
load VOS1_4_Used.txt               % 2014 VOS1 4th Measurement
load VOS1_Avg_Used.txt             % 2014 VOS1 Average 2nd & 4th
load VOS2_2_Used.txt               % 2014 VOS2 2nd Measurement
load VOS2_3_Used.txt               % 2014 VOS2 3rd Measurement
load VOS2_Avg_Used.txt             % 2014 VOS2 Average 2nd & 3rd
load VOS3_12_Used.txt              % 2014 VOS3_12 2nd Measurement
load VOS3_13_Used.txt              % 2014 VOS3_13 2nd Measurement
load VOS3_Avg_Used.txt             % 2014 VOS3 Average 12 and 13 2nd
load VOS4_12_Used.txt              % 2014 VOS4_12 2nd Measurement
load VOS4_13_Used.txt              % 2014 VOS4_13 2nd Measurement
load VOS4_Avg_Used.txt             % 2014 VOS4 Average 12 and 13 2nd
% Control Data
load WaterDielectric_Used.txt
load Air12_Used.txt % Air without Tan delta added to row four
%Water Dielectric data -
load Water3_Used.txt  %  Water with Tan delta added to row four

% Load data from Erdogan, Akyel and Ghannouchi,
% "Dielectric properties of oil sands at 2.45 GHz with TE1,0,11 mode
% determined by a rectangular cavity resonator"
% Journal of Microwave Power and Electromagnetic Energy, 45(1), 2011, pp.15-23.
% % Load Erdogan et al DIELECTRIC data
load Erdogan_LowestGradeOilSand_Used.txt % Erdogan et al's lowest grade Oil Sand
Results
load Erdogan_LowGradeOilSand_Used.txt % Erdogan et al's low grade Oil Sand Results
load Erdogan_HighGradeOilSand_Used.txt % Erdogan et al's High grade Oil Sand Results


% Assign Permittivity data Air
FreqAir12=Air12_Used(:,1); % First Column is Frequency and same for all
ReEAir12=Air12_Used(:,2);% Second Column is Re[e], Air
ImEAir12=Air12_Used(:,3);% 3rd Column Im[e], Air
TandAir12=Air12_Used(:,4);% 4th Column tandelta Air
% Assign Permittivity data Water
FreqWater3=Water3_Used(:,1); % First Column is Frequency and same for all
ReEWater3=Water3_Used(:,2);% Second Column is Re[e], Air
ImEWater3=Water3_Used(:,3);% 3rd Column Im[e], Air
TandWater3=Water3_Used(:,4);% 3rd Column Im[e], Air

%plotting the data
figure(1) % Chapter 5 Fig.5.5.a Permittivities air (Using Air12Data)
plot(FreqAir12/1e9, ReEAir12, '-b', FreqAir12/1e9, ImEAir12, '-k', FreqAir12/1e9,
TandAir12, '-r')
xlabel('Frequency, {\itf} (GHz)')
```

```
ylabel('Permittivity (F/m)')
grid on
title ('Dielectric Properties Air')
legend ('Re[{\it\epsilon_r}], Air', 'Im[{\it\epsilon_r}], Air' ,'Tan{\it\delta}, Air')
pause(1)

%%%%%%%% Cole Cole Model Implementation for Real Permittivity Water %%%%%%
epsInf = 4.22;      % infinite dielectric constant Hasted, 1972
epsStat = 78.6;     % static dielectric constant given by Hasted, 1972
F=0.9e9:101e6:11e9;  %Frequency defined from 0.9 GHz to 11 GHz in 101 steps
alpha = 0.013;      % Exponent parameter. Given by Hasted, 1972
%tau = 8.8*10^(-12); %rexation time. Value for DI water given by Hasted, 1972
tau = 12.8*10^(-12); %Relaxation time. Value for tap water derived by curve fitting
omega = 2*pi*F; % omega changes with F from 0.9 to 11 GHz


for N=1:101 %101 steps to match the frequency
   Top(N)=(epsStat-epsInf)*[1+(omega(N)*tau).^(1-alpha)*sind(0.5*alpha*pi)];
    Bottom(N)=1+2*(omega(N)*tau).^(1-alpha)*sind(0.5*alpha*pi)+(omega(N)*tau).^2*(1-
alpha);
    epsReal(N) = epsInf+Top/Bottom;
end


% Combination Real E measurements and Cole-Cole Model for Fig.5.5.b
figure(2) % Chapter 5 Fig.5.5.b Permittivity Water (using Water3Data)
plot(FreqWater3/1e9, ReEWater3, '-b', FreqWater3/1e9, ImEWater3, '-k',FreqWater3/1e9,
TandWater3, '-r', F/1e9, epsReal, '-.g^')
xlabel('Frequency, {\itf} (GHz)')
ylabel('Permittivity (F/m)')
grid on
title ('Dielectric Properties Water')
legend ('Re[{\it\epsilon_r}],Water', 'Im[{\it\epsilon_r}], Water', 'Tan{\it\delta},
Water', 'Re[{\it\epsilon_r}],Water Cole-Cole')


figure(3) % Also used IEEE RADARCON 2014 Cincinnati MUT A,B, E &F with Erdogan
Permittivity
plot(XBSD, ZBSD100P_1Im, '-b', XLFSD, ZLFSD100P_1Im, '-g', XdeH1/1e9, ZdeH1,'--k',
XdeV1/1e9, ZdeV1,'--r', FreqELGOS/1e9,ImELGOS,'mo',FreqEHGOS/1e9,ImEHGOS,'ms')
xlabel('Frequency, {\itf} (GHz)')
ylabel('Permittivity, {\it\epsilon } (F/m)')
title ('Measured Dielectric Properties of Barefaced Terrain')
legend('{\it\epsilon_r^"} Beach Sand','{\it\epsilon_r^"} Loamy Farm Soil',
'{\it\epsilon_r^"} HOS', '{\it\epsilon_r^"} VOS', '{\it\epsilon_r^"} Low Grade OS',
'{\it\epsilon_r^"} High Grade OS')
pause(1)

figure(4) % Also used IEEE RADARCON 2014 Cincinnati MUT A,B, E &F with Erdogan
Permittivity
plot(XBSD, ZBSD100P_1Re, '-b', XLFSD, ZLFSD100P_1Re, '-g', XdeH1/1e9, YdeH1,'-k',
XdeV1/1e9, YdeV1,'-r',
FreqELGOS/1e9,ReELGOS,'mo',FreqEHGOS/1e9,ReEHGOS,'ms',FreqA/1e9, ImEA100,
':b',FreqB/1e9, ImEB100, ':g',XdeH1/1e9, ZdeH1,':r',XdeV1/1e9,
ZdeV1,':k',FreqELGOS/1e9,ImELGOS,'co',FreqEHGOS/1e9,ImEHGOS,'cs')
xlabel('Frequency, {\itf} (GHz)')
ylabel('Permittivity, {\it\epsilon } (F/m)')
title ('Measured Dielectric Properties of Barefaced Terrain')
legend('{\it\epsilon_r^''} Beach Sand','{\it\epsilon_r^''} Loamy Farm Soil',
'{\it\epsilon_r^''} HOS', '{\it\epsilon_r^''} VOS', '{\it\epsilon_r^''} Low Grade OS',
'{\it\epsilon_r^''} High Grade OS','{\it\epsilon_r^"} Beach Sand','{\it\epsilon_r^"}
Loamy Farm Soil','{\it\epsilon_r^"} HOS', '{\it\epsilon_r^"} VOS','{\it\epsilon_r^"}
Low Grade OS','{\it\epsilon_r^"} High Grade OS')
pause(1)

figure (5)% Real Permittivity
plot(XBSD, ZBSD100P_1Re, '-bd', XLFSD, ZLFSD100P_1Re, '-gd', XdeH1/1e9, YdeH1,'-ks',
XdeV1/1e9, YdeV1,'-rs', FreqELGOS/1e9,ReELGOS,'mo',FreqEHGOS/1e9,ReEHGOS,'ms')
xlabel('Frequency, {\itf} (GHz)')
ylabel('Permittivity, {\it\epsilon } (F/m)')
title ('Measured Dielectric Properties MUT A, B, E and F')
legend('{\it\epsilon_r^''} Beach Sand','{\it\epsilon_r^''} Loamy Farm Soil',
'{\it\epsilon_r^''} HOS', '{\it\epsilon_r^''} VOS', '{\it\epsilon_r^''} Low Grade OS',
'{\it\epsilon_r^''} High Grade OS')
pause(1)


figure(6) %
```

```
plot(FreqA/1e9, ImEA100, '-bd', FreqB/1e9, ImEB100, '-gd', XdeH1/1e9, ZdeH1,'--ks',
XdeV1/1e9, ZdeV1,'--rs', FreqELGOS/1e9,ImELGOS,'mo',FreqEHGOS/1e9,ImEHGOS,'ms')
xlabel('Frequency, {\itf} (GHz)')
ylabel('Permittivity, {\it\epsilon_r^" } (F/m)')
title ('Measured Dielectric Properties MUT A, B, E and F')
legend('{\it\epsilon_r^"} Beach Sand','{\it\epsilon_r^"} Loamy Farm Soil',
'{\it\epsilon_r^"} HOS', '{\it\epsilon_r^"} VOS', '{\it\epsilon_r^"} Low Grade OS',
'{\it\epsilon_r^"} High Grade OS')
pause(1)


%%%%%%%%%%%%%%%%%%%%%%%%%%%%%%%%%%%%%%%%%%%%%%%%%%%%%%%%%%%%%%%%%%%%%%%%%%%%%%%%%%%%%%%%%%%%%%%%%%%%%%
% PLSA and PCA are used to model the dielectric behaviour for a response variable in
the presence % of a large number of predictor variables that are correlated. Both
construct new predictor var % or components as linear combination of the original
predictor variables but in different ways. % Refer to Chapter 4 of Thesis for how they
do this. Here we present the second part of the code %for obtaining the dielectric
discrimination %
%%%%%%%%%%%%%%%%%%%%%%%%%%%%%%%%%%%%%%%%%%%%%%%%%%%%%%%%%%%%%%%%%%%%%%%%%%%%%%%%%%%%%%%%%
clear all
% Load the data
% The data acquisition process has been discussed in Thesis Chapter 4 and in 3 papers:
% • M.Ezeoke, K. Tong and S. Shi (2014), “Modeling Synthetic Aperture Radar Signature
of Agbabu % % Oil Sand for Petroleum Exploration”, Energy Production and Management in
the 21st Century the % % Quest for Sustainable Energy, Vol.2, Eds C.A. Brebbia, E.R.
Magaril and M.Y. Khodorovsky, WIT % % Transactions on Ecology and the Environment,
Vol. 190, pp. 1284 - 1295.
% • Ezeoke, M. and Tong, K. (2013), “Modeling Electromagnetic Reflectivity of Agbabu
Oil Sands % % from Hyperspectral Infrared Reflectance Spectra and Dielectric
Properties at L-, C- and X-band % Frequencies”, Proceedings of the 5th Computational
Intelligence, Communication Systems
% and Networks (CICSyN2013), 5-8 June, Madrid, Spain, pp.125-130, 2013
% • M.Ezeoke and K.Tong (2014), “Polarimetric SAR Classification of Terrain for Land
Degradation % Monitoring”, Proceedings of the 2014 IAF Global Space Applications
Conference (2014 GLAC), 2 - % 4 June, Paris, France, GLAC-2014,S,6B,4,x20699, 2014.
% Hard Oil Sand Dielectric Discrimination Model. This is code Part II


load HOSDielectric.txt
load MeasurementHOSDielectric.txt
load Dielectric_HOS.txt
load Dielectric_HOS2.txt

whos Dielectric_HOS Dielectric_HOS2 MeasurementHOSDielectric

% Assign data Dielectric Permittivity Measurements
XHOS=HOSDielectric(1,:)/1e9; % Permittivity Measurement frequency which is same for
all Loc
                             % First row and all 111 columns

YHOS4_1Re=MeasurementHOSDielectric(1,1); % all the rows but first column
YHOS4_1Im=MeasurementHOSDielectric(2,1); YHOS4_2Re=MeasurementHOSDielectric(3,1);
YHOS4_2Im=MeasurementHOSDielectric(4,1); YHOS5_1Re=MeasurementHOSDielectric(5,1);
YHOS5_1Im=MeasurementHOSDielectric(6,1); YHOS5_2Re=MeasurementHOSDielectric(7,1);
YHOS5_2Im=MeasurementHOSDielectric(8,1); YHOS6_1Re=MeasurementHOSDielectric(9,1);
YHOS6_1Im=MeasurementHOSDielectric(10,1); YHOS6_2Re=MeasurementHOSDielectric(11,1);
YHOS6_2Im=MeasurementHOSDielectric(12,1); YHOS7_1Re=MeasurementHOSDielectric(13,1);
YHOS7_1Im=MeasurementHOSDielectric(14,1); YHOS7_2Re=MeasurementHOSDielectric(15,1);
YHOS7_2Im=MeasurementHOSDielectric(16,1); YHOS8_1Re=MeasurementHOSDielectric(17,1);
YHOS8_1Im=MeasurementHOSDielectric(18,1); YHOS8_2Re=MeasurementHOSDielectric(19,1);
YHOS8_2Im=MeasurementHOSDielectric(20,1); YHOS9_1Re=MeasurementHOSDielectric(21,1);
YHOS9_1Im=MeasurementHOSDielectric(22,1); YHOS9_2Re=MeasurementHOSDielectric(23,1);
YHOS9_2Im=MeasurementHOSDielectric(24,1); YHOS10_1Re=MeasurementHOSDielectric(25,1);
YHOS10_1Im=MeasurementHOSDielectric(26,1); YHOS10_2Re=MeasurementHOSDielectric(27,1);
YHOS10_2Im=MeasurementHOSDielectric(28,1);



ZHOS4_1Re=Dielectric_HOS(1,:); % first column but all the rows
ZHOS4_1Im=Dielectric_HOS(2,:);  ZHOS4_2Re=Dielectric_HOS(3,:);  % second column but
all the rows
ZHOS4_2Im=Dielectric_HOS(4,:);  ZHOS5_1Re=Dielectric_HOS(5,:);  % third column but all
the rows
ZHOS5_1Im=Dielectric_HOS(6,:);  ZHOS5_2Re=Dielectric_HOS(7,:);  % fourth column but
all the rows
```

```
ZHOS5_2Im=Dielectric_HOS(8,:);  ZHOS6_1Re=Dielectric_HOS(9,:);  % Fifth column but all
the rows
ZHOS6_1Im=Dielectric_HOS(10,:);  ZHOS6_2Re=Dielectric_HOS(11,:);  % Sixth column but
all the rows
ZHOS6_2Im=Dielectric_HOS(12,:);  ZHOS7_1Re=Dielectric_HOS(13,:);
ZHOS7_1Im=Dielectric_HOS(14,:); ZHOS7_2Re=Dielectric_HOS(15,:);
ZHOS7_2Im=Dielectric_HOS(16,:);  ZHOS8_1Re=Dielectric_HOS(17,:);
ZHOS8_1Im=Dielectric_HOS(18,:);  ZHOS8_2Re=Dielectric_HOS(19,:);
ZHOS8_2Im=Dielectric_HOS(20,:);  ZHOS9_1Re=Dielectric_HOS(21,:);
ZHOS9_1Im=Dielectric_HOS(22,:); ZHOS9_2Re=Dielectric_HOS(23,:);
ZHOS9_2Im=Dielectric_HOS(24,:); ZHOS10_1Re=Dielectric_HOS(25,:);
ZHOS10_1Im=Dielectric_HOS(26,:); ZHOS10_2Re=Dielectric_HOS(27,:);
ZHOS10_2Im=Dielectric_HOS(28,:);


%%%%%%%%%%%%%%%%%%%%%%%%%%%%%%  Arrange HOS data and plot 3D %%%%%%%%%%%%%%%%%%
  [dumHOS,vHOS] = sort(MeasurementHOSDielectric); % creating 'dumHOS' & 'vHOS' with
values 1-28
LHOS80 = repmat(1:111,28,1); % create 28 x 111 Array with 28 rows and 111
                             % columns. Each column contains the same value
                             % which is equal to the column number i.e 1, 2
                            % Therefore each row is identical from 1...111


for n = 1:28                  % Assign each row the value of wavenumber for plot
    LHOS80(n, 1:111) = Dielectric_HOS2(1,:)/1e9; %Frequency in 1st row Dielectric_HOS2
end


oldorder = get(gcf,'DefaultAxesColorOrder');
set(gcf,'DefaultAxesColorOrder',jet(28)); % 28 Measurements of HOS
figure ()
%plot3(repmat(1:2126,6,1)',repmat(Location(v),1,2126)',VNIR_MIR(v,:)');
plot3(LHOS80',repmat(MeasurementHOSDielectric(vHOS),1,111)',Dielectric_HOS(vHOS,:)');
xlabel('Frequency, {\itf} (GHz)'); ylabel('Measurements');zlabel('Permittivity,
{\it\epsilon } (F/m)') %axis('tight');
title ('Dielectric Permittivity MUT E: HOS4 - HOS10');
legend
('HOS4_1Re','HOS4_1Im','HOS4_2Re','HOS4_2Im','HOS5_1Re','HOS5_1Im','HOS5_2Re','HOS5_2I
m','HOS6_1Re','HOS6_1Im','HOS6_2Re','HOS6_2Im','HOS7_1Re','HOS7_1Im','HOS7_2Re','HOS7_
2Im','HOS8_1Re','HOS8_1Im','HOS8_2Re','HOS8_2Im','HOS9_1Re','HOS9_1Im','HOS9_2Re','HOS
9_2Im','HOS10_1Re','HOS10_1Im','HOS10_2Re','HOS10_2Im');
grid on
%axis ([4600 500 1 6 65 100])
axis('tight');
% similar sequence for HOS, VOS, Beachsand and Loamy Farm soil so only HOS Shown
%%%%%%%%%%%%%%%%%%%%%%%%%%%%%% Fit Data with components %%%%%%%%%%%%%%%%%%
% Fitting the Data with Two Components                                        %
% We Use the |plsregress| function to fit a PLSA model                       %
% with five PLS components and one response                                    %
%%%%%%%%%%%%%%%%%%%%%%%%%%%%%%%%%%%%%%%%%%%%%%%%%%%%%%%%%%%%%%%%%%%%%%%%%%%%%%
MyHOSX = Dielectric_HOS;
MyHOSY = MeasurementHOSDielectric;
[m,p] = size(MyHOSX); % let the array take extent of X
[Xloadings,Yloadings,Xscores,Yscores,betaPLS, PLSPctVar] =
plsregress(MyHOSX,MyHOSY,3);
MyfitPLS = [ones(m,1) MyHOSX]*betaPLS;
% Using three components to explain the variations in the observed |y|
% Next we plot the % of variance in the measurements as function of the
% components i.e. 3 component model. From cross validation it is clear from
% figure 16 that 3 components account for 95% of the variation compared with
% only 85% from 2 components
figure ()plot(1:3,cumsum(100*PLSPctVar(2,:)),'-bo');
xlabel('Number of PLSA components'); ylabel('Percent Variance Explained in Y');
title ('MUT E: HOS4 - HOS10 Dielectric Permittivity Behaviour');
%%%%%%%%%%%%%%%%%%%%%%%%%%%%%% Fit PCA model
% First we perform PCA on X using |pca| function and retaining 2 principal
% components for Figure. Then we use 3 principal components for better
% accuracy in Figure. In essence PCA is a linear regression of the response variable
on the
% three components.
%%%%%%%%%%%%%%%%%%%%%%%%%%%%%%%%%%%%%%%%%%%%%%%%%%%%%%%%%%%%%%%%%%%%%%%%%%%%%%
[PCALoadings,PCAScores,PCAVar] = princomp(MyHOSX);
betaPCA = regress(MyHOSY-mean(MyHOSY), PCAScores(:,1:2));


% Converting PCA results to original spectral data by transforming to
% regression coefficients for the original uncentered variables
betaPCA = PCALoadings(:,1:2)*betaPCA;
```

```
betaPCA = [mean(MyHOSY) - mean(MyHOSX)*betaPCA; betaPCA];
MyfitPCA = [ones(n,1) MyHOSX]*betaPCA;
%%%%%% Plot fitted vs. observed response for the PLSR and PCR fits %%%%%%
% For 2 components
figure () % For 2 components plot(MyHOSY,MyfitPLS,'bo',MyHOSY,MyfitPCA,'r^');
xlabel('Observed Response'); ylabel('Fitted Response');
title ('MUT E: HOS4 - HOS10 Dielectric Discrimination Model');
legend({'PLSA with 2 Components' 'PCA with 2 Components'}, 'location','NW');
% For 3 components
betaPCA3 = regress(MyHOSY-mean(MyHOSY), PCAScores(:,1:3));
betaPCA3 = PCALoadings(:,1:3)*betaPCA3;
betaPCA3 = [mean(MyHOSY) - mean(MyHOSX)*betaPCA3; betaPCA3];
MyfitPCA3 = [ones(n,1) MyHOSX]*betaPCA3;
figure () % For 3 components PCA plot(MyHOSY,MyfitPLS,'bo',MyHOSY,MyfitPCA3,'r^');
xlabel('Observed Response'); ylabel('Fitted Response');
title ('MUT E: HOS4 - HOS10 Dielectric Discrimination Model');
legend({'PLSA with 2 Components' 'PCA with 3 Components'},'location','NW');


% In order to confirm which does a better job at fitting the variation in
% the samples or location |y|, we look at the horizontal scatter of fitted
% values in the plot. We also determine this using the r-squared value from
% both the PCA and PLSA to confirm. R squared refers to the model quality
% determined by square of the correlation coefficient between predicted values
% and measured values


TSS = sum((MyHOSY-mean(MyHOSY)).^2);
RSS_PLS = sum((MyHOSY-MyfitPLS).^2);
rsquaredPLS_HOS = 1 - RSS_PLS/
% 2 Components
RSS_PCA = sum((MyHOSY-MyfitPCA).^2);
rsquaredPCA_HOS = 1 - RSS_PCA/TSS
% 3 Components
RSS_PCA3 = sum((MyHOSY-MyfitPCA3).^2);
rsquaredPCA3_HOS = 1 - RSS_PCA3/TSS
% We finally confirm the predictive power of both models by plotting the
% response variable against the 2 component and 3 component predictors
% first for PLS analysis and later PCA in Figures below
% First for PLSA
figure ()plot3(Xscores(:,1),Xscores(:,2),MyHOSY-mean(MyHOSY),'bo');
title ('MUT E: HOS4 - HOS10 Dielectric Discrimination Model');
legend('PLSA'); grid on; view(-30,30);


% Next for PCA with 2 components
figure ()plot3(PCAScores(:,1),PCAScores(:,2),MyHOSY-mean(MyHOSY),'r^');
title ('MUT E: HOS4 - HOS10 Dielectric Discrimination Model'); legend('PCA');
grid on; view(-30,30);


% While the three PLSA components better predict the observed |MyY|,
% Figure shows that they marginally explain less variance in the observed |MyX|
% than the first three principal components used in the PCA.
figure ()
plot(1:3,100*cumsum(PLSPctVar(1,:)),'b-o',1:3,
100*cumsum(PCAVar(1:3))/sum(PCAVar(1:3)),'r-^');
xlabel('Number of Principal Components'); ylabel('Percent Variance Explained in X');
title ('MUT E: HOS4 - HOS10 Dielectric Permittivity Measurements');
legend({'PLSA' 'PCA'},'location','SE');
 % Cross validation can help us predict the mean squared prediction error
% (MSEP) using a 5-fold cross validation.  for PLSA
 [Xl,Yl,Xs,Ys,beta,pctVar,PLSmsep] = plsregress(MyHOSX,MyHOSY,3,'CV',3);
 % For PCA |crossval| combined with a function to calculate the sum of
% squared errors for PCA may be used to estimate MSEP with 3 fold C-V
%Crossval2 uses Kfold as 3 for three runs rather than 10. Saved it in the
%folder for calling out. Also changed 'leave out' in Crossval2 to refer to
%3 rather than 1 multiple. For Fig only plotted the first 3 components
%for both PCAmsep and PLSmsep too.


PCAmsep=sum(crossval2(@pcrsse,MyHOSX,MyHOSY,'leaveout',3),1)/m;


% We can plot the MSEP for PLSA and PCA to discover how many components are
% required to get the same prediction accuracy. Here we see that three
% components suffice. Also the second component in PCA seems to have slightly
% increased the MSE prediction error of the model. This means that the
% combination of predictor variables contained in that component is not strongly
% correlated with |MyY| or the location. This is explained by the fact that
```

```
% PCA constructs components to explain variation in |X| (permittivity)
% not the location or samples |MyY|.
 figure () plot(1:3,PLSmsep(2,1:3),'b-o',1:3,PCAmsep(1,1:3),'r-^');
xlabel('Number of components'); ylabel('Estimated Mean Squared Prediction Error');
title ('MUT E: HOS4 - HOS10 Dielectric Discrimination Model');
legend({'PLSA' 'PCA'},'location','NE');


%%%%%%%%%%% Model Parsimony %%%%%%%%%%%%%%%%%%%%%%%%%%%%%%%%%%%%%%%%%%%%%%%%
% Using weights we can check how strongly each component in the PLSA
% depends on the original variables and in what direction
% In variable alone
[Xl,Yl,Xs,Ys,beta,pctVar,mse,stats] = plsregress(MyHOSX,MyHOSY,3);
figure () plot(1:111,stats.W,'-'); xlabel('Variable');
ylabel('PLS Weight'); title ('MUT E: HOS4 - HOS10 Dielectric Discrimination Model');
legend({'1st Component' '2nd Component' '3rd Component'}, 'location','NW');


% In Frequency alone
[Xl,Yl,Xs,Ys,beta,pctVar,mse,stats] = plsregress(MyHOSX,MyHOSY,3);
figure () plot(LHOS80(1,1:111),stats.W,'-'); xlabel('Variable [in Frequency, {\itf}
(GHz)]');
ylabel('PLS Weight'); title ('MUT E: HOS4 - HOS10 Dielectric Discrimination Model');
legend({'1st PC' '2nd PC' '3rd PC'}, 'location','NW');


% Using PCA loadings we can check how strongly each component in the PCA
% depends on the original variables and in what direction
% In variable alone
figure () plot(1:111,PCALoadings(:,1:3),'-'); xlabel('Variable');
ylabel('PCA Loading'); title ('MUT E: HOS4 - HOS10 Dielectric Discrimination Model');
legend({'1st PC' '2nd PC' '3rd PC'},'location','NW');


% In frequency alone
figure () plot(LHOS80(1,1:111),PCALoadings(:,1:3),'-'); xlabel('Variable [in
Frequency, {\itf} (GHz)]'); ylabel('PCA Loading'); title ('MUT E: HOS4 - HOS10
Dielectric Discrimination Model');
legend({'1st PC' '2nd PC' '3rd PC'},'location','NW');
```

APPENDIX 6A: Some Target Design Parameters

Target Design Parameters

Wentworth (1922) provides a measure for grain size classification based on the major particle size within the population variation (Table 6A.1). Usually this is determined experimentally using sieve analysis of the particles (Fig. 6.A1). Importantly, both the US Department of Agriculture (USDA) and the UK Agricultural Development and Advisory Service (ADAS) suggest soil texture (or roughness) is also affected by silt not just sand and clay (Fig. 6A.2).

TABLE 6A.1: WENTWORTH SCALE

Diameter (mm)	Phi Class (ϕ)	Modal Class	Sediment
>256	-8	Boulders	Gravel
4 to 64	-2 to -6	Pebbles	
1 to 2	0	Very Coarse	Sand
0.25 to 0.5	+1	Medium	
0.125 to 0.25	2	Fine	
0.015 to 0.031	5	Medium	Silt
0.007 to 0.015	6	Fine	
<0.004	8	Clay	Clay

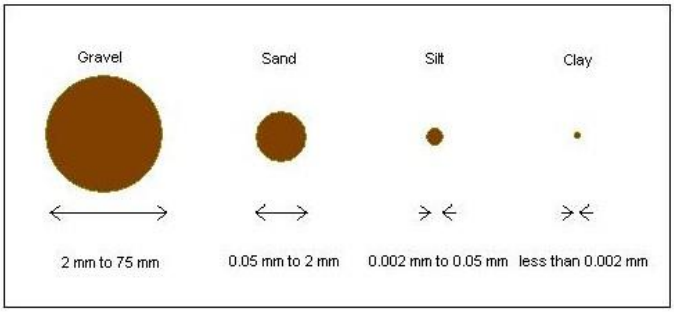

Figure 6.A1. Relative particle sizes of soil components

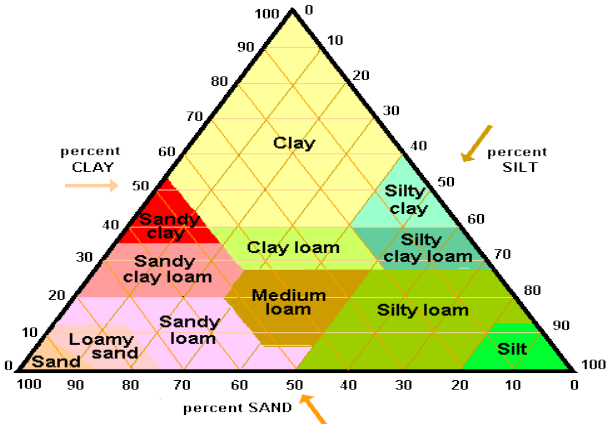

Figure 6.A2. USDA Soil Texture Triangle

APPENDIX 6B: Surface Scattering Plots

In section 6.4.3 we considered the normalised surface scattering plots for the 6 terrain types with different sensor geometries. Here we present the scattering plots for other frequencies discussed in the text but not shown.

Surface scattering plots for $\theta_i = 90°$ and $f = 1$ GHz.

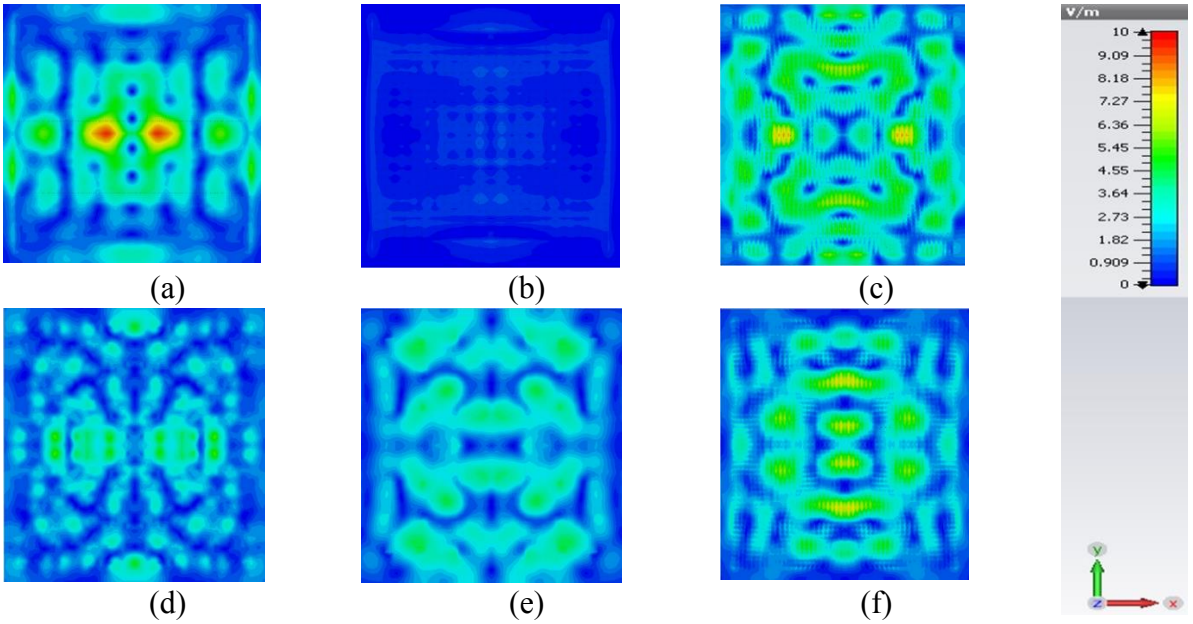

Figure 6B.1: 2D/3D E-field normalized (10 Vm^{-1}) scattering plot from barefaced terrain surface *xy*-plane with $\theta_i = 90°$ and $f = 1$ GHz. (a) MUT A (b) MUT B (c) MUT C (d) MUT D (e) MUT E (f) MUT F

Surface scattering plots for $\theta_i = 90°$ and $f = 5$ GHz.

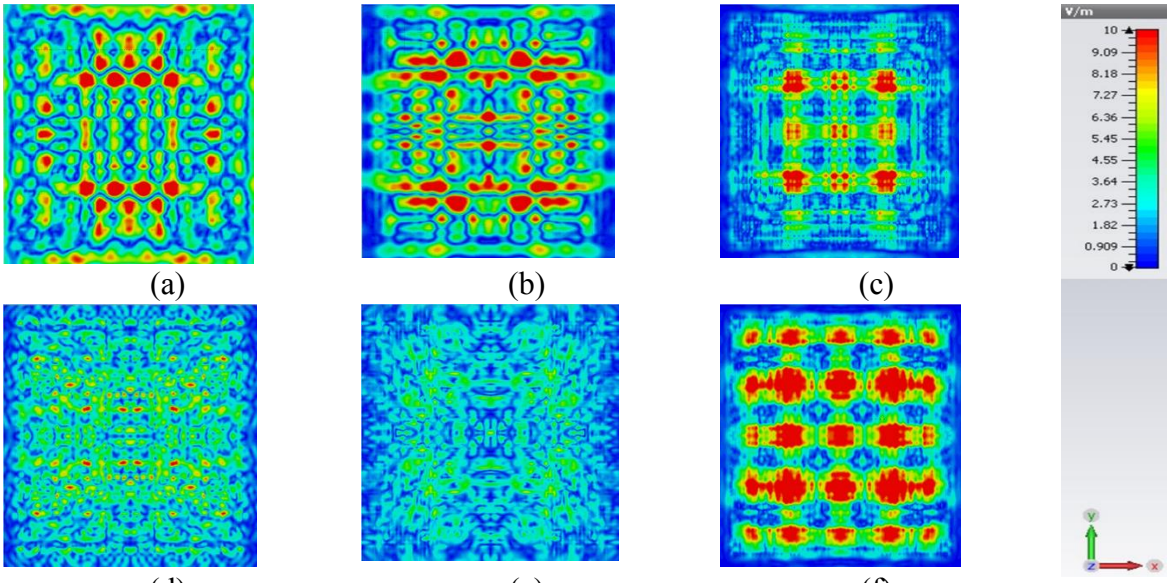

(a) (b) (c)

(d) (e) (f)

Figure 6B.2: 2D/3D E-field normalized (10 Vm^{-1}) scattering plot from barefaced terrain surface *xy*-plane with $\theta_i = 90°$ and $f = 5$ GHz. (a) MUT A (b) MUT B (c) MUT C (d) MUT D (e) MUT E (f) MUT F

Surface scattering plots for $\theta_i = 30°$ and $f = 1$ GHz

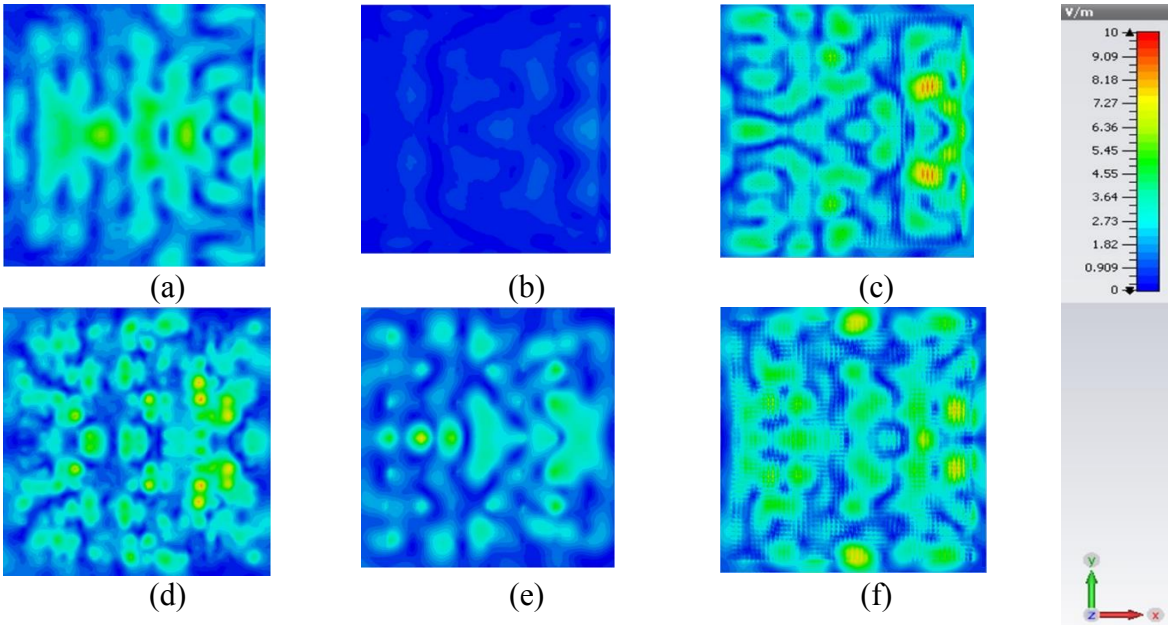

(a) (b) (c)

(d) (e) (f)

Figure 6B.3: 2D/3D E-field normalized (10 Vm^{-1}) scattering plot from barefaced terrain surface *xy*-plane with $\theta_i = 30°$ and $f = 1$ GHz. (a) MUT A (b) MUT B (c) MUT C (d) MUT D (e) MUT E (f) MUT F

Surface scattering plots for $\theta_i = 30°$ and $f = 5$ GHz

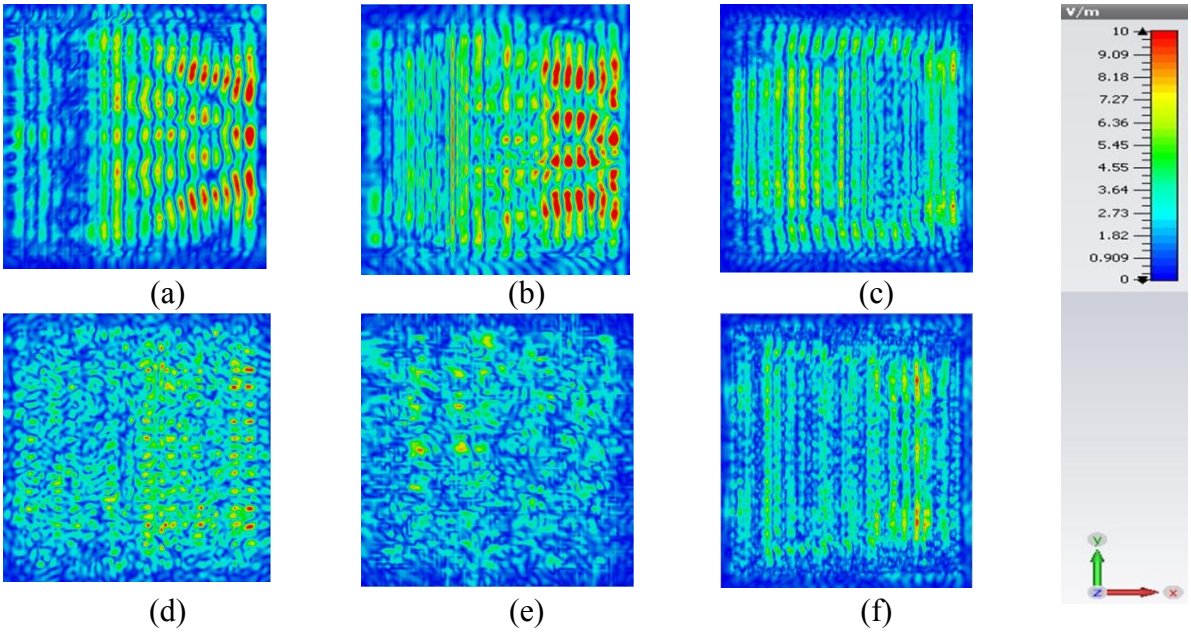

Figure 6B.4: 2D/3D E-field normalized (10 Vm^{-1}) scattering plot from barefaced terrain surface *xy*-plane with $\theta_i = 30°$ and $f = 5$ GHz. (a) MUT A (b) MUT B (c) MUT C (d) MUT D (e) MUT E (f) MUT F

Surface scattering plots for $\theta_i = 45°$ and $f = 1$ GHz

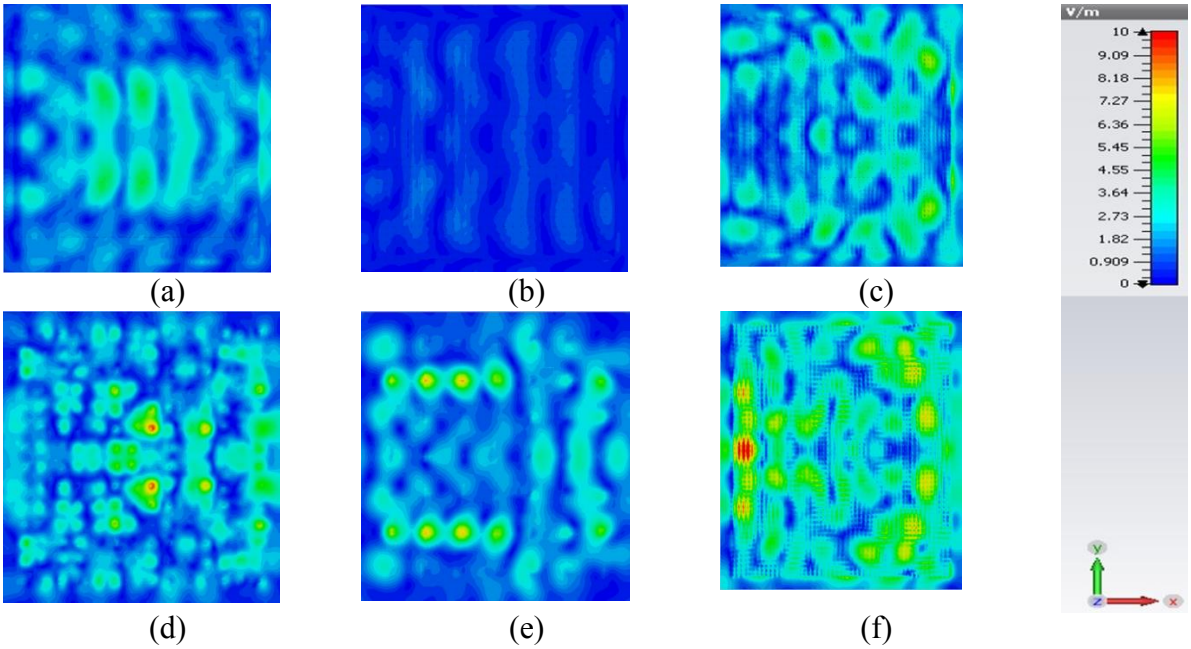

Figure 6B.5: 2D/3D E-field normalized (10 Vm^{-1}) scattering plot from barefaced terrain surface *xy*-plane with $\theta_i = 45°$ and $f = 1$ GHz. (a) MUT A (b) MUT B (c) MUT C (d) MUT D (e) MUT E (f) MUT F

Surface scattering plots for $\theta_i = 45°$ and $f = 5$ GHz

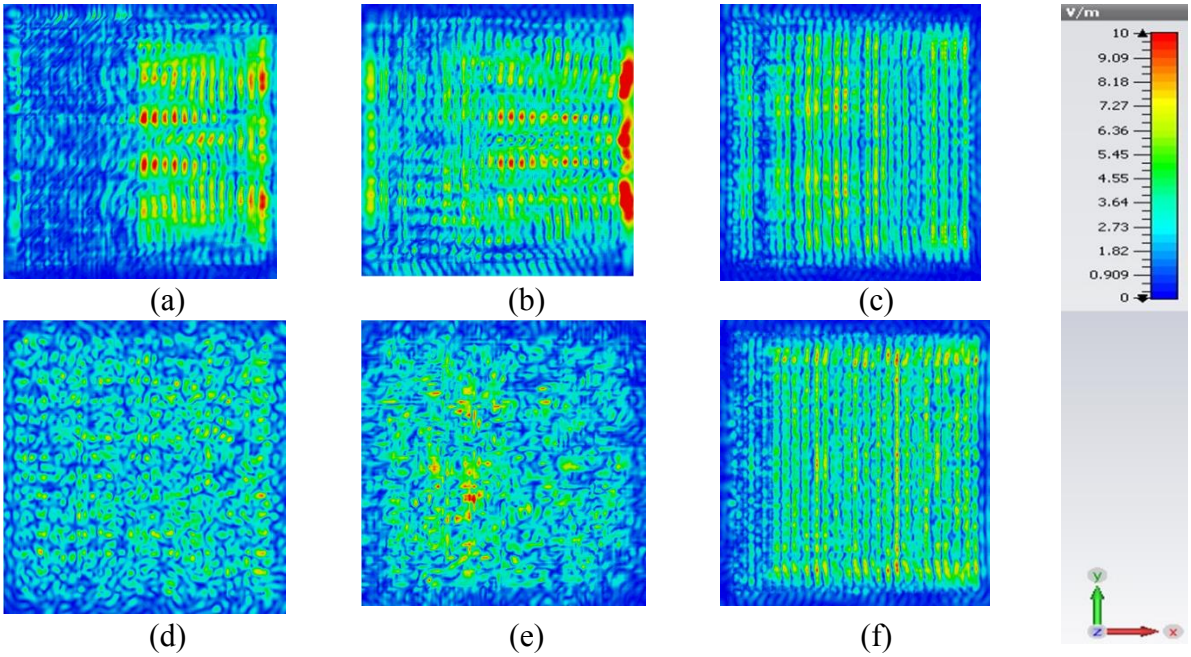

Figure 6B.6: 2D/3D E-field normalized (10 Vm^{-1}) scattering plot from barefaced terrain surface *xy*-plane with $\theta_i = 45°$ and $f = 5$ GHz. (a) MUT A (b) MUT B (c) MUT C (d) MUT D (e) MUT E (f) MUT F

Surface scattering plots for $\theta_i = 60°$ and $f = 1$ GHz

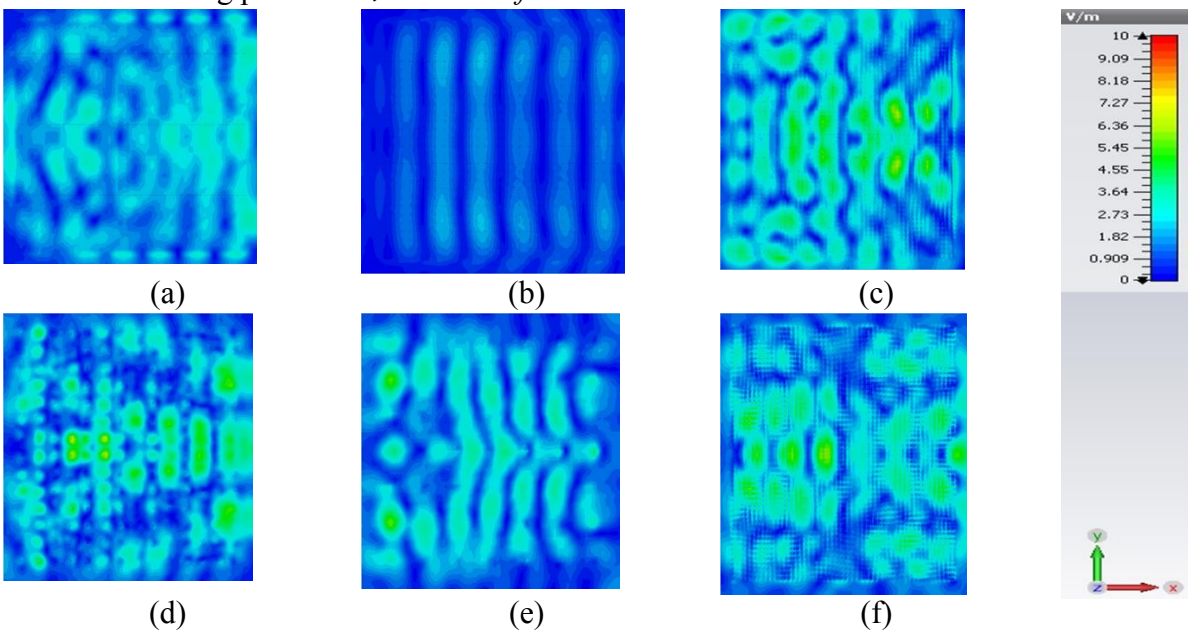

Figure 6B.7: 2D/3D E-field normalized (10 Vm^{-1}) scattering plot from barefaced terrain surface *xy*-plane with $\theta_i = 60°$ and $f = 1$ GHz. (a) MUT A (b) MUT B (c) MUT C (d) MUT D (e) MUT E (f) MUT F

Surface scattering plots for $\theta_i = 60°$ and $f = 5$ GHz

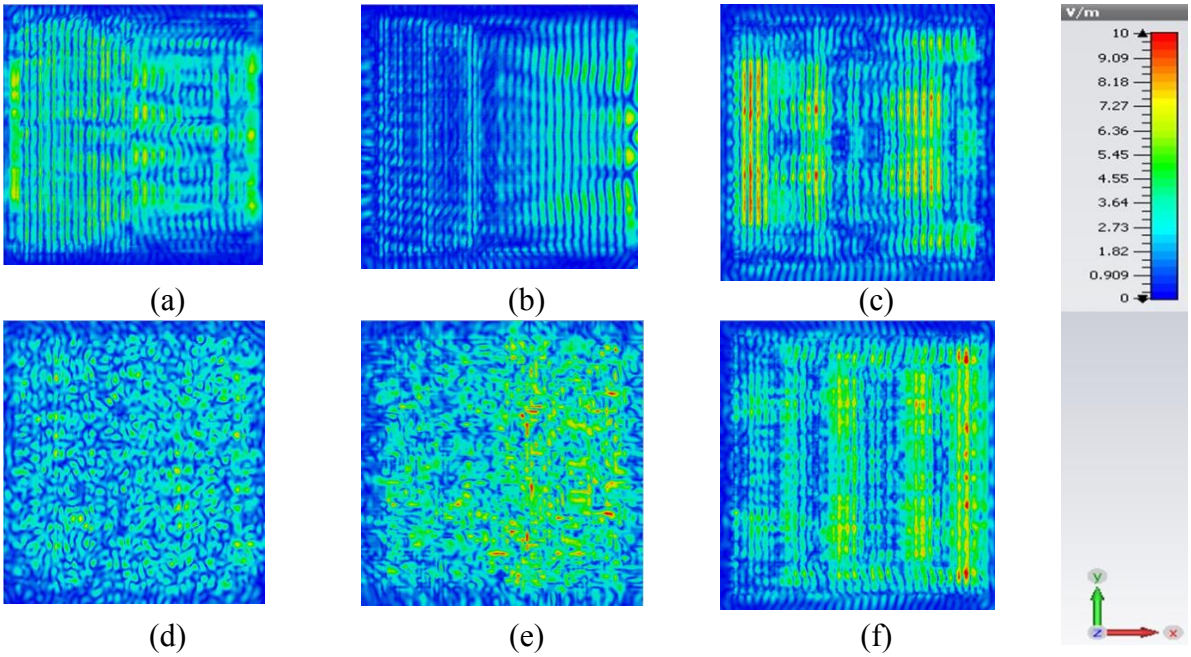

(a) (b) (c)

(d) (e) (f)

Figure 6B.8: 2D/3D E-field normalized (10 Vm^{-1}) scattering plot from barefaced terrain surface *xy*-plane with $\theta_i = 60°$ and $f = 5$ GHz. (a) MUT A (b) MUT B (c) MUT C (d) MUT D (e) MUT E (f) MUT F

APPENDIX 7A: Validation Measurement Sequence

Natural Rubber Coated Black Stand

TABLE 7A.1: MEASUREMENT SEQUENCE AND DATASETS ACQUIRED

Material	$\theta_i = 90°$ HH	$\theta_i = 90°$ VV
LSS alone (open air)		
SPFB alone		
Open pit base (Sharp sand)		
Planar		
Dihedral		
Trihedral		
Beach sand – MUT A		
Loamy Farm Soil – MUT B		
Pebbles – MUT C		
Gravel – MUT D		
Hard Oil Sand – MUT E		
Viscous Oil Sand – MUT F		

Anechoic Chamber

TABLE 7A.2: MEASUREMENT SEQUENCE AND DATASETS ACQUIRED

Material	$\theta_i = +10°$		$\theta_i = +20°$	
	HH	VV	HH	VV
LSS alone (open air)				
SPFB alone				
Planar				
Dihedral				
Trihedral				
Beach sand – MUT A				
Loamy Farm Soil – MUT B				
Pebbles – MUT C				
Gravel – MUT D				
Hard Oil Sand – MUT E				
Viscous Oil Sand – MUT F				

APPENDIX 7B: Code for Scenario 2 SAR Scatterometer

```
%%%%%%%%%%%%%%%%%%%%%%%%%%%%%%%%%%%%%%%%%%%%%%%%%%%%%%%%%%%%%%%%%%%%%%%%%%%%%%%%%%%%%%%%
% The code aggregates data for f = 0.9 - 8 GHz for Scenario 2 of the Validation
Measurement    % % sequence corresponging to 631 data values at each azimuth or
antenna position and 56 azimuth or % LSS positions in all. Data is converted from
frequency domain to time domain for zeroing of   %   % background influence and then
back to frequency domain for combination in phase and magnitude % % and then both
compressed and uncompressed images are plotted although only the uncompressed % % %
plots are presented in Thesis Chapter 7.
%%%%%%%%%%%%%%%%%%%%%%%%%%%%%%%%%%%%%%%%%%%%%%%%%%%%%%%%%%%%%%%%%%%%%%%%%%%%%%%%%%%%%%%%
clear all
close all
clc


c=3e8; load HornAloneG_Used.txt
FreqHornG1=HornAloneG_Used(:,1); % First Column is Frequency
ReHornG1=HornAloneG_Used(:,2);% Second Column is Re[S11]
```

```
PhHornG1=unwrap(HornAloneG_Used(:,3)*2*pi/360);% 3rd Column Phase[S11]


load VVn_OPB.txt
Freq90VVn_OPB=VVn_OPB(:,1)/1e9; % First Column is Frequency
Re90VVn_OPB=VVn_OPB(:,2);% Second Column is Re[S11]
Ph90VVn_OPB=unwrap(VVn_OPB(:,3)*2*pi/360);% 3rd Column Phase[S11]


index=1;
for n=0:1:55

% Beach Sand
MUTA=load(['C:\Users\uceemse\Documents\Post-Transfer\Updated Transfer
Thesis\Finals\Chapter 7\Support\Maurice\Data\VVSAR_BeachSand_' int2str(n) '.txt']);
fMUTA=MUTA(:,1); ampMUTA=MUTA(:,2);
phaseMUTA=unwrap(MUTA(:,3)*2*pi/360);   % convert phase to rad then unwrap
YfMUTA=ampMUTA.*exp(j*phaseMUTA)-Re90VVn_OPB.*exp(1i*Ph90VVn_OPB);  % H(f)%
%adding open pit terrain effect in the above line produces BETTER RESULT
fMUTA=fMUTA; fbinMUTA=fMUTA(2)-fMUTA(1); fmaxMUTA=fMUTA(length(fMUTA));
NfftMUTA=floor(fmaxMUTA/fbinMUTA+1)+1; NzerosMUTA=NfftMUTA-length(fMUTA);
fnewMUTA=[0:2*NfftMUTA-1]*fbinMUTA;
XfMUTA=[YfMUTA;zeros(NzerosMUTA,1);zeros(NfftMUTA,1)];
FsMUTA=max(fnewMUTA); sMUTA=(ifft(XfMUTA)); RESMUTA(:,index)=sMUTA;
tMUTA=([0:2*NfftMUTA-1])/FsMUTA*c/2;

% Loamy Farm Soil
MUTB=load(['C:\Users\uceemse\Documents\Post-Transfer\Updated Transfer
Thesis\Finals\Chapter 7\Support\Maurice\Data\VVSAR_LoamySoil_' int2str(n) '.txt']);
fMUTB=MUTB(:,1); ampMUTB=MUTB(:,2);
phaseMUTB=unwrap(MUTB(:,3)*2*pi/360); % convert phase to rad then unwrap
YfMUTB=ampMUTB.*exp(j*phaseMUTB)-Re90VVn_OPB.*exp(1i*Ph90VVn_OPB);  % H(f)%
%adding open pit terrain effect in the above line produces BETTER RESULT
fMUTB=fMUTB; fbinMUTB=fMUTB(2)-fMUTB(1); fmaxMUTB=fMUTB(length(fMUTB));
NfftMUTB=floor(fmaxMUTB/fbinMUTB+1)+1; NzerosMUTB=NfftMUTB-length(fMUTB);
fnewMUTB=[0:2*NfftMUTB-1]*fbinMUTB;
XfMUTB=[YfMUTB;zeros(NzerosMUTB,1);zeros(NfftMUTB,1)];
FsMUTB=max(fnewMUTB); sMUTB=(ifft(XfMUTB)); RESMUTB(:,index)=sMUTB;
tMUTB=([0:2*NfftMUTB-1])/FsMUTB*c/2;

% Pebbels
MUTC=load(['C:\Users\uceemse\Documents\Post-Transfer\Updated Transfer
Thesis\Finals\Chapter 7\Support\Maurice\Data\VVSAR_Pebble_' int2str(n) '.txt']);
 fMUTC=MUTC(:,1); ampMUTC=MUTC(:,2);
phaseMUTC=unwrap(MUTC(:,3)*2*pi/360);   % convert phase to rad then unwrap
 YfMUTC=ampMUTC.*exp(j*phaseMUTC)-Re90VVn_OPB.*exp(1i*Ph90VVn_OPB);  % H(f)%
%adding open pit terrain effect in the above line produces BETTER RESULT
fMUTC=fMUTC; fbinMUTC=fMUTC(2)-fMUTC(1); fmaxMUTC=fMUTC(length(fMUTC));
NfftMUTC=floor(fmaxMUTC/fbinMUTC+1)+1; NzerosMUTC=NfftMUTC-length(fMUTC);
fnewMUTC=[0:2*NfftMUTC-1]*fbinMUTC;
XfMUTC=[YfMUTC;zeros(NzerosMUTC,1);zeros(NfftMUTC,1)];
FsMUTC=max(fnewMUTC); sMUTC=(ifft(XfMUTC)); RESMUTC(:,index)=sMUTC;
tMUTC=([0:2*NfftMUTC-1])/FsMUTC*c/2;

% Gravel
MUTD=load(['C:\Users\uceemse\Documents\Post-Transfer\Updated Transfer
Thesis\Finals\Chapter 7\Support\Maurice\Data\VVSAR_Gravel_' int2str(n) '.txt']);
 fMUTD=MUTD(:,1); ampMUTD=MUTD(:,2);
phaseMUTD=unwrap(MUTD(:,3)*2*pi/360);   % convert phase to rad then unwrap


YfMUTD=ampMUTD.*exp(j*phaseMUTD)-Re90VVn_OPB.*exp(1i*Ph90VVn_OPB);  % H(f)%
%adding open pit terrain effect in the above line produces BETTER RESULT
fMUTD=fMUTD; fbinMUTD=fMUTD(2)-fMUTD(1); fmaxMUTD=fMUTD(length(fMUTD));
NfftMUTD=floor(fmaxMUTD/fbinMUTD+1)+1; NzerosMUTD=NfftMUTD-length(fMUTD);
fnewMUTD=[0:2*NfftMUTD-1]*fbinMUTD;
XfMUTD=[YfMUTD;zeros(NzerosMUTD,1);zeros(NfftMUTD,1)];
FsMUTD=max(fnewMUTD); sMUTD=(ifft(XfMUTD)); RESMUTD(:,index)=sMUTD;
tMUTD=([0:2*NfftMUTD-1])/FsMUTD*c/2;

% Viscous oil Sand
MUTE=load(['C:\Users\uceemse\Documents\Post-Transfer\Updated Transfer
Thesis\Finals\Chapter 7\Support\Maurice\Data\VVSAR_HOS_' int2str(n) '.txt']);
 fMUTE=MUTE(:,1); ampMUTE=MUTE(:,2); phaseMUTE=unwrap(MUTE(:,3)*2*pi/360);
YfMUTE=ampMUTE.*exp(j*phaseMUTE)-Re90VVn_OPB.*exp(1i*Ph90VVn_OPB);  % H(f)%
%adding open pit terrain effect in the above line produces BETTER RESULT
fMUTE=fMUTE; fbinMUTE=fMUTE(2)-fMUTE(1); fmaxMUTE=fMUTE(length(fMUTE));
NfftMUTE=floor(fmaxMUTE/fbinMUTE+1)+1; NzerosMUTE=NfftMUTE-length(fMUTE);
```

```
fnewMUTE=[0:2*NfftMUTE-1]*fbinMUTE;
XfMUTE=[YfMUTE;zeros(NzerosMUTE,1);zeros(NfftMUTE,1)];
FsMUTE=max(fnewMUTE); sMUTE=(ifft(XfMUTE)); RESMUTE(:,index)=sMUTE;
tMUTE=([0:2*NfftMUTE-1])/FsMUTE*c/2;

% Hard Oil Sand
 MUTF=load(['C:\Users\uceemse\Documents\Post-Transfer\Updated Transfer
Thesis\Finals\Chapter 7\Support\Maurice\Data\VVSAR_VOS_' int2str(n) '.txt']);


fMUTF=MUTF(:,1); ampMUTF=MUTF(:,2); phaseMUTF=unwrap(MUTF(:,3)*2*pi/360);
YfMUTF=ampMUTF.*exp(j*phaseMUTF)-Re90VVn_OPB.*exp(1i*Ph90VVn_OPB);  % H(f)%
fMUTF=fMUTF; fbinMUTF=fMUTF(2)-fMUTF(1); fmaxMUTF=fMUTF(length(fMUTF));
NfftMUTF=floor(fmaxMUTF/fbinMUTF+1)+1; NzerosMUTF=NfftMUTF-length(fMUTF);
fnewMUTF=[0:2*NfftMUTF-1]*fbinMUTF;
XfMUTF=[YfMUTF;zeros(NzerosMUTF,1);zeros(NfftMUTF,1)];
FsMUTF=max(fnewMUTF); sMUTF=(ifft(XfMUTF)); RESMUTF(:,index)=sMUTF;
tMUTF=([0:2*NfftMUTF-1])/FsMUTF*c/2;


index=index+1;
 end


RESabMUTA=abs(RESMUTA); RESabMUTA=RESabMUTA/max(max(RESabMUTA));
RESabMUTB=abs(RESMUTB); RESabMUTB=RESabMUTB/max(max(RESabMUTB));
RESabMUTC=abs(RESMUTC); RESabMUTC=RESabMUTC/max(max(RESabMUTC));
RESabMUTD=abs(RESMUTD); RESabMUTD=RESabMUTD/max(max(RESabMUTD));
RESabMUTE=abs(RESMUTE); RESabMUTE=RESabMUTE/max(max(RESabMUTE));
RESabMUTF=abs(RESMUTF); RESabMUTF=RESabMUTF/max(max(RESabMUTF));
h=figure (1)
imagesc(20*log10(RESabMUTA),[-20 0]); colorbar; axis xy
ylim([0 160]); xlabel('LSS Position, {\ity} (cm)');
ylabel('Range Profile, {\itx} (cm)'); title ('Beach Sand');


AZMUTA=abs(fft(RESMUTA')).^2; AZcompMUTA=abs(ifft(AZMUTA));
h=figure(2)
imagesc(AZcompMUTA'); axis xy
ylim([0 200]); xlabel('LSS Position, {\ity} (cm)');
ylabel('Range Profile, 0.5{\itx} (cm)'); title ('Beach Sand Profile LSS Nadir');


h=figure (3)
imagesc(20*log10(RESabMUTB),[-20 0]); colorbar; axis xy
ylim([0 160]); xlabel('LSS Position, {\ity} (cm)');
ylabel('Range Profile, {\itx} (cm)'); title ('Loamy Farm Soil');


AZMUTB=abs(fft(RESMUTB')).^2; AZcompMUTB=abs(ifft(AZMUTB));
h=figure(4)
imagesc(AZcompMUTB'); axis xy; ylim([0 200]); xlabel('LSS Position, {\ity} (cm)');
ylabel('Range Profile, 0.5{\itx} (cm)'); title ('Loamy Soil Profile LSS Nadir');


h=figure (5)
imagesc(20*log10(RESabMUTC),[-20 0]); colorbar; axis xy; ylim([0 160])
xlabel('LSS Position, {\ity} (cm)'); ylabel('Range Profile, {\itx} (cm)'); title
('Pebbles');


AZMUTC=abs(fft(RESMUTC')).^2; AZcompMUTC=abs(ifft(AZMUTC));
h=figure(6)
imagesc(AZcompMUTC'); axis xy; ylim([0 200]); xlabel('LSS Position, {\ity} (cm)');
ylabel('Range Profile, 0.5{\itx} (cm)'); title ('Pebbles Profile LSS Nadir');


h=figure (7)
imagesc(20*log10(RESabMUTD),[-20 0]); colorbar; axis xy; ylim([0 160]);
xlabel('LSS Position, {\ity} (cm)'); ylabel('Range Profile, {\itx} (cm)'); title
('Gravel');


AZMUTD=abs(fft(RESMUTD')).^2; AZcompMUTD=abs(ifft(AZMUTD));
h=figure(8)
imagesc(AZcompMUTD'); axis xy; ylim([0 200]); xlabel('LSS Position, {\ity} (cm)');
ylabel('Range Profile, 0.5{\itx} (cm)'); title ('Gravel Profile LSS Nadir');


 h=figure (9)
imagesc(20*log10(RESabMUTE),[-20 0]); colorbar; axis xy; ylim([0 160]);
xlabel('LSS Position, {\ity} (cm)'); ylabel('Range Profile, {\itx} (cm)');
```

```
title ('Hard Oil Sand');

AZMUTE=abs(fft(RESMUTE')).^2; AZcompMUTE=abs(ifft(AZMUTE));
h=figure(10)
imagesc(AZcompMUTE');axis xy; ylim([0 200]); xlabel('LSS Position, {\ity} (cm)');
ylabel('Range Profile, 0.5{\itx} (cm)'); title ('Hard Oil Sand Profile LSS Nadir');

 h=figure (11)
imagesc(20*log10(RESabMUTF),[-20 0]); colorbar; axis xy; ylim([0 160]);
xlabel('LSS Position, {\ity} (cm)'); ylabel('Range Profile, {\itx} (cm)');
title ('Viscous Oil Sand');

 AZMUTF=abs(fft(RESMUTF')).^2; AZcompMUTF=abs(ifft(AZMUTF));
h=figure(12)
imagesc(AZcompMUTF'); axis xy; ylim([0 200]); xlabel('LSS Position, {\ity} (cm)');
ylabel('Range Profile, 0.5{\itx} (cm)'); title ('Viscous Oil Sand Profile LSS Nadir');
```